Alma Mater Studiorum · Università di Bologna

Dottorato di ricerca in Fisica
Ciclo XXX

Settore Concorsuale: 02/A1
Settore Scientifico disciplinare: FIS/01

Measurement of CP violation in two-body b-hadron decays with the LHCb experiment

Presentata da: Fabio Ferrari

Coordinatore Dottorato
Prof.ssa Silvia Arcelli

Supervisore
Dott. Angelo Carbone

Co-supervisori
Dott. Stefano Perazzini
Dott. Vincenzo Maria Vagnoni

Esame finale anno 2018

Abstract

The LHCb experiment has been designed to perform flavour-physics measurements at the Large Hadron Collider. Measurements of *CP*-violation are of great importance to shed light on some theoretical open issues and to find evidence for physics beyond the Standard Model of particle physics. Using a data sample corresponding to an integrated luminosity of about $3.0\,\text{fb}^{-1}$ collected by the LHCb experiment during the LHC Run-1, various *CP*-violation measurements with two-body b-hadron decays are performed, along with some subsidiary measurements.

The b-hadron production asymmetries in the LHCb acceptance are measured to be

$$\begin{aligned}
A_{\rm P}(B^+)_{\sqrt{s}=7\,\text{TeV}} &= -0.002 \pm 0.002 \pm 0.004,\\
A_{\rm P}(B^+)_{\sqrt{s}=8\,\text{TeV}} &= -0.007 \pm 0.002 \pm 0.003,\\
A_{\rm P}(B^0)_{\sqrt{s}=7\,\text{TeV}} &= 0.004 \pm 0.009 \pm 0.001,\\
A_{\rm P}(B^0)_{\sqrt{s}=8\,\text{TeV}} &= -0.014 \pm 0.006 \pm 0.001,\\
A_{\rm P}(B_s^0)_{\sqrt{s}=7\,\text{TeV}} &= -0.007 \pm 0.029 \pm 0.006,\\
A_{\rm P}(B_s^0)_{\sqrt{s}=8\,\text{TeV}} &= 0.020 \pm 0.019 \pm 0.006,\\
A_{\rm P}(\Lambda_b^0)_{\sqrt{s}=7\,\text{TeV}} &= -0.001 \pm 0.025 \pm 0.011,\\
A_{\rm P}(\Lambda_b^0)_{\sqrt{s}=8\,\text{TeV}} &= 0.034 \pm 0.016 \pm 0.008,
\end{aligned}$$

where the first uncertainties are statistical and the second systematic.

In particular, the measurement of the Λ_b^0 production asymmetry provides a necessary ingredient for the determination of the physical *CP* asymmetries in $\Lambda_b^0 \to pK^-$ and $\Lambda_b^0 \to p\pi^-$ decays. These quantities are found to be

$$\begin{aligned}
A_{CP}(\Lambda_b^0 \to pK^-) &= -0.019 \pm 0.013 \pm 0.017,\\
A_{CP}(\Lambda_b^0 \to p\pi^-) &= -0.035 \pm 0.017 \pm 0.018,
\end{aligned}$$

where the first uncertainties are statistical and the second systematic.

Finally, the direct and mixing-induced *CP*-violating asymmetries in $B^0 \to \pi^+\pi^-$ and $B_s^0 \to K^+K^-$ decays are measured, together with the direct *CP* asymmetries in $B^0 \to K^+\pi^-$ and $B_s^0 \to \pi^+K^-$ decays. The results are

$$\begin{aligned}
C_{\pi^+\pi^-} &= -0.34 \pm 0.06 \pm 0.01,\\
S_{\pi^+\pi^-} &= -0.63 \pm 0.05 \pm 0.01,\\
C_{K^+K^-} &= 0.20 \pm 0.06 \pm 0.02,\\
S_{K^+K^-} &= 0.18 \pm 0.06 \pm 0.02,\\
A_{K^+K^-}^{\Delta\Gamma} &= -0.79 \pm 0.07 \pm 0.10,\\
A_{CP}(B^0 \to K^+\pi^-) &= -0.084 \pm 0.004 \pm 0.003,
\end{aligned}$$

$$A_{CP}(B_s^0 \to \pi^+ K^-) \quad = \quad 0.213 \pm 0.015 \pm 0.007,$$

where the first uncertainties are statistical and the second systematic. All these *CP*-violation measurements are compatible with the world averages and improve on previous determinations.

Sommario

L'esperimento LHCb è stato progettato per eseguire misure di fisica del sapore al Large Hadron Collider. Misure di violazione di *CP* sono di grande importanza per fare luce su questioni ancora aperte e per trovare effetti di fisica oltre il Modello Standard delle particelle elementari. Utilizzando un campione di dati corrispondente ad una luminosità integrata di circa $3.0\,\text{fb}^{-1}$ acquisito dall'esperimento LHCb durante il Run-1 di LHC, sono state eseguite diverse misure di violazione di *CP* con decadimenti a due corpi di adroni contenenti quark b.

Le asimmetrie di produzione di vari adroni di interesse contenenti quark b sono misurate essere

$$\begin{aligned}
A_{\text{P}}(B^+)_{\sqrt{s}=7\,\text{TeV}} &= -0.002 \pm 0.002 \pm 0.004,\\
A_{\text{P}}(B^+)_{\sqrt{s}=8\,\text{TeV}} &= -0.007 \pm 0.002 \pm 0.003,\\
A_{\text{P}}(B^0)_{\sqrt{s}=7\,\text{TeV}} &= 0.004 \pm 0.009 \pm 0.001,\\
A_{\text{P}}(B^0)_{\sqrt{s}=8\,\text{TeV}} &= -0.014 \pm 0.006 \pm 0.001,\\
A_{\text{P}}(B_s^0)_{\sqrt{s}=7\,\text{TeV}} &= -0.007 \pm 0.029 \pm 0.006,\\
A_{\text{P}}(B_s^0)_{\sqrt{s}=8\,\text{TeV}} &= 0.020 \pm 0.019 \pm 0.006,\\
A_{\text{P}}(\Lambda_b^0)_{\sqrt{s}=7\,\text{TeV}} &= -0.001 \pm 0.025 \pm 0.011,\\
A_{\text{P}}(\Lambda_b^0)_{\sqrt{s}=8\,\text{TeV}} &= 0.034 \pm 0.016 \pm 0.008,
\end{aligned}$$

dove le prime incertezze sono statistiche e le seconde sistematiche.

Utilizzando in particolare la misura dell'asimmetria di produzione del barione Λ_b^0 è possibile determinare le asimmetrie fisiche di *CP* nei decadimenti $\Lambda_b^0 \to pK^-$ e $\Lambda_b^0 \to p\pi^-$. Queste quantità sono trovate essere

$$\begin{aligned}
A_{CP}(\Lambda_b^0 \to pK^-) &= -0.019 \pm 0.013 \pm 0.017,\\
A_{CP}(\Lambda_b^0 \to p\pi^-) &= -0.035 \pm 0.017 \pm 0.018,
\end{aligned}$$

dove le prime incertezze sono statistiche e le seconde sistematiche.

Infine, sono misurati i parametri di violazione di *CP* diretta e indotta dal miscelamento dai decadimenti $B^0 \to \pi^+\pi^-$ e $B_s^0 \to K^+K^-$, assieme alle asimmetrie di *CP* dirette nei decadimenti $B^0 \to K^+\pi^-$ e $B_s^0 \to \pi^+K^-$. I risultati sono

$$\begin{aligned}
C_{\pi^+\pi^-} &= -0.34 \pm 0.06 \pm 0.01,\\
S_{\pi^+\pi^-} &= -0.63 \pm 0.05 \pm 0.01,\\
C_{K^+K^-} &= 0.20 \pm 0.06 \pm 0.02,\\
S_{K^+K^-} &= 0.18 \pm 0.06 \pm 0.02,\\
A_{K^+K^-}^{\Delta\Gamma} &= -0.79 \pm 0.07 \pm 0.10,\\
A_{CP}(B^0 \to K^+\pi^-) &= -0.084 \pm 0.004 \pm 0.003,
\end{aligned}$$

$$A_{CP}(B_s^0 \to \pi^+ K^-) \quad = \quad 0.213 \pm 0.015 \pm 0.007,$$

dove le prime incertezze sono statistiche e le seconde sistematiche. Tutte queste misure di violazione della simmetria *CP* sono compatibili con le medie mondiali e hanno migliore precisione rispetto alle determinazioni precedentemente esistenti.

Contents

Introduction

One of the most intriguing questions in modern physics is why in our observable universe antimatter appears to be almost entirely absent. This question is directly related to the study of *CP* violation in particle physics.

Up to 60 years ago, it was believed that all laws of Nature were invariant under the application of charge-conjugation (C) and parity (P) transformations. After a careful review of all particle experiments conducted until then, Lee and Yang realised in 1956 that there was no experimental reason to believe that the P symmetry was conserved. Hence they proposed a series of experiments that could be carried out to verify that assumption. The suggestion was positively received by madame Wu and her team, which in 1957 found a clear violation of P conservation in the ^{60}Co β decay [1]. After this experimental evidence, the fact that the P symmetry was violated by weak interactions was definitively established. A subsequent experiment made by Goldhaber *et .al.* [2] in 1958 showed that the neutrino is *left-handed*, *i.e.* its spin is antiparallel with respect to its momentum. It was soon pointed out that the independent application of C and P operators to the *left-handed* neutrino (ν_L) led to physical states not observed in Nature (*right-handed* neutrino, ν_R, and *left-handed* anti-neutrino, $\bar{\nu}_L$, respectively), but that the application of the *CP* operator to the ν_L led to the observed $\bar{\nu}_R$. For this reason it was thought that the *CP* symmetry was indeed conserved. However, in 1964, Cronin and Fitch discovered that the *CP* symmetry was broken in a small fraction of K_L^0 decays [3], yielding first experimental evidence for *CP* violation.

Gell-Mann and Zweig developed some years later a classification scheme for hadrons that soon would have become known as "quark model". This model initially comprised only the *up*, *down* and *strange* quarks. In 1963, to preserve the universality of weak interactions, *i.e.* the fact that the coupling constant was the same in all transitions, Nicola Cabibbo introduced a mixing angle θ_C (the so-called Cabibbo angle) and made the hypothesis that the state coupling to the up quark was a superposition of down-type

quarks, *i.e.*

$$d' = d\cos(\theta_C) + s\sin(\theta_C) \ .$$

A few years later, in 1970, Glashow, Iliopoulos, and Maiani proposed to explain the observed suppression of flavour-changing neutral currents (FCNC) processes with the hypothesis that the up quark coupled to a second superposition of down-type quarks, orthogonal to d' and defined as

$$s' = -d\sin(\theta_C) + s\cos(\theta_C) \ .$$

Moreover, to cancel completely the tree-level FCNC diagrams, they also theorised the existence of a fourth quark, *charm* [4]. This prediction was experimentally confirmed four years later by two experimental groups led by Ting at the Brookhaven National Laboratory [5] and by Richter at the Stanford Linear Accelerator [6], through the discovery of the first $c\bar{c}$ resonance, since then called the J/ψ meson.

The d' and s' combinations can be written in matrix notation as

$$\begin{pmatrix} d' \\ s' \end{pmatrix} = \begin{pmatrix} \cos\theta_C & \sin\theta_C \\ -\sin\theta_C & \cos\theta_C \end{pmatrix} \begin{pmatrix} d \\ s \end{pmatrix} \ ,$$

where the 2×2 matrix is known as the Cabibbo matrix.

Soon after, by noticing that *CP* violation could not be explained in a four-quark model, Kobayashi and Maskawa generalized the Cabibbo matrix into the so-called Cabibbo-Kobayashi-Maskawa (CKM) matrix [7]

$$\begin{pmatrix} d' \\ s' \\ b' \end{pmatrix} = \begin{pmatrix} V_{ud} & V_{us} & V_{ub} \\ V_{cd} & V_{cs} & V_{cb} \\ V_{td} & V_{ts} & V_{tb} \end{pmatrix} \begin{pmatrix} d \\ s \\ b \end{pmatrix} \ ,$$

thus predicting the existence of another quark doublet [7]. This hypothesis was then confirmed with the discovery of the *beauty* quark in 1977 by Lederman and collaborators at FermiLab [8] and with the discovery of the *top* quark in 1995 by the CDF [9] and DØ [10] collaborations. The CKM matrix is characterised by four free parameters: three mixing angles and one complex phase, the latter accounting for *CP* violation. This formalism has proven to be very successful in explaining and predicting *CP* violation in different decays. For their work, Kobayashi and Maskawa were awarded the Nobel Prize in 2008.

Since its discovery in 1964, a systematic study of *CP* violation has been carried out by a number of experiments. Another important leap was made owing to the ARGUS collaboration, that observed for the first time and measured in 1987 the mixing of B^0 and $\overline{B}^0$ mesons [11], opening a new avenue for the measurement of *CP* violation using mesons containing the b quark. In 2006, the CDF Collaboration reported the first observation of $B_s^0 - \bar{B}_s^0$ mixing [12], and very recently the LHCb Collaboration that of $D^0 - \bar{D}^0$ mixing from a single experiment [13]. The existence of *CP* violation in the decays of B^0 mesons was actually demonstrated by the BaBar and Belle experiments [14, 15]. Finally, the first observation of *CP* violation in B_s^0 decays was reported by LHCb [16].

CP violation is still nowadays a prominent field of research, with an exhaustive programme of precision measurements being pursued by LHCb, and in a few years by the Belle II experiment in Japan. In particular, charmless two-body decays of *beauty* baryons involve elements of the CKM matrix that could be sensitive to physics beyond the Standard Model (SM), as these decays proceed also through loop-level quark transitions, which are more likely to be affected by sizeable new physics effects. For this reason, it is important to measure *CP* violation in such decays.

The thesis is organised as follows. In the first chapter, theoretical aspects of the SM of particle physics are presented. A short introduction to the SM Lagrangian is given with a brief overview of the CKM formalism and of the present experimental status concerning CKM matrix elements. Then, after a short discussion on flavour-changing neutral currents and neutral-meson mixing, the basic theoretical tools to study *CP* violation are introduced, with particular attention on charmless two-body b-hadron decays.

The second chapter is dedicated to the description of the LHCb detector. It starts with a brief overview of the LHC collider and its operation, and then the LHCb detector and all of its sub-detectors are described in detail. Special attention is payed on sub-detectors devoted to particle identification (PID), which are very relevant for the analysis of the decays under study. Finally, the trigger system used to acquire data during the physics runs is described, along with the data management and computing systems used in the offline analysis.

In the third chapter, the measurement of b-hadron production asymmetries is introduced. After an initial part devoted to the description of the strategy and datasets, the description of the fit models used to measure raw and production asymmetries is given. Finally, the determination of systematic uncertainties is discussed and the approach used to obtain the Λ_b^0 production asymmetry is presented, together with the results.

In the fourth chapter, the measurement of the position of a portion of the LHCb beampipe (beryllium-made) is discussed. This measurement is particularly useful to check whether the simulation reproduces well the position of this passive element. Since that portion of the beampipe is within the acceptance of the LHCb tracking system, in the future it will be possible to measure the relative hadronic cross-sections of various charged particles and antiparticles on beryllium, that will turn out to be valuable inputs to determine the different probabilities for such particles and antiparticles to interact with the detector material.

In the fifth chapter, the measurements of the *CP* asymmetries in $\Lambda_b^0 \to pK^-$ and $\Lambda_b^0 \to p\pi^-$ decays are presented. After a brief discussion on the datasets and event selection, the strategy adopted to evaluate the PID efficiencies is discussed. Then, the fit model is introduced and the results of the fits are presented. The chapter ends with the determination of the systematic uncertainties and the measurement of the instrumental asymmetries needed to derive the physical *CP* asymmetries.

The sixth chapter describes the measurement of the *CP*-violating parameters in $B^0 \to \pi^+\pi^-$ and $B_s^0 \to K^+K^-$ decays, together with the determination of the direct *CP*

asymmetries in $B^0 \to K^+\pi^-$ and $B_s^0 \to \pi^+K^-$ decays. Following a description of the strategy, datasets and event selection, the determination of PID efficiencies is presented. Then, the invariant-mass and decay-time models are described in detail. Subsequently, the determinations of the decay-time resolution and acceptance are discussed in detail, and the calibration of the flavour-tagging algorithms is described. Then the fit results are presented, the assessment of systematic uncertainties is discussed, and the final results are given.

Finally, conclusions are drawn in the seventh chapter.

1 Standard Model and two-body b-hadron decays

1.1 The Standard Model Lagrangian

The Standard Model (SM) Lagrangian can be built from the following fundamental ingredients

1. The gauge symmetry of the Lagrangian (also requiring Poincare invariance). The gauge symmetry is
$$G_{\rm SM} = SU(3)_{\rm C} \times SU(2)_{\rm L} \times U(1)_{\rm Y}. \tag{1.1}$$

2. The representations of fermions and scalars under the symmetry. The fermion generations are three, each one of them consisting in five representations of $G_{\rm SM}$
$$Q^I_{Li}(3,2)_{+1/6}, \quad U^I_{Ri}(3,1)_{+2/3}, \quad D^I_{Ri}(3,1)_{-1/3}, \quad L^I_{Li}(1,2)_{-1/2}, \quad E^I_{Ri}(1,1)_{-1}. \tag{1.2}$$
In this notation, for example, left-handed quarks, Q^I_L, are triplets of $SU(3)_{\rm C}$, doublets of $SU(2)_{\rm L}$, and carry hypercharge $Y = +1/6$. The super-index denotes gauge interaction eigenstates, whereas the sub-index $i = 1, 2, 3$ is the flavour (or generation) index. The other representations stand for right-handed up type quarks (U^I_R), right-handed down type quarks (D^I_R), left-handed leptons (L^I_L) and right-handed leptons (E^I_R). Concerning scalars, there is a single representation
$$\phi(1,2)_{+1/2}. \tag{1.3}$$

3. The pattern of spontaneous symmetry breaking (SSB). The scalar field ϕ has a vacuum expectation value (VEV),
$$\langle \phi \rangle = \begin{pmatrix} 0 \\ v/\sqrt{2} \end{pmatrix} \tag{1.4}$$
which leads to the SSB of the gauge group
$$G_{\rm SM} \to SU(3)_{\rm C} \times U(1)_{\rm EM}. \tag{1.5}$$

Once these ingredients are provided, the most general renormalizable Lagrangian that is invariant under these symmetries and provide the required SSB necessary to have massive particles can be written. The SM Lagrangian ($\mathcal{L}_{\rm SM}$), is the most general renormalizable Lagrangian that is consistent with gauge symmetry (1.1) and the particle content (1.2) and (1.3). For the sake of clarity, the SM Lagrangian can be written as the sum of its various components

$$\mathcal{L}_{\rm SM} = \mathcal{L}_{\rm gauge} + \mathcal{L}_{\rm kin} + \mathcal{L}_{\phi} + \mathcal{L}_{\psi} + \mathcal{L}_{\rm Yukawa}, \tag{1.6}$$

where $\mathcal{L}_{\rm gauge}$ contains the gauge terms, $\mathcal{L}_{\rm kin}$ the kinetic terms, $\mathcal{L}_{\phi}$ the scalar terms, $\mathcal{L}_{\psi}$ the fermion terms and $\mathcal{L}_{\rm Yukawa}$ describes the scalar-fermion interaction. In the following, each piece of the Lagrangian will be described separately.

1.1.1 $\mathcal{L}_{\rm gauge}$

The term $\mathcal{L}_{\rm gauge}$ describes the propagation of gauge fields and is given by

$$\mathcal{L}_{gauge} = -\frac{1}{4} G^a_{\mu\nu} (G^a)^{\mu\nu} - \frac{1}{4} W^d_{\mu\nu} (W^d)^{\mu\nu} - \frac{1}{4} B_{\mu\nu} B^{\mu\nu}, \tag{1.7}$$

with

$$\begin{aligned} G^{\mu\nu}_a &= \partial^\mu G^\nu_a - \partial^\nu G^\mu_a + g_s f^{abc} G^\mu_b G^\nu_c \ , \\ W^{\mu\nu}_d &= \partial^\mu W^\nu_d - \partial^\nu W^\mu_d + g \varepsilon^{def} W^\mu_e W^\nu_f \ , \\ B^{\mu\nu} &= \partial^\mu B^\nu - \partial^\nu B^\mu \ , \end{aligned} \tag{1.8}$$

where

- $G^{\mu\nu}_a$ is the Yang-Mills tensor that represents the eight ($a = 1, 2, \ldots, 8$) gluon fields G^μ_a, g_s is the strong coupling constant and f^{abc} are the $SU(3)_{\rm C}$ structure constants.
- $W^{\mu\nu}_d$ is the weak field tensor that represent three ($d = 1, 2, 3$) gauge fields W^μ_d, g is the Quantum Flavour Dynamics (QFD) coupling constant and ε^{def} are the $SU(2)_{\rm L}$ structure constants.
- $B^{\mu\nu}$ is the electromagnetic tensor that represents the $U(1)_{\rm Y}$ gauge field B^μ.

The presence of the $f^{abc} G^\mu_b G^\nu_c$ and $\varepsilon^{def} W^\mu_e, W^\nu_f$ terms in Eqs. (1.8) suggests that QCD and QFD are non-abelian theories, whose gauge fields can then self-interact. This no longer holds for QED, that being an abelian theory forbids photon self-interaction.

1.1.2 $\mathcal{L}_{\rm kin}$

This term describes the kinetic energy of fermions and their interaction with the gauge fields. In order to maintain gauge invariance, the standard derivative needs to be replaced by a covariant derivative of the form

$$D^\mu = \partial^\mu + ig_s G_a^\mu L_a + igW_b^\mu T_b + ig' B^\mu Y \tag{1.9}$$

where

- L_a are the eight $SU(3)_{\mathrm{C}}$ generators (the 3×3 Gell-Mann matrices);
- T_b are the four $SU(2)_{\mathrm{L}}$ generators (the 2×2 Pauli matrices);
- Y is the $U(1)_{\mathrm{Y}}$ generator.

For example, for the left-handed quarks, the kinetic part of the Lagrangian is

$$\mathcal{L}_{\mathrm{kin}}(Q_L^I) = i\overline{Q_{Li}^I}\gamma_\mu \left(\partial^\mu + \frac{i}{2} g_s G_a^\mu \lambda_a + \frac{i}{2} g W_b^\mu \tau_b + \frac{i}{6} g' B^\mu \right) Q_{Li}^I \tag{1.10}$$

where the identities $L_a \equiv \frac{1}{2}\lambda_a$ and $T_b \equiv \frac{1}{2}\tau_b$ have been used and where γ_μ are the Dirac matrices. This part of the Lagrangian has three parameters (the three coupling constants).

1.1.3 $\mathcal{L}_\phi$

This part of the Lagrangian describes the spontaneous symmetry breaking that allows all SM particles to acquire mass. This Lagrangian is written as

$$\mathcal{L}_\phi = \mu^2 \phi^\dagger \phi - \lambda (\phi^\dagger \phi)^2. \tag{1.11}$$

The most important aspect of the Higgs Mechanism is the introduction of a scalar field ϕ

$$\phi = \frac{1}{\sqrt{2}} \begin{pmatrix} \phi^\dagger \\ \phi^0 \end{pmatrix}, \tag{1.12}$$

assumed to be present everywhere in the space-time and weakly self-interacting. This modifies the vacuum state making it non-symmetric. In this way, masses are dynamically generated thanks to their interaction with the ϕ field, or to be more accurate, with the excitation of this field, the Higgs boson. A convenient bound for the free parameters is $\mu^2 < 0$ and $\lambda > 0$: in this way the Higgs potential assumes the shape of a mexican hat, as shown in Fig. 1.1 and the vacuum state $\phi = 0$ becomes a local maximum that disturbs the symmetry of the system, making it unstable. If one sets $\phi^\dagger = 0,\ \phi^0 = v$ and $Y = 1$ where v is the value of the infinite degenerate minima, then the Higgs field acquires a vacuum expectation value (VEV) $\langle\phi\rangle_0$ expressed as

$$\langle\phi\rangle_0 = \frac{1}{\sqrt{2}} \begin{pmatrix} 0 \\ v \end{pmatrix} \quad \text{with} \quad v = \sqrt{\frac{-\mu^2}{\lambda}} \simeq 246\mathrm{GeV} \tag{1.13}$$

This leads to the SSB that generates four fields W_a^μ $(a = 1, 2, 3)$ and B^μ. The physical fields are defined as

- two charged vector fields $W_\pm^\mu = \frac{1}{\sqrt{2}}(W_1^\mu \mp iW_2^\mu)$ with mass $m_W = gv/2$;

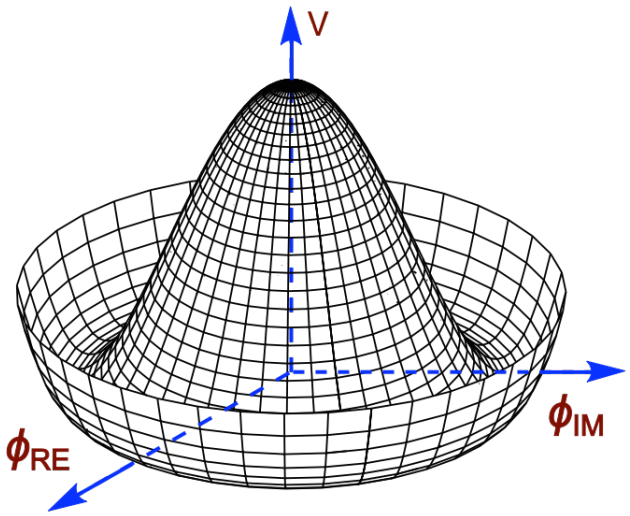

Figure 1.1: *Higgs potential representation with the bonds* $\mu^2 < 0$ *and* $\lambda > 0$.

- one neutral vector field $Z^\mu = \cos\theta_w W_3^\mu - \sin\theta_w B^\mu$ with mass $m_Z = m_W/\cos\theta_w$;
- one photon field $A^\mu = \sin\theta_w W_3^\mu + \cos\theta_w B^\mu$ with mass $m_A = 0$.

As a consequence, a Higgs boson with mass $m_H = \sqrt{-2\mu^2} = \sqrt{2\lambda\mu}$ must exist to allow this mechanism to work correctly. This part of the Lagrangian has two parameters (μ and λ).

1.1.4 $\mathcal{L}_\psi$

This term of the Lagrangian involves only fermion fields and no kinetic terms. In order to have a mass term one would need to have a vector representation of the fermions *i.e.* the left-handed and right-handed fermions would need to have the same representation. For these reasons, this part of the Lagrangian is zero, since the SM is a chiral theory and left-handed and right-handed fermions have different representations.

1.1.5 $\mathcal{L}_{\text{Yukawa}}$

We split the Yukawa part of the Lagrangian in two, the leptonic and the baryonic parts. The leptonic part is given by

$$-\mathcal{L}_{\text{Yukawa}}^{\text{leptons}} = Y_{ij}^e(\overline{L_{Li}^I})\phi E_{Rj}^I + \text{h.c.} \tag{1.14}$$

where Y_{ij}^e is a complex 3×3 matrix containing the Higgs coupling to the leptons. After the Higgs acquires a VEV, these terms lead to charged lepton masses. This part of the Lagrangian has three parameters (the three lepton masses).

The baryonic part of the Yukawa Lagrangian is given by

$$-\mathcal{L}_{\text{Yukawa}}^{\text{quarks}} = Y_{ij}^{d}(\overline{Q_{Li}^{I}})\phi D_{Rj}^{I} + Y_{ij}^{u}(\overline{Q_{Li}^{I}})\phi U_{Rj}^{I} + \text{h.c.} \tag{1.15}$$

where Y_{ij}^{u} and Y_{ij}^{d} are two complex 3×3 matrices containing the Higgs coupling to the up-type and down-type quarks, respectively. This part of the Lagrangian has 10 parameters: the six quark masses and the four parameters of the CKM matrix. In the next Section we will explain how the CKM matrix emerges from this part of the Lagrangian.

1.2 The CKM matrix

There are two important basis regarding the Yukawa interaction: the mass basis, where the masses are diagonal, and the interaction basis, where the $W^{\pm}$ interactions are diagonal. The fact that these two bases are not identical results in flavour changing interactions. The CKM matrix is the matrix that rotates between the two bases.

Since the majority of measurements is done in the mass basis, we write the interaction in that basis. After the $SU(2)_{\text{L}}$ quark doublets are decomposed in their components

$$Q_{Li}^{I} = \begin{pmatrix} U_{Li}^{I} \\ D_{Li}^{I} \end{pmatrix}, \tag{1.16}$$

the quarks Lagrangian can be written as

$$-\mathcal{L}_{M}^{\text{quarks}} = (M_d)_{ij}\overline{D_{Li}^{I}}D_{Rj}^{I} + (M_u)_{ij}\overline{U_{Li}^{I}}U_{Rj}^{I} + \text{h.c.}, \quad M_q = \frac{v}{\sqrt{2}}Y_q. \tag{1.17}$$

In the mass basis, by definition, the mass matrices are diagonal. One can then always find unitary matrices V_{qL} and V_{qR} such that

$$V_{qL}M_qV_{qR}^{\dagger} = M_q^{\text{diag}} \qquad q = u, d \tag{1.18}$$

with M_q^{diag} diagonal and real. In this case, the quark mass eigenstates are given by

$$q_{Li} = (V_{qL})_{ij}q_{Lj}^{I}, \quad q_{Ri} = (V_{qR})_{ij}q_{Rj}^{I} \qquad q = u, d. \tag{1.19}$$

The $W_{\mu}^{\pm}$ interaction can be written in the mass basis and the resulting Lagrangian is

$$-\mathcal{L}_{W^{\pm}}^{\text{quarks}} = \frac{g}{\sqrt{2}}\overline{u_{Li}}\gamma^{\mu}(V_{uL}V_{dL}^{\dagger})_{ij}d_{Lj}W_{\mu}^{+} + \text{h.c.}\ . \tag{1.20}$$

The unitary 3×3 matrix

$$V = V_{uL}V_{dL}^{\dagger}, \quad (VV^{\dagger} = \mathbb{I}) \tag{1.21}$$

is the Cabibbo-Kobayashi-Maskawa mixing matrix for quarks. Since V is not diagonal, this results in the fact that the $W^{\pm}$ gauge bosons couple to mass eigenstates of different generations. This is an unique mechanism in the SM and it is the only source of flavour changing quark interactions.

The elements of V are written as follows

$$V = \begin{pmatrix} V_{ud} & V_{us} & V_{ub} \\ V_{cd} & V_{cs} & V_{cb} \\ V_{td} & V_{ts} & V_{tb} \end{pmatrix} \tag{1.22}$$

One of the main features of the CKM matrix is its unitarity, required since processes involving quarks will not be invariant under a change of the quark field basis representation. This condition fixes the number of free parameters of the matrix. Indeed, a $N \times N$ unitary matrix contains $N(N-1)/2$ mixing angles and $N(N+1)/2$ complex phases. Moreover, we shall note that in the CKM matrix case, the Lagrangian allows to redefine the phase of each quark field obtaining

$$\left.\begin{array}{l} U \to e^{-i\phi_U} U \\ D \to e^{-i\phi_D} D \end{array}\right\} V_{UD} \to e^{i\phi_U} V_{UD} e^{-i\phi_D}. \tag{1.23}$$

These relations imply that $2N-1$ phases will cancel out, being unphysical. Therefore the number of free parameters of a $N \times N$ complex matrix describing mixing between N quarks generations is

$$\underbrace{\frac{1}{2}N(N-1)}_{\text{Number of mixing angles}} + \underbrace{\frac{1}{2}(N-1)(N-2)}_{\text{Number of physical complex phases}} = (N-1)^2. \tag{1.24}$$

From Eq. (1.24) it follows that there will be three mixing angles and one complex phase as free parameters, as already anticipated in the previous Section. The latter is the responsible for *CP* violation in weak interactions, and it is usually called Kobayashi-Maskawa phase ($\delta_{\rm KM}$). In order to see how the three real and one imaginary parameters enter the CKM matrix, we can choose and explicit parameterization, as for example the standard one given by PDG [17]

$$V = \begin{pmatrix} c_{12}c_{13} & s_{12}c_{13} & s_{13}e^{-i\delta} \\ -s_{12}c_{23} - c_{12}s_{23}s_{13}e^{i\delta} & c_{12}c_{23} - s_{12}s_{23}s_{13}e^{i\delta} & s_{23}c_{13} \\ s_{12}s_{23} - c_{12}c_{23}s_{13}e^{i\delta} & -c_{12}s_{23} - s_{12}c_{23}s_{13}e^{i\delta} & c_{23}c_{13} \end{pmatrix}, \tag{1.25}$$

where the notation $s_{ij} = \sin\theta_{ij}$ and $c_{ij} = \cos\theta_{ij}$ has been used and δ is the *CP*-violating complex phase. We can choose the angles θ_{ij} to lie in the interval $[0, \pi/2]$ so that $s_{ij},\ c_{ij} > 0$: this means that the mixing between two quark generations i, j will vanish if the corresponding θ_{ij} is zero.

Another useful parametrisation is the Wolfenstein parametrisation [18], where the four mixing parameters are $\lambda,\ A,\ \rho$ and η. The parameter η represents the *CP*-violating phase. The Wolfenstein parametrisation is an expansion in the small parameter $\lambda = |V_{us}| \approx 0.22$. To $\mathcal{O}(\lambda^3)$ the CKM matrix is given by

$$V = \begin{pmatrix} 1 - \lambda^2/2 & \lambda & A\lambda^3(\rho - i\eta) \\ -\lambda & 1 - \lambda/2 & A\lambda^2 \\ A\lambda^3(1 - \rho - i\eta) & -A\lambda^2 & 1 \end{pmatrix}. \tag{1.26}$$

1.2.1 The Jarlskog invariant

Various parameterisations differ in the way that the freedom of phase rotation is used to leave a single phase in V. One can define, however, a *CP*-violating quantity that is independent from the parametrisation. This quantity, called Jarlskog invariant ($J_{\rm CKM}$), is defined as

$$\Im(V_{ij}V_{kl}V_{il}^{*}V_{kj}^{*}) = J_{\rm CKM}\sum_{m,n=1}^{3}\epsilon_{ikm}\epsilon_{jln}, \quad (i,j,k,l=1,2,3), \tag{1.27}$$

where $\Im$ stands for the imaginary part. In terms of the explicit parametrisation the Jarlskog invariant can be written as

$$J_{\rm CKM} = s_{12}s_{13}s_{23}c_{12}c_{23}c_{13}^{2}\sin\delta. \tag{1.28}$$

The condition of Eq. (1.28) can be also expressed in terms of the mass basis. In this case we see that a necessary and sufficient condition for *CP* violation in the quark sector of the SM is

$$\Delta m_{tc}^{2}\Delta m_{tu}^{2}\Delta m_{cu}^{2}\Delta m_{bs}^{2}\Delta m_{bd}^{2}\Delta m_{sd}^{2}J_{\rm CKM} \neq 0. \tag{1.29}$$

From Eq. (1.29) one immediately sees that the following requirements need to be satisfied in the SM to have $\mathcal{C}_{violation}^{'}$

1. There should not be mass degeneracy within each quark sector;
2. None of the three mixing angles should be zero or $\pi/2$;
3. The phase should be neither 0 or π.

1.2.2 Measurements of CKM matrix elements

It is possible to determine CKM matrix elements through the following tree-level processes:

- $|V_{ud}|$ - Nuclear beta decays ($d \to ue\bar{\nu}_e$ transitions);
- $|V_{us}|$ - Semi-leptonic kaons decays $K \to \pi l\bar{\nu}$ ($s \to ul\bar{\nu}$ transitions);
- $|V_{ub}|$ - Exclusive and inclusive semi-leptonic B-hadron decays ($b \to ul\bar{\nu}$);
- $|V_{cd}|$ - Semi-leptonic D-hadron decays $D \to \pi l\bar{\nu}$ ($c \to dl\bar{\nu}$ transitions) and charm production from ν interaction with matter;
- $|V_{cs}|$ - Semi-leptonic D decays ($c \to sl\bar{\nu}$ transitions) and leptonic D_s decays ($D_s \to l\bar{\nu}$);
- $|V_{cb}|$ - Exclusive and inclusive semi-leptonic B decays to charm ($b \to cl\bar{\nu}$);

- $|V_{tb}|$ - Branching ratio of $t \to Wb$ decay (assuming CKM matrix unitarity) and single top-quark-production cross Section.

For what concerns V_{td} and V_{ts}, their magnitude is not measurable using tree-level processes. Therefore, the optimal way to obtain their values is to extract $|V_{td}/V_{ts}|$ from $B^0 - \bar{B}^0$ and $B_s^0 - \bar{B}_s^0$ oscillations, which are described by box diagrams where u, c, t quarks circulate as virtual states. In Tab. 1.1 the current values of the CKM matrix elements are reported.

Table 1.1: *CKM matrix elements current experimental values with their associated uncertainties taken from Ref. [17].*

CKM matrix element	Experimental value
$\|V_{ud}\|$	0.97425 ± 0.00022
$\|V_{us}\|$	0.2253 ± 0.0008
$\|V_{ub}\|$	$(4.13 \pm 0.49) \cdot 10^{-3}$
$\|V_{cd}\|$	0.225 ± 0.008
$\|V_{cs}\|$	0.986 ± 0.016
$\|V_{cb}\|$	$(41.1 \pm 1.3) \cdot 10^{-3}$
$\|V_{td}\|$	$(8.4 \pm 0.6) \cdot 10^{-3}$
$\|V_{ts}\|$	$(40.0 \pm 2.7) \cdot 10^{-3}$
$\|V_{tb}\|$	1.021 ± 0.032

1.2.3 The Unitary Triangle

A very useful concept is that of unitary triangles. The unitarity of the CKM matrix leads to various relations among the matrix elements. There are twelve equations relating the matrix elements: six for the diagonal terms equal to 1 and six for the off-diagonal terms equal to 0. The equations for the off-diagonal terms can be represented as triangles in the complex plane, all with same area $J_{\mathrm{CKM}}/2$

$$\underbrace{V_{ud}V_{us}^*}_{\mathcal{O}(\lambda)} + \underbrace{V_{cd}V_{cs}^*}_{\mathcal{O}(\lambda)} + \underbrace{V_{td}V_{ts}^*}_{\mathcal{O}(\lambda^5)} = 0 \,, \tag{1.30}$$

$$\underbrace{V_{us}V_{ub}^*}_{\mathcal{O}(\lambda^4)} + \underbrace{V_{cs}V_{cd}^*}_{\mathcal{O}(\lambda^2)} + \underbrace{V_{ts}V_{tb}^*}_{\mathcal{O}(\lambda^2)} = 0 \,, \tag{1.31}$$

$$\underbrace{V_{ud}V_{ub}^*}_{(\rho+i\eta)A\lambda^3} + \underbrace{V_{cd}V_{cb}^*}_{-A\lambda^3} + \underbrace{V_{td}V_{tb}^*}_{(1-\rho-i\eta)A\lambda^3} = 0 \,, \tag{1.32}$$

$$\underbrace{V_{ud}^*V_{cd}}_{\mathcal{O}(\lambda)} + \underbrace{V_{us}^*V_{cs}}_{\mathcal{O}(\lambda)} + \underbrace{V_{ub}^*V_{cb}}_{\mathcal{O}(\lambda^5)} = 0 \,, \tag{1.33}$$

$$\underbrace{V_{cd}^*V_{td}}_{\mathcal{O}(\lambda^4)} + \underbrace{V_{cs}^*V_{ts}}_{\mathcal{O}(\lambda^2)} + \underbrace{V_{cb}^*V_{tb}}_{\mathcal{O}(\lambda^2)} = 0 \,, \tag{1.34}$$

$$\underbrace{V_{ud}^*V_{td}}_{(1-\rho-i\eta)A\lambda^3} + \underbrace{V_{us}^*V_{ts}}_{-A\lambda^3} + \underbrace{V_{ub}^*V_{tb}}_{(\rho+i\eta)A\lambda^3} = 0 \,. \tag{1.35}$$

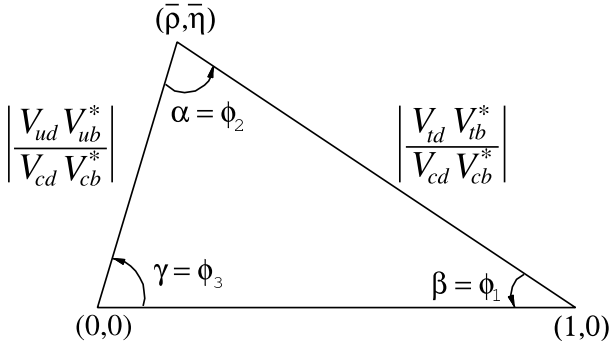

Figure 1.2: *Unitarity triangle drawn in the complex plane corresponding to Eq.* (1.32).

In these equations we have underlined the value of each product at the leading order in λ as obtained from Eq. (1.26), representing the length of the corresponding triangle sides. Dividing for the factor $A\lambda^3$ all the terms involved in Eq. (1.32) and using the definitions

$$\overline{\eta} \equiv \eta \left(1 - \frac{1}{2}\lambda^2\right), \quad \overline{\rho} \equiv \rho \left(1 - \frac{1}{2}\lambda^2\right), \tag{1.36}$$

one obtains the triangle represented in Fig. 1.2, usually referred to as "the Unitary Triangle" (UT). Its importance will be discussed later. The relations between the UT sides and the CKM matrix elements can now be written as

$$R_b \equiv \left|\frac{V_{ud}V_{ub}}{V_{cd}V_{cb}}\right|, \tag{1.37}$$

$$R_t \equiv \left|\frac{V_{td}V_{tb}}{V_{cd}V_{cb}}\right|, \tag{1.38}$$

while the following relations hold for the UT angles

$$V_{ub} = A\lambda^3 \left(\frac{R_b}{1 - \lambda^2/2}\right) e^{-i\gamma}, \tag{1.39}$$

$$V_{td} = A\lambda^3 R_t e^{-i\beta}, \tag{1.40}$$

where the angles γ and β appear.

The angles relations with the CKM matrix elements can finally be written in the following way

$$\alpha \equiv \arg\left(-\frac{V_{td}V_{tb}^*}{V_{ud}V_{ub}^*}\right), \quad \beta \equiv \arg\left(-\frac{V_{cd}V_{cb}^*}{V_{td}V_{tb}^*}\right), \quad \gamma \equiv \arg\left(-\frac{V_{ud}V_{ub}^*}{V_{cd}V_{cb}^*}\right). \tag{1.41}$$

These angles are physical quantities and can be independently measured. Note that in the standard parametrisation we have $\gamma = \delta_{\rm KM}$.

1.2.4 Determination of the UT parameters

Here the state of the art for what concerns the measurements of the UT parameters is discussed; more details about the adopted experimental techniques and the results can be found in Ref. [19]. To determine the parameters, information from both experimental and theoretical sources are needed. The experimental information about UT parameters can be obtained from the following measurements

$|\mathbf{V_{ub}}|/|\mathbf{V_{cb}}|$: This ratio can be obtained through branching fraction measurements of semi-leptonic decays governed by $b \to ul\bar{\nu}$ and $b \to cl\bar{\nu}$ transitions. This quantity is proportional to the UT side between the γ and α angles, expressed as $\frac{(1-\lambda^2/2)V^*_{ub}}{\lambda|V_{cb}|}$.

$\mathbf{\Delta m_d}$: This parameter measures the $B^0 - \bar{B}^0$ mixing frequency. It is proportional to the magnitude of V_{td} and thus to the side of the UT between the α and β angles. However, the relation between Δm_d and V_{td} is plagued by large theoretical uncertainties, thus the quantity $\Delta m_s/\Delta m_d$ is also used as a constrain for the UT.

$\mathbf{\Delta m_s/\Delta m_d}$: Δm_s is the analogue quantity of Δm_d in $B^0_s - \bar{B}^0_s$ mixing; its value is proportional to V_{ts}. The relations between $\Delta m_s/\Delta m_d$, V_{ts} and V_{td} contains some theoretical parameters that can be estimated more precisely with respect to the case of Δm_d.

β: This angle can be determined, mainly, from time-dependent measurements of the $B^0 \to J/\psi K^0$ decays.

$\varepsilon_{\mathbf{K}}$: This quantity is related to the size of *CP* violation in the neutral kaon system.

α: It is possible to measure this UT angle from $B \to \pi\pi$ and $B \to \rho\rho$ decays. Decay amplitudes and *CP* asymmetries of these channels are related to $V_{td}V^*_{tb}$ and $V_{ud}V^*_{ub}$ sides of the UT.

γ: This angle is determined through the $B \to D^{(*)}K^{(*)}$ decays, whose transitions are mediated by the V_{ub} and V_{cb} CKM elements.

$\sin(\mathbf{2}\beta + \gamma)$: Terms proportional to this quantity can be found in time-dependent decay rates of $B \to D^{(*)}\pi$ channels.

The determination of the UT parameters can be achieved, for example, following a Bayesian statistical approach. The unknowns $\overline{\rho}$ and $\overline{\eta}$ are related to a set of N observables x_i by M relations $c_j = \phi_j(x_1, \ldots, x_N, \overline{\rho}, \overline{\eta})$, with $j \in \{1, M\}$. The joint PDF for $\overline{\rho}$ and $\overline{\eta}$ is found using the Bayes theorem; indeed, the conditional distribution $\mathbf{f}$ for $\overline{\rho}$ and $\overline{\eta}$ given the measurements x_i and the constrain relations c_j can be written as

$$\mathbf{f}(\overline{\rho}, \overline{\eta}|x_1, \ldots, x_N, c_1, \ldots, c_M) \propto f(c1, \ldots, c_M|\overline{\rho}, \overline{\eta}, x_1, \ldots, x_N) \cdot f_0(\overline{\rho}, \overline{\eta}) \cdot g_0(x_1, \ldots, x_N), \quad (1.42)$$

where the f on the right side is the probability to obtain the constraint relations $c_1, \ldots, c_M$ for a given set of values $\overline{\rho}$, $\overline{\eta}$ and measurements x_i , f_0 is the *a priori* PDF for $\overline{\rho}$, $\overline{\eta}$ and

finally g_0 is the *a priori* PDF for the observables $x_1, \ldots, x_N$, determined from experimental measurements and theoretical calculations. The following relation can be written

$$f(c1, \ldots, c_M|\overline{\rho}, \overline{\eta}, x_1, \ldots, x_N) = \prod_{j=1}^{M} \delta(c_j - \phi_j(x_1, \ldots, x_n, \overline{\rho}, \overline{\eta})) \tag{1.43}$$

where the δ stands for the Dirac delta function. Then, the joint PDF for $\overline{\rho}, \overline{\eta}$ obtained in Eq. (1.42) becomes

$$\mathbf{f}(\overline{\rho}, \overline{\eta}|x_1, \ldots, x_N, c_1, \ldots, c_M) \propto \prod_{j=1}^{M} \delta(c_j - \phi_j(x_1, \ldots, x_n, \overline{\rho}, \overline{\eta})) \cdot f_0(\overline{\rho}, \overline{\eta}) \cdot \prod_{i=1}^{N} f_i(x_i) \tag{1.44}$$

in which the $f_i(x_i)$ are the distributions of the observables x_i. To determine the joint PDF for $\overline{\rho}$ and $\overline{\eta}$ one must then generate their values, weighted by the constraint relations, through the use of Monte Carlo techniques. We report in Tab. 1.2 the input values used and the best values obtained for the parameters mentioned at the beginning of this Section. The full fit results [19] for the $\overline{\rho}$ and $\overline{\eta}$ parameters result to be

$$\overline{\rho} = 0.153 \pm 0.013, \qquad \overline{\eta} = 0.343 \pm 0.011. \tag{1.45}$$

Finally, a graphical representation of the allowed parameter values is given in Fig. 1.3.

1.3 Flavour-changing neutral currents (FCNC)

So far all the analysed interactions were mediated by $W^{\pm}$ bosons. This kind of interaction goes under the name of flavour-changing charged currents (FCCCs). In the SM, this type of interaction is the only source of flavour changing interaction, and, in particular, of generation changing interaction. On the other hand, there is no *a priori* reason why there cannot be flavour changing neutral currents; yet, experimentally, we see that FCNCs processes are highly suppressed in the SM. For example, the rate of the neutral current decay $K_L^0 \to \mu^+\mu^-$ is a lot more suppressed than its charged current counterpart, $K^+ \to \mu^+\nu_\mu$.

This experimental fact needs to be taken into account by any model aiming to describe the FCNCs; this means that there must be a mechanism in the SM that suppresses this kind of interactions. One way to suppress FCNCs is to make sure that they cannot happen at tree level. There are four neutral bosons in the SM that could mediate tree level FCNCs: g, γ, H^0, and Z.

Concerning the massless gauge bosons, g and γ, their couplings to the fermions are universal, *i.e.* they have the same strength for all the generations, and flavour conserving, due to the gauge symmetry; thus, they cannot mediate FCNCs. Higgs couplings are diagonal in the SM, since they are aligned with the mass matrix. To see this consider the Yukawa Lagrangian in Eq. (1.15) and insert $\Re(\phi^0) \to (v + h)/\sqrt{2}$, obtaining

Table 1.2: *Inputs and results from the SM fit of Ref. [19].*

Parameter	Input value	Full fit	SM prediction	Pull
$\bar{\rho}$	–	–	0.153 ± 0.013	–
$\bar{\eta}$	–	–	0.343 ± 0.011	–
ρ	–	–	0.157 ± 0.014	–
η	–	–	0.352 ± 0.011	–
A	–	–	0.833 ± 0.012	–
λ	0.22534 ± 0.00089	–	0.22497 ± 0.00069	-0.2
$\sin\theta_{12}$	–	–	0.22497 ± 0.00069	–
$\sin\theta_{23}$	–	–	0.04229 ± 0.00057	–
$\sin\theta_{13}$	–	–	0.00368 ± 0.00010	–
$\delta[^\circ]$	–	–	65.9 ± 2.0	–
$\lvert V_{ub}\rvert$	0.00373 ± 0.00021	0.00368 ± 0.00010	0.00366 ± 0.00012	-0.4
$\lvert V_{ub}\rvert$(excl.)	0.00361 ± 0.00013	–	–	$+0.2$
$\lvert V_{ub}\rvert$(incl.)	0.00440 ± 0.00022	–	–	-3.0
$\lvert V_{cb}\rvert$	0.04170 ± 0.00100	0.04229 ± 0.00057	0.04256 ± 0.00069	$+0.7$
$\lvert V_{cb}\rvert$(excl.)	0.0400 ± 0.0011	–	–	$+1.7$
$\lvert V_{cb}\rvert$(incl.)	0.04200 ± 0.00064	–	–	$+0.5$
$\alpha[^\circ]$	94.2 ± 5.0	92.0 ± 2.0	91.0 ± 2.5	-0.6
$\beta[^\circ]$	–	22.11 ± 0.76	23.2 ± 1.2	–
$\gamma[^\circ]$	70.5 ± 5.7	65.8 ± 1.9	65.3 ± 2.0	-0.7
$J_{\mathrm{CKM}} \cdot 10^5$	–	–	3.115 ± 0.093	–
$2\beta + \gamma[^\circ]$	89 ± 54	110.0 ± 2.3	110.2 ± 2.3	$+0.3$
$\sin(2\beta)$	0.680 ± 0.023	0.696 ± 0.018	0.724 ± 0.028	$+1.2$
$\cos(2\beta)$	0.86 ± 0.12	0.716 ± 0.018	0.686 ± 0.030	-1.4
$\beta_s[^\circ]$	0.94 ± 0.94	–	1.042 ± 0.034	$+0.1$
$m_c[\mathrm{GeV/c^2}]$	1.288 ± 0.025	–	–	–
$m_b[\mathrm{GeV/c^2}]$	4.176 ± 0.026	–	–	–
$m_t[\mathrm{GeV/c^2}]$	165.72 ± 0.73	165.53 ± 0.67	160.1 ± 7.4	-0.8
B_k	0.740 ± 0.029	0.751 ± 0.026	0.813 ± 0.065	$+0.9$
f_{B_s}	0.2260 ± 0.0050	0.2238 ± 0.0041	0.2204 ± 0.0070	-0.7
f_{B_s}/f_{B_d}	1.203 ± 0.013	1.202 ± 0.011	1.209 ± 0.034	$+0.1$
B_{B_s}/B_{B_d}	1.032 ± 0.036	1.042 ± 0.029	1.069 ± 0.053	$+0.5$
B_{B_s}	0.888 ± 0.053	0.866 ± 0.035	0.854 ± 0.045	-0.6
B_k	0.740 ± 0.029	0.751 ± 0.026	0.813 ± 0.065	$+0.9$
$\lvert\epsilon_k\rvert \cdot 10^3$	2.228 ± 0.011	2.227 ± 0.011	2.03 ± 0.18	-1.1
$\Delta m_s[\mathrm{ps^{-1}}]$	17.757 ± 0.021	17.755 ± 0.020	17.69 ± 0.93	-0.1
$\Delta m_d[\mathrm{ps^{-1}}]$	0.5063 ± 0.0019	–	–	–
$\Delta\Gamma_d/\Gamma_d$	-0.0020 ± 0.0100	–	0.00497 ± 0.00039	$+0.6$
$\Delta\Gamma_s/\Gamma_s$	0.1240 ± 0.0089	–	0.154 ± 0.012	$+1.9$
A_{SL_d}	0.00020 ± 0.00200	-0.000290 ± 0.000027	-0.000290 ± 0.000027	-0.3
A_{SL_s}	0.0017 ± 0.0030	0.0000127 ± 0.0000012	0.0000127 ± 0.0000012	-0.6
$B(B \to \tau\nu) \cdot 10^4$	1.06 ± 0.20	0.828 ± 0.060	0.807 ± 0.061	-1.3

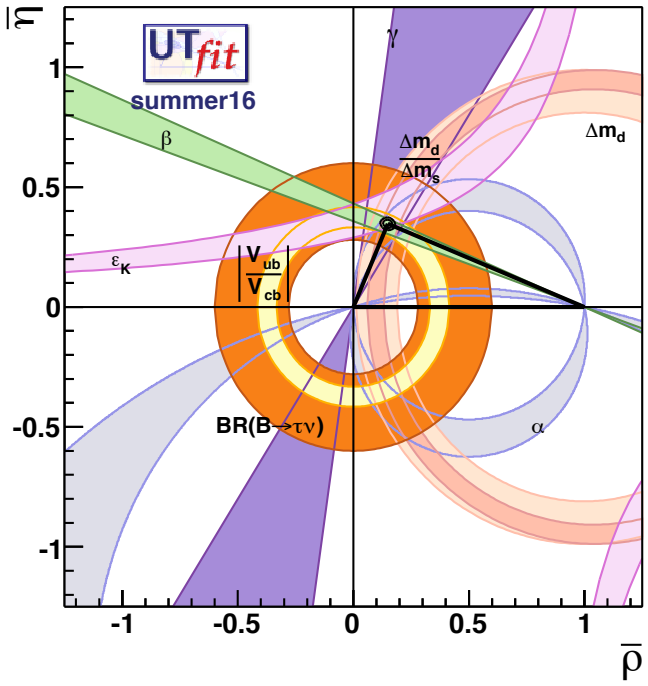

Figure 1.3: *Graphical representation of the allowed parameter ranges as given from the full fit procedure described in Ref. [19]. The* 68% *and* 95% *contours for* $\overline{\rho}$ *and* $\overline{\eta}$ *parameters are also displayed.*

$$\begin{aligned} -\mathcal{L}^{\text{quarks}}_{\text{Yukawa}} &= Y^d_{ij}(\overline{Q^I_{Li}})\phi D^I_{Rj} + Y^u_{ij}(\overline{Q^I_{Li}})\phi U^I_{Rj} = \\ &= \frac{Y^d_{ij}}{\sqrt{2}}(\overline{D^I_{Li}}D^I_{Ri})(v+h) + \frac{Y^u_{ij}}{\sqrt{2}}(\overline{U^I_{Li}}U^I_{Ri})(v+h). \end{aligned} \tag{1.46}$$

By diagonalising the mass matrix one obtains the interaction in the physical basis

$$M_d(\overline{D^I_{Li}}D^I_{Ri})(v+h) + M_u(\overline{U^I_{Li}}U^I_{Ri})(v+h). \tag{1.47}$$

Everything is proportional to $(v+h)$ and this is the proof that the Higgs couplings are aligned with the mass matrix and diagonal. For this reason, the Higgs cannot mediate FCNCs.

Last, we examine the Z-mediated FCNCs. In this case, the coupling to fermions is proportional to $T_3 - q\sin(\theta_w)$ and the Lagrangian in the mass basis is given by (for simplicity, we consider only left-handed quarks)

$$\begin{aligned} -\mathcal{L}_Z &= \frac{g}{\cos(\theta_w)}\left[\overline{u_{Li}}(V_{uL})_{ik}\gamma^\mu\left(\frac{1}{2} - \frac{2}{3}\sin^2(\theta_w)\right)(V_{uL})_{kj}u_{Lj}\right] = \\ &= \frac{g}{\cos(\theta_w)}\left[\overline{u_{Li}}\gamma^\mu\left(\frac{1}{2} - \frac{2}{3}\sin^2(\theta_w)\right)u_{Lj}\right] \end{aligned} \tag{1.48}$$

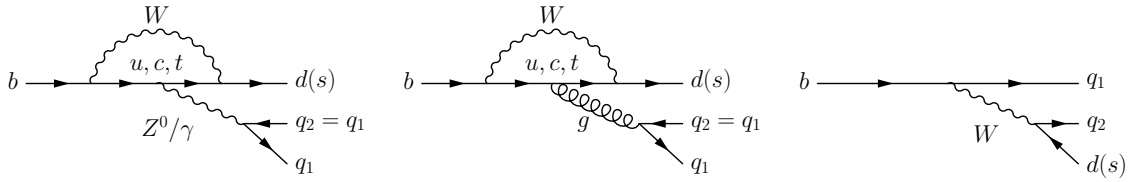

Figure 1.4: *Feynman diagrams representing (left) the penguin EW topology, (center) the penguin QCD topology and (right) the tree-level topology contributing to two-body b-hadron decays.*

since $V_{uL}V_{uL}^{\dagger} = \mathbb{I}$. This means that the interaction is diagonal and universal in flavour, and thus the Z cannot mediate FCNCs. A very important difference between neutral and charged currents is that in the former we insert $V_{uL}V_{uL}^{\dagger} = \mathbb{I}$, whereas in the second we use $V_{uL}V_{dL}^{\dagger}$, that in general is not equal to the identity matrix (it is the CKM matrix).

1.4 Charmless two-body hadronic b decays

Rare b decays involving FCNC transitions are of great interest to look for possible hints of new physics beyond the SM. In the SM, the FCNC transitions arise only at one-loop level, thus providing a sensitive test for the investigation of the gauge structure of the SM. Moreover, the study of weak decays of bottom hadrons can provide valuable information on the CKM matrix due to the fact that b decays involve five matrix elements (V_{cb}, V_{ub}, V_{td}, V_{ts} and V_{td}).

The weak decays concerning heavy baryons containing a b quark may provide important clues on flavour changing currents beyond the SM in a complementary way with respect to B mesons decays. Furthermore, since CP violation has been measured in B^0 and B_s^0 meson decays involving $b \to s$ transitions [16], one expects that there could be deviations also in the b baryons decays involving the same quark transitions. Therefore, the study of rare b decays is of fundamental importance in order to establish possible signals of CP violation that could represent hints for NP.

The Feynman diagrams describing such transitions can be divided into two groups: tree-level topologies and penguin (or loop-level) topologies. In the case of the charmless two-body b-hadron decays the diagrams involved can be classified in three categories:

- $b \to d(s)$ transitions mediated by tree-level topologies;
- $b \to d(s)$ transitions mediated by loop-level QCD topologies;
- $b \to d(s)$ transitions mediated by loop-level EW topologies.

The different Feynman diagrams referring to the topologies listed above are shown in Fig. 5.1.

1.4.1 Effective Hamiltonian approach

To fully describe the weak decays of hadrons, it is also necessary to consider the strong interaction binding together the constituents quarks. Due to the QCD asymptotic freedom, it is possible to treat short-distance corrections, *i.e.* the hard gluons contributions at energies of the order of $\mathcal{O}(M_W)$ down to hadronic scales ≥ 1 GeV, in perturbation theory. The theoretical framework adopted to exploit such property is the so called Operator Product Expansion (OPE) [20, 21].

This approach allows to write the effective Hamiltonian for the hadronic charmless decays as

$$\mathcal{H}_{eff} = \frac{G_F}{\sqrt{2}} \left\{ V_{ub}V_{uq}^*[c_1(\mu)O_1^u(\mu) + c_2(\mu)O_2^u(\mu)] - V_{tb}V_{tq}^* \sum_{i=3}^{10} c_i(\mu)O_i(\mu) \right\} + \text{h.c.} \quad (1.49)$$

where $q = d, s$, G_F is the Fermi constant, and $c_i(\mu)$ are the Wilson coefficients evaluated at the renormalisation scale μ. The operators O_{1-10} are given by the expressions

$$\begin{aligned}
O_1^u &= (\bar{u}b)_{V-A}(\bar{q}u)_{V-A}, \\
O_2^u &= (\bar{u}_\alpha b_\beta)_{V-A}(\bar{q}_\beta u_\alpha)_{V-A}, \\
O_{3(5)} &= (\bar{q}b)_{V-A} \sum_{q'} (\bar{q}'q')_{V-A(V+A)}, \\
O_{4(6)} &= (\bar{q}_\alpha b_\beta)_{V-A} \sum_{q'} (\bar{q}'_\beta q'_\alpha)_{V-A(V+A))}, \\
O_{7(9)} &= \frac{3}{2}(\bar{q}b)_{V-A} \sum_{q'} e_{q'}(\bar{q}'q')_{V+A(V-A)}, \\
O_{8(10)} &= \frac{3}{2}(\bar{q}_\alpha b_\beta)_{V-A} \sum_{q'} e_{q'}(\bar{q}'_\beta q'_\alpha)_{V+A(V-A)}
\end{aligned} \quad (1.50)$$

where $O_{1,2}$ are the tree-level current-current operators, O_{3-6} are the QCD penguin operators, O_{7-10} are the EW penguin operators and $(\bar{q}_1 q_2)_{(V\pm A)}$ denote the usual $(V \pm A)$ currents. The sum over q' runs over all the quark fields active at the scale $\mu = \mathcal{O}(m_b)$, *i.e.* $(q' \in u, d, c, s, b)$.

To conclude, we note that using the unitarity of the CKM matrix ($V_{tr}^* V_{tb} = -V_{ur}^* V_{ub} - V_{cr}^* V_{cb}$), we can write Eq. (1.49) in a more convenient way

$$\mathcal{H}_{eff} = \frac{G_F}{\sqrt{2}} \left\{ \sum_{j=u,c} V_{jr}^* V_{jb} \left[\sum_{k=1}^{2} c_k(\mu)O_k^{jr} + \sum_{k=3}^{10} c_k(\mu)O_k^r \right] \right\}. \quad (1.51)$$

that will prove to be useful in the next Section.

1.4.2 Decay amplitudes

Using the formalism just described the matrix element of a generic $\bar{H}_b \to \bar{f}$ decay can be written as

$$\begin{aligned} A(\bar{H}_b \to \bar{f}) &= \langle \bar{f}|\mathcal{H}_{eff}|\bar{H}_b\rangle = \\ &= \frac{G_F}{\sqrt{2}}\left\{\sum_{j=u,c} V_{jr}^* V_{jb}\left[\sum_{k=1}^{2} c_k(\mu)\langle \bar{f}|O_k^{jr}|\bar{H}_b\rangle + \sum_{k=3}^{10} c_k(\mu)\langle \bar{f}|O_k^{r}|\bar{H}_b\rangle\right]\right\}, \end{aligned} \tag{1.52}$$

while for its *CP* coniugate decay one has

$$\begin{aligned} A(H_b \to f) &= \langle f|\mathcal{H}_{eff}^{\dagger}|H_b\rangle = \\ &= \frac{G_F}{\sqrt{2}}\left\{\sum_{j=u,c} V_{jr}^* V_{jb}\left[\sum_{k=1}^{2} c_k(\mu)\langle f|O_k^{jr\dagger}|H_b\rangle + \sum_{k=3}^{10} c_k(\mu)\langle f|O_k^{r\dagger}|H_b\rangle\right]\right\}. \end{aligned} \tag{1.53}$$

Using the strong interaction invariance under *CP* and noting that $(CP)^\dagger(CP) = \mathbb{I}$ the following relations hold

$$\begin{aligned} (CP)O_k^{jr}(CP)^\dagger &= O_k^{jr}\ , \\ (CP)O_k^{r}(CP)^\dagger &= O_k^{r}\ , \\ (CP)|f\rangle &= e^{i\phi_f}|\bar{f}\rangle\ , \\ (CP)|H_b\rangle &= e^{i\phi_{H_b}}|\bar{H}_b\rangle\ . \end{aligned} \tag{1.54}$$

The equations above allow to rewrite Eq. (1.53) in the following way

$$\begin{aligned} A(H_b \to f) &= e^{i(\phi_{H_b}-\phi_f)}\frac{G_F}{\sqrt{2}} \times \\ &\times \left\{\sum_{j=u,c} V_{jr}^* V_{jb}\left[\sum_{k=1}^{2} c_k(\mu)\langle f|O_k^{jr\dagger}|H_b\rangle + \sum_{k=3}^{10} c_k(\mu)\langle f|O_k^{r\dagger}|H_b\rangle\right]\right\}. \end{aligned} \tag{1.55}$$

Finally, the two decay amplitudes can be expressed as

$$\begin{aligned} A(\bar{H}_b \to \bar{f}) &= e^{i\psi_1}|A_1|e^{i\delta_1} + e^{i\psi_2}|A_2|e^{i\delta_2} \\ A(H_b \to f) &= e^{i(\phi_{H_b}-\phi_f)} \times \left(e^{i\psi_1}|A_1|e^{i\delta_1} + e^{i\psi_2}|A_2|e^{i\delta_2}\right)\ , \end{aligned} \tag{1.56}$$

where $\psi_{1,2}$ denotes the *CP*-violating phase coming from the CKM elements $V_{jr}V_{jb}^*$ and $|A_{1,2}|e^{i\delta 1,2}$ are the *CP*-conserving strong amplitudes coming from

$$|A|e^{i\delta} \sim \sum_k \underbrace{c_k(\mu)}_{\text{perturbative QCD}} \times \underbrace{\langle \bar{f}|c_k(\mu)|\bar{H}_b\rangle}_{\text{non-perturbative QCD}}\ . \tag{1.57}$$

1.5 Meson mixing

A very interesting FCNC process is neutral meson mixing. Since it is a FCNC process, it can proceed only through loop-level diagrams, and thus it is suppressed and difficult to observe. Yet, the importance of meson mixing and oscillations in determining elements of the CKM makes their study worthwhile. We will now introduce the formalism needed to cope with meson mixing, restricting ourselves to the case where there is no *CP* violation; the same formalism will be reused later when we will study *CP* violation in mixing.

1.5.1 Formalism

In the SM we have four neutral mesons that can mix: K^0, D^0, B^0 and B_s^0. The formalism is that of a two-body open system and it is entirely general and thus we will refer from now on to a general neutral meson called P. Before the meson decays, the state is a superposition of two meson states; at $t = 0$ the wave function is given by

$$|\psi(0)\rangle = a(0)|P^0\rangle + b(0)|\overline{P}^0\rangle, \tag{1.58}$$

where one is interested in calculating the values of the time-dependent coefficients $a(t)$ and $b(t)$. All the evolution can be determined by means of a 2×2 effective Hamiltonian $\mathcal{H}$, that is not Hermitian. This matrix can be written in terms of two Hermitian matrices M and Γ as

$$\mathcal{H} = M - \frac{i}{2}\Gamma. \tag{1.59}$$

The diagonal elements in M and Γ are associated with flavour-conserving transitions $P^0(\overline{P}^0) \to P^0(\overline{P}^0)$, whereas off-diagonal terms describe the flavour-changing transitions $P^0 \leftrightarrow \overline{P}^0$. Since $\mathcal{H}$ is not diagonal, P^0 and $\overline{P}^0$ are not mass eigenstates and thus do not have well defined masses and widths: in fact we denote with P_L and P_H the lighter and heavier mass eigenstates. This is an arbitrary choice: indeed, one could also distinguish the two different eigenstates according to their lifetimes, as it is the case for the K mesons. Due to CPT symmetry, we have that $M_{11} = M_{22}$ and $\Gamma_{11} = \Gamma_{22}$. Solving the eigenvalue problem for $\mathcal{H}$, one finds that the eigenstates are given by

$$|P_{L,H}\rangle = p|P^0\rangle \pm q|\overline{P^0}\rangle, \tag{1.60}$$

where the q and p parameters are bounded by the relations $|p^2| + |q^2| = 1$ and

$$\left(\frac{q}{p}\right)^2 = \frac{M_{12}^* - (i/2)\Gamma_{12}^*}{M_{12} - (i/2)\Gamma_{12}}. \tag{1.61}$$

If CP symmetry holds, then

$$\left|\frac{q}{p}\right| = 1. \tag{1.62}$$

The mass and width differences are defined as $\Delta m \equiv M_H - M_L$ and $\Delta\Gamma \equiv \Gamma_H - \Gamma_L$, respectively; note that Δm is positive by definition, whereas the sign of $\Delta\Gamma$ has to be determined experimentally. The average mass and widths are defined as

$$m \equiv= \frac{M_H + M_L}{2}, \quad \Gamma = \frac{\Gamma_H + \Gamma + L}{2}, \tag{1.63}$$

and the dimensionless ratios x and y as

$$x \equiv \frac{\Delta m}{\Gamma}, \quad y \equiv \frac{\Delta\Gamma}{2\Gamma}. \tag{1.64}$$

These quantities will prove to be useful in the next Section, where the time evolution of a neutral meson will be studies.

1.5.2 Time evolution

Assuming CP symmetry conservation, then $|p| = |q| = 1/\sqrt{2}$ and Eq. (1.60) becomes

$$|P_{L,H}\rangle = \frac{1}{\sqrt{2}}\left(|P^0\rangle \pm |\overline{P^0}\rangle\right). \tag{1.65}$$

In an initial state where only P^0 is present, after a time t the state will be

$$|P^0(t)\rangle = \cos\left(\frac{\Delta E t}{2}\right)|P^0\rangle + i\sin\left(\frac{\Delta E t}{2}\right)|\overline{P}^0\rangle, \tag{1.66}$$

and similarly for $\overline{P}^0$. From Eq. (1.66) one sees that the probability $\mathcal{P}$ to measure a specific flavour oscillates in time and it is equal to

$$\begin{aligned}
\mathcal{P}(P^0 \to P^0)[t] &= \left|\langle P^0(t)|P^0\rangle\right|^2 = \frac{1+\cos(\Delta E t)}{2}, \\
\mathcal{P}(P^0 \to \overline{P}^0)[t] &= \left|\langle P^0(t)|\overline{P}^0\rangle\right|^2 = \frac{1-\cos(\Delta E t)}{2}.
\end{aligned} \tag{1.67}$$

In the meson rest frame $\Delta E = \Delta m$ and $t = \tau$; from the first relation we can see that the flavour oscillations happen with a frequency Δm. Also, by measuring the oscillation frequency, the mass splitting between the two mass eigenstates is determined.

1.5.3 Time scales

The study of neutral meson mixing involves two different time scales:

- One scale is the oscillation period and this is given by Δm;
- The other scale is the time when the flavour measurements are done: this time scale is given by the decay width Γ.

The dimensionless ratio $x \equiv \Delta m/\Gamma$ turns out to be an excellent quantity to analyse the different regimes one can have:

1. $x \ll 1$. This is the case of "slow oscillations". In this case the meson does not have time to oscillate and thus, to a good approximation, flavour is conserved. In fact $x \ll 1 \Rightarrow \cos(\Delta m t) \approx 1$, and thus Eqs. (1.67) yield $\mathcal{P}(P^0 \to P^0) \approx 1$ and $\mathcal{P}(P^0 \to \overline{P}^0) \to 0$. This is the case for the D^0 system.
2. $x \gg 1$. We denote this case as "fast oscillations". In this scenario the meson oscillates

several times before decaying and thus the oscillating term, $\cos(\Delta m t)$, practically averages to zero. This means that Eqs. (1.67) yield $\mathcal{P}(P^0 \to P^0) \approx \mathcal{P}(P^0 \to \overline{P}^0) \approx 1/2$. This is the case for the B_s^0 system.

3. $x \sim 1$ In this case the oscillation and decay times are roughly the same. The consequence is that the system has time to oscillate and the oscillations are not averaged out; thus using Eqs. (1.67) one can measure the value of Δm. This is the case for the K^0 and B^0 systems.

Considerations can also be made by observing the values that the dimensionless parameter $y \equiv \Delta\Gamma/(2\Gamma)$ takes

1. $|y| \ll 1$ and $y \ll x$. In this case the width difference of the two mass eigenstates is irrelevant. This is the case for the B^0 system.

2. $y \sim x$. In this scenario the width difference is as important as the oscillation. This is the case for D^0 system ($y \ll 1$) and for the K^0 system ($y \sim 1$).

3. $|y| \sim 1$ and $y \ll x$. In this case the oscillation averages to zero and the width difference shows up as a difference in the lifetimes of the two mass eigenstates. This case is relevant for the B_s^0 system.

In the following, a summary of the order of magnitude of the x and y parameters for each neutral meson is given

$$\begin{aligned} x_K &\sim 1, & y_K &\sim 1, \\ x_D &\sim 10^{-2}, & y_D &\sim 10^{-2}, \\ x_d &\sim 1, & y_d &\leq 10^{-2}, \\ x_s &\sim 10, & y_s &\leq 10^{-1}. \end{aligned} \tag{1.68}$$

1.6 *CP* violation

At this point we are ready to study *CP* violation in detail. As it should be evident by now, *CP* violation is closely related to flavour. Indeed, the source of *CP* violation in the SM is the Kobayashi-Maskawa phase present in the CKM matrix.

1.6.1 How to observe *CP* violation

The *CP* symmetry relates particles with their anti-particles. If *CP* is conserved, one must have

$$\Gamma(A \to B) = \Gamma(\overline{A} \to \overline{B}), \tag{1.69}$$

with A and B representing any possible initial and final state. The only way to find *CP* violation is to look for decays where the equality presented in Eq. (1.69) does not

hold. Even if this is the case, it is not easy to observe *CP* violation, since the deviations from Eq. (1.69) are usually very small.

There are several conditions that need to be fulfilled in order to have *CP* violation. First of all, *CP* violation can arise only in the interference between two decay amplitudes, that must carry different weak and strong phases. Consider for example the $B \to f$ decay amplitude A_f, and the *CP* conjugate process $\overline{B} \to \overline{f}$, whose decay amplitude is $\overline{A}_{\overline{f}}$. There are two kind of phases that could appear in these decay amplitudes. Complex parameters in any Lagrangian term that contributes to the amplitude will appear in complex conjugate form in the *CP*-conjugate amplitude. For this reason, their phases appear in A_f and $\overline{A}_{\overline{f}}$ with opposite signs, and these phases are thus *CP*-odd. In the SM, these phases appear only in $W^{\pm}$ couplings and hence they are also called "weak phases". Possible contributions of intermediate on-shell states in the decay process give rise to a second kind of phases, equal between A_f and $\overline{A}_{\overline{f}}$, and therefore *CP*-even. This phases are also called "strong phases".

Finally, *CP* violation is present only in a SM with three generations and thus any *CP* violating observable must involve all the three generations. Due to the hierarchy of the CKM matrix, these observables are proportional to very small CKM elements.

It is useful to write each contribution a_i to the amplitudes in three parts: its magnitude $|a_i|$, its weak phase ϕ_i, and its strong phase δ_i. If, for example, there are two contributions, $A = a_1 + a_2$, such that

$$\begin{aligned} A_f &= |a_1|e^{i(\delta_1+\phi_1)} + |a_2|e^{i(\delta_2+\phi_2)} \\ \overline{A}_{\overline{f}} &= |a_1|e^{i(\delta_1-\phi_1)} + |a_2|e^{i(\delta_2-\phi_2)}. \end{aligned} \tag{1.70}$$

1.6.2 Types of *CP* violation

When considering *CP* violation in meson decays, there are two types of amplitudes: mixing and decay. Therefore, there must be three ways to observe *CP* violation, depending on which amplitudes interfere:

1. *CP* violation in decay, also called direct *CP* violation.
2. *CP* violation in mixing, also called indirect *CP* violation.
3. *CP* violation in the interference between mixing and decay.

1.6.2.1 *CP* violation in decay

In this case

$$|A(P \to f)| \neq |A(\overline{P} \to \overline{f})| \tag{1.71}$$

and one defines the quantity

$$a_{CP} = \frac{\Gamma(\overline{B} \to \overline{f}) - \Gamma(B \to f)}{\Gamma(\overline{B} \to \overline{f}) + \Gamma(B \to f)} = \frac{|\overline{A}/A|^2 - 1}{|\overline{A}/A|^2 + 1} \tag{1.72}$$

Using Eq. (1.70) with ϕ as the weak phase difference and δ as the strong phase difference, we write

$$A(P \to f) = A(1 + re^{i(\phi+\delta)}), \quad A(P \to \overline{f}) = A(1 + re^{i(-\phi+\delta)}), \tag{1.73}$$

with $r \leq 1$. One finally gets

$$a_{CP} = r \sin(\phi) \sin(\delta). \tag{1.74}$$

This equation shows that one needs two decay amplitudes, *i.e.* $r \neq 0$, with different weak phases, $\phi \neq 0, \pi$ and different strong phases, $\delta \neq 0, \pi$, in order to have direct *CP* violation. Moreover, in order to have a sizable violation, each one of the factors entering Eq. (1.74) needs to be large.

1.6.2.2 *CP* violation in mixing

We will start be re-deriving the formalism introduced in Sec. 1.5 in a more general case, where we allow for *CP* violation. We will concentrate on the B system. Considering a final state f one can write

$$A_f \equiv A(B \to f), \quad \overline{A}_f \equiv A(\overline{B} \to f). \tag{1.75}$$

and define the quantity

$$\lambda_f \equiv \frac{q}{p}\frac{\overline{A}_f}{A_f}. \tag{1.76}$$

The general time evolution of a P^0 and $\overline{P}^0$ meson can be written as

$$\begin{aligned} |P^0(t)\rangle &= g_+(t)|P^0\rangle - (q/p)g_-(t)|\overline{P}^0\rangle, \\ |\overline{P}^0(t)\rangle &= g_+(t)|\overline{P}^0\rangle - (q/p)g_-(t)|P^0\rangle, \end{aligned} \tag{1.77}$$

where we work in the B rest frame and

$$g_\pm(t) \equiv \frac{1}{2}\left(e^{-im_H t - \frac{1}{2}\Gamma_H t} \pm e^{-im_L t - \frac{1}{2}\Gamma_L t}\right). \tag{1.78}$$

Defining $\tau \equiv \Gamma t$ the decay rates can be expressed as

$$\begin{aligned} \Gamma(B \to f)[t] = |A_f|^2 e^{-\tau} \big\{ &(\cosh(y\tau) + \cos(x\tau)) + |\lambda_f|^2 (\cosh(y\tau) - \cos(x\tau)) \\ &-2\Re\left[\lambda_f(\sinh(y\tau) + i\sin(x\tau))\right]\big\}, \\ \Gamma(\overline{B} \to f)[t] = |\overline{A}_f|^2 e^{-\tau} \big\{ &(\cosh(y\tau) + \cos(x\tau)) + |\lambda_f|^{-2} (\cosh(y\tau) - \cos(x\tau)) \\ &-2\Re\left[\lambda_f^{-1}(\sinh(y\tau) + i\sin(x\tau))\right]\big\}. \end{aligned} \tag{1.79}$$

where $\Gamma(B \to f)[t]$ ($\Gamma(\overline{B} \to f)[t]$) is the probability for an initially pure B ($\overline{B}$) meson to decay at time t to a final state f. Terms proportional to $|A_f|^2$ or $|\overline{A}_f|^2$ are associated with

decays that occur without any net oscillation, while terms proportional to $|\lambda|^2$ or $|\lambda|^{-2}$ are associated with decays following a net oscillation. The $\sinh(y\tau)$ and $\sin(x\tau)$ terms are associated with the interference between these two cases.

The *CP* observable asymmetry is defined as

$$\mathcal{A}_f(t) = \frac{\Gamma[\overline{B}(t) \to f] - \Gamma[B(t) \to f]}{\Gamma[\overline{B}(t) \to f] + \Gamma[B(t) \to f]} \tag{1.80}$$

If $\Delta\Gamma = 0$ and $|q/p| = 1$, as expected to a good approximation for the B system, and the decay amplitudes are equal, then the interference between decays with and without mixing is the only source of the asymmetry and

$$\mathcal{A}_f(t) = \Im(\lambda_f)\sin(x\tau) = \sin[\arg(\lambda_f)]\sin(\Delta m t), \tag{1.81}$$

where the equality $\lambda = 1$ is used in the last step. If Δm is know, this provides a clean measurement of the phase λ_f, that is directly related to CKM angles. In the particular case where $f = \overline{f}$, Eq. (1.80) can be written as

$$\begin{aligned}
\mathcal{A}_f(t) &= \frac{\Gamma[\overline{B}(t) \to f] - \Gamma[B(t) \to f]}{\Gamma[\overline{B}(t) \to f] + \Gamma[B(t) \to f]} = \\
&= \frac{(|\lambda_f|^2 - 1)\cos(\Delta m t) + 2\Im(\lambda_f)\sin(\Delta m t)}{(|\lambda_f|^2 + 1)\cosh(\frac{\Delta\Gamma}{2}t) - 2\Re(\lambda_f)\sinh(\frac{\Delta\Gamma}{2}t)} \\
&= \frac{\mathcal{A}^{\rm dir}\cos(\Delta m t) + \mathcal{A}^{\rm mix}\sin(\Delta m t)}{\cosh(\frac{\Delta\Gamma}{2}t) - \mathcal{A}^{\Delta\Gamma}\sinh(\frac{\Delta\Gamma}{2}t)}
\end{aligned} \tag{1.82}$$

where the relation $|q/p| \approx 1$ has been used and the quantities $\mathcal{A}^{\rm dir}$, $\mathcal{A}^{\rm mix}$ and $\mathcal{A}^{\Delta\Gamma}$ are defined as

$$\mathcal{A}^{\rm dir} = \frac{|\lambda_f|^2 - 1}{|\lambda_f|^2 + 1}, \quad \mathcal{A}^{\rm mix} = \frac{2\Im(\lambda_f)}{|\lambda_f|^2 + 1}, \quad \mathcal{A}^{\Delta\Gamma} = \frac{2\Re(\lambda_f)}{|\lambda_f|^2 + 1}. \tag{1.83}$$

These three quantities satisfy the relation

$$|\mathcal{A}^{\rm dir}|^2 + |\mathcal{A}^{\rm mix}|^2 + |\mathcal{A}^{\Delta\Gamma}|^2 = 1. \tag{1.84}$$

The quantity $\mathcal{A}^{\rm dir}$ is the equivalent of the *CP* asymmetry defined in Eq. 1.72. If $\mathcal{A}^{\rm dir} \neq 0$ then direct *CP* violation is present in the process considered. The quantity $\mathcal{A}^{\rm mix}$ depends on the phase of the *CP* violating parameter λ_f. If it is different from zero, then mixing-induced *CP* violation is present, caused by the interference between $B - \overline{B}$ mixing and decay processes.

1.7 Phenomenology of charmless two-body decays

The family of charmless two-body B decays is composed by several decay modes, thus providing several occasions for testing the SM picture of *CP* violation. In the studies

presented in this thesis, eight decay channels are taken into account (not counting the *CP*-conjugate ones): $B^0 \to \pi^+\pi^-$, $B^0 \to K^+\pi^-$, $B^0 \to K^+K^-$, $B^0_s \to K^+K^-$, $B^0_s \to \pi^+K^-$, $B^0_s \to \pi^+\pi^-$, $\Lambda^0_b \to pK^-$ and $\Lambda^0_b \to p\pi^-$. The theoretical framework used to extract the CKM related quantities from these decays is the same discussed in the previous sections. A simple interpretation of *CP* violating observables of charmless two-body B decays in terms of CKM phases is not possible, in contrast to other theoretically clean measurements of *CP* violation in the B sector. Indeed, sizeable QCD ($b \to d(s) + g$ transitions) and EW ($b \to d(s) + \gamma,\ Z^0$ transitions) penguin contributions are present in addition to the $b \to u + W^+$ tree-level transition. Such penguin pollution poses several problems for a clean measurement of CKM phases using these decays, arising from hadronic matrix elements. On the other hand, loops inside the penguin diagrams could be affected by sizeable contributions from NP and thus their study is important.

1.7.1 $B \to h^+h'^-$ decay amplitudes

The SM topologies contributing to charmless two-body $B^0_{(s)}$ are depicted in Fig. 1.5 and the ones contributing to each decay mode are summarised in Tab. 1.3.

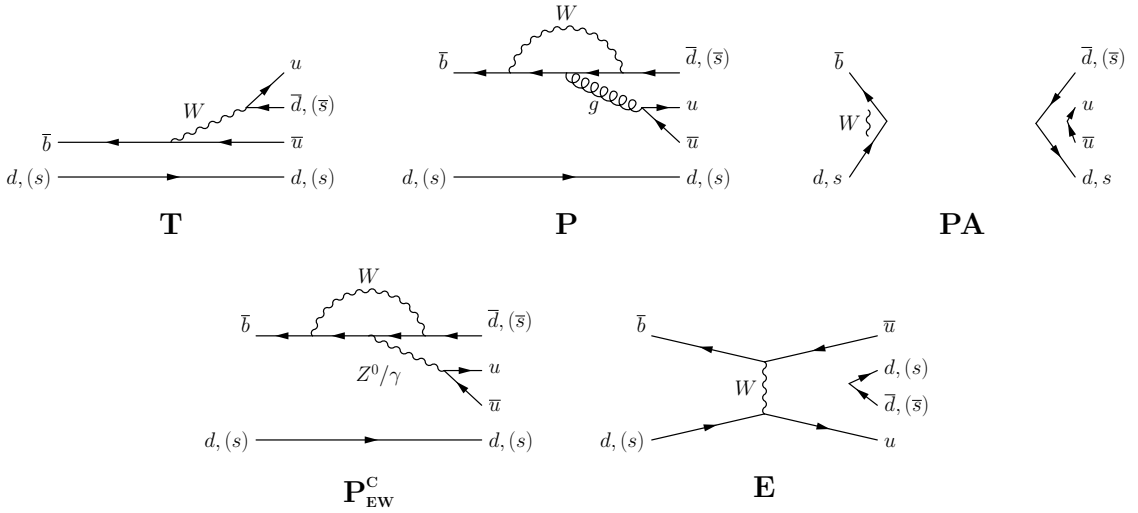

Figure 1.5: *Feynman diagrams contributing to the decay amplitudes of $B \to h^+h'^-$ decays: (T) tree, (P) penguin, (PA) penguin annihilation, (P^C_{EW} colour-suppressed electroweak penguin) and (E) exchange.*

It is useful to show the following relations between the various decay channels

$$\underbrace{B^0 \to K^+K^-}_{PA+E} \qquad d \longleftrightarrow s \qquad \underbrace{B^0_s \to \pi^+\pi^-}_{PA+E} \tag{1.85}$$

$$\underbrace{B^0 \to \pi^+\pi^-}_{T+P+\frac{2}{3}P^C_{EW}+PA+E} \qquad d \longleftrightarrow s \qquad \underbrace{B^0_s \to K^+K^-}_{T+P+\frac{2}{3}P^C_{EW}+PA+E} \tag{1.86}$$

Table 1.3: *Diagrams contributing to the amplitudes of each charmless $B^0_{(s)}$ decay to two charged mesons. See the caption of Fig. 1.5 for the definitions.*

Decay	Topology contributions
$B^0 \to \pi^+\pi^-$	T, P, P^C_{EQ}, PA, E
$B^0 \to K^+\pi^-$	T, P, P^C_{EQ}
$B^0_s \to K^+K^-$	T, P, P^C_{EQ}, PA, E
$B^0_s \to \pi^+K^-$	T, P, P^C_{EQ}
$B^0 \to K^+K^-$	PA, E
$B^0_s \to \pi^+\pi^-$	PA, E

$$\underbrace{B^0 \to K^+K^-}_{PA+E} \qquad d \longleftrightarrow s \qquad \underbrace{B^0_s \to \pi^+\pi^-}_{PA+E} \tag{1.87}$$

$$\underbrace{B^0 \to K^+\pi^-}_{T+P+\frac{2}{3}P^C_{EW}} \qquad d \longleftrightarrow s \qquad \underbrace{B^0_s \to \pi^+K^-}_{T+P+\frac{2}{3}P^C_{EW}} \tag{1.88}$$

$$\underbrace{B^0 \to K^+\pi^-}_{T+P+\frac{2}{3}P^C_{EW}} \qquad d \overset{\text{spect.}}{\longleftrightarrow} s \qquad \underbrace{B^0_s \to K^+K^-}_{T+P+\frac{2}{3}P^C_{EW}+PA+E} \tag{1.89}$$

$$\underbrace{B^0 \to \pi^+\pi^-}_{T+P+\frac{2}{3}P^C_{EW}+PA+E} \qquad d \overset{\text{spect.}}{\longleftrightarrow} s \qquad \underbrace{B^0_s \to \pi^+K^-}_{T+P+\frac{2}{3}P^C_{EW}} \tag{1.90}$$

where we emphasised the diagrams contributing to the transitions and how the channels are interconnected by $SU(3)$ symmetry. The label "spect." means that the two considered transitions differ just for the valence quarks of the B mesons that do not participate to the weak processes governing the decay (spectator quarks). For example, $B^0 \to \pi^+\pi^-$ and $B^0_s \to \pi^+K^-$ differ by the interchange of the spectator quarks, which in the former case is a d while in the latter is a s. For this reason, their strong interaction dynamics are connected by the $U-$spin symmetry. However, $U-$spin symmetry is not fully satisfied, because the diagrams labelled as PA and E contribute to the $B^0 \to \pi^+\pi^-$ decay but not to the $B^0_s \to \pi^+K^-$ decay. Anyway, such contributions are expected to be small and their size can be probed by means of $B^0 \to K^+K^-$ and $B^0_s \to \pi^+\pi^-$ decays, which proceed only through PA and E topologies. Analogous considerations are valid for $B^0_s \to K^+K^-$ and $B^0 \to K^+\pi^-$ decays. On the other hand, both $B^0 \to \pi^+\pi^-$ and $B^0_s \to K^+K^-$, as well as $B^0 \to K^+\pi^-$ and $B^0_s \to \pi^+K^-$ decays are fully $U-$spin symmetric: no dynamical assumptions that some topologies do not contribute significantly, as in the previous cases, are needed.

1.7.1.1 $B^0 \to \pi^+\pi^-$

The decay $B^0 \to \pi^+\pi^-$ originates from $\bar{b} \to \bar{u}u\bar{d}$ quark-level transitions, as shown in Fig. 1.5. Using the formalism introduced in the previous sections, the decay amplitude can be written as

$$A\left(B^0 \to \pi^+\pi^-\right) = \lambda_u^{(d)}\left(A_T^u + A_P^u\right) + \lambda_c^{(d)} A_P^c + \lambda_t^{(d)} A_P^t \tag{1.91}$$

where A_T^u represents the amplitude due to tree-level processes, while A_P^j represent the amplitudes due to QCD and electroweak penguin topologies with internal j quarks ($j \in \{u, c, t\}$). The quantities $\lambda_j^{(d)}$ are defined as $\lambda_j^{(d)} \equiv V_{jd}V_{jb}^*$. Making use of the unitarity of CKM matrix and of the generalised Wolfenstein parameterisation, one obtains

$$A\left(B^0 \to \pi^+\pi^-\right) = \left(1 - \frac{\lambda^2}{2}\right)\mathcal{C}\left[e^{i\gamma} - de^{i\theta}\right] \tag{1.92}$$

where

$$\mathcal{C} \equiv \lambda^3 A R_b\left(A_T^u + A_P^u - A_P^t\right) \tag{1.93}$$

and

$$de^{i\theta} \equiv \frac{1}{\left(1 - \lambda^2/2\right)R_b}\left(\frac{A_P^c - A_P^t}{A_T^u + A_P^u - A_P^t}\right). \tag{1.94}$$

The quantities A, λ, R_b and γ are those defined in Section 1.2. As a consequence, the *CP* violating parameter λ_f becomes

$$\lambda_f = -e^{-2i\beta}\left[\frac{e^{i\gamma} - de^{i\theta}}{e^{-i\gamma} - de^{i\theta}}\right]. \tag{1.95}$$

Inserting Eq. (1.95) into Eqs. (1.83) we obtain

$$\mathcal{A}_{\pi\pi}^{dir} = -\left[\frac{2d\sin\theta\sin\gamma}{1 - 2d\cos\theta\cos\gamma + d^2}\right] \tag{1.96}$$

$$\mathcal{A}_{\pi\pi}^{mix} = \left[\frac{\sin\left(2\beta + 2\gamma\right) - 2d\cos\theta\sin\left(2\beta + \gamma\right) + d^2\sin 2\beta}{1 - 2d\cos\theta\cos\gamma + d^2}\right] \tag{1.97}$$

where β denotes the $B^0 - \bar{B}^0$ mixing phase. The quantity $\mathcal{A}^{\Delta\Gamma}$ has been considered 0 as $\Delta\Gamma_d$ is small [17]. From Eqs. (1.96) one has that the *CP*-violating observables $\mathcal{A}_{\pi\pi}^{dir}$ and $\mathcal{A}_{\pi\pi}^{mix}$ depend on the quantities d, θ, γ and β. Time-dependent *CP* asymmetries relative to this decay mode have been measured by BaBar [22], Belle [23] and LHCb [24] collaborations. The current experimental knowledge of $\mathcal{A}_{\pi\pi}^{dir}$ and $\mathcal{A}_{\pi\pi}^{mix}$ (excluding the results presented in this thesis) is shown in Fig. 1.6.

1.7.1.2 $B^0 \to K^+\pi^-$

The $B^0 \to K^+\pi^-$ decay channel receives contributions both from tree and from penguin amplitudes depicted in Fig. 1.5, but not from PA and E topologies. Within the usual

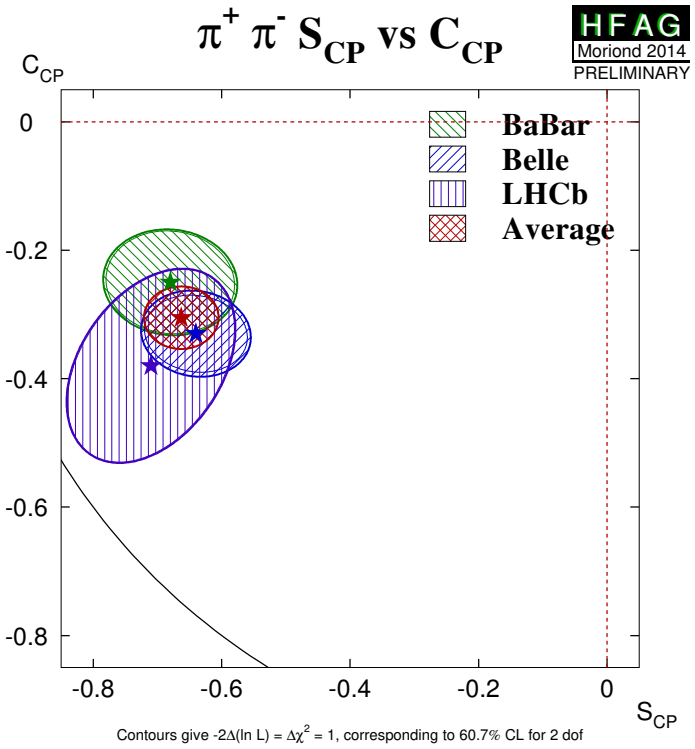

Figure 1.6: *Representation of the measurements of direct* (C_{CP}) *and mixing-induced* (S_{CP}) *CP-violating asymmetries for the* $B^0 \to \pi^+\pi^-$ *decay measured by BaBar [22], Belle [23] and LHCb [24] collaborations. The contours correspond to the* 60.7% *C.L regions.*

formalism and exploiting the CKM matrix unitarity, the decay amplitude of this channel can be written as

$$A\left(B^0 \to K^+\pi^-\right) = -P\left[1 - re^{i\delta}e^{i\gamma}\right] \tag{1.98}$$

where P describes the penguin amplitudes, r describes the amplitude ratios between tree and penguin amplitudes and δ is the *CP* conserving hadronic phase.

The quark level transitions $\bar{b} \to \bar{u}u\bar{s}$ are responsible of tree amplitudes, and contain a CKM factor $V_{ub}^* V_{us}$. On the other hand penguin amplitudes, dominated by a loop diagram with virtual top quark, contain a CKM factor $V_{tb}^* V_{ts}$. Consequently, because of the ratio $V_{ub}^* V_{us}/V_{tb}^* V_{ts} \approx 0.02$, QCD penguin amplitudes are expected to dominate the decay process. EW penguin topologies can contribute to the amplitude only in the colour-suppressed mode and thus are expected to play a minor rôle.

Since $B^0 \to K^+\pi^-$ is a flavour specific decay the instantaneous amplitude $A_{\bar{f}} \equiv A\left(B^0 \to K^-\pi^+\right)$ and $\bar{A}_f \equiv A\left(\bar{B}^0 \to K^+\pi^-\right)$ are zero. Consequently the decay rates are

$$\Gamma_{B^0\to K^+\pi^-}(t) \;=\; |A_f|^2\left[\cosh\left(\frac{\Delta\Gamma}{2}t\right) + \cos\left(\Delta m t\right)\right], \tag{1.99}$$

$$\Gamma_{B^0\to K^-\pi^+}(t) = \left|\bar{A}_{\bar{f}}\right|^2\left[\cosh\left(\frac{\Delta\Gamma}{2}t\right)-\cos\left(\Delta m t\right)\right], \quad (1.100)$$

$$\Gamma_{\bar{B}^0\to K^+\pi^-}(t) = \left|A_f\right|^2\left[\cosh\left(\frac{\Delta\Gamma}{2}t\right)-\cos\left(\Delta m t\right)\right], \quad (1.101)$$

$$\Gamma_{\bar{B}^0\to K^-\pi^+}(t) = \left|\bar{A}_{\bar{f}}\right|^2\left[\cosh\left(\frac{\Delta\Gamma}{2}t\right)+\cos\left(\Delta m t\right)\right]. \quad (1.102)$$

Using the time dependent asymmetry defined in Eq. (1.82) one obtains an asymmetry independent of time

$$\begin{aligned}\mathcal{A}^{\mathcal{CP}}_{K^+\pi^-} &= \frac{\left[\Gamma_{B^0\to K^-\pi^+}(t)+\Gamma_{\bar{B}^0\to K^-\pi^+}(t)\right]-\left[\Gamma_{\bar{B}^0\to K^+\pi^-}(t)+\Gamma_{B^0\to K^+\pi^-}(t)\right]}{\left[\Gamma_{B^0\to K^-\pi^+}(t)+\Gamma_{\bar{B}^0\to K^-\pi^+}(t)\right]+\left[\Gamma_{\bar{B}^0\to K^+\pi^-}(t)+\Gamma_{B^0\to K^+\pi^-}(t)\right]} \\ &= \frac{\left|\bar{A}_{\bar{f}}\right|^2-\left|A_f\right|^2}{\left|\bar{A}_{\bar{f}}\right|^2+\left|A_f\right|^2} = \frac{2r\sin(\delta)\sin(\gamma)}{1+2r\cos(\delta)\cos(\gamma)+r^2}. \end{aligned} \quad (1.103)$$

It is important to note that $\mathcal{A}^{\mathcal{CP}}_{K^+\pi^-}$ is a function of the γ angle of the UT and of the hadronic parameters r and δ. Thus the direct *CP* asymmetry of $B^0\to K^+\pi^-$ contains informations about the γ angle. The current experimental knowledge of direct *CP* asymmetries (excluding the results presented in this thesis) is reported in Tab. 1.4.

Table 1.4: *Current measurements of CP asymmetries of $B^0\to K^+\pi^-$ and $B^0_s\to\pi^+K^-$ decays measured by BaBar [22], Belle [25], CDF [26] and LHCb [27]. The average is performed by the HFLAV group. The first uncertainties are statistical and the second systematic.*

Mode	BaBar	Belle	CDF	LHCb	Average
$B^0\to K^+\pi^-$	$-0.107\pm0.016^{+0.006}_{-0.004}$	$-0.069\pm0.014\pm0.007$	$-0.083\pm0.013\pm0.004$	$-0.080\pm0.007\pm0.003$	-0.082 ± 0.006
$B^0_s\to\pi^+K^-$	-	-	$0.22\pm0.07\pm0.02$	$.27\pm0.04\pm0.01$	0.26 ± 0.04

1.7.1.3 $B^0_s\to K^+K^-$

The $B^0_s\to K^+K^-$ decay is the fully U-spin counterpart of the $B^0\to\pi^+\pi^-$ decay. On the other hand, just changing the s spectator quark of this decay with a d quark we obtain the $B^0\to K^+\pi^-$ decay. Thus, also $B^0\to K^+\pi^-$ results to be U-spin related to $B^0\to K^+K^-$, but only in the case of small contributions from penguin annihilation (PA) and exchange (E) topologies depicted in Fig. 1.5.

Because of the different CKM factors entering the diagrams in the $B^0_s\to K^+K^-$ decay, the penguin processes are dominant. In analogy to Eq. (1.92) we has

$$A\left(B^0_s\to K^+K^-\right) = \lambda\mathcal{C}'\left[e^{i\gamma}+\frac{1}{\varepsilon}d'e^{i\theta'}\right] \quad (1.104)$$

where $\varepsilon \equiv \lambda^2/\left(1-\lambda^2/2\right)$; $\mathcal{C}'$, d' and θ' are the counterpart of $\mathcal{C}$, d and θ in the $B^0 \to \pi^+\pi^-$ case. Calculating the time-dependent *CP* asymmetry terms, one obtains

$$\mathcal{A}_{KK}^{\text{dir}} = -\left[\frac{2d'\sin\theta'\sin\gamma}{1-2d'\cos\theta'\cos\gamma+d'^2}\right], \tag{1.105}$$

$$\mathcal{A}_{KK}^{\text{mix}} = +\left[\frac{\sin\left(2\beta_s+2\gamma\right)-2d'\cos\theta'\sin\left(2\beta_s+\gamma\right)+d'^2\sin 2\beta_s}{1-2d'\cos\theta'\cos\gamma+d'^2}\right], \tag{1.106}$$

$$\mathcal{A}_{\Delta\Gamma}^{KK} = -\left[\frac{d'^2\sin 2\beta_s+2\varepsilon d'\cos\theta'\cos\left(2\beta_s+\gamma\right)+\varepsilon^2\cos\left(2\beta_s+2\gamma\right)}{d'^2+2\varepsilon d'\cos\theta'\cos\gamma+\varepsilon^2 d'^2}\right]. \tag{1.107}$$

Similarly to the $B^0 \to \pi^+\pi^-$ decay, the observables $\mathcal{A}_{KK}^{\text{dir}}$ and $\mathcal{A}_{KK}^{\text{mix}}$ are functions of d', θ', β_s and γ. The only measurement of the direct and mixing-induced *CP*-violating parameters ($C_{K^+K^-}$ and $S_{K^+K^-}$) has been performed by the LHCb collaboration [24] and the values of these quantities are

$$\begin{aligned} C_{K^+K^-} &= 0.14 \pm 0.11 \pm 0.03, \\ S_{K^+K^-} &= 0.30 \pm 0.12 \pm 0.04, \end{aligned}$$

where the first uncertainty is statistical and the second systematic.

1.7.1.4 $B_s^0 \to \pi^+K^-$

The $B_s^0 \to \pi^+K^-$ is the fully U-spin counterpart of $B^0 \to K^+\pi^-$, and is the "spectator" U-spin counterpart of $B^0 \to \pi^+\pi^-$. Within the usual formalism and exploiting the CKM matrix unitarity, the decay amplitude of this channel can be written as

$$A\left(B_s^0 \to \pi^+K^-\right) = P_s\sqrt{\varepsilon}\left[1+\frac{1}{\varepsilon}r_s e^{i\delta_s}e^{i\gamma}\right]. \tag{1.108}$$

As this channel is a "flavour specific" decay, the same considerations on its time-evolution which are valid for the $B^0 \to K^+\pi^-$ decay also hold in this case. Consequently for the direct *CP* asymmetry one has

$$\mathcal{A}_{\mathcal{CP}} = \frac{2r_s\sin\left(\delta_s\right)\sin\left(\gamma\right)}{1+2r_s\cos\left(\delta_s\right)\cos\left(\gamma\right)+r_s^2}. \tag{1.109}$$

1.7.1.5 $B^0 \to K^+K^-$ and $B_s^0 \to \pi^+\pi^-$

Within the SM the amplitudes of these decays are governed by PA and E topologies shown in Fig. 1.5. The first evidence of the $B_s^0 \to \pi^+\pi^-$ decay has been obtained by the CDF collaboration [28], whereas the LHCb collaboration observed both $B_s^0 \to \pi^+\pi^-$ and $B^0 \to K^+K^-$ decays [29].

1.7.2 $\Lambda_b^0 \to h^+h'^-$ decay amplitudes

Examples of Feynman diagrams contributing to the $\Lambda_b^0 \to pK^-$ and $\Lambda_b^0 \to p\pi^-$ decays are shown in Fig. 1.7. CPV could arise from the interference of two amplitudes with non-zero strong and weak relative phases.

1.7.2.1 $\Lambda_b^0 \to pK^-$ and $\Lambda_b^0 \to p\pi^-$

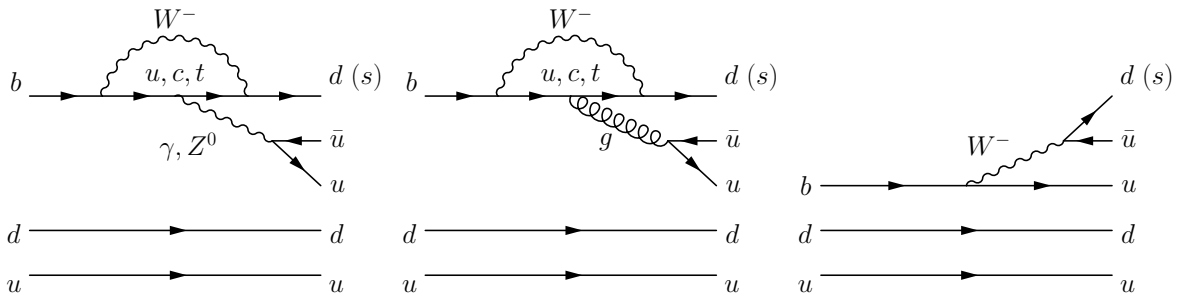

Figure 1.7: *Examples of Feynman diagrams representing (left) the penguin EW topology, (center) the penguin QCD topology and (right) the tree-level topology contributing to* $\Lambda_b^0 \to pK^-$ *(*$b \to su\bar{u}$ *transition) and* $\Lambda_b^0 \to p\pi^-$ *decays (*$b \to du\bar{u}$ *transition).*

The decays of the Λ_b^0 (bud) baryon to two-body charmless final states, pK^- or $p\pi^-$, are expected to have relatively small *CP* asymmetries, up to 6% [30] in the generalised factorisation approach [31]. Using the pQCD formalism, *CP* asymmetries larger than 30% (although with very large uncertainties related to hadronic quantities and scale dependence) have been also predicted [32]. The only measurement of *CP* asymmetries in $\Lambda_b^0 \to pK^-$ and $\Lambda_b^0 \to p\pi^-$ decays to date has been performed by the CDF collaboration [26]. The asymmetries have been found to be compatible with zero within large uncertainties. It is thus important to lower the experimental uncertainty on such quantities in order to make significant comparisons with theoretical predictions.

2 The LHCb detector at the LHC

2.1 The Large Hadron Collider

The Large Hadron Collider [33] is a two-ring hadron accelerator and collider, installed inside a 27 km long tunnel (the same where previously the LEP collider was installed), placed about 100 m underground, as shown in Fig. 2.1. The accelerator is designed to collide protons up to a centre-of-mass energy of 14 TeV, with a peak luminosity of 10^{34} $\mathrm{cm}^{-2}\mathrm{s}^{-1}$, while heavy-ion collisions (Pb-Pb) happen at a centre-of-mass energy of 2.8 TeV per nucleon, with a peak luminosity of 10^{27} $\mathrm{cm}^{-2}\mathrm{s}^{-1}$. Until now, the LHC has collided protons at $\sqrt{s} = 7$ TeV in 2010-2011, $\sqrt{s} = 8$ TeV in 2012, and $\sqrt{s} = 13$ TeV in 2015-2017.

The protons used in the collisions are obtained from ionised hydrogen atoms, once

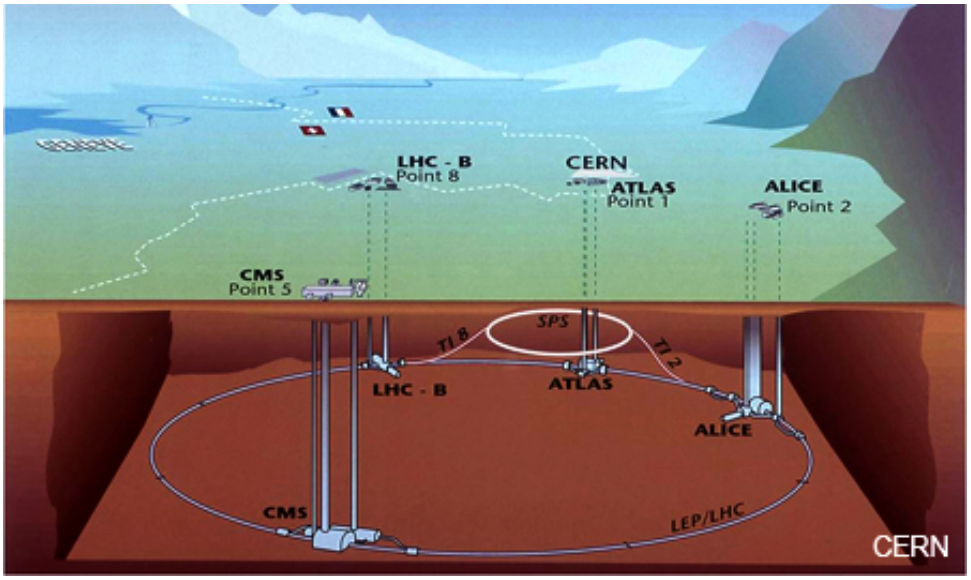

Figure 2.1: *Schematic view of the LHC collider. The collider is built 100 m underground and there are 4 access points to the main experiments (ALICE, ATLAS, CMS, LHCb).*

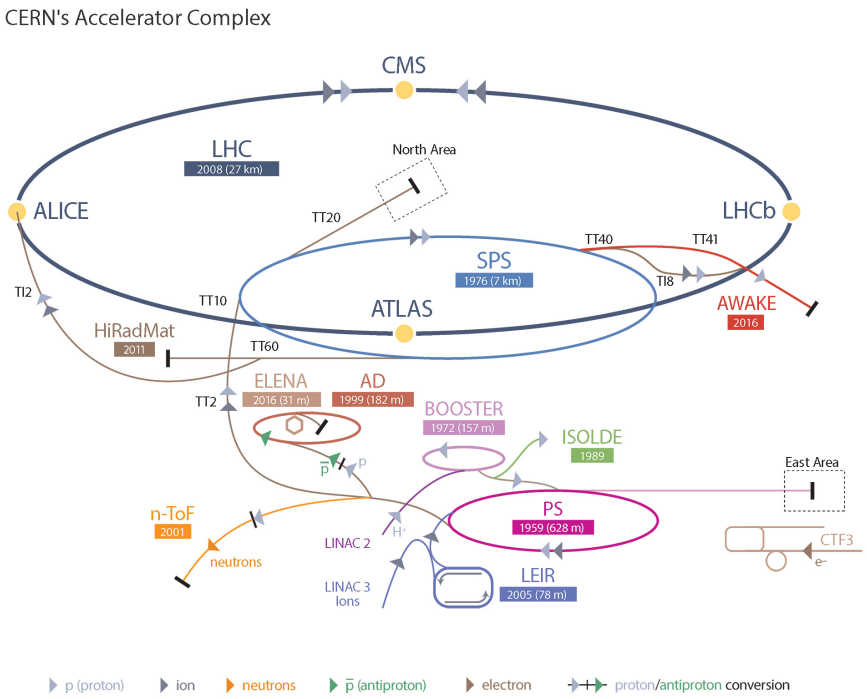

Figure 2.2: *Scheme representing the various machines employed to pre-accelerate the protons that will be injected in the LHC.*

their electrons have been stripped off. As it is not possible to directly accelerate protons from their quasi-rest conditions up to the required energy, it is necessary to pre-accelerate them through a complex of machines, represented in Fig. 2.2. Firstly, protons are injected in Linac2, a linear accelerator that provides the Proton Synchrotron Booster (PSB) with proton bunches of 50 MeV energy. The PSB can accelerate protons at energies up to 1 GeV; after this, the particles are injected in the Proton Synchrotron (PS), where they reach an energy of 26 GeV. Then, the PS delivers the protons to the Super Proton Synchrotron (SPS), where they are accelerated for the last time up to an energy of 450 GeV, before being injected into the LHC via two tunnels, called T12 and T18, shown in Fig. 2.2.

Once in the collider, the protons are kept in their orbits thanks to a magnetic field with an intensity of 8.34 T. To reach such a strong magnetic field it is mandatory to use superconducting magnetic dipoles, that operate at a temperature of 1.9 K (-271.3°C). At the nominal operation regime, the LHC rings store 2808 proton bunch per ring, each of them containing 1.1^{11} protons and colliding with a frequency of 40 MHz (*i.e.* the bunches collide every 25 ns). The LHC has performed very well during Run 1 and Run 2, allowing the LHCb experiment to collect more than 7 fb^{-1} of integrated luminosity (see Fig. 2.3), with an efficiency well over 90%.

It is also important to note that due to the $b\bar{b}$ and $c\bar{c}$ production cross-section dependence on the center-of-mass energy and thanks to several improvements in the LHCb trigger system, the number of b and c decays collected per fb^{-1} is roughly three times

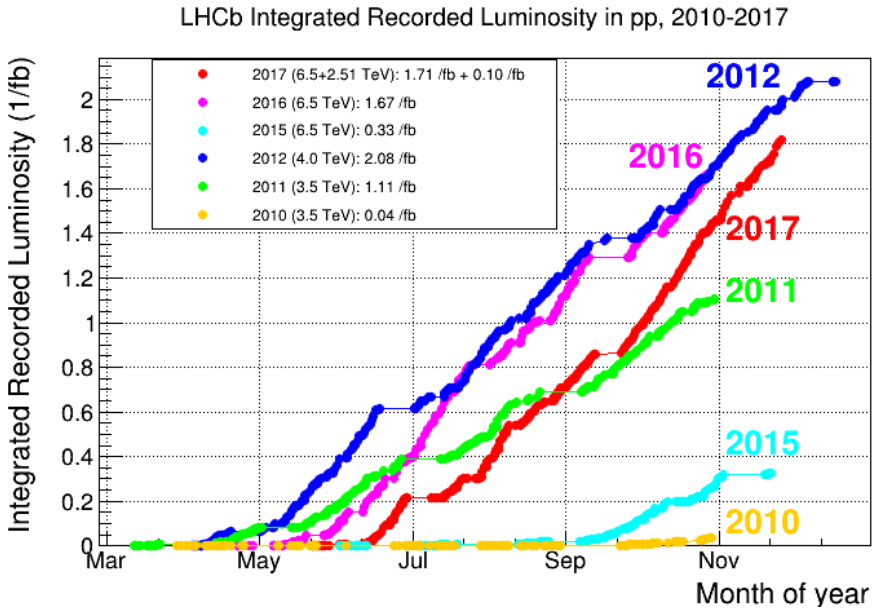

Figure 2.3: *Integrated luminosity recorded by LHCb as a function of the month of the year, divided by years of data taking.*

larger in Run 2 with respect to Run 1 for many decay modes.

Thanks to excellent performance of the LHC and of the LHCb detector, an unprecedented sample of charm and beauty hadrons has been collected. This will allow the LHCb collaboration to perform high precision measurements, improving previous results coming from the BaBar, Belle and CDF Collaborations and possibly allowing the discovery of NP effects.

2.2 The LHCb detector

The LHCb experiment [34] is designed to exploit the great production cross-section of $b\bar{b}$ pairs in pp collision at the LHC center-of-mass energies. The cross-section values are $\sigma(pp \to b\bar{b}X)_{\sqrt{s}=7\text{ TeV}} = (72.0 \pm 0.3 \pm 6.8)\,\mu b$ at $\sqrt{s} = 7$ TeV and $\sigma(pp \to b\bar{b}X)_{\sqrt{s}=13\text{ TeV}} = (154.3 \pm 1.5 \pm 14.3)\,\mu b$ [35] at $\sqrt{s} = 13$ TeV. The same characteristics that allow LHCb to be an ideal experiment for b physics are optimal for the study of c physics as well, also because the $c\bar{c}$ production cross-section is even larger than the $b\bar{b}$ production cross-section, namely $\sigma(pp \to c\bar{c}X)_{\sqrt{s}=7\text{ TeV}} = (1230 \pm 190)\,\mu b$ [36] at $\sqrt{s} = 7$ TeV and $\sigma(pp \to c\bar{c}X)_{\sqrt{s}=13\text{ TeV}} = (2369 \pm 3 \pm 152 \pm 118)\,\mu b$ [37] at $\sqrt{s} = 13$ TeV.

Due to the average imbalance in momentum of two partons that collide during a pp interaction, the b and c quarks are produced strongly boosted along the beam-line. As a consequence, the b and c hadrons at the LHC are produced prominently in the same forward or backward region and with a small angle with respect to the beam direction, as can be seen in Fig. 2.4.

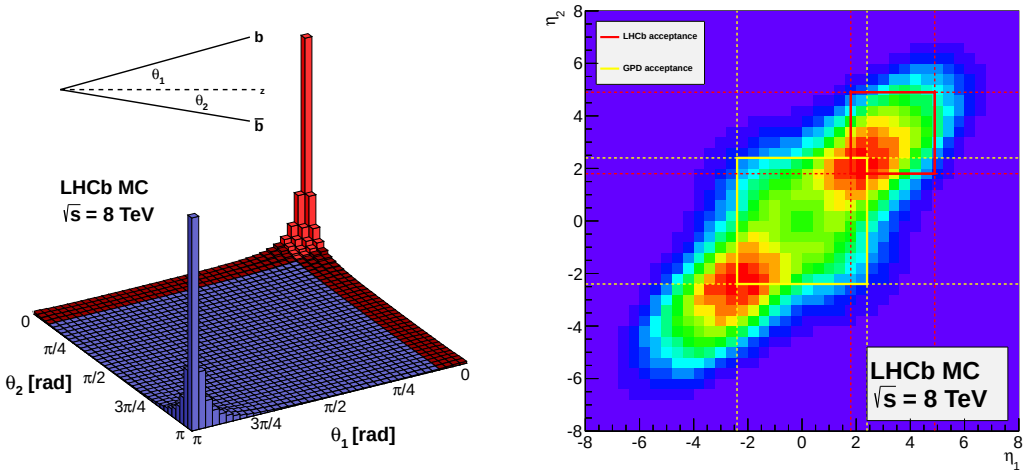

Figure 2.4: *(left) production angles of a $b\bar{b}$ pair with respect to the beam direction and (right) pseudorapidities of the $b\bar{b}$ pair produced in a pp collision as obtained from fully simulated events for a center-of-mass energy of 8 TeV. The LHCb acceptance is highlighted in red in both plots.*

In order to take advantage of this peculiarity, the LHCb detector, in contrast to other LHC detectors, is designed as a forward spectrometer, as can be seen in Fig. 2.5. The LHCb detector geometrical acceptance lies between 10 and 300 *mrad* in the horizontal plane and between 10 and 250 *mrad* in the vertical plane: the difference in the acceptances is justified by the fact that the horizontal plane is also the bending plane for the charged particles deflected by the dipole magnetic field of LHCb. Therefore, the detector can measure particles that lie in a pseudo-rapidity[1] (η) range between 1.8 and 4.9.

[1]The pseudo-rapidity is defined as

$$\eta = -\ln\tan\left(\frac{\theta}{2}\right) = \frac{1}{2}\ln\frac{|\vec{p}|+p_L}{|\vec{p}|-p_L}$$

where θ is the angle between the particle and the beam axis and p_L is the longitudinal momentum.

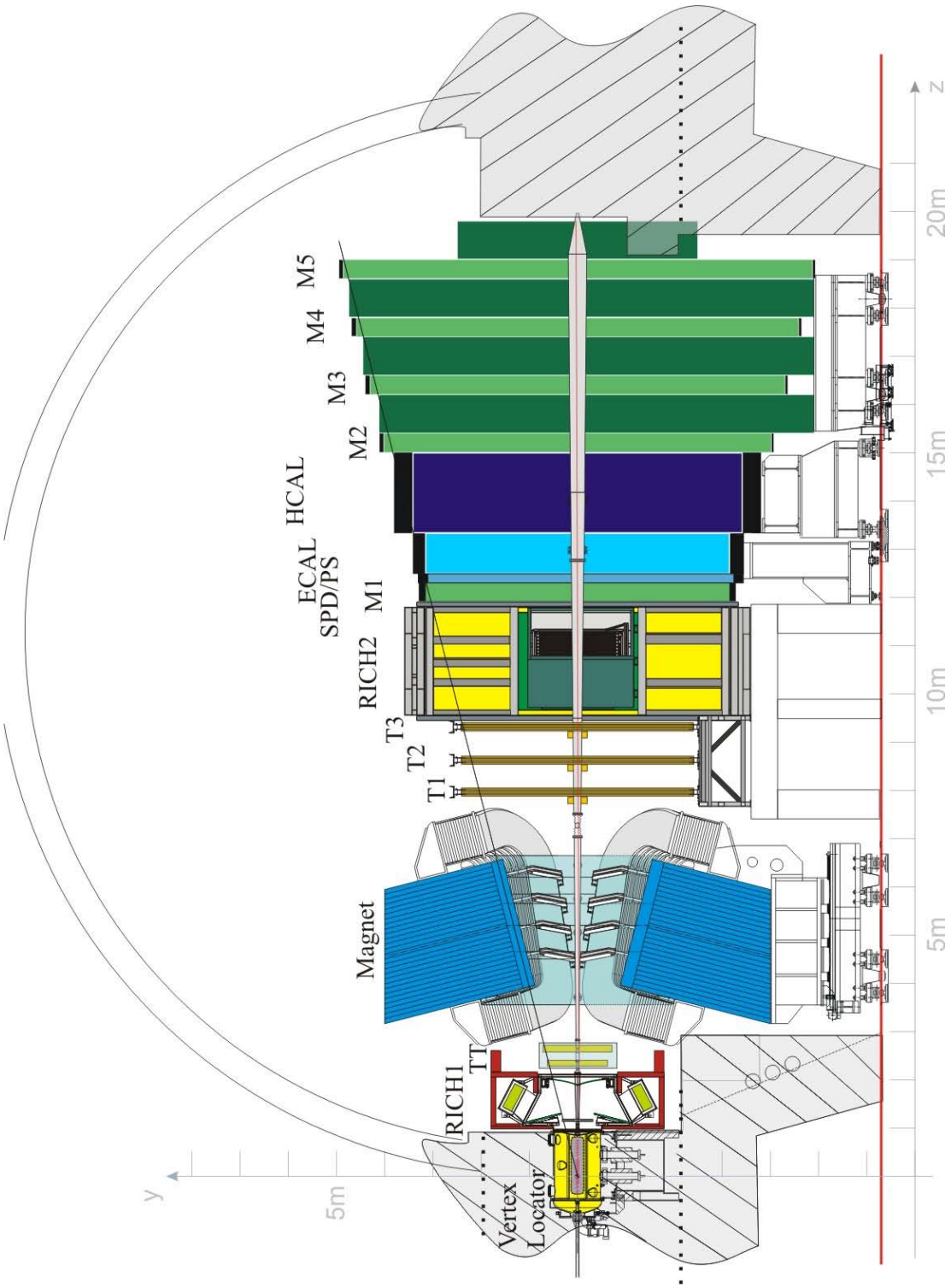

Figure 2.5: *Scheme representing the LHCb detector. From left to right all the sub-detectors are visible: VELO, RICH1, TT, Magnet, Tracking Stations, RICH2, Electromagnetic Calorimeter (ECAL), Hadronic Calorimeter (HCAL) and Muon Stations (M1-M5)*

2.3 LHCb tracking systems

2.3.1 VELO

Non excited beauty and charm hadrons revealed in LHCb flight about 1 cm before decaying and so a distinctive feature of these decays is the presence of a secondary vertex well displaced from the *pp* primary vertex (PV). For this reason and also due to the high track multiplicity in LHC collisions, it is imperative to have a vertex locator with a micro-metric precision in order to select signal events while rejecting most of the background [38]. The VELO is composed by 21 circular silicon modules, installed perpendicularly along the beam line, as shown in Fig. 2.6. Each silicon modules is divided in two halves, to allow the positioning of the VELO during the data taking phase (closed) or during the beam stabilisation phase (open), as can be seen in the bottom part of Fig. 2.6. For this reason, the modules are installed on a movable device placed inside a vacuum vessel; it is important to note that the two halves of a module partly overlap in the closed VELO configuration (as shown in the bottom left part of Fig. 2.6), in order to achieve a better geometrical coverage. The modules are composed by two 220 μm thick silicon micro-strip sensors planes able to measure the distance from the beam (R sensors) and the polar angle (Φ sensors) of hits generated by the ionising particles that cross the VELO. The third coordinate z is simply measured knowing what modules give a signal for a particular particle hit.

The structure of such R and Φ sensors is reported in Fig. 2.7. The R sensors are divided into four parts per halve, each one covering about 45°. The micro-strips composing these parts are modelled in a semi-circular shape and their width increases as the distance from the beam axis becomes greater, since the particles occupancy is greater near it (*i.e.* in high η regions). The micro-strips width ranges from 40 μm near the center to 92 μm far from the beam.

The Φ sensors are divided in an inner and in an outer region. The latter starts at a radius of 17.25 mm and its pitch is set to be roughly half (39.3 μm) that of the inner region (78.3 μm), which ends at the same radius. Inner and outer regions have different skew to the radial direction to improve pattern recognition: they are tilted by 20° and 10° respectively. Furthermore, to improve the track reconstruction, the longitudinally adjacent Φ sensors have opposite skew to each other.

The performances of the VELO detector [39] have been analysed using the the data collected in Run 1. For 2011 data it was found that a 25-track vertex has a resolution in the transverse plane of 13 μm, while the resolution in z is 71 μm, as shown in Fig. 2.8.

The impact parameter (IP)[2] resolution is also measured. Particles that have a decay vertex displaced from the primary vertex, *i.e.* B and D mesons decays, have larger IPs with respect to particles produced near the PV. Therefore, cuts on the IP are very effective in rejecting prompt backgrounds in a given data set. For this reason it is important the IP is measured with the best precision possible. We report in Fig. 2.9 the IP resolution

[2]The IP of a track is defined as the distance between the track and the PV at the track's point of closest approach to the PV.

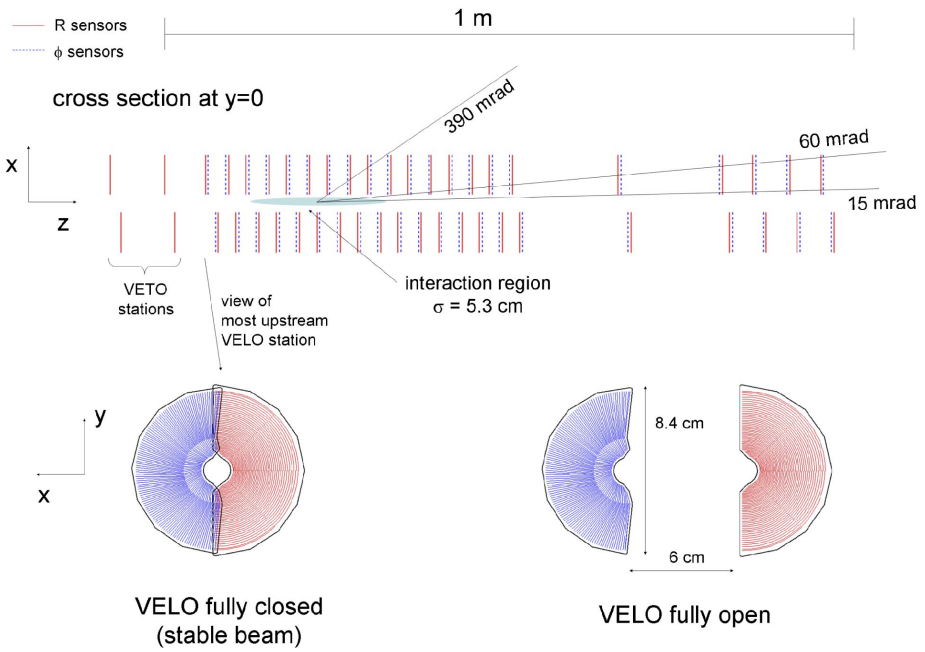

Figure 2.6: *(top) Top view of the VELO and (bottom) frontal view of the VELO in (left) open and (right) closed position, respectively. The R sensors are represented in red while the Φ sensors are drawn in blue.*

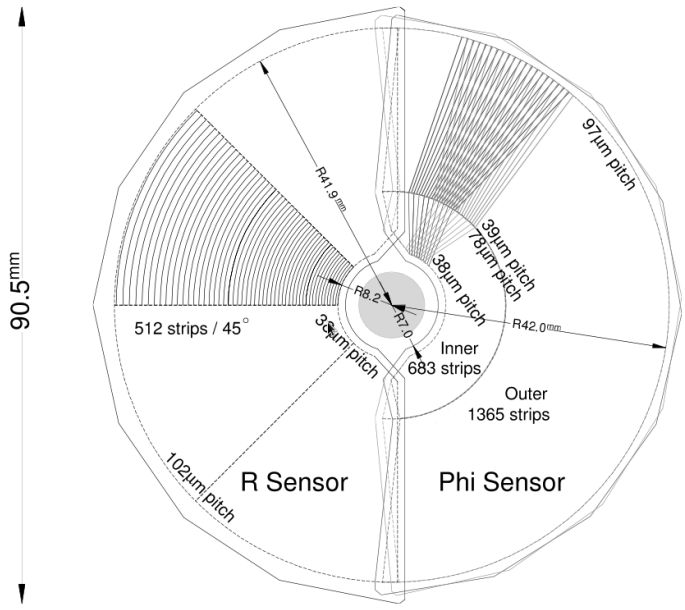

Figure 2.7: *Geometry of the (left) R and (right) Φ sensors of the silicon modules composing the VELO. For completeness, two adjacent Φ modules are drawn in the right part of the figure, to show their opposite skewness.*

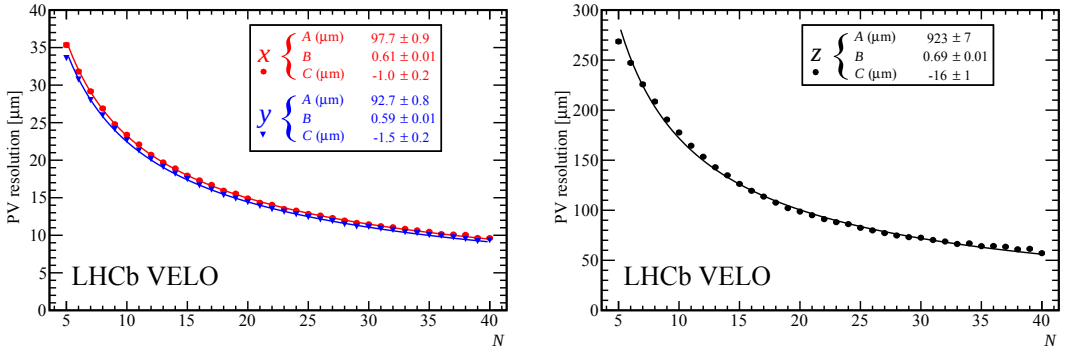

Figure 2.8: *The primary vertex resolution for events with one reconstructed primary vertex, as a function of track multiplicity. (left) The x (red) and y (blue) resolutions are separately shown. (right) The z resolution is shown.*

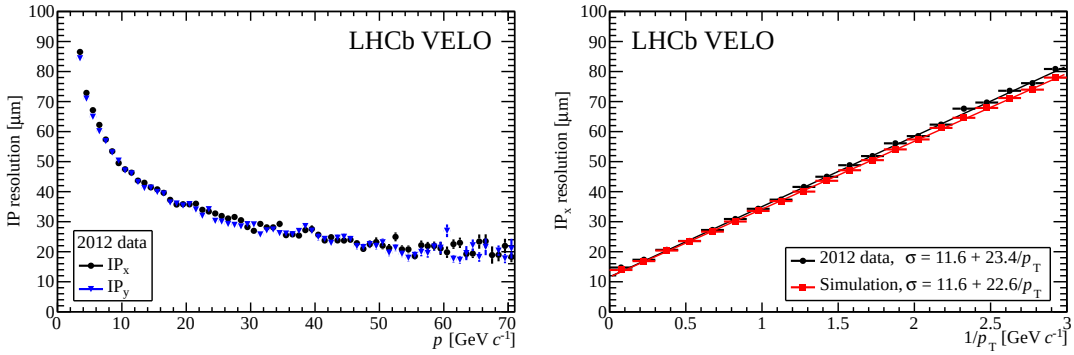

Figure 2.9: *(left)* IP_x *and* IP_y *as a function of the particle momentum and (right)* IP_x *as a function of* $1/p_\mathrm{T}$.

as a function of the particle momentum and $1/p_\mathrm{T}$. The IP resolution along the x and y direction are almost identical and it is asymptotic at high p_T, tending to ~ 12 μm. Also, an excellent agreement between simulation and data is found.

2.3.2 Tracker Turicensis

The Tracker Turicensis is placed after the first Ring Imaging Cherenkov detector RICH1 and before the magnet. The TT task is to provide reference segments used to combine the track reconstructed in the tracking stations with those reconstructed in the VELO, in order to improve the momentum and coordinate resolution.

The system is composed by four stations, divided in two groups called respectively TTa and TTb, at a distance of about 30 cm one from the other and placed approximately 2.4 m after the beam interaction region. A detailed scheme of this sub-detector is shown in Fig. 2.10. Each one of the four stations covers a rectangular region of about 120 cm in height and 150 cm in width. A TT detector layer is composed of silicon micro-strip

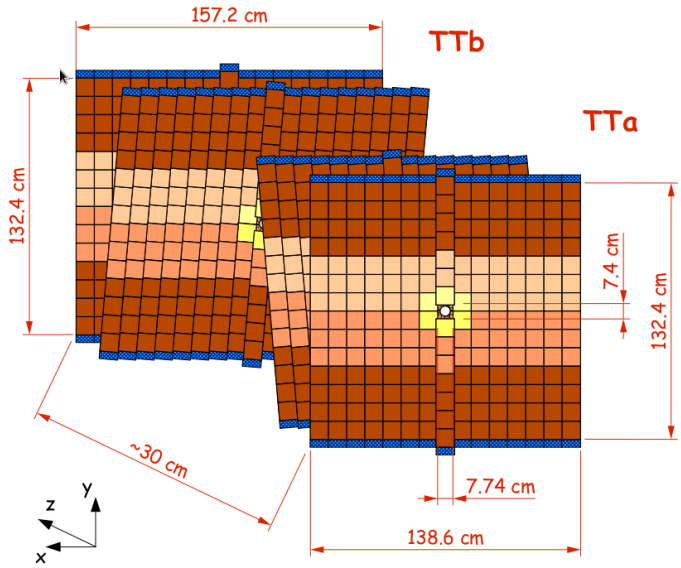

Figure 2.10: *Tracker Turicensis illustration. The first and fourth stations (x-plane) have sensors parallel to the vertical plane, while the second and third stations (called u-plane and v-plane) have sensors tilted by +5° and -5°.*

sensors with a 183 µm pitch, arranged in readout strips up to 38 cm long, to keep the number of readout channels low. In the first and fourth stations the strips are parallel to the vertical plane (x-layer), while in the second and third stations they are tilted by +5° (u-layer) and -5° (v-layer), respectively. This is done to improve the precision of the track reconstruction.

The intrinsic hit efficiency of the silicon sensors can be measured using reconstructed tracks to probe whether or not the expected hits on a track are found. This efficiency is given by the ratio of the number of hits found in a given sensor and the number of hit expected in the same sensor. For the TT, the overall hit efficiency is measured to be greater than 99.7%. Another important quantity to assess the TT performance is the hit resolution, *i.e.* the the residuals between the measured hit position and the extrapolated track position. The residual is evaluated by removing the hit from the track fit and calculating the distance between the hit and the extrapolated track position. The resolution is given by the spread of the residual distribution after correcting for the uncertainty in the track parameters and it is shown in Fig. 2.11. The average hit resolution for 2011 data is 52.6 µm.

2.3.3 Tracking stations

The three tracking stations T1, T2 and T3 are placed behind the magnet. They are divided in two main parts, depending on the distance from the beam pipe. The inner part of the tracking stations is called Inner Tracker, while the outer part is called Outer

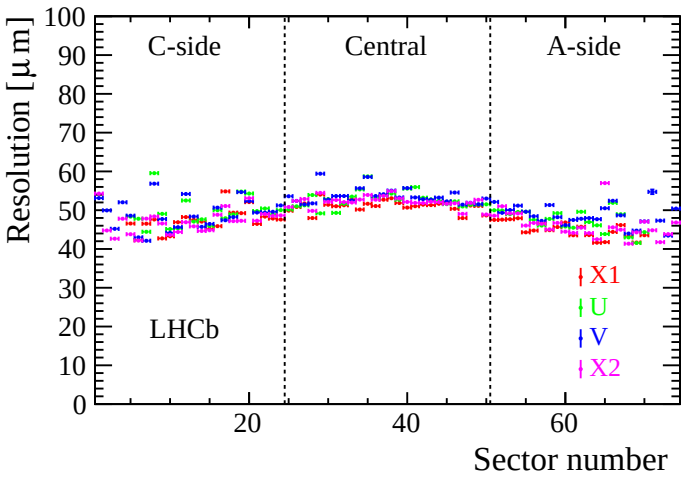

Figure 2.11: *Hit resolution measured for all the four sensors composing the Tracker Turicensis. The labels X1, U, V and X2 correspond to the four detection layers arranged with an* $(x-u-v-x)$ *geometry in the TT box.*

Tracker. They adopt different technologies to detect the particles: the IT is composed by silicon micro-strip sensors, while the OT is made of drift straw tubes.

The Inner Tracker [40] covers the region around the beam pipe and it is arranged in a cross-shaped geometry, that grants optimal coverage while conserving surface; each station consist of four independent boxes arranged as shown in Fig. 2.12. Each box is composed by four planes, as for the TT. The first and fourth planes of the IT have the sensors parallel to the vertical plane (x-layer), while the second and the third planes have the sensors tilted by $+5°$ (u-layer) and -5° (v-layer). The side boxes have to two ladders of micro-strips, with those of the lower sensor connected in series with those of the upper sensor to a single readout channel, while the top and bottom boxes have only one micro-strips ladder. The total IT size is about 1.2 m in the bending plane and about 40 cm in the vertical plane.

The overall hit efficiency for the inner tracker is measured to be greater than 99.8% with an average hit resolution of 50.3 μm. The resolution measured with 2012 data as a function of the sector number is shown in Fig. 2.13.

The Outer Tracker [41] is a gas-filled straw tube detector, covering about 99% of the summed surface of the T1-T3 tracker stations. For each tracking station there are four planes of straw tubes arranged in the same way as the TT and IT silicon micro-strip sensors: the first and the fourth have the tubes parallel to the vertical plane (x-layer), while the second and the third have the tubes tilted by $+5°$ (u-layer) and -5° (v-layer). Moreover, each plane is composed of two rows of tubes, arranged in a honeycomb structure, as shown in Fig. 2.14. The straw tubes have a radius of 5 mm and are filled with a mixture of $Ar/CF_4/CO_2$ gases. At the tube ends, locator pieces support and center the anode wire with a precision better than 100 μm.

Unlike other tracking detectors here described, the OT measures drift times rather

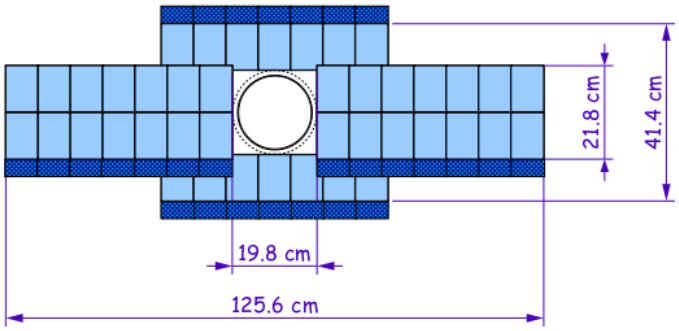

Figure 2.12: *Inner Tracker layer with vertically oriented micro-strip sensors. The four boxes are arranged around the beam pipe and the individual sensors inside the boxes are visible. The deep blue part of each box represents the readout plugs. For completeness, the dimensions of the IT are also reported.*

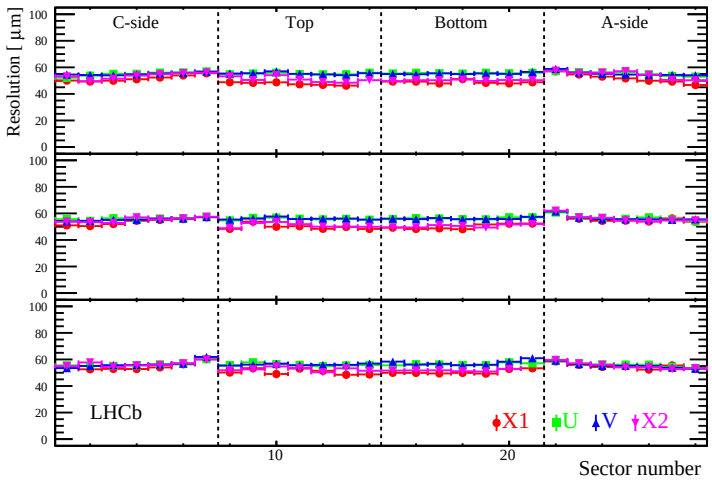

Figure 2.13: *Hit resolution measured for modules in (bottom) IT1, (middle) IT2 and (top) IT3. The labels X1, U, V and X2 correspond to the four detection layers arranged with an* $(x-u-v-x)$ *geometry in the each box.*

than pulse heights. The maximum drift time in the straw tubes is about 35 ns, but to account for variations of the time-of-flight of the particles, the signal propagation time through the wire, and variations in time offset constants in the electronics, three bunch crossings are read out upon a positive L0 trigger on the first bunch crossing, corresponding to a time window of 75 ns. The contribution from earlier and later bunch crossings is visible in the drift time spectrum, shown in Fig. 2.15. The average hit efficiency for tracks in the central half of the straw, *i.e.* close than 1.25 mm to the wire, corresponds to 99.2%. The single hit resolution is obtained by comparing the predicted hit position from the track with the hit position obtained from the drift-time. The resulting resolution is found to be 205 µm, near the design value of 200 µm.

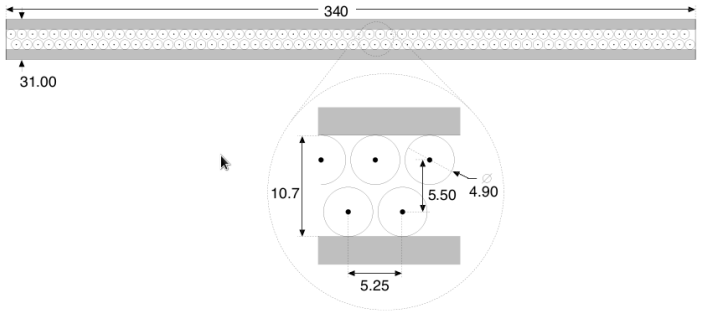

Figure 2.14: *Cross-section of a straw tube plane. The zoomed part shows the honeycomb structure of the two rows of tubes. For completeness, the dimensions (in mm) of the straw tube plane are also reported.*

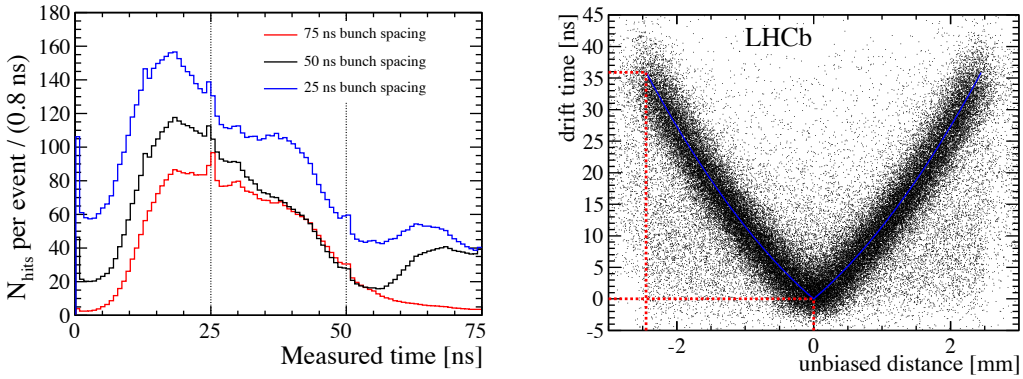

Figure 2.15: *(left) Drift time distribution for the modules located closest to the beam (M8) and (right) drift time versus distance relation. The red-dotted lines indicate the centre and the edge of the straw, corresponding to drift times of 0 and 36 ns, respectively.*

2.3.4 Magnet

All modern experiments measure particle momenta through the curvature in a given magnetic field. For this reason, the LHCb detector is provided with a warm (*i.e.* non super-conducting) magnet dipole placed between the TT and the first tracking station T1 [42]. The magnet geometry has been chosen considering the detector acceptance: in fact, the magnet is formed by two coils shaped in a particular way, in order to become wider as the z coordinate increases. The magnetic field is oriented along the y coordinate, perpendicular to the $x - z$ plane, referred to as the bending plane. In Fig. 2.16 the y component of the magnetic field is reported as a function of the z coordinate and it can be seen that the maximum intensity of the magnetic field is about 1 T, while the magnetic field integral is 4 Tm.

During the data taking, the polarity of the magnetic field is flipped several times, in order to allow the evaluation of any left-right asymmetry in the detector. Indeed, since positive and negative charged particles are bent to opposite directions by the magnetic

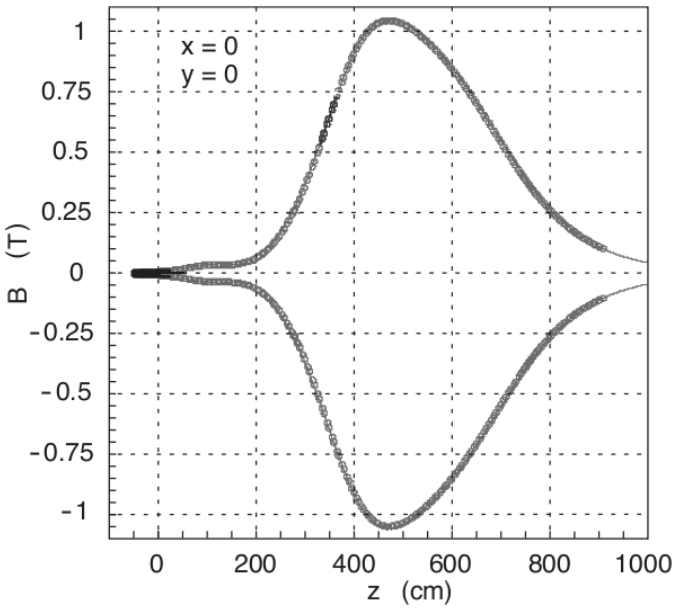

Figure 2.16: *Magnetic field generated by the warm magnetic dipole as a function of the z coordinate. From the plot it is evident that the maximum reached intensity is about 1 T.*

field, any variation in the detection efficiency between the left and the right part of the detector could affect *CP* asymmetry measurements.

2.3.5 Track reconstruction performance

The trajectory of the charged tracks leaving hits in the VELO, TT, IT and OT can be reconstructed using specific algorithms. Depending on their path the tracks are divided in the following categories

Long tracks: these tracks leave hits in all the tracking sub-detectors. Since there are hits in the full tracking system, these tracks have the most precise momentum determination of all tracks and they are therefore the most important tracks for physics analyses.

Upstream tracks: these tracks leave hits only in the VELO and TT. Usually these tracks correspond to low momentum particles that are swept outside the LHCb acceptance by the magnetic field before reaching the tracking stations. However, these tracks pass through the RICH1 and can emit Cherenkov photons if their momentum is greater than 1 GeV/c, thus allowing to perform background-related studies for the RICH sub-detectors.

Downstream tracks: these tracks leave hits only in the TT and tracking stations. Generally, these tracks are generated by the decays of long lived particles, such as

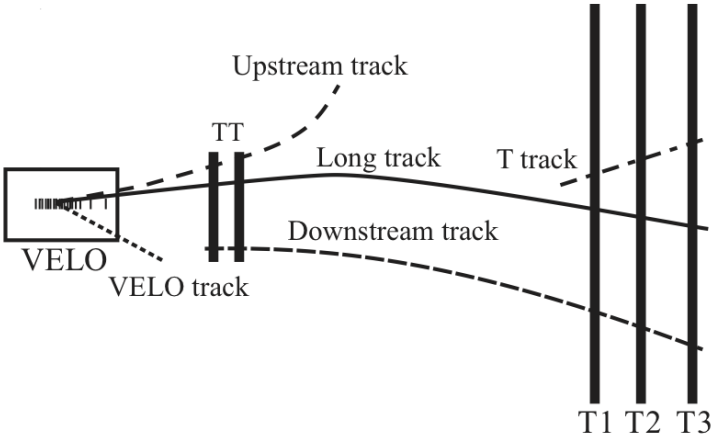

Figure 2.17: *Schematic representation of the different kind of tracks that are reconstructed in LHCb.*

K_S^0 and Λ, that can decay outside the VELO. These tracks are used for physical analysis and detector studies.

VELO tracks: these tracks leave hits only in the VELO. Typically they are generated by large-angle or backward travelling particles.

T tracks: these tracks leave hits only in the tracking stations. Normally, these tracks are generated by secondary interaction and can be used for RICH2 studies.

In Fig. 2.17 a pictorial representation of the different types of tracks that can be reconstructed by the LHCb detector is shown.

Track finding and reconstruction are organised in different steps. The first starts with the definition of segments in the various sub-detectors. Inside the VELO, segments are created matching all hits that lie on a straight line, whereas in the tracking stations a segment is created by matching the hits contained in a section of the first and third station (*e.g.* in the left corner on these two stations) and by using the information given only by one plane of vertically oriented micro-strip sensors. Then, under the hypothesis of a parabolic trajectory, the algorithm calculates the position of the hit in the middle stations and searches for compatible hits. If a signal is found, it is added to the segment and it is used to better determine the parameters of the trajectory. Finally, compatible hits coming from the u-plane and the v-plane are also added, in order to have a 3-dimensional segment.

The reconstruction process is organised in a hierarchical way: the algorithm tries firstly to reconstruct long tracks and then it picks up unused segments to reconstruct downstream and upstream tracks. Long tracks are reconstructed with two algorithms: the first extrapolates VELO segments to the tracking stations, adding to the track the compatible hits in the TT. The second matches VELO and tracking stations segments one to each other, extrapolating VELO segments in the forward direction and tracking stations

segments in the backward direction. Downstream tracks are reconstructed starting from T stations segments and then adding the compatible hits in the TT to those segments. Upstream tracks are obtained extrapolating VELO segments to the Trigger Tracker, adding compatible hits and requiring a non compatibility with any of the tracking station segments. Finally, a bi-directional Kalman filter is applied to better determine the track parameters and then a clone killer compares the reconstructed tracks, two by two. If a pair of tracks shares more than a fixed percentage of hits they are considered clones and only that with more hits (or the best χ^2) is stored.

Track finding efficiency is defined as the probability that the trajectory of a charged track leaving hits in the full tracking system is reconstructed. This efficiency can be measured by means of a tag-and-probe technique with $J/\psi \rightarrow \mu^+\mu^-$ decays. In this method, the *tag* leg, one of the two daughter particles, is fully reconstructed, whereas the *probe* leg, the other daughter, is only partially reconstructed. The tracking efficiency is then obtained by matching the partially reconstructed *probe* with a fully reconstructed long track. If this is possible, then the *probe* is said to be efficient. Two different methods have been used to evaluate the tracking efficiency [43, 44]. As an example, in Fig. 2.18 the results obtained in Ref. [44] are shown: the average tracking efficiency is above 96% in the momentum range 5 GeV/$c < p <$ 200 GeV/c and in the pseudorapidity range $2 < \eta < 5$, which corresponds to the LHCb detector acceptance. The efficiency is slightly lower in 2012 data due to the higher hit multiplicity in the various sub-systems.

2.4 LHCb particle identification systems

2.4.1 RICH1 and RICH2

In order to discriminate between pions, kaons and protons, the LHCb detector employs two Ring Imaging Cherenkov detectors [45]. These sub-detectors are able to discriminate among the different particle hypotheses in a momentum range included between few GeV/c and 150 GeV/c. Cherenkov light detectors exploit the light emitted by particles that travel in a medium faster than the light in the same medium. The relation between the Cherenkov photon emission angle (θ_C) and the refraction index (n) of the radiator is

$$\cos(\theta_C) = \frac{1}{\beta n} \ , \tag{2.1}$$

where $\beta = v/c$ is the particle velocity with respect to the speed of light in vacuum. From this relation, one can notice that Cherenkov light is emitted only by those particles with $c/n < v < c$; in fact, if $v = c/n$ then $cos(\theta_C) = 1$ and so $\theta_C = 0$, while if $v = c$ then $\cos(\theta_C) = 1/n$ and so $\theta_C = \arccos(1/n)$. Thus, it is evident that for particles approaching the speed of light the Cherenkov angle will saturate at the value $\theta_C = \arccos(1/n)$. For these reasons, it is necessary to have different radiators in order to discriminate particles in a wide range of momenta.

RICH1 is optimised to identify tracks with a medium-low momentum, between 1 GeV/c and 50 GeV/c. The structure of the apparatus is reported in the left part of Fig. 2.19. The

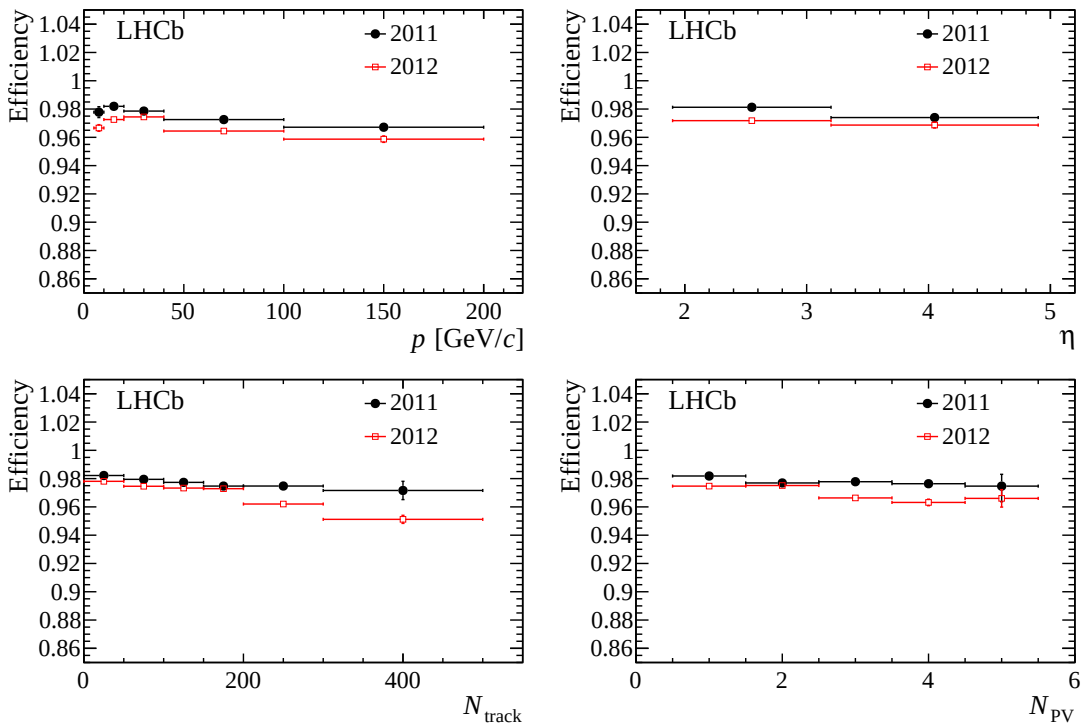

Figure 2.18: *Tracking efficiency as function of (top left) momentum, (top right) pseudorapidity, (bottom left) number of tracks in the event and (bottom right) number of reconstructed primary vertices for 2011 and 2012 data.*

RICH1 is placed immediately after the VELO and its geometrical acceptance (between 25 $mrad$ to 330 $mrad$) is enough to cover practically the whole LHCb detector acceptance. There are two different types of radiators inside RICH1: the first is a 5 cm thick Aerogel layer, with $n = 1.03$, suitable for low momentum particles, while the second, gaseous C_4F_{10} ($n = 1.0015$), fills the remaining part of the detector and is employed to detect particles with higher momenta (up to 50 GeV/c).

RICH2 is placed behind the last tracking station and its geometrical acceptance, 120 $mrad$ in the vertical plane and 100 $mrad$ in the horizontal plane, covers the region of the detector where most of high momentum particles are found. The radiator chosen for this sub-detector is gaseous CF_4, with a refraction index $n = 1.00046$, optimal for the higher momentum region, up to about 150 GeV/c.

The Cherenkov photons emitted in both detectors are conveyed, through a system composed of spherical and plane mirrors, onto a lattice of photo detectors, the Hybrid Photon Detector (HPD). The HPD's are placed in both the RICH sub-detectors outside the LHCb detector acceptance and they are shielded against the residual magnetic field (this is particular important for RICH1, because in this region of the detector the residual magnetic field is not negligible). The shielding is necessary in order to allow the HPD's to operate properly: indeed, the photo-electrons created in the photomultipliers would be bent by the residual magnetic field and this could reduce the HPD's performances. This

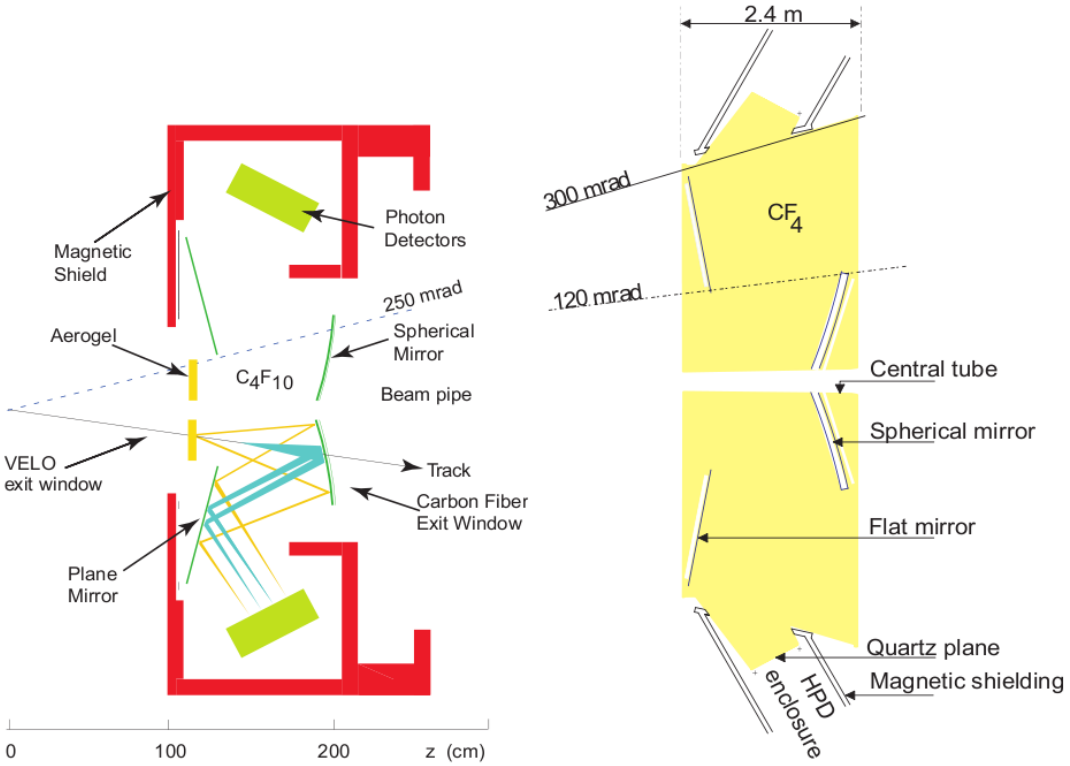

Figure 2.19: *Left: schematic view of the RICH1 sub-detector. It is relevant to note the different Cherenkov photon emission angles of the Aerogel (yellow) and C_4F_{10} (light blue) radiators. Right: schematic view of the RICH2 sub-detector, filled with CF_4 gas.*

configuration allows to have optimal results with signal's rise and fall times ~ 1 *ns*.

RICH detectors are able to discriminate between the various mass hypotheses for a given particle. Indeed, as shown in Fig. 2.20, the photon emission angle is related to the particle mass and to its momentum. Moreover, since the emission covers the full solid angle, we expect to see rings on the HPD plane, with radius proportional to θ_C. The hits on the HPD plane will be distributed around a particular radius value (that corresponds to the Cherenkov emission angle); anyway, due to resolution effects, the distribution will be smeared around the central value. Measuring the photons hit positions, it is then possibile to obtain a value of θ_C for each particle, allowing us to discriminate between the various mass hypotheses.

Due to an irreducible background, given by photons coming from other particles, and due to the complexity of the problem, the following approach has been chosen to achieve the best particle discrimination. For a given set of mass hypotheses, the probability for a single photon to be detected on a single HPD pixel is computed; then, the expected contribution from all sources is compared with the observed number of photons and a likelihood is calculated (the change in the likelihood value depends only on the mass hypotheses assigned to the tracks). Only five mass hypotheses are considered for the

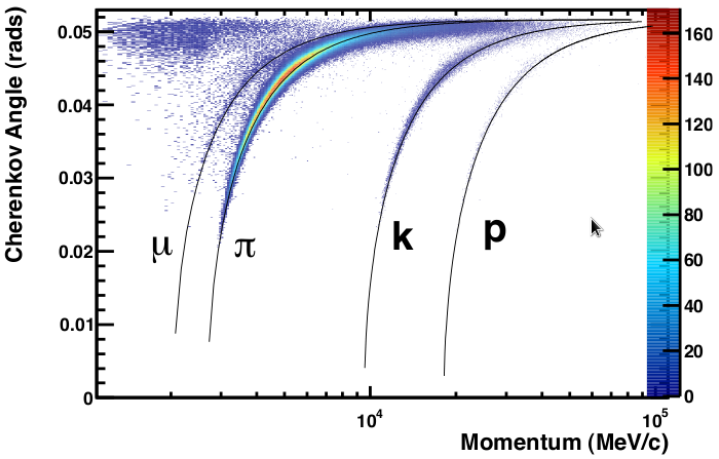

Figure 2.20: *Cherenkov photons emission angle as a function of the particle momentum. The theoretical value (solid line) is superimposed to the experimental results.*

tracks detected: electron, muon, pion, kaon and proton. Since the computation of the likelihood for all tracks would be unfeasible, a different approach is adopted. In fact, the pion mass-hypothesis is used for all the tracks detected and a first global likelihood is computed. Then the hypothesis is changed to e, μ, K and p for one particle at a time and the change in the global likelihood is computed. The chosen mass hypotheses is the one that returns the maximum improvement in the global likelihood. This process is repeated for all tracks, until no improvement is observed in the likelihood value.

The discriminating variable is the so called $\Delta \log \mathcal{L}$. For example, $\Delta \log \mathcal{L}_{K-\pi}(h)$ is the difference between the logarithm of the likelihood under the K and π hypothesis for the particle h:

$$\Delta \log \mathcal{L}_{K-\pi}(h) = \log \mathcal{L}_K(h) - \log \mathcal{L}_\pi(h) \ . \tag{2.2}$$

A large positive value of $\Delta \log \mathcal{L}_{K-\pi}(h)$ corresponds to a high probability that the particle h is a kaon, while a large negative value of $\Delta \log \mathcal{L}_{K-\pi}(h)$ corresponds to a high probability that the particle h is a pion. In Fig. 2.21 we show the $\Delta \log \mathcal{L}_{p-\pi}$ *vs.* $\Delta \log \mathcal{L}_{K-\pi}$ distributions for pions, kaons, and protons [46].

The efficiency of this discriminating method has been widely studied using real data samples with high purity final states selectable only using kinematical cuts, due to their particular kinematic characteristics *e.g.* $K^0_S \to \pi^+\pi^-$, $\Lambda \to p\pi^-$, $D^{*+} \to D^0(K^-\pi^+)\pi^+$, without using the RICH sub-detectors.

The performance of the $\Delta \log \mathcal{L}$ variables are also shown in Fig. 2.22, where the identification efficiency (for correctly identified particles) and mis-identification rate (for wrongly identified particles) are plotted as a function of the track momentum. For example, a 95% kaon identification efficiency can be achieved with a 10% pion mis-identification rate imposing a $\Delta \log \mathcal{L}_{K-\pi} > 0$ requirement. Requiring $\Delta \log \mathcal{L}_{K-\pi} > 5$, one can obtain a 85% kaon efficiency for a 3% pion mis-identification fraction. This demonstrates the

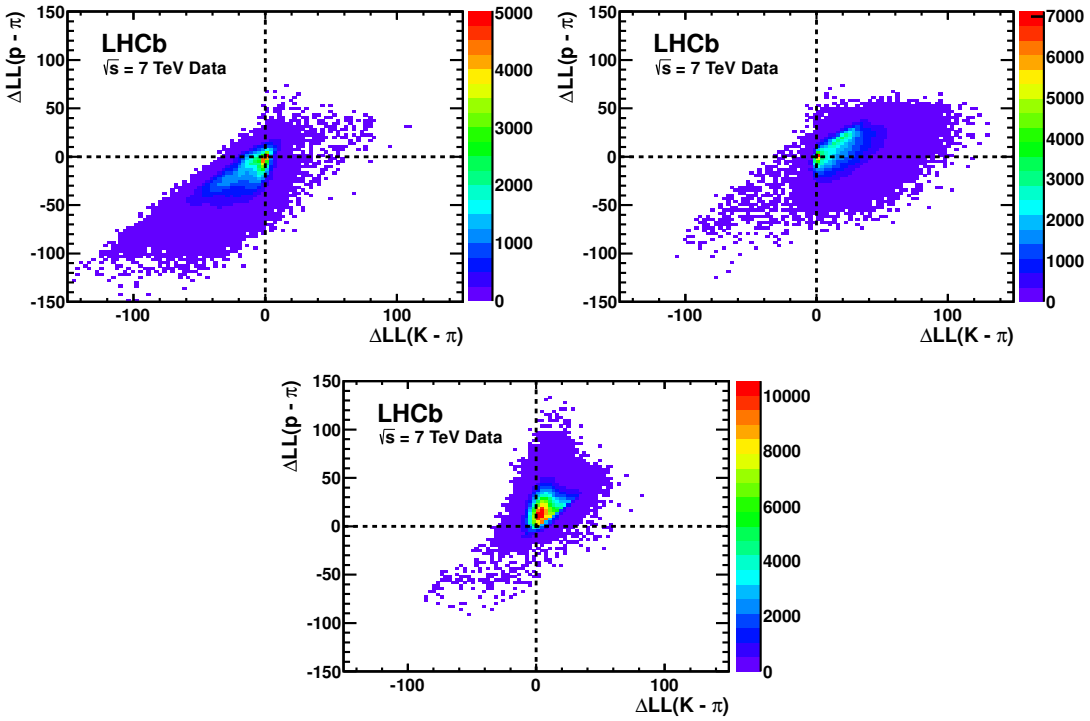

Figure 2.21: *Distribution of* $\Delta \log \mathcal{L}_{p-\pi}$ *against* $\Delta \log \mathcal{L}_{K-\pi}$ *for (top left) pions, (top right) kaons and (bottom) protons.*

excellent performance of the LHCb RICH system.

2.4.2 SPD, PS, ECAL and HCAL

The calorimeter system [47] is employed to measure particles energies, allowing the LHCb detector to efficiently discriminate between $e^{\pm}$, γ and π^0. Moreover, it provides important information for the Level-0 trigger (L0-trigger), by measuring hadron, electron and photon transverse energy (E_{T})[3].
The calorimeter system is composed by four sub-detectors

- Scintillator Pad Detector (SPD);
- Pre-Shower (PS);
- Electromagnetic Calorimeter (ECAL);
- Hadronic Calorimeter (HCAL).

[3]The transverse energy is defined as $E_{\mathrm{T}} = E \sin(\theta)$, where E is the energy measured in the calorimeter and θ is the polar angle of the hits in the calorimeter with respect to the beam pipe.

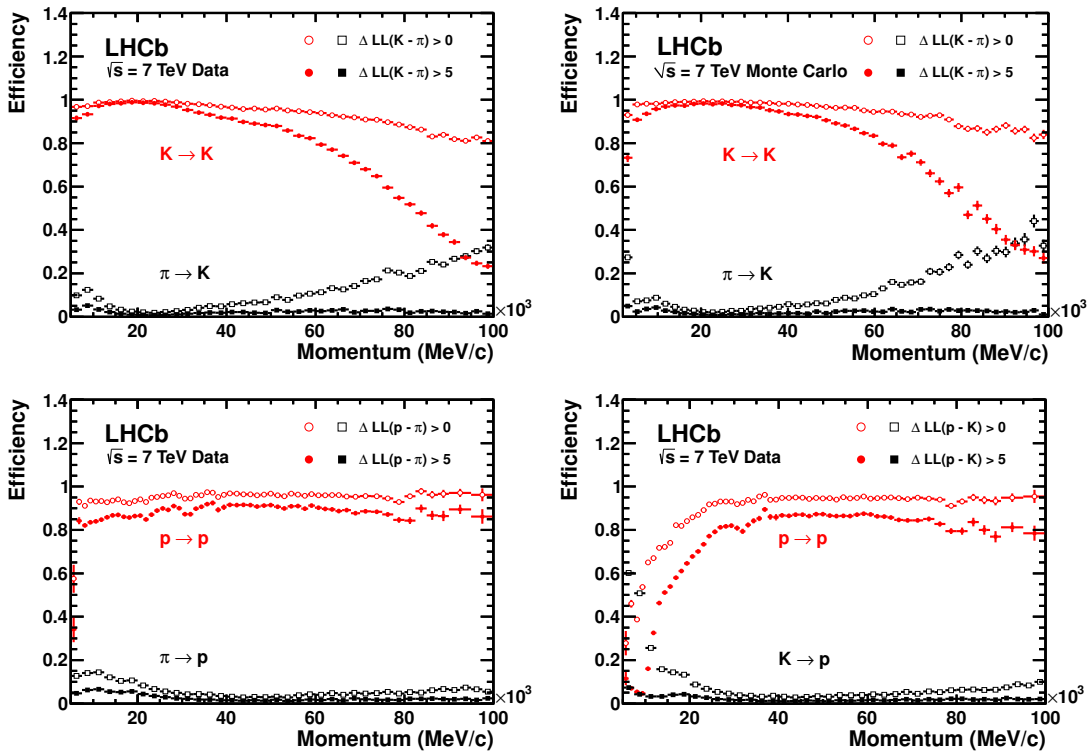

Figure 2.22: *(top) Kaon identification efficiency and pion mis-identification rate as a function of the track momentum for (left) real data and (right) simulated events. (bottom) Proton identification efficiency against (left) pions and (right) kaons. The empty and filled markers represent two different* $\Delta \log \mathcal{L}$ *requirements imposed on the track.*

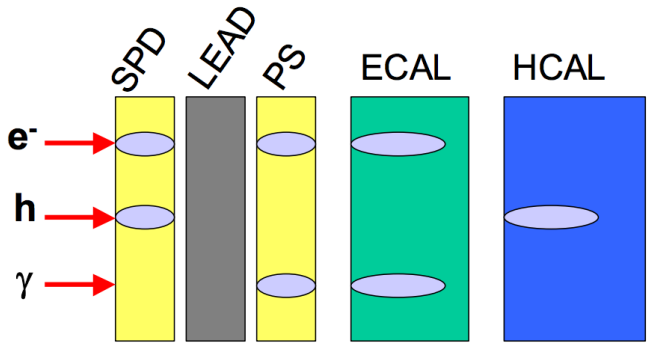

Figure 2.23: *Signal deposited on the different parts of the calorimeter by (top) an electron, (middle) an hadron or (bottom) a photon.*

In Fig. 2.23 we show a schematic representation of the calorimeter system and the interactions of each sub-detector with each type of particle.

Each sub-detector is divided into regions with different dimensions and where differently

sized sensors are used (the smallest sensors, *i.e.* the most precise, are placed in the inner regions, while the biggest are placed in the outer regions). SPD, PS and ECAL are divided in three regions (inner, middle and outer), while the HCAL is divided only in two regions (inner and outer). The sensor size increases as the distance from the beam pipe is greater in order to reach a compromise between occupancy and the number of read-out channels.

The SPD and the PS are the ECAL auxiliary sub-detectors and they are placed in front of it. The SPD is used to discriminate between charged and neutral particles, as the former emits light when crossing a scintillator material while the latter does not. The PS is instead used to obtain a better discrimination between electrons and pions. Both the SPD and the PS consist of scintillating pads with a thickness of 15 mm, interspaced with a 2.5 radiation lengths[4] lead converter. The light produced by the scintillator material is collected using wavelength-shifting fibres (WLS). These fibres are used to transmit the light to multi-anode photomultipliers (MAPMTs) located outside the detector. The SPD and the PS contain about 6000 pads each.

The ECAL is a sampling calorimeter realised using Shashlik technology and separated in independent modules. The Shashlik calorimeters are sampling calorimeters in which the scintillation light is read-out via WLS fibres running perpendicularly to the converter/absorber plates [49]: this technique offers the combination of an easy assembly, good hermiticity and fast time response. A sketch of ECAL is given in Fig. 2.24.

Each ECAL module is composed of 66 lead converter layers (2 mm thick), each one installed between two plastic scintillator layers 4 mm thick. In total, all the layers installed in the ECAL correspond to about 25 radiation lengths and 1.1 nuclear interaction lengths. The WLS fibres bring the light produced by the scintillator material to the read-out photo-multipliers in the back part of the module. The module size and the number of read-out channels differ depending on the region where the module is installed. In the inner region each module has a 4×4 cm^2 section, with 9 read-out channels per module; the middle region contains modules with a 6×6 cm^2 section and 4 read-out channels. Finally, the outer region is composed of 12×12 cm^2 modules with one channel each.

The HCAL main task it to measure the energies of hadronic showers. This information if fundamental for the Level-0 trigger. The HCAL structure is very similar to the ECAL structure, with the difference that each module is composed of scintillator layers 4 mm thick interleaved with steel layers 16 mm thick. This corresponds to roughly 5.6 nuclear interaction lengths in total. In the inner region, modules have a section of 13×13 cm^2, while in the outer region they are 26×26 cm^2. Energy resolutions are given by $\sigma(E)/E = (8.5 - 9.5)\%/\sqrt{E} \oplus 0.8\%$ for ECAL and $\sigma(E)/E = (69 \pm 5)\%/\sqrt{E} \oplus (9 \pm 2)\%$ for HCAL.

[4]The radiation length is defined as

$$X_0 = \frac{A \cdot 716.4\ g/cm^2}{Z(Z+1)\ln(287\sqrt{Z})}$$

where A is the mass number and Z is the atomic number of the material considered. The radiation length corresponds to the distance over which the energy of an electron is reduced by a factor $1/e$ only due radiation loss. For more details see Ref. [48].

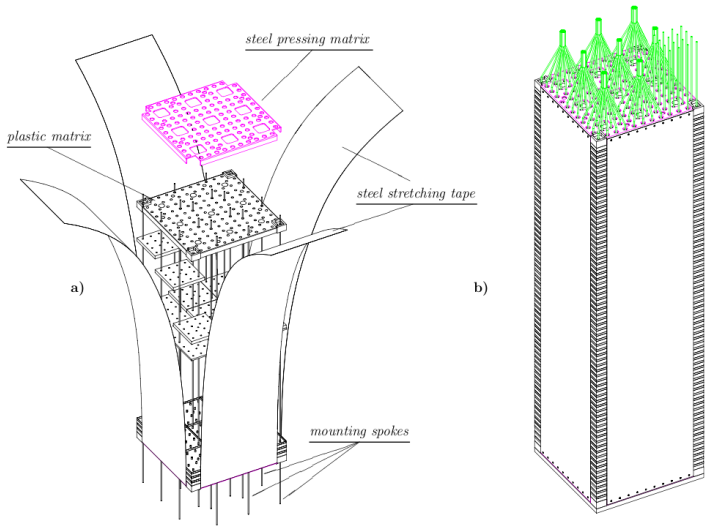

Figure 2.24: *(left) Representation of an ECAL module during the assembly phase. The lead/scintillator layers are clearly visible. (right) Representation of an assembled ECAL module. The green lines connected to an end are the WLS fibres connecting the calorimeter to the photomultipliers.*

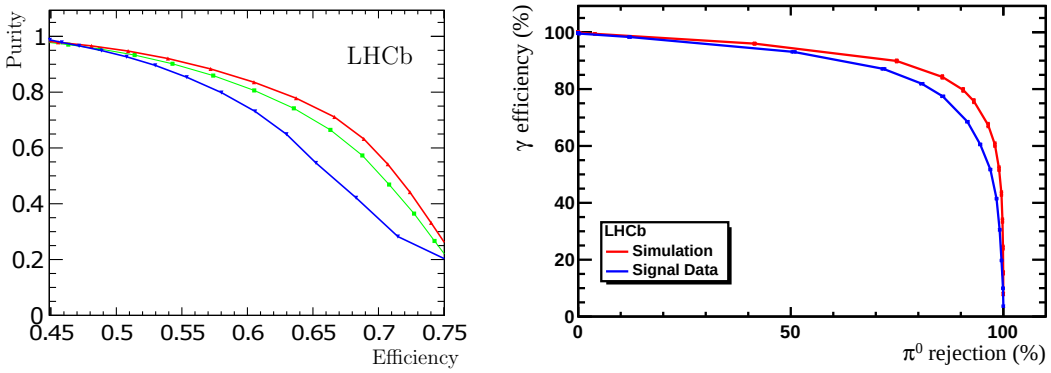

Figure 2.25: *Performance of the photon identification: (left) purity as a function of efficiency for (green) the full photon candidate sample, (blue) converted candidates according to the SPD information and (red) non-converted candidates and (right) photon identification efficiency as a function of π^0 rejection efficiency for the $\gamma - \pi^0$ separation tool for (red line) simulation and (blue line) data.*

The calorimeter system, as already said, is used to discriminate between $e^{\pm}$, γ and π^0. Figure 2.25 shows the photon identification efficiency with respect to the π^0 rejection efficiency for simulation and data.

In order to discriminate between electrons and hadrons, a $\Delta \log \mathcal{L}^{\mathrm{CALO}}{}_{e-h}$ variable is defined as:

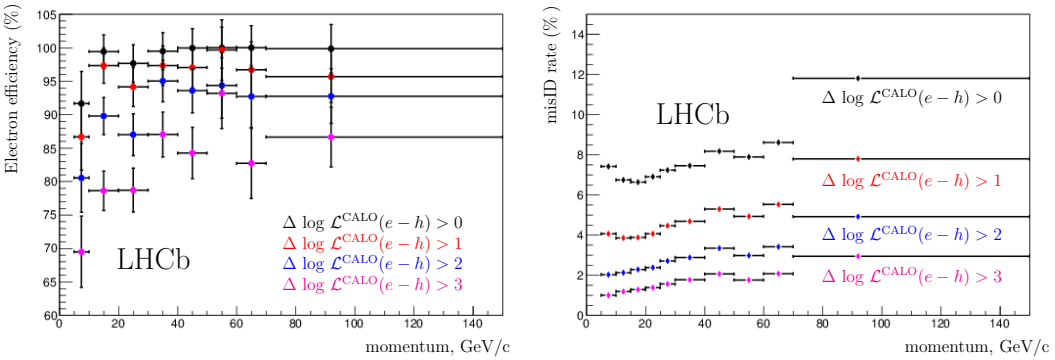

Figure 2.26: *(left) Electron identification efficiency and (right) $e \to h$ mis-identification rate as a function of the track momentum, for various $\Delta \log \mathcal{L}^{\rm CALO}{}_{e-h}$ requirements.*

$$\Delta \log \mathcal{L}^{\rm CALO}{}_{e-h} = \Delta \log \mathcal{L}^{\rm ECAL}{}_{e-h} + \Delta \log \mathcal{L}^{\rm HCAL}{}_{e-h} + \Delta \log \mathcal{L}^{\rm PS}{}_{e-h}. \tag{2.3}$$

In Fig. 2.26 the electron identification efficiency and the $e \to h$ mis-identification rate as a function of the track momentum for various $\Delta \log \mathcal{L}^{\rm CALO}{}_{e-h}$ requirements is shown. With a $\Delta \log \mathcal{L}^{\rm CALO}{}_{e-h} > 2$ requirement, a 90% electron identification efficiency with a 3% $e \to h$ mis-identification rate is achieved.

2.4.3 Muon stations

The final part of the LHCb detector consists of five muon stations, that altogether form the muon sub-detector [50]. Muons with high $p_{\rm T}$ are very important particles since they are used by the tagging algorithm to identify the flavour of the spectator b-hadron produced associated to the signal b-hadron. Moreover, several b-hadron decay chains contain muons, *e.g.* $B_s^0 \to J/\psi\,\phi$, $B^0 \to K^{*0}\mu^+\mu^-$, $B_s^0 \to \mu^+\mu^-$, *etc.*, and for this reason it is fundamental to have an excellent muon identification efficiency keeping the mis-identification rates as low as possible.

The five muon stations (M1-M5) cover an angular acceptance of ± 300 *mrad* in the horizontal plane and ± 200 *mrad* in the vertical plane. The geometrical efficiency for the detection of muons coming from b-hadrons is nearly 46%. The first muon station M1 is placed before the calorimeters, to avoid possible muon multiple scattering effects, that could modify the particle trajectory. The remaining four muon station (M2-M5) are placed after the calorimeter system, at the end of the LHCb detector. A schematic view of the entire muon sub-detector is reported in Fig. 2.27.

Each muon station is divided into four regions (R1-R4, where R1 is the closest to the beam pipe and R4 is the farther). The dimensions of the chambers increase as they are more and more distant from the beam pipe; moreover, also the segmentation of each region increases as the distance from the beam pipe becomes greater, in a ratio 1:2:4:8, as shown in Fig 2.28. In this way, the charged particle occupancy is expected to be about the same

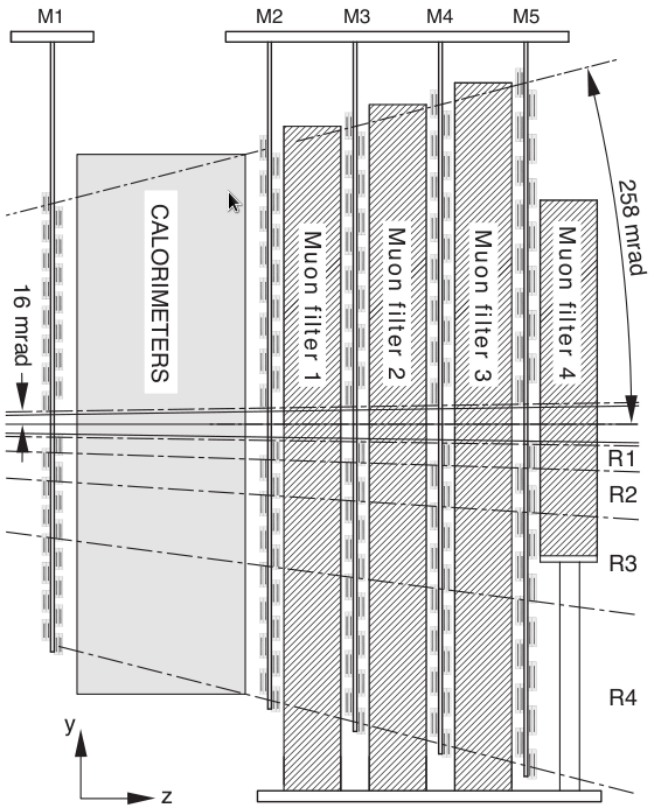

Figure 2.27: *Lateral view of the muon detector. As described in the text, the first muon station (M1) is placed before the calorimeters, while the remaining stations (M2-M4) are placed at the end of the LHCb detector.*

in each region. All the chambers are Multi-Wire Proportional Chambers, except for the inner region of the M1 station, where triple-GEM detectors are employed. MWPCs have four overlapped gaps, each one 5 mm thick and with a distance between wires of about 2 mm. In total, the muon detector contains 1380 MWPCs. The triple-GEM detector consists of three gas electron multiplier foils sandwiched between anode and cathode planes.

The muon identification procedure can be divided in three steps [51]. Firstly, a loose selection is performed on the muon candidates, taking into account the track penetration through the filters and calorimeters (this requirement is called IsMuon). Secondly, a likelihood is computed for the muon and non-muon hypotheses, taking into account the pattern of the hits around the tracks extrapolated to the different muon chambers using the information from the tracking system (muDLL). Finally, informations from the RICH and CALO systems are used and a combined likelihood is calculated.

In Fig. 2.29 the muon identification efficiency and the hadrons mis-identification rate for various combinations of IsMuon and muDLL requirements [51] are reported. Applying both cuts on the muon candidates, one achieves a muon identification efficiency of about

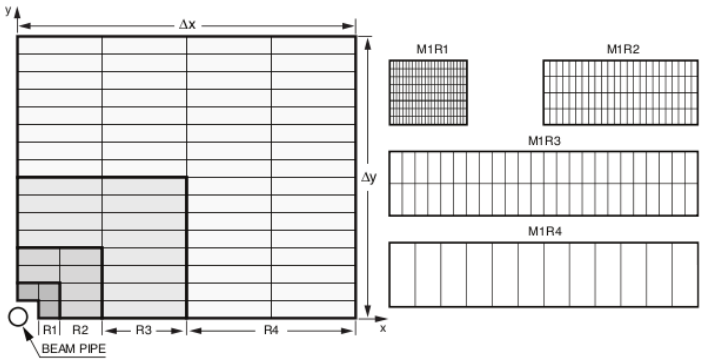

Figure 2.28: *(left) Frontal view of a muon station section where each rectangle represents a chamber and (right) different segmentation types of the four chambers. The inner chambers are more segmented than the outer ones.*

96% with hadrons mis-identification rates generally lower than 1%.

2.5 The LHCb trigger

A good trigger system is fundamental in every high energy physics experiment in order to accept only the interesting events while rejecting at the same time most of the background events. The LHCb trigger system [34,52] has been developed to work at the bunch crossing frequency of the LHC to process the largest number of events possible. The only way to reach the desired performances is to divide the trigger into different levels, each one processing the output of the previous one.

The LHCb trigger system is divided into three levels

Level-0 (L0): this is the first trigger level and it is based on custom electronics. It is fully synchronous with the 40 MHz bunch crossing rate of the LHC and it is designed to perform a first filtering of the events, reducing the input rate of 40 MHz to an output rate of only 1 MHz.

High Level Trigger 1 (HLT1): this is the second trigger level and, in contrast to the first, it is software based. The task of HLT1 is to filter events in an inclusive way and to reduce the rate of accepted events to 50 kHz, starting from an input rate given by the L0 of about 1 Mhz.

High Level Trigger 2 (HLT2): this is the last trigger level and, as the previous one, it is completely software based. The HLT2 takes an input rate of 50 kHz from the HLT1 and reduces it to an output rate of about 3.5 kHz (5 kHz) in 2011 (2012), applying an exclusive selection of beauty and charm decays. The output of HLT2 is finally sent to the mass storage.

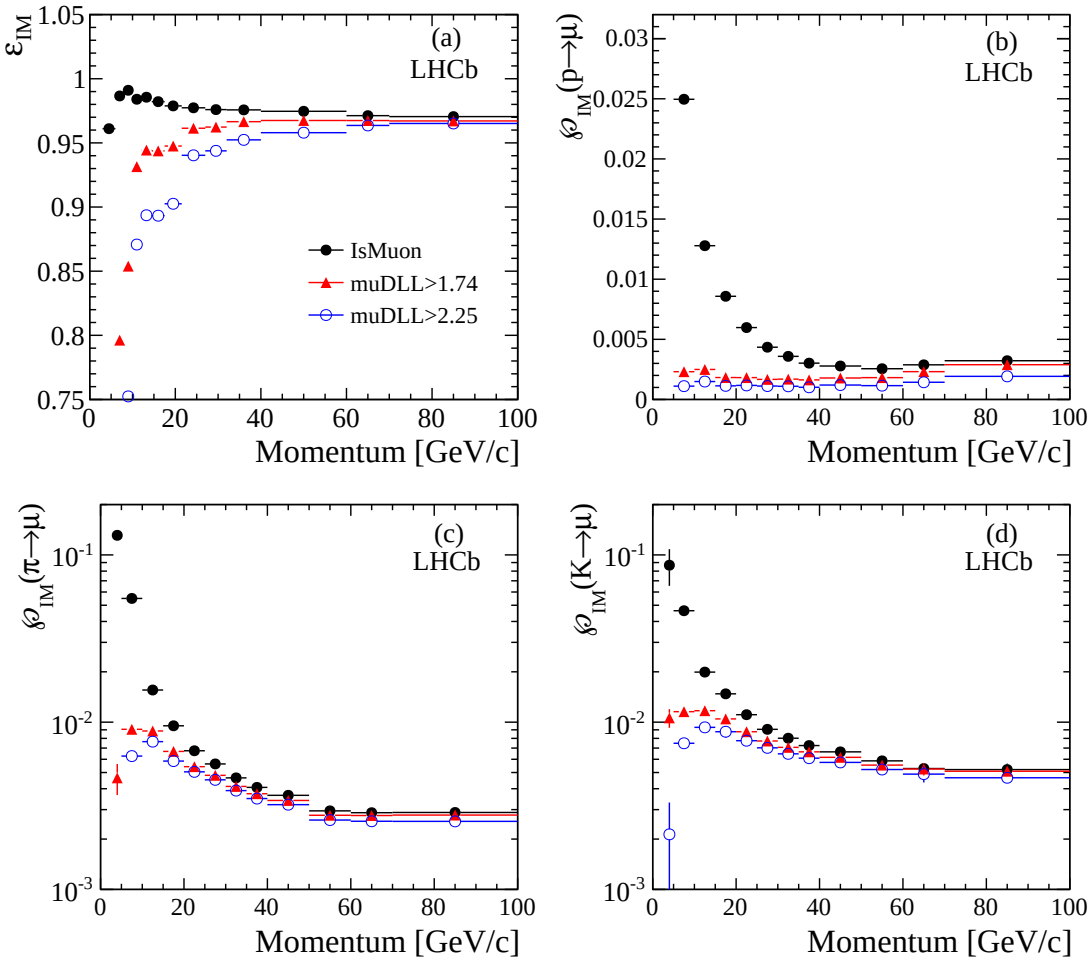

Figure 2.29: *(top left) Muon identification efficiency and (top right) proton, (bottom left) pion, and (bottom right) kaon mis-identification rates as a function of the track momentum. The different markers correspond to various combinations of the IsMuon and muDLL requirements.*

The 2011 and 2012 trigger layouts are reported in Fig. 2.30. In the following, each step of the trigger selection will be described in detail.

2.5.1 Level-0

The L0 trigger uses information coming mainly from the tracking system and from the calorimeter system. In fact, at this level, the trigger decides to keep or discard events based on measures of p_{T} and E_{T} of the particles composing the event. The system uses five independent triggers running in parallel

Photon trigger (`L0Photon`)**:** the highest E_{T} ECAL cluster with 1 or 2 PS cells hit in front of the ECAL cluster and no hit in the SPD cells corresponding to the PS cells. In the inner zone of the ECAL, an ECAL cluster with 3 or 4 PS cells hit in front of

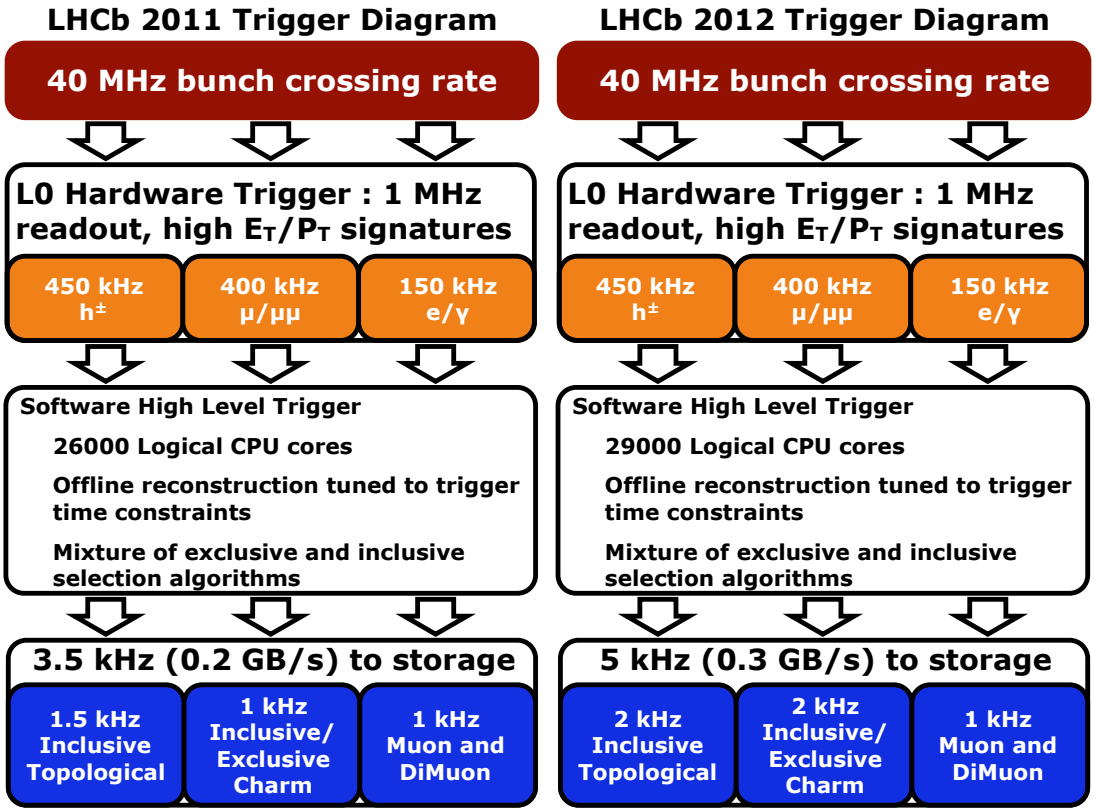

Figure 2.30: *Trigger layout in the LHCb experiment during (left) 2011 and (right) 2012 data taking.*

it is also accepted as photon. The E_{T} of the candidate is the E_{T} deposited in the ECAL alone.

Electron trigger (`L0Electron`)**:** same requirements as for a photon candidate, with in addition at least one SPD cell hit in front of the PS cells.

Hadron (`L0Hadron`) **trigger:** the highest E_{T} HCAL cluster. If there is a highest E_{T} ECAL cluster located in front of the HCAL cluster, the E_{T} of the hadron candidate is the sum of the E_{T} of the HCAL and ECAL clusters

Muon (`L0Muon`) **or DiMuon** (`L0DiMuon`) **trigger:** it uses the information given by the five muon stations. Tracks are reconstructed defining fields of interest around particles hits and then connecting hits in the same field of interest. Events are accepted if at least one muon candidate has a transverse momentum greater than a given threshold (`L0Muon`) (or, in the case of the `L0DiMuon` trigger, if the sum of the two largest transverse momenta of muon candidates is larger than a given threshold).

Furthermore, since in 2010 and 2011 the detector worked at an input rate four times larger than what planned, a system to reject high-occupancy events was developed and

implemented in the L0 trigger. Thanks to its fast response, the SPD can be used to roughly estimate the number of charged particles per event. It has been decided to accept events only if the number of hits in the SPD is less than 600.

2.5.2 High Level Trigger 1

The task of this trigger level is to reduce the input rate from the L0 trigger to a more manageable level. This is done rejecting events with an OT occupancy larger than 20%, because they would occupy more than the $\sim$ 25 ms allowed to the HLT1 to take a decision. After this first rough selection, the remaining events are reconstructed, considering that

- High mass b-hadrons and their production mechanism imply that the particles produced in their decays have a large momentum and transverse momentum compared to other hadrons composed by light quarks.
- The average decay length of b-hadrons produced at the LHC is about 1 cm. As a consequence, their decay products will have a large impact parameter with respect to their primary vertex.
- Each b-hadron decay has at least one final state particle with large p, p_{T} and IP.
- VELO reconstruction time is fast enough to allow the full information on the primary vertex to be used by the HLT1.
- The full reconstruction can be performed only for a limited number of tracks due to limited time available.

The last two points are the reason why the reconstruction is divided in two steps. In the first step VELO tracks and PV are reconstructed. The tracks are selected requiring large impact parameters with respect to the closest PV and a minimum number of hits in the VELO. If the difference between the expected number of hits and the observed number of hits in the VELO is greater than a certain threshold, the track is rejected. After this, forward reconstructed tracks are further selected, requiring minimal p and p_{T} thresholds. Finally, remaining tracks are fitted using a bi-directional Kalman filter with outlier removal, in order to obtain an offline-quality value for the track χ^2 as well as an offline-quality covariance matrix at the first state of the track, allowing a cut on the IP significance squared (χ^2_{IP}). Requirements imposed on the χ^2_{IP} are very efficient in rejecting background, while the track-χ^2 is suitable in rejecting ghost tracks.

2.5.3 High Level Trigger 2

The HLT2 filtering is mainly based on three inclusive selections, the so-called topological lines. In addition, a few dedicated lines for the LHCb core analyses are used.

The main strategy of topological lines is to build multi-body candidates in the following way

- two particles are combined to form a two-body object;
- another input particle is added to the two-body object to form a three-body object and so on;
- the pion mass hypothesis is adopted for all tracks.

In this way, n-body objects are built combining the $(n-1)$-body candidate with another particle (saving CPU time with respect to combining n particles directly). Particles are added to an object only if they respect a cut on the distance of closest approach (DOCA). For example, the two particles forming a two-body object need to have DOCA < 0.15 mm. When a 3-body object is built combining a 2-body object with another particle, another DOCA < 0.15 mm cut is imposed and so on for the construction of further objects.

In addition, HLT2 contains lines which exploit tracks identified as muons. Di-muon candidates are formed and, depending on their mass, cuts are applied on the flight distance and p_{T} of the di-muon candidate. Single muon candidates are accepted requiring a large p_{T} or a combination of χ^2_{IP} and p_{T} cuts.

3 Production asymmetries of b hadrons

The production rates of b and $\bar{b}$ hadrons at the LHC are not expected to be strictly equal, as the two quarks may also combine with u and d valence quarks from the beam remnant. For this reason, one expects *e.g.* a slight excess in the production of B^+ and B^0 over B^- and $\overline{B}^0$ mesons, and b baryons should be produced more abundantly than $\bar{b}$ baryons.

This phenomenon, commonly referred to as production asymmetry, can mimic *CP* violation and it is thus important to measure it in order to disentangle the physical asymmetries from such nuisance ones. In this chapter the procedure followed to measure the Λ_b^0 production asymmetry, $A_{\rm P}(\Lambda_b^0)$, will be described. The Λ_b^0 production asymmetry can be calculated knowing the B^+, B^0, and B_s^0 production asymmetries ($A_{\rm P}(B^+)$, $A_{\rm P}(B^0)$ and $A_{\rm P}(B_s^0)$, respectively) and under certain assumptions. We will present the measurement of all these asymmetries, and then derive $A_{\rm P}(\Lambda_b^0)$.

3.1 Introduction and methodology

The b-mesons production asymmetries are measured by means of $B^0 \to J/\psi\,(\mu^+\mu^-)K^{*0}(K^+\pi^-)$, $B_s^0 \to D_s^-(K^+K^-\pi^-)\pi^+$ and $B^+ \to J/\psi\,(\mu^+\mu^-)K^+$ decays. The Λ_b^0 production asymmetry is determined indirectly from the other asymmetries. Hereafter, K^{*0} is used to refer to the $K^*(892)^0$ and the inclusion of charge-conjugate decay modes is implied throughout, except when referring to the production asymmetries, which are defined as

$$A_{\rm P}\left(B^0\right) = \frac{\sigma(\overline{B^0}) - \sigma\left(B^0\right)}{\sigma(\overline{B^0}) + \sigma\left(B^0\right)}, \tag{3.1}$$

$$A_{\rm P}\left(B_s^0\right) = \frac{\sigma(\overline{B_s^0}) - \sigma\left(B_s^0\right)}{\sigma(\overline{B_s^0}) + \sigma\left(B_s^0\right)}, \tag{3.2}$$

$$A_{\rm P}\left(B^+\right) = \frac{\sigma\left(B^-\right) - \sigma\left(B^+\right)}{\sigma\left(B^+\right) + \sigma\left(B^-\right)}, \tag{3.3}$$

$$A_{\rm P}\left(\Lambda_b^0\right) = \frac{\sigma\left(\Lambda_b^0\right) - \sigma(\overline{\Lambda_b^0})}{\sigma\left(\Lambda_b^0\right) + \sigma(\overline{\Lambda_b^0})}, \tag{3.4}$$

where σ denotes the inclusive production cross-section.

Since production asymmetries are expected to exhibit a dependence on rapidity (y) and transverse momentum ($p_{\rm T}$) [53–55], the measurements are performed also as a function of $p_{\rm T}$ and y of the hadrons within the LHCb detector acceptance, and are then integrated over the ranges $0 < p_{\rm T} < 30\,{\rm GeV}/c$ and/or $2.1 < y < 4.5$ for B^+ and B^0 decays, and $2 < p_{\rm T} < 30\,{\rm GeV}/c$ and/or $2.1 < y < 4.5$ for B_s^0 and Λ_b^0 decays.

3.1.1 Measurement of $A_{\rm P}(B^0)$ and $A_{\rm P}(B_s^0)$

The values of $A_{\rm P}(B^0)$ and $A_{\rm P}(B_s^0)$ are measured by means of a time-dependent analysis, as the decay rate to a flavour-specific final state of a neutral B meson can be written as

$$\begin{aligned} f\left(t,\,\psi,\,\xi\right) \;\propto\; & \left(1 - \psi A_{CP}\right)\left(1 - \psi A_f\right) \\ & \left\{ e^{-\Gamma t}\left[\Omega_+^\xi \cosh\left(\frac{\Delta\Gamma t}{2}\right) + \psi\Omega_-^\xi \cos\left(\Delta m t\right)\right]\right\}, \end{aligned} \tag{3.5}$$

where ψ is the tag of the final state, which assumes the values $\psi = 1$ if the final state is f and $\psi = -1$ if the final state is the CP conjugate $\bar{f}$, ξ is the tag of the initial flavour of the B meson, which assumes the values $\xi = 1$ if it is B and $\xi = -1$ if it is $\bar{B}$ and the terms Ω_+ and Ω_- are defined as

$$\Omega_\pm = \delta_{1,\,\xi}\left(1 - A_{\rm P}\right)\left|\frac{q}{p}\right|^{1-\psi} \pm \delta_{-1,\,\xi}\left(1 + A_{\rm P}\right)\left|\frac{q}{p}\right|^{-1-\psi}, \tag{3.6}$$

where $\delta_{i,\,j}$ is the Kronecker delta. The symbol A_f is detection asymmetry of the final state, defined in terms of the f and $\bar{f}$ detection efficiencies as

$$A_f = \frac{\epsilon_{\bar{f}} - \epsilon_f}{\epsilon_{\bar{f}} + \epsilon_f}. \tag{3.7}$$

The direct CP asymmetry A_{CP} is defined as

$$A_{CP} = \frac{\mathcal{B}\left(\bar{B} \to \bar{f}\right) - \mathcal{B}\left(B \to f\right)}{\mathcal{B}\left(\bar{B} \to \bar{f}\right) + \mathcal{B}\left(B \to f\right)}, \tag{3.8}$$

where $\mathcal{B}$ stands for the branching fraction of the decay considered and $f = J/\psi\,K^{*0}$ for $B^0 \to J/\psi\,K^{*0}$, and $f = D_s^-\pi^+$ for $B_s^0 \to D_s^-\pi^+$ decays.

3.1.2 Measurement of $A_{\rm P}(B^+)$

The quantity $A_{\rm P}(B^+)$ is measured by means of a time-integrated analysis of $B^+ \to J/\psi\,K^+$ decays, with $J/\psi \to \mu^+\mu$, starting from the raw asymmetry defined as

$$A_{\rm raw} \equiv \frac{N(B^- \to J/\psi\,K^-) - N(B^+ \to J/\psi\,K^+)}{N(B^- \to J/\psi\,K^-) + N(B^+ \to J/\psi\,K^+)}, \tag{3.9}$$

where N denotes the observed yields. The raw asymmetry can be written, up to $\mathcal{O}(10^{-6})$ corrections, as

$$A_{\rm raw}(B^+ \to J/\psi\, K^+) = A_{\rm P}(B^+) + A_{\rm D}(K^+) + A_{CP}(B^+ \to J/\psi\, K^+), \tag{3.10}$$

where $A_{\rm D}(K^+)$ is the K^+ detection asymmetry, measured by means of charm control samples as in Ref. [56], and $A_{CP}(B^+ \to J/\psi\, K^+)$ is the *CP* asymmetry in the decay, measured by BaBar, Belle and D0 [57–59]. An improved measurement of the *CP* asymmetry was also made recently by LHCb [60], using an independent data sample selected with different trigger requirements.

3.1.3 Determination of $A_{\rm P}(\Lambda_b^0)$

Since in proton-proton collisions at the LHC b and $\bar{b}$ quarks are predominantly pair-produced via strong interaction processes, we can write the following relation between the Λ_b^0 production asymmetry and the other b-hadron production asymmetries

$$A_{\rm P}(\Lambda_b^0) = -\left[\frac{f_u}{f_{\Lambda_b^0}} A_{\rm P}(B^+) + \frac{f_d}{f_{\Lambda_b^0}} A_{\rm P}(B^0) + \frac{f_s}{f_{\Lambda_b^0}} A_{\rm P}(B_s^0) + \frac{f_c}{f_{\Lambda_b^0}} A_{\rm P}(B_c^+) + \frac{f_{other}}{f_{\Lambda_b^0}} A_{\rm P}({\rm o}ther)\right]$$

where f_u, f_d, f_s, f_c, $f_{\Lambda_b^0}$ and f_{other} are the hadronization fractions of the B^+, B^0, B_s^0, B_c^+ mesons, Λ_b^0 baryons and all the other b-baryon species. The ratios of the hadronization fractions, $f_u/f_{\Lambda_b^0}$, $f_d/f_{\Lambda_b^0}$ and $f_s/f_{\Lambda_b^0}$ are taken from LHCb measurements reported in Refs. [61, 62]. Their dependence on $p_{\rm T}$ and y is taken into account. The terms $(f_c/f_{\Lambda_b^0}) \cdot A_{\rm P}(B_c^+)$ and $(f_{other}/f_{\Lambda_b^0}) \cdot A_{\rm P}({\rm o}ther)$ are of the order of $3 \cdot 10^{-5}$ and $2 \cdot 10^{-3}$, respectively. This is estimated assuming that the value of $A_{\rm P}(B_c^+)$ and $A_{\rm P}({\rm o}ther)$ are of the same order as the B-meson production asymmetries ($\simeq 10^{-2}$) and taking the values of $f_c/f_{\Lambda_b^0}$ and $f_{other}/f_{\Lambda_b^0}$ from simulation. Neglecting these terms, the Λ_b^0 production asymmetry can be measured using the approximate relation

$$A_{\rm P}(\Lambda_b^0) \simeq -\left[\frac{f_u}{f_{\Lambda_b^0}} A_{\rm P}(B^+) + \frac{f_d}{f_{\Lambda_b^0}} A_{\rm P}(B^0) + \frac{f_s}{f_{\Lambda_b^0}} A_{\rm P}(B_s^0)\right]. \tag{3.11}$$

Possible small deviations from this approximation, due in particular to contributions from other b baryons, are taken into account in the evaluation of systematic uncertainties.

3.1.4 Integrated production asymmetries

In addition to the measurements in bins, integrated production asymmetries, where efficiency corrections have been applied, are also provided. The integration of the $A_{\rm P}$ values is performed in the ranges $0 < p_{\rm T} < 30\,{\rm GeV}/c$ and $2.1 < y < 4.5$ for the B^+ and B^0 decays and in the ranges $2 < p_{\rm T} < 30\,{\rm GeV}/c$ and $2.1 < y < 4.5$ for the B_s^0 and Λ_b^0 decays. The integrated value of $A_{\rm P}$ is given by

$$A_{\rm P} = \sum_i \frac{N_i}{\varepsilon_i} A_{{\rm P},i} \Big/ \sum_i \frac{N_i}{\varepsilon_i} \tag{3.12}$$

where the index i runs over the bins, N_i is the number of observed signal events in the i-th bin and ε_i is the efficiency defined as the number of selected events divided by the number of produced events in the i-th bin. The signal yield in each bin can be expressed as

$$N_i = \mathcal{L}\ \sigma_{b\bar{b}}\ 2\ f_q\ \mathcal{B}\ F_i\ \varepsilon_i \tag{3.13}$$

where $\mathcal{L}$ is the integrated luminosity, $\sigma_{b\bar{b}}$ is the $b\bar{b}$ cross-section, f_q is the hadronization fraction for the quark flavour q, with $q \in \{u, d, s\}$, F_i stands for the fraction of the b hadrons produced in the i-th bin and $\mathcal{B}$ is the branching fraction of the b-hadron decay being considered. By substituting N_i/ε_i from Eq. (3.55) into Eq. (3.54), the integrated value of $A_{\rm P}$ becomes

$$A_{\rm P} = \sum_i \omega_i A_{{\rm P},i}. \tag{3.14}$$

where $\omega_i = F_i / \sum_i F_i$. The ω_i values are determined using simulated events, generated with proton-proton collisions at the centre-of-mass energies of 7 and 8 TeV.

3.2 Event selection

3.2.1 Stripping and trigger

Raw data coming from the detector are saved in different streams, depending on which trigger fired and recorded the event. The building of the candidates of interest is performed by the so-called *stripping lines*, that are a collection of algorithms that build different decay chains and save them in the LHCb standard format (DST). The data used in this analysis are the output of the following *stripping lines*

$B^0 \to J/\psi K^{*0}$: `BetaSBd2JpsiKstarDetached` *stripping line* running on the `DIMUON` stream;

$B_s^0 \to D_s^- \pi^+$: `B02DPiD2HHHBeauty2Charm` *stripping line* running on the `BHADRON` stream;

$B^+ \to J/\psi K^+$: `BetaSBu2JpsiKPrescaledLine` *stripping line* running on the `DIMUON` stream;

The selections of $B^+ \to J/\psi K^+$ and $B^0 \to J/\psi K^{*0}$ decays are based on the reconstruction of $J/\psi \to \mu^+\mu^-$ decays combined with either a track identified as a charged kaon or with a K^{*0} decaying to $K^+\pi^-$. The J/ψ candidates are formed from two oppositely charged tracks originating from a common vertex, identified as muons with $p_{\rm T} > 500\,{\rm MeV}/c$. The K^{*0} candidates are formed from two oppositely charged tracks, one identified as a kaon and the other as a pion, originating from the same vertex. They are required to have $p_{\rm T} > 1\,{\rm GeV}/c$ and the $K^+\pi^-$ invariant mass in the range 826–966 MeV/c^2. The invariant mass of B^0 and B^+ candidates, calculated constraining the two muon candidates to have the known J/ψ mass, is required to be in the range 5150–5450 MeV/c^2. The proper decay

time of the B-meson candidate is calculated from a fit that constrains the candidate to originate from the PV with the smallest $\chi^2_{\rm IP}$ with respect to the B candidate. Only B-meson candidates with a decay time greater than 0.2 ps are retained. This lower bound on the decay time rejects a large fraction of the combinatorial background.

In the case of $B^0_s \to D^-_s\pi^+$ decays, the D^-_s candidates are reconstructed using the $K^+K^-\pi^-$ decay channel. Requirements are applied to the D^-_s decay products before combining them to form a common vertex, namely the scalar $p_{\rm T}$ sum of the tracks must exceed 1.8 GeV/c and the largest distance of closest approach between all possible pairs of tracks must be less than 0.5 mm. The D^-_s candidates are then required to be significantly detached from the PV and to have the invariant mass within the range 1949–1989 MeV/c^2. Each D^-_s candidate is subsequently combined with a second charged pion, referred to as the accompanying pion in the following, to form the B-meson decay vertex. The sum of the $p_{\rm T}$ values of the D^-_s and accompanying π^+ must be larger than 5 GeV/c and the decay time of B-meson candidates must be greater than 0.2 ps. Furthermore, the cosine of the angle between the B-meson candidate momentum vector and the vector connecting the PV and B-meson candidate vertex is required to be larger than 0.999.

3.2.2 PID requirements

3.2.2.1 $\mathbf{B^0 \to J/\psi K^*}$ and $\mathbf{B^0_s \to D^-_s\pi^+}$

Before applying the final event selection, the $B^0 \to J/\psi K^{*0}$ candidates that pass the `BetaSBd2JpsiKstarDetached` *stripping line* are required to satisfy the following PID requirements: $\Delta\log\mathcal{L}_{K-\pi} > 2$ to identify kaons and $\Delta\log\mathcal{L}_{K-\pi} < -2$ to identify pions. In the case of the $B^0_s \to D^-_s\pi^+$ candidates, PID requirements are applied to those that pass the `B02DPiD2HHHBeauty2Charm` *stripping line* in order to reduce to a negligible level misidentified backgrounds which may peak in the B mass region. Regarding the $B^0_s \to D^-_s\pi^+$ decay, the main backgrounds are the $B^0 \to D^-(K^+\pi^-\pi^-)\pi^+$ decay, where one of the pion from the D^- is misidentified as a kaon, the $B^0_s \to D^-_s K^+$ decay, where the kaon is misidentified as a pion, and the $\bar{\Lambda}^0_b \to \Lambda^-_c(\bar{p}K^+\pi^-)\pi^+$ where the antiproton from $\overline{\Lambda}^-_c$ is misidentified as a kaon or when the antiproton from $\overline{\Lambda}^-_c$ is misidentified as a pion and the pion from $\overline{\Lambda}^-_c$ as a kaon. To suppress these backgrounds, the following PID requirements are applied

- $\Delta\log\mathcal{L}_{K-\pi} > 5$ for the kaon candidates, when the invariant mass of D^-_s candidates, computed under the $K^+\pi^-\pi^-$ mass hypothesis, is greater than 1830 MeV/c^2. This request is applied only to the kaon candidate with the same charge of the misidentified pion from D^-.

- $\Delta\log\mathcal{L}_{K-p} > 10$ for the kaon candidates, when the invariant mass of D^-_s candidates, computed under the $\bar{p}K^+\pi^-$ mass hypothesis, lies within the window 2225–2315 MeV/c^2. As in the previous case the requirement is applied only to the kaons from D^+_s with the same charge of misidentified proton from $\overline{\Lambda}^-_c$.

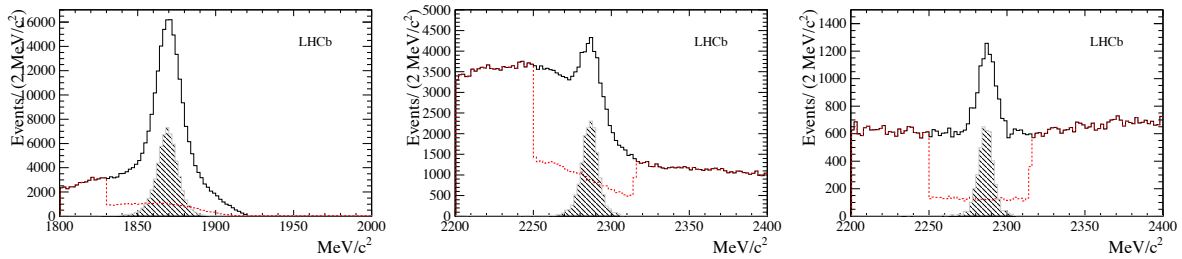

Figure 3.1: *Invariant-mass distribution of offline selected $D_s^- \to K^+K^-\pi^-$ candidates under (left) the $K^+\pi^-\pi^-$ mass hypothesis, (middle) the $\bar{p}K^+\pi^-$ mass hypothesis when the antiproton from $\overline{\Lambda}_c^-$ is misidentified as kaon, and (right) the $\bar{p}K^+\pi^-$ mass hypothesis when the antiproton is misidentified as pion and the pion from $\overline{\Lambda}_c^-$ as a kaon. The dashed red line and solid black line correspond respectively to the cases with and without PID requirements applied. The peaks in the distributions correspond to the mis-identified background.*

- $\Delta \log \mathcal{L}_{p-\pi} < -10$ for the pion candidates, when the invariant mass of D_s^- candidates, computed under the $\bar{p}K^+\pi^-$ mass hypothesis, lies within the window 2225–2315 MeV/c^2. This is applied only for the pion candidates which have the same charge of the misidentified proton from $\overline{\Lambda}_c^-$.

Figure. 3.1 shows the invariant-mass distribution of D_s^- candidates, computed under the $K^+\pi^-\pi^-$ mass hypothesis, the $\bar{p}K^+\pi^-$ mass hypothesis when the antiproton from $\overline{\Lambda}_c^-$ is misidentified as kaon, and the $\bar{p}K^+\pi^-$ mass hypothesis when the proton is misidentified as a pion and the pion from $\overline{\Lambda}_c^-$ as a kaon. An additional source of background is the $B_s^0 \to D_s^- K^+$, where the K^+ is misidentified as a pion. To suppress this background the bachelor pion is required to have $\Delta \log \mathcal{L}_{K-\pi} < -1$. Additional requirements on the invariant mass of D_s^- candidates, that has to lie within the window 1949–1989 MeV/c^2, corresponding to ± 20 MeV/c^2 around the D_s^+ nominal mass, and $\Delta \log \mathcal{L}_{K-\pi} > -3$ for kaons, have been applied.

3.2.2.2 $\mathbf{B^+ \to J/\psi K^+}$

Before applying the final event selection the $B^+ \to J/\psi K^+$ candidates that pass the `BetaSBu2JpsiKPrescaledLine` *stripping line* are required to satisfy the following PID requirements: $\Delta \log \mathcal{L}_{K-\pi} > 2$ for the kaon.

3.2.3 Other selection criteria

For $B^+ \to J/\psi K^+$ decays the kaons are required to have a momentum lower than 70 GeV/c. This is done since the $A_{\rm D}(K^-\pi^+)$ correction can be measured only for momenta lower than this threshold.

3.2.4 Final offline selection

A final selection is applied to the events that satisfy the preselection, PID and (if any) geometric criteria.

3.2.4.1 $B^+ \to J/\psi K^+$

In order to suppress combinatorial background, a selection based on a multivariate analysis method, namely the `Boosted Decision Tree` (BDT) [63, 64], is applied. The BDT optimization is divided into two steps. First the BDT algorithm is trained in order to distinguish between signal and combinatorial background events. In order to achieve this goal, the algorithm utilises two samples: one composed of signal events taken from fully simulated samples and another composed of combinatorial background events from data sidebands. After the training, the algorithm assigns to each event a classifier ($\mu_{\rm BDT}$) ranging from -1 to $+1$. The separation between signal and background events is then achieved by choosing an appropriate threshold for the $\mu_{\rm BDT}$ parameter to maximize a predefined score function. The variables used in the BDT selection are: for the B daughter particles J/ψ and K^+, the transverse momentum (${p_{\rm T}}^{\rm dau}$) and the impact parameter ($d^{\rm dau}_{\rm IP}$); for the B candidates, the transverse momentum (${p_{\rm T}}^{B}$), the distance of flight ($d^{B}_{\rm FL}$) and the impact parameter ($d^{B}_{\rm IP}$). The trigger algorithm in the simulation corresponds to `TCK 0x760037F`. The same preselection and PID requirement applied to the data are also applied to simulated events passing the trigger requirements. Combinatorial background events are isolated in real data from the high invariant-mass sideband, defined as $5.31 < m < 5.45\,{\rm GeV}/c^2$.

Figure. 3.2 shows the correlation matrices between the variables used in the BDT, separately for signal and combinatorial background.

The signal and background yields are estimated by performing unbinned maximum likelihood fits to the mass spectra. The signal component is parameterized using a double-Gaussian convolved with a function taking care of the radiative tail with floating mean and width, while the combinatorial background component is modeled using an exponential function.

A more detailed discussion on the parameterization of signal, combinatorial and partially-reconstructed backgrounds can be found in Sec. 3.4. Figure. 6.4 shows the invariant-mass spectra after applying the final offline selection and the PID requirements on data, with the results of the fits superimposed.

The signal and combinatorial background yields determined from the fits, before the BDT cut, are: $N^{J/\psi K^+}_{\rm sig} = 295\,396 \pm 2\,720$ and $N^{J/\psi K^+}_{\rm bkg} = 649\,580 \pm 2\,756$ for 2011 and $N^{J/\psi K^+}_{\rm sig} = 743\,435 \pm 9\,881$ and $N^{J/\psi K^+}_{\rm bkg} = 2\,049\,164 \pm 9\,916$ for 2012.

The data samples are split into two halves. The first half is used for the training phase of the BDT, while the second to test the presence of possible overtraining effects and to define the optimal requirements on $\mu_{\rm BDT}$. Figure. 3.9 shows the distributions of $\mu_{\rm BDT}$ for signal and background events. The good agreements between the distributions for training and test events witness the absence of possible overtraining effects.

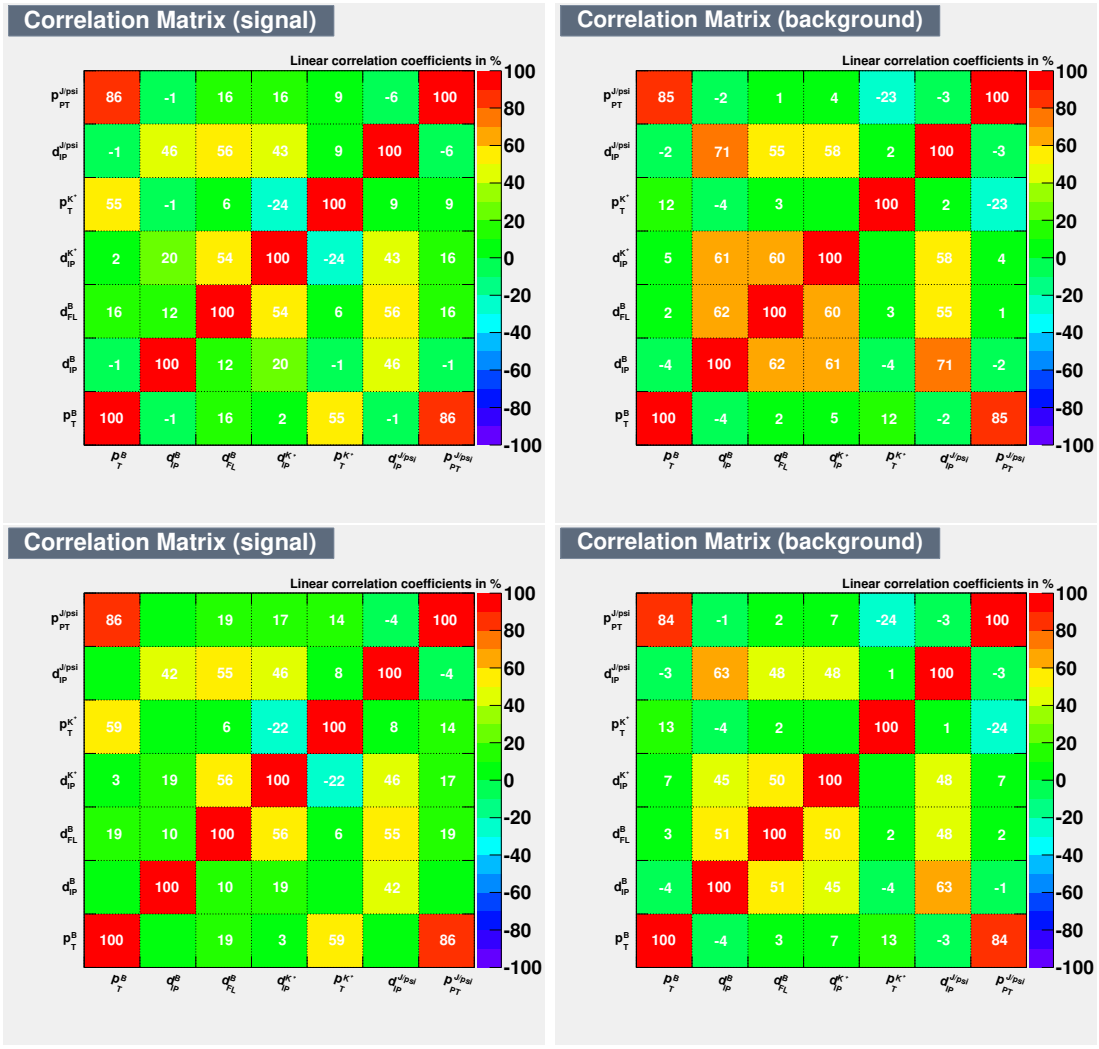

Figure 3.2: *Linear correlation matrices between the variables used in BDT selection: (left) signal and (right) combinatorial background for (top) 2011 and (bottom) 2012* $B^+ \to J/\psi\, K^+$ *decays.*

The optimal requirements on $\mu_{\rm BDT}$ are chosen by maximizing the quantity $\xi = S/\sqrt{(S+B)}$, where S and B represent the number of signal and combinatorial background events within an invariant-mass window corresponding to $\pm 3\sigma$ around the B^0 or B_s^0 masses. As the requirement on $\mu_{\rm BDT}$ can modify the slope of the combinatorial background mass shape, for each $\hat{\mu}$ value an unbinned maximum likelihood fit to the high invariant-mass sideband is performed. The result of each fit is then used to determine the total background yield, by extrapolating to the full invariant-mass window. Figure. 3.5 shows the ξ parameter calculated with events which satisfy the requirement $\mu_{\rm BDT} > \hat{\mu}$, *i.e.* ξ as a function of $\hat{\mu}$. It turns out that the maximum value of ξ is approximately obtained for $\mu_{\rm BDT} > -0.01$ in both 2011 and 2012 datasets.

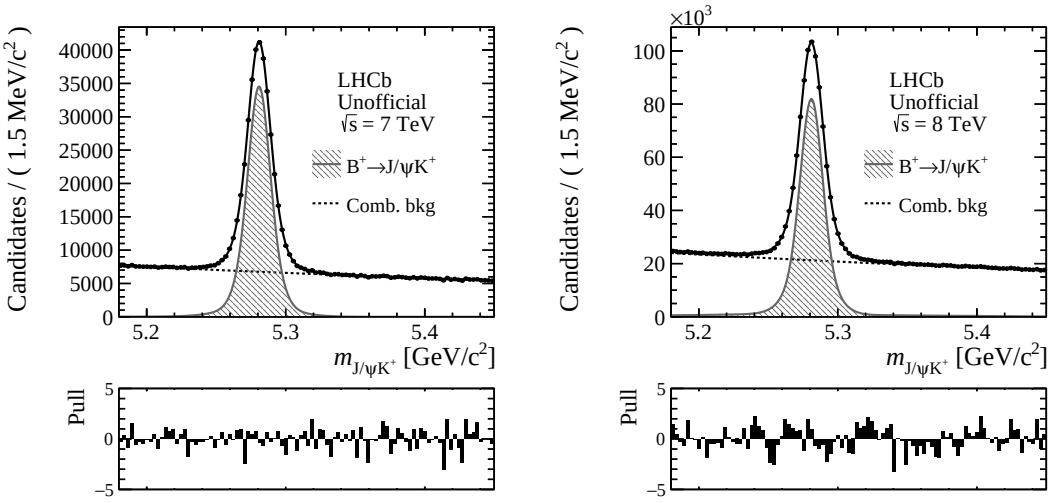

Figure 3.3: *Invariant-mass distributions for $B^+ \to J/\psi K^+$ with the results of the fits superimposed used for the relative normalization of signal and background yields in the BDT optimization: (left) 2011 data and (right) 2012 data.*

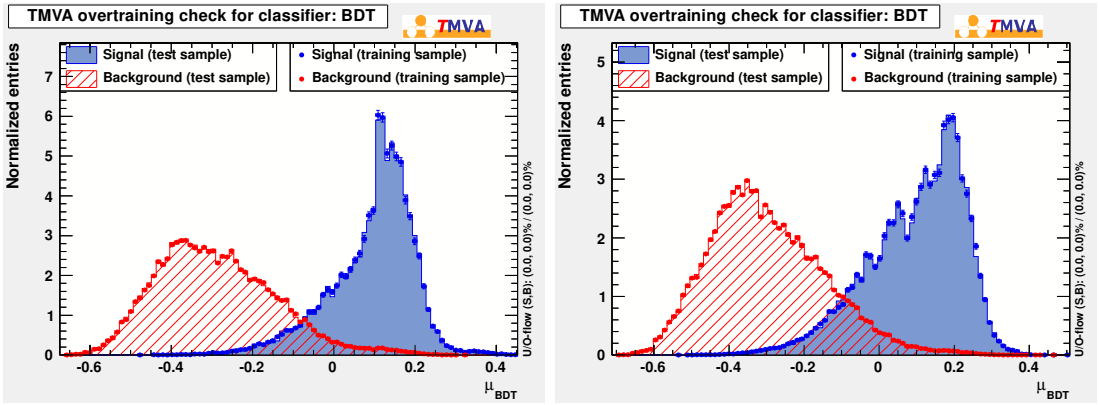

Figure 3.4: *Distributions of $\mu_{\rm BDT}$ for signal and background events for (left) 2011 and (right) 2012 data. The dots correspond to the training samples, while the filled histograms correspond to the test samples.*

3.2.4.2 $\mathbf{B^0 \to J/\psi K^{*0}}$ and $\mathbf{B_s^0 \to D_s^- \pi^+}$

Four different selections are optimized to reject the combinatorial background: one for the $B^0 \to J/\psi K^{*0}$ decay and one for the $B_s^0 \to D_s^- \pi^+$ decay, both for 2011 and 2012 data separately. All of them are based on the BDT method. The variables used in the BDT selection are: for the B daughter particles (J/ψ and K^{*0} in the case of B^0 or D_s^- and π^+ in the case of B_s^0), the transverse momentum ($p_{\rm T}{}^{\rm dau}$) and the impact parameter ($d_{\rm IP}^{\rm dau}$); for the B candidates, the transverse momentum ($p_{\rm T}{}^{B}$), the distance of flight ($d_{\rm FL}^{B}$) and

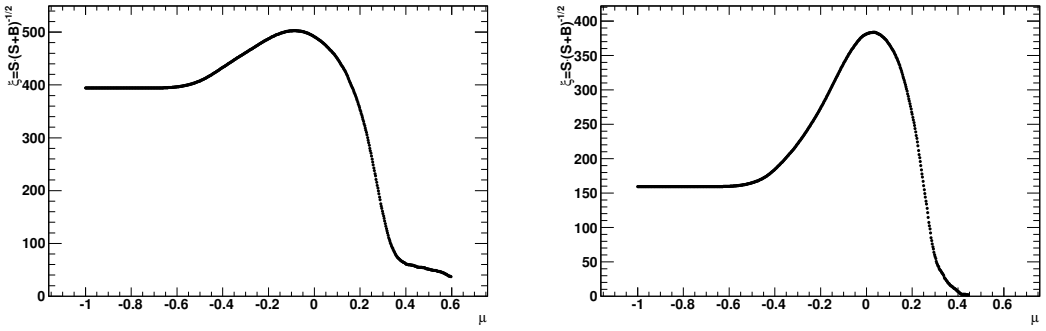

Figure 3.5: *Dependence of* $\xi = S/\sqrt{(S+B)}$ *as a function of the requirement on* $\mu_{\rm BDT} > \hat{\mu}$ *for* $B^+ \to J/\psi\, K^+$ *(left) 2011 and (right) 2012 data.*

the impact parameter ($d^B_{\rm IP}$). The same preselection and PID requirements applied to the data are also applied to simulated events. Combinatorial background events are isolated in real data from the high invariant-mass sidebands, defined as $5.31 < m < 5.34\,{\rm GeV}/c^2$ for the $B^0 \to J/\psi\, K^{*0}$ decay and $5.45 < m < 5.90\,{\rm GeV}/c^2$ for the $B^0_s \to D^-_s\pi^+$ decay.

In Figs. 3.6 and 3.7 the correlation matrices of the variables used in the BDT are shown separately for signal and combinatorial background.

The optimization of the BDT selection requires the knowledge of the relative proportions of signal and background candidates which are present in the sample before the optimization. The signal and background yields are estimated by performing unbinned maximum likelihood fits to the mass spectra. The signal component is parameterized using a double-Gaussian convolved with a function taking care of the radiative tail with floating mean and width, while the combinatorial background component is modeled using an exponential function (see Sec. 3.4 for more details). The component due to partially-reconstructed B decays is taken into account only for the $B^0_s \to D^-_s\pi^+$ decay mode. The shapes, parametrized by means of a kernel estimation technique, are obtained from simulated samples, generated in the exclusive modes $B^0 \to D^{*-}\pi^+$, $B^0 \to D^-\rho^+$, $B^0_s \to D^{*-}_s\pi^+$ and $B^0_s \to D^-_s\rho^+$. The fully simulated events are selected with the same selection applied to the data. The true value of the invariant mass is smeared by a Gaussian resolution model, obtained by a fit to the data where the partially-reconstructed backgrounds were excluded from the mass window.A more detailed discussion on the parameterization of signal, combinatorial and partially-reconstructed backgrounds can be found in Sec. 3.4.

In Fig. 3.8 the invariant-mass spectra after applying the preselection and the PID requirements on data are shown, with the results of the fits superimposed, for $B^0 \to J/\psi\, K^{*0}$ and $B^0_s \to D^-_s\pi^+$ decays.

The signal and combinatorial background yields determined from the fits, before the BDT requirement, are: $N^{J/\psi\,K^*}_{\rm sig} = 100\,840 \pm 835$, $N^{J/\psi\,K^*}_{\rm bkg} = 303\,375 \pm 948$, $N^{D^-_s\pi^+}_{\rm sig} = 17\,823 \pm 304$ and $N^{D^-_s\pi^+}_{\rm bkg} = 29\,937 \pm 580$ for 2011 data and $N^{J/\psi\,K^*}_{\rm sig} = 231\,986 \pm 1\,111$,

Figure 3.6: *Linear correlation matrices of the variables used in BDT selection: (left) signal and (right) combinatorial background for (top) 2011 and (bottom) 2012 $B^0 \to J/\psi\, K^{*0}$ decays.*

$N^{J/\psi\, K^*}_{\rm bkg} = 523\,238 \pm 1\,235$, $N^{D_s^-\pi^+}_{\rm sig} = 40\,913 \pm 443$ and $N^{D_s^-\pi^+}_{\rm bkg} = 58\,666 \pm 872$ for 2012 data.

The data samples are split into two halves. The first half is used for the training phase of the BDT, while the second to test the presence of possible overtraining effects and to define the optimal requirements on $\mu_{\rm BDT}$. In Fig. 3.9 the distributions of $\mu_{\rm BDT}$ for signal and background events are shown. The good agreement between the distributions for training and test events witness the absence of possible overtraining effects.

The optimal requirements on $\mu_{\rm BDT}$ are chosen for each decay by maximizing the quantity $\xi = S/\sqrt{(S+B)}$, where S and B represent the number of signal and combinatorial background events within an invariant-mass window corresponding to $\pm 3\sigma$ around the B^0 or B_s^0 masses. As the requirement on $\mu_{\rm BDT}$ can modify the slope of the combinatorial-

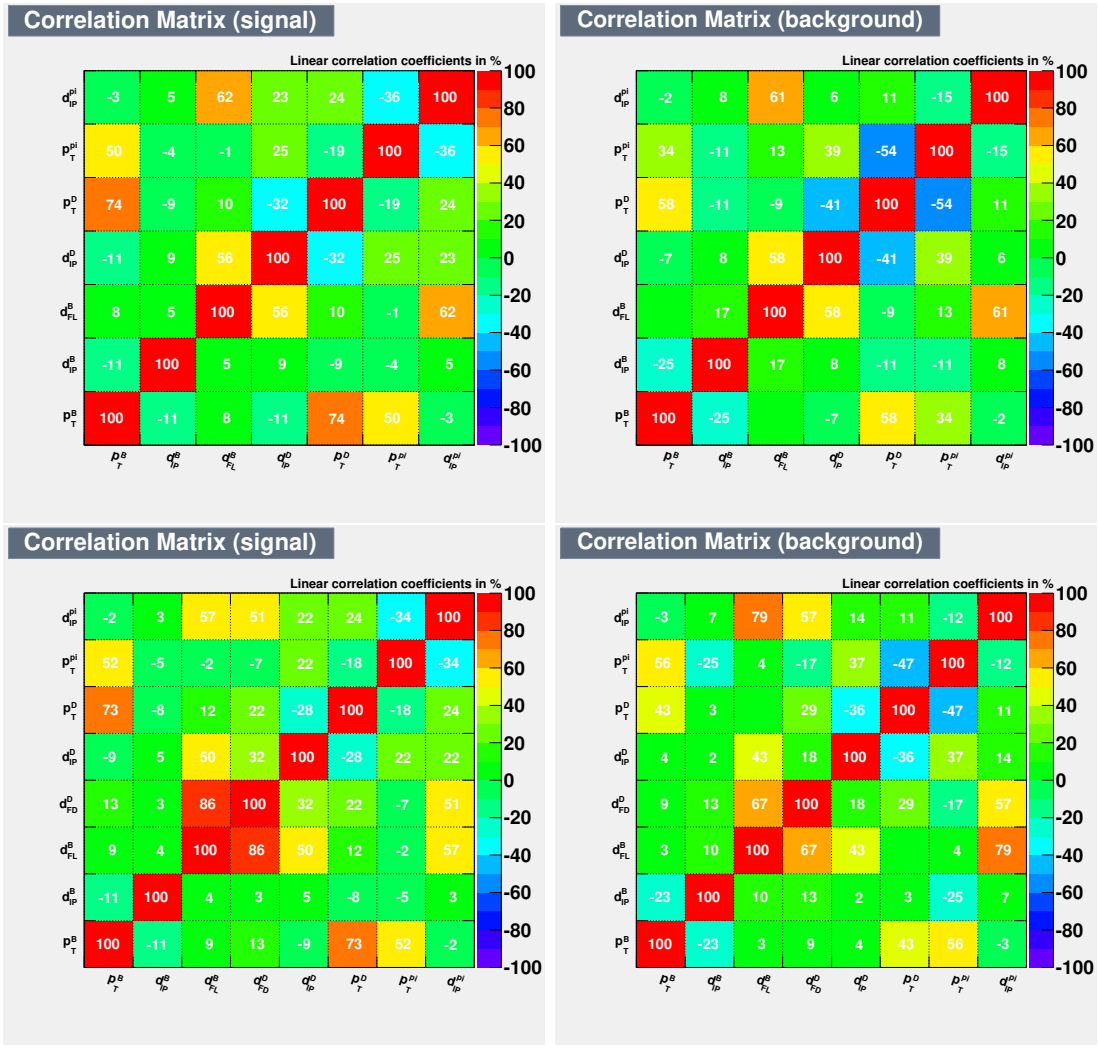

Figure 3.7: *Linear correlation matrices of the variables used in BDT selection: (left) signal and (right) combinatorial background for (top) 2011 and (bottom) 2012* $B_s^0 \to D_s^- \pi^+$ *decays.*

background mass shape, for each $\hat{\mu}$ an unbinned maximum likelihood fit to the high invariant-mass sideband is performed. The result of each fit is then used to determine the total background yield, by extrapolating to the full invariant-mass window. Figure. 3.10 shows ξ calculated with events which satisfy the requirement $\mu_{\rm BDT} > \hat{\mu}$, *i.e.* ξ as a function of $\hat{\mu}$. It turns out that the maximum value of ξ is approximately obtained for $\mu_{\rm BDT} > -0.1$ in the case of the $B^0 \to J/\psi\, K^{*0}$ and $\mu_{\rm BDT} > -0.2$ in the case of the $B_s^0 \to D_s^- \pi^+$ decays for both 2011 and 2012 data sample.

Looking at Fig. 3.10 it is also clear that while for the $B^0 \to J/\psi\, K^{*0}$ decay the BDT selection leads to a sizable improvement in the value of ξ, for the $B_s^0 \to D_s^- \pi^+$ decay the improvement is modest, *i.e.* the preselection requirements are tight enough to reject most of the combinatorial background.

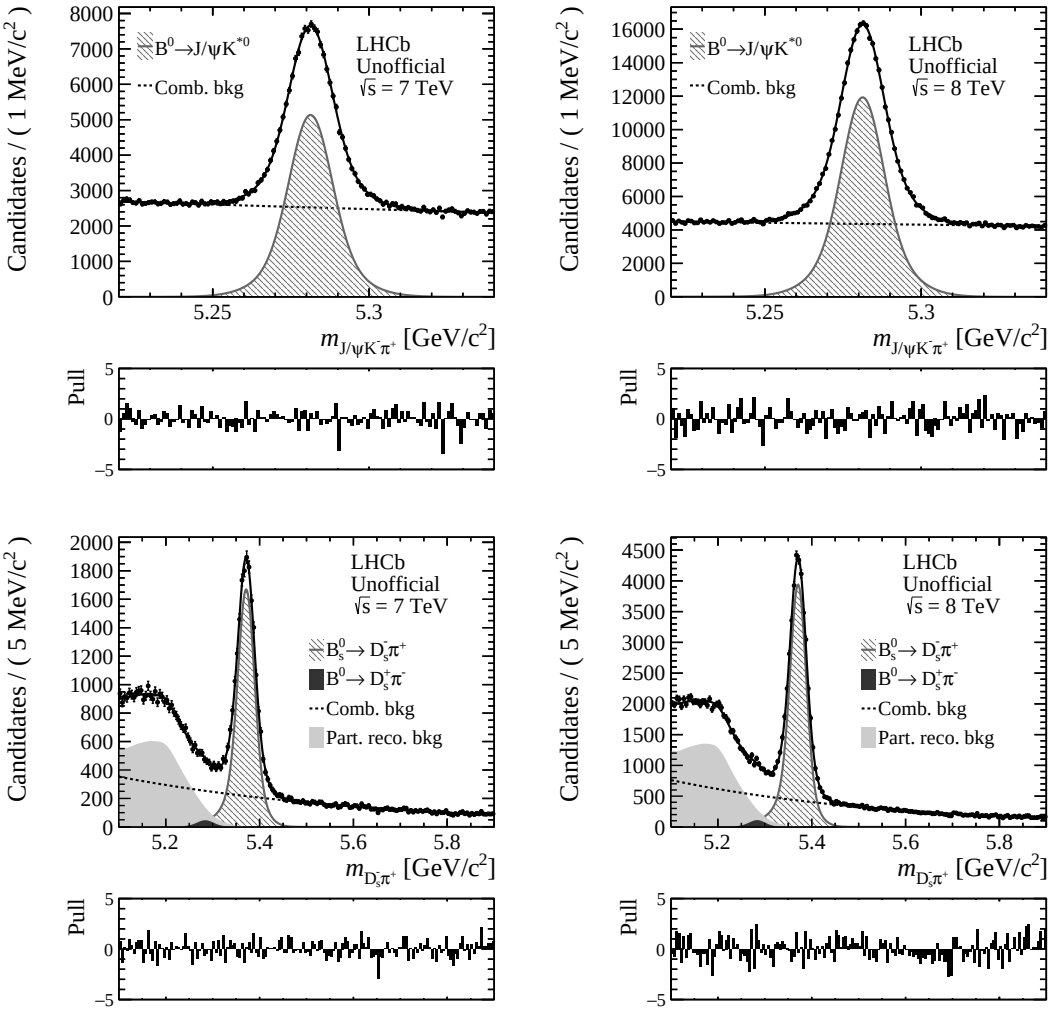

Figure 3.8: *Invariant mass fits used for the relative normalization of signal and background yields in the BDT optimization: (top left) $B^0 \to J/\psi K^{*0}$ 2011 decays, (top right), $B^0 \to J/\psi K^{*0}$ 2012 decays, (bottom left) $B_s^0 \to D_s^- \pi^+$ 2011 decays and (bottom right) $B_s^0 \to D_s^- \pi^+$ 2012 decays.*

3.3 Study of decay-time resolution

Since a time-dependent analysis will be performed for the B^0 and B_s^0 modes, the decay-time resolution needs to be studied in detail. The strategy adopted to study the decay-time resolution consists of reconstructing the decay time of fake-B candidates. The focus is put on the B_s^0 meson, since the accuracy of the decay-time resolution for B^0 mesons plays a negligible role.

A fake-B is formed from a $D^\pm$ decaying to $K^\mp\pi^\pm\pi^\pm$ and a pion track, both coming from the same PV. The bachelor pion is selected in order not to bias the decay time, hence only requirements on momentum and transverse momentum have been applied, avoiding

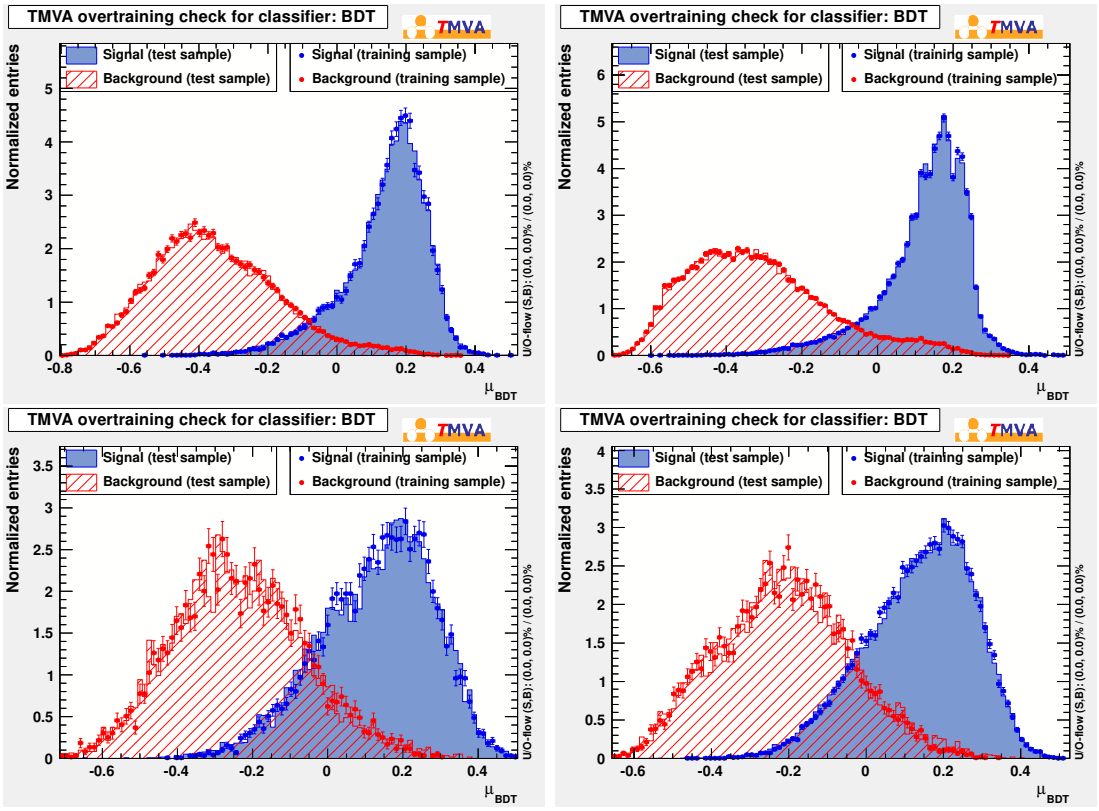

Figure 3.9: *Distributions of* μ_{BDT} *for signal and background events: (top left)* $B^0 \to J/\psi K^{*0}$ *2011 decays, (top right)* $B^0 \to J/\psi K^{*0}$ *2012 decays, (bottom left)* $B_s^0 \to D_s^- \pi^+$ *2011 decays and (bottom right)* $B_s^0 \to D_s^- \pi^+$ *2012 decays.*

the usage of impact parameter variables. The decay-time distribution of the so-formed fake-B candidate yields an estimation of the decay-time resolution of a real $B_s^0 \to D_s^- \pi^+$ decay.

This study is performed using $1\,\text{fb}^{-1}$ of 2011 data, filtered by the `UnbiasedB2DPiWithUnbiasedB2DPi` *stripping line*, which does not apply any requirement on impact parameters nor on the decay time. It has been checked that the decay-time resolution is unchanged for 2012 data (detailed studies are reported in the following sections), even if a different *stripping line* (`B02DKLTUBD2HHHBeauty2CharmLine`) is used. Further requirements are applied in addition to the *stripping line*. They are listed in the following

- the p_{T} of fake-B candidates must exceed $2\,\text{GeV}/c$;
- the smallest impact parameter χ^2 of fake-B candidates, of the $D^{\pm}$ and of the bachelor pion must be less than 9;
- the second smallest impact parameter χ^2 of fake-B candidates must be greater than 20.

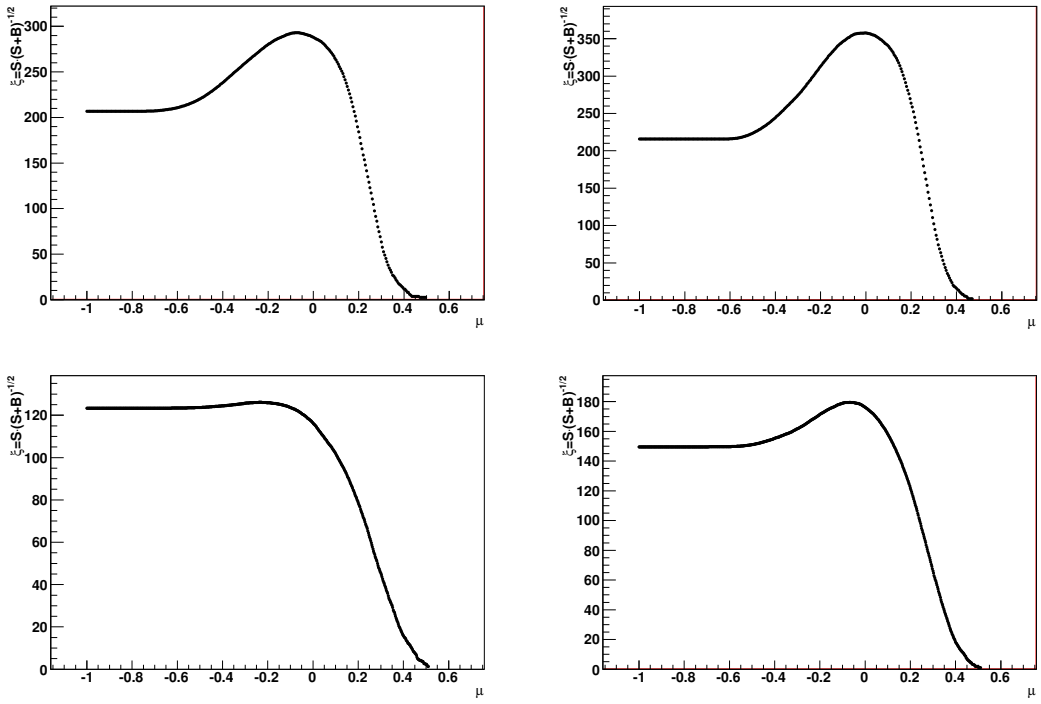

Figure 3.10: *Dependence of* $\xi = S/\sqrt{(S+B)}$ *as a function of the requirement on* $\mu_{\rm BDT} > \hat{\mu}$ *for (top left)* $B^0 \to J/\psi K^{*0}$ *2011 decays, (top right)* $B^0 \to J/\psi K^{*0}$ *2012 decays, (bottom left)* $B_s^0 \to D_s^- \pi^+$ *2011 decays and (bottom right)* $B_s^0 \to D_s^- \pi^+$ *2012 decays.*

These additional requirements are used to remove the fake-B candidates (or rather, their daughters) with a wrong association to the PV.

3.3.1 Validation of the method with simulated events

In order to validate the method, fully simulated $B_s^0 \to D_s^- \pi^+$ events are used. These events need to pass the same requirements (trigger-preselection-PID-BDT) as the real data. The distribution of $t_{\rm rec} - t_{\rm true}$, where $t_{\rm rec}$ is the reconstructed B_s^0 decay time, while $t_{\rm true}$ is the B_s^0 true decay time is shown in Fig. 3.11, with the results of the fit with a double-Gaussian function overlaid.

Then, by making use of the stripping line `UnbiasedB2DPiWithUnbiasedB2DPi` and of the additional requirements mentioned above, fake-B candidates are selected from a fully simulated sample of prompt $D^- \to K^+\pi^-\pi^-$ decays. The decay-time resolution distribution is fitted using again a double-Gaussian function. The data points with the results of the fit overlaid are shown in Fig. 3.12.

The kinematic distributions of fake-B and real B mesons differ, as shown in the left part of Fig. 3.13, where the distributions of p, $p_{\rm T}$, η and azimuthal angle ϕ for fully simulated $B_s^0 \to D_s^- \pi^+$ events and for fake-B decays are compared. The largest difference

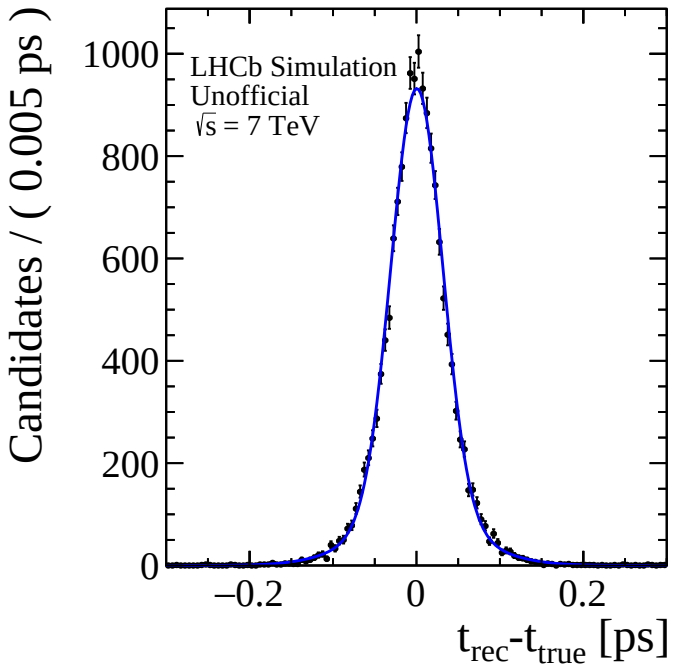

Figure 3.11: $B_s^0 \to D_s^- \pi^+$ *decay-time resolution, resulting from 2011 fully simulated events. The values of the parameters obtained from the fit are reported in Tab. 3.1.*

is observed for p and p_{T}. In order to check whether such differences lead to any significant effect on the decay-time resolution, the kinematics of the fake-B candidates are reweighted in order to match those of the fully simulated B_s^0 mesons. The results of such reweighting procedure are shown in the right part of Fig. 3.13.

By fitting the decay-time distribution of the reweighted data sample, shown in Fig. 3.14, only a slight variation with respect to the unweighted case (see Fig. 3.12) is found. In Tab. 3.1 the values of the double-Gaussian parameters used to fit the decay-time resolution in the case of Monte Carlo signal, fake-B candidates and reweighted fake-B candidates are reported. It is apparent that the effect of having different kinematics is mild. It can then be concluded that it is not necessary to apply a reweighting procedure. The method used to determine the decay-time resolution from fake-B candidates slightly overestimates the resolution, of about 4 fs. This difference will be taken into account as a systematic effect.

3.3.2 Decay-time resolution from data

In contrast to simulated events, here one needs to disentangle prompt D^- mesons from D^- mesons originated from B meson decays. The distribution of the logarithm of the D-meson impact parameter, $\ln(\mathrm{IP}_D)$, is expected to significantly differ between prompt and secondary D^- mesons, and hence can be used to perform such a separation.

Firstly, a background-subtraction is performed (using the *sPlot* technique) on the

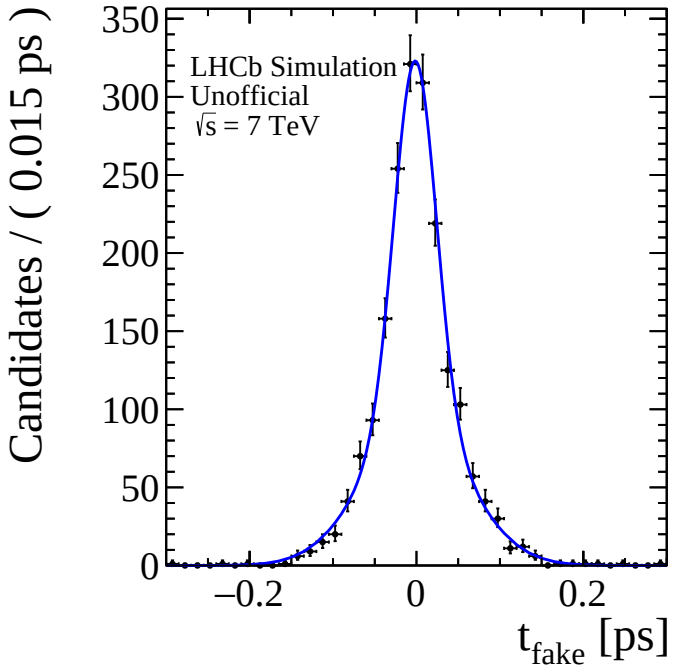

Figure 3.12: *Decay-time resolution from 2011 Monte Carlo fake-B candidates. The values of the parameters obtained from the fit are reported in Tab. 3.1.*

Table 3.1: *Values of the double-Gaussian parameters used to fit the decay-time resolution for 2011 simulated signals, fake-B candidates and reweighted fake-B candidates. The average width is calculated as* $\overline{\sigma} = \sqrt{f_1 \cdot \sigma_1^2 + (1 - f_1) \cdot \sigma_2^2}$ *and error using a Monte Carlo propagation which takes into account the correlation among the parameters.*

Parameter	Signal MC	MC fake-B	MC fake-B reweighted
μ [fs]	0.7 ± 0.4	-1.5 ± 0.9	-2.2 ± 0.9
σ_1 [fs]	32 ± 1	25 ± 2	22 ± 2
σ_2 [fs]	71 ± 2	62 ± 3	58 ± 2
f_1	0.79 ± 0.02	0.51 ± 0.06	0.44 ± 0.05
$\overline{\sigma}$ (average width) [fs]	43 ± 1	47 ± 1	46 ± 1

data sample selected by the `UnbiasedB2DPiWithUnbiasedB2DPi` *stripping line*. The data sample and the fit tothe $D^{\pm}$ invariant-mass spectrum, necessary to obtain the *sWeights*, is shown in Fig. 3.15.

Then the distribution of $\ln(\mathrm{IP}_D)$ is compared between the background-subtracted $D^{\pm}$ candidates from data and the simulated prompt $D^{\pm}$ candidates, to check the presence of a secondary $D^{\pm}$ component. Such a comparison is shown in Fig. 3.16, where the results of

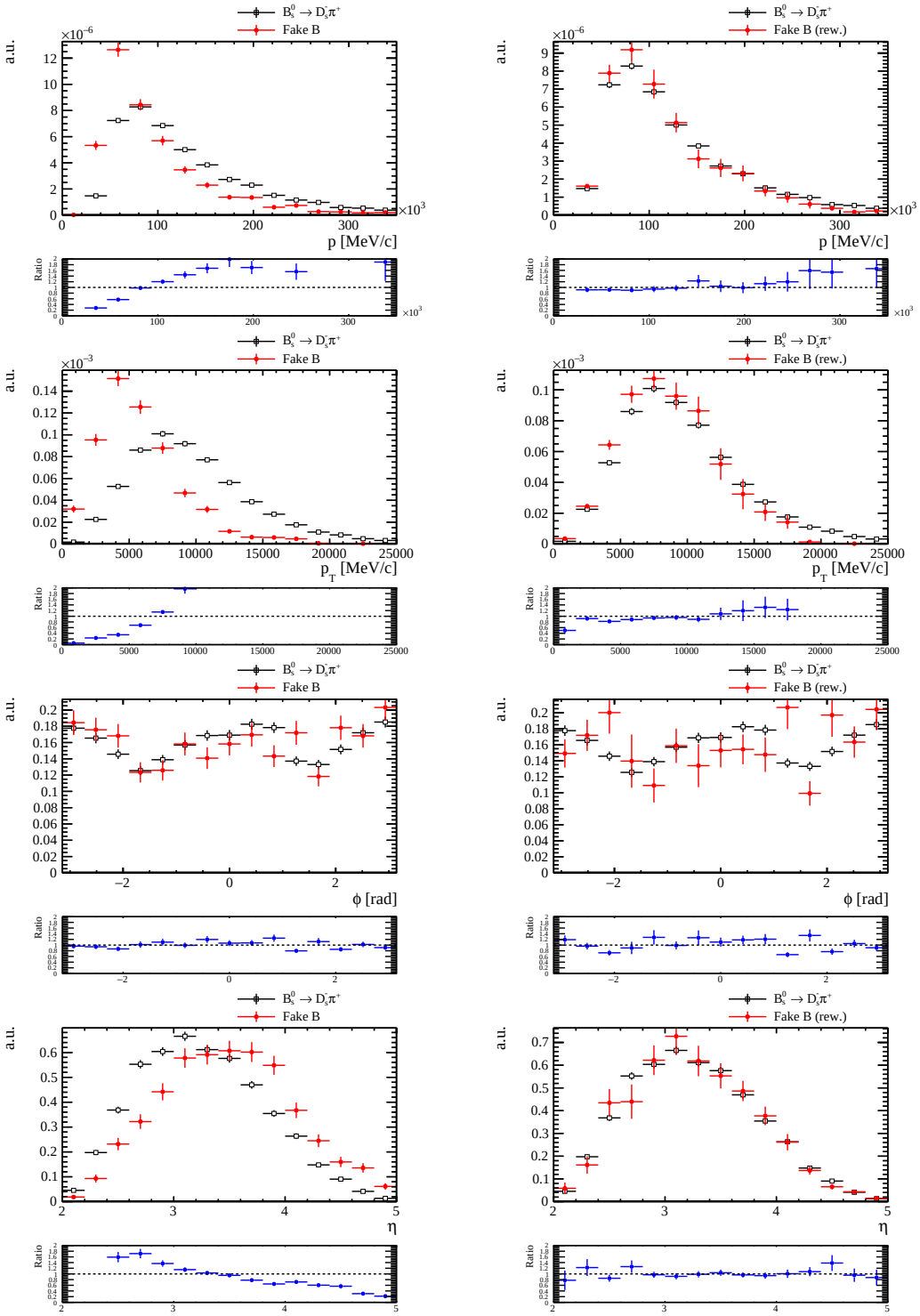

Figure 3.13: *Distribution of (from top to bottom) p, p_T, ϕ and η for (black dots) B_s^0 candidates decaying to $D_s^- \pi^+$ and (red dots) fake-B candidates. The reweighting procedure described in the text has been applied on the plots in the right part, while the plots on the left part represent the original distributions. All the distributions are obtained from 2011 data or simulation.*

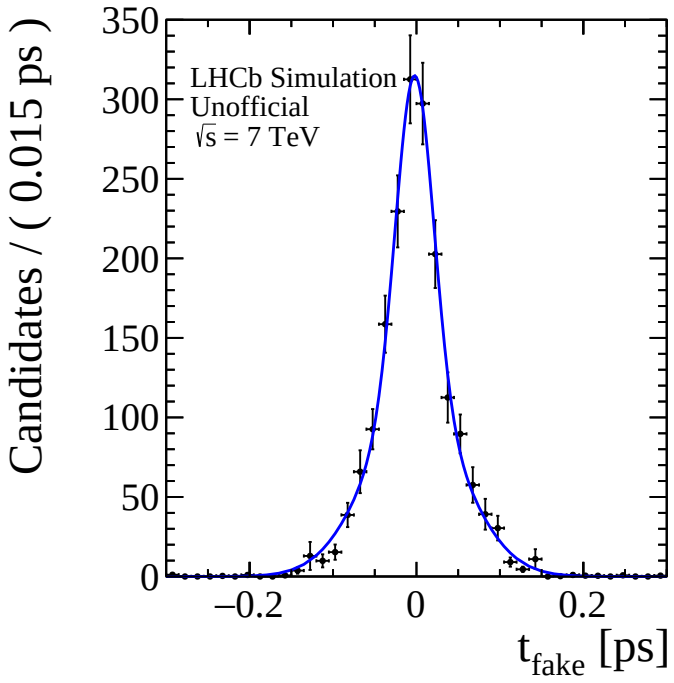

Figure 3.14: *decay-time distribution for 2011 fake-B candidates, once the reweighting procedure is applied.*

fits performed using a `Bukin` function are also overlaid. This function, where x corresponds to $\ln(\mathrm{IP}_D)$ and σ_p, ξ and $\rho_{1,2}$ are free parameters, is defined, for $x < x_1$ and $x > x_2$, as

$$f(x) = A \exp\left[\frac{\xi\sqrt{\xi^2+1}(x-x_1)\sqrt{2\ln 2}}{\sigma_p\left(\sqrt{\xi^2+1}-\xi\right)^2 \ln\left(\sqrt{\xi^2+1}+\xi\right)} + \rho\left(\frac{x-x_i}{x_p-x_i}\right)^2 - \ln 2\right], \quad (3.15)$$

where A is a normalization factor, $\rho = \rho_1$ and $x_i = x_1$ for $x < x_1$, $\rho = \rho_2$ and $x_i = x_2$ for $x > x_2$. For $x_1 < x < x_2$, the function is expressed as

$$f(x) = A \exp\left[-\ln 2 \left(\frac{\ln\left(1 + 2\xi\sqrt{\xi^2+1}\dfrac{x-x_p}{\sigma_p\sqrt{2\ln 2}}\right)}{\ln\left(1+2\xi^2-2\xi\sqrt{\xi^2+1}\right)}\right)^2\right]. \quad (3.16)$$

The values of x_1 and x_2 are given by

$$x_{1,2} = x_p + \sigma_p\sqrt{2\ln 2}\left(\frac{\xi}{\sqrt{\xi^2+1}} \mp 1\right). \quad (3.17)$$

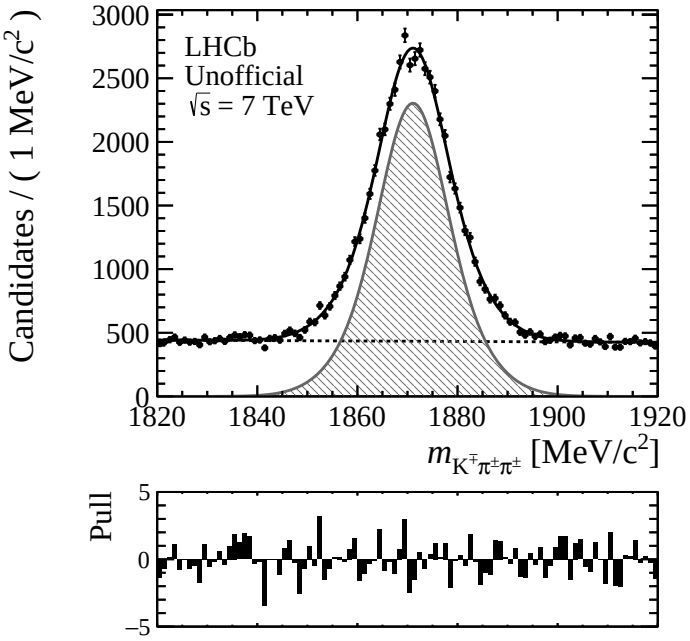

Figure 3.15: *Invariant-mass spectrum of 2011 $D^{\pm}$ candidates used to build the fake-B candidates.*

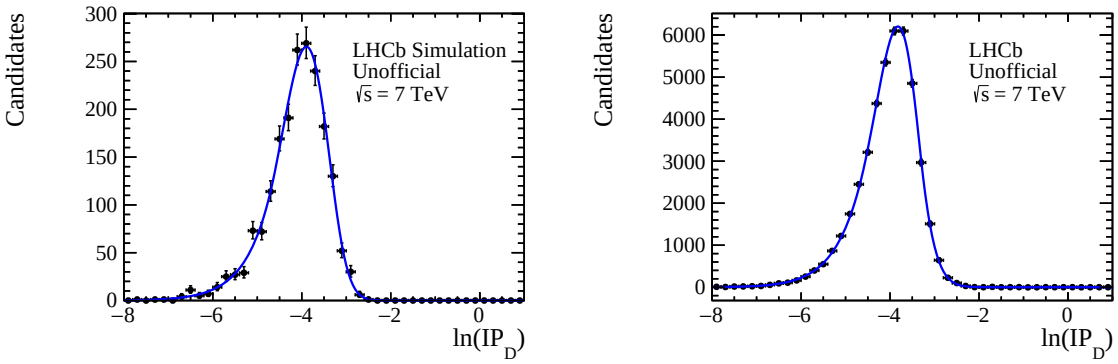

Figure 3.16: *Distributions of* $\ln(\mathrm{IP}_D)$ *for (left) 2011 prompt Monte Carlo $D^{\pm}$ mesons and (right) 2011 $D^{\pm}$ mesons from data used to build the fake-B candidates.*

In Tab. 3.2 the values of the parameters governing the shape of the `Bukin` function obtained from the fits are reported. There is no evidence of a secondary component for fake-B candidates from data. This is due to the requirements applied on the impact parameters.

The final resolution model is obtained by fitting the decay-time distribution of fake-B candidates using a triple-Gaussian function with common mean μ^{res}, widths $\sigma^{\mathrm{res}}_{1,2,3}$

Table 3.2: *Results of the fits to the* $\ln(\mathrm{IP}_D)$ *distributions using a* `Bukin` *function for prompt Monte Carlo* $D^{\pm}$ *mesons and* $D^{\pm}$ *mesons used to form the fake-*B *candidates.*

Parameter	prompt $D^{\pm}$ from MC	$D^{\pm}$ from fake-B
x_p	-3.90 ± 0.03	-3.82 ± 0.06
σ_p	0.55 ± 0.02	0.52 ± 0.03
ξ	-0.12 ± 0.04	-0.17 ± 0.01
ρ_1	-0.02 ± 0.04	-0.05 ± 0.01
ρ_2	-1.08 ± 0.40	-0.48 ± 0.05

.

Table 3.3: *Values of the triple-Gaussian function parameters obtained from a fit to the decay-time distribution of fake-*B *candidates from 2011 data.*

Resolution model parameter	value
μ^{res} [fs]	-1.6 ± 0.2
σ_1^{res} [fs]	17.3 ± 0.6
σ_2^{res} [fs]	49.0 ± 0.9
σ_3^{res} [fs]	101 ± 6
f_1^{res}	0.25 ± 0.01
f_2^{res}	0.68 ± 0.01
$\overline{\sigma}$ (average width) [fs]	49.2 ± 0.3

and fraction of the first and second Gaussian $f_{1,2}^{\mathrm{res}}$. Figure. 3.17 shows the decay-time distribution of fake-B candidates with the results of the fit overlaid. In Tab. 3.3 the values of the triple-Gaussian parameters obtained from the fit are reported.

3.3.3 Uncertainty on decay-time resolution model

Two possible sources of uncertainty are considered. The first is due to the method and it is evaluated by taking the difference between the average resolution width of fully simulated $B_s^0 \to D_s^- \pi^+$ decays and that obtained using fake-B decays. As already said, this difference amounts to 4 fs. The second source of uncertainty comes from taking into account the dependence of the resolution on the decay time. As done in Ref. [65], to study such a dependence the $B_s^0 \to D_s^- \pi^+$ fully simulated sample is divided in bins of decay time and the root mean square (RMS) of $t_{\mathrm{rec}} - t_{\mathrm{true}}$ is plotted for each bin (see Fig. 3.18). The variation observed with respect to the average width (43 fs) is about ± 8 fs. A systematic uncertainty is assigned by rescaling the three widths of the baseline resolution model in order to have an average width differing by ± 8 fs from the baseline one.

Since the analysis is performed in bins of p_{T} and y of the B meson, as it will be

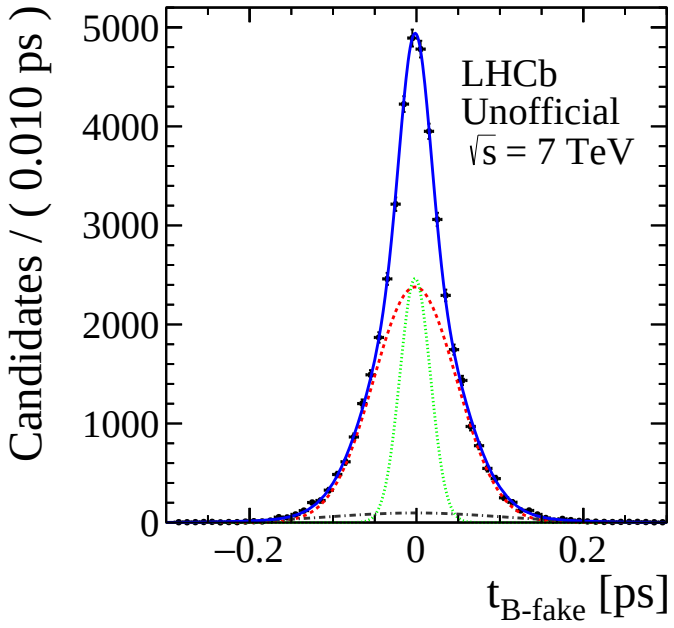

Figure 3.17: *decay-time distribution of fake-B candidates for 2011 data, with the result of the fit overlaid. The three coloured lines represent the three Gaussian functions of the resolution model.*

discussed later, in the case of the B_s^0 the baseline resolution model is also determined for each bin separately. This study is limited to the B_s^0 only, since the resolution model has a non-negligible impact in this case due to the fast B_s^0 oscillations. This discussion is however postponed as the definition of the various kinematic bins needs to be introduced first.

3.3.3.1 Study on 2012 data

In order to check that the proper time resolution is unchanged in 2012 data, the measurement of the fake-B decay-time resolution is repeated using 2012 data. The results are reported in Tab. 3.4, while Fig. 3.19 shows the decay-time resolution of fake-B candidates, with the results of the fit overlaid. A comparison with the results reported in Tab. 3.3 shows no significance differences between 2011 and 2012 studies.

The decay-time resolution is also studied on fully simulated events. The full selection chain, *i.e.* trigger-preselection-PID-BDT, is used to select a sample of $B_s^0 \to D_s^- \pi^+$ fully simulated events and evaluate the decay-time resolution. Figure 3.20 shows the distribution of $t_{\rm rec} - t_{\rm true}$, where $t_{\rm rec}$ is the reconstructed B_s^0 decay time, while $t_{\rm true}$ is the B_s^0 true decay time. The result of a fit with a double-Gaussian function with common mean is overlaid. The results are consistent with the ones obtained with 2011 fully simulated events and are reported in Tab. 3.5.

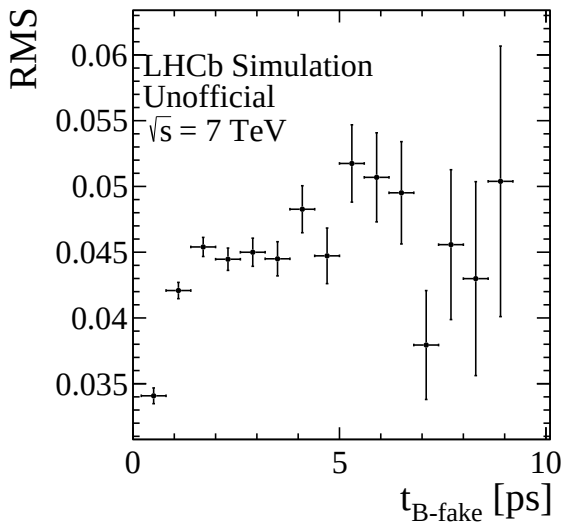

Figure 3.18: *Root mean square (RMS) of* $t_{\rm rec} - t_{\rm true}$ *in bins of decay time for the 2011 fully simulated* $B_s^0 \to D_s^- \pi^+$ *events.*

Table 3.4: *Values of the triple-Gaussian function parameters obtained from a fit to the decay-time distribution of fake-B candidates from 2012 data.*

Resolution model parameter	value
$\mu^{\rm res}$ [fs]	-0.46 ± 0.03
$\sigma_1^{\rm res}$ [fs]	18.2 ± 0.1
$\sigma_2^{\rm res}$ [fs]	50.5 ± 0.2
$\sigma_3^{\rm res}$ [fs]	105 ± 1
$f_1^{\rm res}$	0.28 ± 0.002
$f_2^{\rm res}$	0.66 ± 0.002
$\overline{\sigma}$ (average width) [fs]	49.4 ± 0.3

The study of the dependence of the resolution on the decay time has also been performed and no deviation with respect to the 2011 results are observed. The dependence of the RMS on the decay time are shown in Fig. 3.21.

In conclusion, all the studies performed on 2012 data show no significance differences with respect to those done on 2011 data. For this reason, a triple-Gaussian function with the values of the parameters obtained from the fit to the fake-B decay-time distribution and summarised in Tab. 3.3 is used as baseline model for 2012 data. Systematic uncertainties due to this choice have been assessed in the same way as for 2011 data.

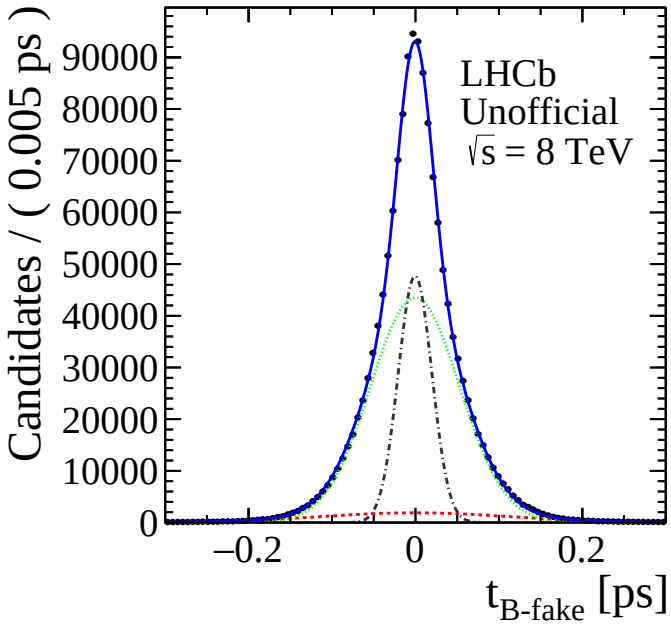

Figure 3.19: *decay-time distribution of fake-B candidates for 2012 data, with the result of the fit overlaid.*

Table 3.5: *Values of the triple-Gaussian parameters used to fit the decay-time resolution for 2012 simulated signals candidates. The average width is calculated as* $\overline{\sigma} = \sqrt{f_1 \cdot \sigma_1^2 + (1-f_1) \cdot \sigma_2^2 + (1-f_1-f_2) \cdot \sigma_3}$ *and error using a Monte Carlo propagation which takes into account the correlation among the parameters.*

Parameter	Signal MC
μ [fs]	$(1 \pm 1) \cdot 10^{-5}$
σ_1 [fs]	26.2 ± 0.7
σ_2 [fs]	49 ± 2
σ_3 [fs]	105 ± 6
f_1	0.43 ± 0.04
f_2	0.53 ± 0.04
$\overline{\sigma}$ (average width) [fs]	43 ± 2

3.4 Fit model

3.4.1 $B^+ \to J/\psi K^+$

3.4.1.1 Signal model

The signal component for $B^+ \to J/\psi K^+$ decays is modeled by convolving a triple-Gaussian function with a function parameterizing the final state QED radiation (FSR). The PDF is

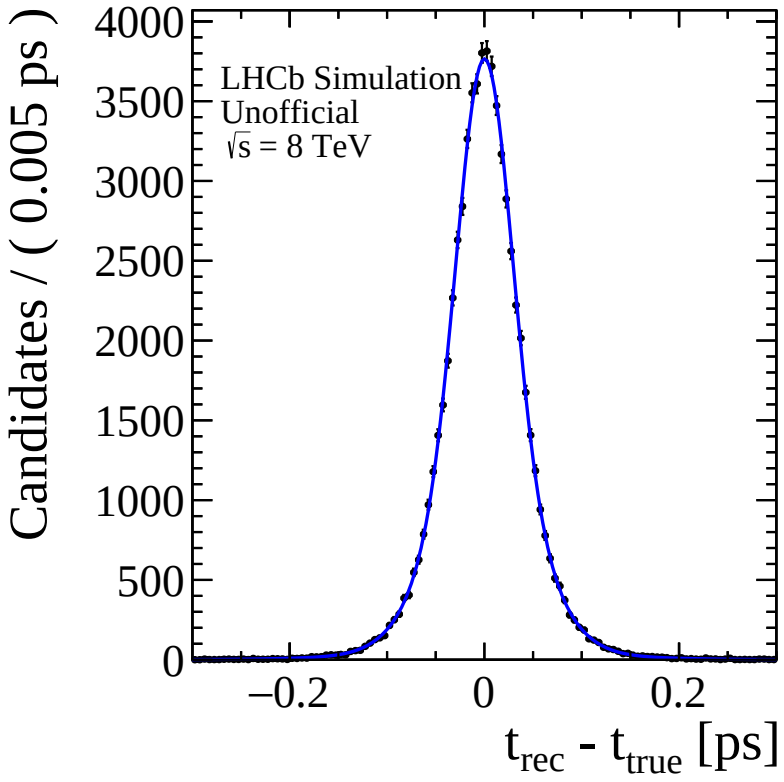

Figure 3.20: $B_s^0 \to D_s^- \pi^+$ *decay-time resolution, resulting from and 2012 simulated events . The values of the parameters obtained from the fit are reported in Tab. 3.5.*

given by

$$g(m) \propto \int_0^{+\infty} (m')^s G\left(m + m'; \mu\right) \mathrm{d}m', \tag{3.18}$$

where G is the sum of three Gaussian functions with different widths and common mean μ. The parameter s governs the amount of final state radiation (FSR) and it is determined using simulated events. Figure. 3.22 shows the invariant-mass spectra for fully simulated truth-matched signal events with the results of the fit overlaid. In both the 2011 and 2012 cases two Gaussian functions are enough to describe the spectra. In Tab. 3.6 the values of the parameters obtained from the fits are reported.

3.4.1.2 Background model

In the case of $B^+ \to J/\psi K^+$ decays we consider only the combinatorial background due to the random association of tracks. The invariant-mass line shape is well described by means of the following PDF

$$\mathcal{P}_{bkg}(m; \xi_{comb}) = K e^{-m\xi^{comb}}, \tag{3.19}$$

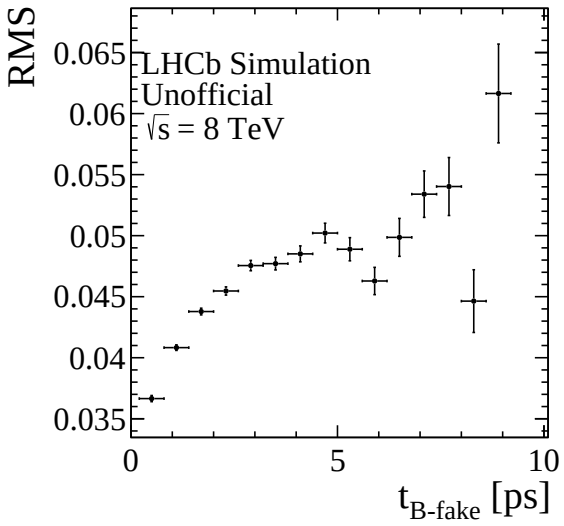

Figure 3.21: *Root mean square (RMS) of* $t_{\rm rec} - t_{\rm true}$ *in bins of decay time for the 2012 fully simulated* $B_s^0 \to D_s^- \pi^+$ *events.*

where K is a normalization factor.

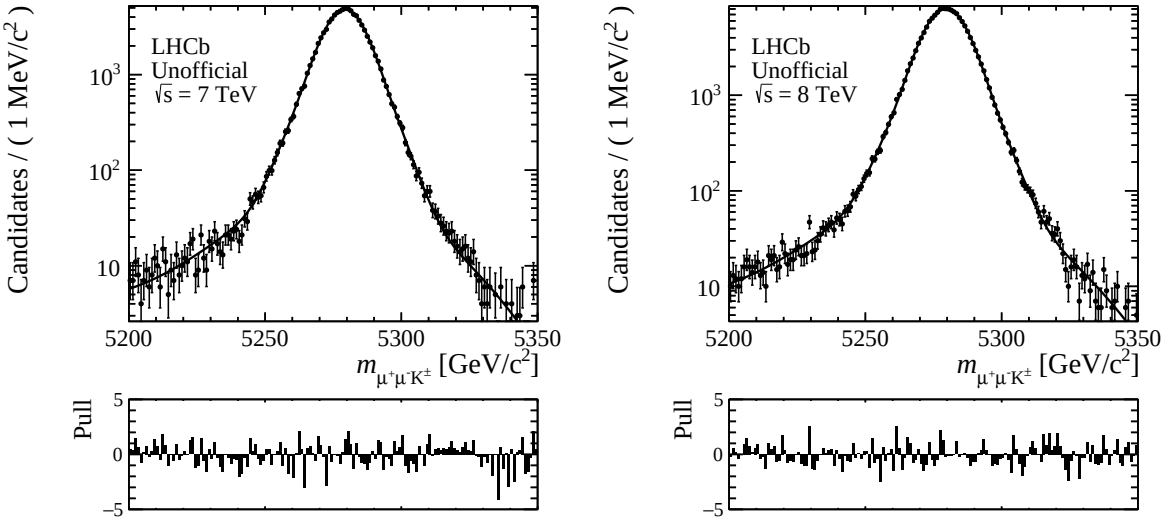

Figure 3.22: *Invariant-mass spectra for (left) 2011 and (right) 2012 fully simulated truth-matched signal events with the results of the fit overlaid.*

Table 3.6: *Values of the signal mass-shape parameters obtained from fits to fully simulated events.*

Parameter	2011	2012
μ [MeV/c^2]	5279.30 ± 0.03	5279.60 ± 0.03
σ_1 [MeV/c^2]	6.5 ± 0.1	6.9 ± 0.1
σ_2 [MeV/c^2]	11.1 ± 0.4	11.8 ± 0.4
σ_2 [MeV/c^2]	26.8 ± 1.7	28.1 ± 1.5
f_1	0.60 ± 0.04	0.67 ± 0.03
f_2	0.030 ± 0.005	0.030 ± 0.004
s	-0.9973 ± 0.0008	-0.9963 ± 0.0006

3.4.2 $B^0 \to J/\psi\, K^{*0}$ and $B_s^0 \to D_s^- \pi^+$

A PDF for the invariant mass and decay time of each channel starting are defined starting from elementary components. For each component, the mass and time parts are factorized, due to their independence.

3.4.2.1 Signal model

The signal component for each decay is modeled convolving a triple-Gaussian function with a function parameterizing the FSR. The PDF is given by

$$g(m) \propto \int_0^{+\infty} (m')^s G\left(m + m'; \mu\right) \mathrm{d}m', \tag{3.20}$$

where G is the sum of three Gaussian functions with different widths and common mean μ. The parameter s governs the amount of FSR and it is determined using simulated events. Figure 3.23 shows the invariant-mass spectra for fully simulated truth-matched signal events with the result of fits overlaid. In the case of the $B^0 \to J/\psi\, K^{*0}$ decay a better description is obtained using a sum of three Gaussian functions, whereas for $B_s^0 \to D_s^- \pi^+$ decay two Gaussian functions are enough. In Tab. 3.7 the values obtained from the fits are reported.

The decay rate to a flavour-specific final state of a neutral B meson is parameterized with the following PDF

$$\begin{aligned} f\left(t, \psi, \xi\right) \;=\; & K\left(1 - \psi A_{CP}\right)\left(1 - \psi A_f\right) \\ & \left\{ e^{-\Gamma t} \left[\Omega_+^\xi \cosh\left(\frac{\Delta\Gamma t}{2}\right) + \psi \Omega_-^\xi \cos\left(\Delta m t\right) \right] \right\} \otimes R\left(t\right) \epsilon\left(t\right), \end{aligned} \tag{3.21}$$

where K is a normalization factor, $\epsilon\left(t\right)$ is the acceptance as a function of the decay time (see Sec. 3.4.2.1), $R\left(t\right)$ is a decay-time resolution function. The three observables are the decay time t, the tag of the final state ψ, which assumes the values $\psi = 1$ if the final state is f and $\psi = -1$ if the final state is the CP conjugate $\bar{f}$, and the tag of the initial

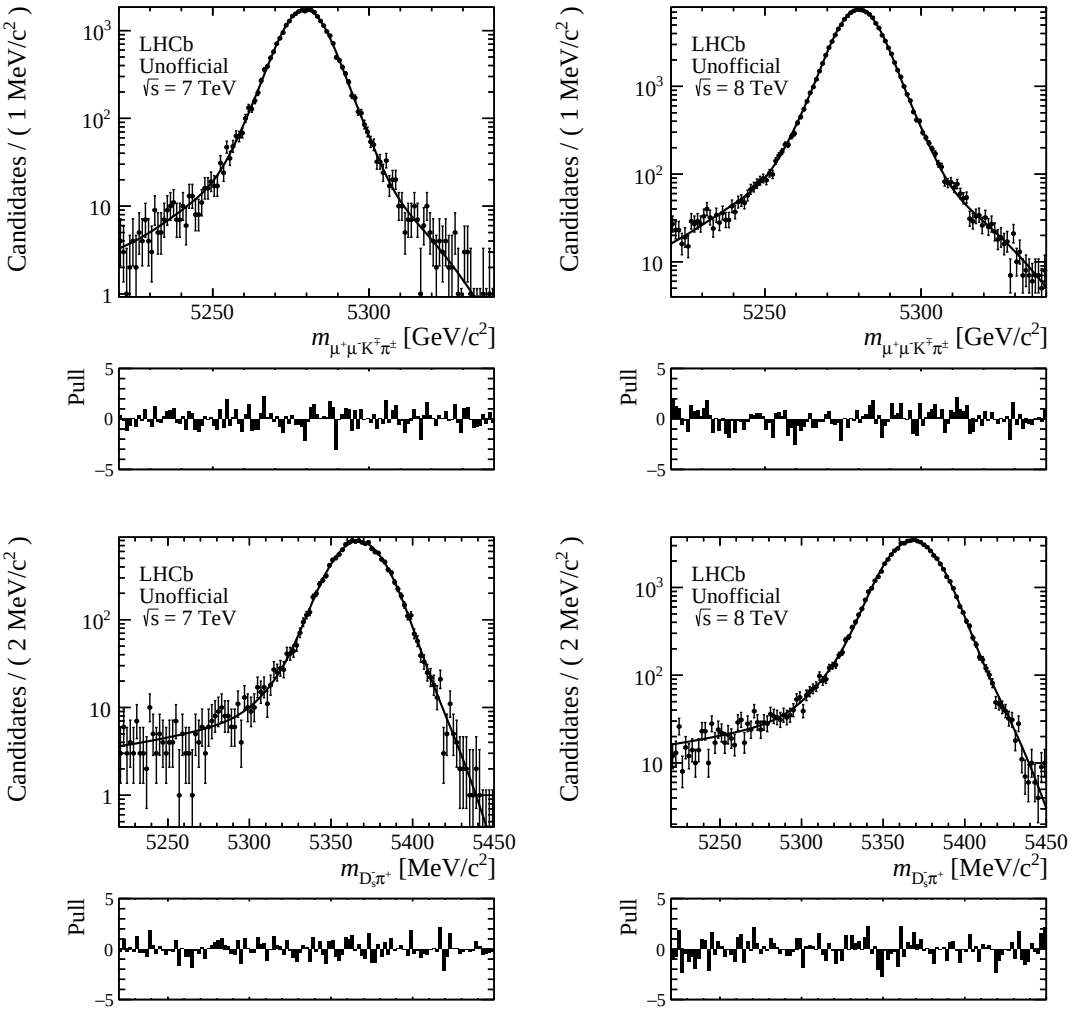

Figure 3.23: *Invariant-mass spectra for fully simulated truth-matched signal events: (top left) $B^0 \to J/\psi K^{*0}$ 2011 data, (top right) $B^0 \to J/\psi K^{*0}$ 2012 data, (bottom left) $B_s^0 \to D_s^- \pi^+$ 2011 data and (bottom right) $B_s^0 \to D_s^- \pi^+$ 2012 data. The results of the fits are overlaid.*

flavour of the B meson ξ, which assumes the values $\xi = 1$ if it is B and $\xi = -1$ if it is $\bar{B}$. The final states are $f = J/\psi K^{*0}$ for $B^0 \to J/\psi K^{*0}$ decays and $f = D_s^- \pi^+$ for $B_s^0 \to D_s^- \pi^+$ decays. The terms Ω_+ and Ω_- are defined as

$$\Omega_\pm = \delta_{1,\xi} (1 - A_{\mathrm{P}}) \left| \frac{q}{p} \right|^{1-\psi} \pm \delta_{-1,\xi} (1 + A_{\mathrm{P}}) \left| \frac{q}{p} \right|^{-1-\psi}, \tag{3.22}$$

where $\delta_{i,j}$ is the Kronecker delta. The symbol A_{P} denotes the production asymmetry of the given $B_{(s)}^0$ meson and A_f is detection asymmetry of the final state, defined in terms of

Table 3.7: *Values of the signal mass shape parameters obtained from fits to fully simulated events.*

Parameter	$B^0 \to J/\psi K^{*0}$ (2011)	$B^0 \to J/\psi K^{*0}$ (2012)	$B_s^0 \to D_s^- \pi^+$ (2011)	$B_s^0 \to D_s^- \pi^+$ (2012)
μ [MeV/c^2]	5279.5 ± 0.04	5280.2 ± 0.02	5367.1 ± 0.14	5368.3 ± 0.1
σ_1 [MeV/c^2]	9.1 ± 0.1	9.9 ± 0.5	14.3 ± 0.3	14.5 ± 0.2
σ_2 [MeV/c^2]	20.8 ± 1.2	5.8 ± 0.1	24.1 ± 1.6	26.0 ± 0.7
σ_3 [MeV/c^2]	5.6 ± 0.1	25.5 ± 1.7	–	–
f_1	0.41 ± 0.02	0.33 ± 0.05	0.83 ± 0.05	0.80 ± 0.02
f_2	0.54 ± 0.02	0.039 ± 0.005	–	–
s	-0.9947 ± 0.0006	-0.9945 ± 0.0003	-0.9834 ± 0.0010	-0.9832 ± 0.0005

the f and $\bar{f}$ detection efficiencies as

$$A_f = \frac{\epsilon_{\bar{f}} - \epsilon_f}{\epsilon_{\bar{f}} + \epsilon_f}. \tag{3.23}$$

The direct *CP* asymmetry A_{CP} is defined as

$$A_{CP} = \frac{\mathcal{B}\left(\bar{B} \to \bar{f}\right) - \mathcal{B}\left(B \to f\right)}{\mathcal{B}\left(\bar{B} \to \bar{f}\right) + \mathcal{B}\left(B \to f\right)}. \tag{3.24}$$

By summing over the initial state tag, the following PDF for untagged decays is obtained

$$\begin{aligned} f\left(t, \psi\right) \;=\; & K\left(1 - \psi A_{CP}\right)\left(1 - \psi A_f\right) \\ & \left\{ e^{-\Gamma t} \left[\Lambda_+ \cosh\left(\frac{\Delta\Gamma t}{2}\right) + \psi \Lambda_- \cos\left(\Delta m t\right) \right] \right\} \otimes R\left(t\right) \epsilon\left(t\right), \end{aligned} \tag{3.25}$$

where the terms Λ_+ and Λ_- are defined as

$$\Lambda_\pm = \left(1 - A_{\mathrm{P}}\right) \left|\frac{q}{p}\right|^{1-\psi} \pm \left(1 + A_{\mathrm{P}}\right) \left|\frac{q}{p}\right|^{-1-\psi}. \tag{3.26}$$

Decay time acceptance Trigger and event selections lead to distortions in the shapes of the decay-time distributions. The signal decay time acceptances are parametrised using fully simulated events. For each simulated decay mode, the trigger and selection requirements are applied as for the real data. Then unbinned maximum likelihood fits to the distributions of the decay time are performed. In the fit all the physical parameters are fixed to their simulated values, *i.e.* average decay widths, decay width differences and mass differences of the B mass eigenstates. As decay-time resolution model a single Gaussian function with 43 fs width is used. A good parameterization for $B^0 \to J/\psi K^{*0}$ decays is empirically found to be

$$\varepsilon_{\mathrm{acc}}\left(t\right) = \frac{1}{2}\left[1 - \mathrm{erf}\left(p_1 t^{p_2}\right)\right]\left(1 + p_3 t\right), \tag{3.27}$$

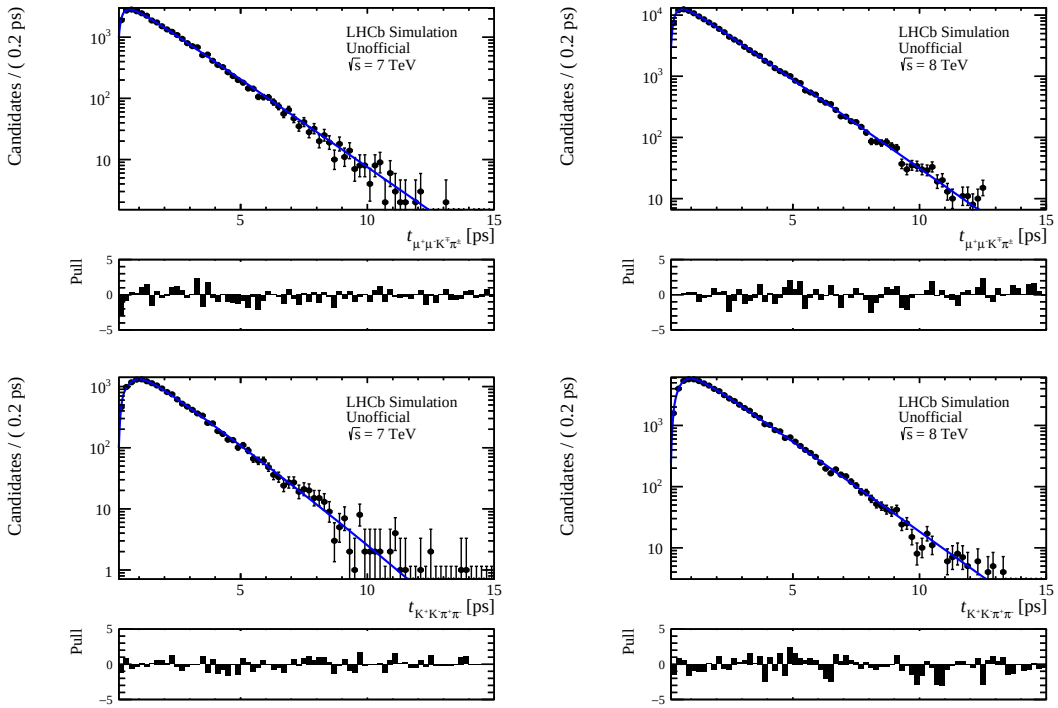

Figure 3.24: *decay-time distributions of fully simulated events with the result of the fits overlaid for (top left) $B^0 \to J/\psi K^{*0}$ 2011, (top right) $B^0 \to J/\psi K^{*0}$ 2012, (bottom left) $B_s^0 \to D_s^- \pi^+$ 2011 and (bottom right) $B_s^0 \to D_s^- \pi^+$ 2012 data.*

while for $B_s^0 \to D_s^- \pi^+$ decays it is

$$\varepsilon_{\rm acc}(t) = \frac{1}{2}\left[1 - \frac{1}{2}{\rm erf}\left(\frac{p_1 - t}{t}\right) - \frac{1}{2}{\rm erf}\left(\frac{p_2 - t}{t}\right)\right](1 + p_3 t)\,, \tag{3.28}$$

where p_1, p_2 and p_3 are free parameters and erf is the error function. In Fig. 3.24 and 3.25 the decay time distribution and decay time acceptances of $B^0 \to J/\psi K^{*0}$ and $B_s^0 \to D_s^- \pi^+$ decays are shown with the results of the fits superimposed. The numerical values of the acceptance parameters obtained from the fits are reported in Tab. 3.8.

3.4.2.2 Background model

Two categories of background are considered: the combinatorial background, due to the random association of tracks, and the partially-reconstructed background, due to decays with a topology similar to that of the signal, but with one or more non reconstructed particles. The latter component is present only in $B_s^0 \to D_s^- \pi^+$ decays.

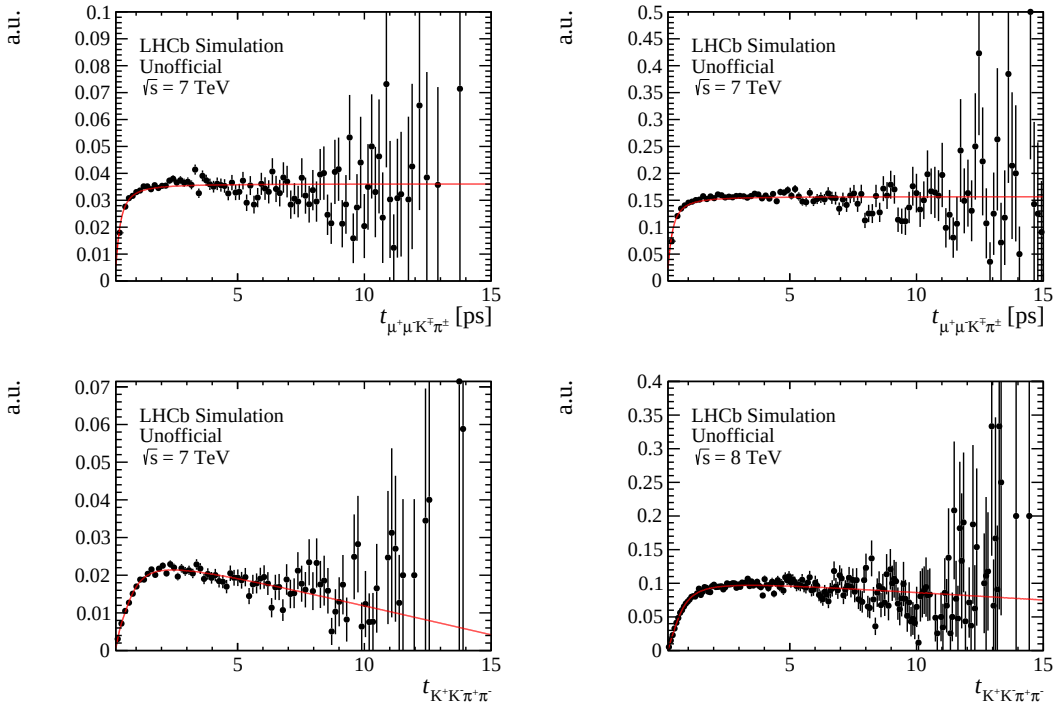

Figure 3.25: *Decay time acceptances of fully simulated events with the result of the fits overlaid for (top left) $B^0 \to J/\psi K^{*0}$ 2011, (top right) $B^0 \to J/\psi K^{*0}$ 2012, (bottom left) $B_s^0 \to D_s^- \pi^+$ 2011 and (bottom right) $B_s^0 \to D_s^- \pi^+$ 2012 data.*

Table 3.8: *Acceptance parameters determined from decay time fits to Monte Carlo signal events. Note that the parameters p_1 and p_2 have different meanings for $B^0 \to J/\psi K^{*0}$ and $B_s^0 \to D_s^- \pi^+$ decays. The decay time is measured in ps.*

Parameter	$B^0 \to J/\psi K^{*0}$ (2011)	$B^0 \to J/\psi K^{*0}$ (2012)	$B_s^0 \to D_s^- \pi^+$ (2011)	$B_s^0 \to D_s^- \pi^+$ (2012)
p_1 $[ps]$	0.13 ± 0.01	0.088 ± 0.006	0.432 ± 0.008	0.471 ± 0.004
p_2 $[ps]$	-1.34 ± 0.06	-1.52 ± 0.05	1.19 ± 0.06	1.08 ± 0.03
p_3 $[ps^{-1}]$	-0.007 ± 0.004	-0.011 ± 0.002	-0.056 ± 0.006	-0.022 ± 0.003

Combinatorial background The invariant-mass line shape is well described in all cases by means of the following PDF

$$B(m) = Ke^{-m\xi^{\text{comb}}}, \tag{3.29}$$

where K is a normalization factor. In order to study the parameterization of the decay-time distributions we focus on the high invariant mass sidebands, that we define as 5.31–5.34 GeV/c^2 for $B^0 \to J/\psi K^{*0}$ and 5.45–5.90 GeV/c^2 for $B_s^0 \to D_s^- \pi^+$ decays. Concerning the $J/\psi K^{*0}$ spectrum, it is empirically found that an accurate description is given by the

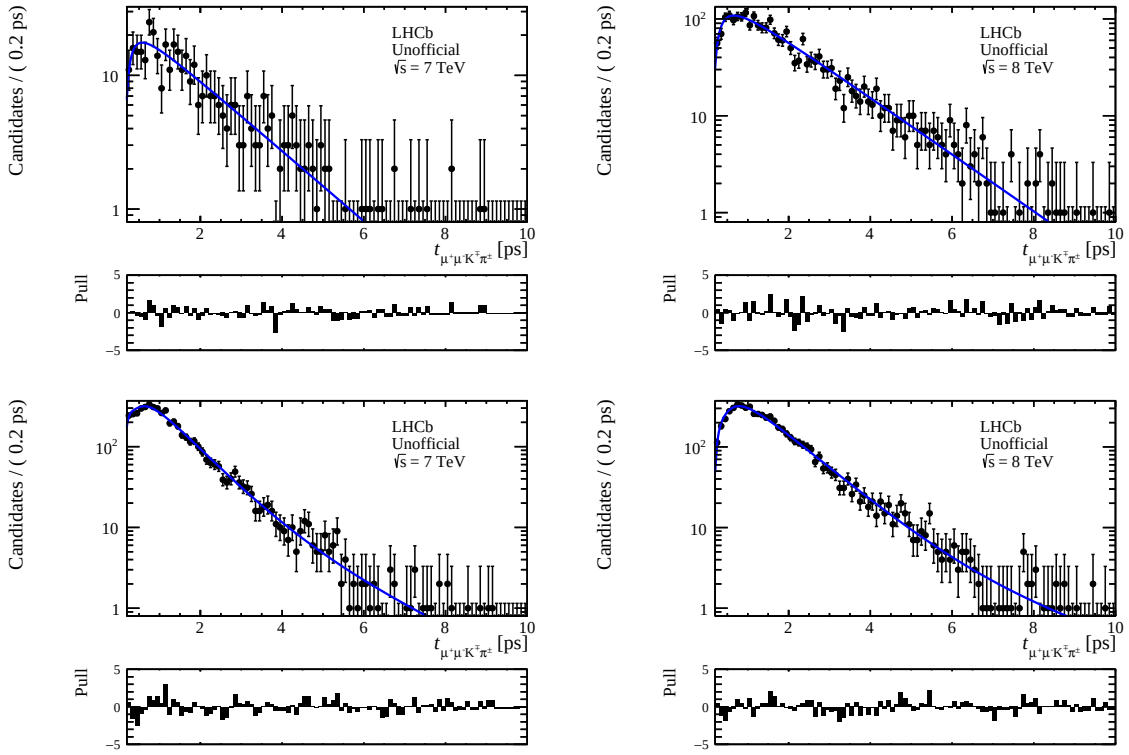

Figure 3.26: *Decay-time distributions of combinatorial background events from high invariant-mass sidebands: (top left) $B^0 \to J/\psi K^{*0}$ 2011 data, (top right), $B^0 \to J/\psi K^{*0}$ 2012, (bottom left) $B_s^0 \to D_s^- \pi^+$ 2011 and (bottom right) $B_s^0 \to D_s^- \pi^+$ 2012 . The result of the fits are superimposed.*

PDF

$$f(t,\,\psi) = K\left(1 - \psi A_{\rm comb}\right)\left[f^{\rm comb} e^{-\Gamma_1^{\rm comb} t} + \left(1 - f^{\rm comb}\right) e^{-\Gamma_2^{\rm comb} t}\right] \varepsilon_{\rm acc}^{\rm comb}(t)\,, \tag{3.30}$$

where K is a normalization factor and $A_{\rm comb}$ is the charge asymmetry of the combinatorial background. For the $J/\psi K^{*0}$ spectrum the effective "acceptance" function $\varepsilon_{\rm acc}^{\rm comb}(t)$ is given by

$$\varepsilon_{\rm acc}^{\rm comb}(t) = \frac{1}{2}\left[1 - {\rm erf}\left(p_1^{\rm comb} t^{p_2^{\rm comb}}\right)\right], \tag{3.31}$$

whereas for the $D_s^-\pi^+$ spectra is given by

$$\varepsilon_{\rm acc}^{\rm comb}(t) = \frac{1}{2}\left[1 - \frac{1}{2}{\rm erf}\left(\frac{p_1^{\rm comb} - t}{t}\right) - \frac{1}{2}{\rm erf}\left(\frac{p_2^{\rm comb} - t}{t}\right)\right]. \tag{3.32}$$

In Fig. 3.26 the decay-time distributions corresponding to the high invariant-mass sidebands are shown with the result of the fits superimposed. The values of the various parameters determined from the fits are reported in Tab. 3.9.

Table 3.9: *Parameters determined from fits to events corresponding to the high mass sidebands. Note that the parameters p_1 and p_2 have different meanings for $B^0 \to J/\psi K^{*0}$ and $B_s^0 \to D_s^- \pi^+$ decays and thus their units of measure differ. The decay time is measured in ps.*

Parameter	$B^0 \to J/\psi K^{*0}$ (2011)	$B^0 \to J/\psi K^{*0}$ (2012)	$B_s^0 \to D_s^- \pi^+$ (2011)	$B_s^0 \to D_s^- \pi^+$ (2012)
$p_1^{\rm comb}$ $[ps^{-1}]$	0.01 ± 0.01	0.0001 ± 0.0002	0.26 ± 0.02	0.39 ± 0.01
$p_2^{\rm comb}$ [no dim. or ps]	-2.6 ± 2.0	-5.1 ± 1.0	0.91 ± 0.07	0.99 ± 0.08
$\Gamma_1^{\rm comb}$ $[ps^{-1}]$	-0.70 ± 0.03	-0.68 ± 0.01	-0.58 ± 0.15	-0.37 ± 0.21
$\Gamma_2^{\rm comb}$ $[ps^{-1}]$	-2.45 ± 0.42	-2.61 ± 0.11	-1.3 ± 0.1	-1.02 ± 0.06
$f^{\rm comb}$	0.16 ± 0.03	0.17 ± 0.01	0.05 ± 0.03	0.02 ± 0.02

Partially-reconstructed background In the case of the $D_s^- \pi^+$ spectrum, a background component due to partially-reconstructed B_s^0 decays is present in the low invariant mass sideband. The main contributions are expected to come from

- $B_s^0 \to D_s^{*-}(D_s^- \gamma, D_s^- \pi^0)\pi^+$ decays with $D_s^- \to K^- K^+ \pi^-$, and a missing γ/π^0;
- $B_s^0 \to D_s^-(K^- K^+ \pi^-)\rho^+(\pi^+ \pi^0)$ decays where the π^0 is missing.

The partially-reconstructed component is parameterised by means of a kernel estimation technique [66] based on invariant-mass distributions obtained from fully simulated events, where the same selection applied to data is used. In order to take into account the discrepancy in resolution between data and fully simulated events, the invariant mass is calculated by smearing with Gaussian-distributed random numbers the value of the true mass, *i.e.* the mass calculated using true momenta. The width of the Gaussian function is extracted from data by fitting the invariant-mass spectrum in the region where no contribution from partially-reconstructed events is present. An average width of $\sim 22\,\mathrm{MeV}/c^2$ is found for both the decay modes. In addition, mass shifts of $5\,\mathrm{MeV}/c^2$ are found in the case of $B_s^0 \to D_s^- \pi^+$ decays, which are included in the mass templates. The invariant mass templates so obtained are shown in Fig. 3.27 for the 2011 case.

As far as the decay-time components are concerned, a good empirical parameterization is given by

$$f\,(t,\ \psi) = K\,(1 - \psi A_{\rm phys})\, e^{-\Gamma^{\rm phys} t} \varepsilon_{\rm acc}^{\rm phys}\,(t)\,, \tag{3.33}$$

where K is a normalization factor and

$$\varepsilon_{\rm acc}^{phys}\,(t) = \frac{1}{2}\left[1 - {\rm erf}\left(p_1^{\rm phys} t^{p_2^{\rm phys}}\right)\right]. \tag{3.34}$$

In Fig. 3.28 the decay-time distribution corresponding to $B_s^0 \to D_s^{*-}\pi^+$ and $B_s^0 \to D_s^- \rho^+$ decays obtained using fully simulated events is shown. In Tab. 3.10 the values of the parameters obtained from the fits are reported.

$\mathbf{B^0 \to D_s^- \pi^+}$ background In the case of $B_s^0 \to D_s^- \pi^+$ decays, a background component due to the $B^0 \to D_s^- \pi^+$ decays is also presented. This component is accounted for in the

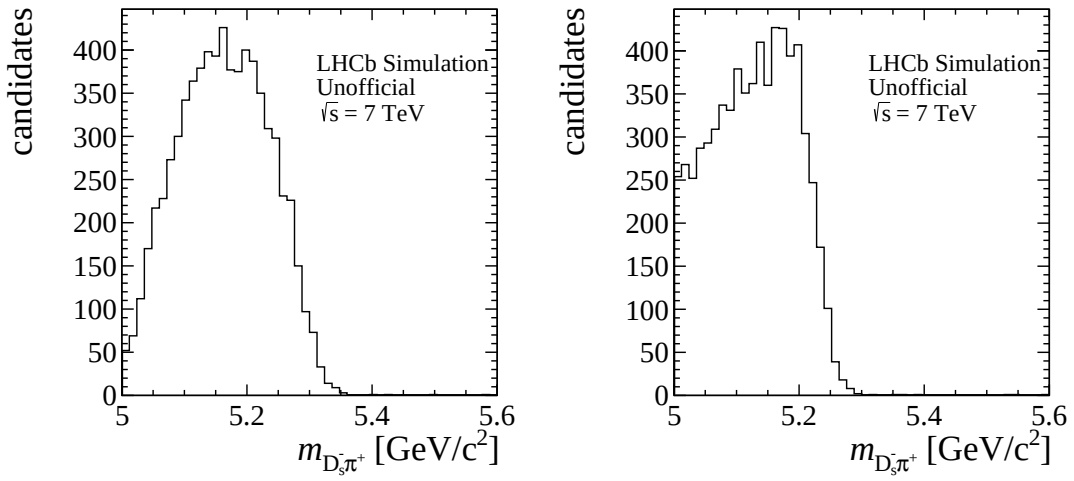

Figure 3.27: *Invariant-mass distributions of 2011 (left) $B_s^0 \to D_s^{*-}\pi^+$ and (right) $B_s^0 \to D_s^-\rho^+$ simulated events.*

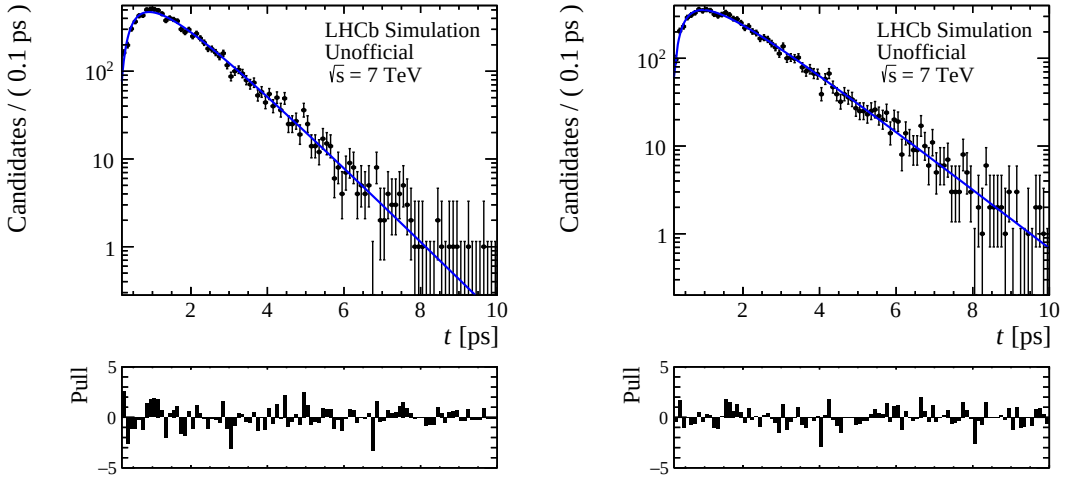

Figure 3.28: *Decay-time spectra of 2011 (left) $B_s^0 \to D_s^{*-}\pi^+$ and (right) $B_s^0 \to D_s^-\rho^+$ decays, obtained using simulated events. The results of the fits are overlaid.*

fits using the same parameterisation adopted for the signal and described in Sec. 3.4.2.1. The invariant-mass resolution model is the same as for the B_s^0 decay, with an average mass shifted by the difference in nominal masses between B^0 and B_s^0 mesons according to the PDG. In the decay time PDF, the production asymmetry is fixed from the $B^0 \to D^-\pi^+$ fit. The $B^0 \to D_s^-\pi^+$ yield is fixed from the ratio between hadronization fractions and branching ratios.

Table 3.10: *Parameters of functions describing the decay-time distributions of partially-reconstructed background decays, as determined from fits to simulated events.*

Parameter	$B^0 \to D^-\pi^+$ BDT	
	$B_s^0 \to D_s^{*-}\pi^+$	$B_s^0 \to D_s^-\rho^+$
p_1^{phys} $[ps^{-1}]$	0.81 ± 0.09	0.66 ± 0.08
p_2^{phys}	-0.44 ± 0.06	-0.51 ± 0.07
$\Gamma^{\rm phys}$ $[ps^{-1}]$	0.78 ± 0.02	0.92 ± 0.02

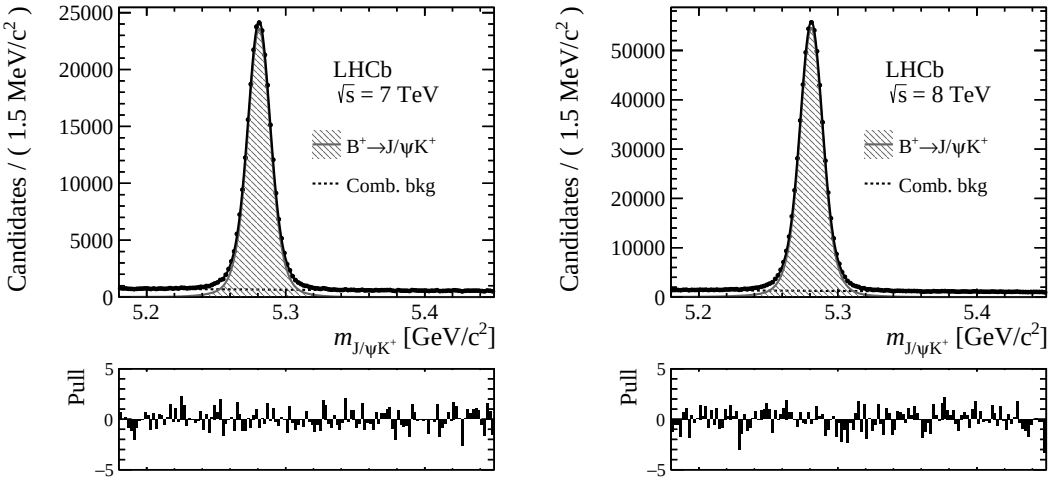

Figure 3.29: *Distributions of invariant mass for (left) $B^+ \to J/\psi K^+$ 2011 and (right) 2012 decays, with the results of the fit overlaid.*

3.5 Fit results

In this Section we present the results of the invariant-mass and decay-time fits used to determine the production asymmetries. We perform global fits to the whole data samples first and then we split the events in bins of $p_{\rm T}$ and η, performing fits for each bin.

3.5.1 $B^+ \to J/\psi K^+$

3.5.1.1 Global fits

Binned maximum likelihood fits to the invariant mass are performed for both 2011 and 2012 data samples. In Fig. 3.29 the results of the fits are shown, while in Tab. 3.11 the values of the parameters obtained from the fits are reported.

Table 3.11: *Values of* $A_{\text{raw}}(B^+ \to J/\psi K^+)$ *and signal yields determined from* $B^+ \to J/\psi K^+$ *using the full 2011 and 2012 data sets.*

Parameter	$B^+ \to J/\psi K^+$ (2011)	$B^+ \to J/\psi K^+$ (2012)
A_{raw}	-0.017 ± 0.002	-0.014 ± 0.001
A_{comb}	-0.018 ± 0.004	-0.009 ± 0.003
N_{sig}	$266\,083 \pm 703$	$620\,354 \pm 1\,083$
N_{comb}	$85\,129 \pm 560$	$164\,094 \pm 848$
f_1	0.35 ± 0.09	0.51 ± 0.02
f_2	0.11 ± 0.05	0.42 ± 0.11
μ [GeV/c^2]	5.2809 ± 0.0001	5.2810 ± 0.0001
σ_1 [GeV/c^2]	0.0067 ± 0.0004	0.0072 ± 0.0001
σ_2 [GeV/c^2]	0.0100 ± 0.0004	0.026 ± 0.001
σ_3 [GeV/c^2]	0.021 ± 0.008	0.011 ± 0.001
ξ^{comb} [c^2/GeV]	-1.14 ± 0.08	-1.11 ± 0.05

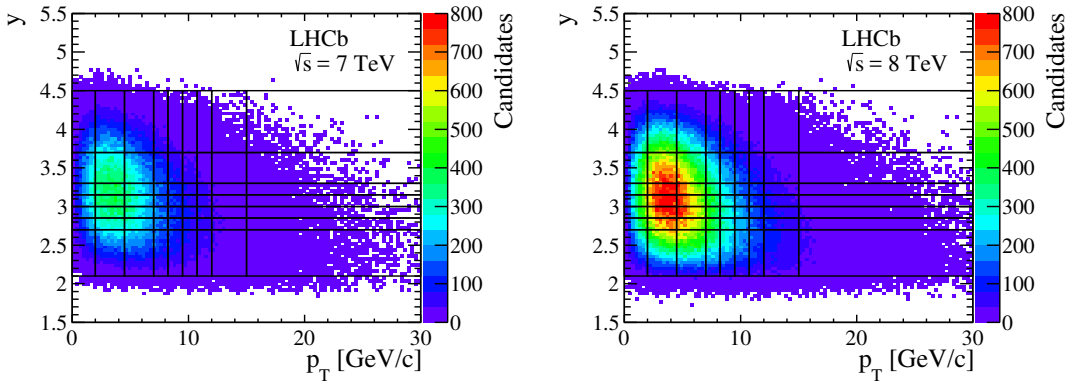

Figure 3.30: *Distributions of* p_{T} *and* y *for background-subtracted* $B^+ \to J/\psi K^+$ *decays for (left) 2011 and (right) 2012 datasets. The adopted binning scheme is superimposed.*

3.5.1.2 Fits in bins of p_{T} and y

To investigate whether the production asymmetry has a dependence on the kinematics of the B^+ mesons, unbinned maximum likelihood fits to the invariant-mass distribution are performed in bins p_{T} and y bin. The definition of the bins is reported in Tab. 3.12. The raw asymmetries are measured in each B^+ kinematic bin and thus the production asymmetries can be evaluated in each bin using Eq. (3.43).

Figure. 3.30 shows the distribution of p_{T} and y for background-subtracted $B^+ \to J/\psi K^+$ events, with the chosen binning scheme superimposed.

The value of $A_{\text{raw}}(B^+ \to J/\psi K^+)$ are reported in Tab. 3.13 for 2011 data and in

Table 3.12: *Bin ranges used to study the dependence of $A_{\rm P}(B^+)$ on $p_{\rm T}$ and y from $B^+ \to J/\psi K^+$ decays.*

Bin	$p_{\rm T}$ range [GeV/c]	y range	Bin	$p_{\rm T}$ range [GeV/c]	y range
0	$2.00 - 4.50$	$2.10 - 2.70$	28	$9.50 - 10.75$	$2.10 - 2.70$
1	$2.00 - 4.50$	$2.70 - 2.85$	29	$9.50 - 10.75$	$2.70 - 2.85$
2	$2.00 - 4.50$	$2.85 - 3.00$	30	$9.50 - 10.75$	$2.85 - 3.00$
3	$2.00 - 4.50$	$3.00 - 3.15$	31	$9.50 - 10.75$	$3.00 - 3.15$
4	$2.00 - 4.50$	$3.15 - 3.30$	32	$9.50 - 10.75$	$3.15 - 3.30$
5	$2.00 - 4.50$	$3.30 - 3.70$	33	$9.50 - 10.75$	$3.30 - 3.70$
6	$2.00 - 4.50$	$3.70 - 4.50$	34	$9.50 - 10.75$	$3.70 - 4.50$
7	$4.50 - 7.00$	$2.10 - 2.70$	35	$10.75 - 12.00$	$2.10 - 2.70$
8	$4.50 - 7.00$	$2.70 - 2.85$	36	$10.75 - 12.00$	$2.70 - 2.85$
9	$4.50 - 7.00$	$2.85 - 3.00$	37	$10.75 - 12.00$	$2.85 - 3.00$
10	$4.50 - 7.00$	$3.00 - 3.15$	38	$10.75 - 12.00$	$3.00 - 3.15$
11	$4.50 - 7.00$	$3.15 - 3.30$	39	$10.75 - 12.00$	$3.15 - 3.30$
12	$4.50 - 7.00$	$3.30 - 3.70$	40	$10.75 - 12.00$	$3.30 - 3.70$
13	$4.50 - 7.00$	$3.70 - 4.50$	41	$10.75 - 12.00$	$3.70 - 4.50$
14	$7.00 - 8.25$	$2.10 - 2.70$	42	$12.00 - 15.00$	$2.10 - 2.70$
15	$7.00 - 8.25$	$2.70 - 2.85$	43	$12.00 - 15.00$	$2.70 - 2.85$
16	$7.00 - 8.25$	$2.85 - 3.00$	44	$12.00 - 15.00$	$2.85 - 3.00$
17	$7.00 - 8.25$	$3.00 - 3.15$	45	$12.00 - 15.00$	$3.00 - 3.15$
18	$7.00 - 8.25$	$3.15 - 3.30$	46	$12.00 - 15.00$	$3.15 - 3.30$
19	$7.00 - 8.25$	$3.30 - 3.70$	47	$12.00 - 15.00$	$3.30 - 3.70$
20	$7.00 - 8.25$	$3.70 - 4.50$	48	$12.00 - 15.00$	$3.70 - 4.50$
21	$8.25 - 9.50$	$2.10 - 2.70$	49	$15.00 - 30.00$	$2.10 - 2.70$
22	$8.25 - 9.50$	$2.70 - 2.85$	50	$15.00 - 30.00$	$2.70 - 2.85$
23	$8.25 - 9.50$	$2.85 - 3.00$	51	$15.00 - 30.00$	$2.85 - 3.00$
24	$8.25 - 9.50$	$3.00 - 3.15$	52	$15.00 - 30.00$	$3.00 - 3.15$
25	$8.25 - 9.50$	$3.15 - 3.30$	53	$15.00 - 30.00$	$3.15 - 3.30$
26	$8.25 - 9.50$	$3.30 - 3.70$	54	$15.00 - 30.00$	$3.30 - 3.70$
27	$8.25 - 9.50$	$3.70 - 4.50$	55	$15.00 - 30.00$	$3.70 - 4.50$

Bin	$p_{\rm T}$ range [GeV/c]	y range
A	$0 - 2$	$2.10 - 2.70$
B	$0 - 2$	$2.70 - 2.85$
C	$0 - 2$	$2.85 - 3.00$
D	$0 - 2$	$3.00 - 3.15$
E	$0 - 2$	$3.15 - 3.30$
F	$0 - 2$	$3.30 - 3.70$
G	$0 - 2$	$3.70 - 4.50$

Table 3.13: *Values of* $A_{\rm raw}(B^+ \to J/\psi K^+)$ *from* $B^+ \to J/\psi K^+$ *fits in the various bins of* $p_{\rm T}$ *and* y *using 2011 data for (left) up and (right) down magnet polarities.*

Up				Down			
Bin	$A_{\rm raw}(B^+ \to J/\psi K^+)$	Bin	$A_{\rm raw}(B^+ \to J/\psi K^+)$	Bin	$A_{\rm raw}(B^+ \to J/\psi K^+)$	Bin	$A_{\rm raw}(B^+ \to J/\psi K^+)$
0	0.006 ± 0.013	28	-0.072 ± 0.028	0	-0.027 ± 0.011	28	-0.010 ± 0.024
1	-0.042 ± 0.017	29	0.008 ± 0.045	1	-0.019 ± 0.015	29	-0.045 ± 0.038
2	-0.005 ± 0.016	30	-0.008 ± 0.044	2	-0.038 ± 0.014	30	-0.056 ± 0.038
3	-0.036 ± 0.015	31	-0.001 ± 0.050	3	-0.041 ± 0.013	31	0.027 ± 0.041
4	-0.015 ± 0.016	32	0.022 ± 0.053	4	-0.001 ± 0.013	32	-0.017 ± 0.047
5	-0.024 ± 0.011	33	-0.035 ± 0.044	5	-0.032 ± 0.009	33	-0.024 ± 0.036
6	-0.007 ± 0.015	34	-0.070 ± 0.061	6	-0.007 ± 0.012	34	-0.076 ± 0.055
7	-0.007 ± 0.014	35	-0.010 ± 0.032	7	-0.011 ± 0.011	35	-0.048 ± 0.027
8	0.001 ± 0.019	36	-0.010 ± 0.052	8	-0.020 ± 0.015	36	-0.027 ± 0.046
9	0.014 ± 0.018	37	-0.073 ± 0.058	9	-0.023 ± 0.015	37	0.024 ± 0.046
10	0.004 ± 0.018	38	-0.005 ± 0.063	10	-0.007 ± 0.015	38	-0.047 ± 0.054
11	-0.016 ± 0.018	39	-0.048 ± 0.069	11	-0.025 ± 0.015	39	-0.025 ± 0.057
12	-0.035 ± 0.013	40	-0.013 ± 0.055	12	-0.025 ± 0.011	40	-0.002 ± 0.048
13	0.020 ± 0.020	41	0.118 ± 0.085	13	-0.032 ± 0.016	41	-0.017 ± 0.071
14	-0.003 ± 0.022	42	0.009 ± 0.027	14	-0.013 ± 0.018	42	-0.015 ± 0.023
15	-0.099 ± 0.032	43	0.046 ± 0.049	15	-0.051 ± 0.027	43	-0.016 ± 0.042
16	0.004 ± 0.030	44	-0.021 ± 0.051	16	-0.040 ± 0.027	44	0.013 ± 0.044
17	0.009 ± 0.033	45	-0.034 ± 0.059	17	-0.023 ± 0.028	45	-0.044 ± 0.051
18	-0.034 ± 0.035	46	0.020 ± 0.067	18	-0.033 ± 0.028	46	-0.113 ± 0.054
19	0.036 ± 0.026	47	-0.004 ± 0.054	19	0.005 ± 0.022	47	-0.006 ± 0.045
20	0.102 ± 0.039	48	-0.038 ± 0.083	20	0.006 ± 0.034	48	0.138 ± 0.071
21	-0.017 ± 0.025	49	0.021 ± 0.029	21	-0.029 ± 0.020	49	-0.016 ± 0.025
22	-0.028 ± 0.039	50	-0.132 ± 0.062	22	-0.016 ± 0.032	50	-0.059 ± 0.052
23	-0.068 ± 0.038	51	-0.050 ± 0.073	23	0.008 ± 0.032	51	-0.077 ± 0.059
24	-0.047 ± 0.038	52	-0.058 ± 0.079	24	-0.094 ± 0.033	52	-0.051 ± 0.067
25	0.019 ± 0.042	53	0.067 ± 0.097	25	0.063 ± 0.037	53	-0.064 ± 0.075
26	-0.009 ± 0.033	54	-0.086 ± 0.077	26	-0.021 ± 0.028	54	0.059 ± 0.066
27	-0.004 ± 0.052	55	-0.242 ± 0.135	27	-0.012 ± 0.045	55	0.017 ± 0.101
Bin	$A_{\rm raw}(B^+ \to J/\psi K^+)$			Bin	$A_{\rm raw}(B^+ \to J/\psi K^+)$		
A	-0.023 ± 0.024			A	0.005 ± 0.020		
B	-0.017 ± 0.030			B	-0.012 ± 0.025		
C	-0.011 ± 0.027			C	-0.010 ± 0.023		
D	-0.013 ± 0.026			D	-0.020 ± 0.022		
E	-0.016 ± 0.026			E	-0.009 ± 0.023		
F	-0.001 ± 0.017			F	-0.001 ± 0.014		
G	-0.017 ± 0.022			G	-0.026 ± 0.018		

Tab. 3.14 for 2012 data for each bin.

In order to measure $A_{\rm P}(B^+)$ in bins of $p_{\rm T}$ and y it is necessary to subtract to $A_{\rm raw}(B^+ \to J/\psi K^+)$ the kaon detection asymmetry. The determination of the kaon detection asymmetry will be discussed in detail in Sec. 3.6.

3.5.2 $B^0 \to J/\psi K^{*0}$ and $B_s^0 \to D_s^- \pi^+$

3.5.2.1 Global fits

Binned maximum likelihood fits to the invariant-mass and decay-time distributions are performed for each decay mode. The oscillation frequencies Δm_d and Δm_s, the mixing

Table 3.14: *Values of* $A_{\rm raw}(B^+ \to J/\psi K^+)$ *from* $B^+ \to J/\psi K^+$ *fits in the various bins of* $p_{\rm T}$ *and* y *using 2012 data for (left) up and (right) down magnet polarities.*

Up				Down			
Bin	$A_{\rm raw}(B^+ \to J/\psi K^+)$	Bin	$A_{\rm raw}(B^+ \to J/\psi K^+)$	Bin	$A_{\rm raw}(B^+ \to J/\psi K^+)$	Bin	$A_{\rm raw}(B^+ \to J/\psi K^+)$
0	-0.012 ± 0.008	28	0.019 ± 0.016	0	0.006 ± 0.007	28	-0.019 ± 0.015
1	-0.003 ± 0.010	29	0.023 ± 0.026	1	-0.026 ± 0.010	29	-0.035 ± 0.025
2	0.003 ± 0.010	30	0.033 ± 0.026	2	-0.015 ± 0.010	30	-0.016 ± 0.025
3	-0.007 ± 0.010	31	-0.010 ± 0.029	3	-0.016 ± 0.009	31	0.013 ± 0.028
4	-0.007 ± 0.010	32	-0.016 ± 0.033	4	-0.009 ± 0.010	32	-0.087 ± 0.033
5	-0.010 ± 0.007	33	-0.043 ± 0.025	5	-0.017 ± 0.007	33	-0.025 ± 0.025
6	-0.019 ± 0.009	34	-0.075 ± 0.039	6	-0.017 ± 0.009	34	0.015 ± 0.038
7	-0.003 ± 0.008	35	-0.002 ± 0.018	7	-0.020 ± 0.007	35	0.027 ± 0.018
8	-0.017 ± 0.011	36	-0.064 ± 0.032	8	0.002 ± 0.011	36	-0.059 ± 0.030
9	0.001 ± 0.011	37	-0.013 ± 0.033	9	-0.018 ± 0.010	37	0.038 ± 0.033
10	-0.024 ± 0.011	38	-0.029 ± 0.037	10	-0.010 ± 0.010	38	0.003 ± 0.037
11	-0.036 ± 0.011	39	0.021 ± 0.039	11	-0.011 ± 0.011	39	0.001 ± 0.040
12	-0.038 ± 0.008	40	-0.061 ± 0.032	12	-0.021 ± 0.008	40	-0.027 ± 0.033
13	-0.013 ± 0.012	41	0.078 ± 0.050	13	-0.017 ± 0.012	41	-0.024 ± 0.050
14	-0.004 ± 0.012	42	0.011 ± 0.015	14	-0.021 ± 0.012	42	-0.009 ± 0.015
15	-0.002 ± 0.018	43	0.002 ± 0.028	15	-0.047 ± 0.019	43	-0.059 ± 0.027
16	-0.018 ± 0.019	44	-0.011 ± 0.030	16	-0.011 ± 0.018	44	0.034 ± 0.029
17	0.005 ± 0.019	45	0.016 ± 0.033	17	-0.003 ± 0.019	45	-0.014 ± 0.034
18	-0.004 ± 0.020	46	0.042 ± 0.038	18	-0.017 ± 0.020	46	-0.071 ± 0.039
19	-0.004 ± 0.016	47	-0.025 ± 0.031	19	-0.006 ± 0.015	47	-0.027 ± 0.030
20	-0.055 ± 0.024	48	-0.001 ± 0.048	20	-0.014 ± 0.024	48	-0.111 ± 0.048
21	-0.018 ± 0.014	49	-0.022 ± 0.016	21	-0.004 ± 0.013	49	-0.030 ± 0.016
22	-0.013 ± 0.022	50	-0.066 ± 0.035	22	-0.013 ± 0.021	50	-0.011 ± 0.036
23	-0.043 ± 0.022	51	-0.020 ± 0.039	23	-0.013 ± 0.022	51	-0.035 ± 0.038
24	-0.034 ± 0.023	52	0.027 ± 0.046	24	-0.023 ± 0.023	52	0.034 ± 0.044
25	-0.027 ± 0.026	53	-0.003 ± 0.053	25	-0.032 ± 0.025	53	-0.019 ± 0.052
26	-0.003 ± 0.020	54	-0.025 ± 0.043	26	-0.014 ± 0.019	54	-0.028 ± 0.044
27	-0.064 ± 0.031	55	-0.040 ± 0.070	27	-0.004 ± 0.031	55	-0.165 ± 0.069
Bin		$A_{\rm raw}(B^+ \to J/\psi K^+)$		Bin		$A_{\rm raw}(B^+ \to J/\psi K^+)$	
A		-0.013 ± 0.014		A		-0.038 ± 0.013	
B		-0.018 ± 0.018		B		-0.003 ± 0.017	
C		0.021 ± 0.017		C		-0.016 ± 0.017	
D		-0.010 ± 0.017		D		-0.003 ± 0.016	
E		-0.040 ± 0.017		E		-0.020 ± 0.017	
F		-0.025 ± 0.011		F		-0.012 ± 0.011	
G		0.009 ± 0.015		G		-0.032 ± 0.014	

parameters $|q/p|_{B^0}$ and $|q/p|_{B_s^0}$, the average decay widths Γ_d and Γ_s and the width differences $\Delta\Gamma_d$ and $\Delta\Gamma_s$ are fixed to the values reported in Tab. 3.15.

In the limit of small *CP* and detection asymmetries, Eq. (3.25) can be written to the first order as

$$\begin{aligned} f(t,\psi) \;\simeq\; & K\left[1-\psi\left(A_{CP}+A_f\right)\right] \\ & \left\{e^{-\Gamma t}\left[\Lambda_+\cosh\left(\frac{\Delta\Gamma t}{2}\right)+\psi\Lambda_-\cos\left(\Delta m t\right)\right]\right\} \otimes R(t)\,\epsilon(t)\,. \end{aligned} \tag{3.35}$$

This means that the fit is only sensitive to the sum of A_{CP} and A_f. In the fit it has been chosen to fix the direct *CP* violation term A_{CP} to zero and to leave the detection

Table 3.15: *Values of the various physical inputs used in the fits.*

Parameter	Value	Reference
Δm_d [ps^{-1}]	0.5065 ± 0.0019	[67]
Δm_s [ps^{-1}]	17.757 ± 0.021	[67]
Γ_d [ps^{-1}]	0.6579 ± 0.0017	[67]
Γ_s [ps^{-1}]	0.6645 ± 0.0018	[67]
$\Delta\Gamma_d$ [ps^{-1}]	0	
$\Delta\Gamma_s$ [ps^{-1}]	0.083 ± 0.006	[67]
$\lvert q/p\rvert_{B^0}$	1.0007 ± 0.0009	[67]
$\lvert q/p\rvert_{B^0_s}$	1.0038 ± 0.0021	[67]

asymmetry A_f as a free parameter. According to Eq. (3.35), one does not expect any impact on the determination of the production asymmetry $A_{\rm P}$ from the choice of the value of A_{CP}. As a cross-check, the fit is repeated by allowing CP violation up to $\pm 1\%$ and, as expected, the impact on the determination of $A_{\rm P}$ turns out to be completely negligible.

In Figs. 3.31 and 3.32 the $\mu\mu K\pi$ and $KK\pi\pi$ invariant mass and decay-time distributions are shown, with the result of the fits overlaid. The raw asymmetries as a function of the decay time for events in the signal mass region are shown in Fig. 3.33.

The values of the parameters determined from the fits are reported in Tab. 3.16. In particular, the values of the production asymmetries from the global fits are found to be

$$A_{\rm P}\left(B^0\right)_{\sqrt{s}=7\,\text{TeV}} = (-1.13 \pm 0.63)\,\%, \tag{3.36}$$

$$A_{\rm P}\left(B^0\right)_{\sqrt{s}=8\,\text{TeV}} = (-1.09 \pm 0.42)\,\%, \tag{3.37}$$

$$A_{\rm P}\left(B^0_s\right)_{\sqrt{s}=7\,\text{TeV}} = (-0.01 \pm 1.66)\,\% \tag{3.38}$$

$$A_{\rm P}\left(B^0_s\right)_{\sqrt{s}=8\,\text{TeV}} = (+0.81 \pm 1.11)\,\%. \tag{3.39}$$

3.5.2.2 Studies with fast pseudoexperiments

Pseudoexperiments are used in order to validate the fit model. In Fig. 3.34 the distributions of the pulls for the quantities $A_{\rm P}$, A_f and $A_{\rm comb}$ obtained by means of 2000 pseudoexperiments using the results of the $B^0 \to J/\psi\, K^{*0}$ and $B^0_s \to D^-_s\pi^+$ global fits as inputs are shown. The value of mean and RMS of the distributions is reported in each plot. A Gaussian function with mean equal to zero and standard deviation equal to one ($\mathcal{G}(0;1)$) is overlaid to each distribution. The results of the χ^2 tests between the $\mathcal{G}(0;1)$ and the distributions are also reported in the plots. The correlation between the three parameters are reported in Tab. 3.17.

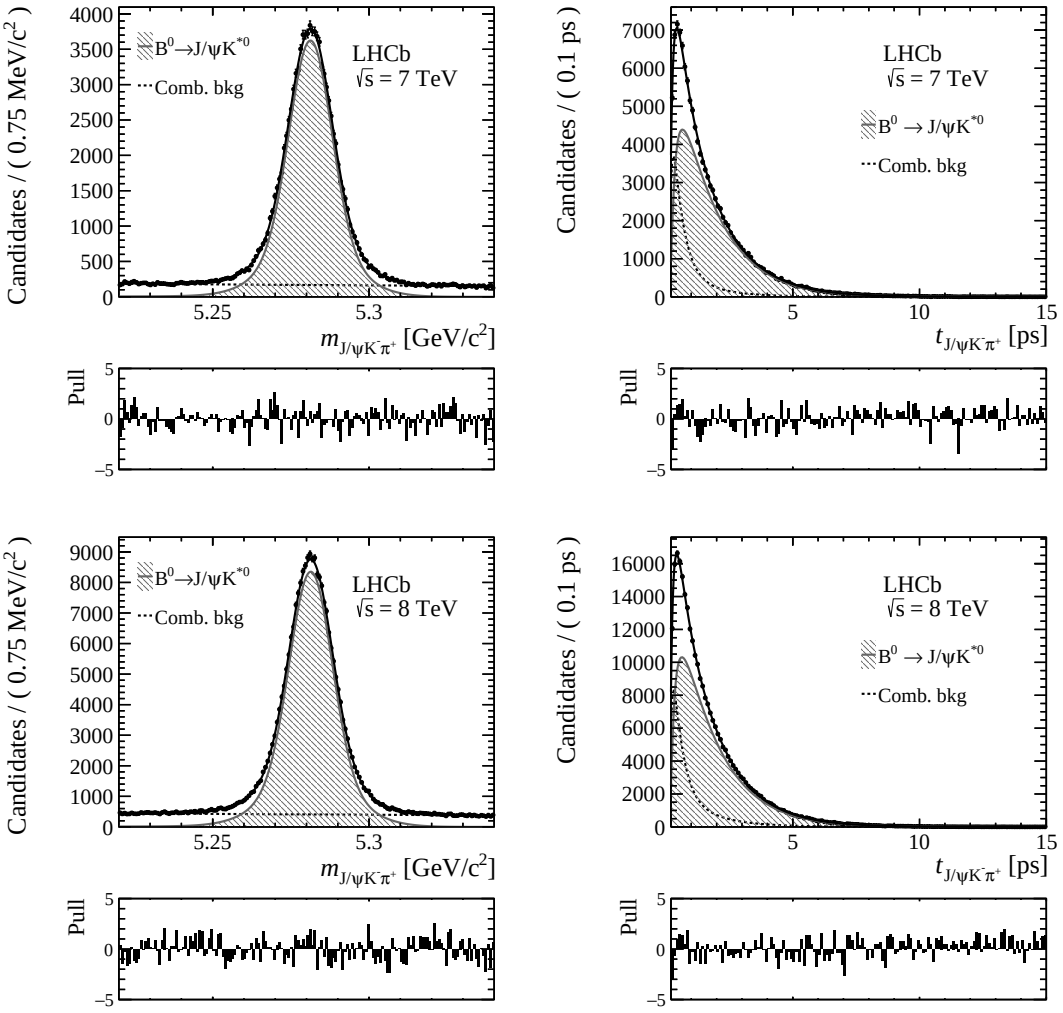

Figure 3.31: *Distributions of (left) invariant mass and (right) decay time for $B^0 \to J/\psi K^{*0}$ (top) 2011 and (bottom) 2012 decays, with the results of the fit overlaid. The dashed line corresponds to the combinatorial background.*

3.5.2.3 Fits in bins of $p_{\rm T}$ and y

Figure. 3.35 shows the two dimensional $p_{\rm T}$ and η distribution for background-subtracted $B^0 \to J/\psi K^{*0}$ and $B_s^0 \to D_s^- \pi^+$ decays, with the chosen binning scheme overlaid. The numerical values of the adopted bin ranges are reported in Tab. 3.12 for the $B^0 \to J/\psi K^{*0}$ decay and in Tab. 3.18 for the $B_s^0 \to D_s^- \pi^+$ decay.

Unbinned maximum likelihood fits to the mass and decay-time distributions are performed in each bin. In the case of $B^0 \to J/\psi K^{*0}$ fit, the combinatorial background is described by the same function used in the corresponding global fit, with parameters fixed to those obtained in the global fit. In the case of the $B_s^0 \to D_s^- \pi^+$ fits, the same model of

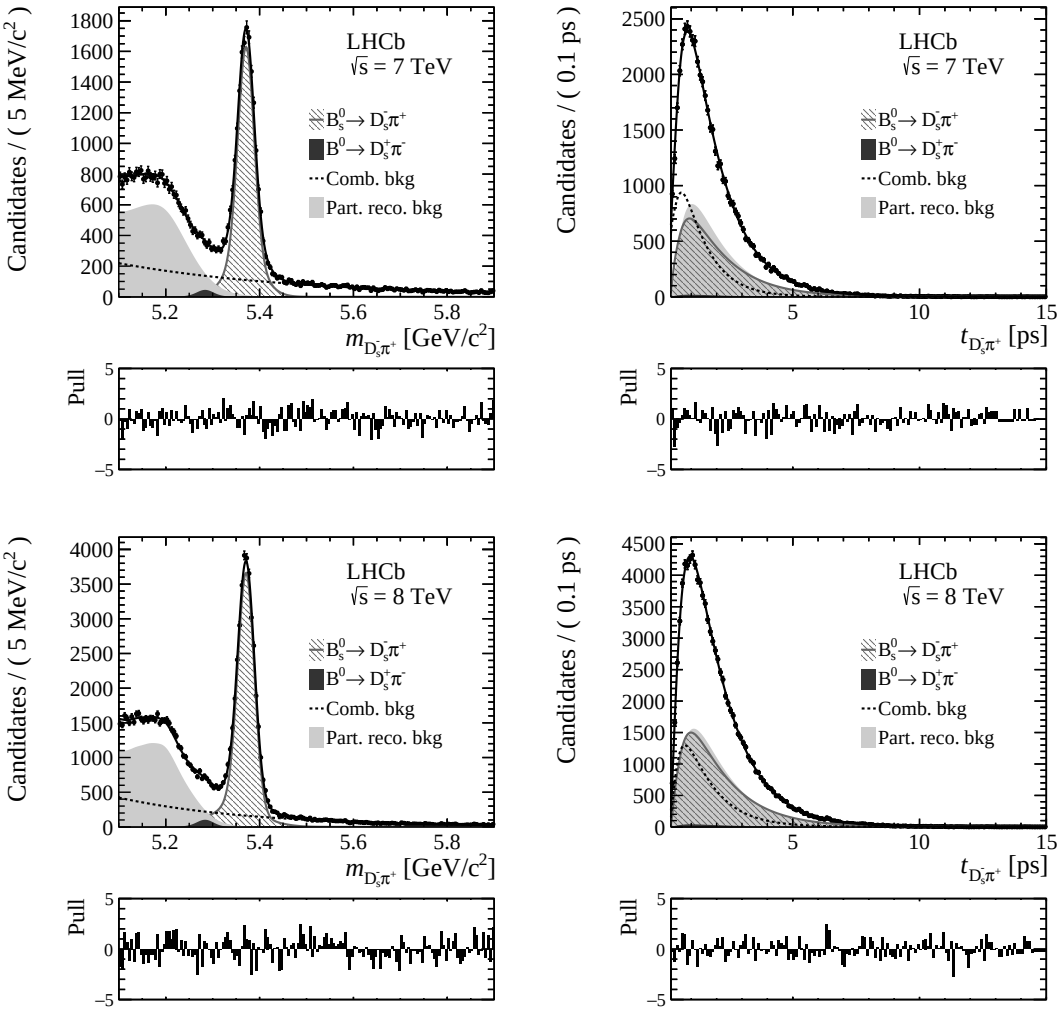

Figure 3.32: *Distributions of (left) invariant mass and (right) decay time for $B_s^0 \to D_s^- \pi^+$ (top) 2011 and (bottom) 2012 decays, with the results of the fit overlaid. The dashed line corresponds to the combinatorial background, while the dotted line corresponds to the partially-reconstructed background.*

the global fits is used, except for the function $\varepsilon_{\rm acc}^{comb}(t)$ that is given by

$$\varepsilon_{\rm acc}^{comb}(t) = \frac{1}{2}\left[1 - {\rm erf}\left(\frac{p^{\rm comb} - t}{t}\right)\right], \tag{3.40}$$

where the parameter $p^{\rm comb}$ is left free to vary, whereas $\Gamma_1^{\rm comb}$ and $\Gamma_2^{\rm comb}$ are fixed to the values obtained in the global fit. In addition, the decay time acceptance for signal events is simplified as

$$\varepsilon_{\rm acc}(t) = \frac{1}{2}\left[1 - {\rm erf}\left(\frac{p_1 - t}{t}\right)\right](1 + p_3 t). \tag{3.41}$$

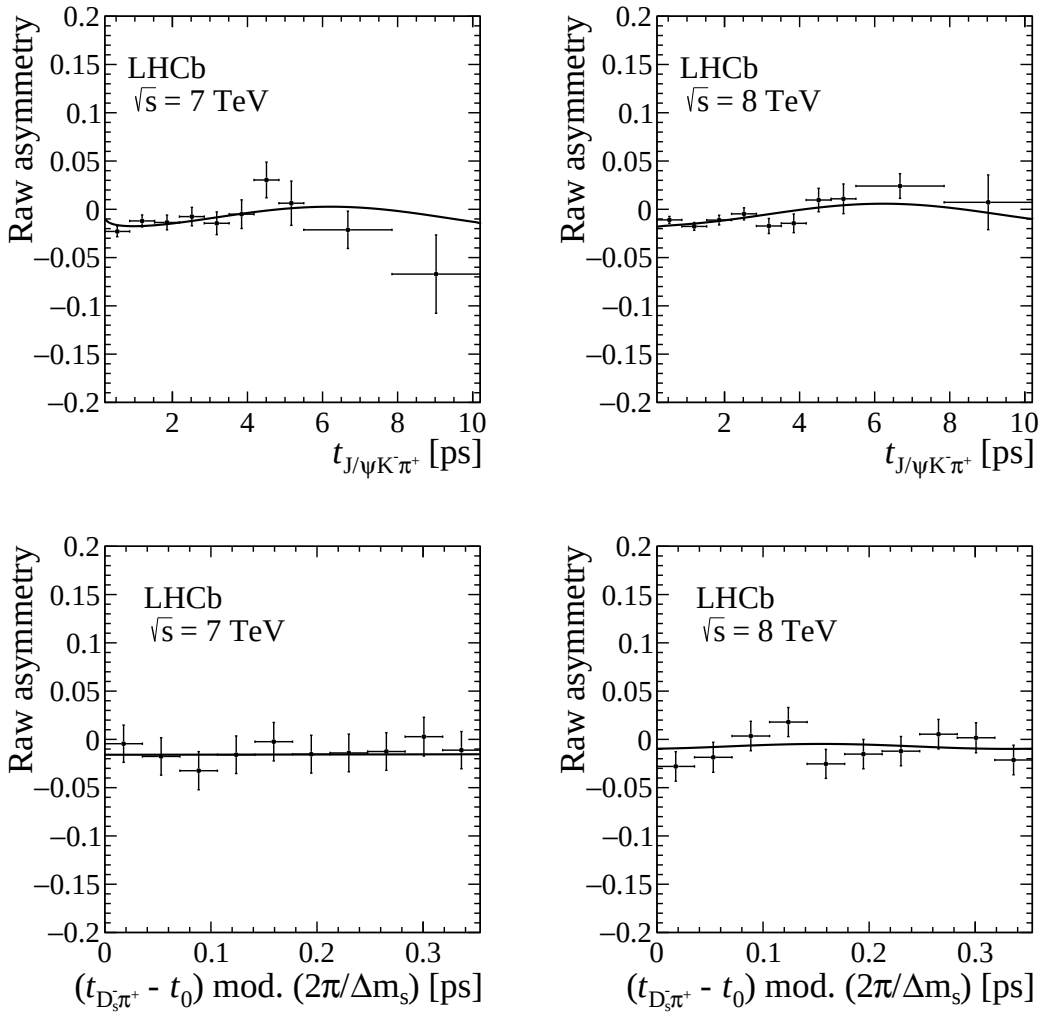

Figure 3.33: *Raw asymmetries as a function of the decay time from the global fits to the (top left)* $B^0 \to J/\psi K^{*0}$ *2011, (top right)* $B^0 \to J/\psi K^{*0}$ *2012, (bottom left)* $B_s^0 \to D_s^- \pi^+$ *2011, and (bottom right)* $B_s^0 \to D_s^- \pi^+$ *2012 data samples. The signal region as* $5.25 < m < 5.31$ GeV/c^2 *for the* $B^0 \to J/\psi K^{*0}$ *mode and as* $5.30 < m < 5.45$ GeV/c^2 *for the* $B_s^0 \to D_s^- \pi^+$ *mode.*

where the parameter p^{comb} is left free to vary in the fit, whereas Γ_1^{comb} and Γ_2^{comb} are fixed to the values obtained in the global fit. Finally, the decay time acceptance for the signals is simplified as

$$\varepsilon_{\text{acc}}(t) = \frac{1}{2}\left[1 - \text{erf}\left(\frac{p_1 - t}{t}\right)\right](1 + p_3 t)\,. \tag{3.42}$$

The values of A_{P} determined from each fit using $B^0 \to J/\psi K^{*0}$ and $B_s^0 \to D_s^- \pi^+$ decays are reported in Tabs. 3.19 and 3.20.

Table 3.16: *Values of the parameters obtained from the global fits to $B^0 \to J/\psi K^{*0}$ and $B_s^0 \to D_s^- \pi^+$ decays for each data-taking year.*

Parameter	$B^0 \to J/\psi K^{*0}$ (2011)	$B^0 \to J/\psi K^{*0}$ (2012)	$B_s^0 \to D_s^- \pi^+$ (2011)	$B_s^0 \to D_s^- \pi^+$ (2012)
Asymmetries				
$A_{\rm P}$	-0.0113 ± 0.0063	-0.0109 ± 0.0042	-0.0001 ± 0.0166	0.0081 ± 0.0111
A_f	-0.0098 ± 0.0046	-0.0056 ± 0.0030	-0.0143 ± 0.0086	-0.0103 ± 0.0058
$A_{\rm comb}$	-0.0029 ± 0.0077	-0.0199 ± 0.0051	-0.0380 ± 0.0130	-0.0175 ± 0.0124
$A^{\rm phys}_{B^0_{(s)} \to D^-_{(s)} \rho^+}$	–	–	-0.0364 ± 0.0651	0.0300 ± 0.0440
$A^{\rm phys}_{B^0_{(s)} \to D^{*-}_{(s)} \pi^+}$	–	–	0.0198 ± 0.0184	-0.0125 ± 0.0141
Yields				
$N_{\rm sig}$	$95\,122 \pm 369$	$221\,973 \pm 569$	$16\,932 \pm 174$	$36\,726 \pm 250$
$N_{\rm comb}$	$26\,931 \pm 260$	$63\,882 \pm 791$	$14\,931 \pm 433$	$23\,528 \pm 711$
$N^{\rm phys}_{B^0_{(s)} \to D^-_{(s)} \rho^+}$	–	–	$3\,697 \pm 437$	$8\,072 \pm 664$
$N^{\rm phys}_{B^0_{(s)} \to D^{*-}_{(s)} \pi^+}$	–	–	$15\,156 \pm 574$	$29\,338 \pm 863$
Signal parameters				
μ [GeV/c^2]	5.2813 ± 0.0001	5.2814 ± 0.0001	5.3715 ± 0.0002	5.3710 ± 0.0001
σ_1 [GeV/c^2]	0.0128 ± 0.0004	0.0092 ± 0.0010	0.0171 ± 0.0003	0.0169 ± 0.0002
σ_2 [GeV/c^2]	0.0067 ± 0.0001	0.0059 ± 0.0002	0.0357 ± 0.0018	0.0356 ± 0.0015
σ_3 [GeV/c^2]	–	0.0189 ± 0.0016	–	–
f_1	0.29 ± 0.02	0.46 ± 0.07	0.74 ± 0.02	0.79 ± 0.01
f_2	–	0.11 ± 0.02	–	–
p_1 [ps]	0.13 ± 0.01	0.129 ± 0.01	0.42 ± 0.01	0.49 ± 0.01
p_2 [ps]	-1.34 ± 0.06	-1.34 ± 0.06	1.00 ± 0.05	1.06 ± 0.04
p_3 [ps^{-1}]	-0.007 ± 0.005	-0.007 ± 0.005	-0.023 ± 0.006	-0.015 ± 0.004
Background parameters				
$\xi^{\rm comb}$ [c^2/GeV]	1.63 ± 0.19	1.38 ± 0.12	2.57 ± 0.10	-3.65 ± 0.10
$p_1^{\rm comb}$ [ps^{-1}]	0.01 ± 0.01	0.015 ± 0.009	0.75 ± 0.04	0.78 ± 0.04
$p_2^{\rm comb}$ [no dim. or ps]	-2.44 ± 0.58	-2.29 ± 0.04	0.21 ± 0.02	0.39 ± 0.01
$p_1^{\rm phys}$ [ps^{-1}]	–	–	0.80 ± 0.11	0.95 ± 0.14
$p_2^{\rm phys}$ [ps^{-1}]	–	–	-0.61 ± 0.08	-0.50 ± 0.07
f^{comb}	0.10 ± 0.01	0.116 ± 0.001	–	–
$\Gamma_1^{\rm comb}$ [ps^{-1}]	0.77 ± 0.03	0.77 ± 0.02	1.07 ± 0.02	-0.91 ± 0.02
$\Gamma_2^{\rm comb}$ [ps^{-1}]	2.65 ± 0.17	2.94 ± 0.14	–	–
$\Gamma^{\rm phys}_{B^0_{(s)} \to D^-_{(s)} \rho^+}$ [ps^{-1}]	–	–	1.57 ± 0.20	-1.45 ± 0.24
$\Gamma^{\rm phys}_{B^0_{(s)} \to D^{*-}_{(s)} \pi^+}$ [ps^{-1}]	–	–	0.83 ± 0.02	-0.81 ± 0.03

3.6 K^- detection asymmetry and $A_{\rm P}(B^+)$

In the following Section the procedure employed to measure the kaon detection asymmetry is described. Once the correction is obtained, the values of $A_{\rm P}(B^+)$ can be calculated starting from the $A_{\rm raw}$ measurements.

The B^+ production asymmetry can be expressed as the sum of various terms

$$A_{\rm P}(B^+) = A_{\rm raw}(B^+ \to J/\psi K^+) - A_{\rm D}(K^-\pi^+) - A_{CP}(B^+ \to J/\psi K^+), \tag{3.43}$$

where $A_{\rm raw}(B^+ \to J/\psi K^+)$ is the raw asymmetry defined as

$$A_{\rm raw} = \frac{N(B^- \to J/\psi K^-) - N(B^+ \to J/\psi K^+)}{N(B^- \to J/\psi K^-) + N(B^+ \to J/\psi K^+)}, \tag{3.44}$$

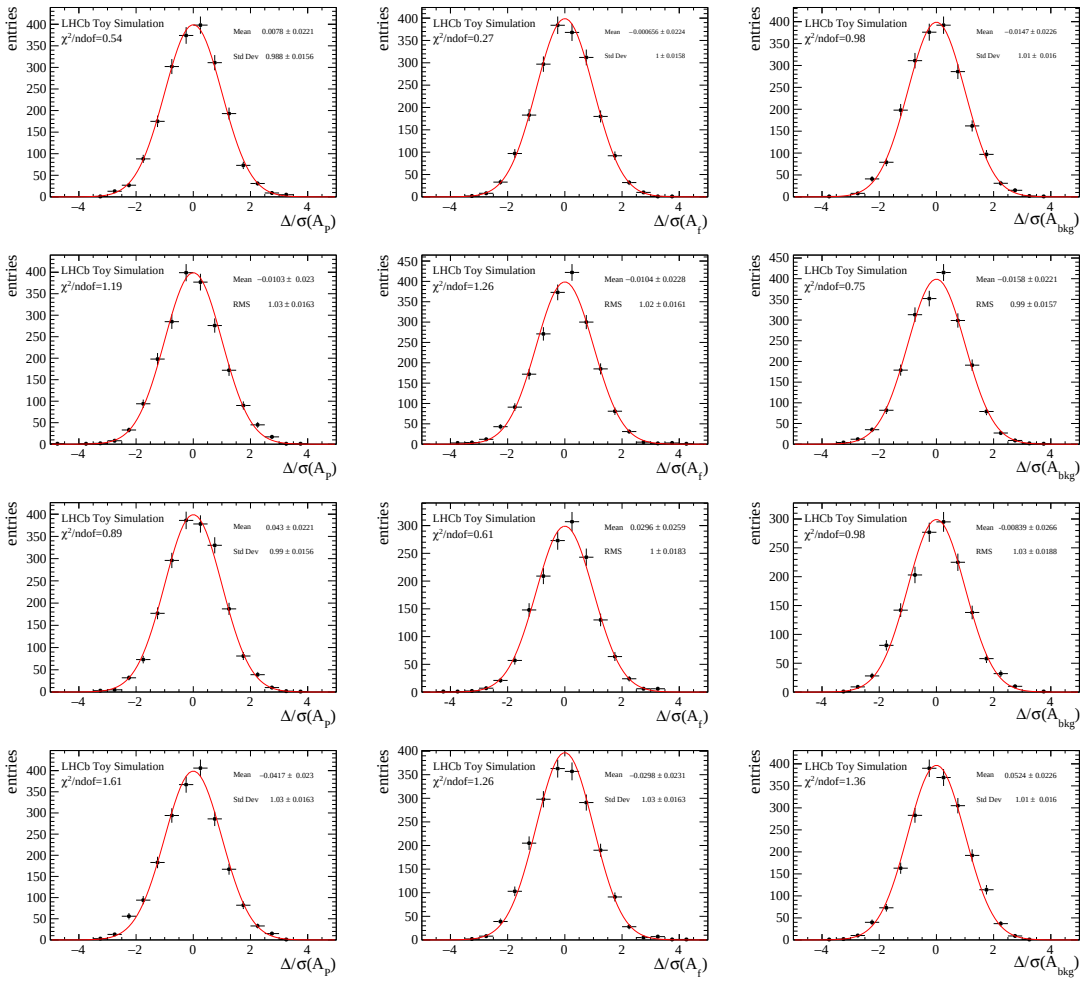

Figure 3.34: *Distributions of the pulls for (left) $A_{\rm P}$, (center) A_f and (right) $A_{\rm comb}$ obtained from global fits to toy Monte Carlo events for (top) 2011 $B^0 \to J/\psi K^{*0}$, (mid top) 2012 $B^0 \to J/\psi K^{*0}$, (mid bottom) 2011 $B_s^0 \to D_s^- \pi^+$ and (bottom) 2012 $B_s^0 \to D_s^- \pi^+$ decays. The value reported in the plots correspond to the mean and RMS of the distributions. The Gaussian function $\mathcal{G}(0;1)$ with mean equal to zero and standard deviation equal to one is overlaid to each distribution. The results of the χ^2 tests between the $\mathcal{G}(0;1)$ and the distributions are also reported in the plots.*

$A_{\rm D}(K^-\pi^+)$ is the kaon detection asymmetry and $A_{CP}(B^+ \to J/\psi K^+)$ is the *CP* asymmetry in the decay.

3.6.1 $A_{\rm D}(K^-)$

In order to measure $A_{\rm D}(K^-) = A_{\rm D}(K^-\pi^+) - A_{\rm D}(\pi^-)$, samples of $D^+ \to K^-\pi^+\pi^+$ and $D^+ \to \overline{K}^0\pi^+$ decays are used to determine the $A_{\rm D}(K^-\pi^+)$ asymmetry and a sample of partially and fully reconstructed $D^{*+} \to D^0(K^-\pi^+\pi^-\pi^+)\pi^+$ is used to estimate the

Table 3.17: *Values of correlations between $A_{\rm P}$, A_f and $A_{\rm comb}$ for 2011 and 2012 $B^0 \to J/\psi K^{*0}$ and $B_s^0 \to D_s^- \pi^+$ decays determined from global fits to toy Monte Carlo events.*

Correlation	$B^0 \to J/\psi K^{*0}$ (2011)	$B^0 \to J/\psi K^{*0}$ (2012)	$B_s^0 \to D_s^- \pi^+$ (2011)	$B_s^0 \to D_s^- \pi^+$ (2012)
$\rho(A_{\rm P},\ A_f)$	-0.60	-0.67	0.04	-0.07
$\rho(A_{\rm P},\ A_{\rm comb})$	-0.13	-0.13	0.04	0.01

Table 3.18: *Bin ranges used to study the dependence of $A_{\rm P}(B_s^0)$ on $p_{\rm T}$ and y from $B_s^0 \to D_s^- \pi^+$*

Bin	$p_{\rm T}$ range [GeV/c]	y range
0	$2.0 - 7.0$	$2.1 - 3.0$
1	$2.0 - 7.0$	$3.0 - 3.3$
2	$2.0 - 7.0$	$3.3 - 4.5$
3	$7.0 - 9.5$	$2.1 - 3.0$
4	$7.0 - 9.5$	$3.0 - 3.3$
5	$7.0 - 9.5$	$3.3 - 4.5$
6	$9.5 - 12.0$	$2.1 - 3.0$
7	$9.5 - 12.0$	$3.0 - 3.3$
8	$9.5 - 12.0$	$3.3 - 4.5$
9	$12.0 - 30.0$	$2.1 - 3.0$
10	$12.0 - 30.0$	$3.0 - 3.3$
11	$12.0 - 30.0$	$3.3 - 4.5$

$A_{\rm D}(\pi^-)$ asymmetry.

The raw asymmetry of the $D^+ \to K^-\pi^+\pi^+$ decay can be written as

$$A_{\rm raw}(D^+ \to K^-\pi^+\pi^+) = A_{\rm P}(D^+) + A_{\rm D}(K^-\pi^+) + A_{\rm D}(\pi^+), \tag{3.45}$$

where $A_{\rm P}(D^+)$ is the production asymmetry of prompt D^+ mesons and $A_{\rm D}(\pi^+)$ is the detection asymmetry of charged pions in the LHCb detector. The raw asymmetry of $D^+ \to \overline{K}^0\pi^+$ decays can be written as

$$A_{\rm raw}(D^+ \to \overline{K}^0\pi^+) = A_{\rm P}(D^+) + A_{\rm D}(\pi^+) - A_{\rm D}(K^0), \tag{3.46}$$

where $A_{\rm D}(K^0)$ is the neutral kaon detection asymmetry and where the relation $A_{\rm D}(\overline{K}^0) = -A_{\rm D}(K^0)$ has been used. This asymmetry includes effects from the *CP* violation in the $K^0 \to \pi^+\pi^-$ decay and from the different interaction rates of K^0 and $\overline{K}^0$ in matter. This quantity has been measured to be $A_{\rm D}(K^0) = (0.054 \pm 0.014)\%$ in a previous LHCb analysis [68] and it is taken as external input.

Taking the difference of the above defined raw asymmetries and subtracting the K^0 detection asymmetry one can measure $A_{\rm D}(K^-\pi^+)$, since

$$A_{\rm D}(K^-\pi^+) = A_{\rm raw}(D^+ \to K^-\pi^+\pi^+) - A_{\rm raw}(D^+ \to \overline{K}^0\pi^+) - A_{\rm D}(K^0). \tag{3.47}$$

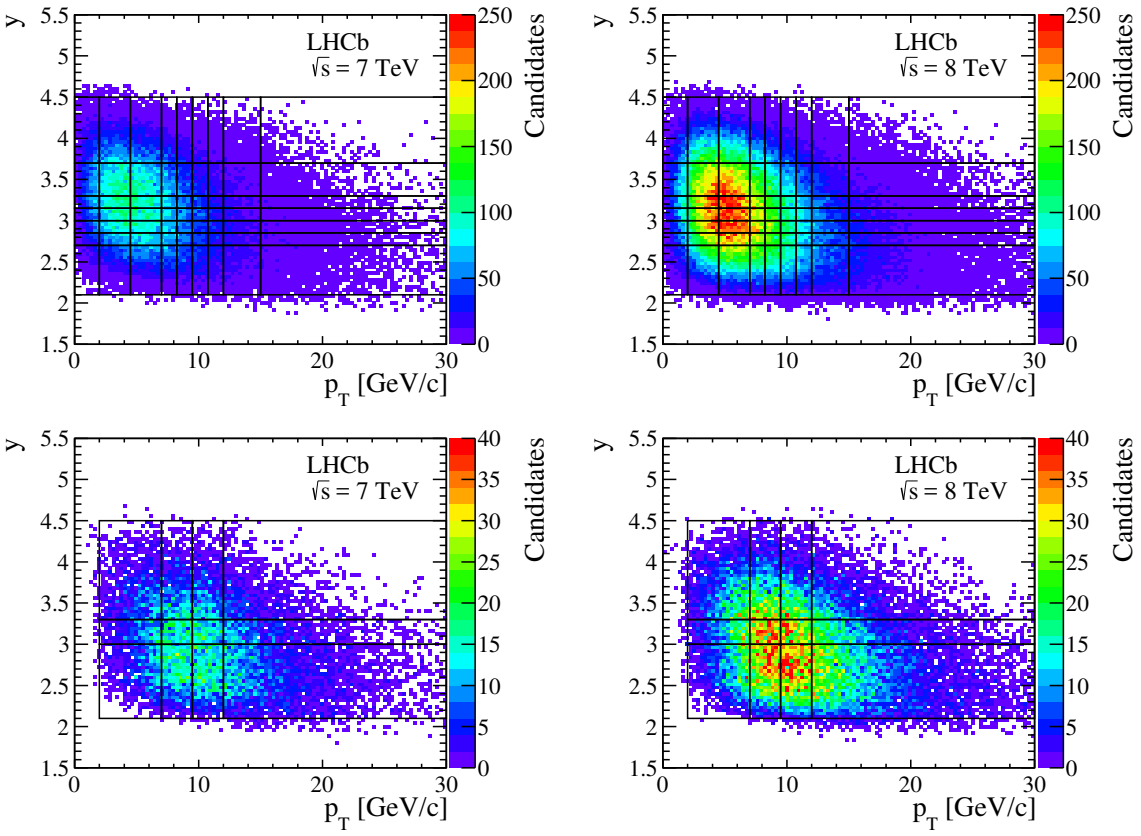

Figure 3.35: *Distribution of $p_{\rm T}$ and y for background-subtracted (top left) $B^0 \to J/\psi K^{*0}$ 2011, (top right) $B^0 \to J/\psi K^{*0}$ 2012, (bottom left) $B^0_s \to D^-_s \pi^+$ 2011 and (bottom right) $B^0_s \to D^-_s \pi^+$ 2012.*

Since $A_{\rm D}(K^-\pi^+)$ depends on the kaon momentum, mainly due to the asymmetry induced by the different interaction cross sections of K^+ and K^- with the detector materials, this quantity is measured in bins of kaon momentum. The bin definition is reported in Tab. 5.19. In order to have statistically independent measurements in each bin, the $D^+ \to K^-\pi^+\pi^+$ and $D^+ \to \overline{K}^0\pi^+$ data samples have been divided in independent sub-samples, applying requirements on the kaon momentum from $D^+ \to K^-\pi^+\pi^+$ and and on the pion daughter of $\overline{K}^0$ from $D^+ \to \overline{K}^0\pi^+$ decays.

The D^+ production asymmetry and the charged pion detection asymmetry cancel out in the difference of the two raw asymmetries only if their kinematic distributions are equal. To ensure this a reweighting procedure is performed, separately for both magnet polarities, years of data taking and bins of kaon momentum. The weights are computed using the normalised, binned, background-subtracted distributions of various kinematic variables for the $K^-\pi^+\pi^+$ and $\overline{K}^0\pi^+$ final states. The p and $p_{\rm T}$ distributions of the D^+ meson and the $p_{\rm T}$ distribution of the pion are reweighted. The chosen pion in the $K^-\pi^+\pi^+$ case is the one that triggered the HLT1, *i.e* the pion with higher momentum. 42 two-dimensional

Table 3.19: *Values of $A_{\rm P}(B^0 \to J/\psi K^{*0})$ determined from $B^0 \to J/\psi K^{*0}$ fits in the various bins of $p_{\rm T}$ and y for (left) 2011 and (right) 2012 data.*

$\sqrt{s} = 7$ TeV				$\sqrt{s} = 8$ TeV			
Bin	$A_{\rm P}(B^0 \to J/\psi K^{*0})$	Bin	$A_{\rm P}(B^0 \to J/\psi K^{*0})$	Bin	$A_{\rm P}(B^0 \to J/\psi K^{*0})$	Bin	$A_{\rm P}(B^0 \to J/\psi K^{*0})$
0	0.069 ± 0.039	28	0.041 ± 0.053	0	-0.019 ± 0.023	28	0.002 ± 0.032
1	0.014 ± 0.041	29	0.023 ± 0.076	1	-0.007 ± 0.029	29	0.043 ± 0.049
2	-0.028 ± 0.038	30	0.010 ± 0.090	2	-0.009 ± 0.028	30	0.051 ± 0.051
3	-0.027 ± 0.036	31	-0.059 ± 0.085	3	-0.021 ± 0.027	31	-0.090 ± 0.050
4	0.014 ± 0.035	32	-0.058 ± 0.077	4	-0.064 ± 0.026	32	-0.022 ± 0.049
5	-0.027 ± 0.023	33	0.062 ± 0.058	5	-0.017 ± 0.017	33	-0.020 ± 0.035
6	-0.027 ± 0.028	34	-0.033 ± 0.095	6	-0.013 ± 0.020	34	-0.085 ± 0.051
7	0.060 ± 0.033	35	0.015 ± 0.064	7	-0.007 ± 0.019	35	0.003 ± 0.036
8	-0.018 ± 0.040	36	-0.010 ± 0.102	8	-0.044 ± 0.026	36	-0.019 ± 0.059
9	-0.017 ± 0.037	37	0.018 ± 0.085	9	0.032 ± 0.023	37	0.020 ± 0.063
10	-0.070 ± 0.037	38	0.148 ± 0.089	10	-0.020 ± 0.023	38	-0.006 ± 0.057
11	-0.044 ± 0.036	39	0.048 ± 0.083	11	-0.025 ± 0.023	39	-0.064 ± 0.058
12	-0.021 ± 0.023	40	0.038 ± 0.073	12	-0.025 ± 0.016	40	0.020 ± 0.045
13	0.019 ± 0.032	41	0.106 ± 0.118	13	-0.002 ± 0.021	41	0.014 ± 0.071
14	-0.024 ± 0.044	42	-0.007 ± 0.045	14	0.008 ± 0.028	42	-0.036 ± 0.028
15	-0.220 ± 0.060	43	0.026 ± 0.092	15	-0.038 ± 0.039	43	-0.001 ± 0.052
16	-0.062 ± 0.060	44	0.023 ± 0.078	16	-0.054 ± 0.038	44	0.026 ± 0.047
17	-0.015 ± 0.059	45	-0.119 ± 0.079	17	-0.058 ± 0.038	45	0.008 ± 0.052
18	-0.004 ± 0.057	46	0.133 ± 0.091	18	-0.012 ± 0.038	46	-0.002 ± 0.049
19	-0.031 ± 0.041	47	0.047 ± 0.059	19	-0.009 ± 0.027	47	-0.053 ± 0.037
20	-0.035 ± 0.052	48	-0.103 ± 0.085	20	-0.049 ± 0.036	48	-0.049 ± 0.061
21	-0.044 ± 0.048	49	0.070 ± 0.046	21	-0.021 ± 0.029	49	0.022 ± 0.027
22	-0.051 ± 0.065	50	-0.001 ± 0.075	22	0.071 ± 0.042	50	-0.020 ± 0.049
23	-0.061 ± 0.067	51	-0.055 ± 0.075	23	0.012 ± 0.039	51	0.088 ± 0.052
24	-0.002 ± 0.070	52	-0.164 ± 0.092	24	0.075 ± 0.041	52	0.012 ± 0.053
25	0.022 ± 0.073	53	0.046 ± 0.112	25	-0.053 ± 0.046	53	0.015 ± 0.063
26	-0.062 ± 0.048	54	-0.019 ± 0.078	26	0.015 ± 0.030	54	-0.065 ± 0.043
27	-0.086 ± 0.064	55	0.169 ± 0.133	27	-0.006 ± 0.045	55	0.039 ± 0.078
Bin		$A_{\rm P}(B^0 \to J/\psi K^{*0})$		Bin		$A_{\rm P}(B^0 \to J/\psi K^{*0})$	
A		0.072 ± 0.077		A		0.007 ± 0.054	
B		-0.111 ± 0.082		B		-0.073 ± 0.072	
C		-0.030 ± 0.073		C		0.050 ± 0.063	
D		-0.085 ± 0.062		D		0.009 ± 0.055	
E		-0.066 ± 0.064		E		0.082 ± 0.062	
F		0.012 ± 0.040		F		0.067 ± 0.037	
G		0.070 ± 0.046		G		-0.042 ± 0.045	
$A_{\rm P}^{\rm avg}(B^0 \to J/\psi K^{*0}) = -0.0112 \pm 0.0063$				$A_{\rm P}^{\rm avg}(B^0 \to J/\psi K^{*0}) = -0.0111 \pm 0.0042$			

bins in p and $p_{\rm T}$ of the D^+ meson and 7 bins in $p_{\rm T}$ of the π^+ are employed.

The weighting function, $f_i(p_D, p_{{\rm T}D}, p_{{\rm T}\pi})$, in the i-th kinematics bin is calculated as

$$f_i(p_D, p_{{\rm T}D}, p_{{\rm T}\pi}) = \frac{N_i^{K\pi\pi}(p_D, p_{{\rm T}D}, p_{{\rm T}\pi})}{N_i^{K^0\pi}(p_D, p_{{\rm T}D}, p_{{\rm T}\pi})} \frac{N_{\rm tot}^{K^0\pi}}{N_{\rm tot}^{K\pi\pi}}, \tag{3.48}$$

Table 3.20: *Values of* $A_{\rm P}(B_s^0 \to D_s^-\pi^+)$ *determined from* $B_s^0 \to D_s^-\pi^+$ *fits in the various bins of* $p_{\rm T}$ *and* y *for (left) 2011 and (right) 2012 data.*

	$\sqrt{s} = 7$ TeV	$\sqrt{s} = 8$ TeV
Bin	$A_{\rm P}(B_s^0 \to D_s^-\pi^+)$	$A_{\rm P}(B_s^0 \to D_s^-\pi^+)$
0	0.017 ± 0.063	0.041 ± 0.042
1	0.031 ± 0.077	-0.024 ± 0.057
2	-0.083 ± 0.056	0.017 ± 0.039
3	0.036 ± 0.048	0.048 ± 0.032
4	0.021 ± 0.068	0.098 ± 0.047
5	0.006 ± 0.058	-0.043 ± 0.039
6	-0.004 ± 0.046	0.007 ± 0.030
7	0.110 ± 0.072	-0.128 ± 0.050
8	0.154 ± 0.072	-0.050 ± 0.046
9	-0.027 ± 0.034	-0.001 ± 0.022
10	-0.054 ± 0.061	0.042 ± 0.042
11	-0.059 ± 0.065	0.054 ± 0.045
$A_{\rm P}^{\rm avg}$	-0.0002 ± 0.0160	$+0.0083 \pm 0.0107$

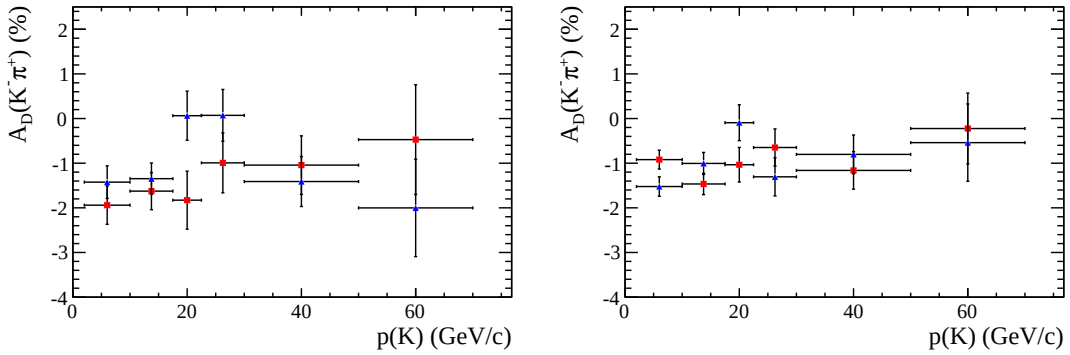

Figure 3.36: *Values of* $A_{\rm D}^j(K^-\pi^+) + A_{\rm D}(K^0)$ *for (top left) 2011 data, (top right) and 2012 data. The red squares refer to magnet up data, while the blue triangles to magnet down.*

where $N_i^{hh(h)}$ is the number of background-subtracted events in the i-th kinematic bin and $N_{\rm tot}^{hh(h)}$ is the total number of background-subtracted events.

The reweighted datasets are used to perform binned fits to D^+ invariant mass in each j-th bin of kaon momentum to extract $A_{\rm raw}^j(D^+ \to K^-\pi^+\pi^+)$ and $A_{\rm raw}^j D^+ \to (\overline{K}^0\pi^+)$. The fit model is the same used to fit the B^+ invariant mass and it is described in Sec. 3.4. In Fig. 3.36 the $A_{\rm D}^j(K^-\pi^+) + A_{\rm D}(K^0) = A_{\rm raw}^j(D^+ \to K^-\pi^+\pi^+) - A_{\rm raw}^j(D^+ \to \overline{K}^0\pi^+)$ values separated by year of data taking and magnet polarity are shown.

Table 3.21: *Values of the PID asymmetries in different kaon momentum bins.*

Bin	2011 Up	2011 Down
1	-0.0031 ± 0.0002	0.0037 ± 0.0001
2	-0.0014 ± 0.0001	0.0027 ± 0.0001
3	-0.0012 ± 0.0001	0.0021 ± 0.0001
4	-0.0003 ± 0.0001	0.0007 ± 0.0001
5	0.0005 ± 0.0001	-0.0004 ± 0.0001
6	0.0026 ± 0.0003	-0.0025 ± 0.0003
Bin	2012 Up	2012 Down
1	-0.0009 ± 0.0001	-0.0033 ± 0.0001
2	-0.0003 ± 0.0001	-0.0019 ± 0.0001
3	0.0000 ± 0.0000	-0.0016 ± 0.0001
4	0.0004 ± 0.0001	-0.0027 ± 0.0001
5	0.0007 ± 0.0001	-0.0045 ± 0.0001
6	0.0070 ± 0.0002	-0.0087 ± 0.0002

In order to make the measurements of $A_{\rm D}^j(K^-\pi^+)$ independent from the asymmetry induced by the PID requirements, the PID asymmetry, $A_{\rm PID}^j(K^-\pi^+)$, needs to be evaluated in each bin. The PID asymmetry in each bin is given by

$$A_{\rm PID}^j(K^-\pi^+) = \frac{\varepsilon^j(K^-\pi^+) - \varepsilon^j(K^+\pi^-)}{\varepsilon^j(K^-\pi^+) + \varepsilon^j(K^+\pi^-)}, \tag{3.49}$$

where ε is the PID requirement efficiency. This asymmetry is due to different efficiencies of the PID requirements on the $K^\mp\pi^\pm$ final states and to compute it the efficiencies of the PID requirements on the $K^-\pi^+$ and $K^+\pi^-$ final states are measured using control samples of $D^{*+} \to D^0(K^-\pi^+)\pi^+$ decays selected without any PID requirement. Since the PID efficiencies depend on the kinematics of the particles, a two-dimensional reweighting of the p and η distributions of the $K\pi$ pairs between the signal and control samples is done. The values of the measured PID asymmetries are reported in Tab. 3.21 and shown figs. 3.37.

3.6.2 $A_{\rm D}(\pi^+)$

In order to measure the pion detection asymmetry, we follow the procedure described in Ref. [69], where the pion detection asymmetry as a function of the pion momentum is measured by means of partially and fully reconstructed $D^{*+} \to D^0(K^-\pi^+\pi^-\pi^+)\pi^+$ decays. The values of the pion interaction asymmetry obtained in this analysis are reported in Tab. 5.21.

The momentum distribution of the π^+ from $D^+ \to K^-\pi^+\pi^+$ decays is different in each bin of kaon momentum. For this reason the measurements of $A_{\rm D}(\pi^+)$ are reweighted

to the pion momentum distribution in every kaon momentum bin. The weights obtained are reported in Tab. A.1. The obtained asymmetries are reported in Tab. 3.23.

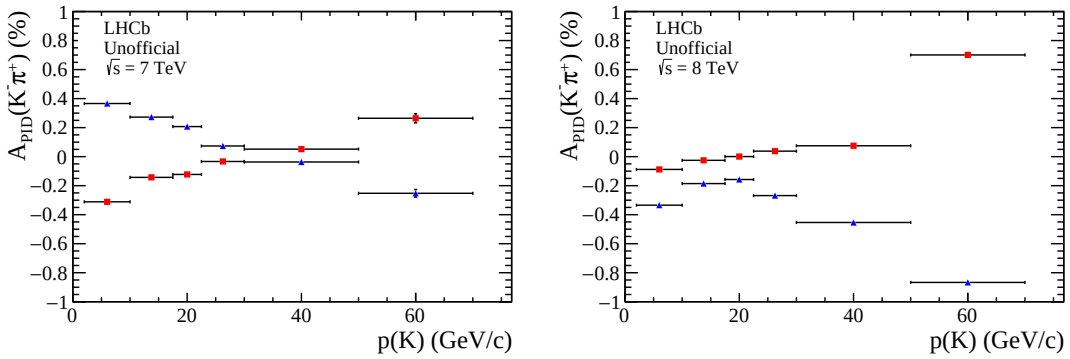

Figure 3.37: *Values of $A^j_{\rm PID}(K^-\pi^+)$ for (left) 2011 and (right) 2012 data for (red squares) up and (blue triangles) down magnet polarities.*

Table 3.22: *Values of the pion detection asymmetry in various ranges of pion momentum as taken from Ref. [69], divided by year and magnet polarity.*

		2011 Up	2011 Down
Bin	π momentum [GeV/c]	$A_{\rm D}(\pi)$	
1	2-6	-0.0045 ± 0.0043	-0.0059 ± 0.0036
2	6-15	-0.0047 ± 0.0029	0.0034 ± 0.0024
3	15-20	-0.0022 ± 0.0042	0.0014 ± 0.0034
4	20-30	-0.0031 ± 0.0045	0.0018 ± 0.0037
5	30-40	-0.0011 ± 0.0068	0.0004 ± 0.0056
6	40-50	0.0088 ± 0.0096	0.0004 ± 0.0080
7	50-100	0.0056 ± 0.0105	-0.0049 ± 0.0088
		2011 Up	2011 Down
Bin	π momentum [GeV/c]	$A_{\rm D}(\pi)$	
1	2-6	-0.0121 ± 0.0021	0.0032 ± 0.0022
2	6-15	-0.0052 ± 0.0015	-0.0000 ± 0.0015
3	15-20	0.0008 ± 0.0021	-0.0012 ± 0.0021
4	20-30	0.0004 ± 0.0022	-0.0012 ± 0.0022
5	30-40	0.0015 ± 0.0033	-0.0073 ± 0.0033
6	40-50	0.0015 ± 0.0048	-0.0050 ± 0.0048
7	50-100	0.0062 ± 0.0051	-0.0107 ± 0.0051

Table 3.23: *Pion detection asymmetries relative to each kaon momentum bin in which we measure* $A^j_{\rm D}(K^-\pi^+)$

.

Kaon momentum bins	$A^j_{\rm D}(\pi)$	
	2011 Up	2011 Down
1	-0.0027 ± 0.0021	0.0019 ± 0.0017
2	-0.0013 ± 0.0024	0.0012 ± 0.0020
3	-0.0000 ± 0.0028	0.0006 ± 0.0023
4	0.0009 ± 0.0032	0.0001 ± 0.0026
5	0.0021 ± 0.0040	-0.0008 ± 0.0034
6	0.0031 ± 0.0050	-0.0016 ± 0.0042
Kaon momentum bins	$A^j_{\rm D}(\pi)$	
	2012 Up	2012 Down
1	-0.0012 ± 0.0010	-0.0015 ± 0.0010
2	0.0001 ± 0.0011	-0.0028 ± 0.0011
3	0.0009 ± 0.0013	-0.0039 ± 0.0013
4	0.0014 ± 0.0015	-0.0047 ± 0.0015
5	0.0022 ± 0.0019	-0.0058 ± 0.0019
6	0.0030 ± 0.0023	-0.0069 ± 0.0023

3.6.3 $A_{\rm D}(K^-)$

In conclusion, the values of $A^j_{\rm D}(K^-)$ are obtained from the following relation

$$A^j_{\rm D}(K^-) = A_{\rm raw}(D^+ \to K^-\pi^+\pi^+) - A_{\rm raw}(D^+ \to \overline{K}^0\pi^+) - A_{\rm D}(K^0) - A_{\rm PID}(K^-\pi^+). \quad (3.50)$$

As the value of $A_{\rm D}(K^0)$ is a constant shift to $A^j_{\rm D}(K^-)$ and $A^j_{\rm D}(K^-)$ will be used in a weighted average when applied to the B^+ system (see next Section), we report the value of $A^j_{\rm D}(K^-) + A_{\rm D}(K^0)$, in each bin of kaon momentum, in Tab. 5.19 and in Fig. 3.38. In this way all the statistical errors are uncorrelated amongst the bins. The value of $A^j_{\rm D}(K^-)$ are independent of PID requirements and can be considered to correct kaon detection asymmetry in any analysis, following the approach described in the next Section.

3.6.4 Applying corrections to B^+ data sample

The momentum distribution of the K^+ coming from $B^+ \to J/\psi\, K^+$ is different in each $(p_{\rm T}, y)$ bin of the B^+. For this reason the measurements of $A^j_{\rm D}(K^-) + A_{\rm D}(K^0)$ need to be reweighted according to the distribution of the kaon momentum in every $(p_{\rm T}, y)$ bin. In the i-th B^+ $p_{\rm T}$ and y bin the kaon detection asymmetry is given by

$$A^i_{\rm D}(K^-) = \sum_j f_{i,j} \left(A^j_{\rm D}(K^-) + A_{\rm D}(K^0) \right) - A_{\rm D}(K^0), \quad (3.51)$$

Table 3.24: *Values of* $A_{\rm D}^{j}(K^-) + A_{\rm D}(K^0)$ *divided by year and magnet polarity.*

		$A_{\rm D}^{j}(K^-) + A_{\rm D}(K^0)$[%]			
Bin	$p(K)$ [GeV/c]	2011 Up	2011 Down	2012 Up	2012 Down
1	2 - 10	-1.36 ± 0.48	-1.98 ± 0.40	-0.71 ± 0.23	-1.04 ± 0.24
2	10 - 17.5	-1.35 ± 0.48	-1.74 ± 0.40	-1.45 ± 0.26	-0.54 ± 0.27
3	17.5 – 22.5	-1.70 ± 0.71	-0.20 ± 0.59	-1.12 ± 0.41	0.45 ± 0.42
4	22.5 - 30	-1.05 ± 0.74	-0.01 ± 0.64	-0.83 ± 0.44	-0.57 ± 0.45
5	30 - 50	-1.30 ± 0.77	-1.30 ± 0.65	-1.46 ± 0.46	0.23 ± 0.47
6	50 - 70	-1.05 ± 1.33	-1.59 ± 1.17	-1.23 ± 0.83	1.01 ± 0.90

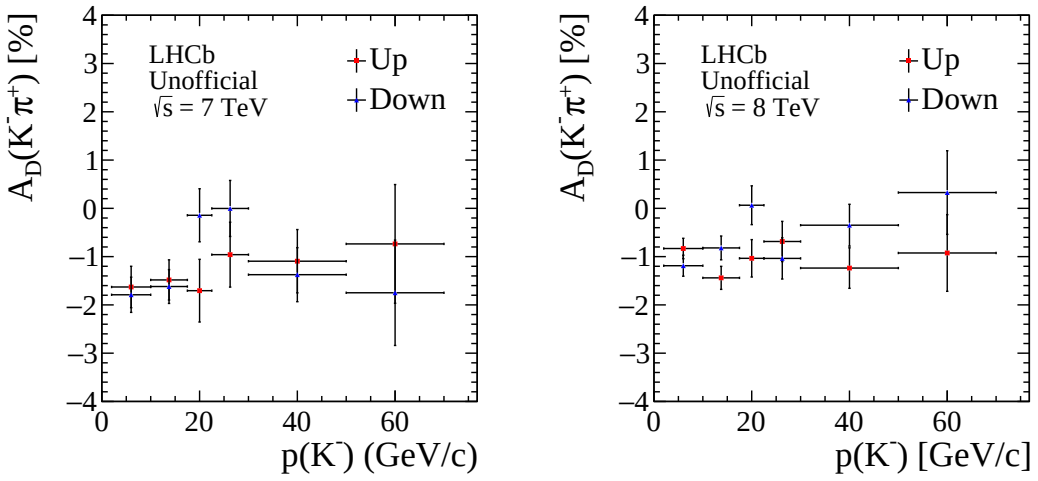

Figure 3.38: *Values of* $A_{\rm D}^{j}(K^-) + A_{\rm D}(K^0)$*, for (top left) 2011 data, (top right) and 2012 data. The red dots refer to magnet up data, while the blue ones to magnet down.*

where the $f_{i,j}$ coefficients are calculated as the fraction of kaons in the $j-$th kaon momentum bin for each i-th B^+ bin. The values of $f_{i,j}$ coefficients are reported in Tabs. A.2 and A.3 for 2011 data and in Tabs. A.4 and A.5 for 2012 data. In Tabs. A.6 and A.7 the values of $A_{\rm D}^{i}(K^-)$ for each magnet polarity and year of data taking are summarised.

The $A_{\rm D}^{i}(K^-)$ measured are independent of PID asymmetries, as previously described, and for this reason, in order to use these measurements to measure $A_{\rm P}(B^+)$, it is necessary to calculate the PID asymmetry due to the kaon coming from the $B^+ \to J/\psi\, K^+$ decay for each i-th B^+ $(p_{\rm T}, y)$ bin. This quantity is defined as

$$A_{\rm PID}^{i}(B^+ \to J/\psi\, K^+) = \frac{\varepsilon^i(K^-) - \varepsilon^i(K^+)}{\varepsilon^i(K^-) + \varepsilon^i(K^+)}\ . \tag{3.52}$$

The PID requirement efficiencies are measured separately for K^- and K^+ using charm control samples, reweigthing the kinematics of the control samples to match the kinematics of K^+ from B^+. The asymmetries found are reported in Tabs. A.8 and A.9 for 2011 and 2012 decays, respectively.

The B^+ production asymmetry in each i-th is given by

$$A^i_{\rm P}(B^+) = A^i_{\rm raw}(B^+ \to J/\psi K^+) - A^i_{\rm D}(K^+) - A^i_{\rm PID}(B^+ \to J/\psi K^+) - A_{CP}(B^+ \to J/\psi K^+) \quad (3.53)$$

where the i index runs over the B^+ $(p_{\rm T}, y)$ bins. In Tabs. 3.25 and 3.26 the final results are reported.

3.7 $A_{\rm P}$ integrated over $p_{\rm T}$ and y

The integration is performed in the ranges $0 < p_{\rm T} < 30$ GeV/c and 2.1 <y< 4.5 for the B^+ and B^0 mesons and in the ranges $2 < p_{\rm T} < 30$ GeV/c and 2.1 <y< 4.5 for the B^0_s meson. The $A_{\rm P}$ integrated value is given by

$$A_{\rm P} = \frac{\sum_i \frac{N_i}{\varepsilon_i} A_{{\rm P},i}}{\sum_i \frac{N_i}{\varepsilon_i}}, \quad (3.54)$$

where the index i runs over the kinematic bins, N_i is the number of signal events in each bin and ε_i is the efficiency in each bin defined as the number of selected events divided by the number of produced events. The signal yield in each bin can be expressed as

$$N_i = \mathcal{L} \cdot \sigma_{b\bar{b}} \cdot 2 \cdot f_X \cdot \mathcal{B} \cdot f_i \cdot \varepsilon_i, \quad (3.55)$$

where $\mathcal{L}$ is the integrated luminosity, $\sigma_{b\bar{b}}$ is the $b\bar{b}$ production cross-section, f_X, where $X = u,\ d,$ or s is the $B^+,\ B^0$ orB^0_s hadronization fraction, f_i is the fraction of B mesons produced in the $i-$th bin and $\mathcal{B}$ is the branching fraction of the B decay. By substituting N_i/ε_i from Eq. (3.55) into Eq. (3.54), the integrated value of $A_{\rm P}$ can be expressed as

$$A_{\rm P} = \sum_i \omega_i A_{{\rm P},i}\ , \quad (3.56)$$

where $\omega_i = f_i / \sum_i f_i$. The values of the ω_i are determined using simulated events. Signal events for $B^+ \to J/\psi K^+$ are generated using PYTHIA without any generator level cut. The values of ω_i are also extracted from data using $B^+ \to J/\psi K^+$ decays. In this case $\omega_i^{\rm data}$ is given by

$$\omega_i^{\rm data} = \frac{N_i}{\varepsilon_i^{\rm sel} \cdot \varepsilon_i^{\rm trig} \cdot \varepsilon_i^{\rm PID}} \Big/ \sum_i \frac{N_i}{\varepsilon_i^{\rm sel} \cdot \varepsilon_i^{\rm trig} \cdot \varepsilon_i^{\rm PID}}, \quad (3.57)$$

where

- N_i is the yield int the $i-$th bin;
- $\varepsilon_i^{\rm sel}$ is defined as the number of selected events, without trigger and PID requirements, in the $i-$th bin divided by the number of produced events in that bin;

Table 3.25: *Values of $A_{\rm P}(B^+)$ determined in the various bins of $p_{\rm T}$ and y, where the first error is statistical, the second is systematic, the third is due to the external input $A_{CP}(B^+ \to J/\psi K^+)$, and the fourth is due to the external input $A_{\rm D}(K^0)$.*

Bin	$A_{\rm P}(B^+)$ [$\sqrt{s} = 7$ TeV]	Bin	$A_{\rm P}(B^+)$ [$\sqrt{s} = 7$ TeV]
0	$0.0007 \pm 0.0089 \pm 0.0019 \pm 0.0028 \pm 0.0001$	28	$-0.0249 \pm 0.0182 \pm 0.0019 \pm 0.0028 \pm 0.0001$
1	$-0.0171 \pm 0.0113 \pm 0.0018 \pm 0.0028 \pm 0.0001$	29	$-0.0113 \pm 0.0292 \pm 0.0024 \pm 0.0028 \pm 0.0001$
2	$-0.0120 \pm 0.0105 \pm 0.0018 \pm 0.0028 \pm 0.0001$	30	$-0.0241 \pm 0.0290 \pm 0.0029 \pm 0.0028 \pm 0.0001$
3	$-0.0269 \pm 0.0102 \pm 0.0019 \pm 0.0028 \pm 0.0001$	31	$0.0267 \pm 0.0318 \pm 0.0031 \pm 0.0028 \pm 0.0001$
4	$0.0043 \pm 0.0103 \pm 0.0021 \pm 0.0028 \pm 0.0001$	32	$0.0118 \pm 0.0352 \pm 0.0034 \pm 0.0028 \pm 0.0001$
5	$-0.0167 \pm 0.0072 \pm 0.0025 \pm 0.0028 \pm 0.0001$	33	$-0.0164 \pm 0.0281 \pm 0.0034 \pm 0.0028 \pm 0.0001$
6	$0.0053 \pm 0.0099 \pm 0.0030 \pm 0.0028 \pm 0.0001$	34	$-0.0605 \pm 0.0411 \pm 0.0035 \pm 0.0028 \pm 0.0001$
7	$0.0023 \pm 0.0088 \pm 0.0018 \pm 0.0028 \pm 0.0001$	35	$-0.0200 \pm 0.0206 \pm 0.0020 \pm 0.0028 \pm 0.0001$
8	$-0.0002 \pm 0.0120 \pm 0.0019 \pm 0.0028 \pm 0.0001$	36	$-0.0068 \pm 0.0344 \pm 0.0028 \pm 0.0028 \pm 0.0001$
9	$0.0034 \pm 0.0116 \pm 0.0021 \pm 0.0028 \pm 0.0001$	37	$-0.0017 \pm 0.0362 \pm 0.0030 \pm 0.0028 \pm 0.0001$
10	$0.0092 \pm 0.0115 \pm 0.0022 \pm 0.0028 \pm 0.0001$	38	$-0.0181 \pm 0.0411 \pm 0.0032 \pm 0.0028 \pm 0.0001$
11	$-0.0092 \pm 0.0120 \pm 0.0025 \pm 0.0028 \pm 0.0001$	39	$-0.0239 \pm 0.0441 \pm 0.0033 \pm 0.0028 \pm 0.0001$
12	$-0.0168 \pm 0.0088 \pm 0.0028 \pm 0.0028 \pm 0.0001$	40	$0.0058 \pm 0.0362 \pm 0.0034 \pm 0.0028 \pm 0.0001$
13	$0.0010 \pm 0.0129 \pm 0.0029 \pm 0.0028 \pm 0.0001$	41	$0.0485 \pm 0.0548 \pm 0.0038 \pm 0.0028 \pm 0.0001$
14	$0.0031 \pm 0.0140 \pm 0.0018 \pm 0.0028 \pm 0.0001$	42	$0.0059 \pm 0.0174 \pm 0.0021 \pm 0.0028 \pm 0.0001$
15	$-0.0591 \pm 0.0208 \pm 0.0022 \pm 0.0028 \pm 0.0001$	43	$0.0210 \pm 0.0321 \pm 0.0032 \pm 0.0028 \pm 0.0001$
16	$-0.0089 \pm 0.0203 \pm 0.0023 \pm 0.0028 \pm 0.0001$	44	$0.0092 \pm 0.0334 \pm 0.0052 \pm 0.0028 \pm 0.0001$
17	$0.0016 \pm 0.0213 \pm 0.0027 \pm 0.0028 \pm 0.0001$	45	$-0.0267 \pm 0.0386 \pm 0.0037 \pm 0.0028 \pm 0.0001$
18	$-0.0205 \pm 0.0222 \pm 0.0029 \pm 0.0028 \pm 0.0001$	46	$-0.0516 \pm 0.0421 \pm 0.0031 \pm 0.0028 \pm 0.0001$
19	$0.0303 \pm 0.0172 \pm 0.0031 \pm 0.0028 \pm 0.0001$	47	$0.0071 \pm 0.0349 \pm 0.0039 \pm 0.0028 \pm 0.0001$
20	$0.0603 \pm 0.0259 \pm 0.0032 \pm 0.0028 \pm 0.0001$	48	$0.0748 \pm 0.0542 \pm 0.0036 \pm 0.0028 \pm 0.0001$
21	$-0.0134 \pm 0.0157 \pm 0.0019 \pm 0.0028 \pm 0.0001$	49	$0.0116 \pm 0.0188 \pm 0.0023 \pm 0.0028 \pm 0.0001$
22	$-0.0099 \pm 0.0246 \pm 0.0022 \pm 0.0028 \pm 0.0001$	50	$-0.0763 \pm 0.0401 \pm 0.0032 \pm 0.0028 \pm 0.0001$
23	$-0.0112 \pm 0.0246 \pm 0.0025 \pm 0.0028 \pm 0.0001$	51	$-0.0541 \pm 0.0458 \pm 0.0032 \pm 0.0028 \pm 0.0001$
24	$-0.0613 \pm 0.0251 \pm 0.0029 \pm 0.0028 \pm 0.0001$	52	$-0.0449 \pm 0.0512 \pm 0.0032 \pm 0.0028 \pm 0.0001$
25	$0.0552 \pm 0.0279 \pm 0.0030 \pm 0.0028 \pm 0.0001$	53	$0.0011 \pm 0.0599 \pm 0.0065 \pm 0.0028 \pm 0.0001$
26	$-0.0038 \pm 0.0216 \pm 0.0031 \pm 0.0028 \pm 0.0001$	54	$0.0089 \pm 0.0502 \pm 0.0035 \pm 0.0028 \pm 0.0001$
27	$0.0047 \pm 0.0342 \pm 0.0033 \pm 0.0028 \pm 0.0001$	55	$-0.0662 \pm 0.0827 \pm 0.0183 \pm 0.0028 \pm 0.0001$

Bin	$A_{\rm P}(B^+)$ [$\sqrt{s} = 7$ TeV]
A	$0.0085 \pm 0.0157 \pm 0.0021 \pm 0.0028 \pm 0.0001$
B	$-0.0014 \pm 0.0192 \pm 0.0019 \pm 0.0028 \pm 0.0001$
C	$0.0016 \pm 0.0177 \pm 0.0018 \pm 0.0028 \pm 0.0001$
D	$-0.0052 \pm 0.0171 \pm 0.0018 \pm 0.0028 \pm 0.0001$
E	$-0.0006 \pm 0.0171 \pm 0.0019 \pm 0.0028 \pm 0.0001$
F	$0.0107 \pm 0.0111 \pm 0.0022 \pm 0.0028 \pm 0.0001$
G	$-0.0104 \pm 0.0142 \pm 0.0032 \pm 0.0028 \pm 0.0001$

- $\varepsilon_i^{\rm PID}$ is defined as the number of selected events, including PID requirements, in the $i-$th bin divided by the number of selected events without trigger and PID requirements in that bin;
- $\varepsilon_i^{\rm trig}$ is defined as the number of selected events, including PID requirements and trigger, in the $i-$th bin divided by the number of selected events including PID requirements in that bin.

Table 3.26: *Values of $A_{\rm P}(B^+)$ determined in the various bins of $p_{\rm T}$ and y, where the first error is statistical, the second is systematic, the third is due to the external input $A_{CP}(B^+ \to J/\psi\, K^+)$, and the fourth is due to the external input $A_{\rm D}(K^0)$.*

Bin	$A_{\rm P}(B^+)$ [$\sqrt{s} = 8$ TeV]	Bin	$A_{\rm P}(B^+)$ [$\sqrt{s} = 8$ TeV]
0	$0.0050 \pm 0.0054 \pm 0.0011 \pm 0.0028 \pm 0.0001$	28	$0.0060 \pm 0.0109 \pm 0.0013 \pm 0.0028 \pm 0.0001$
1	$-0.0076 \pm 0.0073 \pm 0.0011 \pm 0.0028 \pm 0.0001$	29	$-0.0011 \pm 0.0183 \pm 0.0020 \pm 0.0028 \pm 0.0001$
2	$0.0009 \pm 0.0070 \pm 0.0012 \pm 0.0028 \pm 0.0001$	30	$0.0122 \pm 0.0183 \pm 0.0021 \pm 0.0028 \pm 0.0001$
3	$-0.0046 \pm 0.0069 \pm 0.0012 \pm 0.0028 \pm 0.0001$	31	$0.0067 \pm 0.0205 \pm 0.0022 \pm 0.0028 \pm 0.0001$
4	$-0.0018 \pm 0.0070 \pm 0.0013 \pm 0.0028 \pm 0.0001$	32	$-0.0462 \pm 0.0233 \pm 0.0023 \pm 0.0028 \pm 0.0001$
5	$-0.0081 \pm 0.0049 \pm 0.0016 \pm 0.0028 \pm 0.0001$	33	$-0.0290 \pm 0.0181 \pm 0.0023 \pm 0.0028 \pm 0.0001$
6	$-0.0133 \pm 0.0068 \pm 0.0020 \pm 0.0028 \pm 0.0001$	34	$-0.0243 \pm 0.0273 \pm 0.0023 \pm 0.0028 \pm 0.0001$
7	$-0.0045 \pm 0.0054 \pm 0.0011 \pm 0.0028 \pm 0.0001$	35	$0.0191 \pm 0.0128 \pm 0.0013 \pm 0.0028 \pm 0.0001$
8	$-0.0002 \pm 0.0077 \pm 0.0012 \pm 0.0028 \pm 0.0001$	36	$-0.0562 \pm 0.0220 \pm 0.0017 \pm 0.0028 \pm 0.0001$
9	$-0.0019 \pm 0.0075 \pm 0.0013 \pm 0.0028 \pm 0.0001$	37	$0.0172 \pm 0.0233 \pm 0.0021 \pm 0.0028 \pm 0.0001$
10	$-0.0107 \pm 0.0076 \pm 0.0014 \pm 0.0028 \pm 0.0001$	38	$-0.0080 \pm 0.0262 \pm 0.0033 \pm 0.0028 \pm 0.0001$
11	$-0.0175 \pm 0.0078 \pm 0.0017 \pm 0.0028 \pm 0.0001$	39	$0.0162 \pm 0.0282 \pm 0.0024 \pm 0.0028 \pm 0.0001$
12	$-0.0241 \pm 0.0059 \pm 0.0019 \pm 0.0028 \pm 0.0001$	40	$-0.0393 \pm 0.0233 \pm 0.0023 \pm 0.0028 \pm 0.0001$
13	$-0.0101 \pm 0.0087 \pm 0.0020 \pm 0.0028 \pm 0.0001$	41	$0.0317 \pm 0.0353 \pm 0.0023 \pm 0.0028 \pm 0.0001$
14	$-0.0052 \pm 0.0086 \pm 0.0011 \pm 0.0028 \pm 0.0001$	42	$0.0067 \pm 0.0107 \pm 0.0014 \pm 0.0028 \pm 0.0001$
15	$-0.0177 \pm 0.0131 \pm 0.0015 \pm 0.0028 \pm 0.0001$	43	$-0.0232 \pm 0.0195 \pm 0.0019 \pm 0.0028 \pm 0.0001$
16	$-0.0083 \pm 0.0132 \pm 0.0016 \pm 0.0028 \pm 0.0001$	44	$0.0171 \pm 0.0212 \pm 0.0037 \pm 0.0028 \pm 0.0001$
17	$0.0065 \pm 0.0134 \pm 0.0019 \pm 0.0028 \pm 0.0001$	45	$0.0065 \pm 0.0241 \pm 0.0035 \pm 0.0028 \pm 0.0001$
18	$-0.0055 \pm 0.0144 \pm 0.0027 \pm 0.0028 \pm 0.0001$	46	$-0.0101 \pm 0.0274 \pm 0.0023 \pm 0.0028 \pm 0.0001$
19	$-0.0003 \pm 0.0111 \pm 0.0021 \pm 0.0028 \pm 0.0001$	47	$-0.0214 \pm 0.0219 \pm 0.0025 \pm 0.0028 \pm 0.0001$
20	$-0.0300 \pm 0.0168 \pm 0.0021 \pm 0.0028 \pm 0.0001$	48	$-0.0511 \pm 0.0340 \pm 0.0024 \pm 0.0028 \pm 0.0001$
21	$-0.0038 \pm 0.0097 \pm 0.0012 \pm 0.0028 \pm 0.0001$	49	$-0.0203 \pm 0.0115 \pm 0.0016 \pm 0.0028 \pm 0.0001$
22	$-0.0070 \pm 0.0153 \pm 0.0015 \pm 0.0028 \pm 0.0001$	50	$-0.0340 \pm 0.0253 \pm 0.0021 \pm 0.0028 \pm 0.0001$
23	$-0.0228 \pm 0.0157 \pm 0.0017 \pm 0.0028 \pm 0.0001$	51	$-0.0231 \pm 0.0277 \pm 0.0047 \pm 0.0028 \pm 0.0001$
24	$-0.0236 \pm 0.0164 \pm 0.0022 \pm 0.0028 \pm 0.0001$	52	$0.0347 \pm 0.0317 \pm 0.0022 \pm 0.0028 \pm 0.0001$
25	$-0.0252 \pm 0.0182 \pm 0.0029 \pm 0.0028 \pm 0.0001$	53	$-0.0064 \pm 0.0379 \pm 0.0061 \pm 0.0028 \pm 0.0001$
26	$-0.0036 \pm 0.0141 \pm 0.0022 \pm 0.0028 \pm 0.0001$	54	$-0.0221 \pm 0.0311 \pm 0.0030 \pm 0.0028 \pm 0.0001$
27	$-0.0293 \pm 0.0220 \pm 0.0022 \pm 0.0028 \pm 0.0001$	55	$-0.0987 \pm 0.0496 \pm 0.0055 \pm 0.0028 \pm 0.0001$

Bin	$A_{\rm P}(B^+)$ [$\sqrt{s} = 8$ TeV]
A	$-0.0178 \pm 0.0097 \pm 0.0012 \pm 0.0028 \pm 0.0001$
B	$-0.0027 \pm 0.0127 \pm 0.0011 \pm 0.0028 \pm 0.0001$
C	$0.0093 \pm 0.0120 \pm 0.0011 \pm 0.0028 \pm 0.0001$
D	$0.0005 \pm 0.0119 \pm 0.0012 \pm 0.0028 \pm 0.0001$
E	$-0.0230 \pm 0.0120 \pm 0.0015 \pm 0.0028 \pm 0.0001$
F	$-0.0120 \pm 0.0080 \pm 0.0015 \pm 0.0028 \pm 0.0001$
G	$-0.0077 \pm 0.0104 \pm 0.0022 \pm 0.0028 \pm 0.0001$

3.7.1 $B^+ \to J/\psi\, K^+$

The values of $\varepsilon_i^{\rm sel}$ and $\varepsilon_i^{\rm trig}$ are determined from simulated events, while in order to account for the discrepancy between PID performances in data and simulated events, $\varepsilon_i^{\rm PID}$ is determined from data, using a dedicated calibration sample of $D^{*+} \to D^0(K^-\pi^+)\pi^+$ events and making use of the `PIDCalib` package. The efficiencies and the corresponding values of $\omega_i^{\rm data}$ and ω_i from simulation are reported in Tabs. A.10 and A.11. In Fig. 3.39

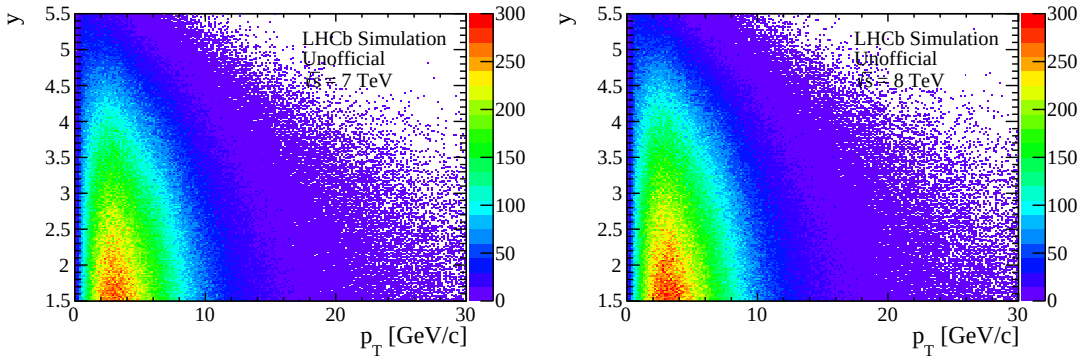

Figure 3.39: *Distribution of p_{T} and y for simulated B^+ mesons produced without generator level cuts at centre-of-mass energies of (left) $\sqrt{s} = 7$ TeV and (right) $\sqrt{s} = 8$ TeV.*

the two-dimensional p_{T} and y distributions of fully simulated events generated without using generator level cuts are shown.

The values of ω_i and ω_i^{data} exhibit systematic differences. The difference in the central value between the integrated $A_{\mathrm{P}}(B^+)$ calculated using either ω_i or ω_i^{data} will be assigned as a systematic uncertainty to the final integrated value of the production asymmetry.

3.7.2 $B^0 \to J/\psi K^{*0}$ and $B_s^0 \to D_s^- \pi^+$

The values of ω_i are determined using simulated events. Signal events for $B^0 \to J/\psi K^{*0}$ and $B_s^0 \to D_s^- \pi^+$ are generated using PYTHIA 8 without any generator level cut. In Tabs. A.12 and A.13 the values of ω_i for $B^0 \to J/\psi K^{*0}$ 2011 and 2012 decays using the binning scheme of Tab. 3.12 are reported, whereas in Tab. A.14 the values of ω_i for $B_s^0 \to D_s^- \pi^+$ 2011 and 2012 decays using the binning scheme of Tab. 3.18 are reported. In Figs. 3.40 and 3.41 the two-dimensional p_{T} and y distributions of fully simulated events generated without using generator level cuts.

The values of ω_i and ω_i^{data} exhibit systematic differences. The difference in the central value between $A_{\mathrm{P}}(B^0 \to J/\psi K^{*0})$ calculated using either ω_i or ω_i^{data} will be assigned as a systematic uncertainty for both $A_{\mathrm{P}}(B^0)$ and $A_{\mathrm{P}}(B_s^0)$.

3.8 Systematic uncertainties

To estimate the contribution of each single source we repeat the fit for each single bin after having modified the baseline fit model. The shifts from the relevant baseline values are accounted for as systematic uncertainties.

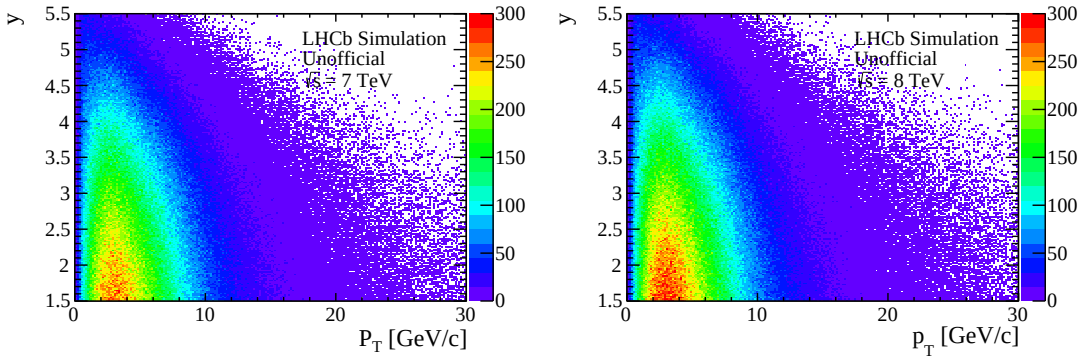

Figure 3.40: *Distribution of p_{T} and y for simulated B^0 mesons produced without generator level cuts at centre-of-mass energies of (left) $\sqrt{s} = 7$ TeV and (right) $\sqrt{s} = 8$ TeV.*

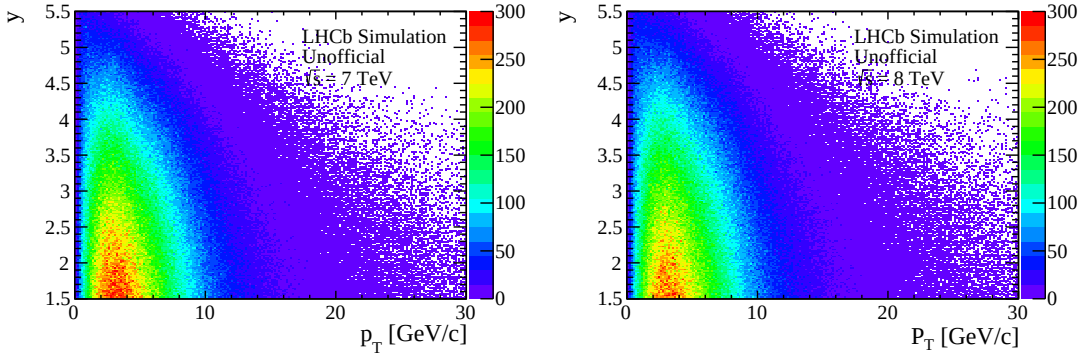

Figure 3.41: *Distribution of p_{T} and y for simulated B_s^0 mesons produced without generator level cuts at centre-of-mass energies of (left) $\sqrt{s} = 7$ TeV and (right) $\sqrt{s} = 8$ TeV.*

3.8.1 $B^+ \to J/\psi\, K^+$

The following sources of systematics uncertainties affecting the determination of the production asymmetries are considered

- inaccuracies in the shapes of any component (signal and combinatorial background);

To estimate a systematic uncertainty related to the parameterization of FSR on the signal mass distributions, the parameter s is varied by $\pm 1\sigma$ of the corresponding value obtained from fits to simulated events. A systematic uncertainty related to the invariant-mass resolution model is estimated by repeating the fit using a double-Gaussian function without the correction for the FSR. The systematic uncertainty related to the parametrization of the mass shape for the combinatorial background is investigated by replacing the exponential function with a straight line.

A summary of the numerical values of all systematic uncertainties for each bin is reported in Tabs. A.15 and A.16.

3.8.2 $B^0 \to J/\psi\, K^{*0}$ and $B_s^0 \to D_s^- \pi^+$

The following sources of systematic uncertainties affecting the determination of the production asymmetries are considered

- invariant mass
  - inaccuracies in the shapes of any component (signals, combinatorial and partially-reconstructed backgrounds);
- decay time
  - inaccuracies in the resolution and acceptance functions;
  - uncertainties on the external inputs ($|q/p|_{B^0}$, $|q/p|_{B_s^0}$, Δm_d, Δm_s, $\Delta\Gamma_s$, Γ_d and Γ_s);

To estimate a systematic uncertainty related to the parameterization of FSR on the signal mass distributions, the parameter s is varied by $\pm 1\sigma$ of the corresponding value obtained from fits to simulated events. A systematic uncertainty related to the invariant-mass resolution model is estimated by repeating the fit using a single Gaussian function without the correction for FSR. The systematic uncertainty related to the parameterization of the mass shape for the combinatorial background is investigated by replacing the exponential function with a straight line. Concerning the partially-reconstructed background, a systematic uncertainty is obtained by repeating the fits while excluding the low mass sideband, *i.e.* applying the requirement $m > 5.33\,\mathrm{GeV}/c^2$ for $B_s^0 \to D_s^- \pi^+$ decays. In the case of $B_s^0 \to D_s^- \pi^-$ decays the $B^0 \to D_s^- \pi^+$ yields are fixed to the ones obtained from the fit and varied by $\pm 1\sigma$. To estimate an uncertainty related to the parameterization of signal decay time acceptances, an alternative acceptance function with respect to that used for the $B^0 \to J/\psi\, K^{*0}$ is used. Effects of inaccuracies in the knowledge of the decay-time resolution are estimated by rescaling the widths of the baseline model in order to obtain an average resolution width differing by ± 8 fs, corresponding to the uncertainty estimated in Sec. 3.3, with respect to the baseline one. Effects due to a possible bias in the decay time are also accounted for by introducing a bias of ± 2 fs in the decay-time resolution model. The determination of the systematic uncertainties related to the $|q/p|$ input value needs a special treatement, as A_{P} turns out to be correlated with $|q/p|$. For this reasons, any variation of $|q/p|$ turns into the same shift of A_{P} in each of the kinematic bins, *i.e.* such systematic uncertainties are 100% correlated between the various bins.

A summary of the numerical values of all systematic uncertainties for each bin is reported in Tabs. A.17, A.18, A.19 and A.20.

3.9 Final integrated results

The overall production asymmetries integrated over the ranges $0 < p_{\mathrm{T}} < 30$ GeV/c and $2.1 < y < 4.5$ for B^+ and B^0 mesons and over the ranges $0 < p_{\mathrm{T}} < 30$ GeV/c and

$2.1 < y < 4.5$ for the B_s^0 meson are determined. The values of the production asymmetries from global fits are found to be

$$\begin{aligned} A_{\rm P}(B^0)_{\sqrt{s}=7\,\text{TeV}} &= (-1.13 \pm 0.63)\,\%, \\ A_{\rm P}(B^0)_{\sqrt{s}=8\,\text{TeV}} &= (-1.09 \pm 0.42)\,\%, \\ A_{\rm P}(B_s^0)_{\sqrt{s}=7\,\text{TeV}} &= (-0.01 \pm 1.66)\,\%, \\ A_{\rm P}(B_s^0)_{\sqrt{s}=8\,\text{TeV}} &= (\ \ 0.82 \pm 1.11)\,\%. \end{aligned}$$

The integrated values of the production asymmetries are obtained according to Eq. (3.56), where the values of ω_i are obtained from simulation, as discussed in Sec. 3.7. Concerning the B^+ production asymmetry, the weighted mean between up and down magnet polarities is taken before performing the integration. The central values become

$$\begin{aligned} A_{\rm P}(B^+)_{\sqrt{s}=7\,\text{TeV}} &= -0.0023, \\ A_{\rm P}(B^0)_{\sqrt{s}=8\,\text{TeV}} &= -0.0074, \\ A_{\rm P}(B^0)_{\sqrt{s}=7\,\text{TeV}} &= \ \ 0.0044, \\ A_{\rm P}(B^0)_{\sqrt{s}=8\,\text{TeV}} &= -0.0140, \\ A_{\rm P}(B_s^0)_{\sqrt{s}=7\,\text{TeV}} &= -0.0065, \\ A_{\rm P}(B_s^0)_{\sqrt{s}=8\,\text{TeV}} &= \ \ 0.0198. \end{aligned}$$

The statistical and systematic uncertainties are calculated by error propagation as

$$\sigma_{\rm stat} = \sqrt{\sum_i \left(\omega_i\, \sigma_{\rm stat}\left(A_{\rm P}^i\right)\right)^2}, \tag{3.58}$$

$$\sigma_{\rm syst} = \sigma_{\rm syst}\left(A_{\rm P}\right), \tag{3.59}$$

where the last equation is due to the equality of the correlated uncertainties in all bins.

Other systematic effects need to be taken into account. The statistical uncertainties on the values of ω_i are propagated as

$$\sigma_\omega = \sqrt{\sum_i \left(A_{\rm P}^i\, \sigma_{\rm stat}\left(\omega_i\right)\right)^2}. \tag{3.60}$$

Furthermore, as already mentioned in Sec. 3.7, a systematic uncertainty related to the determination of ω_i from simulation is computed. This is defined as the difference between the central values of $A_{\rm P}$ calculated using either ω_i or $\omega_i^{\rm data}$. The systematic uncertainties obtained are reported in Tab. 3.27. In the case of B_s^0 the same systematic calculated for the B^0 is used.

The final result for the integrated values of $A_{\rm P}(B^+)$, $A_{\rm P}(B^0)$ and $A_{\rm P}(B_s^0)$ are

$$\begin{aligned} A_{\rm P}(B^+)_{\sqrt{s}=7\,\text{TeV}} &= -0.0023 \pm 0.0024\ (\text{stat}) \pm 0.0037\ (\text{syst}), \\ A_{\rm P}(B^+)_{\sqrt{s}=8\,\text{TeV}} &= -0.0074 \pm 0.0015\ (\text{stat}) \pm 0.0032\ (\text{syst}), \end{aligned}$$

Table 3.27: *Systematic uncertainties on the integrated $A_{\rm P}$ due to the difference between ω_i or $\omega_i^{\rm data}$.*

Decay and year	$\lvert A_{\rm P,MC} - A_{\rm P,data}\rvert$
$B^+ \to J/\psi\, K^+$ (2011)	0.0002
$B^+ \to J/\psi\, K^+$ (2012)	0.0002
$B^0 \to J/\psi\, K^{*0}$ (2011)	0.0003
$B^0 \to J/\psi\, K^{*0}$ (2012)	0.0003
$B_s^0 \to D_s^- \pi^+$ (2011)	0.0003
$B_s^0 \to D_s^- \pi^+$ (2012)	0.0003

Table 3.28: *Values of the production asymmetries in bins of $p_{\rm T}$, integrated over y, for B^+ and B^0 mesons for data collected in proton-proton collisions at the centre-of-mass energy of 7 TeV. The first uncertainties are statistical and the second systematic. The uncertainties among the bins are correlated due to the external inputs: $A_{CP}(B^+ \to J/\psi\, K^+)$ and $A_{\rm D}(\overline{K}^0)$ for $A_{\rm P}(B^+)$, and $\lvert q/p\rvert$ for $A_{\rm P}(B^0)$.*

$p_{\rm T}$ [GeV/c]	$A_{\rm P}(B^+)_{\sqrt{s}=7\text{ TeV}}$	$A_{\rm P}(B^0)_{\sqrt{s}=7\text{ TeV}}$
(0.00, 2.00)	$0.0015 \pm 0.0067 \pm 0.0036$	$0.0215 \pm 0.0297 \pm 0.0025$
(2.00, 4.50)	$-0.0050 \pm 0.0040 \pm 0.0037$	$0.0123 \pm 0.0163 \pm 0.0078$
(4.50, 7.00)	$-0.0010 \pm 0.0045 \pm 0.0038$	$0.0124 \pm 0.0150 \pm 0.0042$
(7.00, 8.25)	$0.0083 \pm 0.0080 \pm 0.0041$	$-0.0440 \pm 0.0219 \pm 0.0012$
(8.25, 9.50)	$-0.0078 \pm 0.0096 \pm 0.0039$	$-0.0476 \pm 0.0248 \pm 0.0038$
(9.50, 10.75)	$-0.0220 \pm 0.0114 \pm 0.0044$	$0.0155 \pm 0.0297 \pm 0.0056$
(10.75, 12.00)	$-0.0045 \pm 0.0138 \pm 0.0043$	$0.0404 \pm 0.0357 \pm 0.0040$
(12.00, 15.00)	$0.0107 \pm 0.0124 \pm 0.0053$	$-0.0050 \pm 0.0269 \pm 0.0035$
(15.00, 30.00)	$-0.0146 \pm 0.0150 \pm 0.0065$	$0.0333 \pm 0.0298 \pm 0.0077$

$$
\begin{aligned}
A_{\rm P}(B^0)_{\sqrt{s}=7\,\text{TeV}} &= 0.0044 \pm 0.0088\ (\text{stat}) \pm 0.0011\ (\text{syst}),\\
A_{\rm P}(B^0)_{\sqrt{s}=8\,\text{TeV}} &= -0.0140 \pm 0.0055\ (\text{stat}) \pm 0.0010\ (\text{syst}),\\
A_{\rm P}(B_s^0)_{\sqrt{s}=7\,\text{TeV}} &= -0.0065 \pm 0.0288\ (\text{stat}) \pm 0.0059\ (\text{syst}),\\
A_{\rm P}(B_s^0)_{\sqrt{s}=8\,\text{TeV}} &= 0.0198 \pm 0.0190\ (\text{stat}) \pm 0.0059\ (\text{syst}),
\end{aligned}
$$

In Tabs. 3.28, 3.29, 3.30, 3.31, 3.32, and 3.33 the values of $A_{\rm P}(B^+)$, $A_{\rm P}(B^0)$, and $A_{\rm P}(B_s^0)$ integrated over y and $p_{\rm T}$ separately for 2011 and 2012 data samples are reported. The dependence of $A_{\rm P}(B^+)$, $A_{\rm P}(B^0)$, and $A_{\rm P}(B_s^0)$ on $p_{\rm T}$ and y are shown in Figs. 3.42, 3.43, and 3.44.

Table 3.29: *Values of the production asymmetries in bins of y, integrated over $p_{\rm T}$, for B^+ and B^0 mesons for data collected in proton-proton collisions at the centre-of-mass energy of 7 TeV. The first uncertainties are statistical and the second systematic. The uncertainties among the bins are correlated due to the external inputs: $A_{CP}(B^+ \to J/\psi K^+)$ and $A_{\rm D}(\overline{K}^0)$ for $A_{\rm P}(B^+)$, and $|q/p|$ for $A_{\rm P}(B^0)$.*

y	$A_{\rm P}(B^+)_{\sqrt{s}=7\text{ TeV}}$	$A_{\rm P}(B^0)_{\sqrt{s}=7\text{ TeV}}$
$(2.10, 2.70)$	$0.0007 \pm 0.0047 \pm 0.0036$	$0.0488 \pm 0.0205 \pm 0.0017$
$(2.70, 2.85)$	$-0.0131 \pm 0.0064 \pm 0.0036$	$-0.0366 \pm 0.0232 \pm 0.0027$
$(2.85, 3.00)$	$-0.0063 \pm 0.0061 \pm 0.0037$	$-0.0251 \pm 0.0213 \pm 0.0010$
$(3.00, 3.15)$	$-0.0125 \pm 0.0061 \pm 0.0039$	$-0.0478 \pm 0.0203 \pm 0.0017$
$(3.15, 3.30)$	$-0.0009 \pm 0.0063 \pm 0.0039$	$-0.0130 \pm 0.0203 \pm 0.0018$
$(3.30, 3.70)$	$-0.0060 \pm 0.0044 \pm 0.0043$	$-0.0143 \pm 0.0133 \pm 0.0017$
$(3.70, 4.50)$	$0.0041 \pm 0.0062 \pm 0.0046$	$0.0044 \pm 0.0173 \pm 0.0045$

Table 3.30: *Values of the production asymmetries in bins of $p_{\rm T}$, integrated over y, for B^+ and B^0 mesons for data collected in proton-proton collisions at the centre-of-mass energy of 8 TeV. The first uncertainties are statistical and the second systematic. The uncertainties among the bins are correlated due to the external inputs: $A_{CP}(B^+ \to J/\psi K^+)$ and $A_{\rm D}(\overline{K}^0)$ for $A_{\rm P}(B^+)$, and $|q/p|$ for $A_{\rm P}(B^0)$.*

$p_{\rm T}$ [GeV/c]	$A_{\rm P}(B^+)_{\sqrt{s}=8\text{ TeV}}$	$A_{\rm P}(B^0)_{\sqrt{s}=8\text{ TeV}}$
$(0.00, 2.00)$	$-0.0105 \pm 0.0045 \pm 0.0031$	$0.0065 \pm 0.0230 \pm 0.0017$
$(2.00, 4.50)$	$-0.0033 \pm 0.0026 \pm 0.0031$	$-0.0188 \pm 0.0103 \pm 0.0009$
$(4.50, 7.00)$	$-0.0093 \pm 0.0029 \pm 0.0032$	$-0.0111 \pm 0.0092 \pm 0.0011$
$(7.00, 8.25)$	$-0.0094 \pm 0.0051 \pm 0.0033$	$-0.0192 \pm 0.0141 \pm 0.0015$
$(8.25, 9.50)$	$-0.0126 \pm 0.0061 \pm 0.0033$	$0.0015 \pm 0.0155 \pm 0.0009$
$(9.50, 10.75)$	$-0.0073 \pm 0.0073 \pm 0.0034$	$-0.0156 \pm 0.0177 \pm 0.0013$
$(10.75, 12.00)$	$0.0036 \pm 0.0090 \pm 0.0034$	$0.0017 \pm 0.0210 \pm 0.0027$
$(12.00, 15.00)$	$-0.0082 \pm 0.0079 \pm 0.0035$	$-0.0270 \pm 0.0171 \pm 0.0009$
$(15.00, 30.00)$	$-0.0251 \pm 0.0095 \pm 0.0040$	$0.0137 \pm 0.0177 \pm 0.0009$

Table 3.31: *Values of the production asymmetries in bins of y, integrated over p_{T}, for B^+ and B^0 mesons for data collected in proton-proton collisions at the centre-of-mass energy of 8 TeV. The first uncertainties are statistical and the second systematic. The uncertainties among the bins are correlated due to the external inputs: $A_{CP}(B^+ \to J/\psi K^+)$ and $A_{\mathrm{D}}(\overline{K}^0)$ for $A_{\mathrm{P}}(B^+)$, and $|q/p|$ for $A_{\mathrm{P}}(B^0)$.*

y	$A_{\mathrm{P}}(B^+)_{\sqrt{s}=8\text{ TeV}}$	$A_{\mathrm{P}}(B^0)_{\sqrt{s}=8\text{ TeV}}$
$(2.10, 2.70)$	$-0.0023 \pm 0.0029 \pm 0.0031$	$-0.0082 \pm 0.0128 \pm 0.0012$
$(2.70, 2.85)$	$-0.0080 \pm 0.0041 \pm 0.0031$	$-0.0237 \pm 0.0173 \pm 0.0009$
$(2.85, 3.00)$	$0.0003 \pm 0.0040 \pm 0.0032$	$0.0148 \pm 0.0159 \pm 0.0015$
$(3.00, 3.15)$	$-0.0038 \pm 0.0040 \pm 0.0032$	$-0.0140 \pm 0.0151 \pm 0.0009$
$(3.15, 3.30)$	$-0.0123 \pm 0.0042 \pm 0.0034$	$-0.0193 \pm 0.0158 \pm 0.0021$
$(3.30, 3.70)$	$-0.0138 \pm 0.0030 \pm 0.0034$	$-0.0029 \pm 0.0103 \pm 0.0010$
$(3.70, 4.50)$	$-0.0144 \pm 0.0042 \pm 0.0037$	$-0.0201 \pm 0.0137 \pm 0.0010$

Table 3.32: *Values of the production asymmetries in bins of p_{T}, integrated over y, for the B_s^0 meson for data collected in proton-proton collisions at the centre-of-mass energy of 7 and 8 TeV. The first uncertainties are statistical and the second systematic. The uncertainties among the bins are correlated due to the external inputs: $|q/p|_{B_s^0}$ for $A_{\mathrm{P}}(B_s^0)$.*

p_{T} [GeV/c]	$A_{\mathrm{P}}(B_s^0)_{\sqrt{s}=7\text{ TeV}}$	$A_{\mathrm{P}}(B_s^0)_{\sqrt{s}=8\text{ TeV}}$
$(2.0, 7.0)$	$-0.0166 \pm 0.0393 \pm 0.0082$	$0.0292 \pm 0.0200 \pm 0.0096$
$(7.0, 9.5)$	$0.0247 \pm 0.0334 \pm 0.0050$	$0.0367 \pm 0.0302 \pm 0.0127$
$(9.5, 12.0)$	$0.0566 \pm 0.0349 \pm 0.0096$	$0.0442 \pm 0.0437 \pm 0.0164$
$(12.0, 30.0)$	$-0.0382 \pm 0.0273 \pm 0.0054$	$0.0902 \pm 0.0612 \pm 0.0253$

Table 3.33: *Values of the production asymmetries in bins of y, integrated over p_{T}, for the B_s^0 meson for data collected in proton-proton collisions at the centre-of-mass energy of 7 and 8 TeV. The first uncertainties are statistical and the second systematic. The uncertainties among the bins are correlated due to the external inputs: $|q/p|_{B_s^0}$ for $A_{\mathrm{P}}(B_s^0)$.*

y	$A_{\mathrm{P}}(B_s^0)_{\sqrt{s}=7\text{ TeV}}$	$A_{\mathrm{P}}(B_s^0)_{\sqrt{s}=8\text{ TeV}}$
$(2.1, 3.0)$	$0.0151 \pm 0.0445 \pm 0.0088$	$0.0028 \pm 0.0247 \pm 0.0107$
$(3.0, 3.3)$	$0.0296 \pm 0.0566 \pm 0.0111$	$0.0792 \pm 0.0317 \pm 0.0138$
$(3.3, 4.5)$	$-0.0554 \pm 0.0432 \pm 0.0101$	$0.0682 \pm 0.0242 \pm 0.0142$

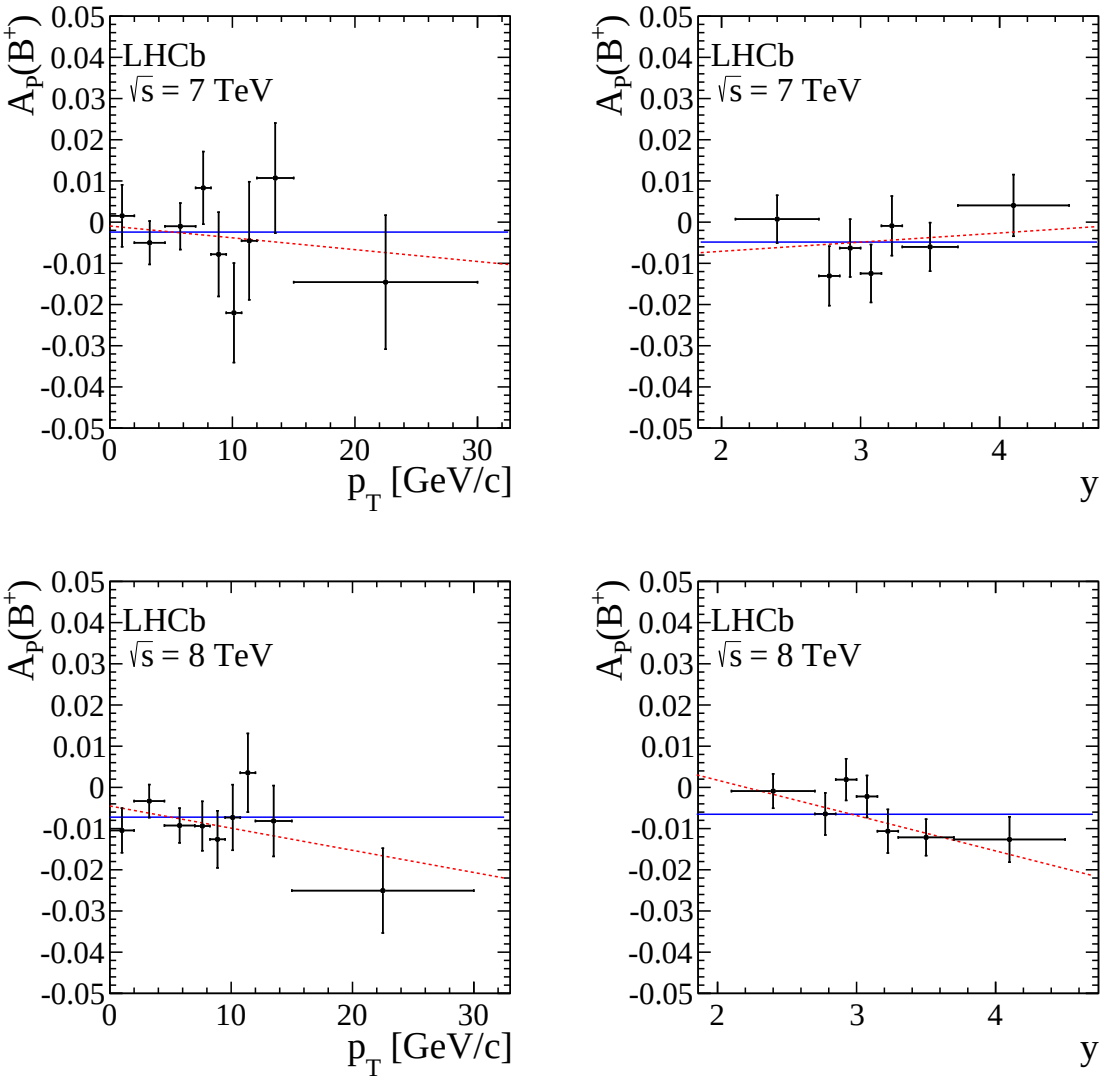

Figure 3.42: *Dependence of $A_{\rm P}(B^+)$, for data collected in proton-proton collisions with centre-of-mass of energies of (top) 7 and (bottom) 8 TeV, on (left) $p_{\rm T}$ and (right) y. The results of fits using a straight line with zero (solid line) or floating slope parameter (dashed line) are also shown. The fits take into account the correlations amongst the bins.*

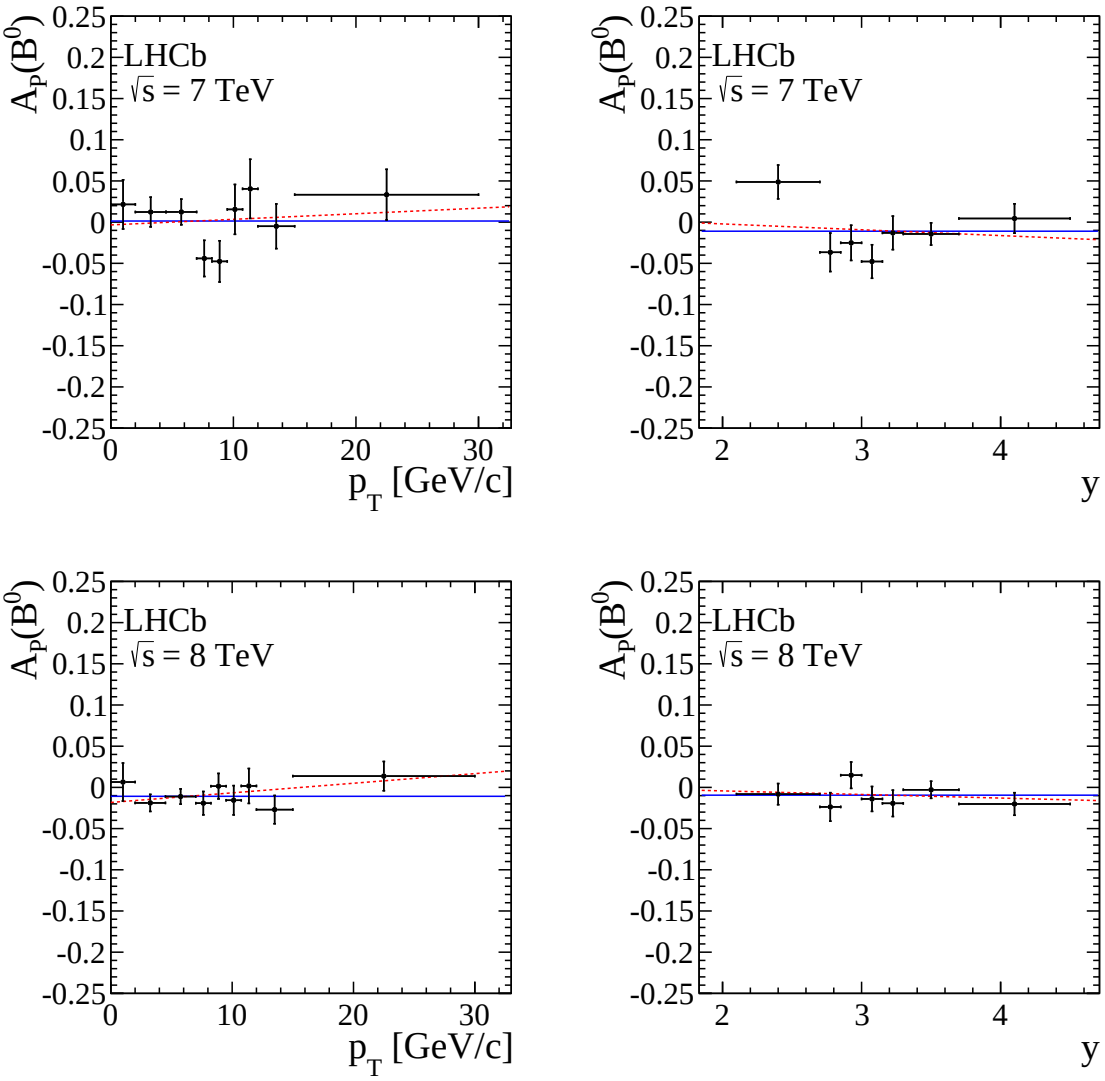

Figure 3.43: *Dependence of $A_{\rm P}(B^0)$, for data collected in proton-proton collisions with centre-of-mass of energies of (top) 7 and (bottom) 8 TeV, on (left) $p_{\rm T}$ and (right) y. The results of fits using a straight line with zero (solid line) or floating slope parameter (dashed line) are also shown. The fits take into account the correlations amongst the bins.*

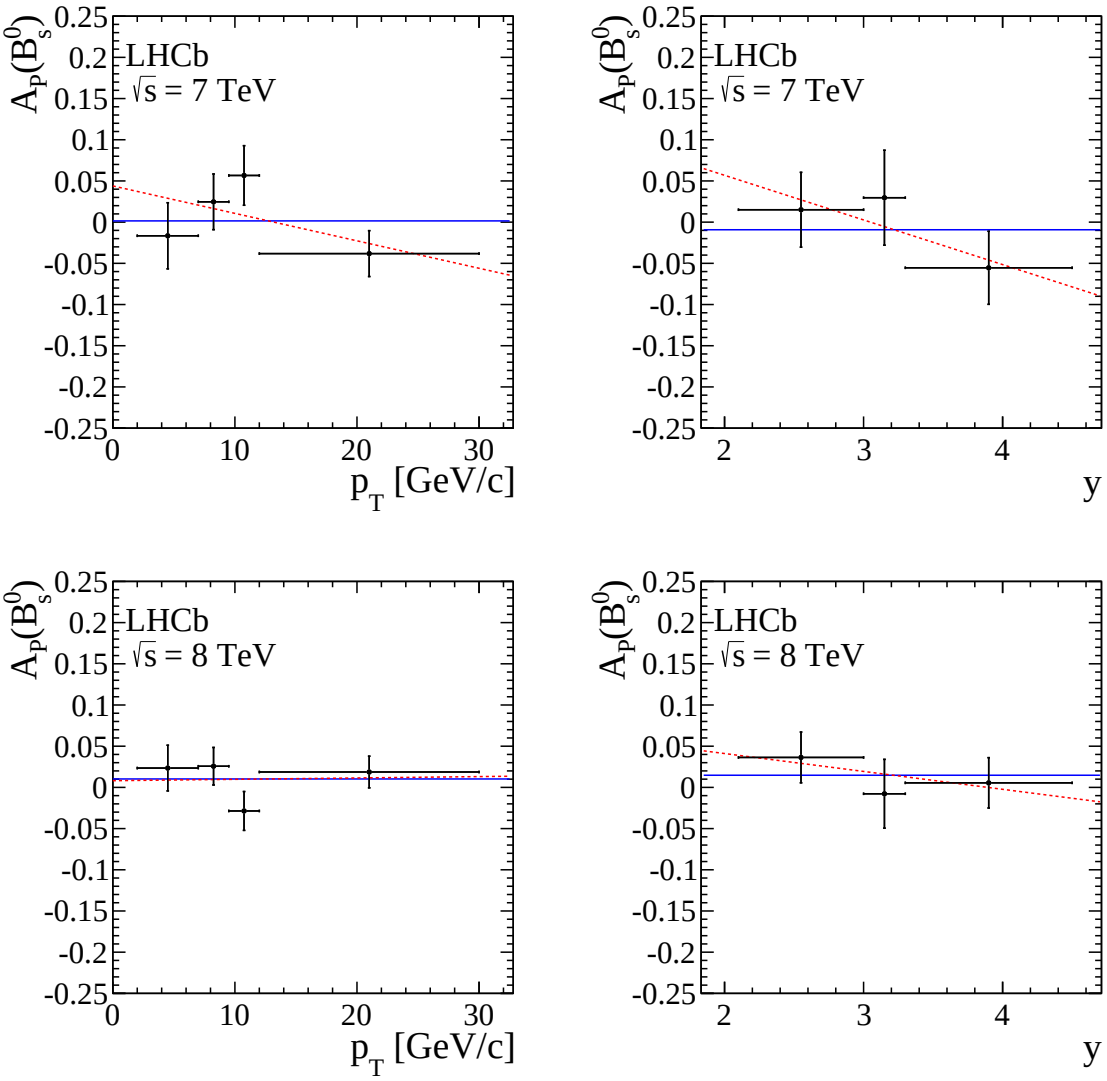

Figure 3.44: *Dependence of $A_{\rm P}(B_s^0)$, for data collected in proton-proton collisions with centre-of-mass of energies of (top) 7 and (bottom) 8 TeV, on (left) $p_{\rm T}$ and (right) y. The results of fits with a straight line with zero (solid line) or floating slope parameter (dashed line) are also shown. The fits take into account the correlations amongst the bins.*

3.10 Λ_b^0 production asymmetry determination

3.10.1 Formalism

Since b-quark and $\bar{b}$-quark are predominantly produced in pairs, the following relation is valid

$$N_{\bar{B}^0} - N_{B^0} + N_{B^-} - N_{B^+} + N_{\bar{B}_s^0} - N_{B_s^0} + N_{\Lambda_b^0} - N_{\bar{\Lambda}_b^0} + \\ + N_{B_c^-} - N_{B_c^+} + N_{b-\text{baryons}} - N_{\bar{b}\text{baryons}} = 0, \tag{3.61}$$

where N_h (with $h = B^+$, B^0, B_s^0, B_c^+, Λ_b^0 or b-baryons) is the number of hadrons of a certain type produced and b-baryons refers to all the b-baryons except Λ_b^0. The production asymmetries can then be expressed as

$$A_{\text{P}}(B^0) = \frac{N_{\bar{B}^0} - N_{B^0}}{N_{\bar{B}^0} + N_{B^0}} = \frac{N_{\bar{B}^0} - N_{B^0}}{f_d} N_{\text{tot}}, \tag{3.62}$$

$$A_{\text{P}}(B_s^0) = \frac{N_{\bar{B}_s^0} - N_{B_s^0}}{N_{\bar{B}_s^0} + N_{B_s^0}} = \frac{N_{\bar{B}_s^0} - N_{B_s^0}}{f_s} N_{\text{tot}}, \tag{3.63}$$

$$A_{\text{P}}(B^+) = \frac{N_{B^-} - N_{B^+}}{N_{B^-} + N_{B^+}} = \frac{N_{B^-} - N_{B^+}}{f_u} N_{\text{tot}}, \tag{3.64}$$

$$A_{\text{P}}(\Lambda_b^0) = \frac{N_{\Lambda_b^0} - N_{\bar{\Lambda}_b^0}}{N_{\Lambda_b^0} + N_{\bar{\Lambda}_b^0}} = \frac{N_{\Lambda_b^0} - N_{\bar{\Lambda}_b^0}}{f_{\Lambda_b^0}} N_{\text{tot}}, \tag{3.65}$$

$$A_{\text{P}}(B_c^+) = \frac{N_{B_c^-} - N_{B_c^+}}{N_{B_c^-} + N_{B_c^+}} = \frac{N_{B_c^-} - N_{B_c^+}}{f_c} N_{\text{tot}}, \tag{3.66}$$

$$A_{\text{P}}(b-\text{baryons}) = \frac{N_{b-\text{baryons}} - N_{\bar{b}-\text{baryons}}}{N_{b-\text{baryons}} + N_{\bar{b}-\text{baryons}}} = \frac{N_{b-\text{baryons}} - N_{\bar{b}-\text{baryons}}}{f_{(b\bar{b})-\text{baryons}}} N_{\text{tot}}, \tag{3.67}$$

where the f_i (with $i = d$, s, u, c, Λ_b^0 or $(b\bar{b})-$baryons) are the hadronization fractions and N_{tot} is the total number of produced b-hadrons.

Using Eqs. (3.62), (3.62), (3.63), (3.64), (3.65), (3.66) and (3.67), the Λ_b^0 production asymmetry can be expressed as a function of the meson and baryon production asymmetries

$$A_{\text{P}}(\Lambda_b^0) = -\left[\frac{f_d}{f_{\Lambda_b^0}} A_{\text{P}}(B^0) + \frac{f_u}{f_{\Lambda_b^0}} A_{\text{P}}(B^+) + \frac{f_s}{f_{\Lambda_b^0}} A_{\text{P}}(B_s^0) + \frac{f_c}{f_{\Lambda_b^0}} A_{\text{P}}(B_c^+) + \right. \\ \left. + \frac{f_{b\bar{b}-\text{baryons}}}{f_{\Lambda_b^0}} A_{\text{P}}(b-\text{baryons})\right]. \tag{3.68}$$

For the final results, the terms $\frac{f_c}{f_{\Lambda_b^0}} A_{\text{P}}(B_c^+)$ and $\frac{f_{b\bar{b}-\text{baryons}}}{f_{\Lambda_b^0}} A_{\text{P}}(b-\text{baryons})$ are considered to be negligible. This assumption is verified by means of about 14×10^6 simulated events, generated with PYTHIA at $\sqrt{s} = 7$ TeV and $\sqrt{s} = 8$ TeV. Using simulated events one finds $f_c = 0.000209 \pm 0.000006$ and $f_{b\bar{b}-\text{baryons}} = 0.01290 \pm 0.00005$. Considering

that f_u and f_d are $\mathcal{O}(40\%)$ and f_s is $\mathcal{O}(10\%)$ and assuming that the production asymmetries $A_{\rm P}(B_c^+)$ and $A_{\rm P}(b-{\rm baryons})$ are $\mathcal{O}(1\%)$, one can neglect the terms $\frac{f_c}{f_{\Lambda_b^0}} A_{\rm P}(B_c^+)$ and $\frac{f_{b\bar{b}-{\rm baryons}}}{f_{\Lambda_b^0}} A_{\rm P}(b-{\rm baryons})$ in Eq. (3.68). Therefore, the Λ_b^0 production asymmetry is measured using the approximate relation

$$A_{\rm P}(\Lambda_b^0) = -\left[\frac{f_u}{f_{\Lambda_b^0}} A_{\rm P}(B^+) + \frac{f_d}{f_{\Lambda_b^0}} A_{\rm P}(B^0) + \frac{f_s}{f_{\Lambda_b^0}} A_{\rm P}(B_s^0)\right]. \tag{3.69}$$

where the values of $A_{\rm P}(B^+)$, $A_{\rm P}(B^0)$ and $A_{\rm P}(B_s^0)$ correspond to the measurements described in the previous sections and the values of the hadronization fractions from external inputs [61, 70].

The hadronization fractions depend on kinematics and two-dimensional dependences are needed in the integration equation. In the f_s case, the only dependence observed is on the $p_{\rm T}$ of the meson, while in the f_d case, the hadronization fraction depends both on $p_{\rm T}$ and y of the meson. However, since only the one dimensional dependences are reported for f_d, only the $p_{\rm T}$ dependence of the hadronization fraction is considered and systematic uncertainty is assigned to account for the neglected y dependence.

In order to measure Λ_b^0 production asymmetry in kinematics bins, the binning scheme adopted is the one used to measure the B_s^0 production asymmetry. The integrated values in each bin are given by the following relation

$$A_{\rm P}^k(\Lambda_b^0) = -\frac{f_u}{f_{\Lambda_b}}(\langle p_{\rm T}\rangle)_k A_{\rm P}^k(B^+) - \frac{f_d}{f_{\Lambda_b}}(\langle p_T\rangle)_k A_{\rm P}^k(B^0) - \frac{f_s}{f_{\Lambda_b}}(\langle p_{\rm T}\rangle)_k A_{\rm P}^k(B_s^0), \tag{3.70}$$

where $A_{\rm P}^k(B^+) = \sum_{k'} \omega_{k'} A_{\rm P}^{k,k'}(B^+)$ and $A_{\rm P}^k(B^0) = \sum_{k'} \omega_{k'} A_{\rm P}^{k,k'}(B^0)$ and the k' index runs over the fourth or sixth bins in the $p_{\rm T}$ and y plane of the B^+ or B^0 binning scheme corresponding to the k-th bin in B_s^0 binning scheme. In fact the binning schemes have been defined in such a way that each bin in the $p_{\rm T}$ and y plane defined for the measurement of B_s^0 production asymmetries corresponds to four or six bins in the $p_{\rm T}$ and y plane of the binning scheme used to measure the B^0 and B^+ production asymmetries. The quantities $\frac{f_i}{f_j}(\langle p_{\rm T}\rangle)_k$ are the ratio of hadronization fractions computed for the average value of $p_{\rm T}$ in the bin and $\omega_{k'}$ are the normalized fraction of b-mesons produced in the four or six bins.

3.10.2 Systematic uncertainties on Λ_b^0 production asymmetry

Systematic uncertainties are assigned propagating in Eq. (3.70) the uncertainties related to the measurements used as inputs

- B^0, B^+ and B_s^0 systematics on production asymmetry measurements;
- systematics on the hadronization fractions;
- total errors (statistical and systematic) on the external inputs $A_{CP}(B^+ \to J/\psi\, K^+)$ and $A_{\rm D}(\overline{K}^0)$.

Table 3.34: *Values $\delta\xi^k$ calculated in bins of $p_{\rm T}$ and y of Λ_b*

Bin	$\delta\xi^k$ [$\sqrt{s} = 7$ TeV]	$\delta\xi^k$ [$\sqrt{s} = 8$ TeV]
0	-0.003 ± 0.001	-0.001 ± 0.001
1	-0.004 ± 0.002	-0.002 ± 0.002
2	-0.007 ± 0.001	-0.009 ± 0.001
3	-0.001 ± 0.002	-0.002 ± 0.002
4	-0.001 ± 0.004	-0.004 ± 0.004
5	-0.004 ± 0.003	-0.007 ± 0.003
6	-0.001 ± 0.003	0.001 ± 0.003
7	0.001 ± 0.006	-0.003 ± 0.006
8	-0.005 ± 0.005	-0.001 ± 0.004
9	-0.002 ± 0.003	-0.002 ± 0.003
10	-0.006 ± 0.007	0.002 ± 0.006
11	0.008 ± 0.005	-0.002 ± 0.005

In addition a systematic uncertainty related to Eq. (3.70) is assigned, where $A_{\rm P}^k$ is calculated assuming that the number of hadrons containing a b quark in the k-th bin, N_b^k, is equal to the number of hadrons containing a $\bar{b}$ quark, $N_{\bar{b}}^k$, in the same bin. This assumption is strictly valid in the full phase space, but it may be that $N_b^k \neq N_{\bar{b}}^k$ in a specific kinematic bin. In this case the Λ_b^0 production asymmetry would be biased by the quantity

$$\delta\xi^k = \frac{N_b^k - N_{\bar{b}}^k}{N^k} \cdot \frac{1}{f_{\Lambda_b^0}}, \tag{3.71}$$

where N^k is the total number of b-hadrons produced in the k-th bin. In Tab. 3.34 are reported the value of $\delta\xi^k$, obtained from fully simulated events.

The systematic uncertainties, $\sigma_{\delta\xi}^k$, are assigned in each bin as the half of the maximum variation from zero of the quantities $\delta\xi^k \pm \sigma(\delta\xi^k)$. As previously discussed the terms $\frac{f_c}{f_{\Lambda_b^0}}(\langle p_{\rm T}\rangle)_k A_{\rm P}^k(B_c^+)$ and $\frac{f_{b\bar{b}-\text{baryons}}}{f_{\Lambda_b^0}}(\langle p_{\rm T}\rangle)_k A_{\rm P}^k(b-\text{baryons})$ in Eq. (3.70) have been neglected. As the B_c^+ hadronization fraction is estimated to be $\mathcal{O}(0.02\%)$ from simulated events, one can safely neglect the related term. This is not completely true in the case of the term $f_{b\bar{b}-\text{baryons}}$ which is $\mathcal{O}(1\%)$ and requires the estimation of a systematic uncertainty due its neglection. Among all the b-baryon and excluding the Λ_b^0, the Ξ_b is the one produced more abundantly, as shown in Tab. 3.35. For this reason the neglected term can be evaluated as

$$\frac{f_{b\bar{b}-\text{baryons}}}{f_{\Lambda_b^0}}(\langle p_{\rm T}\rangle)_k A_{\rm P}^k(b-\text{baryons}) = \frac{f_{\Xi_b}}{f_{\Lambda_b^0}}(\langle p_{\rm T}\rangle) A_{\rm P}^k(\Xi_b), \tag{3.72}$$

where for f_{Ξ_b} we use the value reported in Tab. 3.35. The value of $A_{\rm P}(\Xi_b)$ is found to be two times larger than the value $A_{\rm P}(\Lambda_b^0)$ in the fully simulated events. For this reason

Table 3.35: *Values of b-baryons hadronization fractions obtained from fully simulated events.*

Bin	f_c	f_{Ξ_b}	f_{other}	$f_{\Lambda_b^0}$
$\sqrt{s} = 7$ TeV				
0	0.00021 ± 0.00001	0.01270 ± 0.00010	0.00020 ± 0.00001	0.09066 ± 0.00028
1	0.00025 ± 0.00003	0.01246 ± 0.00020	0.00017 ± 0.00002	0.08959 ± 0.00054
2	0.00022 ± 0.00002	0.01285 ± 0.00013	0.00019 ± 0.00002	0.08999 ± 0.00035
3	0.00015 ± 0.00003	0.01271 ± 0.00023	0.00017 ± 0.00003	0.08953 ± 0.00062
4	0.00014 ± 0.00005	0.01259 ± 0.00047	0.00027 ± 0.00007	0.08782 ± 0.00125
5	0.00020 ± 0.00004	0.01296 ± 0.00033	0.00013 ± 0.00003	0.08608 ± 0.00085
6	0.00016 ± 0.00004	0.01267 ± 0.00035	0.00013 ± 0.00004	0.08592 ± 0.00090
7	0.00021 ± 0.00009	0.01269 ± 0.00072	0.00000 ± 0.00000	0.08736 ± 0.00190
8	0.00032 ± 0.00008	0.01155 ± 0.00049	0.00008 ± 0.00004	0.08517 ± 0.00134
9	0.00018 ± 0.00004	0.01281 ± 0.00036	0.00014 ± 0.00004	0.08471 ± 0.00092
10	0.00014 ± 0.00008	0.01348 ± 0.00080	0.00009 ± 0.00007	0.08389 ± 0.00199
11	0.00014 ± 0.00006	0.01253 ± 0.00060	0.00009 ± 0.00005	0.08372 ± 0.00155
$\sqrt{s} = 8$ TeV				
0	0.00023 ± 0.00001	0.01279 ± 0.00010	0.00019 ± 0.00001	0.09025 ± 0.00027
1	0.00021 ± 0.00003	0.01256 ± 0.00020	0.00015 ± 0.00002	0.09007 ± 0.00053
2	0.00023 ± 0.00002	0.01273 ± 0.00013	0.00021 ± 0.00002	0.08972 ± 0.00034
3	0.00021 ± 0.00003	0.01254 ± 0.00023	0.00015 ± 0.00002	0.08818 ± 0.00060
4	0.00018 ± 0.00005	0.01280 ± 0.00046	0.00020 ± 0.00006	0.08803 ± 0.00121
5	0.00016 ± 0.00003	0.01234 ± 0.00030	0.00017 ± 0.00004	0.08674 ± 0.00080
6	0.00021 ± 0.00004	0.01247 ± 0.00033	0.00013 ± 0.00003	0.08869 ± 0.00088
7	0.00026 ± 0.00010	0.01222 ± 0.00068	0.00019 ± 0.00008	0.08468 ± 0.00178
8	0.00016 ± 0.00005	0.01250 ± 0.00048	0.00013 ± 0.00005	0.08733 ± 0.00126
9	0.00020 ± 0.00004	0.01246 ± 0.00033	0.00017 ± 0.00004	0.08579 ± 0.00088
10	0.00029 ± 0.00011	0.01197 ± 0.00070	0.00021 ± 0.00009	0.08718 ± 0.00190
11	0.00012 ± 0.00005	0.01268 ± 0.00054	0.00012 ± 0.00005	0.08428 ± 0.00140

we estimate the systematic uncertainties as $\sigma_{\text{syst}}(\Xi_b) = 2 \cdot \sigma(A_{\text{P}}(\Lambda_b^0))$, where $\sigma(A_{\text{P}}(\Lambda_b^0))$ is the statistical uncertainty of the measured value of $A_{\text{P}}(\Lambda_b^0)$. The values so calculated are reported in Tab. 3.36 and are assigned as systematic uncertainties in each kinematic bin.

3.10.3 Final results

In Tab. 5.24 the values of the Λ_b^0 production asymmetry measured in different kinematic are reported, where the first uncertainty is statistical, the second systematic, not correlated among the bins and the third systematic, but correlated among the bins. The latter uncertainty is the same for the same p_{T}-bin, as it corresponds to the values of the external inputs multiplied by the average values of the ratios of the hadronization fractions in that

Table 3.36: *Summary of the total systematic uncertainties.*

Bin	$\sqrt{s} = 7$ TeV			
	$\sigma_{\rm syst}(B^0,\, B_s^0,\, B^+,\, f_i)$	$\sigma_{\rm syst}(\delta\xi)$	$\sigma_{\rm syst}(\Xi_b)$	$\sigma_{\rm syst}(tot)$
0	0.01440	0.00414	0.01424	0.02067
1	0.01153	0.00665	0.01500	0.02005
2	0.00983	0.00968	0.01147	0.01794
3	0.02251	0.00544	0.01978	0.03045
4	0.00980	0.00735	0.02617	0.02890
5	0.02257	0.01022	0.02318	0.03393
6	0.01963	0.00707	0.02905	0.03576
7	0.01462	0.01252	0.04004	0.04443
8	0.02379	0.01657	0.03833	0.04806
9	0.01851	0.01500	0.03773	0.04462
10	0.03921	0.03561	0.07386	0.09089
11	0.02618	0.03680	0.06469	0.07890
	$\sqrt{s} = 8$ TeV			
0	0.00888	0.00176	0.00900	0.01277
1	0.01110	0.00458	0.01092	0.01623
2	0.00755	0.01212	0.00807	0.01641
3	0.00677	0.00611	0.01236	0.01535
4	0.01271	0.01287	0.01713	0.02491
5	0.01125	0.01541	0.01491	0.02422
6	0.00879	0.00637	0.01671	0.01992
7	0.02553	0.01524	0.02531	0.03905
8	0.01680	0.01003	0.02401	0.03097
9	0.00867	0.01347	0.02213	0.02732
10	0.01831	0.02262	0.03781	0.04772
11	0.04437	0.01896	0.04248	0.06429

$p_{\rm T}$ bin. In Tabs. A.21 and A.22 the total correlations amongst the bins are reported.

The integrated Λ_b^0 production asymmetry is given by the relation

$$A_{\rm P}(\Lambda_b^0) = \sum_k \omega_k A_{\rm P}^k(\Lambda_b^0)\ . \tag{3.73}$$

where ω_k is the fraction of Λ_b baryons produced in pp collisions in the k-th bin and is obtained using simulated events. The values of the ω_k are reported in Tab. 3.38. In Fig. 3.45 the distribution of the produced Λ_b^0 baryons in the $(p_{\rm T}, y)$ plane is shown.

The value of Λ_b^0 production asymmetry integrated in the range $2 < p_{\rm T}(\,{\rm GeV}/c) < 30$ and $2.1 < y < 4.5$ is measured to be

$$A_{\rm P}(\Lambda_b^0)_{\sqrt{s}=7} = -0.0011 \pm 0.0253 \pm 0.0104 \pm 0.0028$$

Table 3.37: *Values of the Λ_b^0 production asymmetry in different kinematic bins.*

$p_{\rm T}$ [GeV/c]	y	$A_{\rm P}(\Lambda_b^0)$ [$\sqrt{s} = 7$ TeV]	$A_{\rm P}(\Lambda_b^0)$ [$\sqrt{s} = 8$ TeV]
$(2.00, 7.00)$	$(2.10, 3.00)$	$-0.0892 \pm 0.0508 \pm 0.0214$	$0.0032 \pm 0.0318 \pm 0.0139$
$(2.00, 7.00)$	$(3.00, 3.30)$	$0.0507 \pm 0.0539 \pm 0.0208$	$0.0929 \pm 0.0392 \pm 0.0171$
$(2.00, 7.00)$	$(3.30, 4.50)$	$0.0849 \pm 0.0401 \pm 0.0188$	$0.0437 \pm 0.0284 \pm 0.0173$
$(7.00, 9.50)$	$(2.10, 3.00)$	$0.1374 \pm 0.0697 \pm 0.0313$	$0.0069 \pm 0.0434 \pm 0.0169$
$(7.00, 9.50)$	$(3.00, 3.30)$	$0.0138 \pm 0.0913 \pm 0.0298$	$0.0076 \pm 0.0589 \pm 0.0259$
$(7.00, 9.50)$	$(3.30, 4.50)$	$0.0466 \pm 0.0770 \pm 0.0347$	$0.1053 \pm 0.0524 \pm 0.0252$
$(9.50, 12.00)$	$(2.10, 3.00)$	$-0.0128 \pm 0.0985 \pm 0.0367$	$-0.0512 \pm 0.0594 \pm 0.0215$
$(9.50, 12.00)$	$(3.00, 3.30)$	$-0.0848 \pm 0.1379 \pm 0.0452$	$0.2355 \pm 0.0877 \pm 0.0399$
$(9.50, 12.00)$	$(3.30, 4.50)$	$-0.1523 \pm 0.1414 \pm 0.0488$	$0.1531 \pm 0.0838 \pm 0.0320$
$(12.00, 30.00)$	$(2.10, 3.00)$	$-0.0720 \pm 0.1248 \pm 0.0465$	$0.0453 \pm 0.0762 \pm 0.0300$
$(12.00, 30.00)$	$(3.00, 3.30)$	$0.3291 \pm 0.2299 \pm 0.0918$	$-0.0934 \pm 0.1377 \pm 0.0493$
$(12.00, 30.00)$	$(3.30, 4.50)$	$-0.0571 \pm 0.2162 \pm 0.0800$	$0.3173 \pm 0.1411 \pm 0.0655$

Table 3.38: *Values of the ω_k weights obtained from (left) 2011 and (right) 2012 MC events used to perform the integration.*

Bin	$\omega_k(2011)$	$\omega_k(2012)$
0	0.4053 ± 0.0008	0.3927 ± 0.0010
1	0.1024 ± 0.0004	0.1010 ± 0.0005
2	0.2493 ± 0.0007	0.2536 ± 0.0008
3	0.0782 ± 0.0004	0.0774 ± 0.0004
4	0.0183 ± 0.0002	0.0186 ± 0.0002
5	0.0387 ± 0.0003	0.0417 ± 0.0003
6	0.0343 ± 0.0002	0.0356 ± 0.0003
7	0.0081 ± 0.0001	0.0080 ± 0.0001
8	0.0153 ± 0.0002	0.0172 ± 0.0002
9	0.0323 ± 0.0002	0.0340 ± 0.0003
10	0.0067 ± 0.0001	0.0075 ± 0.0001
11	0.0111 ± 0.0001	0.0127 ± 0.0002

$$A_{\rm P}(\Lambda_b^0)_{\sqrt{s}=8} = -0.0344 \pm 0.0161 \pm 0.0071 \pm 0.0028$$

where the first uncertainty is statistical, the second systematic and the third is due to the $A_{CP}(B^+ \to J/\psi\, K^+)$ measurement needed as input.

The $p_{\rm T}$ and y integrated values of $A_{\rm P}(\Lambda_b^0)$ are reported in Tab. 3.39. The correlation among the bins is reported in Tabs. A.23 and A.24.

The dependencies of $A_{\rm P}(\Lambda_b^0)$ on $p_{\rm T}$ and y with the results of the fits superimposed are

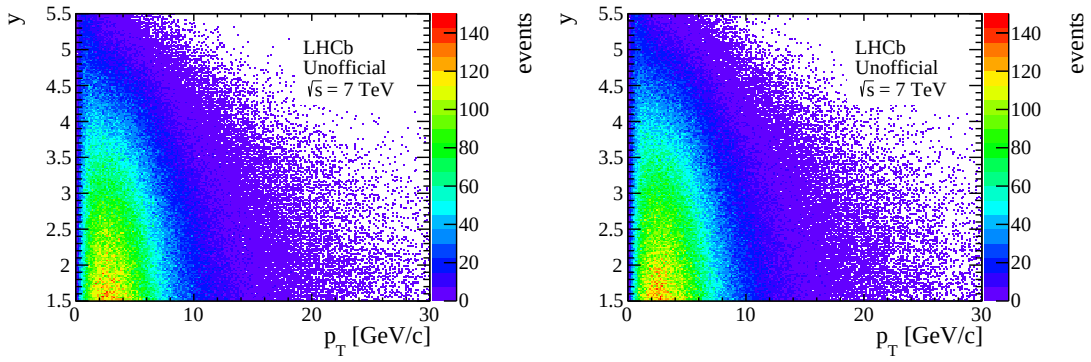

Figure 3.45: *Distributions of $p_{\rm T}$ and y for simulated events at (left) $\sqrt{s} = 7$ TeV and (right) $\sqrt{s} = 8$ TeV.*

Table 3.39: *$A_{\rm P}(\Lambda_b^0)$ results as function of (top) $p_{\rm T}$ and (bottom) y for (left) $\sqrt{s} = 7$ TeV and (right) $\sqrt{s} = 8$ TeV centre-of-mass energies. The first uncertainty is statistical, the second systamatic uncorrelated and the third systematic correlated among the bins.*

$p_{\rm T}$[GeV/c]	$A_{\rm P}(\Lambda_b^0)$ [$\sqrt{s} = 7$ TeV]	$A_{\rm P}(\Lambda_b^0)$ [$\sqrt{s} = 8$ TeV]
$(2.0, 7.0)$	$-0.01303 \pm 0.03113 \pm 0.01284 \pm 0.00351$	$0.02916 \pm 0.01998 \pm 0.00899 \pm 0.00348$
$(7.0, 9.5)$	$0.09483 \pm 0.04759 \pm 0.02051 \pm 0.00460$	$0.03668 \pm 0.03016 \pm 0.01181 \pm 0.00451$
$(9.5, 12.0)$	$-0.05964 \pm 0.07224 \pm 0.02560 \pm 0.00535$	$0.04416 \pm 0.04366 \pm 0.01549 \pm 0.00536$
$(12.0, 30.0)$	$-0.01462 \pm 0.09853 \pm 0.03581 \pm 0.00860$	$0.09024 \pm 0.06121 \pm 0.02382 \pm 0.00848$
y	$A_{\rm P}(\Lambda_b^0)$ [$\sqrt{s} = 7$ TeV]	$A_{\rm P}(\Lambda_b^0)$ [$\sqrt{s} = 8$ TeV]
$(2.1, 3.0)$	$-0.05108 \pm 0.03989 \pm 0.01621 \pm 0.00423$	$0.00280 \pm 0.02472 \pm 0.00979 \pm 0.00419$
$(3.0, 3.3)$	$0.05142 \pm 0.04482 \pm 0.01650 \pm 0.00432$	$0.07919 \pm 0.03174 \pm 0.01309 \pm 0.00429$
$(3.3, 4.5)$	$0.06383 \pm 0.03478 \pm 0.01528 \pm 0.00445$	$0.06816 \pm 0.02424 \pm 0.01351 \pm 0.00440$

shown in Fig. 3.46. The fits are performed using a first order polynomial function and a straight line, in order to check whether a dependence is present. In Tab. A.25 the values of the parameters obtained from the fits are reported.

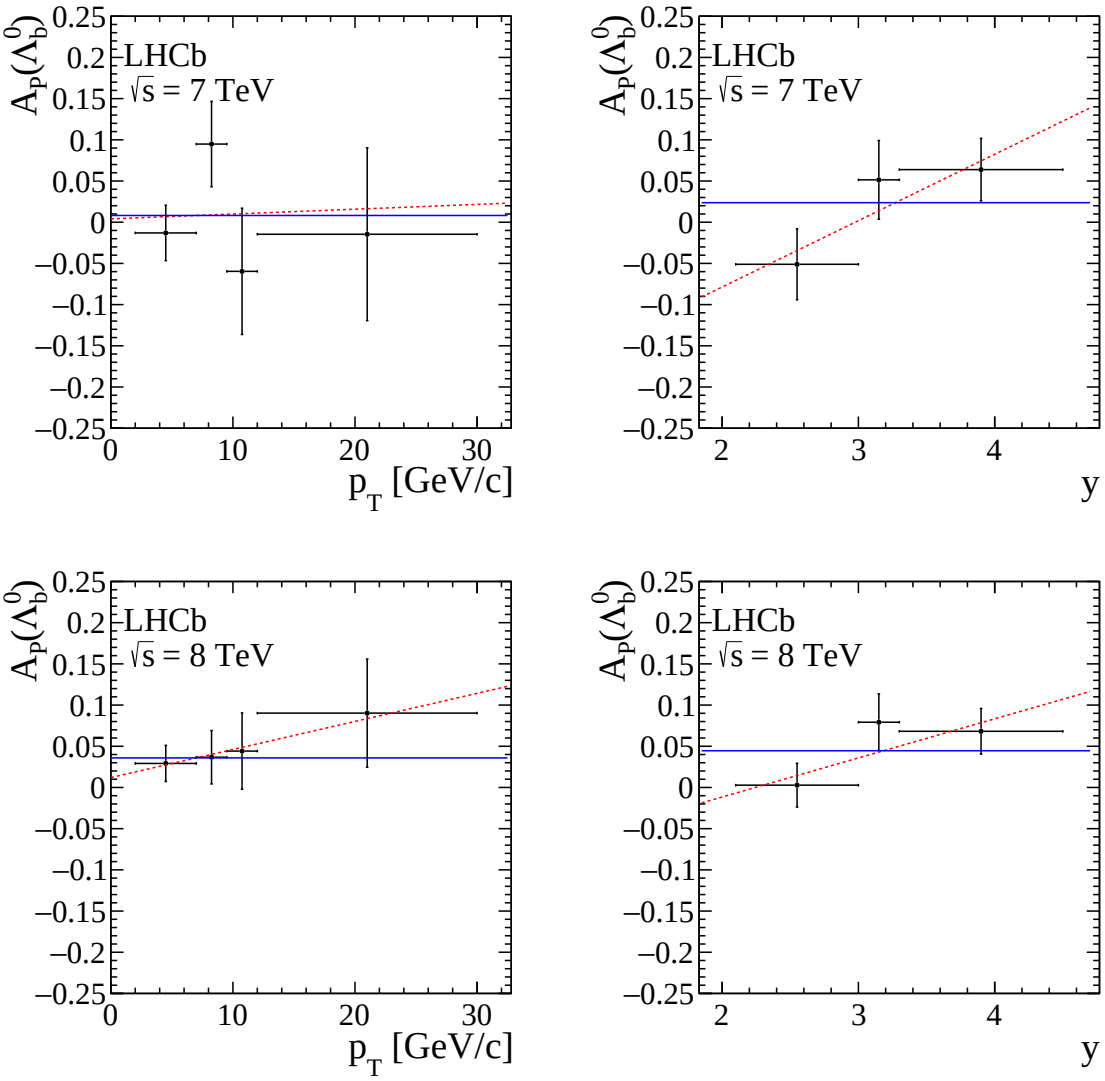

Figure 3.46: *Dependence of $A_P(\Lambda_b^0)$ on (left) p_T and (right) y with the results of a fit with a straight line (solid blue line) and first order polynomial function (black dashed line) overlaid. In the fits we take into account the correlations among bins.*

4 Measurement of the position of the UX85-1 beampipe

The measurement of the position of LHCb detector elements is important for several reasons. First of all, one can check if the design position of sub-detectors is the same as the real position. Discrepancies in these quantities could indicate misalignments in the detector that need to be corrected for. Moreover, the simulation of detector elements is implemented starting from their design reference and differences could lead to inaccuracies in simulated events.

Measurements of the VELO absolute position [71, 72] and of the RF foil aperture [73] have been performed previously by using hadronic interactions of particles originating from beam-gas events. By reconstructing the vertex position of these interactions, one can effectively perform a tomography of the whole sub-detector.

In this chapter an accurate measurement of the position of a beryllium-made portion of the beampipe placed within the acceptance of the LHCb tracking system is presented. Future evolutions of this work will enable the relative hadronic cross-sections of various charged particles and antiparticles on beryllium to be measured, providing valuable inputs to determine detection asymmetries and reduce the associated systematic uncertainties.

4.1 Introduction

The position of the 25 mrad conical section of the UX85-1 beampipe [34] is measured using vertices created by hadronic interactions in the beampipe material using pp collision data. This section is located between the VELO exit window and the end of the RICH1 sub-detector. In particular, we focus on the part with a z coordinate between 1080 and 1600 mm from the origin, corresponding approximately to the centre of the interaction region. The shape of the beampipe in this region is conical and the design parameters are listed in Tab. 4.1.

Tracks originating from the vertices due to hadronic interactions are reconstructed only as downstream tracks (hence without information from the vertex detector) and

Table 4.1: *Design parameters of the portion of UX85-1 with* $1080 < z < 1600$ *mm.*

Parameter	Value
angle	25 mrad
inner radius ($z = 1080$ mm)	27.000 mm
inner radius ($z = 1600$ mm)	40.003 mm
outer radius ($z = 1080$ mm)	28.000 mm
outer radius ($z = 1600$ mm)	41.003 mm

thus the determination of the vertices is less precise with respect to that presented in Refs. [71–73]. As a cross-check, we also perform an alternative measurement with long tracks (with more precise information from the vertex detector) by means of $J/\psi \to \mu^+\mu^-$ decays.

4.2 Dataset and selection

The analysis is performed using the output of the `BHADRONCOMPLETEEVENT.DST` stream. The hadronic interaction vertices are reconstructed by combining pairs of tracks using the CombineParticles algorithm in DaVinci [74]. The requirements imposed on the tracks and on the vertex during this step are reported in Tab. 4.2.

Table 4.2: *Summary of the requirements applied on the tracks and on the reconstructed vertex.*

Requirement	Value
Each track	
p	> 2.0 GeV/c
χ^2_{IP}	> 25
track χ^2/ndf	< 5
track `GHOSTPROB`	< 0.5
Track combination	
χ^2_{DOCA}	< 16
Reconstructed vertex	
χ^2_{vtx}/ndf	< 9
z_{vtx}	> 800 mm
z_{vtx}	< 2200 mm

The $J/\psi \to \mu^+\mu^-$ sample used in the cross-check is obtained from the `LEPTONIC.MDST`

stream for Run-1 data and from the `Turbo` [75] stream for Run-2 data. In this case, since the sample has already very low background, the only selection applied online requires the $\mu^+\mu^-$ invariant mass to be less than 200 MeV/c^2 from the J/ψ nominal mass and that the χ^2 of the vertex is less than 25.

4.2.1 Simulated samples

Fully simulated events are used to define the resolution model. Since vertices from two tracks are build, the decay type is not relevant. Fully simulated samples have been used with 2011 and 2012 data taking conditions only, since this is sufficient for these studies. In these samples the 2011 and 2012 data taking conditions, trigger, reconstruction and stripping have been reproduced in order to have events as comparable as possible with real data. Two distinct trigger configurations are TCKs 0x40760037 and 0x409f0045 have been emulated for the 2011 and 2012 samples, respectively. The requirements listed in Tab. 4.2 are also imposed on fully simulated events.

4.2.2 Offline selection

The data need to be selected offline before proceeding further in the analysis. Since we are interested in decays from secondary interactions inside the beampipe material, we need to veto two-track decays outside the beampipe. The majority of these events are $K^0_S \to \pi^+\pi^-$ decays. We veto this contribution by requiring the two track invariant mass under the $\pi^+\pi^-$ hypothesis to be lower than 480 or higher than 520 MeV/c^2. The amount of ghost candidates present in the data sample when using downstream tracks is high. In addition to standard requirements applied for cleaning the sample from the presence of misreconstructed tracks, a quantity that helps select good two-tracks vertices is the angle between the two particles ($\alpha_{1,2}$). Tracks with a small opening angle are more likely to be ghost and thus we require $\alpha_{1,2}$ to be greater than 0.05 rad. The summary of the requirements applied in the offline selection is reported in Tab. 4.3. The results of the selection are shown in Fig. 4.1. The selection applied to fully simulated events is the same.

Table 4.3: *Summary of offline selection requirements.*

Requirement	Value
$m_{\pi^+\pi^-}$	$(< 480$ OR $> 520)$ MeV/c^2
$\alpha_{1,2}$	> 0.05 rad

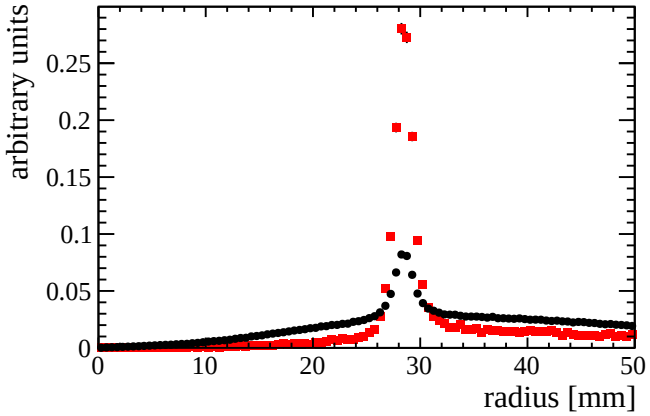

Figure 4.1: *Distribution of the radius (black dots) before and (red squares) after the offline selection summarised in Tab. 4.3. Both distributions are normalised to unitary area. The data are from the 2012 Down sample in the slice* $1120 < z < 1130$ *mm.*

4.3 Fit model

The fit model includes three components. The first two components are studied by means of fully simulated events, whereas the third is modelled from data.

Signal: these are events where the z coordinates of the reconstructed and true vertices lie within one z bin (10 mm) and with the true radius within ± 0.5 mm from the position calculated from the design reference;

Misreconstructed background: these are events where the z coordinate of the reconstructed vertex lies within one z bin (10 mm) whereas the z coordinate of the true vertex lies in the adjacent bins. The true radius is also required to be within ± 0.5 mm from the position calculated from the design reference;

Large-radius background: these are events mostly populating the right-hand sideband.

The signal model is given by

$$\mathcal{P}_{\text{sig}} = \text{erf}\left(\frac{r-\mu+0.5}{\sqrt{2}\sigma}\right) - \text{erf}\left(\frac{r-\mu-0.5}{\sqrt{2}\sigma}\right), \tag{4.1}$$

where erf is the error function. This expression represents the analytical convolution of the real signal model (a step function of width 0.5 mm with mean equal to the design value) with a Gaussian resolution function.

The misreconstructed background model can be expressed as the convolution of the real signal model with a Johnson SU function [76]

$$\mathcal{P}_{\text{bkg}} = [\Theta(r-\mu-0.5) - \Theta(r-\mu+0.5)] \otimes \mathcal{J}(r; 0, \sigma, \delta, \gamma), \tag{4.2}$$

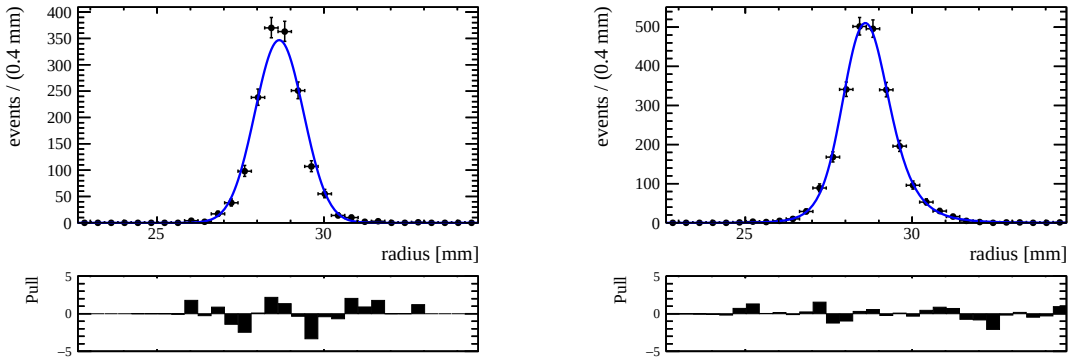

Figure 4.2: *Distribution of the radius for (left) signal events and (right) misreconstrcted background events. The results of the fits with the model described in the text are overlaid. These data are relative to 2011 Down fully simulated samples, in the (*$1120 < z < 1130$ *mm) interval.*

where Θ is the Heavisde function and the Johnson function is defined as

$$\mathcal{J}(r;\mu,\sigma,\delta,\gamma) = \frac{e^{-\frac{1}{2}\left[\gamma+\delta\sinh^{-1}\left(\frac{x-\mu}{\sigma}\right)\right]^2}}{\sqrt{1+\left(\frac{x-\mu}{\sigma}\right)^2}}, \tag{4.3}$$

that accounts for the asymmetric tail of the distribution. In Fig. 4.2 we show fully simulated events for the signal and misreconstructed background cases fitted with models just described.

The large-radius background is empirically parameterised using the same model as for the signal with a very broad step function that is non-zero where the signal step function is zero

$$\mathcal{P}_{\text{high}} = \text{erf}\left(\frac{r-\mu-0.5}{\sqrt{2}\sigma}\right) - \text{erf}\left(\frac{r-100}{\sqrt{2}\sigma}\right). \tag{4.4}$$

The total fit model is given by

$$\mathcal{P} = f_2\left[f_1\mathcal{P}_{\text{sig}} + (1-f_1)\mathcal{P}_{\text{high}}\right] + (1-f_2)\mathcal{P}_{\text{bkg}}. \tag{4.5}$$

As an example, the result of the fit to the $(1120 < z < 1130$ mm) interval for the 2011 Down dataset is shown in Fig. 4.3.

4.4 Strategy

Using the fit model described in Sec. 4.3, fits to the beampipe radius in slices of the z coordinate are performed. The fully simulated datasets are further divided in eight different ϕ intervals, as defined in Tab. 4.4. The fits to the beampipe radius are repeated separately for each ϕ interval. For each ϕ sector fits to the radius as a function of the z coordinate are performed with a linear function

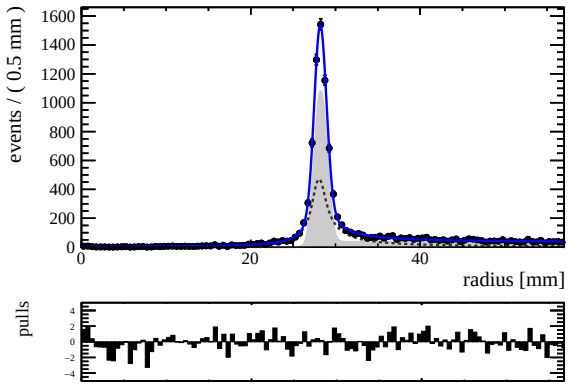

Figure 4.3: *Distribution of the radius for a z interval ($1110 < z < 1120$ mm) for 2011 Down data. The result of the fit is overlaid.*

Table 4.4: *Definition of the ϕ bins. In the case of fully simulated events, only the bins not labelled with the "bis" tag are used.*

Bin	Value [rad]	Bin	Value [rad]
1	$-0.15 < \phi < +0.15$	5	$+2.99 < \phi$ OR $\phi < -2.99$
1bis	$+0.24 < \phi < +0.54$	5bis	$-2.90 < \phi < -2.60$
2	$+0.64 < \phi < +0.94$	6	$-2.51 < \phi < -2.21$
2bis	$+1.03 < \phi < +1.33$	6bis	$-2.11 < \phi < -1.81$
3	$+1.42 < \phi < +1.72$	7	$-1.72 < \phi < -1.42$
3bis	$+1.81 < \phi < +2.11$	7bis	$-1.33 < \phi < -1.03$
4	$+2.21 < \phi < +2.51$	8	$-0.94 < \phi < -0.64$
4bis	$+2.60 < \phi < +2.90$	8bis	$-0.54 < \phi < -0.24$

$$R(z) = m(z - z_0) + q, \tag{4.6}$$

where z_0 is chosen to lie in the mid point of the investigated z range (*i.e.*, $z_0 = 1215$ mm for the 2011, 2012 and 2015 data samples and $z_0 = 1340$ mm for the 2016 data sample). The results of the fits to 2012 Down fully simulated events are shown in Fig. 4.4.
For the data, the number of sectors is increased to 16, as defined in Tab. 4.4. The results of the fit to 2012 Down data are shown in Figs. 4.5 and 4.6. The results for the m and q parameters obtained for each ϕ sector, magnet polarity and data taking year are reported in Tab. 4.5 for fully simulated events and in Tabs. 4.6 and 4.7 for data. In Appendix B.1 we show the difference between the measured and design radial distance of the beampipe position in various ϕ sectors. In Appendix B.2 the procedure employed to measure the beampipe radius and center position as a function of the z coordinate is described.

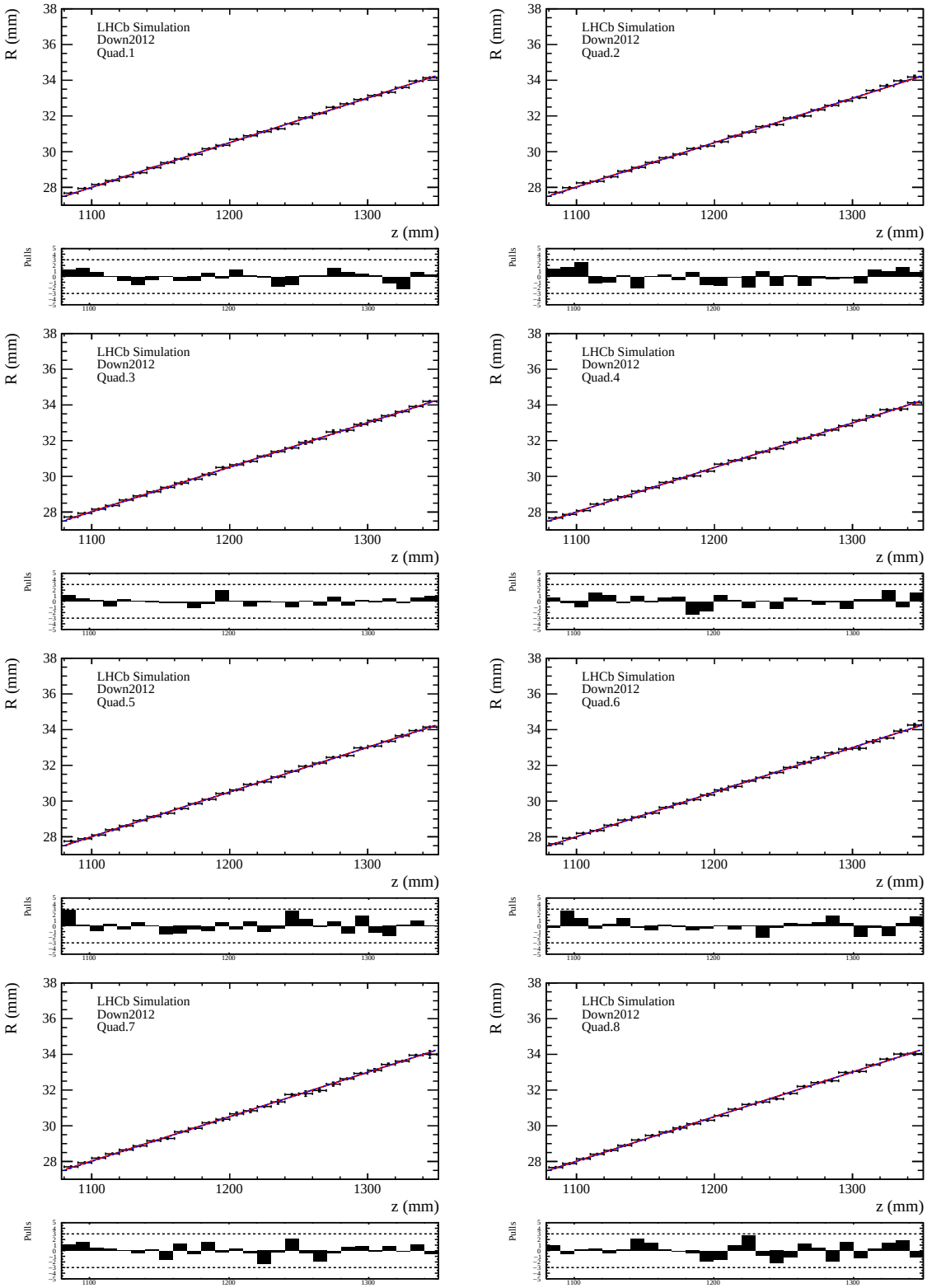

Figure 4.4: *Beampipe radius as a function of the z coordinate for different ϕ sectors for 2012 Down fully simulated events. The results of a linear fit to the data are overlaid (red line). The blue dashed line represents the design position of the beampipe, as implemented in the LHCb simulation. This is not clearly visible as it is perfectly aligned with the fit line.*

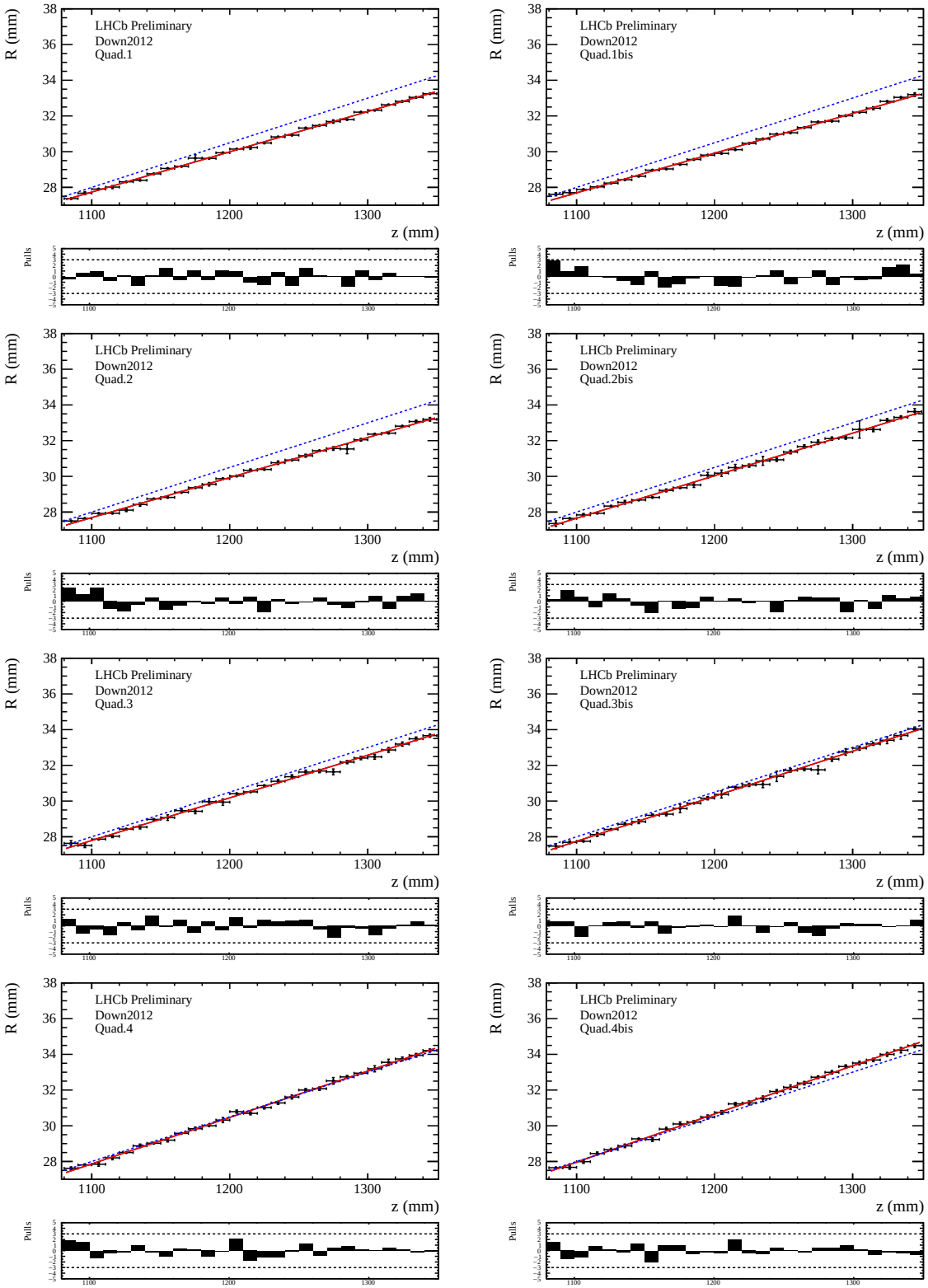

Figure 4.5: *Beampipe radius as a function of the z coordinate for different ϕ sectors for 2012 Down data. The results of a linear fit to the data are overlaid (red line). The blue dashed line represents the design position of the beampipe, as implemented in the LHCb simulation.*

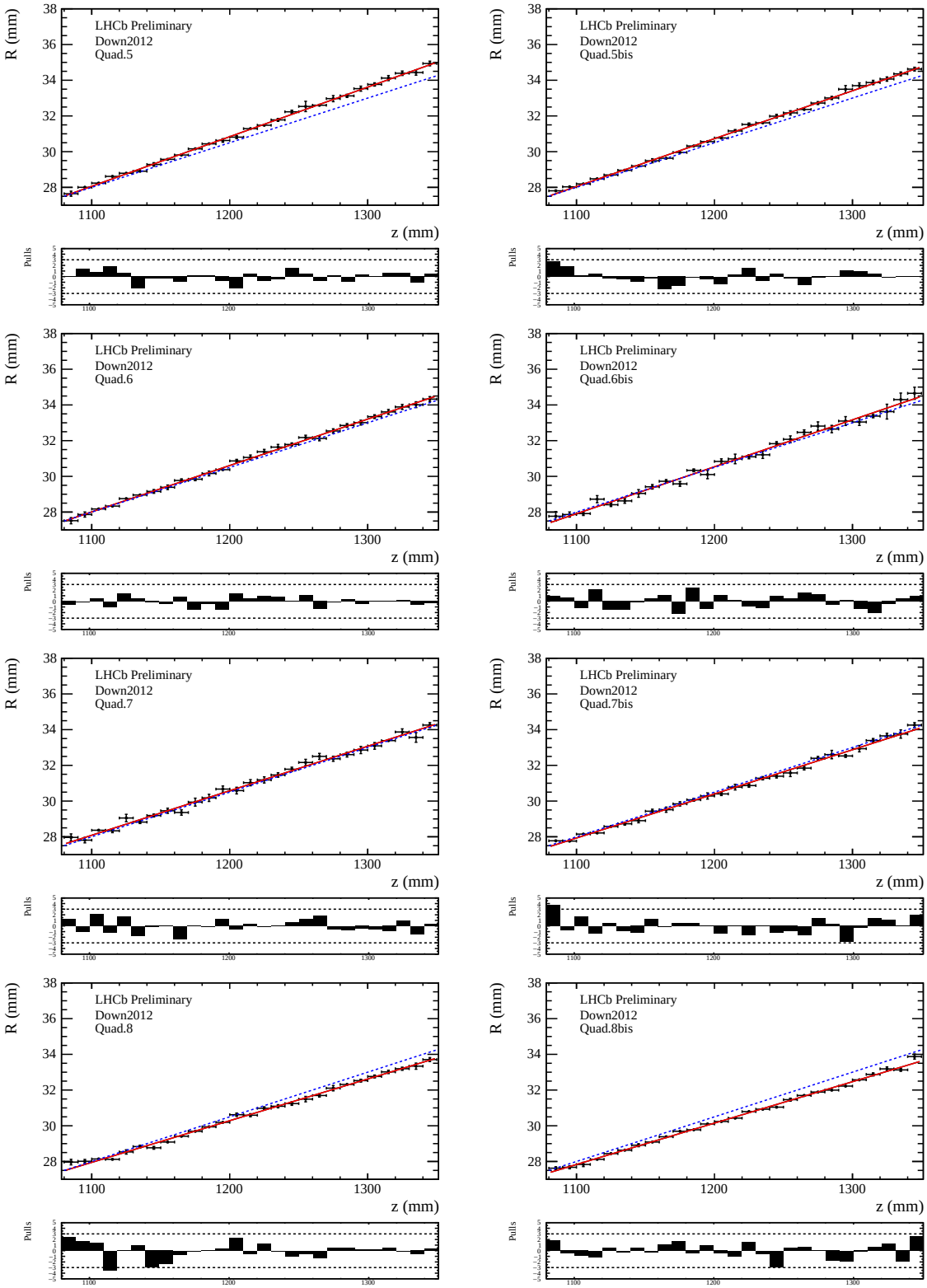

Figure 4.6: *Beampipe radius as a function of the z coordinate for different ϕ sectors for 2012 Down data. The results of a linear fit to the data are overlaid (red line). The blue dashed line represents the design position of the beampipe, as implemented in the LHCb simulation.*

Table 4.5: *Values of the m and q parameters obtained from fits to fully simulated events. The value of z_0 is 1215 mm.*

	2011 Up		2011 Down		2012 Up		2012 Down	
	m	q [mm]	m	q [mm]	m	q [mm]	m	q [mm]
Bin 1	25.3 ± 0.4	30.89 ± 0.03	24.7 ± 0.4	30.89 ± 0.03	24.8 ± 0.3	30.89 ± 0.03	25.0 ± 0.3	30.88 ± 0.03
Bin 2	25.1 ± 0.4	30.87 ± 0.03	24.7 ± 0.4	30.87 ± 0.03	24.9 ± 0.3	30.90 ± 0.03	24.8 ± 0.3	30.88 ± 0.03
Bin 3	25.2 ± 0.4	30.89 ± 0.03	24.8 ± 0.3	30.92 ± 0.03	24.7 ± 0.3	30.86 ± 0.03	24.9 ± 0.3	30.90 ± 0.03
Bin 4	25.1 ± 0.4	30.89 ± 0.03	24.5 ± 0.4	30.89 ± 0.03	24.6 ± 0.3	30.87 ± 0.03	24.9 ± 0.3	30.87 ± 0.03
Bin 5	25.0 ± 0.4	30.88 ± 0.03	24.9 ± 0.4	30.87 ± 0.03	24.9 ± 0.3	30.89 ± 0.03	25.0 ± 0.3	30.89 ± 0.03
Bin 6	25.0 ± 0.4	30.88 ± 0.03	24.6 ± 0.4	30.88 ± 0.03	24.5 ± 0.3	30.87 ± 0.03	24.9 ± 0.3	30.87 ± 0.03
Bin 7	24.9 ± 0.4	30.90 ± 0.03	25.2 ± 0.4	30.93 ± 0.03	24.8 ± 0.4	30.89 ± 0.03	24.8 ± 0.4	30.88 ± 0.03
Bin 8	24.8 ± 0.4	30.90 ± 0.03	25.3 ± 0.4	30.88 ± 0.03	24.8 ± 0.3	30.90 ± 0.03	25.0 ± 0.3	30.89 ± 0.03

Table 4.6: *Values of the m and q parameters obtained from fits to the data using 2011 and 2012 samples. The value of z_0 is 1215 mm in both cases.*

	2011 Up		2011 Down		2012 Up		2012 Down	
	m	q [mm]	m	q [mm]	m	q [mm]	m	q [mm]
Bin 1	22.4 ± 0.4	30.31 ± 0.03	22.2 ± 0.3	30.30 ± 0.03	22.4 ± 0.3	30.29 ± 0.02	22.5 ± 0.3	30.33 ± 0.03
Bin 1bis	22.3 ± 0.4	30.29 ± 0.03	22.4 ± 0.4	30.22 ± 0.03	22.1 ± 0.3	30.20 ± 0.02	22.2 ± 0.3	30.25 ± 0.02
Bin 2	22.2 ± 0.4	30.27 ± 0.03	23.0 ± 0.4	30.28 ± 0.03	22.2 ± 0.3	30.21 ± 0.03	22.4 ± 0.3	30.27 ± 0.03
Bin 2bis	23.3 ± 0.4	30.45 ± 0.03	23.3 ± 0.4	30.40 ± 0.03	23.6 ± 0.4	30.36 ± 0.03	23.8 ± 0.4	30.39 ± 0.03
Bin 3	23.7 ± 0.5	30.49 ± 0.04	24.5 ± 0.5	30.57 ± 0.03	24.0 ± 0.4	30.53 ± 0.03	23.9 ± 0.4	30.54 ± 0.03
Bin 3bis	25.0 ± 0.5	30.67 ± 0.04	25.6 ± 0.5	30.67 ± 0.04	25.1 ± 0.4	30.62 ± 0.03	25.2 ± 0.4	30.65 ± 0.03
Bin 4	26.4 ± 0.5	30.85 ± 0.04	25.8 ± 0.4	30.84 ± 0.04	26.5 ± 0.4	30.82 ± 0.03	26.0 ± 0.4	30.85 ± 0.03
Bin 4bis	26.9 ± 0.5	31.13 ± 0.04	26.9 ± 0.5	31.09 ± 0.04	27.2 ± 0.4	31.09 ± 0.03	27.0 ± 0.4	31.06 ± 0.03
Bin 5	27.4 ± 0.5	31.25 ± 0.03	27.7 ± 0.4	31.27 ± 0.03	27.9 ± 0.4	31.25 ± 0.03	27.8 ± 0.4	31.26 ± 0.03
Bin 5bis	27.3 ± 0.4	31.15 ± 0.03	26.9 ± 0.4	31.12 ± 0.03	27.0 ± 0.4	31.12 ± 0.03	26.8 ± 0.4	31.13 ± 0.03
Bin 6	27.1 ± 0.5	31.01 ± 0.04	27.7 ± 0.6	30.95 ± 0.04	26.8 ± 0.4	30.99 ± 0.03	26.0 ± 0.4	31.00 ± 0.03
Bin 6bis	26.4 ± 0.5	30.94 ± 0.04	26.6 ± 0.5	30.95 ± 0.04	26.8 ± 0.5	30.96 ± 0.04	26.3 ± 0.6	30.93 ± 0.04
Bin 7	25.7 ± 0.6	30.95 ± 0.05	25.1 ± 0.5	30.94 ± 0.04	25.0 ± 0.4	30.93 ± 0.03	24.9 ± 0.5	30.95 ± 0.04
Bin 7bis	25.2 ± 0.5	30.84 ± 0.04	25.3 ± 0.5	30.76 ± 0.04	24.3 ± 0.4	30.80 ± 0.03	24.7 ± 0.4	30.77 ± 0.03
Bin 8	23.8 ± 0.5	30.67 ± 0.04	23.7 ± 0.4	30.64 ± 0.03	23.7 ± 0.4	30.63 ± 0.03	23.4 ± 0.4	30.64 ± 0.03
Bin 8bis	23.4 ± 0.4	30.57 ± 0.03	22.9 ± 0.4	30.49 ± 0.03	23.0 ± 0.3	30.47 ± 0.03	23.2 ± 0.4	30.50 ± 0.03

Table 4.7: *Values of the m and q parameters obtained from fits to the data using 2015 and 2016 samples. The value of z_0 is 1215 mm in 2015 and 1340 mm in 2016.*

	2015 Up		2015 Down		2016 Up		2016 Down	
	m	q [mm]	m	q [mm]	m	q [mm]	m	q [mm]
Bin 1	22.0 ± 0.4	30.44 ± 0.03	22.1 ± 0.4	30.34 ± 0.03	22.6 ± 0.1	33.27 ± 0.02	22.6 ± 0.1	33.27 ± 0.02
Bin 1bis	22.0 ± 0.4	30.30 ± 0.03	21.9 ± 0.4	30.34 ± 0.03	22.8 ± 0.1	33.23 ± 0.02	22.7 ± 0.1	33.23 ± 0.02
Bin 2	21.3 ± 0.5	30.29 ± 0.04	22.5 ± 0.4	30.43 ± 0.03	23.2 ± 0.1	33.34 ± 0.02	23.5 ± 0.1	33.43 ± 0.02
Bin 2bis	24.4 ± 0.5	30.74 ± 0.04	23.9 ± 0.5	30.72 ± 0.04	23.5 ± 0.1	33.47 ± 0.02	23.5 ± 0.2	33.56 ± 0.02
Bin 3	24.8 ± 0.6	30.97 ± 0.04	24.9 ± 0.5	30.92 ± 0.04	24.6 ± 0.2	32.58 ± 0.02	24.4 ± 0.2	32.60 ± 0.02
Bin 3bis	25.0 ± 0.5	30.91 ± 0.04	26.1 ± 0.5	30.98 ± 0.04	25.3 ± 0.1	34.01 ± 0.02	25.4 ± 0.1	34.10 ± 0.02
Bin 4	27.0 ± 0.6	31.03 ± 0.04	25.8 ± 0.4	30.97 ± 0.03	25.7 ± 0.2	34.16 ± 0.02	25.9 ± 0.1	34.19 ± 0.02
Bin 4bis	27.6 ± 0.5	31.08 ± 0.04	26.3 ± 0.5	31.07 ± 0.03	26.9 ± 0.1	34.37 ± 0.02	26.9 ± 0.1	34.36 ± 0.02
Bin 5	27.2 ± 0.5	31.12 ± 0.04	27.3 ± 0.4	31.17 ± 0.03	27.3 ± 0.1	34.57 ± 0.02	27.5 ± 0.1	34.59 ± 0.02
Bin 5bis	26.7 ± 0.5	31.05 ± 0.04	27.4 ± 0.5	31.03 ± 0.04	27.4 ± 0.1	34.46 ± 0.02	27.3 ± 0.1	34.45 ± 0.02
Bin 6	26.6 ± 0.5	30.89 ± 0.04	27.0 ± 0.6	30.92 ± 0.04	26.9 ± 0.2	34.35 ± 0.02	27.0 ± 0.1	34.32 ± 0.02
Bin 6bis	25.9 ± 0.6	31.05 ± 0.05	26.3 ± 0.5	30.99 ± 0.04	26.1 ± 0.2	34.34 ± 0.02	26.4 ± 0.2	34.32 ± 0.02
Bin 7	25.3 ± 0.5	31.10 ± 0.04	24.7 ± 0.5	30.93 ± 0.04	25.3 ± 0.2	32.98 ± 0.02	25.4 ± 0.2	34.18 ± 0.02
Bin 7bis	24.6 ± 0.5	30.95 ± 0.04	24.9 ± 0.5	30.88 ± 0.04	23.8 ± 0.2	33.92 ± 0.02	23.9 ± 0.1	33.90 ± 0.02
Bin 8	23.5 ± 0.7	30.78 ± 0.05	22.8 ± 0.4	30.68 ± 0.03	23.0 ± 0.1	33.66 ± 0.02	23.2 ± 0.1	33.67 ± 0.02
Bin 8bis	22.7 ± 0.4	30.60 ± 0.03	23.3 ± 0.4	30.57 ± 0.03	22.9 ± 0.1	33.46 ± 0.02	22.8 ± 0.1	33.44 ± 0.02

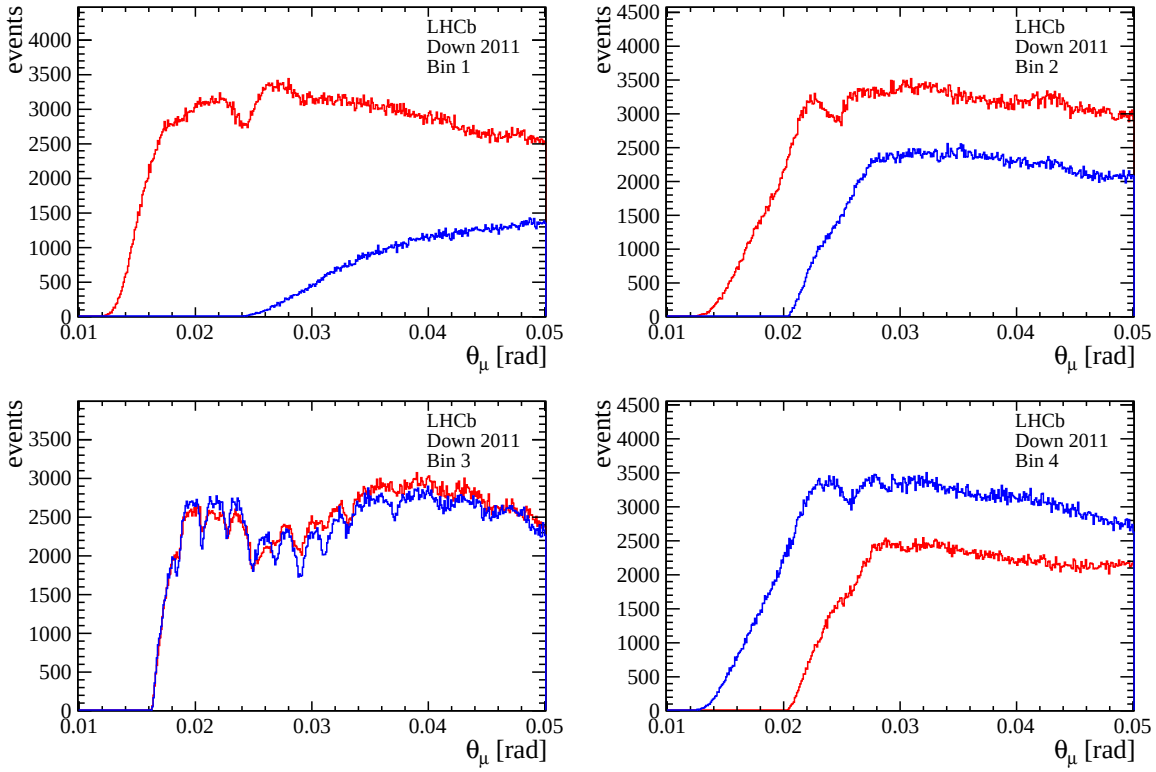

Figure 4.7: *Angular distributions in the first four ϕ bins for (red line) μ^+ and (blue line) μ^- particles coming from $J/\psi \to \mu^+\mu^-$ events.*

4.4.1 Results

The angular coefficients reported in Tabs. 4.6 and 4.7 are different with respect to those obtained from the LHCb simulation, that agree well with the design values. From Figs. 4.5 and 4.6 the beampipe appears to be slightly tilted towards the right part of LHCb (observing the detector from the VELO towards the muon stations). The results obtained for 2011, 2012 and 2015, independently from the magnet polarity, agree very well within the uncertainties, whereas the results found with 2016 data, although compatible between Up and Down magnet polarities, are in tension with the others.

4.5 Cross-check using $J/\psi \to \mu^+\mu^-$ decays

In order to cross-check the beampipe position reconstructed using secondary interactions and downstream tracks, $J/\psi \to \mu^+\mu^-$ decays with long tracks are employed. Figures 4.7 and 4.8 shows the angular distributions of the reconstructed muons. The angle θ_μ is the opening angle respect to the z axis.

A dip in the distributions is evident around the beampipe design angle. This is due to the fact that muons with this particular θ_μ value cross the beampipe and thus they

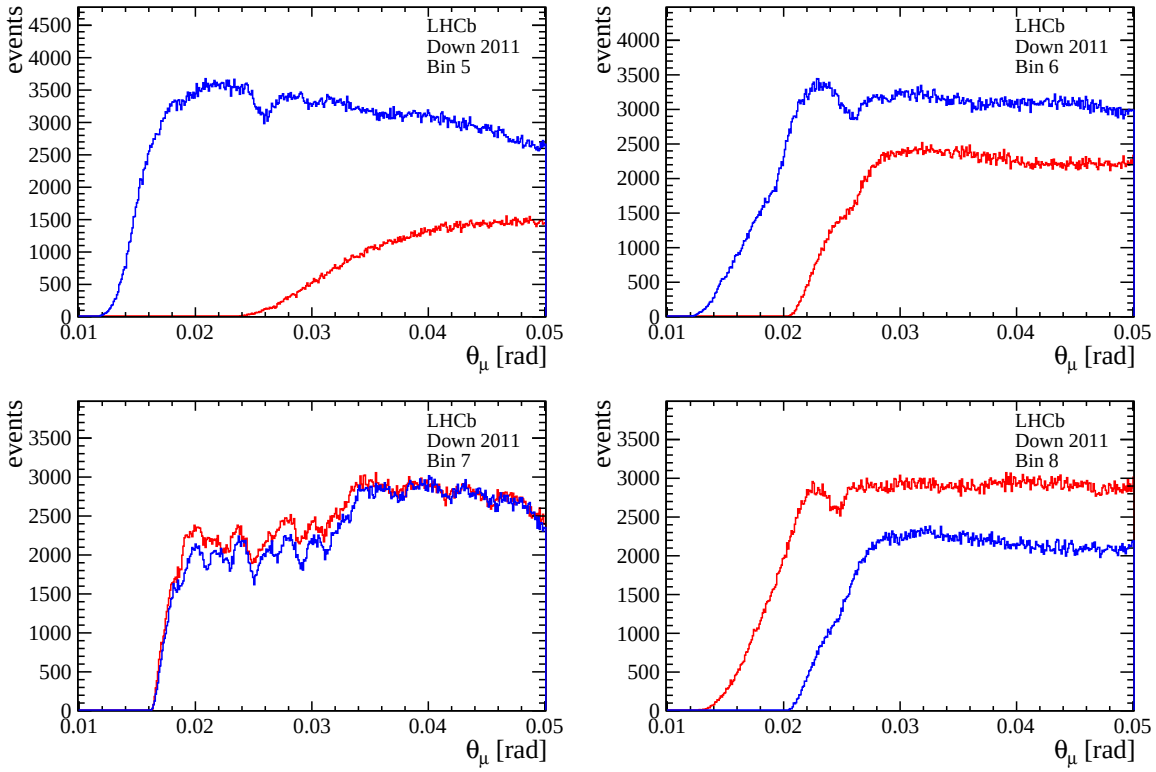

Figure 4.8: *Angular distributions in the first four ϕ bins for (red line) μ^+ and (blue line) μ^- particles coming from $J/\psi \to \mu^+\mu^-$ events.*

undergo multiple scattering. If the scattering angle is large enough, the LHCb tracking systems are not able to reconstruct the muons and thus the dip in the muon angular distribution appears. The dip position depends on the track origin coordinates. Indeed, tracks with different origin vertices will cross the maximum of the beampipe material with different angles. As it is apparent from the figure, the sectors 3 and 7 exhibit a much more irregular behaviour, and are thus discarded.

We measure the dip position as a function of the z coordinate of the J/ψ decay vertex. This is done be means of binned maximum likelihood fits to the θ_μ distributions, divided in several z intervals.

4.5.1 Fit model

The function chosen to parameterise the dip is a Gaussian function ($\mathcal{G}$), whereas a third order Chebychev polynomial ($\mathcal{C}$) is used to model the continuum. The total fit model is thus

$$\mathcal{P} = -N_{\text{sig}}\mathcal{G}(\theta_\mu; \mu, \sigma) + N_{\text{bkg}}\mathcal{C}(\theta_\mu; p_0, p_1, p_2), \tag{4.7}$$

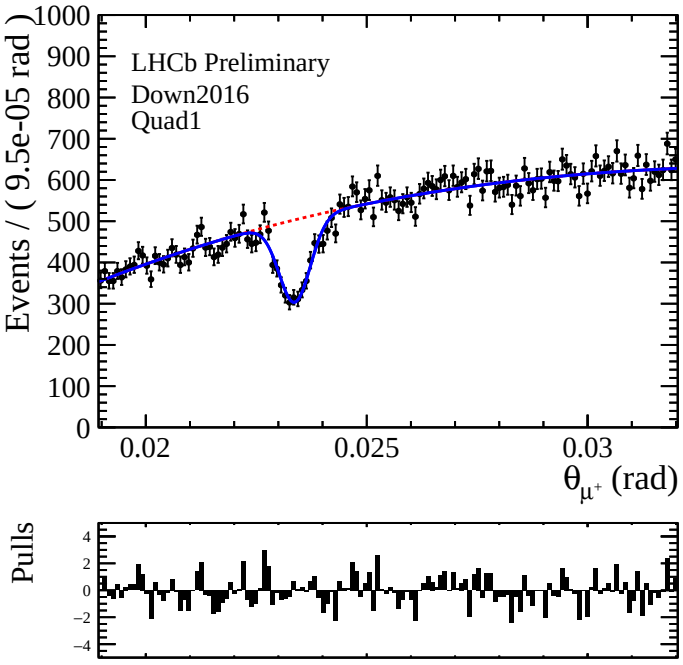

Figure 4.9: *Example of a fit to the muon angular distribution. This sample is relative to the 2016 Down dataset in the* $-60 < z_{\text{endvtx}} < -40$ *mm and* $-0.15 < \phi < 0.15$ *rad intervals.*

where μ and σ are the mean and the width of the Gaussian function and p_0, p_1 and p_2 are the parameters governing the polynomial shape. An example of the fit results is shown in Fig. 4.9.

4.5.2 Extrapolation of θ_μ

To obtain an extrapolation of θ_μ, we determine the z coordinate of the distance of closest approach (z_{DOCA}) between the beampipe position extrapolation (measured with downstream tracks) and the line passing through the point $(x_{\text{mean}}, y_{\text{mean}})$ and parallel to the z axis, where x_{mean} and y_{mean} are the means of the J/ψ decay vertex distributions. The values of DOCA and z_{DOCA} for each sector, polarity and data-taking year are reported in Tabs. 4.8, 4.9, 4.10 and 4.11.

The values of x_{mean} and y_{mean} are taken from the J/ψ decay vertex distributions and are reported in Tabs. 4.8, 4.9, 4.10 and 4.11; as an example, we show these distribution in the first ϕ sector of the 2012 Down sample in Fig. 4.10.
The $\theta_\mu(z_{\text{endvtx}})$ distributions are fitted with a linear relation

$$\theta_\mu(z_{\text{endvtx}}) = m_\theta(z_{\text{endvtx}} - z_{\text{endvtx,0}}) + \theta_0 \ , \tag{4.8}$$

where $z_{\text{endvtx,0}} = 10(30)$ mm for 2011 and 2015 (2012 and 2016) data. An example fit to the $\theta_\mu(z_{\text{endvtx}})$ distribution is shown in Fig. 4.11.

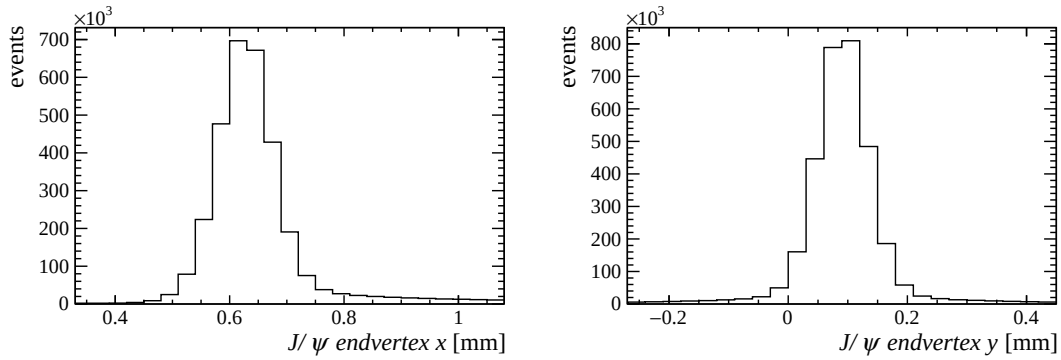

Figure 4.10: *Distribution of the (left) x and (right) y coordinate of the J/ψ decay vertices relative to the first ϕ sector of the 2012 Down sample.*

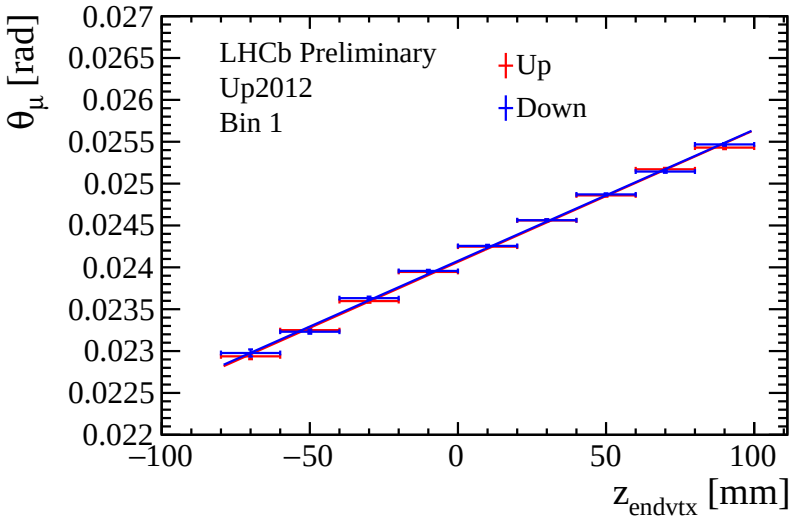

Figure 4.11: *Results of the fits to the muon angle at the dip as a function of the J/ψ z_{endvtx} coordinate for 2012 data.*

The extrapolated value of the beampipe opening angle can then be obtained using the relation

$$\theta_{\text{DOCA}} = m_\theta(z_{\text{DOCA}} - z_{\text{endvtx},0}) + \theta_0, \tag{4.9}$$

where m_θ and θ_0 are obtained from the fits to the $\theta_\mu(z_{\text{endvtx}})$ distributions.
The θ_{DOCA} values thus obtained are listed in Tabs. 4.8, 4.9, 4.10 and 4.11, together with the angles obtained from the downstream fits.

Table 4.8: *Values of the beampipe angle with respect to the z axis as obtained from the fits to the vertices formed by downstream tracks* ($\theta_{\text{downstream}}$) *and through the cross-check with* $J/\psi \to \mu^+\mu^-$ *decays* (θ_{DOCA}) *for 2011 data. We report also the DOCA and z coordinate of the DOCA, as well as the values of the x, y and z means of the* J/ψ *decay vertex distributions. Note that the uncertainty associated to* x_{mean}, y_{mean} *and* z_{mean} *is the RMS of the relative distributions.*

Sample and bin	$\theta_{\text{downstream}}$ [rad]	θ_{DOCA} [rad]	z_{DOCA} [mm]	DOCA [mm]	x_{mean} [mm]	y_{mean} [mm]	z_{mean} [mm]
Down2011 Bin 1	0.0222 ± 0.0003	0.0221 ± 0.0003	-127.51 ± 17.00	0.02 ± 0.08	0.51 ± 0.09	-0.02 ± 0.08	-0.0 ± 37.2
Up2011 Bin 1	0.0224 ± 0.0004	0.0223 ± 0.0003	-114.56 ± 17.89	0.01 ± 0.08	0.51 ± 0.09	-0.01 ± 0.08	1.8 ± 41.2
Down2011 Bin 1bis	0.0224 ± 0.0003	0.0224 ± 0.0003	-112.60 ± 17.32	0.19 ± 0.28	0.50 ± 0.08	0.00 ± 0.08	0.0 ± 37.2
Up2011 Bin 1bis	0.0223 ± 0.0004	0.0223 ± 0.0003	-119.92 ± 19.29	0.18 ± 0.31	0.50 ± 0.08	0.01 ± 0.08	1.8 ± 41.2
Down2011 Bin 2	0.0230 ± 0.0004	0.0230 ± 0.0003	-87.58 ± 17.85	0.34 ± 0.41	0.49 ± 0.08	0.02 ± 0.08	0.0 ± 37.2
Up2011 Bin 2	0.0222 ± 0.0004	0.0223 ± 0.0003	-129.37 ± 19.46	0.33 ± 0.43	0.49 ± 0.08	0.02 ± 0.08	1.9 ± 41.2
Down2011 Bin 2bis	0.0233 ± 0.0004	0.0233 ± 0.0003	-80.08 ± 19.40	0.43 ± 0.33	0.47 ± 0.08	0.03 ± 0.08	0.3 ± 37.2
Up2011 Bin 2bis	0.0233 ± 0.0004	0.0232 ± 0.0003	-85.07 ± 18.06	0.43 ± 0.30	0.48 ± 0.08	0.03 ± 0.08	2.2 ± 41.3
Down2011 Bin 3bis	0.0256 ± 0.0004	0.0258 ± 0.0002	12.23 ± 16.53	0.41 ± 0.31	0.44 ± 0.08	0.03 ± 0.09	0.3 ± 37.2
Up2011 Bin 3bis	0.0250 ± 0.0004	0.0253 ± 0.0002	-19.61 ± 17.37	0.42 ± 0.32	0.44 ± 0.08	0.03 ± 0.08	2.2 ± 41.2
Down2011 Bin 4	0.0258 ± 0.0004	0.0260 ± 0.0002	9.06 ± 16.24	0.31 ± 0.43	0.42 ± 0.08	0.02 ± 0.08	0.2 ± 37.2
Up2011 Bin 4	0.0264 ± 0.0004	0.0264 ± 0.0002	36.76 ± 15.78	0.32 ± 0.42	0.43 ± 0.08	0.02 ± 0.08	2.1 ± 41.3
Down2011 Bin 4bis	0.0269 ± 0.0004	0.0268 ± 0.0002	46.08 ± 15.15	0.16 ± 0.30	0.41 ± 0.08	0.00 ± 0.08	0.1 ± 37.2
Up2011 Bin 4bis	0.0269 ± 0.0005	0.0267 ± 0.0002	43.36 ± 15.74	0.17 ± 0.31	0.42 ± 0.08	0.01 ± 0.08	1.9 ± 41.3
Down2011 Bin 5	0.0277 ± 0.0004	0.0273 ± 0.0002	72.69 ± 13.22	0.02 ± 0.08	0.41 ± 0.09	-0.02 ± 0.08	0.1 ± 37.2
Up2011 Bin 5	0.0274 ± 0.0004	0.0272 ± 0.0003	58.20 ± 14.81	0.01 ± 0.08	0.41 ± 0.09	-0.01 ± 0.08	2.0 ± 41.2
Down2011 Bin 5bis	0.0269 ± 0.0004	0.0270 ± 0.0002	45.91 ± 13.92	0.19 ± 0.28	0.41 ± 0.08	-0.03 ± 0.08	0.1 ± 37.2
Up2011 Bin 5bis	0.0273 ± 0.0004	0.0273 ± 0.0003	61.18 ± 14.19	0.18 ± 0.28	0.42 ± 0.08	-0.02 ± 0.08	1.9 ± 41.2
Down2011 Bin 6	0.0277 ± 0.0005	0.0276 ± 0.0003	87.37 ± 17.24	0.33 ± 0.48	0.42 ± 0.08	-0.05 ± 0.08	0.1 ± 37.2
Up2011 Bin 6	0.0271 ± 0.0005	0.0271 ± 0.0003	60.34 ± 17.56	0.33 ± 0.48	0.43 ± 0.08	-0.04 ± 0.08	1.9 ± 41.2
Down2011 Bin 6bis	0.0266 ± 0.0005	0.0266 ± 0.0003	46.47 ± 17.89	0.43 ± 0.34	0.44 ± 0.08	-0.06 ± 0.09	0.3 ± 37.2
Up2011 Bin 6bis	0.0264 ± 0.0005	0.0266 ± 0.0003	36.90 ± 16.94	0.43 ± 0.32	0.44 ± 0.08	-0.05 ± 0.08	2.1 ± 41.3
Down2011 Bin 7bis	0.0253 ± 0.0005	0.0248 ± 0.0002	6.17 ± 18.47	0.42 ± 0.34	0.48 ± 0.08	-0.06 ± 0.09	0.3 ± 37.2
Up2011 Bin 7bis	0.0252 ± 0.0005	0.0247 ± 0.0002	-1.11 ± 18.41	0.43 ± 0.33	0.48 ± 0.08	-0.05 ± 0.09	2.1 ± 41.3
Down2011 Bin 8	0.0237 ± 0.0004	0.0237 ± 0.0003	-59.55 ± 18.46	0.32 ± 0.44	0.49 ± 0.08	-0.05 ± 0.08	0.1 ± 37.2
Up2011 Bin 8	0.0238 ± 0.0004	0.0238 ± 0.0003	-56.86 ± 19.61	0.32 ± 0.47	0.50 ± 0.08	-0.04 ± 0.08	2.0 ± 41.2
Down2011 Bin 8bis	0.0229 ± 0.0004	0.0229 ± 0.0003	-93.03 ± 18.21	0.16 ± 0.30	0.50 ± 0.08	-0.03 ± 0.08	0.1 ± 37.2
Up2011 Bin 8bis	0.0234 ± 0.0004	0.0232 ± 0.0003	-73.37 ± 18.96	0.17 ± 0.32	0.51 ± 0.08	-0.02 ± 0.08	2.0 ± 41.3

Table 4.9: *Values of the beampipe angle with respect to the z axis as obtained from the fits to the vertices formed by downstream tracks* ($\theta_{\text{downstream}}$) *and through the cross-check with* $J/\psi \to \mu^+\mu^-$ *decays* (θ_{DOCA}) *for 2012 data. We report also the DOCA and z coordinate of the DOCA, as well as the values of the x, y and z means of the* J/ψ *decay vertex distributions. Note that the uncertainty associated to* x_{mean}, y_{mean} *and* z_{mean} *is the RMS of the relative distributions.*

Sample and bin	$\theta_{\text{downstream}}$ [rad]	θ_{DOCA} [rad]	z_{DOCA} [mm]	DOCA [mm]	x_{mean} [mm]	y_{mean} [mm]	z_{mean} [mm]
Down2012 Bin 1	0.0226 ± 0.0003	0.0225 ± 0.0003	-100.03 ± 15.72	0.09 ± 0.08	0.68 ± 0.09	0.09 ± 0.08	19.7 ± 42.9
Up2012 Bin 1	0.0224 ± 0.0003	0.0224 ± 0.0003	-105.01 ± 15.43	0.10 ± 0.08	0.69 ± 0.09	0.10 ± 0.08	18.7 ± 43.3
Down2012 Bin 1bis	0.0222 ± 0.0003	0.0222 ± 0.0003	-116.41 ± 16.29	0.15 ± 0.26	0.67 ± 0.09	0.11 ± 0.08	19.9 ± 42.9
Up2012 Bin 1bis	0.0221 ± 0.0003	0.0221 ± 0.0003	-120.10 ± 15.92	0.15 ± 0.26	0.68 ± 0.09	0.12 ± 0.08	18.9 ± 43.3
Down2012 Bin 2	0.0224 ± 0.0003	0.0226 ± 0.0003	-109.30 ± 16.37	0.38 ± 0.37	0.66 ± 0.08	0.13 ± 0.08	19.9 ± 42.9
Up2012 Bin 2	0.0222 ± 0.0003	0.0223 ± 0.0003	-120.93 ± 16.34	0.37 ± 0.36	0.67 ± 0.09	0.14 ± 0.09	18.9 ± 43.3
Down2012 Bin 2bis	0.0238 ± 0.0004	0.0237 ± 0.0003	-44.88 ± 16.88	0.54 ± 0.29	0.64 ± 0.08	0.14 ± 0.09	20.2 ± 42.9
Up2012 Bin 2bis	0.0236 ± 0.0004	0.0235 ± 0.0003	-54.69 ± 17.17	0.54 ± 0.29	0.65 ± 0.08	0.15 ± 0.09	19.3 ± 43.3
Down2012 Bin 3bis	0.0252 ± 0.0004	0.0255 ± 0.0002	-3.82 ± 16.11	0.61 ± 0.30	0.60 ± 0.08	0.14 ± 0.09	20.2 ± 42.9
Up2012 Bin 3bis	0.0251 ± 0.0004	0.0254 ± 0.0002	-9.74 ± 15.70	0.62 ± 0.29	0.61 ± 0.08	0.15 ± 0.09	19.4 ± 43.4
Down2012 Bin 4	0.0260 ± 0.0004	0.0261 ± 0.0002	15.43 ± 14.29	0.50 ± 0.38	0.58 ± 0.09	0.13 ± 0.08	20.0 ± 42.9
Up2012 Bin 4	0.0266 ± 0.0004	0.0265 ± 0.0002	42.13 ± 13.58	0.51 ± 0.37	0.59 ± 0.09	0.14 ± 0.09	19.1 ± 43.3
Down2012 Bin 4bis	0.0270 ± 0.0004	0.0269 ± 0.0002	44.29 ± 13.70	0.32 ± 0.27	0.57 ± 0.09	0.11 ± 0.08	19.9 ± 42.9
Up2012 Bin 4bis	0.0272 ± 0.0004	0.0271 ± 0.0002	53.21 ± 13.24	0.33 ± 0.27	0.58 ± 0.09	0.12 ± 0.08	19.0 ± 43.3
Down2012 Bin 5	0.0278 ± 0.0004	0.0275 ± 0.0002	68.90 ± 13.50	0.09 ± 0.08	0.57 ± 0.09	0.09 ± 0.08	19.9 ± 42.9
Up2012 Bin 5	0.0280 ± 0.0004	0.0277 ± 0.0002	76.08 ± 12.35	0.10 ± 0.08	0.57 ± 0.09	0.10 ± 0.08	18.9 ± 43.3
Down2012 Bin 5bis	0.0268 ± 0.0004	0.0269 ± 0.0002	32.82 ± 13.66	0.15 ± 0.27	0.57 ± 0.09	0.07 ± 0.08	19.9 ± 42.9
Up2012 Bin 5bis	0.0270 ± 0.0004	0.0270 ± 0.0002	39.90 ± 13.19	0.15 ± 0.26	0.58 ± 0.09	0.08 ± 0.08	18.9 ± 43.3
Down2012 Bin 6	0.0260 ± 0.0004	0.0263 ± 0.0003	4.53 ± 15.61	0.37 ± 0.41	0.58 ± 0.09	0.05 ± 0.08	19.9 ± 42.9
Up2012 Bin 6	0.0268 ± 0.0004	0.0269 ± 0.0002	40.39 ± 14.07	0.37 ± 0.39	0.59 ± 0.09	0.06 ± 0.08	18.8 ± 43.3
Down2012 Bin 6bis	0.0263 ± 0.0006	0.0265 ± 0.0004	28.12 ± 19.87	0.54 ± 0.38	0.60 ± 0.08	0.04 ± 0.09	20.2 ± 42.9
Up2012 Bin 6bis	0.0268 ± 0.0004	0.0269 ± 0.0003	48.62 ± 15.11	0.54 ± 0.30	0.61 ± 0.08	0.05 ± 0.09	19.2 ± 43.4
Down2012 Bin 7bis	0.0247 ± 0.0004	0.0244 ± 0.0002	-21.44 ± 16.57	0.61 ± 0.30	0.65 ± 0.08	0.04 ± 0.09	20.2 ± 42.9
Up2012 Bin 7bis	0.0243 ± 0.0004	0.0242 ± 0.0002	-43.20 ± 17.73	0.62 ± 0.31	0.65 ± 0.08	0.05 ± 0.09	19.3 ± 43.3
Down2012 Bin 8	0.0234 ± 0.0004	0.0234 ± 0.0002	-77.74 ± 16.82	0.51 ± 0.39	0.66 ± 0.08	0.05 ± 0.08	19.9 ± 42.9
Up2012 Bin 8	0.0237 ± 0.0003	0.0237 ± 0.0002	-57.25 ± 15.43	0.52 ± 0.37	0.67 ± 0.09	0.06 ± 0.08	19.0 ± 43.3
Down2012 Bin 8bis	0.0232 ± 0.0003	0.0231 ± 0.0003	-74.82 ± 16.22	0.32 ± 0.27	0.67 ± 0.09	0.07 ± 0.08	20.0 ± 42.9
Up2012 Bin 8bis	0.0230 ± 0.0003	0.0229 ± 0.0002	-84.91 ± 15.11	0.34 ± 0.25	0.68 ± 0.09	0.08 ± 0.08	18.8 ± 43.3

Table 4.10: *Values of the beampipe angle with respect to the z axis as obtained from the fits to the vertices formed by downstream tracks ($\theta_{\text{downstream}}$) and through the cross-check with $J/\psi \to \mu^+\mu^-$ decays (θ_{DOCA}) for 2015 data. We report also the DOCA and z coordinate of the DOCA, as well as the values of the x, y and z means of the J/ψ decay vertex distributions. Note that the uncertainty associated to x_{mean}, y_{mean} and z_{mean} is the RMS of the relative distributions.*

Sample and bin	$\theta_{\text{downstream}}$ [rad]	θ_{DOCA} [rad]	z_{DOCA} [mm]	DOCA [mm]	x_{mean} [mm]	y_{mean} [mm]	z_{mean} [mm]
Down2015 Bin 1	0.0221 ± 0.0003	0.0223 ± 0.0003	-121.61 ± 17.87	0.09 ± 0.08	0.95 ± 0.09	0.09 ± 0.08	4.7 ± 36.2
Up2015 Bin 1	0.0220 ± 0.0004	0.0220 ± 0.0004	-130.72 ± 23.01	0.13 ± 0.08	0.94 ± 0.09	0.13 ± 0.08	2.1 ± 39.1
Down2015 Bin 1bis	0.0219 ± 0.0004	0.0221 ± 0.0003	-136.19 ± 19.17	0.22 ± 0.30	0.94 ± 0.09	0.11 ± 0.08	4.8 ± 36.2
Up2015 Bin 1bis	0.0220 ± 0.0004	0.0221 ± 0.0004	-125.12 ± 21.96	0.18 ± 0.34	0.93 ± 0.09	0.15 ± 0.08	2.1 ± 39.1
Down2015 Bin 2	0.0225 ± 0.0004	0.0228 ± 0.0003	-109.75 ± 19.96	0.49 ± 0.45	0.92 ± 0.09	0.13 ± 0.08	4.7 ± 36.2
Up2015 Bin 2	0.0213 ± 0.0005	0.0218 ± 0.0005	-173.18 ± 28.67	0.46 ± 0.61	0.92 ± 0.08	0.17 ± 0.09	2.1 ± 39.1
Down2015 Bin 2bis	0.0239 ± 0.0005	0.0241 ± 0.0003	-51.83 ± 20.93	0.69 ± 0.36	0.91 ± 0.08	0.14 ± 0.09	5.1 ± 36.2
Up2015 Bin 2bis	0.0244 ± 0.0005	0.0245 ± 0.0004	-25.79 ± 21.29	0.67 ± 0.37	0.90 ± 0.08	0.18 ± 0.09	2.5 ± 39.1
Down2015 Bin 3bis	0.0261 ± 0.0005	0.0259 ± 0.0003	20.05 ± 17.42	0.76 ± 0.33	0.77 ± 0.08	0.14 ± 0.09	4.8 ± 36.1
Up2015 Bin 3bis	0.0250 ± 0.0005	0.0251 ± 0.0003	-25.65 ± 19.27	0.77 ± 0.35	0.76 ± 0.08	0.18 ± 0.09	2.4 ± 39.1
Down2015 Bin 4	0.0258 ± 0.0004	0.0257 ± 0.0002	-2.51 ± 15.42	0.62 ± 0.41	0.75 ± 0.08	0.13 ± 0.09	4.7 ± 36.2
Up2015 Bin 4	0.0270 ± 0.0005	0.0266 ± 0.0003	52.67 ± 18.37	0.64 ± 0.50	0.74 ± 0.09	0.17 ± 0.09	2.2 ± 39.1
Down2015 Bin 4bis	0.0263 ± 0.0004	0.0261 ± 0.0002	10.78 ± 15.93	0.38 ± 0.31	0.74 ± 0.09	0.11 ± 0.08	4.7 ± 36.1
Up2015 Bin 4bis	0.0276 ± 0.0005	0.0268 ± 0.0002	65.31 ± 15.51	0.42 ± 0.31	0.73 ± 0.09	0.15 ± 0.08	2.2 ± 39.1
Down2015 Bin 5	0.0273 ± 0.0004	0.0268 ± 0.0002	47.83 ± 13.61	0.09 ± 0.08	0.73 ± 0.09	0.09 ± 0.08	4.6 ± 36.1
Up2015 Bin 5	0.0272 ± 0.0005	0.0267 ± 0.0002	45.98 ± 15.02	0.13 ± 0.08	0.72 ± 0.09	0.13 ± 0.08	2.2 ± 39.1
Down2015 Bin 5bis	0.0274 ± 0.0004	0.0264 ± 0.0002	56.81 ± 14.31	0.22 ± 0.29	0.74 ± 0.09	0.07 ± 0.08	4.7 ± 36.2
Up2015 Bin 5bis	0.0267 ± 0.0005	0.0261 ± 0.0002	25.26 ± 16.92	0.18 ± 0.33	0.73 ± 0.09	0.11 ± 0.08	2.2 ± 39.1
Down2015 Bin 6	0.0270 ± 0.0006	0.0268 ± 0.0004	47.39 ± 19.12	0.49 ± 0.53	0.75 ± 0.08	0.05 ± 0.09	4.7 ± 36.2
Up2015 Bin 6	0.0267 ± 0.0005	0.0267 ± 0.0004	33.62 ± 18.42	0.46 ± 0.50	0.74 ± 0.09	0.10 ± 0.09	2.2 ± 39.1
Down2015 Bin 6bis	0.0263 ± 0.0005	0.0260 ± 0.0003	22.29 ± 19.20	0.69 ± 0.37	0.77 ± 0.08	0.04 ± 0.09	4.9 ± 36.2
Up2015 Bin 6bis	0.0259 ± 0.0006	0.0256 ± 0.0003	3.49 ± 21.37	0.67 ± 0.40	0.76 ± 0.08	0.08 ± 0.09	2.4 ± 39.1
Down2015 Bin 7bis	0.0249 ± 0.0005	0.0246 ± 0.0003	-16.72 ± 19.15	0.76 ± 0.34	0.91 ± 0.08	0.04 ± 0.09	4.9 ± 36.2
Up2015 Bin 7bis	0.0246 ± 0.0005	0.0244 ± 0.0003	-33.31 ± 21.68	0.77 ± 0.38	0.90 ± 0.08	0.08 ± 0.09	2.3 ± 39.1
Down2015 Bin 8	0.0228 ± 0.0004	0.0229 ± 0.0003	-108.48 ± 21.35	0.62 ± 0.48	0.93 ± 0.09	0.05 ± 0.09	4.7 ± 36.2
Up2015 Bin 8	0.0235 ± 0.0006	0.0235 ± 0.0005	-72.36 ± 29.34	0.65 ± 0.69	0.92 ± 0.09	0.09 ± 0.09	2.1 ± 39.1
Down2015 Bin 8bis	0.0233 ± 0.0004	0.0233 ± 0.0003	-65.36 ± 17.94	0.39 ± 0.30	0.94 ± 0.09	0.07 ± 0.08	4.8 ± 36.2
Up2015 Bin 8bis	0.0227 ± 0.0004	0.0229 ± 0.0003	-101.93 ± 20.47	0.42 ± 0.33	0.93 ± 0.09	0.11 ± 0.08	2.2 ± 39.1

Table 4.11: *Values of the beampipe angle with respect to the z axis as obtained from the fits to the vertices formed by downstream tracks* ($\theta_{\text{downstream}}$) *and through the cross-check with* $J/\psi \to \mu^+\mu^-$ *decays* (θ_{DOCA}) *for 2016 data. We report also the DOCA and z coordinate of the DOCA, as well as the values of the x, y and z means of the* J/ψ *decay vertex distributions. Note that the uncertainty associated to* x_{mean}, y_{mean} *and* z_{mean} *is the RMS of the relative distributions.*

Sample and bin	$\theta_{\text{downstream}}$ [rad]	θ_{DOCA} [rad]	z_{DOCA} [mm]	DOCA [mm]	x_{mean} [mm]	y_{mean} [mm]	z_{mean} [mm]
Down2016 Bin 1	0.0226 ± 0.0001	0.0227 ± 0.0001	-93.93 ± 6.46	0.18 ± 0.08	0.90 ± 0.09	-0.18 ± 0.08	0.3 ± 35.8
Up2016 Bin 1	0.0226 ± 0.0001	0.0227 ± 0.0001	-92.85 ± 6.48	0.19 ± 0.08	0.99 ± 0.09	-0.19 ± 0.08	2.0 ± 39.6
Down2016 Bin 1bis	0.0227 ± 0.0001	0.0229 ± 0.0001	-87.82 ± 6.55	0.49 ± 0.12	0.99 ± 0.08	-0.16 ± 0.08	0.3 ± 35.8
Up2016 Bin 1bis	0.0228 ± 0.0001	0.0229 ± 0.0001	-85.36 ± 6.14	0.50 ± 0.12	0.99 ± 0.08	-0.17 ± 0.08	2.1 ± 39.6
Down2016 Bin 2	0.0235 ± 0.0001	0.0237 ± 0.0001	-58.62 ± 6.10	0.72 ± 0.15	0.98 ± 0.08	-0.14 ± 0.08	0.3 ± 35.8
Up2016 Bin 2	0.0232 ± 0.0001	0.0234 ± 0.0001	-76.20 ± 6.20	0.73 ± 0.15	0.98 ± 0.08	-0.16 ± 0.08	2.1 ± 39.6
Down2016 Bin 2bis	0.0235 ± 0.0001	0.0238 ± 0.0001	-78.69 ± 6.87	0.95 ± 0.13	0.96 ± 0.08	-0.13 ± 0.09	0.5 ± 35.8
Up2016 Bin 2bis	0.0235 ± 0.0001	0.0237 ± 0.0001	-78.36 ± 6.69	0.95 ± 0.13	0.96 ± 0.08	-0.15 ± 0.09	2.3 ± 39.7
Down2016 Bin 3bis	0.0254 ± 0.0001	0.0254 ± 0.0001	-18.16 ± 5.80	0.70 ± 0.13	0.92 ± 0.08	-0.13 ± 0.09	0.5 ± 35.8
Up2016 Bin 3bis	0.0253 ± 0.0001	0.0254 ± 0.0001	-21.71 ± 5.85	0.70 ± 0.13	0.92 ± 0.08	-0.15 ± 0.09	2.3 ± 39.7
Down2016 Bin 4	0.0259 ± 0.0001	0.0259 ± 0.0001	-4.45 ± 5.50	0.46 ± 0.16	0.90 ± 0.08	-0.14 ± 0.08	0.4 ± 35.8
Up2016 Bin 4	0.0257 ± 0.0001	0.0257 ± 0.0001	-14.27 ± 5.74	0.46 ± 0.16	0.90 ± 0.08	-0.15 ± 0.08	2.2 ± 39.7
Down2016 Bin 4bis	0.0269 ± 0.0001	0.0266 ± 0.0001	34.69 ± 4.92	0.15 ± 0.12	0.79 ± 0.08	-0.16 ± 0.08	0.3 ± 35.8
Up2016 Bin 4bis	0.0269 ± 0.0001	0.0265 ± 0.0001	31.92 ± 4.94	0.14 ± 0.12	0.79 ± 0.08	-0.17 ± 0.08	2.1 ± 39.6
Down2016 Bin 5	0.0275 ± 0.0001	0.0269 ± 0.0001	51.57 ± 4.79	0.18 ± 0.08	0.78 ± 0.09	-0.18 ± 0.08	0.4 ± 35.8
Up2016 Bin 5	0.0274 ± 0.0001	0.0267 ± 0.0001	46.93 ± 4.91	0.19 ± 0.08	0.78 ± 0.09	-0.19 ± 0.08	2.1 ± 39.7
Down2016 Bin 5bis	0.0273 ± 0.0001	0.0265 ± 0.0001	53.05 ± 4.84	0.49 ± 0.12	0.79 ± 0.08	-0.20 ± 0.08	0.4 ± 35.8
Up2016 Bin 5bis	0.0274 ± 0.0001	0.0265 ± 0.0001	57.16 ± 4.81	0.49 ± 0.12	0.79 ± 0.08	-0.21 ± 0.08	2.2 ± 39.7
Down2016 Bin 6	0.0271 ± 0.0001	0.0269 ± 0.0001	55.78 ± 5.04	0.72 ± 0.15	0.90 ± 0.08	-0.21 ± 0.08	0.3 ± 35.7
Up2016 Bin 6	0.0269 ± 0.0001	0.0267 ± 0.0001	46.00 ± 5.25	0.72 ± 0.15	0.90 ± 0.08	-0.22 ± 0.08	2.1 ± 39.6
Down2016 Bin 6bis	0.0264 ± 0.0002	0.0261 ± 0.0001	36.63 ± 5.74	0.94 ± 0.13	0.92 ± 0.08	-0.23 ± 0.09	0.5 ± 35.8
Up2016 Bin 6bis	0.0261 ± 0.0002	0.0259 ± 0.0001	20.41 ± 5.68	0.95 ± 0.12	0.92 ± 0.08	-0.23 ± 0.09	2.3 ± 39.7
Down2016 Bin 7bis	0.0239 ± 0.0001	0.0239 ± 0.0001	-56.29 ± 6.36	0.71 ± 0.13	0.96 ± 0.08	-0.23 ± 0.09	0.5 ± 35.8
Up2016 Bin 7bis	0.0238 ± 0.0002	0.0238 ± 0.0001	-60.92 ± 6.85	0.71 ± 0.13	0.96 ± 0.08	-0.23 ± 0.09	2.2 ± 39.7
Down2016 Bin 8	0.0232 ± 0.0001	0.0234 ± 0.0001	-78.27 ± 6.45	0.47 ± 0.16	0.98 ± 0.08	-0.22 ± 0.08	0.4 ± 35.7
Up2016 Bin 8	0.0230 ± 0.0001	0.0231 ± 0.0001	-91.06 ± 6.87	0.46 ± 0.17	0.98 ± 0.08	-0.22 ± 0.08	2.2 ± 39.6
Down2016 Bin 8bis	0.0228 ± 0.0001	0.0229 ± 0.0001	-88.04 ± 6.33	0.16 ± 0.12	0.99 ± 0.09	-0.20 ± 0.08	0.3 ± 35.8
Up2016 Bin 8bis	0.0229 ± 0.0001	0.0229 ± 0.0001	-84.58 ± 6.50	0.15 ± 0.12	0.99 ± 0.08	-0.21 ± 0.08	2.1 ± 39.6

Table 4.12: *Parameters from the fits to the beampipe axis divided by data-taking year and magnet polarity.*

			z = 1080 mm		z = 2210 mm	
Sample	m_x [$\times 10^{-3}$]	m_y [$\times 10^{-3}$]	q_x [mm]	q_y [mm]	q_x [mm]	q_y [mm]
Down2011	2.51 ± 0.09	-0.60 ± 0.11	0.076 ± 0.012	-0.107 ± 0.015	2.913 ± 0.087	-0.780 ± 0.112
Up2011	2.42 ± 0.10	-0.83 ± 0.11	0.068 ± 0.013	-0.094 ± 0.015	2.808 ± 0.097	-1.037 ± 0.116
Down2012	2.30 ± 0.07	-0.51 ± 0.08	0.084 ± 0.009	-0.133 ± 0.011	2.680 ± 0.069	-0.709 ± 0.086
Up2012	2.63 ± 0.06	-0.63 ± 0.08	0.066 ± 0.008	-0.135 ± 0.011	3.036 ± 0.062	-0.848 ± 0.081
Down2015	2.42 ± 0.08	-0.36 ± 0.10	0.024 ± 0.012	-0.018 ± 0.014	2.759 ± 0.086	-0.422 ± 0.105
Up2015	2.62 ± 0.11	-0.36 ± 0.14	-0.032 ± 0.014	-0.057 ± 0.017	2.930 ± 0.115	-0.459 ± 0.144
Down2016	2.38 ± 0.02	-0.41 ± 0.02	-0.022 ± 0.004	-0.053 ± 0.005	2.673 ± 0.017	-0.516 ± 0.024
Up2016	2.34 ± 0.02	-0.40 ± 0.02	0.001 ± 0.004	-0.101 ± 0.005	2.643 ± 0.018	-0.557 ± 0.024

4.6 Discussion and conclusions

The beampipe angles obtained in Section 4.4 for 2011, 2012 and 2015 data are in excellent agreement within statistical uncertainties with those obtained with $J/\psi \to \mu^+\mu^-$ decays. In the 2016 case, where the statistical uncertainties are smaller, some tensions are observed in a few ϕ bins, suggesting possibile systematic uncertainties at a few hundred μrad level.

As described in Appendix B.2, we measured the beampipe radius and center position as a function of the z coordinate. To check the position of the beampipe axis, we fit the x and y coordinates of the beampipe center as a function of the z coordinate with linear functions. The results of the fits are reported in Tab. 4.12. As an example, the data points relative to 2012 Down data with the results of the fits overlaid are shown in Fig. 4.12. Finally, in Fig. 4.13 we show the measured radial distance in every z bin with the results of the circle fits overlaid and with the fitted axis position for the 2016 Down sample.

Discrepancies with respect to the design position have been found in all data-taking years, independently of the magnet polarity. The beampipe position appears as approximately stable across the years, tilted towards the positive x values by about 2.5 μrad and slightly towards the negative y values by about 0.5 μrad if compared to design position in the LHCb reference frame. Lateral movements are found to be at the level of 10 μrad at $z = 1080$ mm and 300 μrad at $z = 2210$ mm, with angular changes at the level of 100 μrad, across the years of data taking.

This kind of measurements can be used to monitor position and movements of the beampipe and to correct the LHCb simulation in order to reproduce more accurately its position.

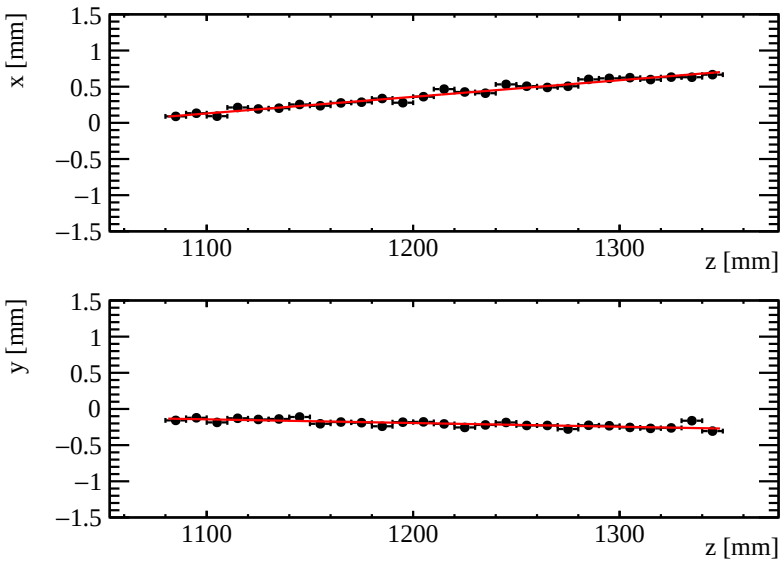

Figure 4.12: *Fitted (top) x and (bottom) y coordinates of the beampipe axis as a function of the z coordinate. The results of fits with linear function are overlaid. The data are 2012 Down sample.*

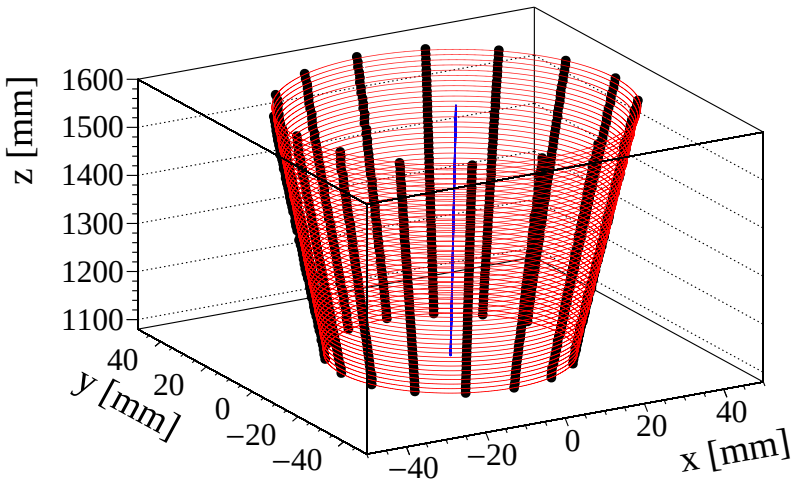

Figure 4.13: *3-D representation of the beampipe obtained drawing all the measured radial distances in every z slice with the results of the circle fits overlaid and with the repesentation of the beampipe axis for 2016 Down sample.*

5

Measurement of $\Lambda_b^0 \to pK^-$ and $\Lambda_b^0 \to p\pi^-$ *CP* asymmetries

5.1 Introduction

CP violation was initially discovered in neutral kaon decays [77], and much later was also observed in the B^0 [78, 79] and B_s^0 systems [27]. Moreover, evidence of *CP* violation in the baryon sector has been found [80]. The decays of the Λ_b^0 (bud) baryon to two-body charmless final states, pK^- or $p\pi^-$, are expected to have relatively small *CP* asymmetries, up to 6% [30] in the generalized factorization approach [31]. Using the pQCD formalism, *CP* asymmetries larger than 30% (although with very large uncertainties related to hadronic quantities and scale dependence) have been also predicted [32]. The only measurement of *CP* asymmetries in $\Lambda_b^0 \to pK^-$ and $\Lambda_b^0 \to p\pi^-$ decays to date has been performed by the CDF collaboration [26]. The asymmetries have been found to be compatible with zero within large uncertainties. It is thus important to lower the experimental uncertainty on such quantities in order to make significant comparisons with theoretical predictions.

Examples of Feynman diagrams contributing to the $\Lambda_b^0 \to pK^-$ and $\Lambda_b^0 \to p\pi^-$ decays are shown in Fig. 5.1. *CP* violation could arise from the interference of two amplitudes with nonzero strong and weak relative phases.

5.2 Analysis strategy

The direct *CP* asymmetries in $\Lambda_b^0 \to pK^-$ and $\Lambda_b^0 \to p\pi^-$ decays can be expressed as the sum of various contributions

$$A_{CP}(pK^-) = A_{\rm raw}(pK^-) - A_{\rm D}(p) - A_{\rm D}(K^-) - A_{\rm PID}(pK^-) - A_{\rm P}(\Lambda_b^0), \quad (5.1)$$

$$A_{CP}(p\pi^-) = A_{\rm raw}(p\pi^-) - A_{\rm D}(p) - A_{\rm D}(\pi^-) - A_{\rm PID}(p\pi^-) - A_{\rm P}(\Lambda_b^0), \quad (5.2)$$

where $A_{\rm raw}(pK^-)$ and $A_{\rm raw}(p\pi^-)$ are the raw asymmetries, $A_{\rm D}(h)$ is the h detection asymmetry, $A_{\rm PID}(pK^-)$ and $A_{\rm PID}(p\pi^-)$ are the asymmetries due to the PID cuts on the

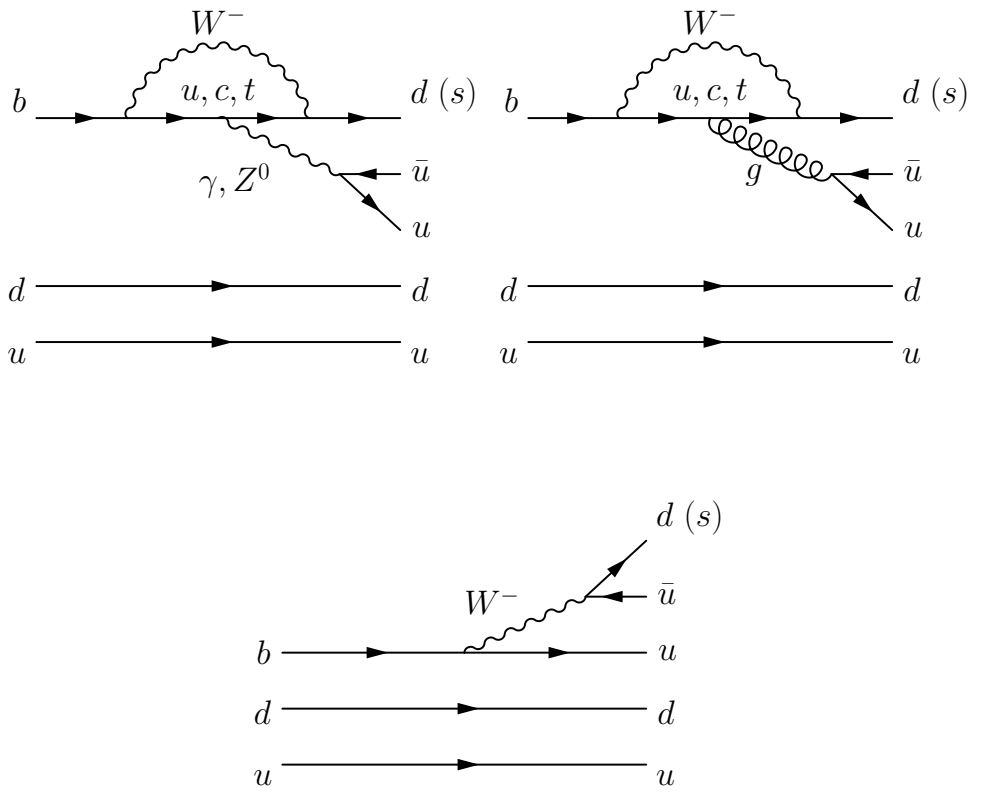

Figure 5.1: *Examples of Feynman diagrams representing (top left) the penguin EW topology, (top right) the penguin QCD topology and (bottom) the tree-level topology contributing to* $\Lambda_b^0 \to pK^-$ *(*$b \to su\bar{u}$ *transition) and* $\Lambda_b^0 \to p\pi^-$ *decays (*$b \to du\bar{u}$ *transition).*

final state particles and $A_{\rm P}(\Lambda_b^0)$ is the Λ_b^0 production asymmetry.

The raw asymmetries can be measured by means of simultaneous invariant-mass fits to the $\Lambda_b^0 \to ph$ spectra and to the other two-body B decays (in order extract the component of cross-feed backgrounds contributing to the spectra of the decays of interest) and are defined as

$$A_{\rm raw}(pK^-) = \frac{N(\Lambda_b^0 \to pK^-) - N(\overline{\Lambda}_b^0 \to \overline{p}K^+)}{N(\Lambda_b^0 \to pK^-) + N(\overline{\Lambda}_b^0 \to \overline{p}K^+)}, \tag{5.3}$$

$$A_{\rm raw}(p\pi^-) = \frac{N(\Lambda_b^0 \to p\pi^-) - N(\overline{\Lambda}_b^0 \to \overline{p}\pi^+)}{N(\Lambda_b^0 \to p\pi^-) + N(\overline{\Lambda}_b^0 \to \overline{p}\pi^+)}, \tag{5.4}$$

where N is the signal yield of a given decay.

The proton detection asymmetry is measured by means of fully simulated events. The $K\pi$ detection asymmetry is measured by means of $D^+ \to K^-\pi^+\pi^+$ and $D^+ \to K_S^0\pi^+$ decays and then corrected for the pion detection asymmetry in order to obtain the kaon detection asymmetry, as described in Refs. [81]. The pion detection asymmetry is taken as an external input [82], measured by means of $D^{*+} \to D^0(K^-\pi^+\pi^-\pi^+)\pi^+$ decays.

Table 5.1: *Total integrated luminosity corresponding to the pp collisions collected by LHCb, separated by year and magnet polarity. Uncertainties are not included.*

	2011	2012
Magnet Down	584.26 pb^{-1}	1068.07 pb^{-1}
Magnet Up	434.42 pb^{-1}	1038.83 pb^{-1}
Mag. Down + Mag. Up	1018.68 pb^{-1}	2106.90 pb^{-1}
Total	3125.58 pb^{-1}	

The PID asymmetries are defined as

$$A_{\rm PID}(pK^-) = \frac{\varepsilon_{\rm PID}(pK^-) - \varepsilon_{\rm PID}(\overline{p}K^+)}{\varepsilon_{\rm PID}(pK^-) + \varepsilon_{\rm PID}(\overline{p}K^+)}, \tag{5.5}$$

$$A_{\rm PID}(p\pi^-) = \frac{\varepsilon_{\rm PID}(p\pi^-) - \varepsilon_{\rm PID}(\overline{p}\pi^+)}{\varepsilon_{\rm PID}(p\pi^-) + \varepsilon_{\rm PID}(\overline{p}\pi^+)}, \tag{5.6}$$

where the PID efficiencies are obtained from samples of $D^{*+} \to D^0(K^-\pi^+)\pi^+$, $\Lambda \to p\pi^-$ and $\Lambda_c^+ \to pK^-\pi^+$ decays where the PID requirements are not imposed in order to assign the identity to the final state particles.

The Λ_b^0 production asymmetry is derived using the results from Ref. [81], accounting for the $\Lambda_b^0 \to ph$ kinematics in order to get the integrated value on the signal channels.

5.3 Data set and event selection

The data sample used in this analysis is composed of *pp* collisions collected during 2011 and 2012 corresponding to an integrated luminosity of 3 fb^{-1}. The total integrated luminosity divided by year and magnet polarity is reported in Tab. 6.3.

The sample used is the output of the `StrippingB2HHBDT` *stripping line*, run in the `Stripping20r1` (for 2011 data) and `Stripping20r0p1` (for 2012 data) stripping campaigns, upon the sample reconstructed with the `Reco14` version of reconstruction software. The `StrippingB2HHBDT` algorithm combines pairs of oppositely charged tracks in order to form two-body *b*-hadron decay candidates, where the pion mass hypothesis is assumed for the final state particles. Only tracks with large transverse momentum ($p_{\rm T}$), large impact parameter ($d_{\rm IP}$) with respect to all the primary vertices (PVs), small normalized χ^2 (χ^2/ndf) and small probability to be a *ghost-track* (`GhostProb`) are used. Pairs of tracks with a small distance of closest approach ($d_{\rm CA}$) are fitted to a common vertex in order to form the *b*-candidate. Only the candidates with a large transverse momentum ${p_{\rm T}}^{H_b}$, a small impact parameter with respect to all the PVs ($d_{\rm IP}^{H_b}$) and a large decay time ($t_{\pi\pi}$, computed assuming decay into the $\pi^+\pi^-$ final state) are selected by the algorithm are reported. In Tab. 6.4 the values of the requirements applied in this step of the stripping selection. The purity of the sample is then increased using a multivariate `Boosted Decision Tree`

(BDT) algorithm. The BDT algorithm discriminates between signal and combinatorial background on the basis of the smallest and largest $p_{\rm T}$ of the two tracks, the smallest and largest $d_{\rm IP}$ of the two tracks, the $d_{\rm CA}$ between the two tracks, the quality of the common vertex fit of the two tracks ($\chi^2_{\rm vtx}$), the ${p_{\rm T}}^{H_b}$ and $d^{H_b}_{\rm IP}$ of the b-hadron candidate, and the distance of flight (FD) of the b-hadron candidate with respect to the associated PV[1].

Table 5.2: *Summary of the values of the cuts used to form the two-body b-hadron decay candidates by the* `StrippingB2HHBDTLine`*, prior to the application of the BDT algorithm. The meaning of the various symbols is explained in the text.*

Cut type	value
Track χ^2/ndf	< 3
Track `GhostProb`	< 0.5
Track $p_{\rm T}$ [GeV/c]	> 1.0
Track $d_{\rm IP}$ [µm]	> 120
$d_{\rm CA}$ [µm]	< 100
$d^{H_b}_{\rm IP}$[µm]	< 120
$t_{\pi\pi}$ [ps]	> 0.6
${p_{\rm T}}^{H_b}$ [GeV/c]	> 1.2

No particular trigger requirement is applied on the sample surviving the `StrippingB2HHBDTLine` algorithm. In Fig. 6.1 the $m_{\pi^+\pi^-}$ distribution of the events surviving the preselection is reported.

5.3.1 Simulated samples

We use simulated samples of all two-body b-hadron decays under study, produced with the `Sim08/Digi13` version of the simulation framework. In these samples the 2011 and 2012 data taking conditions, trigger, reconstruction and stripping have been reproduced in order to have events as similar as possible to real data. Two distinct trigger configurations are emulated for the 2011 and 2012 samples, respectively. Simulated events have been produced with statistics that reproduces the observed ratio between 2011 and 2012 integrated luminosities. Moreover, the ratio between the statistics collected with different magnet polarities is also respected. In Tab. 6.5 we report the amount of simulated events for all two-body b-hadron decays. Reconstructed candidates are required to be associated with a true two-body b-hadron decay.

[1]The candidate is associated to the primary vertex with the smallest χ^2 of the impact parameter.

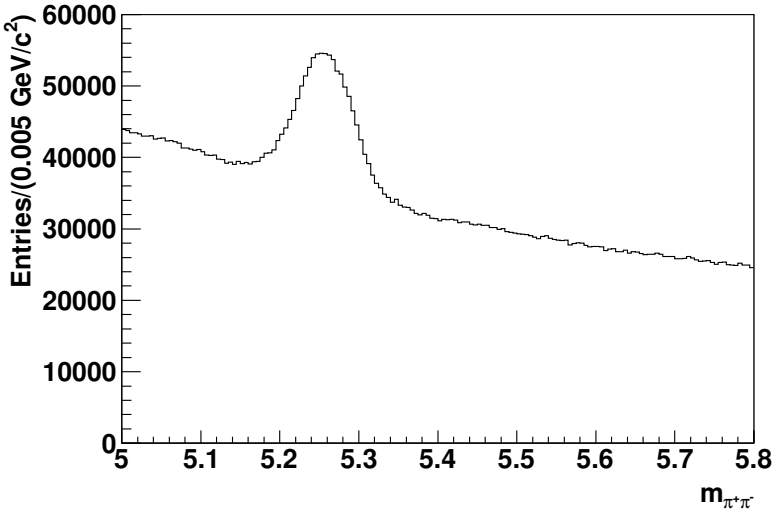

Figure 5.2: *Distribution of invariant mass under the $\pi^+\pi^-$ final state hypothesis for the events passing the* `StrippingB2HHBDTLine` *requirements.*

Table 5.3: *Number of generated events, separated by data taking year.*

Decay	2011	2012
$B^0 \to K^+\pi^-$	1541196	3068989
$B^0 \to \pi^+\pi^-$	1527244	3067742
$B^0 \to K^+K^-$	1027248	2035242
$B_s^0 \to K^+K^-$	1532248	3052242
$B_s^0 \to \pi^+K^-$	1514494	3071739
$B_s^0 \to \pi^+\pi^-$	1024500	2030741
$\Lambda_b^0 \to pK^-$	1558992	3031739
$\Lambda_b^0 \to p\pi^-$	1541498	3026736

5.4 PID calibration

The PID calibration is of fundamental importance for this analysis. The invariant-mass distribution of $\Lambda_b^0 \to pK^-$ and $\Lambda_b^0 \to p\pi^-$ decays peaks in a region where also other two-body B decays, with one or both the final state particles mis-identified, contribute with peaking backgrounds that need to be accounted for. The discriminating variables chosen to distinguish between pions, kaons, and protons are the $\Delta \log \mathcal{L}$ variables [83]. A comparison of the performances of $\Delta \log \mathcal{L}$ and ProbNN variables is done in Ref. [84]. The calibration sample for pions and kaons comes from the `StrippingNoPIDDstarWithD02RSKPiLine` *stripping line*, where $D^{*+} \to D^0 (\to K^-\pi^+)\, \pi_s^+$ decays are reconstructed. In order to determine PID efficiencies for protons we use the joint output of the `StrippingLam0LLLine1V0ForPID`

and `StrippingLam0LLLine2V0ForPID` *stripping lines*, where the $\Lambda \to p\pi^-$ decays are reconstructed. The difference between these lines is that the second has a requirement on the proton momentum ($p > 40$ GeV/c), whereas the first has no requirements and it is prescaled. Using both lines helps in improving the phase space coverage. In addition, also protons from $\Lambda_c^+ \to pK^-\pi^+$ decays are used. The kinematic features of these decays enable the identity of the final state particles to be determined without using any PID information. The residual background contamination has been removed from the samples using the *sPlot* technique [85]. The *sWeight-ed* samples are those provided as part of the `PIDCalibTool` package.

5.4.1 Calibration of PID efficiencies for kaon, pions and protons

The procedure of PID calibration has been developed taking into account the following considerations.

- Since the aim is to distinguish between three types of particles (pions, kaons and protons) a complete set of PID discriminators consists of two $\Delta \log \mathcal{L}$ variables for each final state particle. For example, in order to select kaons we need to apply requirements on both $\Delta \log \mathcal{L}_{K-\pi}$ (in order to reject pions) and $\Delta \log \mathcal{L}_{K-p}$ (in order to reject protons). If a particle satisfies the criteria defined to select kaons, then the kaon hypothesis is assigned to that particle.

- The value of $\Delta \log \mathcal{L}$ depends directly from the momentum of the particle through its relation with the emission angle of Cherenkov photons. In addition, since the two RICH detectors have different angular acceptances and have radiators optimised for different momentum regions, the $\Delta \log \mathcal{L}$ values show a dependence also on the pseudo-rapidity (η) of the particle.

- Several studies [83] performed by the LHCb collaboration showed a degradation of RICH performances in events with high occupancy. This effect can be parameterised studying the dependence of $\Delta \log \mathcal{L}$ with respect to the number of tracks N_{tracks} in the event.

- The kinematics of particles coming from two-body b-hadron decays are different from those of pions, kaons and protons contained in the calibration samples. This is evident from the distributions reported in Fig. 5.3, where background subtracted calibration samples are compared with samples of two-body b-hadron decays from fully simulated events.

- The distribution of N_{tracks} in two-body b-hadron decays results to be slightly different with respect to the distribution observed in the calibration samples. This difference is shown in Fig. 5.4, where the distributions of N_{tracks} for $D^{*+} \to D^0(K^-\pi^+)\pi^+$, $\Lambda \to p\pi^-$ and two-body b-hadron decays are superimposed.

As a first step, for a given set of PID requirements, maps of PID efficiencies in bins of p, η and N_{tracks} are determined. For example, in a given region of p, η and N_{tracks}, the

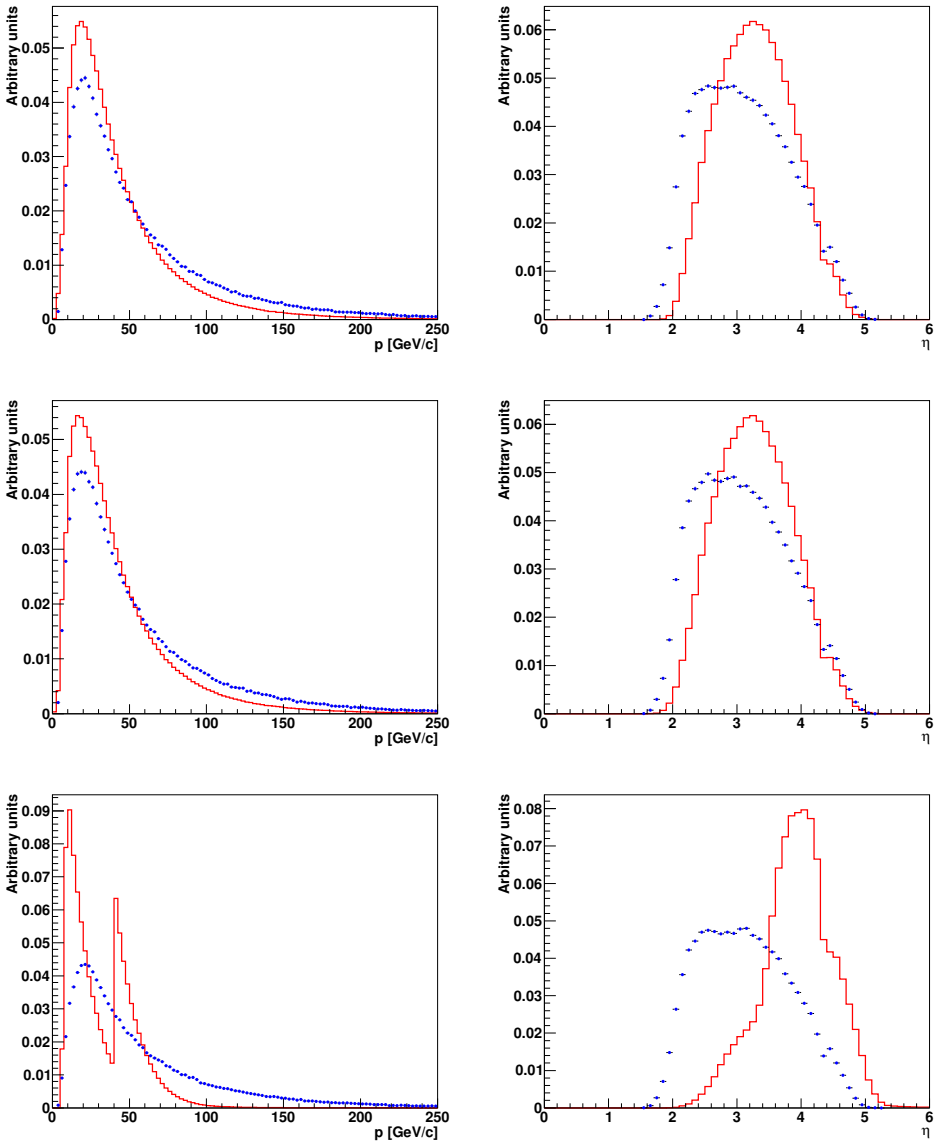

Figure 5.3: *Comparison between (left) p and (right) η distributions for (top) kaons,(middle) pions and (bottom) protons from (blue dots) fully simulated two-body b-hadron decays and (red line) calibration samples. The distributions are normalised to unitary area.*

efficiency of a PID requirement applied to kaons, is given by the number of calibration kaons satisfying that requirement divided by the total number of calibration kaons in that region. The binning scheme is

Track momentum: 2 bins for $0 < p < 10\,\text{GeV}/c$; 45 bins for $10 < p < 100\,\text{GeV}/c$; 20 bins for $100 < p < 150\,\text{GeV}/c$; 4 bins for $150 < p < 500\,\text{GeV}/c$;

Track η: 10 bins for $1 < \eta < 6$;

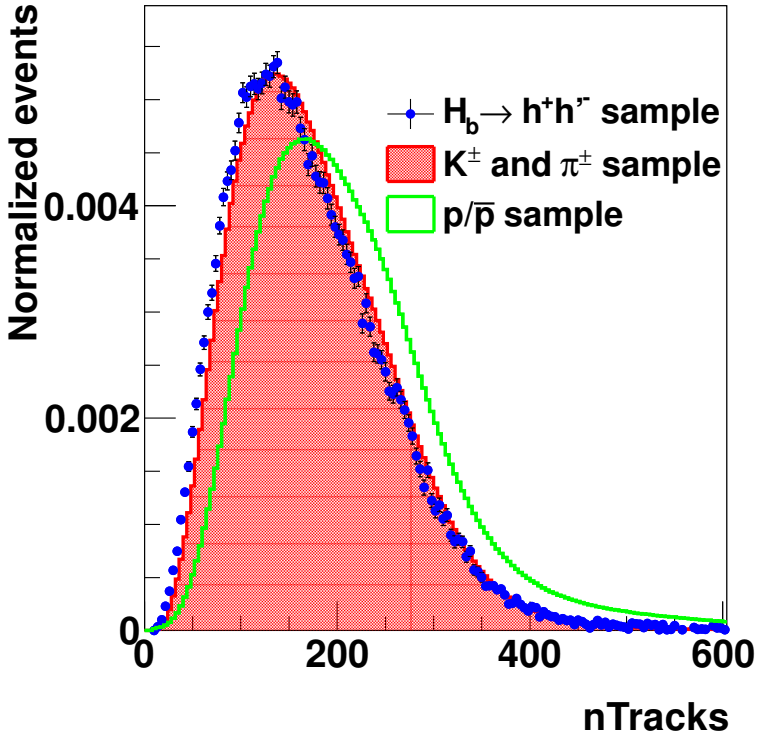

Figure 5.4: *N_{tracks} distribution relative to the calibration samples coming from (red line) $D^{*+} \to D^0(K^-\pi^+)\pi^+$ and (green line) $\Lambda \to p\pi^-$ decays. The distribution of N_{tracks} for two-body b-hadron decay candidates is also shown (blue dots).*

Number of tracks: 4 bins for $0 < N_{\text{tracks}} < 400$ and 1 bin for $400 < N_{\text{tracks}} < 600$.

Since the event occupancy and the kinematic of a particle are independent quantities, we integrate out the dependency of PID efficiency on N_{tracks}. If we knew the analytic expression for the PID efficiency as a function of p, η and N_{tracks} ($\varepsilon\,(p, \eta, N_{\text{tracks}})$) and the distribution of N_{tracks} for the two-body b-hadron decay sample ($f\,(N_{\text{tracks}})$), the procedure could be formalized by the following equation

$$\bar{\varepsilon}\,(p, \eta) = \int \varepsilon\,(p, \eta, N_{\text{tracks}}) \cdot f\,(N_{\text{tracks}})\,\mathrm{d}N_{\text{tracks}}, \tag{5.7}$$

where $\bar{\varepsilon}\,(p, \eta)$ is the PID efficiency as a function of p and η for a particle in the same occupancy regime that we observe in the two-body b-hadron decays. The integration in Eq. (5.7) has been computed as

$$\bar{\varepsilon}\,(p_i, \eta_j) = \frac{1}{N} \sum_{k=1}^{N} \varepsilon\,(p_i, \eta_j, N_{\text{tracks},k})\,, \tag{5.8}$$

where $\bar{\varepsilon}(p_i, \eta_j)$ is the final PID efficiency corresponding to the i-th bin of particle momentum and j-th bin of particle pseudorapidity; $\varepsilon(p_i, \eta_j, N_{\text{tracks}})$ is the PID efficiency corresponding to the i-th bin of particle momentum, the j-th bin of particle pseudorapidity, and k-th bin of N_{tracks}; N is a number large enough to avoid statistical fluctuations in the average (several trials proved $N = 200000$ to be sufficiently large without consuming too much computing power). For each term of the sum the value of $N_{\text{tracks},k}$ has been randomly extracted according to the distribution of N_{tracks} for the two-body b-hadron decay sample. Such a distribution is reported in Fig. 5.4 together with those corresponding to the calibration samples. All the distributions reported in Fig. 5.4 are background subtracted.

The final outcomes of this procedure are the maps of PID efficiencies in bins of p and η for particles coming from two-body b-hadron decays. As a reference, in Fig. 5.5 we report the PID efficiency maps for pions, kaons and protons relative to the requirement $\Delta \log \mathcal{L}_{K-\pi} > 3$ AND $\Delta \log \mathcal{L}_{K-p} > -5$.

5.4.2 Determination of PID efficiencies for two-body b-hadron decays

The efficiency of a PID requirement applied on a two-body b-hadron decay is estimated using the following equation:

$$\hat{\varepsilon}_{h^+h'^-} = \frac{1}{N} \sum_{i=1}^{N} \bar{\varepsilon}_{h^+}\left(p_i^+, \eta_i^+\right) \cdot \bar{\varepsilon}_{h'^-}\left(p_i^-, \eta_i^-\right), \tag{5.9}$$

where N is the number of decay candidates, $\bar{\varepsilon}_{h^+}(\cdot)$ and $\bar{\varepsilon}_{h'^-}(\cdot)$ are the efficiencies as a function of p and η as determined from Eq. (5.8), $p_i^{+(-)}$ and $\eta_i^{+(-)}$ are the momentum and the pseudorapidity of the positive (negative) particle in the i-th candidate. Candidates from fully simulated events are used.

5.4.2.1 Determination of PID efficiencies for $\Lambda_b^0 \to pK^-$ and $\Lambda_b^0 \to p\pi^-$ decays

The distributions of p and η in the calibration sample for protons do not cover all the p and η phase space of the protons coming from Λ_b^0 decays. We report the plots of the various particle distributions in the $p - \eta$ phase space for calibration samples in Fig. 5.6 and for simulated two-body b-hadron decay events in Figs. 5.7 and 5.8. To address this issue we use samples of simulated $\Lambda_b^0 \to pK^-$ and $\Lambda_b^0 \to p\pi^-$ decays.

First of all we define two zones in the $p - \eta$ plane, called *fiducial* and *non-fiducial* regions. The *fiducial* region is determined through different cuts on p and η as the zone where the calibration sample for protons contains a significant number of events. The *non-fiducial* zone covers the remaining phase space, where there are very few events from the calibration sample. The *fiducial* region can be expressed in terms of conditions on the values of p and η of the protons as

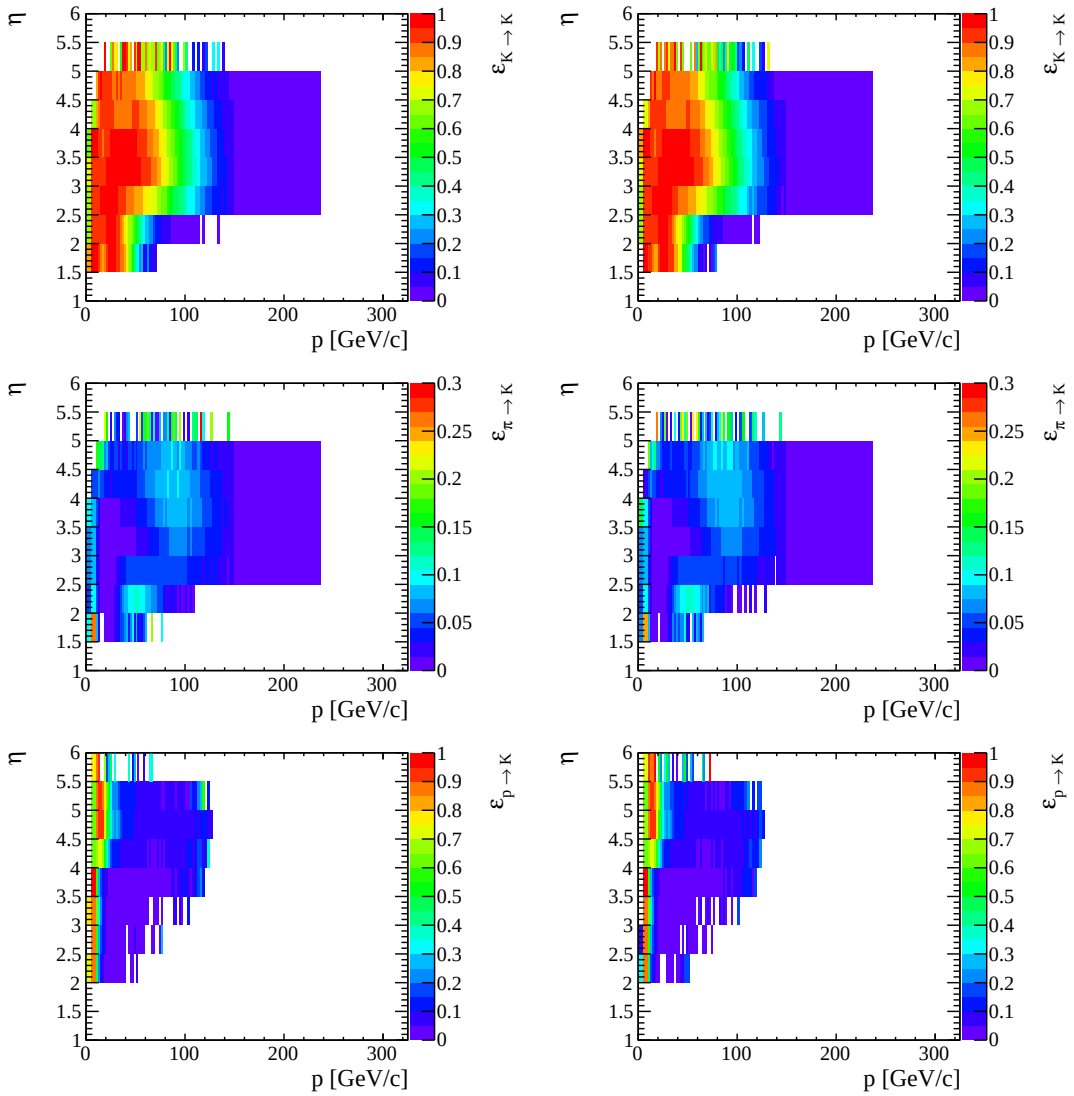

Figure 5.5: *Kaon PID efficiencies after the application of the requirements* $\Delta \log \mathcal{L}_{K-\pi} > 3$ *and* $\Delta \log \Delta \log \mathcal{L}_{K-p} > -5$ *under the (first row) kaon, (second row) pion and (third row) proton hypotheses in bins of* p *and* η*. The first column corresponds to the cases* K^-*,* π^- *and* $\bar{p}$ *while the second to* K^+*,* π^+ *and* p*.*

$$
\begin{aligned}
&(\eta > 2 \quad \text{AND} \quad p < 25\,\text{GeV}/c) \quad \text{OR} \\
&(\eta > p \cdot m_2 + q_2 \quad \text{AND} \quad p \geq 25\,\text{GeV}/c \quad \text{AND} \quad p < 120\ \text{GeV}/c) \quad \text{OR} \\
&(\eta > p \cdot m_3 + q_3 \quad \text{AND} \quad p \geq 120\ \text{GeV}/c),
\end{aligned} \tag{5.10}
$$

where $m_2 = 0.0184\ c/\text{GeV}$, $q_2 = 1.539$, $m_3 = 0.150\ c/\text{GeV}$ and $q_3 = -14.25$.

Since the *non-fiducial* region is not covered by the calibration sample, the PID efficiency in that region is determined with the aid of simulation. The efficiency from simulation

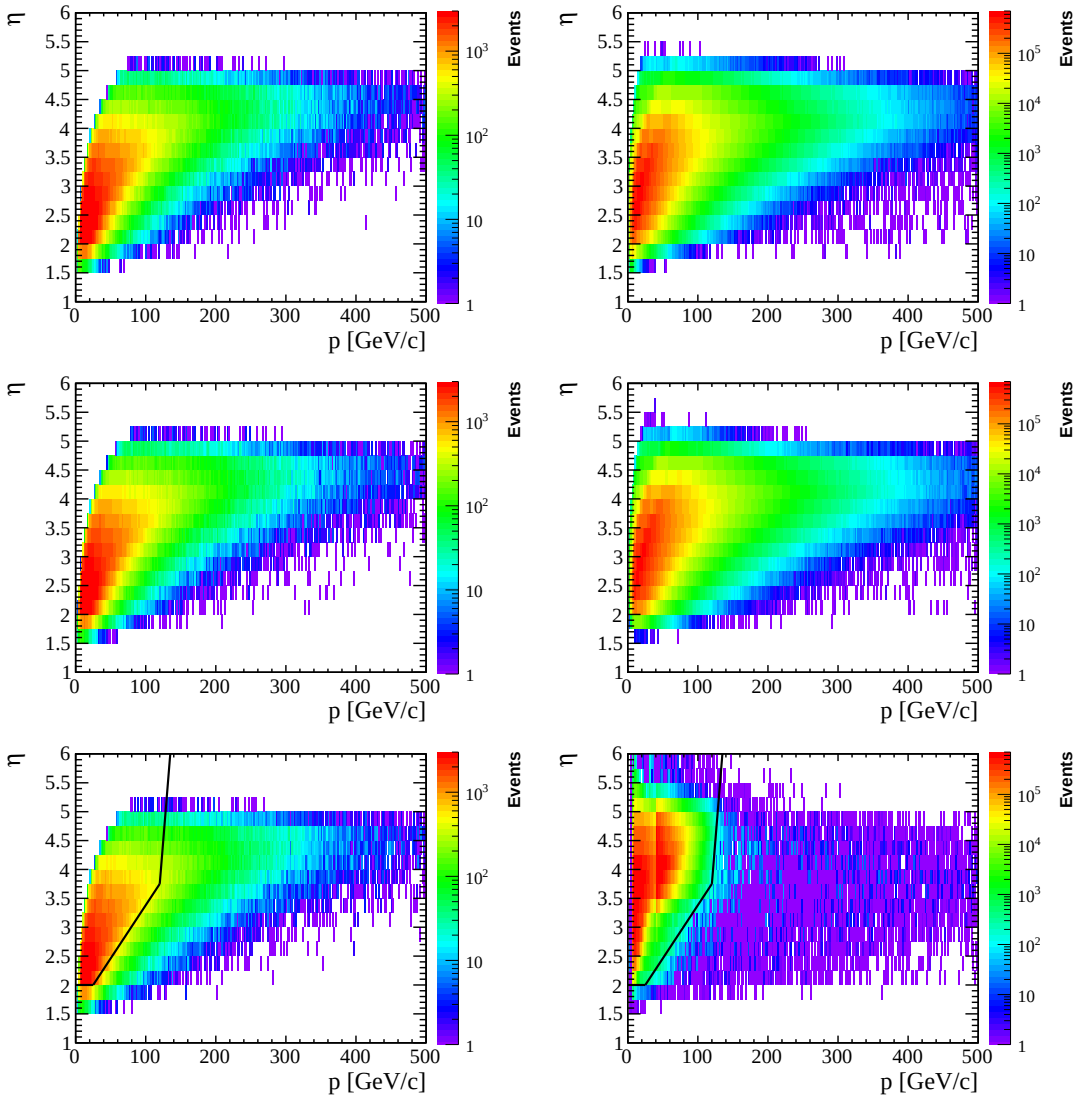

Figure 5.6: *Distribution in the $p - \eta$ plane for (top) kaons, (middle) pions and (bottom) protons coming from (left) two-body b-hadron decays and (right) PID calibration samples. The distribution related to two-body b-hadron decays are taken from fully simulated events, while those related to PID calibration samples are obtained from background-subtracted events, as explained in the text. In the case of protons a black line is drawn to separate the region populated by protons in the calibration sample (*fiducial *region) from the rest of phase space (*non-fiducial *region).*

is rescaled by a factor that takes into account the different PID performances between simulated events and data. Such a factor is defined by

$$\mathcal{K} = \frac{\varepsilon_F}{\varepsilon_F^{MC}}, \tag{5.11}$$

where ε_F is the PID efficiency in the *fiducial* region calculated applying the calibration

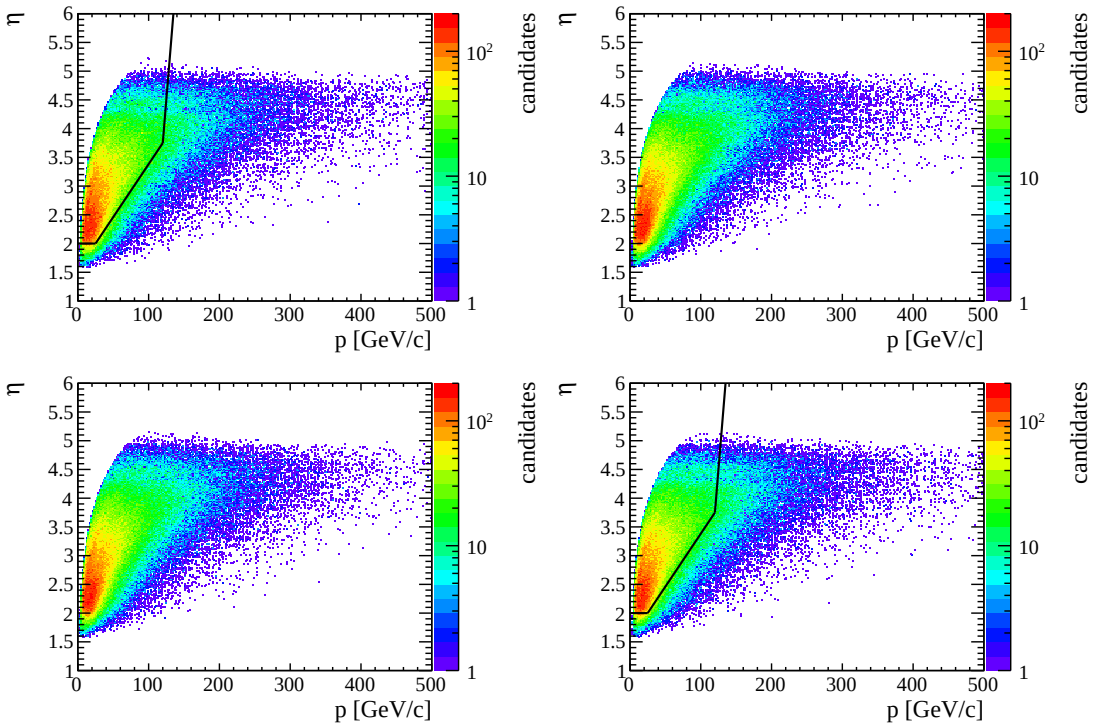

Figure 5.7: *Distributions in the $p-\eta$ plane corresponding to (top row) $\Lambda_b^0 \to pK^-$ and (bottom row) $\Lambda_b^0 \to K^+\overline{p}$ from the simulated data samples (the coloured scale indicates the number of events). The first column contains the plots relative to the positive particle present in each decay while the second column contains the plots relative to the negative particle present in each decay. The black line drawn in the p and $\bar{p}$ plots represent the boundary between the* fiducial *region (on the left of the boundary) and the* non-fiducial *region (on the right of the boundary) as defined in Eq.*(5.10).

procedure described in the previous paragraph by Eq. (5.9) and ε_F^{MC} is the PID efficiency in the *fiducial* region determined from simulated events. The final efficiency is then calculated as

$$\varepsilon = f \cdot \varepsilon_F + (1-f) \cdot \mathcal{K} \cdot \varepsilon_{NO-F}^{MC}, \tag{5.12}$$

where f is the fraction of events inside the *fiducial* region and ε_{NO-F}^{MC} is the PID efficiency relative to the *non-fiducial* region determined from simulation.

5.4.3 Determination of uncertainties on PID efficiencies

All uncertainties that are discussed in this Section will be summed in quadrature to obtain the final uncertainty on PID efficiencies. The uncertainties for all the decay modes and final state hypotheses are estimated only for the final configuration of cuts and are reported in Tabs 5.9 and 5.10.

Two sources of uncertainties that can contribute to the determination of PID efficiencies are considered. The first one is statistical in nature, *i.e.* it comes from the finite size

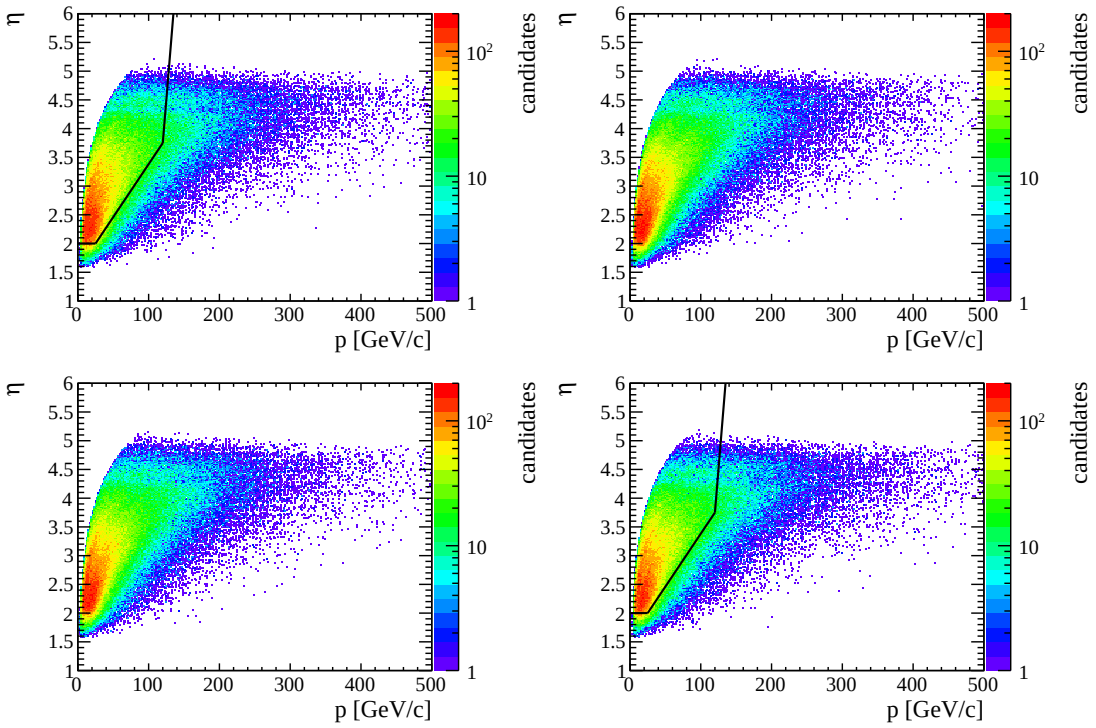

Figure 5.8: *Distributions in the $p - \eta$ plane corresponding to (top row) $\Lambda_b^0 \to p\pi^-$ and (bottom row) $\Lambda_b^0 \to \pi^+\overline{p}$ from the simulated data samples (the coloured scale indicates the number of events). The first column contains the plots relative to the positive particle present in each decay while the second column contains the plots relative to the negative particle present in each decay. The black line drawn in the p and $\bar{p}$ plots represent the boundary between the* fiducial *region (on the left of the boundary) and the* non-fiducial *region (on the right of the boundary) as defined in Eq.* (5.10).

of the calibration sample, used to determine the maps of PID efficiencies, and of the two-body b-hadron decay sample used as reference for the phase space of the particles. The corresponding uncertainty can be determined by simple error propagation.

The second source is related to the method used to transport the PID efficiencies obtained from the calibration sample to the phase space of two-body b-hadron decays. In order to assess a systematic uncertainty we alternatively varied the binning of each variable and we determined again the PID efficiencies for all two-body b-hadron decays. The number of bins of each kinematic variable is doubled and halved in turn. Furthermore, the baseline binning is modified, introducing a further variable, the azimuthal angle of the track, ϕ, with 4 bins. The largest variation between the baseline efficiency and the efficiency determined with each configuration is eventually taken as systematic uncertainty.

5.4.3.1 Determination of uncertainties on PID efficiencies for $\Lambda_b^0 \to pK^-$ and $\Lambda_b^0 \to p\pi^-$ decays

In the case of $\Lambda_b^0 \to pK^-$ and $\Lambda_b^0 \to p\pi^-$ decays we also assess a systematic uncertainty coming from the separation of the sample in the *fiducial* and *non-fiducial* regions. With the procedure described in the previous Section, we assumed that the ratio between the PID efficiency determined in data and simulation does not change moving from the *fiducial* to the *non-fiducial* region. In order to associate a systematic uncertainty to this assumption, we determine the PID efficiencies in the two regions for the two-body b-hadron decays whose phase space is completely covered by the calibration samples. For the $B^0 \to K^+\pi^-$, $B^0 \to \pi^+\pi^-$ and $B^0 \to K^+K^-$ decays we measure the quantity

$$\delta = \frac{\varepsilon_F}{\varepsilon_F^{MC}} - \frac{\varepsilon_{NO-F}}{\varepsilon_{NO-F}^{MC}}, \tag{5.13}$$

under the final state hypotheses $\pi^+\pi^-$, $K^+\pi^-$, $K^-\pi^+$, K^+K^-, pK^-, $\overline{p}K^+$, $p\pi^-$ and $\overline{p}\pi^+$. We observe that the value of δ strongly depends on the number of mis-identified particles in the final state. This is expected, since the simulation is known to reproduce PID efficiencies with limited accuracy (with differences of about 10%), and is even less accurated when predicting small misidentification probabilities. Consequently, we separate the estimated values of δ in three categories: the case where both final state particles are correctly identified, that where one of the two final state particles are misidentified, and that where both final state particles are misidentified. For each category we isolate the largest value of $|\delta|$, corresponding to 0.9, 2 and 4, respectively. The PID efficiencies for $\Lambda_b^0 \to pK^-$ and $\Lambda_b^0 \to p\pi^-$ decays are estimated again using Equation (5.12) but changing the value of the factor $\mathcal{K}$ to $\mathcal{K}_{\rm min} = 0$ and to $\mathcal{K}_{\rm max} = \mathcal{K} + |\delta|$, respectively. The largest deviation with respect to the efficiency estimated with the baseline value of $\mathcal{K}$ is considered as an additional systematic uncertainty.

5.5 Invariant-mass models

The strategy we adopted to optimise the event selection is based on the knowledge of the model used to fit the invariant-mass spectra of selected events. In this Section we present the studies performed in order to determine the various probability density functions (PDFs) used to parameterise all contributions to the spectra. We identified 4 components

Signal: two-body b-hadron decays where the final state particles are correctly identified.

Cross-feed background: two-body b-hadron decays in which the identity of one or both the final state particles is wrongly assigned. This background is particularly dangerous since it peaks at the signal distribution.

Partially reconstructed background: multibody decays of b-hadrons with at least two oppositely charged bodies.

Combinatorial background: candidates composed by pairs of oppositely charged tracks not coming from the same decay chain.

5.5.1 Signal model

The signal distribution is parameterised with a power law function, in order to take into account the QED final state radiation, convolved with a double Gaussian resolution

$$g(m) = A \cdot [\Theta(m_{H_b} - m') \cdot (m_{H_b} - m')^s \otimes G_2(m - m';\ \delta_m, f_1, \sigma_1, \sigma_2)]\,, \tag{5.14}$$

where m is the reconstructed invariant mass, m_{H_b} is the mass of the considered B hadron taken from Ref. [17], Θ is the step-function, A is a normalisation constant, s is a parameter governing the radiative component, G_2 stands for a double Gaussian function of mean δ_m, widths σ_1 and σ_2 and relative fraction of the first Gaussian function f_1, and $\otimes$ stands for the convolution product. Note that the value of the parameter s can be computed analytically using QED, as described in Ref. [86]. A caveat is due for the case of Λ_b^0 decays: the theoretical formalism in Ref. [86] is valid for B meson decays to two pseudoscalars. However, the same formalism is used also for the case of Λ_b^0 decays, verifying the goodness of the assumption using simulated events where photon emission is introduced with the PHOTOS generator [87].

In the study presented in Ref. [88] it has been shown that Eq (5.14) must be corrected to account for the reconstruction efficiency of two-body b-hadron decays as a function of the invariant mass itself. Such a dependence can be parameterised to first order

$$\varepsilon\,(m) \propto 1 + p_0 \cdot |m - m_{H_b}|\,, \tag{5.15}$$

where p_0 is the parameter governing the shape determined from fully simulated events. Thus the model used to describe the signal mass shape is written as

$$h(m) = A \cdot \varepsilon\,(m) \cdot [\Theta(m_{H_b} - m') \cdot (m_{H_b} - m')^s \otimes G_2(m - m';\ \delta_m, f_1, \sigma_1, \sigma_2)]\,. \tag{5.16}$$

To validate the model, binned maximum likelihood fits are performed to the invariant-mass shapes of simulated signal events passing the preselection and reconstructed under the correct mass hypothesis for the two final state particles. A slightly different model, with respect to Eq (5.16), is used to accommodate for the very large tail on the right hand side of the signal peaks. A third, wide, Gaussian function is added to the model, outside the convolution product with the power law function. The contribution of this additional Gaussian component is found to be about 1% of the total. This component is ignored in the baseline fits, and a systematic uncertainty due to this will be assessed (see Section 5.8).

In Figs 5.9 and 5.10 we report the distribution of the invariant mass for all two-body b-hadron decays with the result of the best fit superimposed (the black dashed line represents the wide Gaussian function not included in the resolution model). The values of s and p_0 are reported in Tab. 5.4 together with those of $s_{th.}$ obtained following the theoretical computation reported in Reference [86].

The values of s obtained from the fits to the simulated samples are all in good agreement with the theoretical predictions. However, a systematic uncertainty is also considered.

As far as the parameter p_0 is concerned, its uncertainty depends mainly on the selection requirement applied to the pointing of the b-hadron candidate to the PV. In the event of

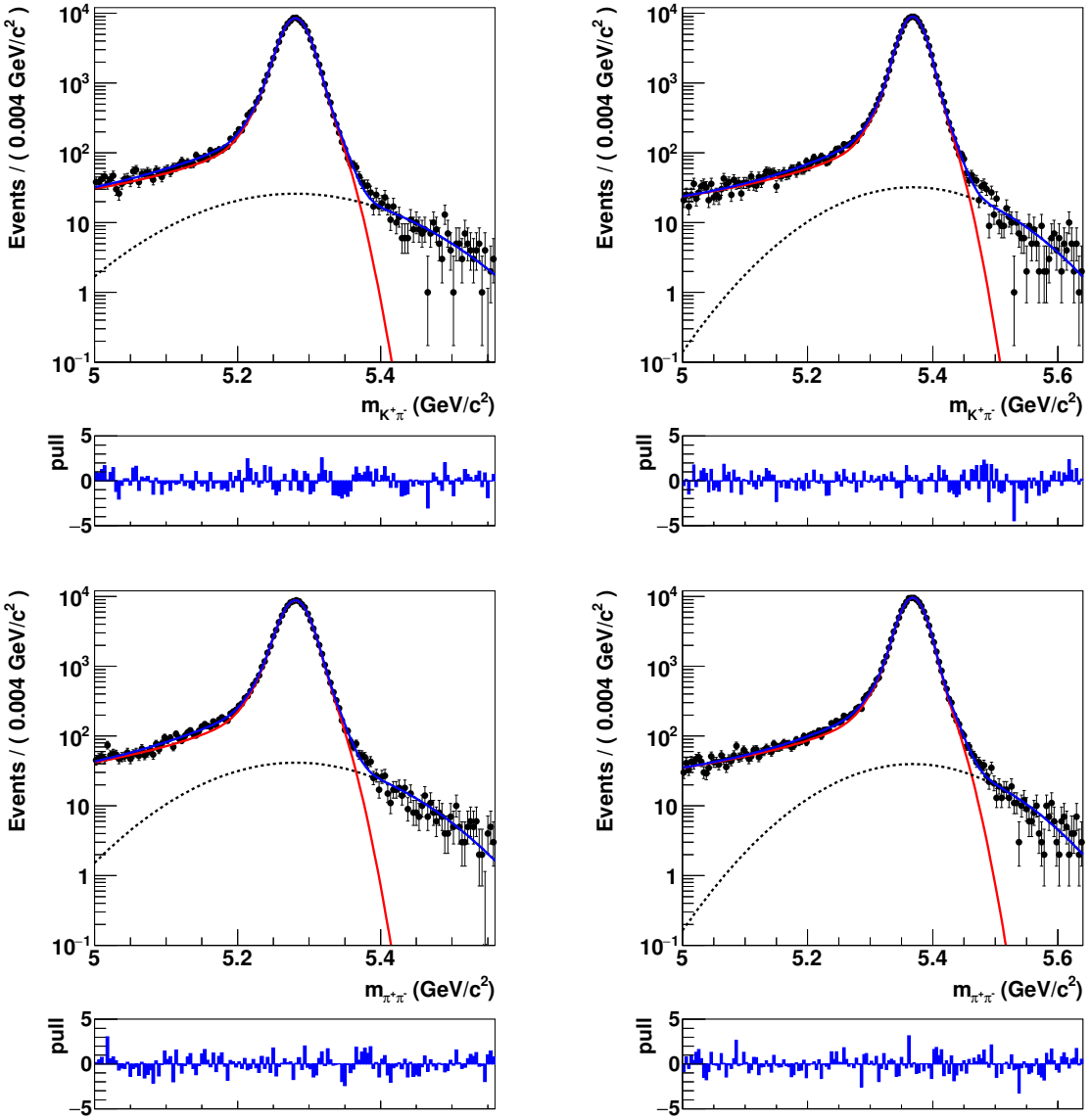

Figure 5.9: *Distribution of invariant mass for fully simulated (top left)* $B^0 \to K^+\pi^-$*, (top right)* $B_s^0 \to \pi^+K^-$*, (bottom left)* $B^0 \to \pi^+\pi^-$ *and (bottom right)* $B_s^0 \to \pi^+\pi^-$ *decays passing the preselection described in Section 5.3. The result of the best fit using the model described in the text in Section 5.5.1 is overlaid.*

missing or exceeding momentum of the charged daughters with respect to the true value, the reconstructed b-hadron momentum is no longer perfectly aligned with the real flight direction. Consequently, a dependence of the efficiency on the B invariant-mass value is introduced.

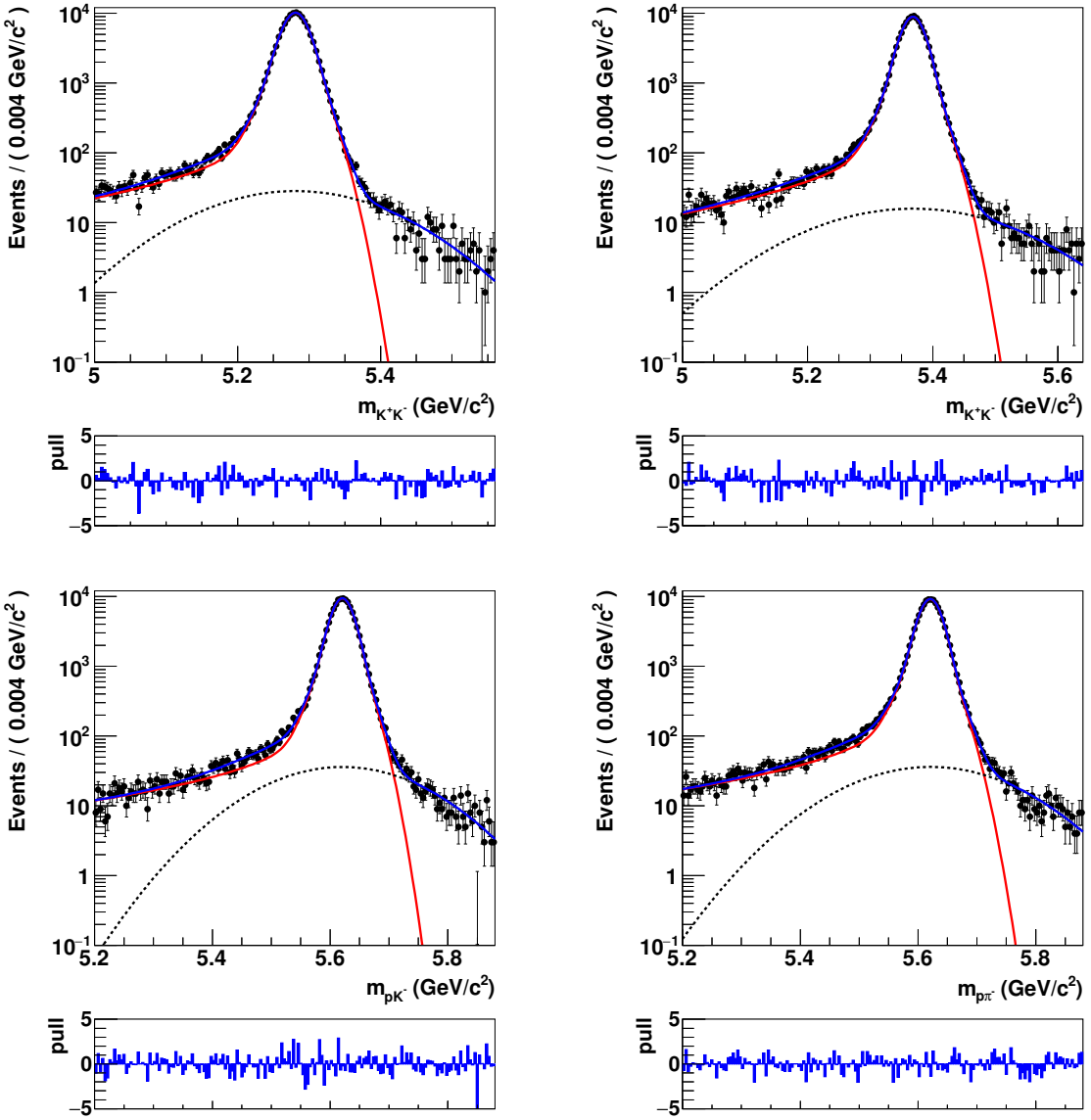

Figure 5.10: *Distribution of invariant mass for fully simulated (top left) $B^0 \to K^+K^-$, (top right) $B_s^0 \to K^+K^-$, (bottom left) $\Lambda_b^0 \to pK^-$ and (bottom right) $\Lambda_b^0 \to p\pi^-$ decays passing the preselection described in Section 5.3. The result of the best fit using the model described in the text in Section 5.5.1 is overlaid.*

5.5.2 Cross-feed background model

The parameterisation of the model used to describe the cross-feed backgrounds is studied using fully simulated signal decays. The procedure consists of two steps: a dataset containing the invariant mass computed under the wrong hypothesis is produced and then

Table 5.4: *Values of the parameters p_0 and s governing the line shape defined by Eq.* (5.16)*, extracted adapting the PDF to fully simulated two-body b-hadron simulated events surviving the preselection presented in Section 5.5.1. The theoretical expectations of the s parameter ($s_{th.}$) have been computed following Reference [86] and are reported as well.*

Decay	$s_{th.}$	s	p_0 [c^2/GeV]
$B^0 \to K^+\pi^-$	-0.9768	-0.9758 ± 0.0011	-0.66 ± 0.25
$B^0 \to \pi^+\pi^-$	-0.9709	-0.9690 ± 0.0012	-0.53 ± 0.22
$B^0 \to K^+K^-$	-0.9827	-0.9824 ± 0.0007	-1.02 ± 0.22
$B_s^0 \to K^+K^-$	-0.9826	-0.9823 ± 0.0007	-1.03 ± 0.17
$B_s^0 \to \pi^+K^-$	-0.9766	-0.9762 ± 0.0008	-0.57 ± 0.16
$B_s^0 \to \pi^+\pi^-$	-0.9707	-0.9694 ± 0.0009	-0.55 ± 0.14
$\Lambda_b^0 \to pK^-$	-0.9852	-0.9860 ± 0.0007	-0.54 ± 0.18
$\Lambda_b^0 \to p\pi^-$	-0.9793	-0.9791 ± 0.0008	-0.62 ± 0.14

the shape is built by applying a kernel estimation method [89] to the dataset.

The reconstructed invariant mass of any two-body decay under a given $h^+h'^-$ final state hypothesis can be written as

$$m_W(h^+h'^-) = \sqrt{m_{h^+}^2 + m_{h'^-}^2 + 2\left(\sqrt{(m_{h^+}^2 + p_+^2)(m_{h'^-}^2 + p_-^2)} - \vec{p}_+ \cdot \vec{p}_-\right)}\,. \tag{5.17}$$

where m_{h^+} and $m_{h'^-}$ are the masses corresponding to the hypothesis, $\vec{p}_{+(-)}$ is the momentum of the positive (negative) particle obtained from the simulation and $p_{+(-)}$ stands for the module of $\vec{p}_{+(-)}$.

The datasets have been created from simulated two-body b-hadron decays, computing for each event the wrong invariant mass using the true momenta of the final state particles (obtained accessing Monte Carlo truth information). In order to describe the cross-feed mass shapes it is necessary to take into account the effect of PID requirements. Since their application alters the momentum distribution of tracks, they have the effect of deforming the invariant-mass distributions obtained through the procedure described above. To address this, a weight to each simulated event is applied as

$$w_i = \varepsilon_{h^+}\left(p_i^+, \eta_i^+\right) \cdot \varepsilon_{h'^-}\left(p_i^-, \eta_i^-\right), \tag{5.18}$$

where $\varepsilon_{h^\pm}$ are the PID efficiencies of the positive and negative particles obtained from the efficiency maps presented in Section 5.4, and $p_i^\pm$ and $\eta_i^\pm$ are the momenta and pseudorapidities in the i-th event. The kernel estimation method is applied to these weighted datasets. An example of invariant-mass distributions for the wrong mass hypothesis is shown in Fig. 5.11, together with the results of the application of the kernel estimation method to the distributions. Finally, in the invariant-mass fits, the obtained non-parametric PDF are convolved with the same invariant-mass resolution used for the

signal line shapes. A study has been dedicated to the validation of the method described above, as reported in Appendix C.1.

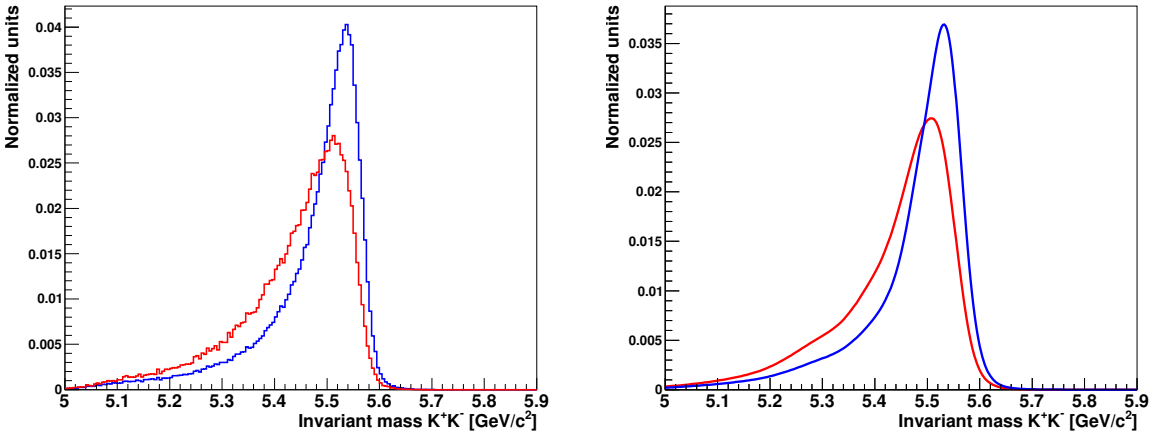

Figure 5.11: *Invariant-mass distributions for wrong mass hypothesis calculated by means of Eq.* (5.17) *for the $\Lambda_b^0 \to pK^-$ decay reconstructed as (left) K^+K^- and (right) the corresponding PDFs obtained using a kernel estimation technique applied to a sub-sample of the same data. The blue lines represent the distributions without taking into account the deformation induced by PID requirements, while the red lines represent the weighted distributions and the relative PDF, where the weights are calculated using the PID efficiencies.*

5.5.3 Partially reconstructed multi-body b-hadron decays

This type of background originates from partially reconstructed decays where one or more final state particles are not reconstructed. As documented in Appendix C.1, an ARGUS function convolved with a resolution model provides a good empirical modelling of this background component. The final PDF is

$$p(m) = A \cdot \left[m' \sqrt{1 - m'^2/m_0^2} \cdot e^{c\left(1-m'^2/m_0^2\right)} \otimes G_2(m - m';\ \delta_m, f_1, \sigma_1, \sigma_2) \right]. \qquad (5.19)$$

Since the lightest particle that can be missed in the reconstruction of the candidate is a π^0, the end point of the ARGUS functions is fixed to $m_{B^0} - m_{\pi^0}$, $m_{B_s^0} - m_{\pi^0}$ and $m_{\Lambda_b^0} - m_{\pi^0}$ for partially reconstructed backgrounds coming from B^0, B_s^0 and Λ_b^0 decays, respectively. Another possible source of partially reconstructed background is the component due to three-body decays of the B^+ meson (like $B^+ \to h^+h'^-\pi^+$). This component is not parameterised explicitly as its shape is almost equal to that of partially reconstructed B^0-meson decays.

5.5.4 Combinatorial background model

The combinatorial background component has been modelled with an exponential function

$$c_f(m) = B_f e^{-k_f m}, \tag{5.20}$$

where k_f is left free to vary in the fit procedure and B_f is a normalisation factor, for the spectrum corresponding to the final state f ($f = \pi^+\pi^-$, $K^+\pi^-$, K^+K^-, pK^-, $p\pi^-$).

5.6 Offline-selection optimisation

The sample obtained from the pre-selection must be further refined offline in order to obtain the best statistical sensitivity on the *CP* asymmetries. The offline selection is composed of two distinct parts

- a kinematic and geometrical selection applied to all the decay channels and based on a BDT multivariate algorithm;
- a specific final state selection based on the application of PID requirements.

Note that both the selection criteria must be optimized simultaneously to obtain the combination of criteria that yields the smallest uncertainty for each *CP* asymmetry. Before describing the offline procedure used to optimise the offline selection criteria, it is appropriate to make some considerations

- The kinematic and geometrical requirements imposed by the BDT selection reduce the amount of combinatorial background present in each invariant-mass spectrum, while PID requirements are needed in order to decrease the number of cross-feed (misidentified) background candidates. However, PID requirements also modify the composition and the amount of combinatorial background.
- For each set of BDT and PID requirements we need to determine the number of signal, cross-feed background, partially reconstructed background and combinatorial background candidates. The grid of BDT and PID requirements is reported in Tab. 5.5.
- The pK^- and $p\pi^-$ invariant-mass spectra are formed by different components. Since the raw asymmetries are obtained by fitting a model to the spectra, the sensitivity on these quantities depends not only on the amount of signal and background candidates in the sample, but also on the fitting model itself.

Then the procedure is the following. First of all we train a BDT for each set of PID requirements, chosen in order to cover a wide region of the $\Delta \log \mathcal{L}$ distributions. Secondly, we select different samples of fully reconstructed pK^- and $p\pi^-$ final states, one for each combination of BDT and PID requirements. Then we perform maximum likelihood fits to the invariant-mass spectra, determining the relevant parameters of the model. Finally, ten

pseudoexperiments for each set of requirements are performed, generating and fitting the data. Thus we use the results of these pseudoexperiments to find the requirements that yield the best sensitivity on each *CP* asymmetry. The optimisation procedure is performed separately and independently for the $\Lambda_b^0 \to pK^-$ and $\Lambda_b^0 \to p\pi^-$ decays, as described in the next sections. In the following we will refer to the selection optimised for $\Lambda_b^0 \to pK^-$ decays as Selection A, while to that optimised for $\Lambda_b^0 \to p\pi^-$ decays as Selection B.

Table 5.5: *List of the PID and BDT requirements explored during the optimisation procedure for (top) Selection A and (bottom) Selection B.*

Selection A		
Variables		Values used
$\Delta\log\mathcal{L}_{p-\pi}(p)$	$>$	5, 7, 9, 11, 13, 15
$\Delta\log\mathcal{L}_{p-K}(p)$	$>$	1, 3, 5, 7, 9, 11, 13, 15
$\Delta\log\mathcal{L}_{K-\pi}(K)$	$>$	0, 1, 3, 5, 7
$\Delta\log\mathcal{L}_{K-p}(K)$	$>$	$\max(-\Delta\log\mathcal{L}_{p-K}(p), -11) \to -1$ (step-size: 2) ; 0
BDT	$>$	$0 \to 0.4$; (step-size: 0.04)
Selection B		
Variables		Values used
$\Delta\log\mathcal{L}_{p-\pi}(p)$	$>$	5, 7, 9, 11, 13, 15
$\Delta\log\mathcal{L}_{p-K}(p)$	$>$	1, 3, 5, 7, 9, 11, 13, 15
$\Delta\log\mathcal{L}_{K-\pi}(\pi)$	$<$	-7, -5, -3, -1, 0
$\Delta\log\mathcal{L}_{p-\pi}(\pi)$	$<$	0 ; 1 $\to \min(\Delta\log\mathcal{L}_{p-\pi}(p), 11)$ (step-size: 2)
BDT	$>$	$0 \to 0.4$ (step-size: 0.04)

5.6.1 BDT training

The training of the BDT algorithm is performed considering that the application of PID modifies the amount and composition of combinatorial background. For this reason a training is made for each configuration of explored PID requirements. The signal sample is taken from fully simulated $\Lambda_b^0 \to pK^-$ and $\Lambda_b^0 \to p\pi^-$ events. The background sample is extracted from real data, selecting events passing the PID requirements used to isolate pK^- and $p\pi^-$ final states with an invariant mass (reconstructed under the $\pi\pi$ hypothesis) larger than 5.6 GeV/c^2. The variables used to select the two-body b-hadron candidates are the same used in the `StrippingB2HHBDT` (listed in Section 5.3), plus the minimum and maximum χ^2 of the impact parameter of the two tracks computed with respect to all the PVs ($\chi^2(d_{\rm IP})$), the χ^2 of the impact parameter of the b-hadron candidate with respect to the associated PV ($\chi^2(d_{\rm IP}^{H_b})$), and the χ^2 of the distance of flight of the b-hadron candidate with respect to the associated PV (χ^2(FD)). The list of variables is reported in Tab. 6.7. The distributions of the variables listed in Tab. 6.7, and their correlations, are reported in Figs. 5.12 and 5.13 for both background and signal events.

In our analysis we train three BDTs for each set of PID requirements. This is done in order to avoid the overtraining of the BDT and the risk of biasing the result. We randomly

Table 5.6: *List of variables used to train the BDT algorithms. The meaning of the symbols is explained in the text.*

BDT variables		
$\min({p_{\rm T}}^+, {p_{\rm T}}^-)$	$\min(d^+_{\rm IP}, d^-_{\rm IP})$	$\min(\chi^2(d^+_{\rm IP}), \chi^2(d^-_{\rm IP}))$
$\max({p_{\rm T}}^+, {p_{\rm T}}^-)$	$\max(d^+_{\rm IP}, d^-_{\rm IP})$	$\max(\chi^2(d^+_{\rm IP}), \chi^2(d^-_{\rm IP}))$
$d_{\rm CA}$	$\chi^2_{\rm vtx}$	
${p_{\rm T}}^{H_b}$	$d^{H_b}_{\rm IP}$	$\chi^2(d^{H_b}_{\rm IP})$
FD	$\chi^2({\rm FD})$	

divide the total data sample into three different and independent sub-samples: `S1`, `S2`, and `S3`. Then we train a BDT for each sub-sample (`BDT1`, `BDT2`, and `BDT3` respectively). `BDT1` is used to select the events of `S2` in the optimisation procedure while in the final analysis we will apply `BDT1` to `S3`. The same applies also to `BDT2` and `BDT3`. We report in Fig. 5.14 the distributions of the multivariate classifier μ_{BDT} relative to the training, optimisation, and final analysis phases of the BDT, corresponding to the PID requirements found by the optimisation procedure for the $\Lambda^0_b \to pK^-$ final state and listed in Tab. 5.8.

5.6.2 Optimization procedure

The first step of the optimisation procedure consists in determining the amount of signal events, cross-feed background events, partially-reconstructed background events, and combinatorial background events surviving each combination of PID and BDT requirements. The PID requirements used to select protons for the pK^- and $p\pi^-$ final states require the $\Delta\log\mathcal{L}_{p-K}$ and $\Delta\log\mathcal{L}_{p-\pi}$ variables to be greater than a given threshold, while to choose kaons we ask $\Delta\log\mathcal{L}_{K-\pi}$ and $\Delta\log\mathcal{L}_{K-p}$ to be greater than a given threshold. Finally, we impose $\Delta\log\mathcal{L}_{K-\pi}$ and $\Delta\log\mathcal{L}_{p-\pi}$ to be smaller than a given threshold when discriminating pions from kaons and protons. Note that the value of the $\Delta\log\mathcal{L}_{K-p}$ and $\Delta\log\mathcal{L}_{p-\pi}$ variables used to select kaons and pions for pK^- and $p\pi^-$ final states are constrained to be mutually exclusive with respect to the $\Delta\log\mathcal{L}_{p-\pi}$ and $\Delta\log\mathcal{L}_{p-K}$ requirements employed to select protons. This is done in order to avoid double counting amoung the different final states.
We perform maximum likelihood fits to the selected samples in order to obtain the various yields and the other relevant parameters of the fitting model; note that in this step the two *CP*-conjugate final states of each decay are not distinguished, hence no asymmetry is measured. The model used to describe the data is that described in Section 5.5. As an example, we report in Figs. 5.15 and 5.16 two normalisation fits corresponding to the pK^- and $p\pi^-$ invariant-mass spectra.

The yields of signal, partially-reconstructed background and combinatorial background events are left free to vary in the fit procedure.

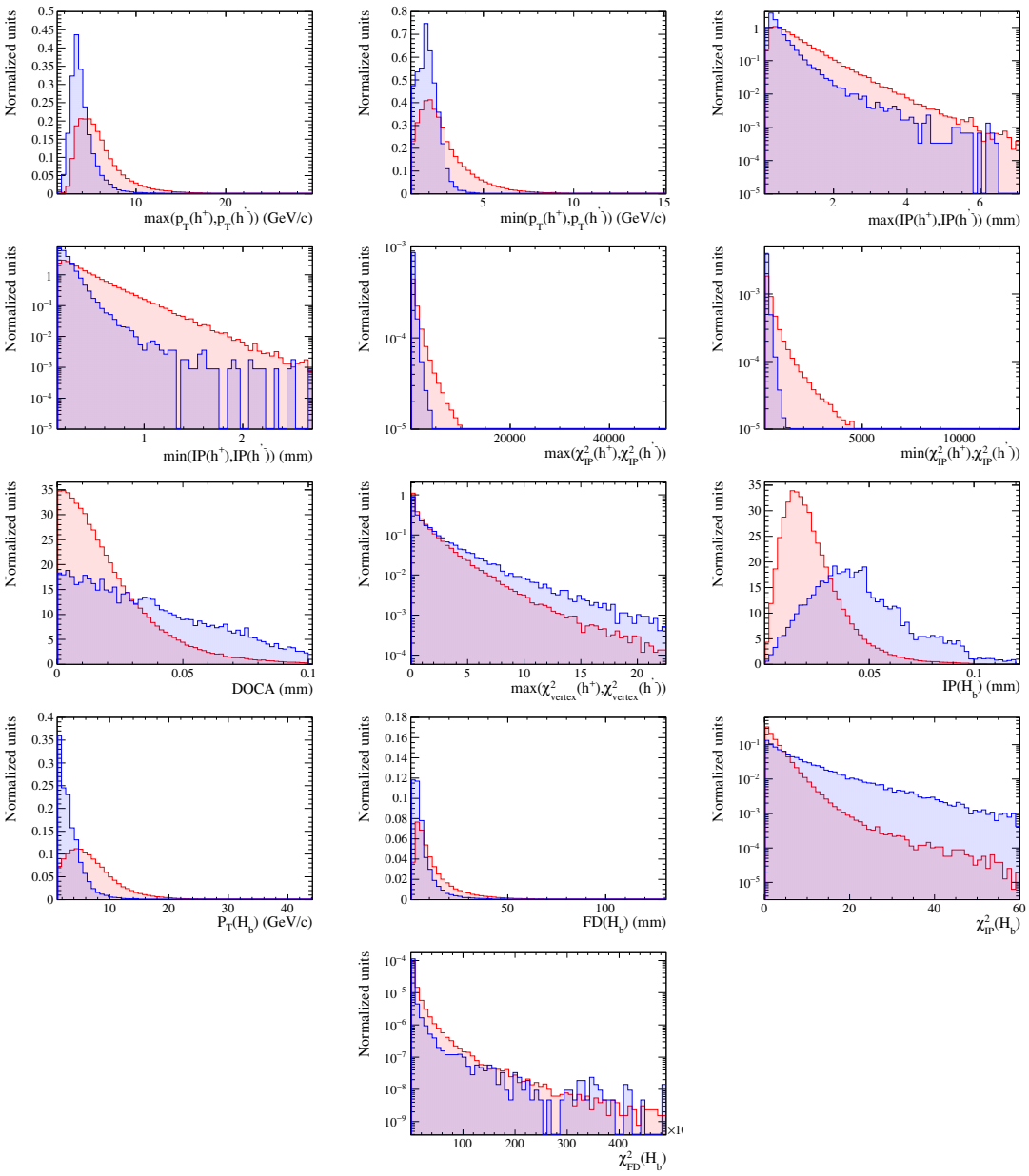

Figure 5.12: *Distribution of the variables used in the BDT training for (red) signal and (blue) background events. The dataset corresponds to Selection A and to the* `BDT1` *training.*

The number of cross-feed background events is calculated in a different way. First of all, we consider only cross-feed background contributions to the pK^- and $p\pi^-$ invariant-mass spectra where just one final state particle is misidentified. This is because the amount of decays where the identity of both final state particles is wrongly assigned turns out to be negligible. Thus, the cross-feed backgrounds considered in the fit model are

- $\overline{B}^0 \to \pi^+K^-$, $B_s^0 \to \pi^+K^-$, $B_s^0 \to K^+K^-$, and $\Lambda_b^0 \to p\pi^-$ decays for the $\Lambda_b^0 \to pK^-$

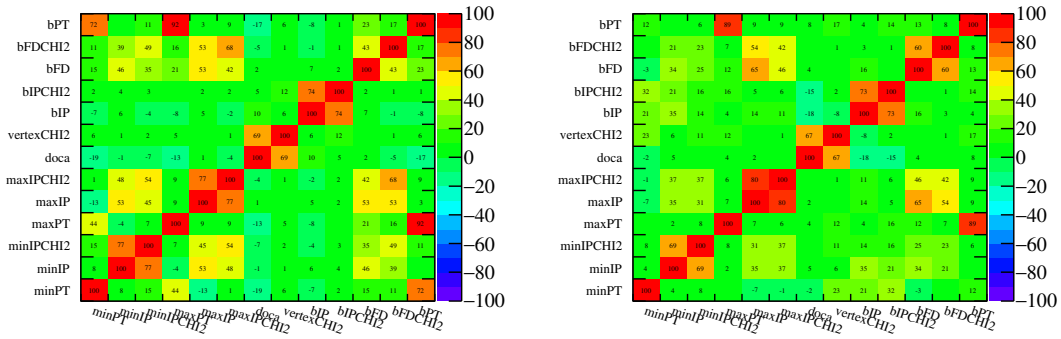

Figure 5.13: *Correlation matrices of the variables used to train the BDT for (left) signal and (right) background events.*

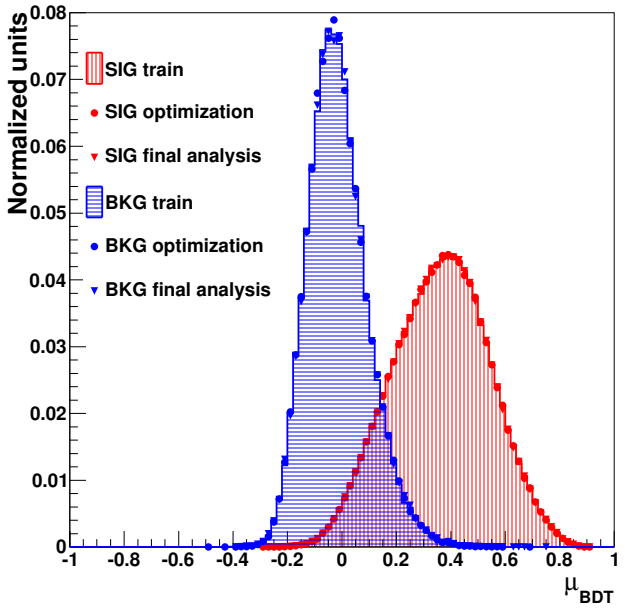

Figure 5.14: *Plots showing the distributions of the multivariate classifier μ_{BDT} relative to the (line) training, (dot) optimization, and (triangle) final analysis phases, divided for (red) signal and (blue) background events. The BDT selections are those used in the analysis of the pK^- final state with the optimised requirements listed in Tab. 5.8.*

invariant-mass spectrum;

- $B^0 \to K^+\pi^-$, $\overline{B}{}^0_s \to K^+\pi^-$, $B^0 \to \pi^+\pi^-$, and $\Lambda^0_b \to pK^-$ decays for the $\Lambda^0_b \to p\pi^-$ invariant-mass spectrum.

We determine the number of $B^0 \to K^+\pi^-$ ($\overline{B}{}^0 \to \pi^+K^-$) decays directly from the fits to the pK^- ($p\pi^-$) invariant-mass spectrum. The yields of the other cross-feed backgrounds

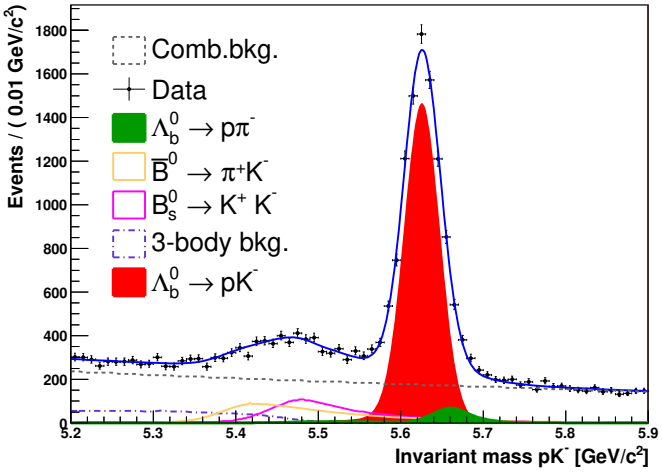

Figure 5.15: *$\Lambda_b^0 \to pK^-$ invariant-mass spectrum as generated using the model defined in Section 5.5 and selected requiring $\Delta\log\mathcal{L}_{p-\pi}(p) > 11$, $\Delta\log\mathcal{L}_{p-K}(p) > 7$, $\Delta\log\mathcal{L}_{K-\pi}(K) > 1$, $\Delta\log\mathcal{L}_{K-p}(K) > -7$ and BDT > 0.2. The results of the binned maximum likelihood fit are superimposed.*

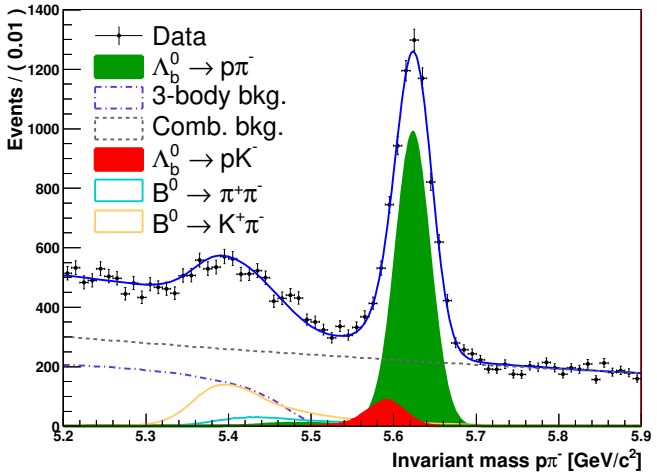

Figure 5.16: *$\Lambda_b^0 \to p\pi^-$ invariant-mass spectrum as generated using the model defined in Section 5.5 and selected requiring $\Delta\log\mathcal{L}_{p-\pi}(p) > 13$,$\Delta\log\mathcal{L}_{p-K}(p) > 7$, $\Delta\log\mathcal{L}_{K-\pi}(\pi) < -1$, $\Delta\log\mathcal{L}_{p-\pi}(\pi) < 7$ and BDT > 0.2. The results of the binned maximum likelihood fit are superimposed.*

coming from B mesons, *i.e.* $B_s^0 \to \pi^+K^-$ and $B_s^0 \to K^+K^-$ ($B^0 \to K^+\pi^-$ and $B^0 \to \pi^+\pi^-$), are constrained to the $B^0 \to K^+\pi^-$ ($B_s^0 \to \pi^+K^-$) yield, while the yields of cross-feed backgrounds coming from the other Λ_b^0 decay are constrained to the yields of the signal.

Table 5.7: *Values from Ref. [90] and used in Eq.* (5.21). *The first uncertainties are statistical, whereas the second are systematic.*

	Values used
$\mathcal{B}(B^0 \to \pi^+\pi^-)/\mathcal{B}(B^0 \to K^+\pi^-)$	$0.262 \pm 0.009 \pm 0.017$
$\mathcal{B}(B_s^0 \to K^+K^-)/(B^0 \to K^+\pi^-) \cdot (f_s/f_d)$	$0.316 \pm 0.009 \pm 0.019$
$\mathcal{B}(B_s^0 \to \pi^+K^-)/\mathcal{B}(B^0 \to K^+\pi^-) \cdot (f_s/f_d)$	$0.074 \pm 0.006 \pm 0.006$
$\mathcal{B}(\Lambda_b^0 \to p\pi^-)/\mathcal{B}(\Lambda_b^0 \to pK^-)$	$0.86 \pm 0.08 \pm 0.05$

Table 5.8: *Optimal PID and BDT requirements found by the optimisation procedure for the* $\Lambda_b^0 \to pK^-$ *(Selection A) and* $\Lambda_b^0 \to p\pi^-$ *(Selection B) decays.*

Selection A			Selection B		
Cut		Value found	Cut		Value found
$\Delta \log \mathcal{L}_{p-\pi}(p)$	$>$	11	$\Delta \log \mathcal{L}_{p-\pi}(p)$	$>$	11
$\Delta \log \mathcal{L}_{p-K}(p)$	$>$	7	$\Delta \log \mathcal{L}_{p-K}(p)$	$>$	7
$\Delta \log \mathcal{L}_{K-\pi}(K)$	$>$	0	$\Delta \log \mathcal{L}_{K-\pi}(\pi)$	$<$	0
$\Delta \log \mathcal{L}_{K-p}(K)$	$>$	-7	$\Delta \log \mathcal{L}_{p-\pi}(\pi)$	$<$	9
BDT	$>$	0.16	BDT	$>$	0.2

The relation used to constrain the yields is

$$N_i = N_j \cdot \frac{\mathcal{B}(i)}{\mathcal{B}(j)} \frac{f_i}{f_j} \frac{\varepsilon_i}{\varepsilon_j}, \tag{5.21}$$

where N_j represents the yield of the considered cross-feed background, N_i represents the yield of the reference decay, $\mathcal{B}$ stands for the branching ratio, f is the hadronisation fraction of the b hadron, and ε is the PID efficiency of the decay under the pK^- ($p\pi^-$) hypothesis. The values of $\mathcal{B}(i)/\mathcal{B}(j) \cdot (f_i/f_j)$ are taken as an external input from a previous LHCb measurement [90] and are reported in Tab. 5.7. We report in Tabs. 5.9 and 5.10 the value of the PID efficiencies obtained from the calibration procedure described in Section 5.4 using the optimal PID and BDT requirements found for the pK^- and $p\pi^-$ final states by means of the optimisation procedure.
Then, we perform ten pseudoexperiments for each combination of BDT and PID requirements, generating and then fitting the model to the data. Note that in this step we introduce the asymmetry between the two *CP*-conjugate modes for each component, generating the data with null asymmetries and then leaving them free to vary in the fit.

Finally we take the average of the ten uncertainties on each signal raw asymmetry for each set of BDT and PID requirements and we identify the criteria that give the smallest average of the statistical uncertainties on the asymmetry. The optimal values of the requirements found for the $\Lambda_b^0 \to pK^-$ and $\Lambda_b^0 \to p\pi^-$ decays are listed in Tab. 5.8.

Table 5.9: *PID efficiencies (in %) for the various mass hypotheses obtained using optimised PID requirements for Selection A.*

Decay	Final state hypothesis							
	$K^+\pi^-$	π^+K^-	$\pi^+\pi^-$	K^+K^-	pK^-	$K^+\bar{p}$	$p\pi^-$	$\pi^+\bar{p}$
$B^0 \to K^+\pi^-$	57.894 ± 0.750	0.054 ± 0.003	1.225 ± 0.054	2.515 ± 0.056	0.121 ± 0.001	0.697 ± 0.056	0.337 ± 0.008	0.012 ± 0.001
$B_s^0 \to K^+\pi^-$	57.894 ± 0.750	0.054 ± 0.003	1.225 ± 0.054	2.515 ± 0.056	0.121 ± 0.001	0.697 ± 0.056	0.337 ± 0.008	0.012 ± 0.001
$B^0 \to \pi^+K^-$	0.054 ± 0.003	57.877 ± 0.796	1.226 ± 0.057	2.522 ± 0.057	0.702 ± 0.061	0.125 ± 0.001	0.012 ± 0.001	0.337 ± 0.010
$B_s^0 \to \pi^+K^-$	0.054 ± 0.003	57.877 ± 0.796	1.226 ± 0.057	2.522 ± 0.057	0.702 ± 0.061	0.125 ± 0.001	0.012 ± 0.001	0.337 ± 0.010
$B^0 \to \pi^+\pi^-$	2.383 ± 0.057	2.377 ± 0.055	54.785 ± 0.820	0.106 ± 0.003	0.076 ± 0.003	0.077 ± 0.003	0.569 ± 0.055	0.560 ± 0.049
$B_s^0 \to \pi^+\pi^-$	2.383 ± 0.057	2.377 ± 0.055	54.785 ± 0.820	0.106 ± 0.003	0.076 ± 0.003	0.077 ± 0.003	0.569 ± 0.055	0.560 ± 0.049
$B^0 \to K^+K^-$	1.296 ± 0.057	1.295 ± 0.054	0.027 ± 0.003	61.172 ± 0.722	0.929 ± 0.022	0.943 ± 0.020	0.008 ± 0.000	0.008 ± 0.000
$B_s^0 \to K^+K^-$	1.296 ± 0.057	1.295 ± 0.054	0.027 ± 0.003	61.172 ± 0.722	0.929 ± 0.022	0.943 ± 0.020	0.008 ± 0.000	0.008 ± 0.000
$\Lambda_b^0 \to pK^-$	0.154 ± 0.059	0.575 ± 0.544	0.013 ± 0.011	6.439 ± 2.610	64.792 ± 10.966	0.184 ± 0.237	1.113 ± 0.179	0.003 ± 0.003
$\Lambda_b^0 \to K^+\bar{p}$	0.668 ± 0.500	0.152 ± 0.041	0.014 ± 0.009	6.431 ± 2.484	0.194 ± 0.226	65.139 ± 11.654	0.004 ± 0.003	1.121 ± 0.153
$\Lambda_b^0 \to p\pi^-$	6.089 ± 2.435	0.022 ± 0.020	0.539 ± 0.512	0.263 ± 0.158	8.737 ± 1.912	0.180 ± 0.163	49.876 ± 9.229	0.005 ± 0.028
$\Lambda_b^0 \to \pi^+\bar{p}$	0.027 ± 0.019	6.216 ± 2.481	0.659 ± 0.496	0.281 ± 0.158	0.149 ± 0.128	8.856 ± 1.880	0.006 ± 0.005	51.190 ± 8.593

Table 5.10: *PID efficiencies (in %) for the various mass hypotheses obtained using optimised PID requirements for Selection B.*

Decay	Final state hypothesis							
	$K^+\pi^-$	π^+K^-	$\pi^+\pi^-$	K^+K^-	pK^-	$K^+\bar{p}$	$p\pi^-$	$\pi^+\bar{p}$
$B^0 \to K^+\pi^-$	56.643 ± 0.775	0.056 ± 0.003	1.250 ± 0.061	2.519 ± 0.058	0.015 ± 0.000	0.563 ± 0.050	0.868 ± 0.020	0.054 ± 0.003
$B_s^0 \to K^+\pi^-$	56.643 ± 0.775	0.056 ± 0.003	1.250 ± 0.061	2.519 ± 0.058	0.015 ± 0.000	0.563 ± 0.050	0.868 ± 0.020	0.054 ± 0.003
$B^0 \to \pi^+K^-$	0.056 ± 0.003	56.629 ± 0.824	1.257 ± 0.063	2.518 ± 0.060	0.571 ± 0.055	0.015 ± 0.000	0.054 ± 0.004	0.878 ± 0.020
$B_s^0 \to \pi^+K^-$	0.056 ± 0.003	56.629 ± 0.824	1.257 ± 0.063	2.518 ± 0.060	0.571 ± 0.055	0.015 ± 0.000	0.054 ± 0.004	0.878 ± 0.020
$B^0 \to \pi^+\pi^-$	2.379 ± 0.061	2.380 ± 0.057	53.611 ± 0.835	0.108 ± 0.003	0.022 ± 0.002	0.022 ± 0.002	0.654 ± 0.058	0.646 ± 0.053
$B_s^0 \to \pi^+\pi^-$	2.379 ± 0.061	2.380 ± 0.057	53.611 ± 0.835	0.108 ± 0.003	0.022 ± 0.002	0.022 ± 0.002	0.654 ± 0.058	0.646 ± 0.053
$B^0 \to K^+K^-$	1.328 ± 0.063	1.321 ± 0.060	0.029 ± 0.003	59.843 ± 0.761	0.344 ± 0.010	0.345 ± 0.010	0.085 ± 0.003	0.087 ± 0.002
$B_s^0 \to K^+K^-$	1.328 ± 0.063	1.321 ± 0.060	0.029 ± 0.003	59.843 ± 0.761	0.344 ± 0.010	0.345 ± 0.010	0.085 ± 0.003	0.087 ± 0.002
$\Lambda_b^0 \to pK^-$	0.158 ± 0.066	0.569 ± 0.549	0.013 ± 0.011	6.160 ± 2.661	52.002 ± 10.067	0.039 ± 0.027	6.058 ± 1.194	0.032 ± 0.030
$\Lambda_b^0 \to K^+\bar{p}$	0.660 ± 0.509	0.158 ± 0.047	0.014 ± 0.009	6.136 ± 2.522	0.036 ± 0.022	53.509 ± 9.435	0.032 ± 0.028	6.103 ± 1.170
$\Lambda_b^0 \to p\pi^-$	5.816 ± 2.454	0.022 ± 0.020	0.535 ± 0.518	0.262 ± 0.166	2.214 ± 0.509	0.060 ± 0.024	61.422 ± 10.954	0.028 ± 0.030
$\Lambda_b^0 \to \pi^+\bar{p}$	0.028 ± 0.020	5.946 ± 2.520	0.658 ± 0.510	0.277 ± 0.160	0.060 ± 0.035	2.261 ± 0.486	0.018 ± 0.012	61.624 ± 11.585

We also show in Figs. 5.17 and 5.18 and a graphical representation of the predicted statistical uncertainties relative to the two raw asymmetries as a function of the PID and BDT requirements. For each plot we use the values listed in Tab. 5.8 for the requirements not represented, letting the requirement vary over the values used in the optimisation procedure.

The optimised requirements for $\Delta \log \mathcal{L}_{K-\pi}(K)$ and $\Delta \log \mathcal{L}_{K-\pi}(\pi)$ are on the border of the region probed. This is because $\Delta \log \mathcal{L}_{K-\pi}$ is the variable that allows pK^- and $p\pi^-$ final states to be separated. A large contribution of $\Lambda_b^0 \to pK^-$ decays at the $\Lambda_b^0 \to p\pi^-$ peak (and vice versa) may lead to larger systematic uncertainties. As a consequence, the requirement on the $\Lambda_b^0 \to p\pi^-$ PID variable is not further loosened.

5.7 Modification to the invariant-mass model

The invariant-mass model used to fit the spectra is the same described in Sec. 5.5. We apply a few tunings in order to achieve a better stability in the final fits to the data..

5.7.1 Constraints to the invariant-mass resolution model

While performing fast toy studies to validate the fits, some instabilities related to the model used to parameterise the invariant-mass resolution were observed. In order to constrain some of the parameters governing the invariant-mass resolution model we use fully simulated events. We fix the value of the fraction (f) between the two Gaussians of the resolution model to what is observed in simulated $B_s^0 \to K^+K^-$ events, and this parameter is common between all the spectra. In addition, in order to take into account the dependence of σ_1 and σ_2 from the PID requirements, we fix the ratios $\sigma_{1(2)}(K^+\pi^-)/\sigma_{1(2)}(K^+K^-)$, $\sigma_{1(2)}(\pi^+\pi^-)/\sigma_{1(2)}(K^+K^-)$, $\sigma_{1(2)}(pK^-)/\sigma_{1(2)}(K^+K^-)$ and $\sigma_{1(2)}(p\pi^-)/\sigma_{1(2)}(K^+K^-)$ to the values determined from simulation. A complete study and validation of this approach has been done in Ref. [84].
The values of the fractions and the ratio of the widths of the Gaussian functions obtained from the fit to fully simulated events are reported in Tab. 5.11.

5.7.2 Determination of invariant-mass efficiency for the final selections

The values of the p_0 parameters reported in Tab. 5.4, governing the invariant-mass acceptance of the signal model, are determined again from fully simulated events surviving the final kinematic selection and weighted according to the PID efficiency maps of Section 5.4. The values of p_0 for all the decay channels are reported in Tab. 5.12.

5.7.3 Constraints to the partially reconstructed background

Another source of fit instability is observed in the parameters governing the exponential decrease of the ARGUS function in the pK^- and $p\pi^-$ spectra. This is due to the fact

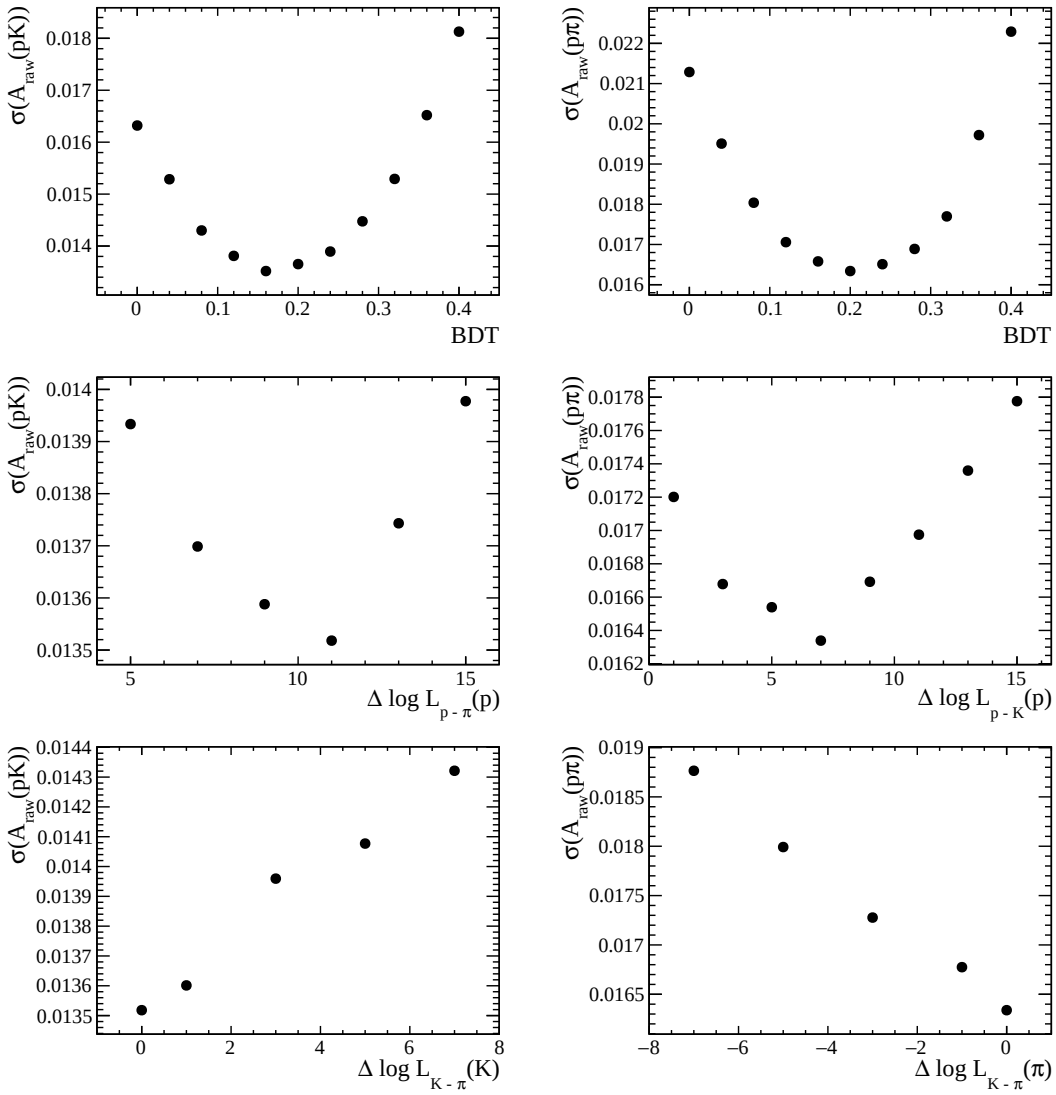

Figure 5.17: *Plots showing the predicted uncertainty on (left) $A_{raw}(pK^-)$ and (right) $A_{raw}(p\pi^-)$ as a function of the BDT requirements. In each plot the other requirements are fixed to the values found by the optimisation procedure.*

that we have no sensitivity on the extraction of the relevant parameters. A very good fit is however obtained by fixing the value of the two c parameters (see Eq. (5.19)) to zero.

5.7.4 Determination of the yields of cross-feed background

In contrast to the fits presented in Section 5.6, now all the cross-feed components are considered in the mass model. The amount of these contributions is constrained to the amount of the same decay where the final state is correctly identified. For example, the

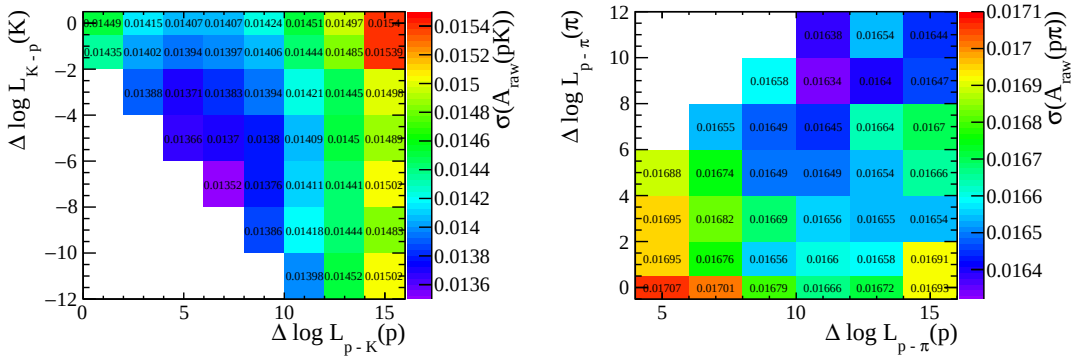

Figure 5.18: *Plots showing the predicted uncertainty on (left) $A_{raw}(pK^-)$ and (right) $A_{raw}(p\pi^-)$ as a function of the PID requirements. In each plot the other requirements are fixed to the values found by the optimisation procedure.*

Table 5.11: *Fraction (f) of the first Gaussian function contributing to the invariant-mass resolution model as used in the final fits. The ratios between the widths of the two Gaussian functions contributing to the invariant-mass resolution model for different final states, with respect to those determined for the K^+K^- spectrum, are obtained from fully simulated events. The strategy used to determine each ratio is explained in Ref. [84].*

Selection A	
Variable	Value
f	0.82 ± 0.02
$\sigma_1(K^+\pi^-)/\sigma_1(K^+K^-)$	0.994 ± 0.008
$\sigma_1(\pi^+\pi^-)/\sigma_1(K^+K^-)$	1.005 ± 0.009
$\sigma_1(pK^-)/\sigma_1(K^+K^-)$	1.024 ± 0.010
$\sigma_1(p\pi^-)/\sigma_1(K^+K^-)$	1.056 ± 0.009
$\sigma_2(K^+\pi^-)/\sigma_2(K^+K^-)$	1.00 ± 0.03
$\sigma_2(\pi^+\pi^-)/\sigma_2(K^+K^-)$	0.99 ± 0.03
$\sigma_2(pK^-)/\sigma_2(K^+K^-)$	1.07 ± 0.04
$\sigma_2(p\pi^-)/\sigma_2(K^+K^-)$	1.16 ± 0.03

Selection B	
Variable	Value
f	0.88 ± 0.02
$\sigma_1(K^+\pi^-)/\sigma_1(K^+K^-)$	0.991 ± 0.008
$\sigma_1(\pi^+\pi^-)/\sigma_1(K^+K^-)$	1.004 ± 0.009
$\sigma_1(pK^-)/\sigma_1(K^+K^-)$	1.016 ± 0.011
$\sigma_1(p\pi^-)/\sigma_1(K^+K^-)$	1.068 ± 0.011
$\sigma_2(K^+\pi^-)/\sigma_2(K^+K^-)$	0.99 ± 0.03
$\sigma_2(\pi^+\pi^-)/\sigma_2(K^+K^-)$	1.00 ± 0.04
$\sigma_2(pK^-)/\sigma_2(K^+K^-)$	1.04 ± 0.04
$\sigma_2(p\pi^-)/\sigma_2(K^+K^-)$	1.15 ± 0.04

yield of $B^0 \to K^+\pi^-$ decays in the K^+K^- spectrum

$$N_{K^+K^-}\left(B^0 \to K^+\pi^-\right) = N\left(B^0 \to K^+\pi^-\right) \cdot \frac{\varepsilon_{K^+K^-}\left(B^0 \to K^+\pi^-\right)}{\varepsilon_{K^+\pi^-}\left(B^0 \to K^+\pi^-\right)}, \tag{5.22}$$

where $N_{K^+K^-}\left(B^0 \to K^+\pi^-\right)$ is the number of $B^0 \to K^+\pi^-$ decays present in the K^+K^- mass spectrum, $N\left(B^0 \to K^+\pi^-\right)$ is the number of $B^0 \to K^+\pi^-$ decays correctly identified by the PID requirements, $\varepsilon_{K^+K^-}\left(B^0 \to K^+\pi^-\right)$ is the probability to assign the K^+K^- hypothesis to a $B^0 \to K^+\pi^-$ decay, and $\varepsilon\left(B^0 \to K^+\pi^-\right)$ is the probability to assign the correct mass hypothesis to a $B^0 \to K^+\pi^-$ decay.

Table 5.12: *Values of the parameter p_0 governing the shape of the invariant-mass acceptance $\varepsilon(m)$ used in the signal model, as determined from fits to the invariant-mass spectrum of fully simulated two-body b-hadron decays.*

Selection A	
Decay	p_0 [c^2/GeV]
$B^0 \to K^+\pi^-$	-0.68 ± 0.07
$B^0 \to \pi^+\pi^-$	-0.35 ± 0.07
$B^0 \to K^+K^-$	-1.01 ± 0.10
$B_s^0 \to \pi^+K^-$	-0.86 ± 0.05
$B_s^0 \to \pi^+\pi^-$	-0.66 ± 0.06
$B_s^0 \to K^+K^-$	-0.98 ± 0.06
$\Lambda_b^0 \to pK^-$	-1.16 ± 0.05
$\Lambda_b^0 \to p\pi^-$	-0.93 ± 0.05

Selection B	
Decay	p_0 [c^2/GeV]
$B^0 \to K^+\pi^-$	-0.85 ± 0.08
$B^0 \to \pi^+\pi^-$	-0.55 ± 0.07
$B^0 \to K^+K^-$	-1.14 ± 0.10
$B_s^0 \to \pi^+K^-$	-1.07 ± 0.05
$B_s^0 \to \pi^+\pi^-$	-0.90 ± 0.06
$B_s^0 \to K^+K^-$	-1.18 ± 0.06
$\Lambda_b^0 \to pK^-$	-1.23 ± 0.06
$\Lambda_b^0 \to p\pi^-$	-1.12 ± 0.05

5.8 Systematic uncertainties

In this section the studies performed in order to asses the main systematic uncertainties affecting the determination of the raw asymmetries of $\Lambda_b^0 \to pK^-$ and $\Lambda_b^0 \to p\pi^-$ decays are presented. The study is based on fast simulated pseudoexperiments generated according to the baseline invariant-mass model. Then, both the baseline model and alternative models are fitted to the generated samples. The distributions of the difference between the raw asymmetries of the $\Lambda_b^0 \to pK^-$ and $\Lambda_b^0 \to p\pi^-$ decays, as obtained using the baseline and alternative models, are used to estimate the systematic uncertainties, calculated as the sums in quadrature of the mean and width of each distribution.

The following sources of systematic uncertainties are considered

- parameterisation of the effect on the invariant-mass shape of signals due to soft photon emission by the final state particles;
- parameterisation of the acceptance as a function of the invariant-mass introduced by the selection criteria;
- parameterisation of the invariant-mass shape used to model two-body b-hadron decays;
- parameterisation of the invariant-mass shape of the combinatorial background component;
- parameterisation of the invariant-mass shape of cross-feed backgrounds;
- parameterisation of the invariant-mass shape of partially reconstructed three-body B decays;

- calibration of PID efficiencies.

5.8.1 Parameterisation of final state radiation

In order to assess a systematic uncertainty due to the parameterisation of final state radiation, the value of the parameter governing the low-mass tail of the signal models is changed by $\pm 1\sigma$ with respect to the baseline value, where σ is the uncertainty on the s parameter determined by fitting fully simulated samples, as reported in Tab. 5.4.

5.8.2 Invariant-mass acceptance

The systematic uncertainty due to the acceptance introduced by the selection criteria in the invariant-mass shape of signals is established varying the value of the parameter p_0 governing the acceptance. In Section 5.7 the values of the p_0 parameter for all the two-body b-hadron decays were determined for the two optimised selections (Selection A and Selection B). For Selection A the values of p_0 range between -1.16 and -0.49, hence fits are performed by fixing alternatively the value of p_0 for all two-body b-hadron decays to these two values. The same thing is done for Selection B, but in this case the maximum and minimum values of p_0 correspond to -0.55 and -1.23, respectively.

5.8.3 Signal invariant-mass model

The modelling of the invariant-mass shape of two-body b-hadron decays does not take into account possible large tails due to bad reconstruction. Studying the mass shape of fully simulated decay events, the large tails can be parameterised with a very wide Gaussian function. This is evident in Fig. 5.19, where the reconstructed invariant mass of fully simulated $B_s^0 \to K^+K^-$ decays is shown, with the result of the best fit overlaid. The model adapted to data is the same as used in Section 5.5.1. The dashed black curve represents a very wide Gaussian function, modelling the tails due to bad reconstruction. In order to assess a systematic uncertainty the alternative model shown in Fig. 5.19 is used to parameterise the invariant-mass shape of signals. The fraction and the width of the additional Gaussian function have been taken from fits to fully simulated events for each decay mode and selection and are reported in Tab. 5.13.

5.8.4 Combinatorial-background invariant-mass model

The systematic uncertainty associated with the parameterisation of the combinatorial background is assessed by substituting the exponential function with a straight line.

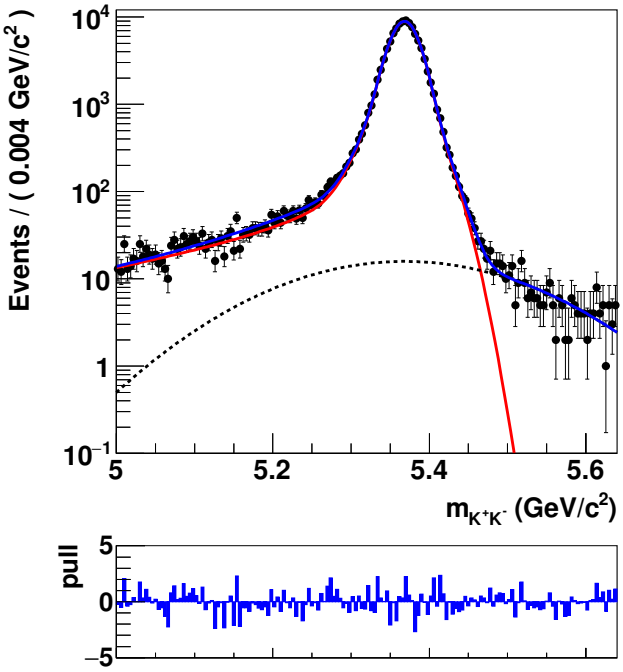

Figure 5.19: *Fit to fully simulated $B_s^0 \to K^+K^-$ decays. The red curve represents the model defined in Sec. 5.5.1. The black dashed curve is a Gaussian function with very wide width used to parameterise the large tails. The blue curve is the sum of the two components.*

Table 5.13: *Values of fraction and widths of the wide Gaussian component used to assess a systematic uncertainty on the signal model.*

	Selection A		Selection B	
Decay	$f_{\text{wide Gaussian}}$	$\sigma_{\text{wide Gaussian}}[\text{GeV}/c^2]$	$f_{\text{wide Gaussian}}$	$\sigma_{\text{wide Gaussian}}[\text{GeV}/c^2]$
$B^0 \to K^+\pi^-$	0.013 ± 0.001	0.087 ± 0.006	0.014 ± 0.001	0.086 ± 0.005
$B_s^0 \to \pi^+K^-$	0.014 ± 0.001	0.093 ± 0.005	0.013 ± 0.001	0.095 ± 0.006
$B^0 \to \pi^+\pi^-$	0.017 ± 0.001	0.084 ± 0.005	0.016 ± 0.001	0.085 ± 0.005
$B_s^0 \to \pi^+\pi^-$	0.016 ± 0.002	0.089 ± 0.006	0.015 ± 0.002	0.092 ± 0.007
$B^0 \to K^+K^-$	0.013 ± 0.002	0.086 ± 0.007	0.012 ± 0.001	0.090 ± 0.008
$B_s^0 \to K^+K^-$	0.011 ± 0.001	0.101 ± 0.007	0.011 ± 0.001	0.099 ± 0.008
$\Lambda_b^0 \to pK^-$	0.017 ± 0.001	0.114 ± 0.004	0.016 ± 0.001	0.115 ± 0.005
$\Lambda_b^0 \to p\pi^-$	0.017 ± 0.001	0.122 ± 0.005	0.019 ± 0.001	0.122 ± 0.005

5.8.5 Parameterisation of partially reconstructed backgrounds in the pK^- and $p\pi^-$ spectra

In order to estimate the systematic uncertainty due to the parameterisation of partially-reconstructed $\Lambda_b^0 \to pK^-X$ and $\Lambda_b^0 \to p\pi^-X$ decays, the fit to the invariant-mass spectrum

is repeated by removing the invariant-mass window where this particular source of background lays, *i.e.* $m_{pK^-} < 5.5\,\text{GeV}/c^2$ and $m_{p\pi^-} < 5.5\,\text{GeV}/c^2$, respectively.

5.8.6 Parameterisation of cross-feed backgrounds invariant-mass shape

The systematic uncertainty related to the modelling of the cross-feed backgrounds is studied modifying the invariant-mass resolution model used to smear the PDF generated from fully simulated events. Since the invariant-mass distributions are generated using the true information, any large tail introduced by the reconstruction is not taken into account. Hence, a third Gaussian function with a very wide width is added to the resolution model, as done for the study of the systematic uncertainty related to the signal model. This fraction and width are the same as in Tab. 5.13.

5.8.7 Summary of systematic uncertainties related to the invariant-mass model

In Figs. 5.20, 5.21, 5.22 and 5.23 the distributions of the difference between the raw asymmetries of the $\Lambda_b^0 \to pK^-$ and $\Lambda_b^0 \to p\pi^-$ decays, using the baseline model and the alternative model, are reported.

5.8.8 Systematic uncertainties related to PID calibration

The treatment of systematic uncertainties coming from possible residual mis-calibration of PID efficiencies is slightly different with respect to the other cases. Ten samples are generated using the baseline model. Then 250 fits are performed, varying the values of the PID efficiencies used in the fit. The PID efficiencies are varied extracting them uniformly in the range $\varepsilon \pm \delta_\varepsilon$, where the values ε and the associated errors δ_ε are taken from Tabs. 5.9 and 5.10. For each sample the width of the distribution of the raw asymmetries for the $\Lambda_b^0 \to pK^-$ and $\Lambda_b^0 \to p\pi^-$ decays is taken as an uncertainty due to PID calibration. The largest width obtained from the ten samples is taken as systematic uncertainty. In Fig. 5.24 the distribution of the difference between the fitted raw asymmetries and the baseline asymmetry for the cases with the largest widths, are reported.

5.8.9 Summary of systematic uncertainties

Table 5.14 reports the values of all the systematic uncertainties discussed in this section.

5.9 Results of invariant-mass fits

In this section, the results of the simultaneous invariant-mass fits to the two-body b-hadron decay spectra perfomed to measure $A_{\text{raw}}(pK^-)$ and $A_{\text{raw}}(p\pi^-)$ are presented. The binned maximum likelihood fits features 43 free parameters

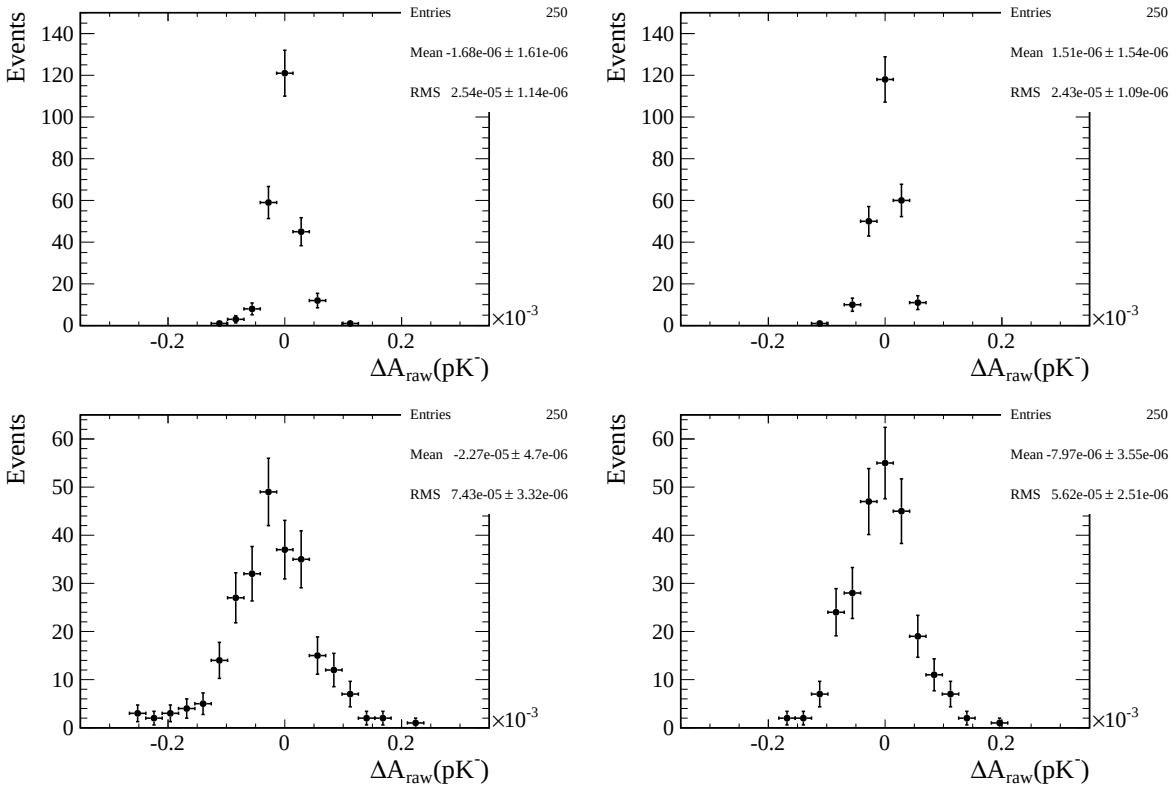

Figure 5.20: *Distributions of the difference between the raw asymmetries of the $\Lambda_b^0 \to pK^-$ decays as obtained from the fits to pseudoexperiments using the baseline and the alternative invariant-mass model. Each plot corresponds to a different alternative model, as explained in the text. Top row: the parameter governing the radiative tail is modified by $\pm 1\sigma$ of its uncertainty, as determined from fully simulated two-body b-hadron decaya samples. Bottom row: the parameter governing the invariant-mass acceptance on the signal is fixed to the lowest and highest values among all decays.*

Table 5.14: *Summary of the systematic uncertainties found in this section.*

Source of systematics uncertainty	$A_{\rm raw}(pK^-)[\%]$	$A_{\rm raw}(p\pi^-)[\%]$
Radiative tail	0.003	0.005
Invariant-mass acceptance	0.008	0.006
Signal model	0.008	0.010
Combinatorial background model	0.005	0.008
Cross-feed model	0.002	0.003
Partially reconstructed model	0.232	0.467
Particle identification	0.572	0.739
Sum in quadrature	0.617	0.874

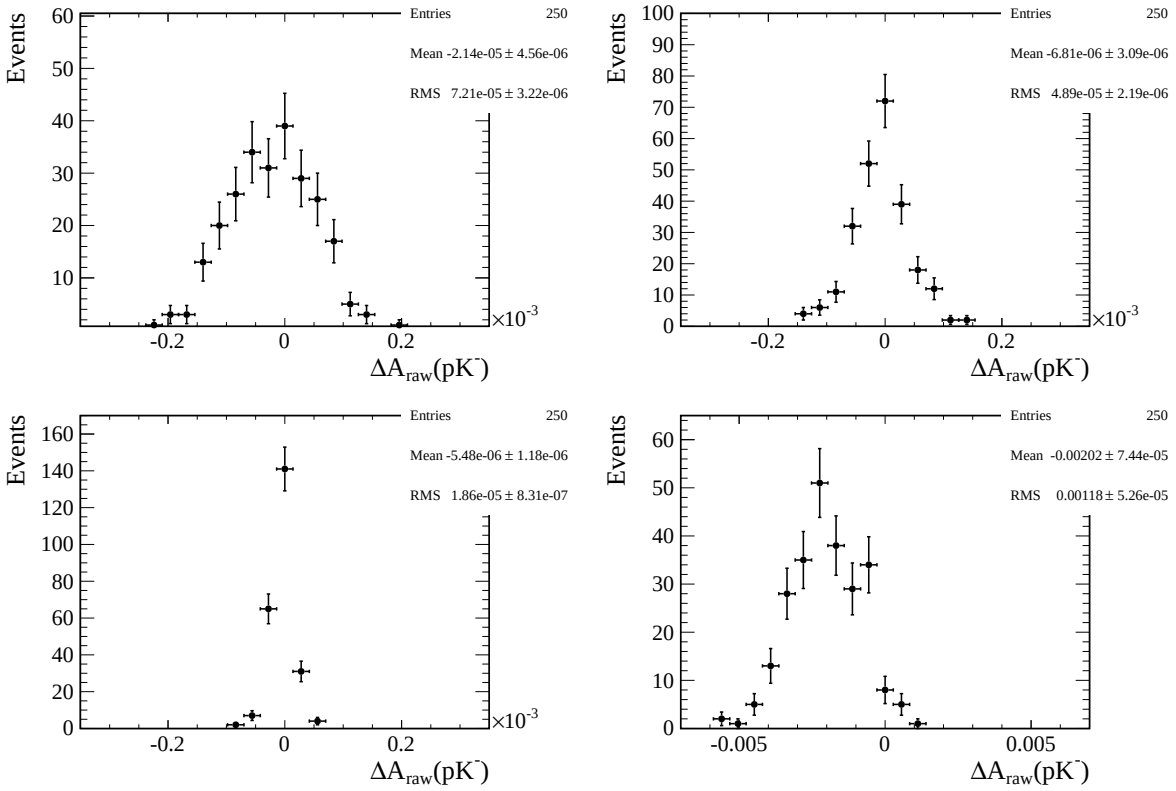

Figure 5.21: *Distributions of the difference between the raw asymmetries of the $\Lambda_b^0 \to pK^-$ decays as obtained from the fits to pseudoexperiments using the baseline and the alternative invariant-mass model. Each plot corresponds to a different alternative model, as explained in the text. Top row: (left) alternative model for signal shape and (right) alternative model for combinatorial background shape. Bottom row: (left) alternative parameterisation of cross-feed backgrounds and (right) alternative fit model ignoring events with $m_{pK^-} < 5.5\,\mathrm{GeV}/c^2$.*

- four raw asymmetries for the two-body b-hadron decay modes: $A_{\rm raw}(B^0 \to K^+\pi^-)$, $A_{\rm raw}(B_s^0 \to \pi^+K^-)$, $A_{\rm raw}(B^0 \to K^+\pi^-)$, $A_{\rm raw}(\Lambda_b^0 \to pK^-)$, $A_{\rm raw}(\Lambda_b^0 \to p\pi^-)$;
- three raw asymmetries for the combinatorial backgrounds relative to the $K^+\pi^-$, pK^- and $p\pi^-$ final states;
- four raw asymmetries for the three-body partially reconstructed background components in the $K^+\pi^-$, pK^-, $p\pi^-$ invariant-mass spectra; the number of parameters results to be greater than the number of final states since for the $K^+\pi^-$ two sources of partially reconstructed backgrounds are considered, one from B^0 decays and the other from B_s^0 decays;
- eight signal yields for the two-body b-hadron decay modes: $N_{\rm sig}(B^0 \to K^+\pi^-)$, $N_{\rm sig}(B^0 \to K^+K^-)$, $N_{\rm sig}(B^0 \to \pi^+\pi^-)$, $N_{\rm sig}(B_s^0 \to \pi^+K^-)$, $N_{\rm sig}(B_s^0 \to K^+K^-)$, $N_{\rm sig}(B_s^0 \to \pi^+\pi^-)$, $N_{\rm sig}(\Lambda_b^0 \to pK^-)$, $N_{\rm sig}(\Lambda_b^0 \to p\pi^-)$;

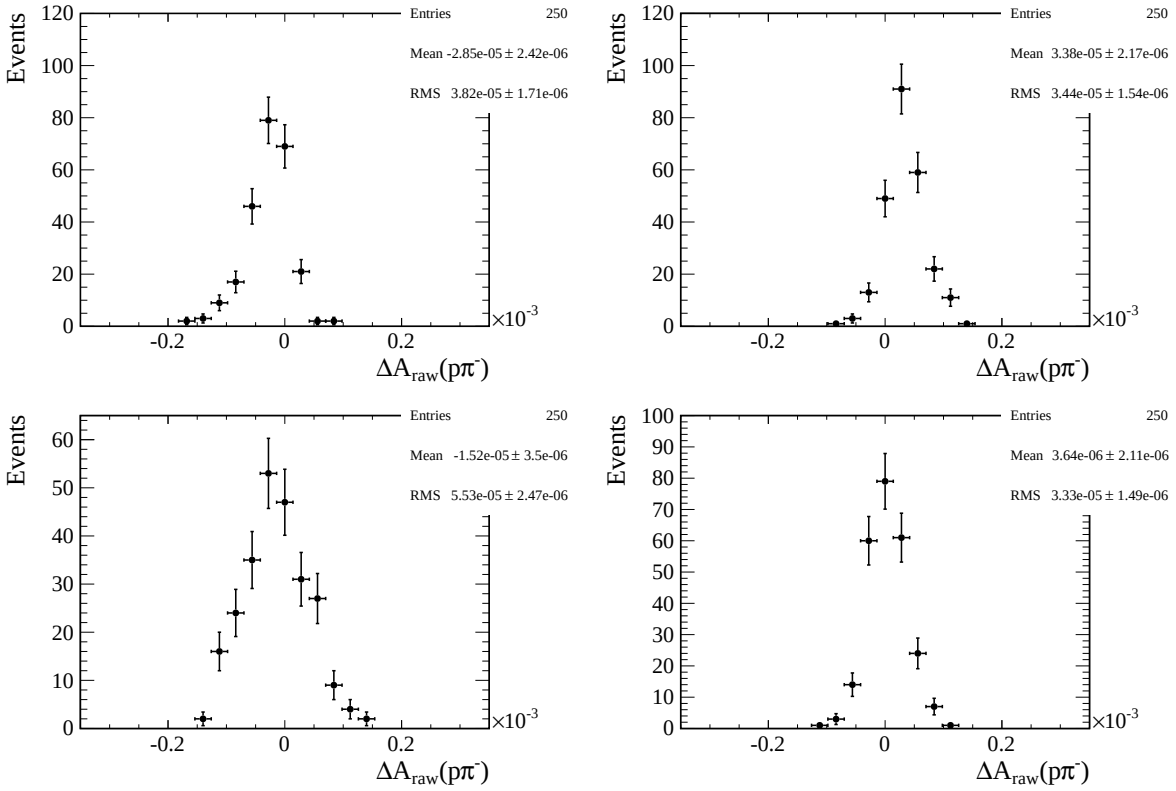

Figure 5.22: *Distributions of the difference between the raw asymmetries of the $\Lambda_b^0 \to p\pi^-$ decays as obtained from the fits to pseudoexperiments using the baseline and the alternative invariant-mass model. Each plot corresponds to a different alternative model, as explained in the text. Top row: the parameter governing the radiative tail has been modified by $\pm 1\sigma$ of its uncertainty determined from fully simulated two-body b-hadron samples. Bottom row: the parameter governing the invariant-mass acceptance on the signal is fixed to the lowest and highest values among all decays.*

- five yields for the combinatorial background relative to $K^+\pi^-$, K^+K^-, $\pi^+\pi^-$, pK^- and $p\pi^-$ final states;
- six yields for the three-body partially reconstructed background components contributing to the $K^+\pi^-$, K^+K^-, $\pi^+\pi^-$, pK^- and $p\pi^-$ final states; as for the raw asymmetries, the $K^+\pi^-$ spectrum is parameterized using two yields instead of one;
- three parameters governing the exponential tail of the ARGUS PDF that models the three-body partially reconstructed background in the $K^+\pi^-$, pK^-, $p\pi^-$ invariant-mass spectra; in this case the parameter governing the ARGUS shape in the $K^+\pi^-$ is in common between B^0 and B_s^0 modes; in the case of pK^- and $p\pi^-$ final states the values of the parameters are fixed to zero as there is no sensitivity to determine them from data;

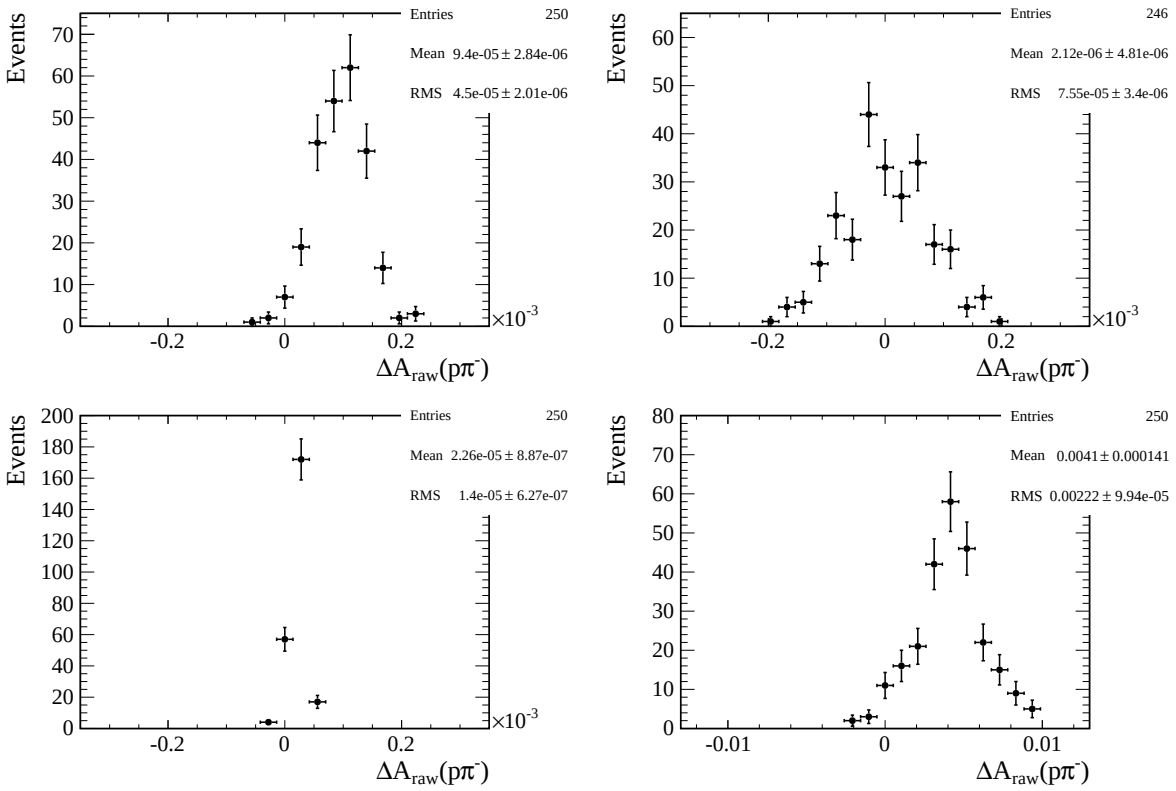

Figure 5.23: *Distributions of the difference between the raw asymmetries of the $\Lambda_b^0 \to p\pi^-$ decays as obtained from the fits to pseudoexperiments using the baseline and the alternative invariant-mass model. Each plot corresponds to a different alternative model, as explained in the text. Top row: (left) alternative model for signal shape and (right) alternative model for combinatorial background shape. Bottom row: (left) alternative parameterisation of cross-feed backgrounds and (right) alternative fit model ignoring events with $m_{p\pi^-} < 5.5\,\mathrm{GeV}/c^2$.*

- three mean values (defined as δ_m in Eq. 5.14), of the Gaussian functions describing the invariant-mass resolution; the means are three since we are considering three different kinds of b hadrons: B^0, B_s^0 and Λ_b^0;
- two standard deviations, for the K^+K^- final state, relative to the Gaussian functions composing the mass resolution for the K^+K^- invariant-mass spectra.
- five exponential slopes for the combinatorial background relative to the $K^+\pi^-$, K^+K^-, $\pi^+\pi^-$, pK^- and $p\pi^-$.

The PID selection criteria for pK^- and $p\pi^-$ final states are taken from Ref. [90] and are reported in Tab. 5.15.

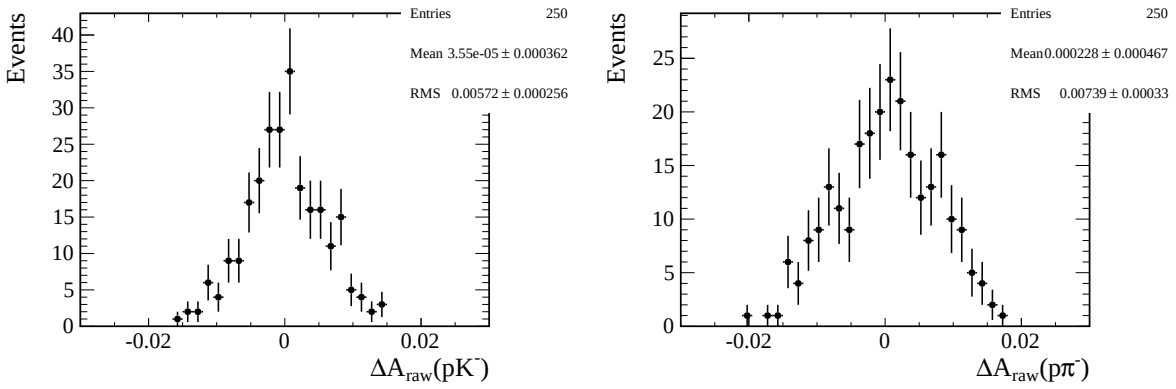

Figure 5.24: *Distributions of the difference between the raw asymmetries and the baseline asymmetry of the (left) $\Lambda_b^0 \to pK^-$ and (right) $\Lambda_b^0 \to p\pi^-$ decays as obtained from the fits to a pseudoexperiments by modifying each time the PID efficiencies by their uncertainties.*

Table 5.15: *PID selection criteria for the $K^+\pi^-$, K^+K^-, and $\pi^+\pi^-$ mass hypotheses. To obtain the charge conjugate final states, h^+ and h'^- must be exchanged.*

$K^+\pi^-$			K^+K^-			$\pi^+\pi^-$		
Cut		Value	Cut		Value	Cut		Value
$\Delta\log\mathcal{L}_{K-\pi}(h^+)$	$>$	3	$\Delta\log\mathcal{L}_{K-\pi}(h^+)$	$>$	3	$\Delta\log\mathcal{L}_{K-\pi}(h^+)$	$<$	-3
$\Delta\log\mathcal{L}_{K-p}(h^+)$	$>$	-5	$\Delta\log\mathcal{L}_{K-p}(h^+)$	$>$	-5	$\Delta\log\mathcal{L}_{p-\pi}(h^+)$	$<$	5
$\Delta\log\mathcal{L}_{K-\pi}(h'^-)$	$<$	-3	$\Delta\log\mathcal{L}_{K-\pi}(h'^-)$	$>$	3	$\Delta\log\mathcal{L}_{K-\pi}(h'^-)$	$<$	-3
$\Delta\log\mathcal{L}_{p-\pi}(h'^-)$	$<$	5	$\Delta\log\mathcal{L}_{K-p}(h'^-)$	$>$	-5	$\Delta\log\mathcal{L}_{p-\pi}(h'^-)$	$<$	5

Table 5.16: *PID selection criteria applied for the pK^- and $p\pi^-$ mass hypotheses when the selection is optimised for the other final state. To obtain the charge conjugate final states, h^+ and h'^- must be exchanged.*

Selection B			Selection A		
pK^-			$p\pi^-$		
Cut		Value	Cut		Value
$\Delta\log\mathcal{L}_{p-\pi}(h^+)$	$>$	10	$\Delta\log\mathcal{L}_{p-\pi}(h^+)$	$>$	10
$\Delta\log\mathcal{L}_{p-K}(h^+)$	$>$	10	$\Delta\log\mathcal{L}_{p-K}(h^+)$	$>$	10
$\Delta\log\mathcal{L}_{K-\pi}(h'^-)$	$>$	3	$\Delta\log\mathcal{L}_{K-\pi}(h'^-)$	$<$	-3
$\Delta\log\mathcal{L}_{K-p}(h'^-)$	$>$	-5	$\Delta\log\mathcal{L}_{p-\pi}(h'^-)$	$<$	5

5.9.1 Invariant-mass fits for Selection A

In the left part of Tab.5.17 the signal yields for all the two-body b-hadron decays are reported, as obtained from the invariant-mass fits to the data sample selected using Selection A. The pK^- raw asymmetry is also reported. In Figs. 5.25 and 5.26 the fits to all the invariant-mass spectra after the requirements imposed by selection A are shown.

Table 5.17: *Values of yields and Λ_b^0 modes raw asymmetries obtained from the invariant-mass fits with (left) Selection A and (right) Selection B.*

Selection A		Selection B	
Parameter	Fit result	Parameter	Fit result
$N_{\rm sig}(B^0 \to K^+\pi^-)$	123853 ± 440	$N_{\rm sig}(B^0 \to K^+\pi^-)$	111148 ± 400
$N_{\rm sig}(B^0 \to K^+K^-)$	882 ± 96	$N_{\rm sig}(B^0 \to K^+K^-)$	843 ± 82
$N_{\rm sig}(B^0 \to \pi^+\pi^-)$	31551 ± 232	$N_{\rm sig}(B^0 \to \pi^+\pi^-)$	28372 ± 207
$N_{\rm sig}(B_s^0 \to \pi^+K^-)$	9278 ± 173	$N_{\rm sig}(B_s^0 \to \pi^+K^-)$	8121 ± 150
$N_{\rm sig}(B_s^0 \to K^+K^-)$	44310 ± 252	$N_{\rm sig}(B_s^0 \to K^+K^-)$	39610 ± 230
$N_{\rm sig}(B_s^0 \to \pi^+\pi^-)$	948 ± 90	$N_{\rm sig}(B_s^0 \to \pi^+\pi^-)$	780 ± 67
$N_{\rm sig}(\Lambda_b^0 \to pK^-)$	8847 ± 124	$N_{\rm sig}(\Lambda_b^0 \to pK^-)$	6483 ± 94
$N_{\rm sig}(\Lambda_b^0 \to p\pi^-)$	5514 ± 100	$N_{\rm sig}(\Lambda_b^0 \to p\pi^-)$	6025 ± 105
$A_{\rm raw}(pK^-)$	$(1.004 \pm 1.349)\%$	$A_{\rm raw}(p\pi^-)$	$(0.482 \pm 1.669)\%$

5.9.2 Invariant-mass fits for Selection B

In the right part of Tab. 5.17 the signal yields for all the two-body b-hadron decays are reported, as obtained from the invariant-mass fits to the data sample selected using Selection B. The $p\pi^-$ raw asymmetry is also reported. In Figs. 5.27 and 5.28 the fits to all the invariant-mass spectra after the requirements imposed by selection A are shown.

5.9.3 Studies with fast pseudoexperiments

In order to validate the global fit the baseline invariant-mass model is used to generate and fit 1000 pseudoexperiments. The yields of the various two-body b-hadron decay modes used in the fast generation are reported in Tab. 5.17. The pull distributions for the pK^- and $p\pi^-$ raw asymmetries are shown in Fig. 5.29.

5.10 Instrumental and production asymmetries

In order to get the physical *CP* asymmetries, one needs to subtract from the raw asymmetries different sources of instrumental and production asymmetries

$$A_{CP}(pK^-) = A_{\rm raw}(pK^-) - A_{\rm D}(p) - A_{\rm D}(K^-) - A_{\rm PID}(pK^-) - A_{\rm P}(\Lambda_b^0), \quad (5.23)$$

$$A_{CP}(p\pi^-) = A_{\rm raw}(p\pi^-) - A_{\rm D}(p) - A_{\rm D}(\pi^-) - A_{\rm PID}(p\pi^-) - A_{\rm P}(\Lambda_b^0). \quad (5.24)$$

In the following we will discuss the determination of each nuisance asymmetry.

5.10.1 Proton detection asymmetry

As of today, no data-driven methods have been developed in order to measure the proton detection asymmetry. This is due to the fact that in order to measure the proton detection

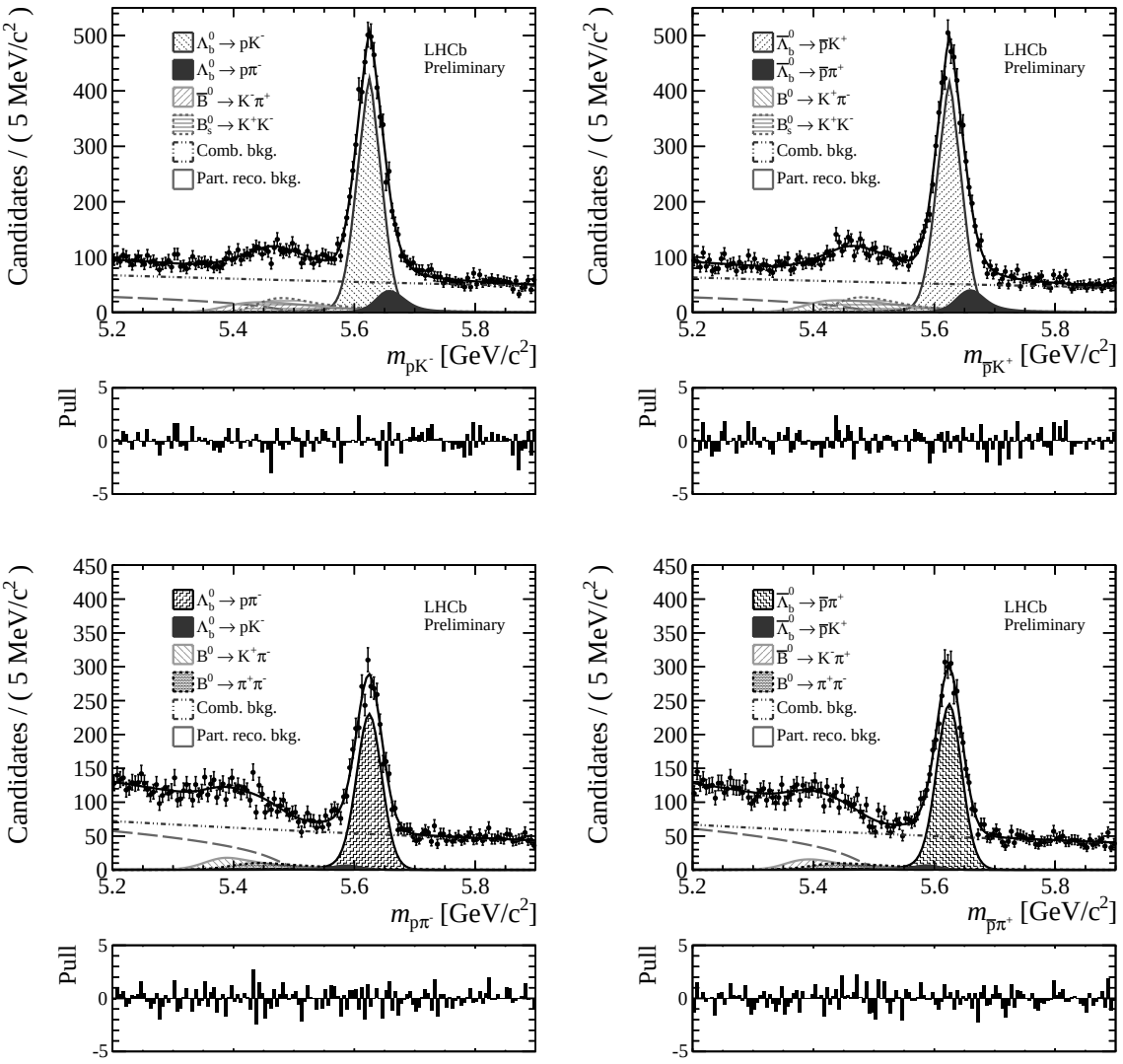

Figure 5.25: *Invariant-mass distributions of the (top left) pK^-, (top right) $\overline{p}K^+$, (bottom left) $p\pi^-$ and (bottom right) $\overline{p}\pi^+$ spectra after selection A. The curves superimposed to the data points represent the result of the best fit.*

asymmetry one should identify a decay channel that is reconstructible even if the proton is not reconstructed. In this way one could calculate a reconstruction efficiency taking the ratio of the number of partially reconstructed decays over the number of fully reconstructed decays. The problem with this approach is that no decay channel with sufficient statistics and with the proper characteristic has been identified yet. Fully simulated events are then used to determine the proton detection asymmetry. Extensive studies were performed to compare the proton and antiproton cross-sections with the detector material used in the simulation with existing measurements. A good agreement is observed. The main

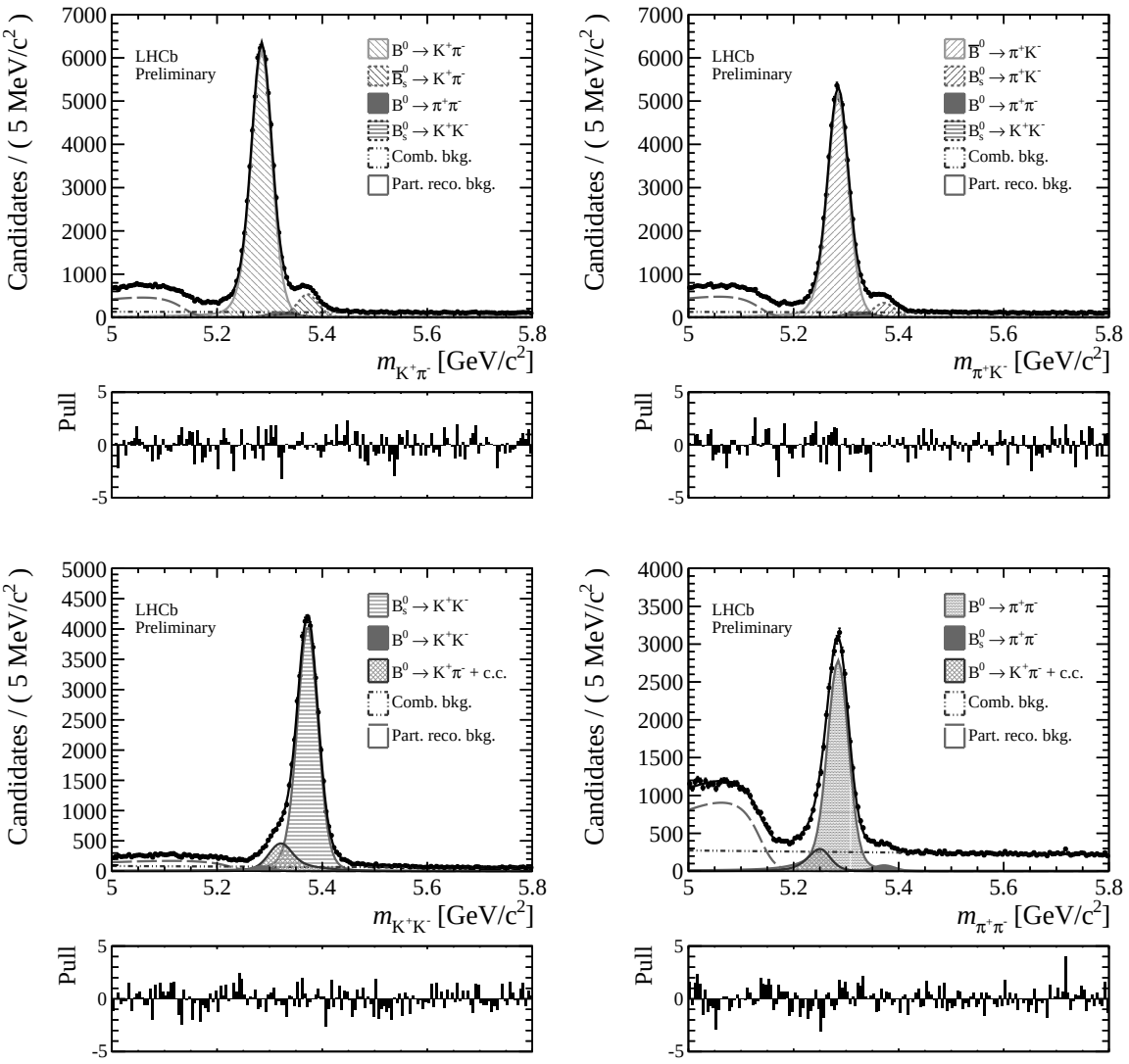

Figure 5.26: *Invariant-mass distribution of the (top left) $K^+\pi^-$, (top right) $K^-\pi^+$, (bottom left) K^+K^- and (bottom right) $\pi^+\pi^-$ spectra after selection A. The curves superimposed to the data points represent the result of the best fit.*

systematic uncertainty is given by the imperfect knowledge of the detector material.

The proton (antiproton) reconstruction efficiency is calculated as

$$\varepsilon_{\text{rec.}}(p(\overline{p})) = \frac{N^{MC}_{\text{rec.}}(p(\overline{p}))}{N^{MC}_{\text{gen.}}(p(\overline{p}))}, \tag{5.25}$$

where $N^{MC}_{\text{rec.}}$ is the number of reconstructed decays and $N^{MC}_{\text{gen.}}$ is the number of generated $\Lambda_b^0 \to \Lambda_c^+ \ (pK^-\pi^+)\mu^-\overline{\nu}_\mu$ decays. These efficiencies are measured as a function of the

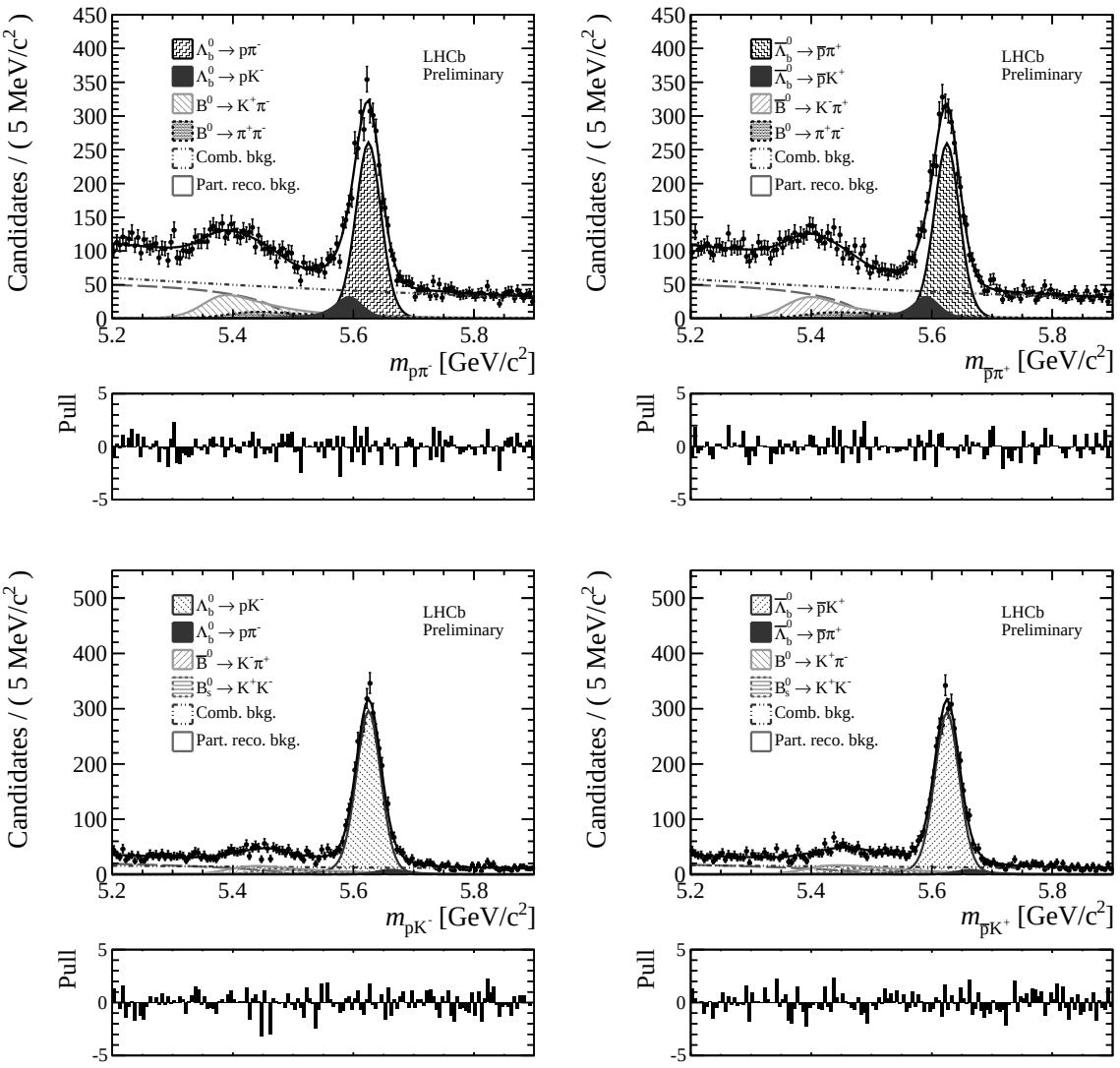

Figure 5.27: *Invariant-mass distribution of the (top left) $p\pi^-$, (top right) $\overline{p}\pi^+$, (bottom left) pK^- and (bottom right) $\overline{p}K^+$ spectra after selection B. The curves superimposed to the data points represent the result of the best fit.*

proton momentum, since it is known that the interaction cross-sections of protons and antiprotons in the detector material depend on the particle momentum.

The measured efficiency as a function of the momentum are reported in Tab. 5.18, together with the proton detection asymmetry, that is defined as

$$A_{\rm D}^j(p) = \frac{\varepsilon_{\rm rec.}^j(p) - \varepsilon_{\rm rec.}^j(\overline{p})}{\varepsilon_{\rm rec.}^j(p) + \varepsilon_{\rm rec.}^j(\overline{p})} \ , \tag{5.26}$$

where the index j runs over the proton momentum bins, as defined in Tab. 5.18. The

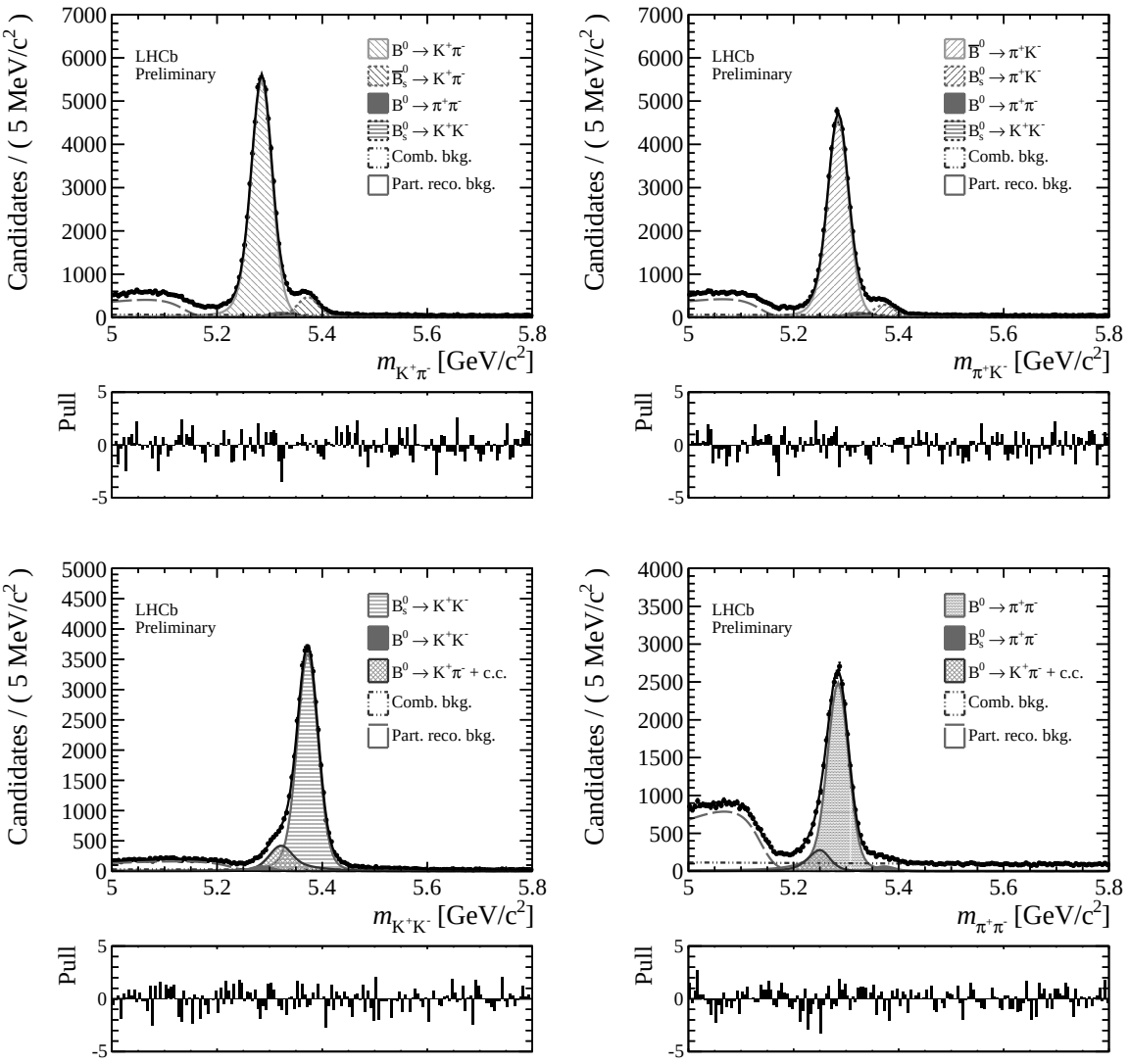

Figure 5.28: *Invariant-mass distribution of the (top left) $K^+\pi^-$, (top right) $K^-\pi^+$, (bottom left) K^+K^- and (bottom right) $\pi^+\pi^-$ spectra after selection B. The curves superimposed to the data points represent the result of the best fit.*

proton detection asymmetry as a function of the proton momentum is shown in Fig. 5.30.

The last two columns of Tab. 5.18 reports the weights, defined as $w_j = \sum_i s_{i,j} / \sum_i s_i$, where $s_{i,j}$ is the sWeight relative to the i-th event contained in the j-th proton momentum bin and the index i runs over all the events in the $\Lambda_b^0 \to pK^-$ and $\Lambda_b^0 \to p\pi^-$ samples. The background-subtracted proton momentum distributions for $\Lambda_b^0 \to pK^-$ and $\Lambda_b^0 \to p\pi^-$ decasy are shown in Fig. 5.31. The value of the proton detection asymmetry relative to

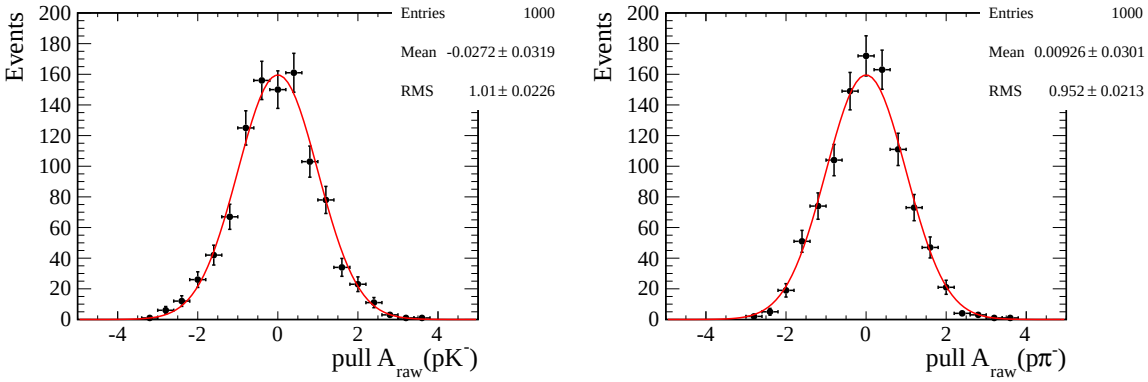

Figure 5.29: *Pull distributions relative to the (left) $\Lambda_b^0 \to pK^-$ and (right) $\Lambda_b^0 \to p\pi^-$ raw asymmetries. Gaussian functions with mean equal to zero and width equal to one are superimposed.*

Table 5.18: *Reconstruction efficiencies for fully simulated protons and antiprotons, proton detection asymmetry and weights calculated from the background-subtracted momentum distributions of $\Lambda_b^0 \to pK^-$ and $\Lambda_b^0 \to p\pi^-$ decays, respectively. Note that the for the asymmetry the first uncertainty is statistical and the second is due to the limited knowledge of the LHCb material budget. This systematic uncertainty is 100% correlated among the bins.*

Bin	p GeV/c	$\varepsilon_{\text{rec.}}(p)$	$\varepsilon_{\text{rec.}}(\overline{p})$	$A_{\text{D}}^j(p)$ [%]	$\omega_j^{\Lambda_b^0 \to pK^-}$	$\omega_j^{\Lambda_b^0 \to p\pi^-}$
1	$(9, 12)$	0.7442 ± 0.0005	0.7045 ± 0.0005	$2.737 \pm 0.047 \pm 0.263$	0.010 ± 0.002	0.005 ± 0.001
2	$(12, 15)$	0.7692 ± 0.0005	0.7350 ± 0.0005	$2.272 \pm 0.050 \pm 0.237$	0.048 ± 0.003	0.042 ± 0.003
3	$(15, 25)$	0.7884 ± 0.0003	0.7597 ± 0.0004	$1.858 \pm 0.032 \pm 0.204$	0.214 ± 0.007	0.218 ± 0.007
4	$(25, 30)$	0.7933 ± 0.0006	0.7694 ± 0.0006	$1.530 \pm 0.055 \pm 0.174$	0.102 ± 0.004	0.109 ± 0.005
5	$(30, 35)$	0.7804 ± 0.0007	0.7602 ± 0.0007	$1.306 \pm 0.064 \pm 0.166$	0.092 ± 0.004	0.097 ± 0.004
6	$(35, 40)$	0.7426 ± 0.0008	0.7226 ± 0.0008	$1.369 \pm 0.078 \pm 0.153$	0.086 ± 0.004	0.091 ± 0.004
7	$(40, 50)$	0.7128 ± 0.0007	0.6975 ± 0.0007	$1.083 \pm 0.067 \pm 0.140$	0.122 ± 0.004	0.131 ± 0.005
8	$(50, 60)$	0.6656 ± 0.0008	0.6515 ± 0.0008	$1.068 \pm 0.087 \pm 0.135$	0.091 ± 0.004	0.090 ± 0.004
9	$(60, 70)$	0.5963 ± 0.0009	0.5883 ± 0.0010	$0.680 \pm 0.114 \pm 0.125$	0.068 ± 0.003	0.068 ± 0.004
10	$(70, 100)$	0.5587 ± 0.0008	0.5522 ± 0.0008	$0.579 \pm 0.100 \pm 0.118$	0.120 ± 0.004	0.118 ± 0.005
11	$(100, 250)$	0.5262 ± 0.0010	0.5195 ± 0.0010	$0.642 \pm 0.135 \pm 0.118$	0.046 ± 0.003	0.032 ± 0.003

the $\Lambda_b^0 \to pK^-$ and $\Lambda_b^0 \to p\pi^-$ decays is found to be

$$A_{\text{D}}^{\Lambda_b^0 \to pK^-}(p) = \sum_j \omega_j^{\Lambda_b^0 \to pK^-} A_{\text{D}}^j(p) = (+1.296 \pm 0.030 \pm 0.161)\% \ ,$$

$$A_{\text{D}}^{\Lambda_b^0 \to p\pi^-}(p) = \sum_j \omega_j^{\Lambda_b^0 \to p\pi^-} A_{\text{D}}^j(p) = (+1.294 \pm 0.031 \pm 0.161)\% \ ,$$

where the first uncertainty is statistical and the second is due to limited knowledge of the LHCb material budget.

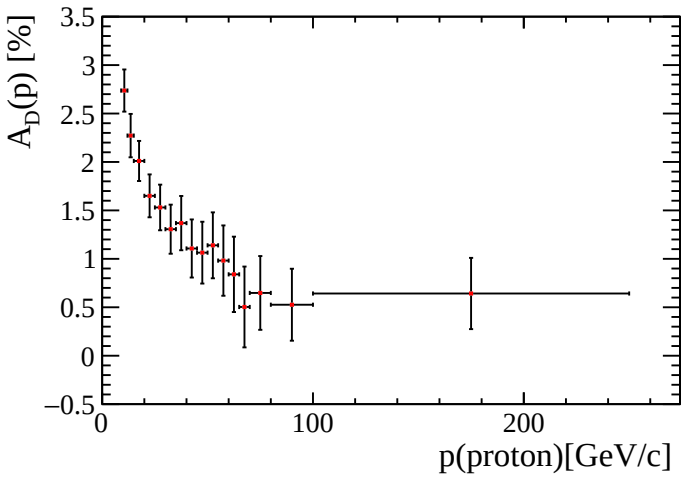

Figure 5.30: *Values of $A_{\rm D}^{j}(p)$ as a function of the proton momentum.*

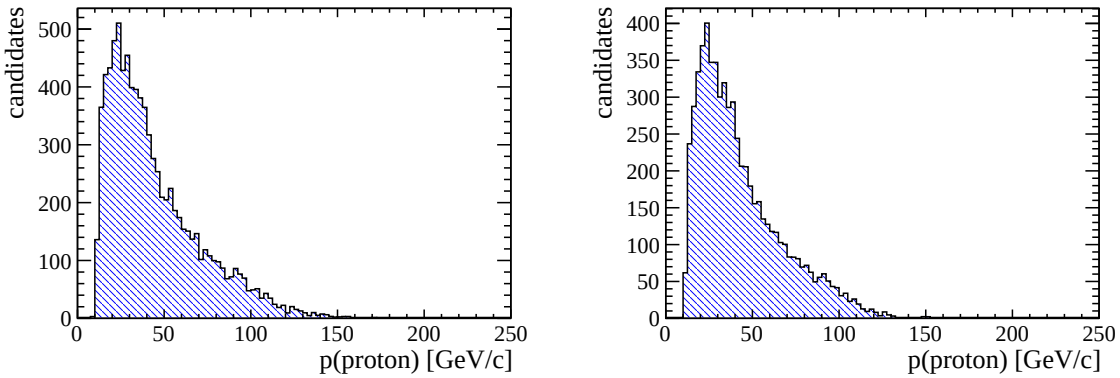

Figure 5.31: *Background-subtracted proton momentum distributions for (left) $\Lambda_b^0 \to pK^-$ and (right) $\Lambda_b^0 \to p\pi^-$ decays.*

5.10.2 Kaon detection asymmetry

The kaon detection asymmetry is defined as

$$A_{\rm D}(K^-) = \frac{\varepsilon_{\rm rec.}(K^-) - \varepsilon_{\rm rec.}(K^+)}{\varepsilon_{\rm rec.}(K^-) + \varepsilon_{\rm rec.}(K^+)}, \tag{5.27}$$

where $\varepsilon_{\rm rec.}$ stands for the reconstruction efficiency of the given particle. The kaon detection asymmetry can be obtained by $D^+ \to K^-\pi^+\pi^+$ and $D^+ \to K^0_S\pi^+$ control modes. A full discussion on the procedure employed to obtain the kaon detection asymmetry is reported in Ref. [81]; here we report in Tab .5.19 only the values of the kaon detection asymmetry as a function of the kaon momentum as obtained in Ref. [81]. The values are shown in Fig. 5.32.

Table 5.19: *Values of $A_{\rm D}^j(K^-) + A_{\rm D}(K^0)$, divided by data taking year and magnet polarity.*

		$A_{\rm D}^j(K^-) + A_{\rm D}(K^0)$[%]			
Bin	$p(K)$ [GeV/c]	2011 Up	2011 Down	2012 Up	2012 Down
1	2 - 10	-1.36 ± 0.48	-1.98 ± 0.40	-0.71 ± 0.23	-1.04 ± 0.24
2	10 - 17.5	-1.35 ± 0.48	-1.74 ± 0.40	-1.45 ± 0.26	-0.54 ± 0.27
3	17.5 - 22.5	-1.70 ± 0.71	-0.20 ± 0.59	-1.12 ± 0.41	0.45 ± 0.42
4	22.5 - 30	-1.05 ± 0.74	-0.01 ± 0.64	-0.83 ± 0.44	-0.57 ± 0.45
5	30 - 50	-1.30 ± 0.77	-1.30 ± 0.65	-1.46 ± 0.46	0.23 ± 0.47
6	50 - 70	-1.05 ± 1.33	-1.59 ± 1.17	-1.23 ± 0.83	1.01 ± 0.90

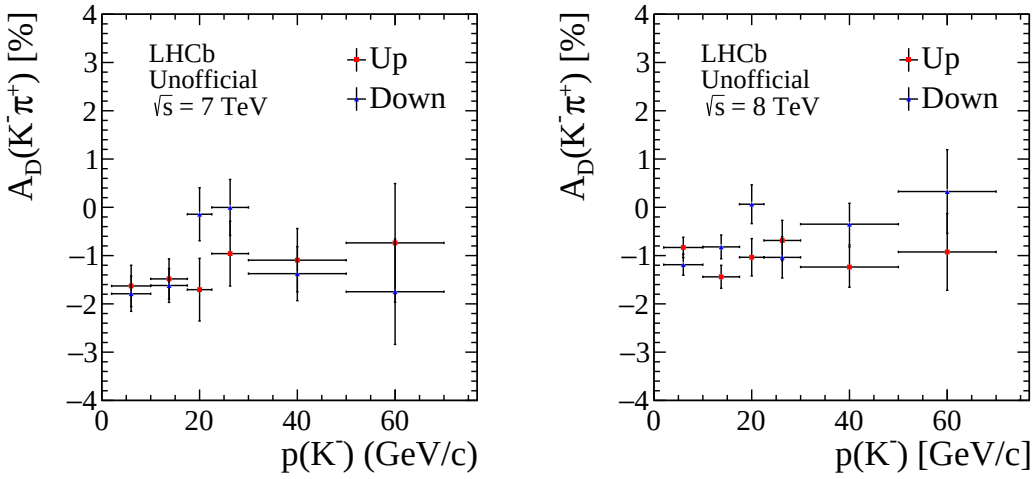

Figure 5.32: *Values of $A_{\rm D}^j(K^-) + A_{\rm D}(K^0)$, for (top left) 2011 data, (top right) and 2012 data. The red dots refer to magnet up data, while the blue ones to magnet down.*

Since this analysis is performed on the whole Run 1 data sample, we take the arithmetic mean between Up and Down values contained in Tab. 5.19, separately for 2011 and 2012. Finally, we take the weighted average between the 2011 and 2012 values. The final numbers as a function of the kaon momentum are reported in Tab. 5.20.

In order to calculate the kaon detection asymmetry on the $\Lambda_b^0 \to pK^-$ sample we need to reweight the values of Tab. 5.20 to match the kaon momentum distribution of kaons from $\Lambda_b^0 \to pK^-$. In Fig. 5.33 the background-subtracted kaon momentum distribution from $\Lambda_b^0 \to pK^-$ decays is shown. From this distribution we can calculate weights, given by the formula $w_j = \sum_i s_{i,j} / \sum_i s_i$, where $s_{i,j}$ is the sWeight relative to the i-th event contained in the j-th kaon momentum bin and the index i runs over all the events in the sample. The values of the weights w_j are reported in Tab. 5.20.

Since the measurement of the kaon detection asymmetry is performed up to 70 GeV/c,

Table 5.20: *Values of $A_{\rm D}^j(K^-) + A_{\rm D}(K^0)$ obtained taking the arithmetic average of up and down values (separately by year) reported in Tab. 5.19 and finally the weighted average between 2011 and 2012 values. The central value and uncertainty in the last bin are obtained as explained in the text. The weights are reported in the last column.*

Bin	$p(K)$ [GeV/c]	$A_{\rm D}^j(K^-) + A_{\rm D}(K^0)$[%]	w_j
1	$2 - 10$	-1.050 ± 0.147	0.034 ± 0.002
2	$10 - 17.5$	-1.141 ± 0.161	0.129 ± 0.004
3	$17.5 - 22.5$	-0.512 ± 0.248	0.095 ± 0.003
4	$22.5 - 30$	-0.650 ± 0.265	0.135 ± 0.004
5	$30 - 50$	-0.820 ± 0.275	0.259 ± 0.005
6	$50 - 70$	-0.501 ± 0.504	0.149 ± 0.004
7	$70 - 250$	-0.501 ± 1.007	0.199 ± 0.005

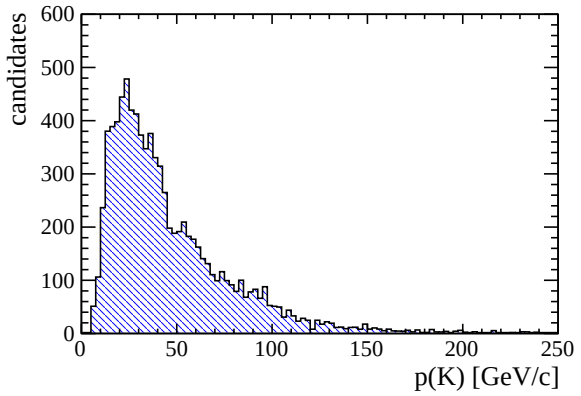

Figure 5.33: *Background-subtracted momentum distribution of kaons from $\Lambda_b^0 \to pK^-$ decays.*

whereas the distribution shown in Fig. 5.33 extends well above that value, a bin from 70 to 250 GeV/c of kaon momentum is added, taking the central value of the last bin and doubling its uncertainty. The last bin will thus take the value $A_{\rm D}^7(K^-) + A_{\rm D}(K^0) = (-0.501 \pm 1.007)\%$. The correction due to the K^0 detection asymmetry is calculated in Ref. [91] and it is $A_{\rm D}(K^0) = 0.054 \pm 0.014\%$.

The value of the kaon detection asymmetry relative to $\Lambda_b^0 \to pK^-$ decays is found to be

$$A_{\rm D}(K^-) = \left[\sum_j \omega_j A_{\rm D}^j(K^-)\right] - A_{\rm D}(K^0) = (-0.760 \pm 0.231)\% \ .$$

Table 5.21: *Values of the pion detection asymmetry in various ranges of pion momentum, divided by year and magnet polarity.*

2011			
		Up	Down
Bin	π momentum [GeV/c]	$A_{\rm D}(\pi^+)$ [%]	
1	2-6	-0.45 ± 0.43	-0.59 ± 0.36
2	6-15	-0.47 ± 0.29	0.34 ± 0.24
3	15-20	-0.22 ± 0.42	0.14 ± 0.34
4	20-30	-0.31 ± 0.45	0.18 ± 0.37
5	30-40	-0.11 ± 0.68	0.04 ± 0.56
6	40-50	0.88 ± 0.96	0.04 ± 0.80
7	50-100	0.56 ± 1.05	-0.49 ± 0.88
2012			
		Up	Down
Bin	π momentum [GeV/c]	$A_{\rm D}(\pi^+)$ [%]	
1	2-6	-1.21 ± 0.21	0.32 ± 0.22
2	6-15	-0.52 ± 0.15	-0.00 ± 0.15
3	15-20	0.08 ± 0.21	-0.12 ± 0.21
4	20-30	0.04 ± 0.22	-0.12 ± 0.22
5	30-40	0.15 ± 0.33	-0.73 ± 0.33
6	40-50	0.15 ± 0.48	-0.50 ± 0.48
7	50-100	0.62 ± 0.51	-1.07 ± 0.51

5.10.3 Pion detection asymmetry

The pion detection asymmetry is defined as

$$A_{\rm D}(\pi^-) = \frac{\varepsilon_{\rm rec.}(\pi^-) - \varepsilon_{\rm rec.}(\pi^+)}{\varepsilon_{\rm rec.}(\pi^-) + \varepsilon_{\rm rec.}(\pi^+)}, \tag{5.28}$$

where $\varepsilon_{\rm rec.}$ stands for the reconstruction efficiency of the given particle. The pion detection asymmetry has been measured by means of partially reconstructed $D^{*+} \to D^0(K^-\pi^+\pi^-\pi^+)\pi^+$ decays, as documented in Ref. [82]. Here we report in Tab. 5.21 only the values of the asymmetry, calculated in the same way as described in Ref. [81].
As for the kaon detection asymmetry, firstly we take the arithmetical average between magnet polarities and then we perform a weighted average between 2011 and 2012 measurements. The final values are reported in Tab. 5.22.

To calculate the pion detection asymmetry on the $\Lambda_b^0 \to p\pi^-$ sample, the values of Tab. 5.22 are reweighted to match the pion momentum distribution in $\Lambda_b^0 \to p\pi^-$ decays. In Fig. 5.34 the background-subtracted pion momentum distribution is shown. From this distribution weights are calculated according to the formula $w_j = \sum_i s_{i,j} / \sum_i s_i$, where

Table 5.22: *Values of $A_{\rm D}^{j}(\pi^+)$ obtained taking the arithmetic average of up and down values (separately by year) reported in Tab. 5.21 and finally the weighted average between 2011 and 2012 values. The central value and uncetrainty in the last bin are obtained as explained in the text. The weights are reported in the last column.*

Bin	$p(\pi)$ [GeV/c]	$A_{\rm D}^{j}(\pi^-)$[%]	ω_j
1	$2-6$	0.460 ± 0.136	0.005 ± 0.001
2	$6-15$	0.215 ± 0.091	0.104 ± 0.004
3	$15-20$	0.024 ± 0.128	0.112 ± 0.004
4	$20-30$	0.047 ± 0.137	0.185 ± 0.006
5	$30-40$	0.233 ± 0.206	0.149 ± 0.005
6	$40-50$	0.033 ± 0.297	0.104 ± 0.004
7	$50-100$	0.173 ± 0.320	0.259 ± 0.007
8	$100-250$	0.173 ± 0.640	0.082 ± 0.004

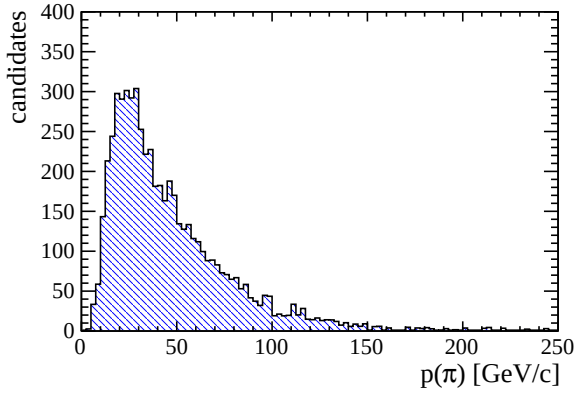

Figure 5.34: *Background-subtracted momentum distribution of pions from $\Lambda_b^0 \to p\pi^-$ decays.*

$s_{i,j}$ is the sWeight relative to the i-th event contained in the j-th pion momentum bin and the index i runs over all the events in the sample. The values of the weights w_j are reported in Tab. 5.22.

Also in this case, a bin from 100 to 250 GeV/c of pion momentum is added by taking the central value of the last bin and doubling its uncertainty. The last bin will thus take the value $A_{\rm D}^{8}(\pi^-) = (0.173 \pm 0.640)\%$.

The value of the pion detection asymmetry relative to the $\Lambda_b^0 \to p\pi^-$ decays is found to be

$$A_{\rm D}(\pi^-) = \left[\sum_j \omega_j A_{\rm D}^{j}(\pi^-)\right] = (0.133 \pm 0.112)\% \ .$$

Table 5.23: *Values of the PID asymmetries computed from the PID efficiencies of the* fiducial *and* non-fiducial *regions with calibration samples and fully simulated events for both selections.*

Selection A				
	$A_{\rm PID}^{\rm data}(f)_F[\%]$	$A_{\rm PID}^{\rm data}(f)_{NO-F}[\%]$	$A_{\rm PID}^{\rm MC}(f)_F[\%]$	$A_{\rm PID}^{\rm MC}(f)_{NO-F}[\%]$
$B^0 \to K^+\pi^-$	0.129	-0.537	0.106	1.309
$\Lambda_b^0 \to pK^-$	-0.156	–	-0.170	-0.865
Selection B				
	$A_{\rm PID}^{\rm data}(f)_F[\%]$	$A_{\rm PID}^{\rm data}(f)_{NO-F}[\%]$	$A_{\rm PID}^{\rm MC}(f)_F[\%]$	$A_{\rm PID}^{\rm MC}(f)_{NO-F}[\%]$
$B^0 \to K^+\pi^-$	0.112	-0.443	0.083	1.390
$\Lambda_b^0 \to p\pi^-$	-0.117	–	-0.265	-0.434

5.10.4 PID asymmetries

PID requirements on the the pK^- and $p\pi^-$ final states can induce asymmetries that need to be taken into account. The PID asymmetries are defined as

$$A_{\rm PID}(pK^-) = \frac{\varepsilon_{\rm PID}(pK^-) - \varepsilon_{\rm PID}(\overline{p}K^+)}{\varepsilon_{\rm PID}(pK^-) + \varepsilon_{\rm PID}(\overline{p}K^+)}, \tag{5.29}$$

$$A_{\rm PID}(p\pi^-) = \frac{\varepsilon_{\rm PID}(p\pi^-) - \varepsilon_{\rm PID}(\overline{p}\pi^+)}{\varepsilon_{\rm PID}(p\pi^-) + \varepsilon_{\rm PID}(\overline{p}\pi^+),} \tag{5.30}$$

where $\varepsilon_{\rm PID}(f)$ is the PID efficiency for the final state f. The simplest way to compute these asymmetries would be to take the numbers from Tabs. 5.9 and 5.10 for $\Lambda_b^0 \to pK^-$ and $\Lambda_b^0 \to p\pi^-$ decays, but since the systematic uncertainty assigned to the efficiencies due to the usage of the *non-fiducial* region is of the order of 10%, the uncertainty associated to the asymmetries would end up being too large.

In order to estimate the PID asymmetries in an alternative way, we firstly compute the PID efficiencies for the Λ_b^0 decays both in the *fiducial* and *non-fiducial* regions separately; the asymmetries calculated from these numbers are reported in Tab. 5.23.

The total PID asymmetry on the final state f can be written then as:

$$A_{\rm PID}(f) = f_{\rm cand.} \cdot A_{\rm PID}^{\rm data}(f)_F + (1 - f_{\rm cand.}) \cdot A_{\rm PID}^{\rm MC}(f)_{NO-F}, \tag{5.31}$$

where $f_{\rm cand.}$ is the fraction of Λ_b^0 candidates inside the *fiducial* region (the 80% of Λ_b^0 candidates lies in this region), $A_{\rm PID}^{\rm data}(f)_F$ and $A_{\rm PID}^{\rm MC}(f)_{NO-F}$ are the PID asymmetries evaluated in the *fiducial* and *non-fiducial* regions respectively.

To associate an uncertainty to the PID asymmetries, they are computed for kaons and pions from $B^0 \to K^+\pi^-$ and $B^0 \to \pi^+K^-$ decays. These asymmetries are reported in Tab. 5.23. The error on the Λ_b^0 final states PID asymmetries is estimated by adding and subtracting to $A_{\rm PID}^{\rm MC}(f)_{NO-F}$ a shift Δ, defined as:

Table 5.24: *Results from Ref. [81] for the Λ_b^0 production asymmetry in bins of $p_{\rm T}$ and y.*

Bin	$p_{\rm T}$ [GeV/c]	y	$A_{\rm P}(\Lambda_b^0)$ [$\sqrt{s} = 7$ TeV]	$A_{\rm P}(\Lambda_b^0)$ [$\sqrt{s} = 8$ TeV]
1	(2.00, 7.00)	(2.10, 3.00)	$-0.0892 \pm 0.0508 \pm 0.0214$	$0.0032 \pm 0.0318 \pm 0.0139$
2	(2.00, 7.00)	(3.00, 3.30)	$0.0507 \pm 0.0539 \pm 0.0208$	$0.0929 \pm 0.0392 \pm 0.0171$
3	(2.00, 7.00)	(3.30, 4.50)	$0.0849 \pm 0.0401 \pm 0.0188$	$0.0437 \pm 0.0284 \pm 0.0173$
4	(7.00, 9.50)	(2.10, 3.00)	$0.1374 \pm 0.0697 \pm 0.0313$	$0.0069 \pm 0.0434 \pm 0.0169$
5	(7.00, 9.50)	(3.00, 3.30)	$0.0138 \pm 0.0913 \pm 0.0298$	$0.0076 \pm 0.0589 \pm 0.0259$
6	(7.00, 9.50)	(3.30, 4.50)	$0.0466 \pm 0.0770 \pm 0.0347$	$0.1053 \pm 0.0524 \pm 0.0252$
7	(9.50, 12.00)	(2.10, 3.00)	$-0.0128 \pm 0.0985 \pm 0.0367$	$-0.0512 \pm 0.0594 \pm 0.0215$
8	(9.50, 12.00)	(3.00, 3.30)	$-0.0848 \pm 0.1379 \pm 0.0452$	$0.2355 \pm 0.0877 \pm 0.0399$
9	(9.50, 12.00)	(3.30, 4.50)	$-0.1523 \pm 0.1414 \pm 0.0488$	$0.1531 \pm 0.0838 \pm 0.0320$
10	(12.00, 30.00)	(2.10, 3.00)	$-0.0720 \pm 0.1248 \pm 0.0465$	$0.0453 \pm 0.0762 \pm 0.0300$
11	(12.00, 30.00)	(3.00, 3.30)	$0.3291 \pm 0.2299 \pm 0.0918$	$-0.0934 \pm 0.1377 \pm 0.0493$
12	(12.00, 30.00)	(3.30, 4.50)	$-0.0571 \pm 0.2162 \pm 0.0800$	$0.3173 \pm 0.1411 \pm 0.0655$

$$\Delta \equiv |A_{\rm PID}^{\rm MC}(K^+\pi^-)_{NO-F} - A_{\rm PID}^{\rm data}(K^+\pi^-)_{NO-F}|, \tag{5.32}$$

and computing again the PID asymmetry. The uncertainty is obtained taking the biggest diffrence between the original asymmetry and the new asymmetries.
The final PID asymmetries computed with this method and their uncertainties are:

$$\begin{aligned} A_{\rm PID}(pK^-) &= (-0.298 \pm 0.738)\%, \\ A_{\rm PID}(p\pi^-) &= (-0.180 \pm 0.733)\% \ . \end{aligned}$$

5.10.5 Λ_b^0 production asymmetry

The Λ_b^0 production asymmetry is defined as

$$A_{\rm P}(\Lambda_b^0) = \frac{\sigma(\Lambda_b^0) - \sigma(\overline{\Lambda}_b^0)}{\sigma(\Lambda_b^0) + \sigma(\overline{\Lambda}_b^0)}, \tag{5.33}$$

where σ stands for the production cross-section. The values of the Λ_b^0 production asymmetry in bins of $p_{\rm T}$ and y are taken from Ref. [81] and are reported in Tab. 5.24.

To calculate the Λ_b^0 production asymmetry on the $\Lambda_b^0 \to pK^-$ and $\Lambda_b^0 \to p\pi^-$ samples the values of Tab. 5.24 are reweighted to match the Λ_b^0 $p_{\rm T}$ and y distribution from $\Lambda_b^0 \to pK^-$ and $\Lambda_b^0 \to p\pi^-$ decays. In Fig. 5.35 the background-subtracted transverse momentum and rapidity distributions of Λ_b^0 from $\Lambda_b^0 \to pK^-$ and $\Lambda_b^0 \to p\pi^-$ decays are shown. From these distributions weights are calculated according to the formula $w_j = \sum_i s_{i,j} / \sum_i s_i$, where $s_{i,j}$ is the sWeight relative to the i-th event contained in the j-th $(p_{\rm T}, y)$ bin and the index i runs over all the events in the sample. The values of the weights w_j are reported in Tab. 5.25.

Table 5.25: *Weights obtained from the background-subtracted $p_{\rm T}$ and y distributions of $\Lambda_b^0 \to pK^-$ and $\Lambda_b^0 \to p\pi^-$ decays.*

Bin	$p_{\rm T}$ [GeV/c]	y	$\omega_j^{\Lambda_b^0\to pK^-,2011}$	$\omega_j^{\Lambda_b^0\to pK^-,2012}$	$\omega_j^{\Lambda_b^0\to p\pi^-,2011}$	$\omega_j^{\Lambda_b^0\to p\pi^-,2012}$
1	(2.00, 7.00)	(2.10, 3.00)	0.308 ± 0.011	0.308 ± 0.007	0.278 ± 0.013	0.286 ± 0.009
2	(2.00, 7.00)	(3.00, 3.30)	0.128 ± 0.007	0.122 ± 0.005	0.129 ± 0.009	0.113 ± 0.006
3	(2.00, 7.00)	(3.30, 4.50)	0.177 ± 0.008	0.168 ± 0.006	0.179 ± 0.010	0.160 ± 0.007
4	(7.00, 9.50)	(2.10, 3.00)	0.126 ± 0.007	0.138 ± 0.005	0.144 ± 0.009	0.150 ± 0.006
5	(7.00, 9.50)	(3.00, 3.30)	0.045 ± 0.004	0.039 ± 0.003	0.045 ± 0.005	0.038 ± 0.003
6	(7.00, 9.50)	(3.30, 4.50)	0.051 ± 0.004	0.050 ± 0.003	0.038 ± 0.005	0.041 ± 0.003
7	(9.50, 12.00)	(2.10, 3.00)	0.069 ± 0.005	0.071 ± 0.004	0.069 ± 0.006	0.076 ± 0.005
8	(9.50, 12.00)	(3.00, 3.30)	0.014 ± 0.002	0.023 ± 0.002	0.019 ± 0.003	0.023 ± 0.002
9	(9.50, 12.00)	(3.30, 4.50)	0.017 ± 0.003	0.018 ± 0.002	0.015 ± 0.003	0.016 ± 0.002
10	(12.00, 30.00)	(2.10, 3.00)	0.050 ± 0.004	0.044 ± 0.003	0.059 ± 0.006	0.070 ± 0.004
11	(12.00, 30.00)	(3.00, 3.30)	0.010 ± 0.002	0.012 ± 0.001	0.012 ± 0.003	0.014 ± 0.002
12	(12.00, 30.00)	(3.30, 4.50)	0.005 ± 0.001	0.007 ± 0.001	0.012 ± 0.003	0.013 ± 0.002

About 5% of Λ_b^0 candidates have a $p_{\rm T}$ lower than 2 GeV/c and the production asymmetry that could arise from these events would not be corrected for by using the measurements reported in Tab. 5.24. Since in Ref. [81] no sizeable dependence of the production asymmetries on the transverse momentum of the Λ_b^0 baryon is observed, these events are included in bins 1, 2, or 3, depending on their rapidity.

The integrated values of the Λ_b^0 production asymmetries are calculated as

$$A_{\rm P}(\Lambda_b^0) = \sum_j \omega_j A_{\rm P}^j(\Lambda_b^0) \ . \tag{5.34}$$

These values divided by year and decay are found to be

$$\begin{aligned}
A_{\rm P}(\Lambda_b^0 \to pK^-)_{\sqrt{s}=7\ \rm TeV} &= (0.896 \pm 2.353 \pm 0.978)\% \ , \\
A_{\rm P}(\Lambda_b^0 \to pK^-)_{\sqrt{s}=8\ \rm TeV} &= (3.375 \pm 1.516 \pm 0.677)\% \ , \\
A_{\rm P}(\Lambda_b^0 \to p\pi^-)_{\sqrt{s}=7\ \rm TeV} &= (1.379 \pm 2.344 \pm 0.972)\% \ , \\
A_{\rm P}(\Lambda_b^0 \to p\pi^-)_{\sqrt{s}=8\ \rm TeV} &= (3.397 \pm 1.537 \pm 0.674)\% \ .
\end{aligned}$$

The weighted average of the 2011 and 2012 results for the production asymmetries are then used to obtain the final result.

5.10.6 Summary of systematic uncertainties

Table 5.26 reports the values of all the systematic uncertainties discussed in this Section together with the results obtained in Sec. 5.8. In the last row, the sum in quadrature of all the systematic uncertainties is computed. This is the systematic uncertainty quoted on the final measurements.

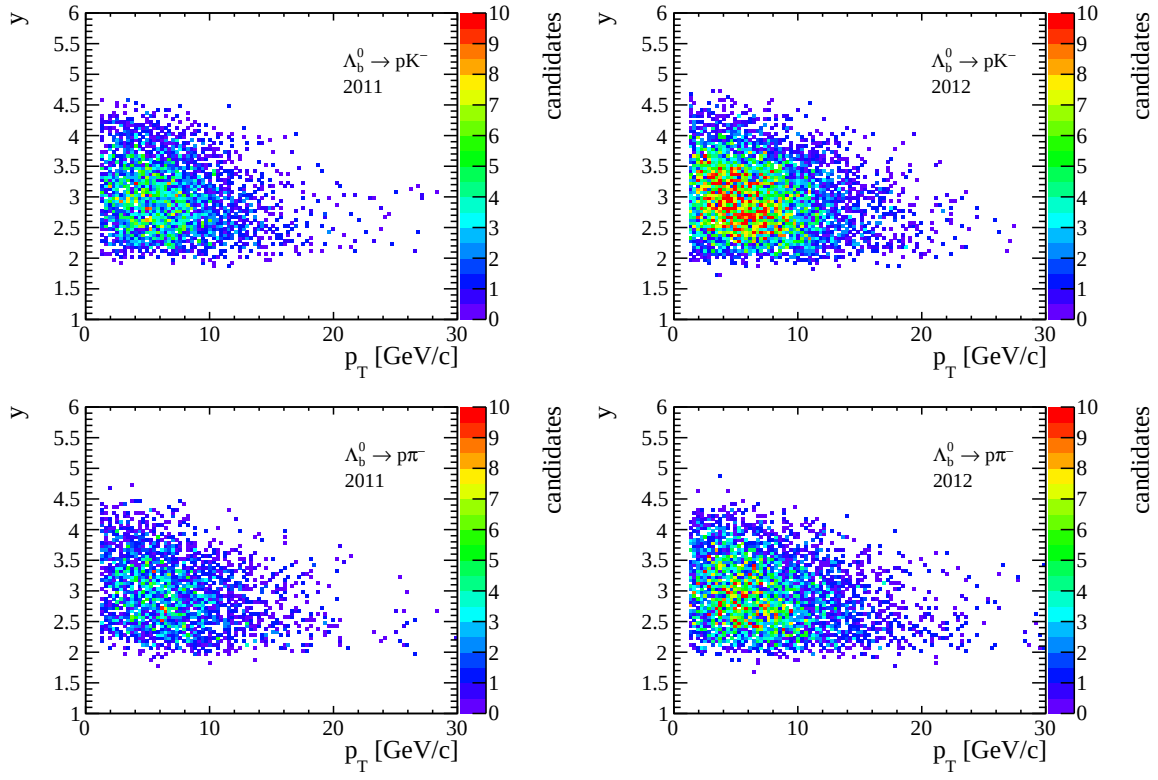

Figure 5.35: *Background-subtracted distributions of transverse momentum and rapidity of the Λ_b^0 from (top left) $\Lambda_b^0 \to pK^-$ 2011, (top right) $\Lambda_b^0 \to pK^-$ 2012, (bottom left) $\Lambda_b^0 \to p\pi^-$ 2011 and (bottom right) $\Lambda_b^0 \to p\pi^-$ 2012 decays.*

Table 5.26: *Summary of systematic uncertainties relative to (left) $\Lambda_b^0 \to pK^-$ and (right) $\Lambda_b^0 \to p\pi^-$. In the last row, the sum in quadrature of all the systematic uncertainties is computed.*

Source	$\Lambda_b^0 \to pK^-$ [%]	$\Lambda_b^0 \to p\pi^-$ [%]
Fit model	0.618	0.874
$A_{\rm D}(K^-)$	0.231	–
$A_{\rm D}(\pi^-)$	–	0.112
$A_{\rm D}(p)$	0.164	0.164
$A_{\rm PID}$	0.738	0.733
$A_{\rm P}(\Lambda_b^0)$	1.391	1.400
Sum in quadrature	1.715	1.816

5.11 Conclusions

Taking the raw asymmetries measured in Section 5.9, the instrumental and production asymmetries determined in Section 5.10, and plugging the values into Eqs. 5.23, the

following results are obtained

$$\begin{aligned} A_{CP}(pK^-) &= (-1.870 \pm 1.349 \pm 1.715)\%, \\ A_{CP}(p\pi^-) &= (-3.547 \pm 1.669 \pm 1.816)\%, \end{aligned}$$

where the first uncertainty is statistical and the second systematic.

These results are consistent with the hypothesis of no *CP* violation and are currrently the world's best measurements of these *CP* asymmetries, significantly improving on the previous CDF determinations [92].

6 Measurement of time-dependent and time-integrated CP-violating asymmetries in $B^0_{(s)} \to h^+h'^-$ decays

6.1 Introduction

The study of CP violation in charmless decays of neutral $B^0_{(s)}$ mesons to two-body charged pions or kaons provides relevant tests of the CKM picture [7, 93] in the SM, and is a sensitive probe to search for the presence of non SM physics [94–98]. Quantitative SM predictions for CP violation in these decays are challenging because of the presence in the decay amplitudes of so-called penguin diagrams in addition to tree diagrams, leading to hadronic factors which cannot be accurately calculated from QCD at present. The presence of penguin diagrams represents a limitation for an easy exploitation of the measurements in this sector, but, on the other hand, such diagrams may also receive contributions from new physics. It is then important to combine several measurements from such two-body decays, exploiting approximate flavour symmetries in order to cancel the unknown hadronic factors.

Measurements of time-integrated CP asymmetries with $B^0 \to K^+\pi^-$ and $B^0_s \to \pi^+K^-$ decays have already been performed [99–103]. Moreover, the branching fractions of charmless charged two-body b-hadron decays [104, 105] have been also measured and recently the LHCb collaboration published the first observation of the annihilation decay $B^0 \to K^+K^-$ [106]. A measurement of time-dependent CP violation in the $B^0 \to \pi^+\pi^-$ and the $B^0_s \to K^+K^-$ decays has also been made, using data collected during 2011 [65,107,108]. The results have been used to determine the CKM angle γ and the B^0_s mixing phase $-2\beta_s$ [109]. Finally, a preliminary measurement of $C_{\pi^+\pi^-}$, $S_{\pi^+\pi^-}$, $C_{K^+K^-}$, $S_{K^+K^-}$ and $A^{\Delta\Gamma}_{K^+K^-}$ using the full Run 1 sample has been performed. In that measurement only the information provided by the Opposite Side (OS) taggers [110] has been exploited. In this document the preliminary result is updated adding also the information provided by the Same Side (SS) taggers. In addition, also updates of the measurements of the direct CP asymmetries in the $B^0 \to K^+\pi^-$ and $B^0_s \to \pi^+K^-$ decays are presented.

The *CP* asymmetry as a function of time for neutral B mesons decaying to a *CP* eigenstate f is given by

$$\mathcal{A}(t) = \frac{\Gamma_{\bar{B}^0_{(s)}\to f}(t) - \Gamma_{B^0_{(s)}\to f}(t)}{\Gamma_{\bar{B}^0_{(s)}\to f}(t) + \Gamma_{B^0_{(s)}\to f}(t)} = \frac{-C_f \cos(\Delta m_{d(s)} t) + S_f \sin(\Delta m_{d(s)} t)}{\cosh\left(\frac{\Delta\Gamma_{d(s)}}{2} t\right) + A_f^{\Delta\Gamma} \sinh\left(\frac{\Delta\Gamma_{d(s)}}{2} t\right)}, \tag{6.1}$$

where $\Delta m_{d(s)}$ and $\Delta\Gamma_{d(s)}$ are the mass and width differences of the $B^0_{(s)} - \bar{B}^0_{(s)}$ system mass eigenstates, and the quantities C_f, S_f and $A_f^{\Delta\Gamma}$ are defined as

$$\begin{aligned} C_f &= \frac{1 - |\lambda_f|^2}{1 + |\lambda_f|^2}, \\ S_f &= \frac{2\mathrm{Im}(\lambda_f)}{1 + |\lambda_f|^2}, \\ A_f^{\Delta\Gamma} &= -\frac{2\mathrm{Re}(\lambda_f)}{1 + |\lambda_f|^2}, \end{aligned} \tag{6.2}$$

with λ_f given by

$$\lambda_f = \frac{q}{p}\frac{\bar{A}_f}{A_f}. \tag{6.3}$$

The term λ_f is related to the $B^0_{(s)} - \bar{B}^0_{(s)}$ mixing (q/p) and to the decay amplitudes of the $B_{(s)} \to f$ decay (A_f) and of the $\overline{B}_{(s)} \to f$ decay ($\bar{A}_f$). The present formulation assumes *CPT* invariance. Moreover, assuming negligible *CP* violation in mixing ($|q/p| = 1$), the terms C_f and S_f parameterise direct and mixing-induced *CP* violation, respectively. For a detailed definition see Ref. [67].

The direct *CP* asymmetry for a B meson decaying to a flavour-specific final state is defined as

$$A_{CP} = \frac{\left|\bar{A}_{\bar{f}}\right|^2 - |A_f|^2}{\left|\bar{A}_{\bar{f}}\right|^2 + |A_f|^2}, \tag{6.4}$$

where $\left|\bar{A}_{\bar{f}}\right|$ and $|A_f|$ are the instantaneous decay amplitudes of the $\overline{B} \to \bar{f}$ and $B \to f$ decays, respectively, as in Eq. (6.3).

The current experimental knowledge of these quantities is summarised in Tab. 6.1, for the time-dependent *CP*-violating parameters, and in Tab. 6.2 for the direct *CP* asymmetries.

6.2 Analysis strategy

The *CP*-violating parameters are determined by means of unbinned maximum likelihood fits performed simultaneously to the samples of the candidates selected in the $\pi^+\pi^-$, K^+K^- and $K^\pm\pi^\mp$ final states. By performing the fit simultaneously to the three spectra one has the advantage that several common quantities that can be determined at once taking automatically all correlations into account. These quantities notably include the

Table 6.1: *Current knowledge of direct and mixing-induced CP-violating asymmetries in $B^0 \to \pi^+\pi^-$ and $B^0_s \to K^+K^-$ decays [67], performed by the BaBar [22], Belle [23] and LHCb [110] experiments. The last column in each table reports the correlation between the two asymmetries.*

Experiment	$C_{\pi^+\pi^-}$	$S_{\pi^+\pi^-}$	$\rho(C_{\pi^+\pi^-}, S_{\pi^+\pi^-})$
BaBar	$-0.25 \pm 0.08 \pm 0.02$	$-0.68 \pm 0.10 \pm 0.03$	-0.06
Belle	$-0.33 \pm 0.06 \pm 0.03$	$-0.64 \pm 0.08 \pm 0.03$	-0.10
LHCb	$-0.24 \pm 0.07 \pm 0.01$	$-0.68 \pm 0.06 \pm 0.01$	0.38
HFLAV average	-0.27 ± 0.04	-0.68 ± 0.04	0.14

Experiment	$C_{K^+K^-}$	$S_{K^+K^-}$	$A^{\Delta\Gamma}_{K^+K^-}$	$\rho(C_{K^+K^-}, S_{K^+K^-})$
LHCb	$0.22 \pm 0.06 \pm 0.02$	$0.24 \pm 0.06 \pm 0.02$	$-0.75 \pm 0.07 \pm 0.11$	-0.005

Table 6.2: *Current knowledge of direct CP asymmetries in $B^0 \to K^+\pi^-$ and $B^0_s \to \pi^+K^-$ decays.*

Experiment	$A_{CP}(B^0 \to K^+\pi^-)$	$A_{CP}(B^0_s \to \pi^+K^-)$
BaBar	$-0.107 \pm 0.016^{+0.006}_{-0.004}$	–
Belle	$-0.069 \pm 0.014 \pm 0.007$	–
CDF	$-0.083 \pm 0.013 \pm 0.004$	$0.22 \pm 0.07 \pm 0.02$
LHCb	$-0.080 \pm 0.007 \pm 0.003$	$0.27 \pm 0.04 \pm 0.01$
HFLAV average	-0.082 ± 0.006	0.26 ± 0.04

calibration parameters of the flavour tagging (discussed in Sec. 6.9.1) and the production asymmetry between B^0 and B^0_s mesons (entering the equations of the experimental tagged decay-time rates described in Sec. 6.6.1). The simultaneous fit also allows the contamination due to misidentified two-body b-hadron decays to be determined by relating the corresponding yields in the various spectra using PID efficiency ratios. The observables of the fits are

- the final state ψ;
- the invariant mass m;
- the decay time t;
- the flavour tag ξ_{tag};
- the predicted mistag probability η_{tag};
- the predicted decay-time uncertainty δ_t computed by the reconstruction algorithms.

The information on the flavour tagging and the predicted decay-time uncertainty are used on a per-event basis.

Table 6.3: *Total integrated luminosity corresponding to the pp collisions collected by LHCb used in this analysis. They are separated by year and magnet polarity. Uncertainties are not included.*

	2011	2012
Magnet Down	$556.29\,\text{pb}^{-1}$	$980.85\,\text{pb}^{-1}$
Magnet Up	$414.33\,\text{pb}^{-1}$	$979.33\,\text{pb}^{-1}$
Mag. Down + Mag. Up	$970.62\,\text{pb}^{-1}$	$1960.18\,\text{pb}^{-1}$
Total	$2930.80\,\text{pb}^{-1}$	

This chapter is organised as follows. In Sec. 6.3 the data sample is defined and the optimisation of the event selection is described in Sec. 6.4. In Secs. 6.5 to 6.9, the description of the model used to parameterise the shapes of the various components entering the unbinned maximum likelihood fits is given: description of the invariant-mass model (Sec. 6.5); description of the decay-time model (Sec. 6.6); description of the models used to parameterise the per-event decay-time uncertainty (Sec. 6.7); determination of the decay-time acceptance (Sec. 6.8), and the description of the distribution used to parameterise the shapes of the predicted mistag probabilities for the so-called opposite-side (OS) and same-side (SS) taggers (Sec. 6.9). In Sec. 6.7, the method used to calibrate the relation between the per-event decay-time uncertainty and the actual experimental resolution on the decay-time is also presented. Similarly, Sec. 6.9 contains an explanation of the method used to calibrate the predicted mistag probability determined by the various flavour-tagging algorithms. The fit results are presented in Sec. 6.10, together with several cross-checks. In Sec. 6.11 the corrections needed to obtain the time-integrated *CP* asymmetries are described. The assessment of systematic uncertainties is discussed in Sec. 6.12.

6.3 Data sample, stripping and trigger

The data sample used in this analysis is composed of *pp* collisions collected during 2011 and 2012. The total integrated luminosity of about $3\,\text{fb}^{-1}$ is divided by year and magnet polarity as reported in Tab. 6.3. [1]

6.3.1 Stripping selection

The sample used is the output of the so-called `StrippingB2HHBDTLine` stripping line reprocessed during Summer 2015 in order to include the information provided by up-to-date flavour tagging algorithms. The `StrippingB2HHBDTLine` (already used in Ref. [106]) is composed of two steps. In the first step, a preselection is performed on the combinations

[1] The luminosities reported in Tab. 6.3 do not sum up to the total luminosity collected by LHCb during Run 1 due to the loss of some data files in the relevant physics stream occurred at a Tier-1 computing site.

Table 6.4: *Summary of the values of the requirements used to form the two-body b-hadron decay candidates by the* ***StrippingB2HHBDTLine****, previous to the application of the BDT algorithm. The meaning of the various symbols is explained in the text.*

Cut type	value
Track χ^2/ndf	< 3
Track `GhostProb`	< 0.5
Track $p_{\rm T}$ [GeV/c]	> 1.0
Track $d_{\rm IP}$ [µm]	> 120
$d_{\rm CA}$ [µm]	< 100
$d^{H_b}_{\rm IP}$[µm]	< 120
$t_{\pi\pi}$ [ps]	> 0.6
$p^{H_b}_{\rm T}$ [GeV/c]	> 1.2

of pairs of oppositely charged tracks, used to form two-body b-hadron candidates, where the pion mass hypothesis is assumed for the final state particles. The second step is used to increase the purity of the sample by means of a multivariate `Boosted Decision Tree` (BDT) classifier [63]. The preselection uses tracks with large transverse momentum ($p_{\rm T}$), large impact parameter ($d_{\rm IP}$) with respect to all the primary vertices (PVs), small normalised χ^2 (χ^2/ndf) and small probablity to be a *ghost-track* (`GhostProb`). Pairs of tracks with a small distance of closest approach ($d_{\rm CA}$) are fitted to a common vertex in order to form the b-hadron candidate. Only candidates with a large transverse momentum $p^{H_b}_{\rm T}$, a small impact parameter with respect to all the PVs ($d^{H_b}_{\rm IP}$) and a large decay time ($t_{\pi\pi}$, computed assuming decay into $\pi^+\pi^-$ final state) are selected by the algorithm. In Tab. 6.4 the values of the requirements applied in the first step of the stripping selection are reported. In the second step, the BDT algorithm discriminates between signal and combinatorial background on the basis of the smallest and largest $p_{\rm T}$ of the two tracks, the smallest and largest $d_{\rm IP}$ of the two tracks, the $d_{\rm CA}$ between the two tracks, the quality of the common vertex fit of the two tracks ($\chi^2_{\rm vtx}$), the $p^{H_b}_{\rm T}$ and $d^{H_b}_{\rm IP}$ of the two-body b-hadron candidate, and the distance of flight (FD) of the b-hadron candidate with respect to the associated PV[2].

6.3.2 Trigger requirements

The following trigger requirements are applied to the events surviving the stripping selection

L0 Trigger: `L0Hadron_TOS OR L0Global_TIS`. The event is accepted if the particles composing the two-body b-hadron candidate fired the `L0Hadron` trigger, *i.e.* the event is triggered by the signal candidate (`L0Hadron_TOS`), or if the other particles not

[2]The candidate is associated to the primary vertex with the smallest χ^2 of the impact parameter.

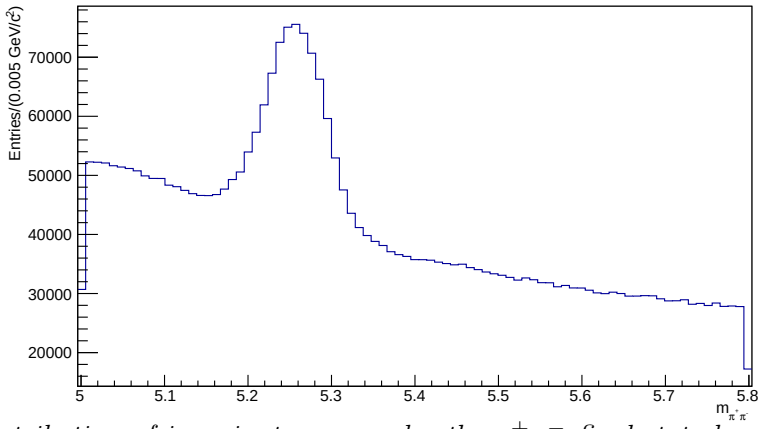

Figure 6.1: *Distribution of invariant mass under the $\pi^+\pi^-$ final state hypothesis for the events surviving the* `StrippingB2HHBDTLine` *stripping selection and the trigger requirements described in the text. The total amount of events is about 3.75 millions.*

belonging to the signal candidate fired at least one of the `L0` triggers (`L0Global_TIS`). The definition of the different `L0` triggers is reported in Sec. 2.5.

Hlt1: `Hlt1TrackAllL0Decision_TOS`. The event is accepted if the tracks passing the `L0` decision and belonging to the signal candidate also satisfy the requirements of this trigger [111]. This algorithm is efficient in selecting beauty and charm decays, requiring their daughters to have momenta larger than 10 GeV/c as well as a transverse momentum greater than 1.7 GeV/c.

Hlt2: `Hlt2B2HHDecision_TOS OR Hlt2Topo2BodyBBDTDecision_TOS`. The signal b-hadron candidate and its daughters need to satisfy the requirements of at least one of these triggers. The first one is specialised in selecting two-body b-hadron decays using a set of specifically-tuned kinematic and geometric requirements on each daughter particles as well as on their combination, whereas the second one is a more generic trigger that selects two-body decays requiring the tracks to satisfy some basic $p_{\rm T}$, $\chi^2_{\rm IP}$ and DOCA requirements. The full list of requirements for both trigger lines is reported in Ref. [111].

In Fig. 6.1 the $m_{\pi^+\pi^-}$ distribution corresponding to the events surviving the preselection is shown.

6.3.3 Simulated samples

Simulated samples of $B^0 \to K^+\pi^-$, $B^0_s \to \pi^+K^-$, $B^0 \to \pi^+\pi^-$, $B^0_s \to \pi^+\pi^-$, $B^0_s \to K^+K^-$, $\Lambda^0_b \to pK^-$ and $\Lambda^0_b \to p\pi^-$ decays[3], produced with the `Sim08b/Digi13` version of the simulation framework, are used. In these samples the 2011 and 2012 data taking

[3]Charge conjugation is implied throughout, unless stated otherwise.

Table 6.5: *Number of generated events containing two-body b-hadron decays, separated by data-taking conditions.*

Decay	Number of 2011 events	Number of 2012 Events
$B^0 \to K^+\pi^-$	1541196	3068989
$B^0 \to \pi^+\pi^-$	1527244	3067742
$B^0_s \to K^+K^-$	1532248	3052242
$B^0_s \to \pi^+K^-$	1514494	3071739
$B^0_s \to \pi^+\pi^-$	1024500	2030741
$\Lambda^0_b \to pK^-$	1558992	3031739
$\Lambda^0_b \to p\pi^-$	1541498	3026736

conditions, trigger, reconstruction, stripping and flavour tagging are reproduced in order to have simulated events resembling as close as possible real data. Two distinct trigger configurations are emulated for the 2011 and 2012 samples. Simulated events have been produced with a number of events that reproduces the observed ratios between the integrated luminosities collected with the different magnet polarities during 2011 and 2012. In Tab. 6.5 the size of simulated samples of all two-body b-hadron decays is reported. Reconstructed candidates are required to be associated with a true decay.

6.4 Particle identification and multivariate selections

The final event selection is separated into two steps. In the first one, $\Delta \log \mathcal{L}$ variables are used to separate the output of the `StrippingB2HHBDTLine` stripping line into mutually exclusive samples corresponding to the $K^\pm\pi^\mp$, $\pi^+\pi^-$ and K^+K^- final state hypotheses. In the second step, a BDT is used to further suppress the combinatorial background.

6.4.1 Particle identification criteria

Before applying the final event selection, the candidates which satisfy the requirements of the `StrippingB2HHBDTLine` stripping line are separated into different final states by means of $\Delta \log \mathcal{L}$ variables. As discussed in Ref. [65], the main source of cross-feed background below the $B^0 \to \pi^+\pi^-$ and $B^0_s \to K^+K^-$ invariant-mass peaks comes from the $B^0 \to K^+\pi^-$ decays, where one of the two final state particles is misidentified. In order to reduce this background, requirements on the $\Delta \log \mathcal{L}_{K-\pi}$ variable are applied. Particle identification (PID) requirements are optimised to reduce the amount of the $B^0 \to K^+\pi^-$ contamination to approximately 10% of the corresponding signal yields. Past experience with the two-body b-hadron decay modes [65, 107] proved that with this level of contamination systematic uncertainties related to the description of the cross-feed backgrounds can be kept under control. Larger contamination will lead to a more difficult

Table 6.6: *PID selection criteria applied for the identification of the final states.*

$K^+\pi^-$	$\pi^+\pi^-$	K^+K^-
$\Delta\log\mathcal{L}_{K-\pi}(h^+) > 5$	$\Delta\log\mathcal{L}_{K-\pi} < -3$	$\Delta\log\mathcal{L}_{K-\pi}(h^+) > 4$
$\Delta\log\mathcal{L}_{K-p}(h^+) > -5$	$\Delta\log\mathcal{L}_{p-\pi} < 5$	$\Delta\log\mathcal{L}_{K-p}(h^+) > -5$
$\Delta\log\mathcal{L}_{K-\pi}(h^-) < -5$	$\Delta\log\mathcal{L}_{K-\pi}(h^-) < -3$	$\Delta\log\mathcal{L}_{K-\pi}(h^-) > 4$
$\Delta\log\mathcal{L}_{p-\pi}(h^-) < 5$	$\Delta\log\mathcal{L}_{p-\pi}(h^-) < 5$	$\Delta\log\mathcal{L}_{K-p}(h^-) > -5$

description of the data and to larger systematic uncertainties, compared to a small gain in signal efficiency.

The amount of $B^0 \to K^+\pi^-$ contamination with respect to the signal yields in the $\pi^+\pi^-$ and K^+K^- spectra is determined to be

$$B_{K^+K^-} = \frac{\varepsilon(K^+\pi^- \to K^+K^-)}{\varepsilon(K^+\pi^- \to K^+\pi^-)} \cdot \frac{f_d}{f_s} \cdot \frac{\mathcal{B}(B^0 \to K^+\pi^-)}{\mathcal{B}(B_s^0 \to K^+K^-)}, \tag{6.5}$$

$$B_{\pi^+\pi^-} = \frac{\varepsilon(K^+\pi^- \to \pi^+\pi^-)}{\varepsilon(K^+\pi^- \to K^+\pi^-)} \cdot \frac{\mathcal{B}(B^0 \to K^+\pi^-)}{\mathcal{B}(B^0 \to \pi^+\pi^-)}, \tag{6.6}$$

where ε is the PID efficiency for a given final state to be identified or misidentified, $\mathcal{B}$ stands for the branching ratio of a given decay, and f_s and f_d are the probabilities of a b quark to hadronise into a B_s^0 or a B^0 meson, respectively. The calibration of the PID efficiencies is performed using a data driven method, following the same procedure described in Section 4 of Ref. [106]. As calibration samples background-subtracted datasets of $D^{*+} \to D^0(K^-\pi^+)\pi^+$ and $\Lambda \to p\pi^-$ decays are used. The procedure is briefly summarised in the following. Firstly, maps of PID efficiencies for different particles and different requirements are built as a function of particle momentum, pseudorapidity and number of tracks in the event. Then the dependency on the event occupancy is averaged over the distribution of the number of tracks in two-body b-hadron events, obtaining maps of PID efficiencies as a function of particle momentum and pseudorapidity. The final efficiencies are averaged over the distributions of momentum and pseudorapidity of final state particles of two-body b-hadron decays, using fully simulated events as a proxy. The ratios of branching fractions, corrected for the factor f_d/f_s in the case of the $B_s^0 \to K^+K^-$ decay, are taken from Ref. [105]. Fixed requirements $\Delta\log\mathcal{L}_{K-p} > -5$ (for the K^+K^- spectrum) and $\Delta\log\mathcal{L}_{p-\pi} < 5$ (for the $\pi^+\pi^-$ spectrum) are also used to suppress $\Lambda_b^0 \to pK^-$ and $\Lambda_b^0 \to p\pi^-$ cross-feed backgrounds. In Fig. 6.2 the relative yield of the $B^0 \to K^+\pi^-$ decay with respect to the $B_s^0 \to K^+K^-$ and $B^0 \to \pi^+\pi^-$ decays is reported as a function of the requirement on the $\Delta\log\mathcal{L}_{K-\pi}$ variable. The optimal PID requirements for the $K^\pm\pi^\mp$ spectrum are chosen following the same strategy, *i.e.* reducing the contamination of the $B^0 \to \pi^+\pi^-$ and $B_s^0 \to K^+K^-$ decays to about 10% of the $B_s^0 \to \pi^+K^-$ decay. The final PID requirements for the K^+K^-, $\pi^+\pi^-$ and $K^\pm\pi^\mp$ spectra are reported in Tab. 6.6.

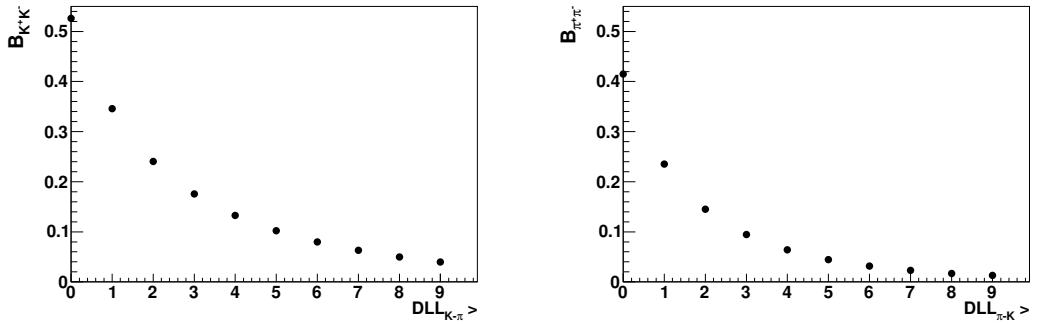

Figure 6.2: *Relative yields of the $B^0 \to K^+\pi^-$ decay with respect to (left) $B^0_s \to K^+K^-$ and (right) $B^0 \to \pi^+\pi^-$ decays as a function of the requirement on the $\Delta \log \mathcal{L}_{K-\pi}$ variable applied to both final state particles.*

6.4.2 BDT selection

A final selection is applied to events passing the stripping line and the PID criteria. Two different selections are optimised to reject the combinatorial background: one for the $B^0 \to \pi^+\pi^-$ decay (in the rest of the text referred to as $BDT_{\pi^+\pi^-}$) and the other for the $B^0_s \to K^+K^-$ decay (in the rest of the text referred to as $BDT_{K^+K^-}$). Both selections are based on a BDT classifier. The default configuration of the BDT algorithms provided within the TMVA package [112] is used, training 100 trees for each BDT and using the `Adaptive Boost` method [113]. The sum of 2011 and 2012 samples is used to train a single BDT algorithm. Possible differences between 2011 and 2012 samples are investigated, finding no significant discrepancy. More details of this comparison are reported in App. D.1.

The BDT training is performed separately for the events surviving the K^+K^- and $\pi^+\pi^-$ PID requirements. The events used to model the combinatorial background are taken from the high invariant-mass sideband corresponding to the requirement $m > 5.6\,\text{GeV}/c^2$ (where m is the invariant-mass computed under the K^+K^- or the $\pi^+\pi^-$ hypotheses, according to the signal under consideration). The parameterisation of signal events is studied on simulated samples and presented in Sec. 6.3.3.

In order to avoid any bias in the determination of the best selection, a strategy that prevents the application of a BDT algorithm on any event either used to train the BDT or used to find the best requirement on the BDT output is adopted. The signal and background samples have been randomly separated into three subsamples (`S1`, `S2` and `S3`). Different instances of the BDT algorithm have been trained for each subsample: `BDT1`, `BDT2` and `BDT3` for `S1`, `S2` and `S3`, respectively. In the second phase of the optimisation, requirements are applied to `BDT1` for the events from `S2`, to `BDT2` for events from `S3` and to `BDT3` for events from `S1`. The final analysis is performed putting requirements on `BDT1` for events from `S3`, on `BDT2` for events from `S1` and on `BDT3` for events from `S2`.

The variables used to describe the $B^0 \to \pi^+\pi^-$ and the $B^0_s \to K^+K^-$ decays are: the minimum and maximum p_T of the two final state tracks, the minimum and maximum χ^2 of

Table 6.7: *List of variables used to train the BDT algorithms. The meaning of the symbols is explained in the text.*

BDT variables	
$\min(p_{\rm T}^+, p_{\rm T}^-)$	$\log(\min(\chi^2(d_{\rm IP}^+), \chi^2(d_{\rm IP}^-)))$
$\max(p_{\rm T}^+, p_{\rm T}^-)$	$\log(\max(\chi^2(d_{\rm IP}^+), \chi^2(d_{\rm IP}^-)))$
$d_{\rm CA}$	$\chi^2_{\rm vtx}$
$p_{\rm T}^{H_b}$	$\chi^2(d_{\rm IP}^{H_b})$
$\log(\chi^2({\rm FD}))$	

the impact parameter of the two tracks computed with respect to all the primary vertices ($\chi^2(d_{\rm IP})$), the distance of closest approach ($d_{\rm CA}$) between the two tracks, the quality of the common vertex fit of the two tracks ($\chi^2_{\rm vtx}$), the $p_{\rm T}$ of the b-hadron candidate ($p_{\rm T}^{H_b}$), the χ^2 of the impact parameter of the b-hadron candidate with respect to the associated primary vertex ($\chi^2(d_{\rm IP}^{H_b})$), and the χ^2 of the distance of flight of the b-hadron candidate with respect to the associated primary vertex ($\chi^2({\rm FD})$). A logarithmic transformation is applied to the distance of flight of the b-hadron candidate and the maximum and minimum χ^2 of the impact parameter of the two tracks making the resulting distributions more Gaussian-like. The list of the variables is reported in Tab. 6.7.

The distributions of the variables listed in Tab. 6.7 and their correlations are reported in Figs. D.1 to D.8 in App. D.1 for both background and signal events. In Fig. 6.3 the distributions of the output of the BDT algorithms, corresponding to $BDT_{\pi^+\pi^-}$ and $BDT_{K^+K^-}$ selections, are shown. The label `Train` has been employed to identify the distributions obtained from the samples used to train the three algorithms, whereas the label `Optim.` is employed to identify the distributions used in the optimisation phase of the selection. The label `Final` is employed to identify the distributions used in the final analysis. As it can be seen, the distributions are in agreement in all cases.

The optimal requirement on the BDT output is chosen by maximising the quantity $\xi = S/\sqrt{(S+B)}$, where S and B represent the number of signal and combinatorial background events within ± 60 MeV/c^2 (corresponding to about $\pm 3\sigma$) of the B^0 or B_s^0 masses. This method requires the knowledge of the amount of signals which are present in the initial sample. We estimate the initial signal yields by performing an unbinned maximum likelihood fit to the mass spectra using a simpler model. The invariant-mass spectra receives contributions mainly from the signals ($B_s^0 \to K^+K^-$ and $B^0 \to \pi^+\pi^-$), the main cross-feed background ($B^0 \to K^+\pi^-$), the combinatorial background and the partially reconstructed $B \to h^+h^-X$ decays. The signal component is parameterised using the sum of a Gaussian function and a Johnson function (an extended description of this model can be found in Sec. 6.5.1). The combinatorial background component is modelled using an exponential function. The component due to partially reconstructed multibody B decays, populating the low invariant-mass region, is parameterised by an ARGUS function [114] convolved with a Gaussian resolution function having the same

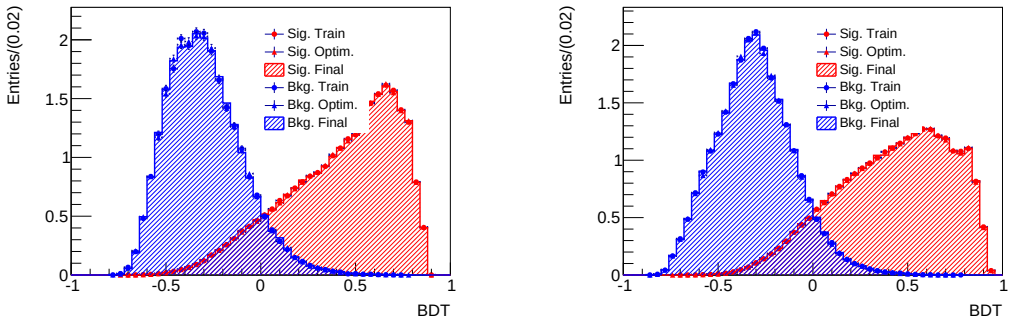

Figure 6.3: *Distributions of the BDT variable for (blue) background-like and the (red) signal-like events taken from the samples used to train the BDT algorithms. Background-like events have been selected applying the PID requirement optimised for the (left) K^+K^- and (right) $\pi^+\pi^-$ spectra on top of the preselection presented in Section 6.3 and the requirement $m_{(K^+K^-,\pi^+\pi^-)} > 5.6\,\mathrm{GeV}/c^2$. Circles represent the distribution of `BDT1` for `S1` sample, `BDT2` for `S2` and `BDT3` for `S3`. Triangles represent the distribution of `BDT1` for `S2` sample, `BDT2` for `S3` sample and `BDT3` for `S1` sample. Filled histograms represent the distribution of `BDT1` for `S3` sample, `BDT2` for `S1` sample and `BDT3` for `S2` sample.*

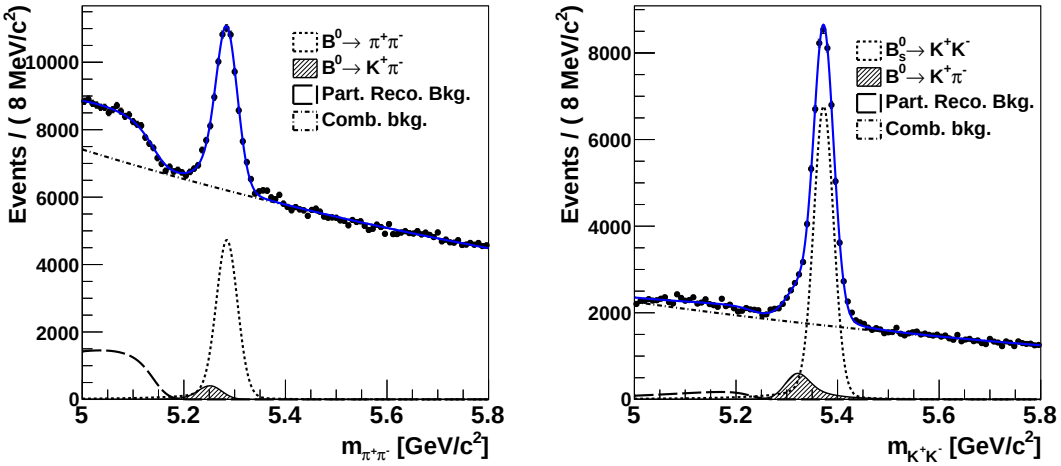

Figure 6.4: *Invariant-mass fits used for the relative normalization of signal and background yields in the BDT optimization for (left) $B^0 \to \pi^+\pi^-$ and (rigth) $B^0_s \to K^+K^-$ decays.*

width of the one used for the signal model. The cross-feed background due to misidentified $B^0 \to K^+\pi^-$ decays is modelled using the same method described in Sec. 5.2 of Ref. [106] and summarised in Sec. 6.5.2 of this thesis. Figure 6.4 shows the $\pi^+\pi^-$ and K^+K^- invariant-mass spectra after applying the preselection and the PID requirements, with the results of the fits superimposed. The signal yields determined from the fits are $N(B^0 \to \pi^+\pi^-) = 33644 \pm 462$ and $N(B^0_s \to K^+K^-) = 45042 \pm 299$. The amount of signal

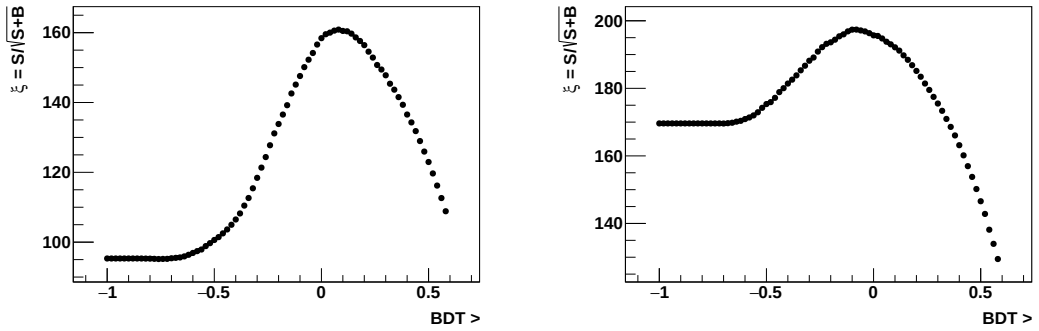

Figure 6.5: *Estimated* $\xi = S/\sqrt{(S+B)}$ *value as a function of the requirement applied on the BDT output for (left)* $B^0 \to \pi^+\pi^-$ *and (right)* $B_s^0 \to K^+K^-$ *decays.*

candidates surviving each BDT requirement is then estimated from these initial numbers and from the efficiencies of the BDT cuts applied to simulated events. The amount of the combinatorial background is instead determined from an unbinned maximum likelihood fit to the high invariant-mass sideband using an exponential function. The result of each fit is used to extrapolate the total background yields in the ± 60 MeV/c^2 invariant-mass window around the signal peak. Figure 6.5 shows the ξ value calculated as a function of the requirement on the BDT variable for the $B^0 \to \pi^+\pi^-$ and $B_s^0 \to K^+K^-$. The maximum value of ξ for $B^0 \to \pi^+\pi^-$ decays is obtained requiring the BDT classifier output to be greater than 0.1, while for $B_s^0 \to K^+K^-$ decays the optimal requirement is BDT > -0.1. The efficiencies of the requirement optimised for the $B^0 \to \pi^+\pi^-$ decay are $83.3 \pm 1.2\%$ and $6.57 \pm 0.07\%$ for signal and background, respectively. The efficiencies of the requirement optimised for the $B_s^0 \to K^+K^-$ decay are $93.9 \pm 0.8\%$ and $19.2 \pm 0.3\%$ for signal and background, respectively. The simplified models used in Fig. 6.4 are adapted to the selected samples applying the two different BDT requirements. A slight modification to the model used for the $\pi^+\pi^-$ spectrum is introduced. Due to the much lower combinatorial background the components due to the $B_s^0 \to \pi^+\pi^-$ decays cannot be neglected. This component has been described with the same model used for $B^0 \to \pi^+\pi^-$ decays. The results are shown in Fig. 6.6 and the values of the figure of merit ξ obtained from these fits are reported in Tab. 6.8. It can be seen that the change in ξ between using $BDT_{\pi^+\pi^-}$ and $BDT_{K^+K^-}$ is at the level of a relative 10%. Such a small difference does not impact significantly on the final uncertainties of C_f and S_f. For this reason the same BDT algorithm and BDT requirement for the analysis of both decays, notably the one corresponding to $BDT_{\pi^+\pi^-}$, is eventually used. This leads to a simplification of the analysis, avoiding the need to repeat twice several studies. In particular, having to perform the analysis with two different selections poses severals problems on how to determine properly the correlations among the relevant variables. Finally, the smaller amount of combinatorial background surviving the selection $BDT_{\pi^+\pi^-}$ helps improve the description of the distributions of the various spectra in the final fit.

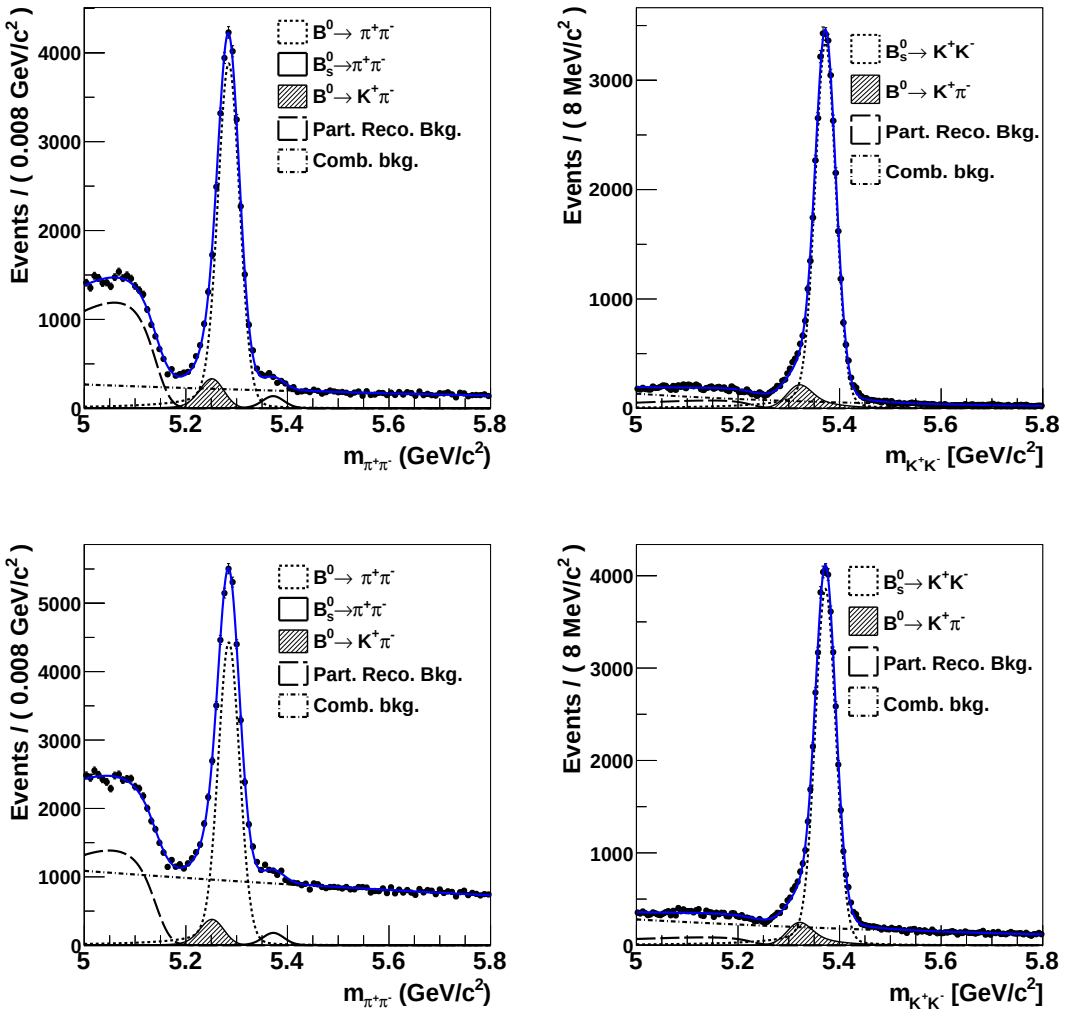

Figure 6.6: *Invariant-mass fits to (left) $\pi^+\pi^-$ and (right) K^+K^- spectra for events surviving the BDT requirement (top) $BDT_{\pi^+\pi^-}$ and (bottom) $BDT_{K^+K^-}$. The model used to fit the data is described in the text.*

6.5 Invariant-mass models

The invariant-mass models used to describe the cross-feed background, the combinatorial background and the partially reconstructed background are mainly the same as those used in Ref. [106], where more detailed explanations and validation studies are also reported. In the following a brief summary of the various models is reported. The parameterisation of the invariant-mass model for signal events, instead, is changed with respect to Ref. [106] in order to reduce the CPU consumption of the fitting code.

Table 6.8: *Values of the figure of merit* $\xi = S/\sqrt{S+B}$ *(within* $\pm 60\,\mathrm{MeV}/c^2$ *of the signal peaks) determined from the fits shown in Fig. 6.6.*

Selection	$B^0 \to \pi^+\pi^-$	$B_s^0 \to K^+K^-$
$BDT_{\pi^+\pi^-}$	159.024	189.012
$BDT_{K^+K^-}$	146.668	195.869

6.5.1 Invariant-mass model for signals

The shape of the signal components invariant mass (m) is studied on fully simulated events and is described by the following equation

$$\mathcal{P}_{sig.}(m) = (1 - f_J)G(m; \mu + \delta, \sigma_1, \sigma_2, f_g) + f_{tail}J(m; \mu, \delta, \alpha_1, \alpha_2), \tag{6.7}$$

where $G(m; \mu + \delta, \sigma_1, \sigma_2)$ is the sum of two Gaussian functions with common mean $\mu + \delta$ and widths σ_1 and σ_2, μ is fixed to the masses of the B^0 or B_s^0 mesons taken from the PDG [17], while the parameter δ is left free to vary to take into account a possible offset in the determination of the invariant mass, f_g is the relative fraction between the two Gaussian functions and $J(m; \mu, \delta, \alpha_1, \alpha_2)$ is a Johnson function, here parameterised as

$$J(m) = \frac{\alpha_2}{\sigma_1\sqrt{2\pi(1+z^2)}} \exp\left[-\frac{1}{2}\left(\alpha_1 + \alpha_2 \sinh^{-1} z\right)^2\right], \tag{6.8}$$

where $z \equiv \left[\frac{m-(\mu+\delta)}{\sigma_1}\right]$ and α_1 and α_2 are two parameters governing the left- and right-hand side tails of the shape. In the fit to data, the parameters α_1, α_2 and f_{tail} are fixed to the values determined from the fit of the model to fully simulated events, while the other parameters are left free to be adjusted by the fits. In Fig. 6.7 the invariant-mass distributions of fully simulated two-body b-hadron decays are reported with the result of the best fit overlaid. The values of the parameters that are fixed in the fit to data are reported in Tab. 6.9.

6.5.2 Invariant-mass model of cross-feed backgrounds

The invariant-mass model used for the cross-feed backgrounds is based on a kernel estimation method [89] applied to fully simulated two-body b-hadron decays. Simulated events are selected applying the same BDT requirement optimised as described in Sec. 6.4.2, while the effect of the PID requirements is estimated applying an event-per-event weight to simulated events, according to the PID efficiencies calibrated from data. A more detailed explanation and validation of the method can be found in Sec. 5.2 and App. B of Ref. [106]. The amount of each cross-feed background component is determined as the product of the yield of the respective decay mode with the ratio of the PID efficiencies

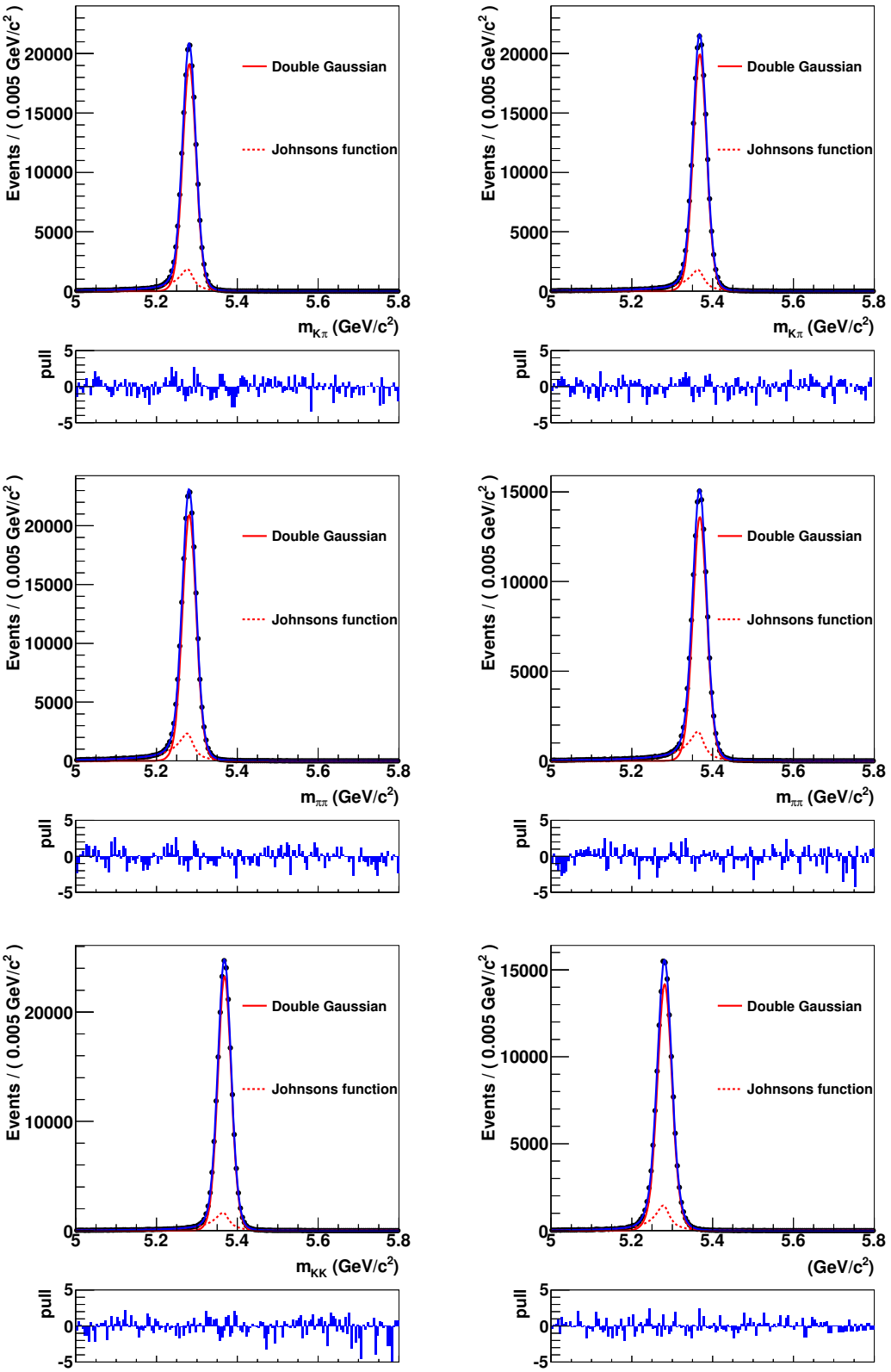

Figure 6.7: *Invariant-mass distributions for (from top left to bottom right) $B^0 \to K^+\pi^-$, $B^0_s \to \pi^+K^-$, $B^0 \to \pi^+\pi^-$, $B^0_s \to \pi^+\pi^-$, $B^0_s \to K^+K^-$ and $B^0 \to K^+K^-$ simulated decays. The result of the best fit with the model described in Eq.* (6.7) *is superimposed.*

Table 6.9: *Parameters of the PDF given in Eq.* (6.7) *obtained from unbinned maximum likelihood fits to simulated two-body b-hadron decays, that are fixed in the fit to data.*

Decay	f_{tail}	α_1	α_2
$B^0 \to K^+\pi^-$	0.1506 ± 0.0047	0.703 ± 0.018	0.5423 ± 0.0089
$B_s^0 \to \pi^+K^-$	0.1482 ± 0.0038	0.719 ± 0.015	0.5261 ± 0.0074
$B^0 \to \pi^+\pi^-$	0.1743 ± 0.0042	0.773 ± 0.016	0.5289 ± 0.0076
$B_s^0 \to \pi^+\pi^-$	0.1863 ± 0.0050	0.745 ± 0.016	0.5373 ± 0.0076
$B_s^0 \to K^+K^-$	0.1184 ± 0.0033	0.639 ± 0.015	0.5122 ± 0.0082
$B^0 \to K^+K^-$	0.1336 ± 0.0076	0.603 ± 0.014	0.5037 ± 0.0103

corresponding to the signal and background final state hypotheses. For example, the yields of the $B^0 \to K^+\pi^-$ decay in the $\pi^+\pi^-$ spectrum is calculated as

$$N_{\pi^+\pi^-}(B^0 \to K^+\pi^-) = N(B^0 \to K^+\pi^-) \cdot \frac{\varepsilon_{\pi^+\pi^-}(B^0 \to K^+\pi^-)}{\varepsilon_{K^+\pi^-}(B^0 \to K^+\pi^-)}, \tag{6.9}$$

where $N_{\pi^+\pi^-}(B^0 \to K^+\pi^-)$ is the number of the $B^0 \to K^+\pi^-$ decays present in the $\pi^+\pi^-$ spectrum, $N(B^0 \to K^+\pi^-)$ is the number of the $B^0 \to K^+\pi^-$ decays correctly identified by the PID requirements, $\varepsilon_{\pi^+\pi^-}(B^0 \to K^+\pi^-)$ is the probability to assign the $\pi^+\pi^-$ hypothesis to a $B^0 \to K^+\pi^-$ decay, and $\varepsilon_{K^+\pi^-}(B^0 \to K^+\pi^-)$ is the probability to assign the correct mass hypothesis to a $B^0 \to K^+\pi^-$ decay. In the final fits to data the PID efficiencies are computed using as a proxy for the kinematics of the final state particles the background-subtracted samples of two-body b-hadron decays, obtained using the method described in App. D.

6.5.3 Invariant-mass model of partially reconstructed backgrounds

The component due to partially-reconstructed three-body B decays in the $\pi^+\pi^-$ and K^+K^- spectra is described convolving a double Gaussian resolution function with an ARGUS function [114] (see also Eq. (D.1) in Appendix D), whereas that in the $K^\pm\pi^\mp$ spectrum is described convolving a Gaussian function with the sum of two ARGUS functions, in order to better take into account not only B^0, but also a lower fraction of B_s^0 three-body decays. This model was already used in previous analyses of two-body b-hadron decays (see for example Refs. [65, 101, 106, 107]), and proved to reproduce properly the shapes of the partially reconstructed backgrounds. The end points (m_0) of the ARGUS functions are fixed to the values $m_{B^0} - m_{\pi^0}$ (when parameterising B^0 partially reconstructed backgrounds), and $m_{B_s^0} - m_{\pi^0}$ (when parameterising B_s^0 partially reconstructed backgrounds), where m_{B^0}, $m_{B_s^0}$ and m_{π^0} are taken from the PDG [17]. The widths of the double Gaussian resolution are the parameters σ_1 and σ_2 of Eq. (6.7), while the mean is the parameter δ of the same equation. In this way, the resolution function

used to smear the ARGUS functions is the same as that used for the resolution of the signals and a possible shift in the reconstruction of the invariant mass is taken properly into account by the parameter δ.

6.5.4 Invariant-mass model of combinatorial background

The combinatorial background is modelled by an exponential PDF for all final state hypotheses. Independent parameters are used for the slopes of the exponential functions in the different spectra and they are free to vary in the fits to data.

6.6 Decay-time models

In this section the PDFs used to describe the distributions of decay-time for all the components contributing to the $K^+\pi^-$, $\pi^+\pi^-$ and K^+K^- spectra are introduced.

6.6.1 Tagged decay-time model for signals

In the following, the description of the decay-time model for the signals is reported. The decay-time models include also the components related to the decay-time resolution, the decay-time acceptance and the flavour-tagging observables. These parts will be described with more details in Secs. 6.7, 6.8 and 6.9, respectively.

6.6.1.1 $B^0_{(s)} \to K\pi$ decays

The dependence on time of the decay rate of a flavour specific $B \to f$ decay and of its CP conjugate $\overline{B} \to \bar{f}$ is given by the PDF

$$\begin{aligned} f\left(\vec{\theta}\right) =& K^{-1}\left(1-\psi A_{CP}\right)\left(1-\psi A_f\right)\cdot\{ \\ & \left[(1-A_{\rm P})\Omega_{sig}(\vec{\theta}_{tag})+(1+A_{\rm P})\bar{\Omega}_{sig}(\vec{\theta}_{tag})\right]H_+\left(t,\,\delta_t\right)+ \\ & \psi\left[(1-A_{\rm P})\Omega_{sig}(\vec{\theta}_{tag})-(1+A_{\rm P})\bar{\Omega}_{sig}(\vec{\theta}_{tag})\right]H_-\left(t,\,\delta_t\right)\Big\}\,, \end{aligned} \tag{6.10}$$

where $\vec{\theta} = \{\psi, \xi_{\rm OS}, \xi_{\rm SS}, \eta_{\rm OS}, \eta_{\rm SS}, t, \delta_t\}$ represents the set of observables used in the fit, the variable ψ is the final state tag assuming the value $+1$ for the final state f and -1 for the final state $\bar{f}$, $\xi_{\rm OS}$ and $\xi_{\rm SS}$ are the flavour tag, for OS and SS taggers, $\eta_{\rm OS}$ and $\eta_{\rm SS}$ are the predicted mistag probabilities, for OS and SS taggers, $\Omega_{sig}(\vec{\theta}_{tag})$ and $\bar{\Omega}_{sig}(\vec{\theta}_{tag})$ are the probability functions for the flavour-tagging observables that will be described in Sec. 6.9 with $\vec{\theta}_{tag} = \{\xi_{\rm OS}, \xi_{\rm SS}, \eta_{\rm OS}, \eta_{\rm SS}\}$, and K is the normalisation factor

$$K = 4\left(1+A_{CP}A_f\right)\int\int H_+\left(t',\,\delta'_t\right)\mathrm{d}t'\mathrm{d}\delta'_t + 4A_{\rm P}\left(A_{CP}+A_f\right)\int\int H_-\left(t',\,\delta'_t\right)\mathrm{d}t'\mathrm{d}\delta'_t. \tag{6.11}$$

The functions $H_+(t,\delta_t)$ and $H_-(t,\delta_t)$ are defined as

$$H_+(t,\,\delta_t) = \left[e^{-\Gamma t'}\cosh\left(\frac{\Delta\Gamma}{2}t'\right)\right]\otimes R(t-t'|\delta_t)\cdot g(\delta_t)\cdot\varepsilon_{\rm acc}(t), \tag{6.12}$$

$$H_-(t,\,\delta_t) = \left[e^{-\Gamma t'}\cos(\Delta m t')\right]\otimes R(t-t'|\delta_t)\cdot g(\delta_t)\cdot\varepsilon_{\rm acc}(t), \tag{6.13}$$

where Γ is the average decay width of the B meson, $\Delta\Gamma$ is the decay-width difference between the mass eigenstates, Δm is the mass difference between the mass eigenstates, R is the per-event decay-time resolution model as a function of the uncertainty on the decay time (δ_t) predicted by the reconstruction algorithms, $g(\delta_t)$ is the distribution of δ_t (see Sec. 6.7 for more details), $\varepsilon_{\rm acc}$ is the decay-time acceptance and $\otimes$ stands for convolution product. The parameters A_{CP}, A_f and $A_{\rm P}$ represent the direct *CP* asymmetry, the asymmetry of final state reconstruction efficiencies and the B meson production asymmetry, respectively. They are defined as

$$A_{CP} = \frac{\mathcal{B}\left(\bar{B}\to\bar{f}\right)-\mathcal{B}\left(B\to f\right)}{\mathcal{B}\left(\bar{B}\to\bar{f}\right)+\mathcal{B}\left(B\to f\right)}, \tag{6.14}$$

$$A_f = \frac{\varepsilon_{\rm tot}\left(\bar{f}\right)-\varepsilon_{\rm tot}\left(f\right)}{\varepsilon_{\rm tot}\left(\bar{f}\right)+\varepsilon_{\rm tot}\left(f\right)}, \tag{6.15}$$

$$A_{\rm P} = \frac{\mathcal{R}\left(\bar{B}\right)-\mathcal{R}\left(B\right)}{\mathcal{R}\left(\bar{B}\right)+\mathcal{R}\left(B\right)}, \tag{6.16}$$

where $\mathcal{B}$ denotes the branching fraction, $\varepsilon_{\rm tot}$ is the total efficiency in reconstructing and selecting the final state f or $\bar{f}$, and $\mathcal{R}$ is the production rate of the given B or $\overline{B}$ meson. Note that in Eq. (6.10), up to a very good approximation, A_{CP} and A_f can be substituted with a single asymmetry $A_{raw} = A_{CP} + A_f$, that will be the variable determined from the fit. The determination of A_f, necessary to determine the *CP* asymmetry, will be discussed in Sec. 6.11.

6.6.1.2 $B^0 \to \pi^+\pi^-$ and $B_s^0 \to K^+K^-$ decays

In this case, the final states f and $\bar{f}$ are the same, hence the observable ψ is not necessary anymore and is removed from $\vec{\theta}$. The time-dependent decay rates are described by

$$\begin{aligned} f\left(\vec{\theta}\right) = K^{-1}\Big\{&\left[(1-A_{\rm P})\,\Omega\left(\vec{\theta}_{tag}\right)+(1+A_{\rm P})\,\bar{\Omega}\left(\vec{\theta}_{tag}\right)\right]I_+(t,\,\delta_t)+\\ &\left[(1-A_{\rm P})\,\Omega\left(\vec{\theta}_{tag}\right)-(1+A_{\rm P})\,\bar{\Omega}\left(\vec{\theta}_{tag}\right)\right]I_-(t,\,\delta_t)\Big\}, \end{aligned} \tag{6.17}$$

where the normalization factor K is

$$K = 2\int\int I_+(t',\,\delta_t')\,{\rm d}t'{\rm d}\delta_t' - 2A_{\rm P}\int\int I_+(t',\,\delta_t')\,{\rm d}t'{\rm d}\delta_t'. \tag{6.18}$$

The functions $I_+(t)$ and $I_-(t)$ are

$$I_+(t,\,\delta_t) = \left\{e^{-\Gamma t'}\left[\cosh\left(\frac{\Delta\Gamma}{2}t'\right)-A_f^{\Delta\Gamma}\sinh\left(\frac{\Delta\Gamma}{2}t'\right)\right]\right\}\otimes$$

$$R\left(t-t'|\delta_t\right)\cdot g\left(\delta_t\right)\cdot\varepsilon_{\rm acc}\left(t\right), \tag{6.19}$$

$$I_-\left(t,\,\delta_t\right) = \left\{e^{-\Gamma t'}\left[C_f\cos\left(\Delta m t'\right)-S_f\sin\left(\Delta m t'\right)\right]\right\}\otimes R\left(t-t'|\delta_t\right)\cdot g\left(\delta_t\right)\cdot\varepsilon_{\rm acc}\left(t\right). \tag{6.20}$$

The parameter $A_f^{\Delta\Gamma}$ can be parameterised as

$$A_f^{\Delta\Gamma} = \pm\sqrt{1-C_f^2-S_f^2}, \tag{6.21}$$

where the ambiguity in the sign of this relation reflects the invariance of the decay rates under the exchange $\left(\Delta\Gamma,\,A_f^{\Delta\Gamma}\right)\to\left(-\Delta\Gamma,\,-A_f^{\Delta\Gamma}\right)$. In the case of the $B^0\to\pi^+\pi^-$ decay, where $\Delta\Gamma$ can be assumed negligible, the ambiguity is not relevant, in contrast to the case of the $B^0_s\to K^+K^-$ decay. Alternatively, as done in this analysis, $A_f^{\Delta\Gamma}$ can also be left free to vary in the fit and the validity of the relation verified *a posteriori*.

6.6.2 Cross-feed background decay-time model

In the following, the expressions for the decay-time PDFs of the cross-feed background components are reported, assuming that the decay time calculated under the wrong mass hypothesis is not significantly different from the correct one. This assumption is then verified by means of fully simulated events, as already proved in Sec. 5.4.3 of Ref. [115]. The components considered are

- the $B^0\to\pi^+\pi^-$ and $B^0_s\to K^+K^-$ decays with final states misidentified as $K^+\pi^-$;
- the $B^0\to K^+\pi^-$ decay with final state misidentified as $\pi^+\pi^-$ or K^+K^-;
- the $\Lambda^0_b\to pK^-$ decay with final state misidentified as K^+K^-.

Further contributions, due to double misidentification, are found to be negligible given the PID requirements used to separate the $K^+\pi^-$, $\pi^+\pi^-$ and K^+K^- spectra.

6.6.2.1 $B^0\to\pi^+\pi^-$ and $B^0_s\to K^+K^-$ decays under the $K^+\pi^-$ hypothesis

As the final states of $B^0\to\pi^+\pi^-$ and $B^0_s\to K^+K^-$ decays are self-conjugate, their decay rates do not depend explicitly on ψ. Thus the PDF in this case is written as

$$f\left(\vec{\theta}\right) = K^{-1}\left\{\left[\left(1-A_{\rm P}\right)\Omega_{sig}\left(\vec{\theta}_{tag}\right)+\left(1+A_{\rm P}\right)\bar{\Omega}_{sig}\left(\vec{\theta}_{tag}\right)\right]I_+\left(t,\delta_t\right)+\left[\left(1-A_{\rm P}\right)\Omega_{sig}\left(\vec{\theta}_{tag}\right)-\left(1+A_{\rm P}\right)\bar{\Omega}_{sig}\left(\vec{\theta}_{tag}\right)\right]I_-\left(t,\delta_t\right)\right\}, \tag{6.22}$$

where $\vec{\theta}=\{\psi,\xi_{OS},\xi_{SS},\eta_{OS},\eta_{SS},t,\delta_t\}$. The dependence on ψ is implicit as $B^0\to\pi^+\pi^-$ and $B^0_s\to K^+K^-$ can be misidentified as both $K^+\pi^-$ and $K^-\pi^+$ final states. The normalisation factor K is given by

$$K = 4\int\int I_+\left(t',\delta'_t\right)\mathrm{d}t'\mathrm{d}\delta'_t - 4A_{\rm P}\int\int I_+\left(t',\delta'_t\right)\mathrm{d}t'\mathrm{d}\delta'_t. \tag{6.23}$$

6.6.2.2 $B^0 \to K^+\pi^-$ decays with final state identified as $\pi^+\pi^-$ or K^+K^-

In this case, the information provided by the observation of the two $K^+\pi^-$ and $K^-\pi^+$ final states is lost. This effect corresponds to integrate away ψ from the PDF given in Eq. (6.10). The parameterization of this cross-feed background is

$$f\left(\vec{\theta}\right) = K^{-1}\left\{\left(1+A_{CP}A_f\right)\left[\left(1-A_{\rm P}\right)\Omega_{sig}\left(\vec{\theta}_{tag}\right)+\left(1+A_{\rm P}\right)\bar{\Omega}_{sig}\left(\vec{\theta}_{tag}\right)\right]H_+(t,\delta_t)- \left(A_{CP}+A_f\right)\left[\left(1-A_{\rm P}\right)\Omega_{sig}\left(\vec{\theta}_{tag}\right)-\left(1+A_{\rm P}\right)\bar{\Omega}_{sig}\left(\vec{\theta}_{tag}\right)\right]H_-(t,\delta_t)\right\}, \tag{6.24}$$

where the variable ψ is removed from $\vec{\theta}$ and the normalization factor K is

$$K = 2\left(1+A_{CP}A_f\right)\int\int H_+\left(t',\delta_t'\right)\mathrm{d}t'\mathrm{d}\delta_t' + 2A_{\rm P}\left(A_{CP}+A_f\right)\int\int H_-\left(t',\delta_t'\right)\mathrm{d}t'\mathrm{d}\delta_t'. \tag{6.25}$$

6.6.2.3 $\Lambda_b^0 \to pK^-$ decays with final state identified as K^+K^-

Also in this case, the information provided by the observation of the two pK^- and $\overline{p}K^+$ final states is lost, and again this effect corresponds to integrate away ψ from the PDF given in Eq. (6.10). In addition, the time-dependent decay rate of the Λ_b^0 baryon is a pure exponential. Therefore, the tagged time-dependent rate of $\Lambda_b^0 \to pK^-$ misidentified as K^+K^- final state can be written as

$$\begin{aligned} f\left(\vec{\theta}\right) = K^{-1}\Big[&\left(1-A_{\rm P}\right)\left(1-A_f\right)\left(1-A_{CP}\right)\Omega_{sig}\left(\vec{\theta}_{tag}\right) \\ &+\left(1+A_{\rm P}\right)\left(1+A_f\right)\left(1+A_{CP}\right)\bar{\Omega}_{sig}\left(\vec{\theta}_{tag}\right)\Big]T\left(t,\,\delta_t\right), \end{aligned} \tag{6.26}$$

where $T\left(t,\delta_t\right)$ is

$$T\left(t,\,\delta_t\right) = e^{-\Gamma t'} \otimes R\left(t-t'|\delta_t\right)\cdot g\left(\delta_t\right)\cdot\varepsilon_{\rm acc}\left(t\right). \tag{6.27}$$

In this case Γ is the decay width of the Λ_b^0 baryon, $A_{\rm P}$ is the production asymmetry of the Λ_b^0 baryon, A_f is the detection asymmetry of the pK^- and $\overline{p}K^+$ final states and A_{CP} is the CP asymmetry of the $\Lambda_b^0 \to pK^-$ decay. The functions $\Omega_{sig}\left(\xi,\eta\right)$ and $\bar{\Omega}_{sig}\left(\xi,\eta\right)$ determine the probability of a Λ_b^0 baryon to be tagged as a B meson or a $\overline{B}$ meson respectively. The normalisation factor K is given by

$$K = 2\left(1+A_{CP}A_f+A_{CP}A_P+A_fA_P\right)\int\int T\left(t',\,\delta_t'\right)\mathrm{d}t'\mathrm{d}\delta_t'. \tag{6.28}$$

6.6.3 Combinatorial background

In order to study the parameterisation of the decay-time distribution for combinatorial background events we focus on the high invariant mass sideband, that is defined as $m > 5.6$ GeV/c^2. For the combinatorial background in the $K^\pm\pi^\mp$ spectrum it is empirically

found that the PDF can be written as

$$f\left(\vec{\theta}\right) = K^{-1}\left(1 - \psi A_{CP}^{comb}\right)\Omega_{comb}(\vec{\theta}_{tag}) \cdot g_{comb}(\delta_t) \quad \times \\ \left[f_{comb} \cdot e^{-\Gamma_1^{comb} t}\varepsilon_{acc}^{comb}(t) + (1 - f_{comb})\, e^{-\Gamma_2^{comb} t}\varepsilon_{acc}^{comb}(t)\right], \tag{6.29}$$

where $\vec{\theta} = \{\psi, \xi_{OS}, \xi_{SS}, \eta_{OS}, \eta_{SS}, t, \delta_t\}$, $\Omega_{comb}(\vec{\theta}_{tag})$ is the probability function for the flavour-tagging observables that will be discussed in Sec. 6.9, $g_{comb}(\delta_t)$ is the distribution of δ_t for the combinatorial background and K is the normalisation constant

$$K = 2\int g_{comb}(\delta_t')\mathrm{d}\delta_t' \int \left[f_{comb} \cdot e^{-\Gamma_1^{comb} t'}\varepsilon_{acc}^{comb}(t') + (1 - f_{comb})\, e^{-\Gamma_2^{comb} t'}\varepsilon_{acc}^{comb}(t')\right]\mathrm{d}t'. \tag{6.30}$$

The parameter $A_{CP}^{\rm comb}$ is the charge asymmetry of the combinatorial background and Γ_1^{comb}, Γ_2^{comb} and f_{comb} are free parameters to be determined by the fit. The effective function $\varepsilon_{\rm acc}^{\rm comb}(t)$ is the analog of the decay time acceptance for signal decays. It has been empirically found that using the parameterisation

$$\varepsilon_{\rm acc}^{\rm comb}(t) = \frac{1}{2}\left[1 - \mathrm{erf}\left(\frac{a - t}{a \cdot t}\right)\right], \tag{6.31}$$

where a is a free parameter to be determined in the fit, a good agreement between the model and the decay time distribution in the high invariant mass sidebands is obtained. For the $\pi^+\pi^-$ and K^+K^- spectra, the same parameterisation is used, apart from the fact that the PDF does not depend on the two different charge-conjugate final states that have to be considered in the $K^\pm\pi^\mp$ case. In Fig. 6.8 the decay-time distributions of events from the high invariant mass sideband of the $K^\pm\pi^\mp$, $\pi^+\pi^-$ and K^+K^- spectra are shown, with the results of fits superimposed.

6.6.4 Partially reconstructed background

The decay time distribution of partially reconstructed B decays in the $\pi^+\pi^-$ and K^+K^- spectra are described by the empirical parameterisation

$$f\left(\vec{\theta}\right) = K^{-1}\Omega_{phys}(\vec{\theta}_{tag}) \cdot g_{\rm phys}(\delta_t) \cdot e^{-\Gamma^{\rm phys} t}\varepsilon_{\rm acc}^{\rm phys}(t), \tag{6.32}$$

where $\Omega_{phys}(\vec{\theta}_{\rm tag})$ is the probability function for the flavour-tagging observables that will be discussed in Section 6.9, $g_{\rm phys}(\delta_t)$ is the distribution of δ_t for partially reconstructed backgrounds and K is a normalisation factor. The effective function $\varepsilon_{\rm acc}^{\rm phys}(t)$ is given by

$$\varepsilon_{\rm acc}^{\rm phys}(t) = \frac{1}{2}\left[1 - \mathrm{erf}\left(\frac{b - t}{b \cdot t}\right)\right], \tag{6.33}$$

where b is a free parameter of the fit.

For the $K^+\pi^-$ spectrum the parameterisation of the partially reconstructed background is the same adopted for the $B^0 \to K^+\pi^-$ decays and reported in Eq. (6.10), with

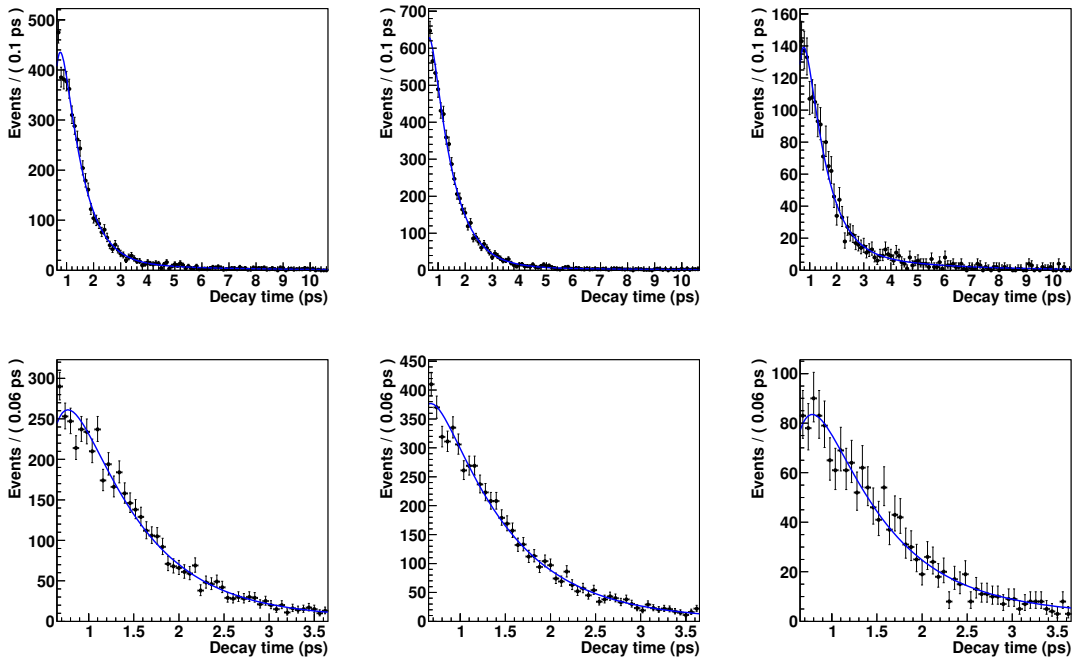

Figure 6.8: *Decay time distributions for events in the high invariant mass sideband ($m > 5.6\,\mathrm{GeV}/c^2$) for the (top left) $K^{\pm}\pi^{\mp}$, (top middle) $\pi^+\pi^-$ and (top right) K^+K^- spectra. The result of the best fit to data is superimposed to the data points. In the bottom row a zoom in the low decay time region is also shown.*

independent parameters governing the calibration of the flavour tagging and the oscillation frequency Δm that are left free to be adjusted by the fit. The parameter governing the exponential part of the equation (Γ) is fixed to 0.6 ps^{-1}. The acceptance function is described using cubic splines (as explained in Ref. [116]) with 6 knots placed at 0.7, 1, 1.5, 2, 3 and 10 ps. The coefficients governing the contribution of each cubic polynomial are left free to vary in the fit. The need to describe this component differently from the the partially reconstructed backgrounds in the $\pi^+\pi^-$ and K^+K^- spectra is due to the observation of a time-dependent asymmetry in the low-mass region of the $K^+\pi^-$ spectrum, as it will be shown in Sec. 6.10.

6.7 Decay-time resolution

The calibration of the decay-time resolution is of fundamental importance for time-dependent *CP* violation measurements. In fact, a non-negligible value of the decay time resolution introduces a dilution factor on the parameters C_f and S_f, corresponding to approximately

$$D_{\sigma_t} = e^{-\frac{\Delta m^2_{d,s}\cdot\sigma_t^2}{2}}, \tag{6.34}$$

where $\Delta m_{d,s}$ are the mass differences between the two mass eigenstates of the considered neutral B systems and σ_t is the width of the decay time resolution. The relation between the observed value of the *CP*-violating parameter $C_f^{obs.}$ ($S_f^{obs.}$) is then $C_f^{obs.} = D_{\sigma_t} \cdot C_f$ ($S_f^{obs.} = D_{\sigma_t} \cdot S_f$). The determination of σ_t is particularly important for the B_s^0 decays, because of the large value of Δm_s. In the case of the B^0 meson, instead, the value of Δm_d is such that even a value of σ_t as large as 150 fs will result in a dilution factor $D \approx 0.997$, hence a three per mille deviation of the observed *CP*-violating parameters with respect to their real values.

The calibration of the decay time-resolution for two-body b-hadron decays is performed in the following steps

- the functional dependence between the predicted decay time error δ_t and the decay time resolution σ_t is studied using fully simulated $B_s^0 \to \pi^+K^-$, $B_s^0 \to K^+K^-$ and $B_s^0 \to D_s^-\pi^+$ decays, with particular attention in checking that different kinematics of the decays have no impact;

- the model describing the decay-time resolution is also determined from fully simulated $B_s^0 \to \pi^+K^-$ and $B_s^0 \to D_s^-\pi^+$ events, studying the distribution of the difference between the true and reconstructed decay time as a function of δ_t;

- the calibration of the functional relation between δ_t and σ_t is performed by means of fits to the tagged time-dependent decay rates of the flavour specific $B_s^0 \to D_s^-\pi^+$ decay; the possibility of using this method to calibrate the decay time resolution is validated using fully simulated $B_s^0 \to \pi^+K^-$ and $B_s^0 \to D_s^-\pi^+$ decays.

In the following sections the studies corresponding to the steps outlined above will be presented.

6.7.1 Relation between δ_t and σ_t

In order to study the relation between the predicted decay-time uncertainty δ_t and the decay-time resolution σ_t, fully simulated $B_s^0 \to \pi^+K^-$, $B_s^0 \to K^+K^-$ and $B_s^0 \to D_s^-\pi^+$ events are used. The $B_s^0 \to \pi^+K^-$ and $B_s^0 \to K^+K^-$ decays are selected by applying the same BDT requirements optimised in Sec. 6.4.2. For the $B_s^0 \to D_s^-\pi^+$ decays, fully simulated events where the D_s^- is forced to decay to the $K^+K^-\pi^-$ final state are used, requiring the match between the reconstructed decay and the Monte Carlo truth information. The decay time is computed constraining the D_s^- mass to the known value. The same reconstruction version and trigger configurations used for the two-body b-hadron sample are employed to process the simulated $B_s^0 \to D_s^-\pi^+$ events. In order to take into account possible effects related to the kinematics of the involved decays, an event-per-event weight is applied to the $B_s^0 \to \pi^+K^-$ and to the $B_s^0 \to K^+K^-$ simulated events, corresponding to the PID efficiencies as a function of the momentum and pseudorapidity of the final state particles. In the case of fully simulated $B_s^0 \to D_s^-\pi^+$ decays, a two-dimensional reweighting of the B momentum and pseudorapidity to the distributions of the $B_s^0 \to K^+K^-$ decays is performed.

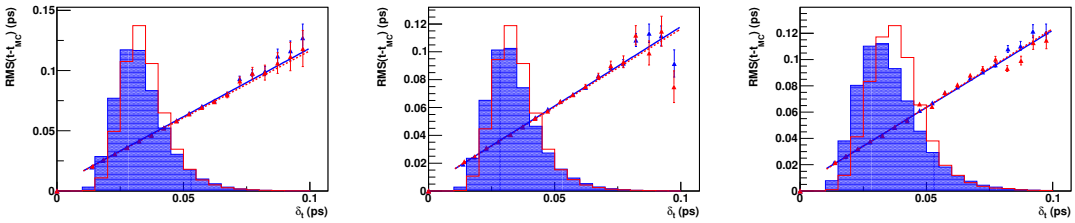

Figure 6.9: *The triangles represent the dependency between δ_t and the RMS of $t - t_{MC}$ for fully simulated (left) $B_s^0 \to \pi^+K^-$, (middle) $B_s^0 \to K^+K^-$ and (right) $B_s^0 \to D_s^-\pi^+$ decays. Blue triangles represent the case where PID effect or kinematic reweighting (as explained in the text) have not been applied. Red triangles represent the cases where the PID effect and the kinematic reweighting have been taken into account. The solid blue (dashed red) line represent the best fit to the blue (red) triangles using Eq.* (6.35)*. The distributions of δ_t are also reported for (blue filled histogram) unweighted and (red histogram) weighted samples.*

Table 6.10: *Parameters governing the linear relation of Eq.* (6.35) *between the predicted decay time error δ_t and RMS($\tau_{err.}$) for fully simulated $B_s^0 \to \pi^+K^-$, $B_s^0 \to K^+K^-$ and $B_s^0 \to D_s^-\pi^+$ decays.*

Decay	Unweighted			Weighted		
	q_0 [fs]	q_1	$\rho(q_0, q_1)$	q_0 [fs]	q_1	$\rho(q_0, q_1)$
$B_s^0 \to \pi^+K^-$	38.97 ± 0.05	1.136 ± 0.006	0.13	38.44 ± 0.08	1.113 ± 0.010	-0.19
$B_s^0 \to K^+K^-$	38.26 ± 0.05	1.140 ± 0.006	0.11	38.00 ± 0.08	1.120 ± 0.010	-0.16
$B_s^0 \to D_s^-\pi^+$	40.07 ± 0.05	1.174 ± 0.005	0.10	40.05 ± 0.06	1.195 ± 0.006	-0.23

The samples are divided into 20 bins of δ_t and in each bin the RMS of the quantity $\tau_{err.} = t - t_{MC}$ is computed, where t is the reconstructed decay time and t_{MC} is the true decay time of the generated B meson. In Fig. 6.9 the relation between δ_t and the RMS of $\tau_{err.}$ for $B_s^0 \to \pi^+K^-$, $B_s^0 \to K^+K^-$ and $B_s^0 \to D_s^-\pi^+$ fully simulated events is shown. The distributions of the δ_t observable are also shown. The linear relation

$$\mathrm{RMS}(\tau_{err.}) = q_0 + q_1 \cdot (\delta_t - \hat{\delta}_t), \tag{6.35}$$

where $\hat{\delta}_t$ has been fixed to 30 fs (corresponding approximately to the average of the δ_t distributions), describes very well the observed dependence. The PID and kinematic reweighting are found to have an impact on the δ_t distributions. However, they do not have a significant effect on the linear relation between δ_t and RMS($\tau_{err.}$). Indeed, the values of the parameters q_0 and q_1, reported in Tab. 6.10 result to be almost unaffected.

Table 6.11: *Calibration parameters of the decay-time resolution for fully simulated $B^0_s \to \pi^+K^-$ and $B^0_s \to D^-_s\pi^+$ decays. The results are obtained from the unbinned maximum likelihood fit of the model described in Eq.* (6.36) *to the distributions of fully simulated candidates.*

Parameter	$B^0_s \to \pi^+K^-$	$B^0_s \to D^-_s\pi^+$
μ [fs]	0.070 ± 0.052	-0.069 ± 0.067
q_0 [fs]	35.102 ± 0.077	36.735 ± 0.096
q_1	1.0990 ± 0.0065	1.158 ± 0.010
r_σ	3.081 ± 0.032	2.975 ± 0.042
f_τ	0.97119 ± 0.00082	0.97145 ± 0.00109

6.7.2 Determination of the decay-time resolution model

In order to determine the model used to parameterise the decay-time resolution, two-dimensional unbinned maximum likelihood fits to the δ_t and the $\tau_{err.}$ distributions of $B^0_s \to \pi^+K^-$ and $B^0_s \to D^-_s\pi^+$ fully simulated events are performed. The distributions are modelled using the PDF

$$T(\delta_t, \tau_{err.}) = [f_\tau \cdot G(\tau_{err.}; \mu, \sigma_1(\delta_t)|\delta_t) + (1 - f_\tau) \cdot G(\tau_{err.}; \mu, \sigma_2(\delta_t))] \cdot g(\delta_t), \qquad (6.36)$$

where $G(\tau_{err.}; \mu, \sigma_{1,2}(\delta_t)|\delta_t)$ are Gaussian functions with common mean μ and widths σ_1 and σ_2 and $g(\delta_t)$ is an histogram describing the distribution of δ_t. The dependence of σ_1 and σ_2 on δ_t are parameterised in the following way

$$\sigma_1(\delta_t) = q_0 + q_1 \cdot (\delta_t - \hat{\delta}_t), \qquad (6.37)$$

$$\sigma_2(\delta_t) = r_\sigma \cdot \sigma_1(\delta_t). \qquad (6.38)$$

In Tab. 6.11 the values of the parameters obtained from the fit are reported, while the plots of $\tau_{err.}$ are shown in Fig. 6.10, with the result of the best fit superimposed. No significant deviation of μ from 0 is observed. In addition, the parameters f_τ and r_σ are in good agreement between the $B^0_s \to \pi^+K^-$ and $B^0_s \to D^-_s\pi^+$ decays.

6.7.3 Calibration of decay-time resolution using tagged time-dependent fits

In order to probe the possibility of calibrating the decay time resolution from tagged time dependent fits, simulated samples of $B^0_s \to \pi^+K^-$ and $B^0_s \to D^-_s\pi^+$ decays are used. The tagged decay time distributions have been fitted using the model described in Eq. (6.10), where the resolution function is parameterised using the sum of two Gaussian functions

$$R(t - t'|\delta_t) = f_\tau \cdot G(t - t'; \mu, \sigma_1(\delta_t)|\delta_t) + (1 - f_\tau) \cdot G(t - t'; \mu, \sigma_2(\delta_t)), \qquad (6.39)$$

where G is defined as in Eq. (6.36) and the dependencies of σ_1 and σ_2 on δ_t are the same of Eqs. (6.37) and (6.38). The parameters q_0 and q_1 are left free to be adjusted by the

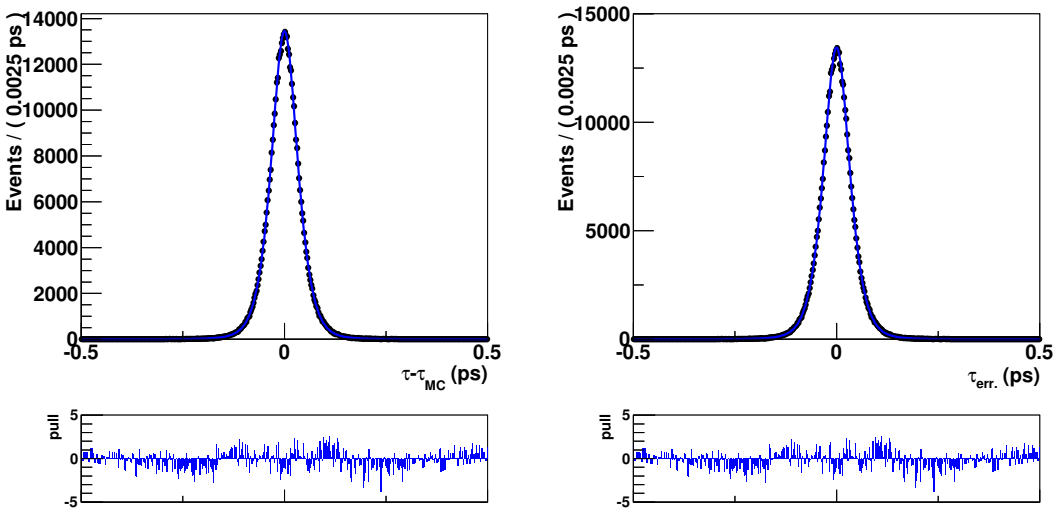

Figure 6.10: *Distribution of $\tau_{\rm err.}$ for fully simulated (left) $B_s^0 \to \pi^+ K^-$ and (right) $B_s^0 \to D_s^- \pi^+$ decays. The result of the best fit with the model described in Eq.* (6.36) *to the data points is superimposed.*

Table 6.12: *Calibration parameters of the decay-time resolution for fully simulated $B_s^0 \to \pi^+ K^-$ and $B_s^0 \to D_s^- \pi^+$ decays. The results are obtained from tagged time-dependent unbinned maximum likelihood fits to the distributions of simulated candidates, as described in the text.*

	q_0 [fs]	q_1	$\rho(q_0, q_1)$
$B_s^0 \to \pi^+ K^-$	34.71 ± 0.27	1.041 ± 0.028	-0.44
$B_s^0 \to D_s^- \pi^+$	35.84 ± 0.21	1.143 ± 0.018	-0.33

fit, while the mean of the Gaussian functions μ is fixed to 0, and the values of r_σ and f_τ are fixed to the weighted average between the values reported in Tab. 6.11. The decay width Γ_s and decay width difference $\Delta\Gamma_s$ are fixed to their simulated values corresponding to $\Gamma_s = 0.6654$ ps^{-1} and $\Delta\Gamma_s = 0.0916$ ps^{-1}, while the coefficients of the cubic splines governing the decay-time acceptance are left free to be adjusted by the fit. In addition, we make use of the Monte Carlo truth information to tag the flavour of the B candidate, hence fixing tagging efficiencies to 1 and mistag probabilities to 0.

Since the final calibration on data is performed using $B_s^0 \to D_s^- \pi^+$ events having different kinematic distributions with respect to two-body b-hadron charmless events, the PID-weighted sample for $B_s^0 \to \pi^+ K^-$ decays and the unweighted sample for $B_s^0 \to D_s^- \pi^+$ decays are fitted. In Fig. 6.11 we report the decay-time distribution of the two decay modes with the result of the best fit overlaid. The corresponding time-dependent asymmetries are shown as well. Numerical results for q_0 and q_1 are reported in Tab. 6.12. The values of

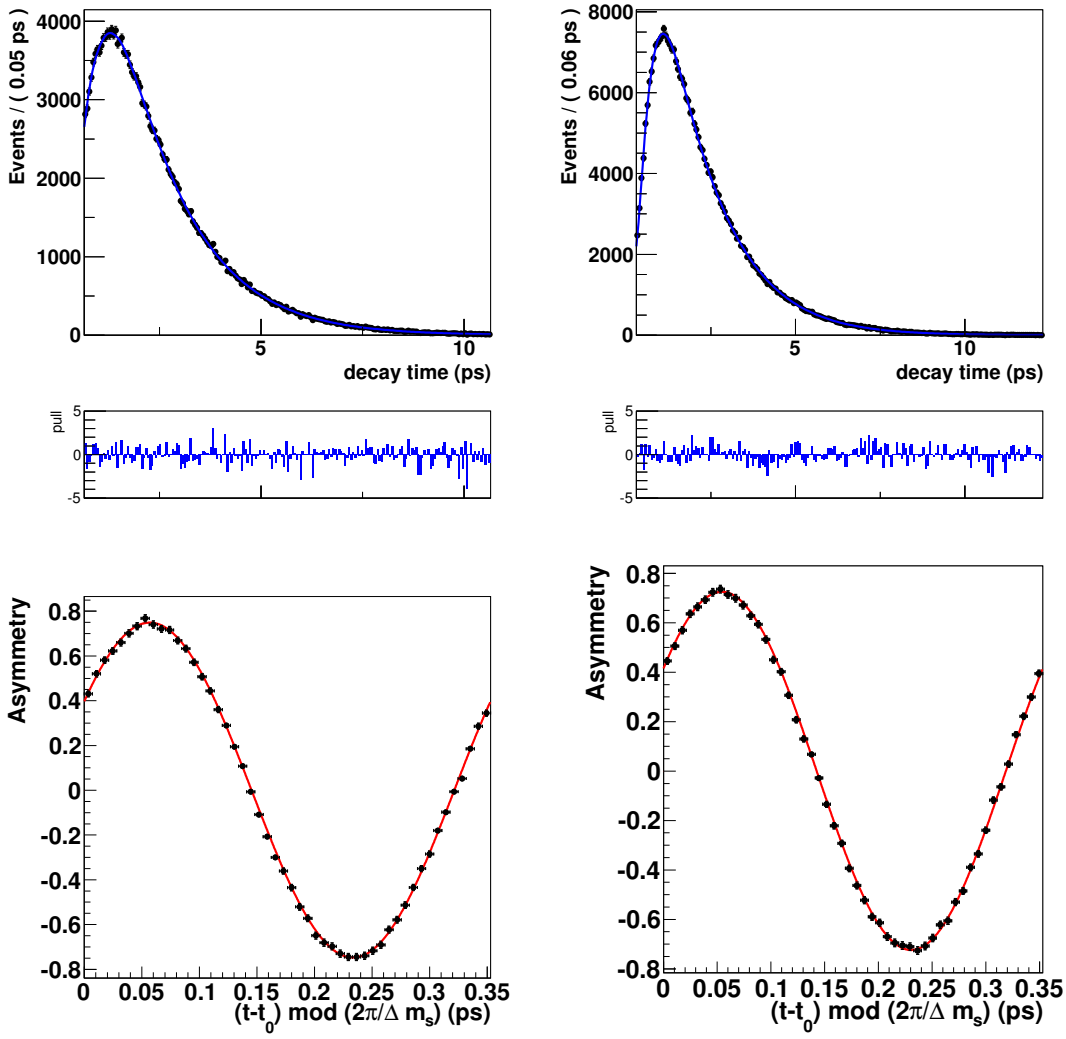

Figure 6.11: *(top) distributions of decay-time and (bottom) time-dependent asymmetries for fully simulated (left) $B^0_s \to \pi^+K^-$ and (right) $B^0_s \to D^-_s\pi^+$ decays. The results of the best fits are superimposed.*

q_0 and q_1 obtained from the time-dependent fit are slightly different with respect to those reported in Tab. 6.11. The differences are about 1 fs for q_0 and 0.01-0.06 for q_1. These discrepancies, as well as the differences observed between the calibration parameters for $B^0_s \to \pi^+K^-$ and $B^0_s \to D^-_s\pi^+$ decays, will be treated as a source of systematic uncertainty.

6.7.4 Calibration of the decay-time resolution from data

The calibration of the decay-time resolution from data is performed by means of unbinned maximum likelihood fits to the tagged decay-time distribution of $B^0 \to D^-\pi^+$ and $B_s^0 \to D_s^-\pi^+$ decays. Samples of *sWeighted* events, obtained using the *sPlot* [85] technique used to perform the official calibrations of the flavour tagging and that are provided by the LHCb flavour tagging group are employed. The two samples are fitted simultaneously using the model described in Eq. (6.10) with the decay-time resolution parameterised as in Eq. (6.39). The decay width and decay-width differences $\Gamma_{d,s}$ and $\Delta\Gamma_{d,s}$ are fixed to the HFLAV averages [67] (reported in Tab. 6.20), while the coefficients of the cubic splines are free to vary, as well as the values of $\Delta m_{d,s}$. The two decay modes share the parameters governing the calibration of the opposite side tagger and of the decay-time resolution.

Since the decay-time resolution has a negligible effect on the $B^0 \to D^-\pi^+$ decay, from this sample it is possible to determine the calibration of the flavour tagging, fixing the dilution factor of the oscillation amplitude due to the mistag probability. The calibration of the decay time resolution is hence determined measuring the additional dilution of the oscillation amplitude in the $B_s^0 \to D_s^-\pi^+$ decay. In Fig. 6.12 the decay-time distributions and the time-dependent asymmetries for the $B^0 \to D^-\pi^+$ and $B_s^0 \to D_s^-\pi^+$ samples are shown, respectively. As for the fit to simulated events, the values of μ, r_σ and f_τ are fixed to 0, 3 and 0.971 respectively (according to the value reported in Tab. 6.11). The numerical values for the parameters q_0 and q_1 are

$$\begin{aligned} q_0 &= 46.1 \pm 2.5 fs, \\ q_1 &= 0.81 \pm 0.23, \\ \rho(q_0, q_1) &= -0.32, \end{aligned} \tag{6.40}$$

6.7.5 Parameterisation of the δ_t distributions

In order to describe the distributions of δ_t for all components contributing to the spectra, a similar strategy as that used for the distributions of the predicted mistag probability η is followed (see Sec. 6.9). The background-subtracted sample of two-body b-hadron decays obtained with the procedure described in App. D is used to create histograms that are taken as templates to describe the distribution of δ_t for two-body b-hadron charmless decays. The study shown in Fig. 6.9 demonstrates that different PID requirements have an important effect on the distribution of δ_t. Hence the *sWeight* associated to each B candidate by the *sPlot* method is multiplied by the PID efficiency of the candidate as a function of the momentum and pseudorapidity of its final state tracks. The histograms obtained in this way are used to describe the distributions of δ_t for the different two-body b-hadron decay modes.

The same strategy used for the predicted mistag probability described in Secs. 6.9.2 and 6.9.2.1 is used also for the combinatorial and partially-reconstructed backgrounds.

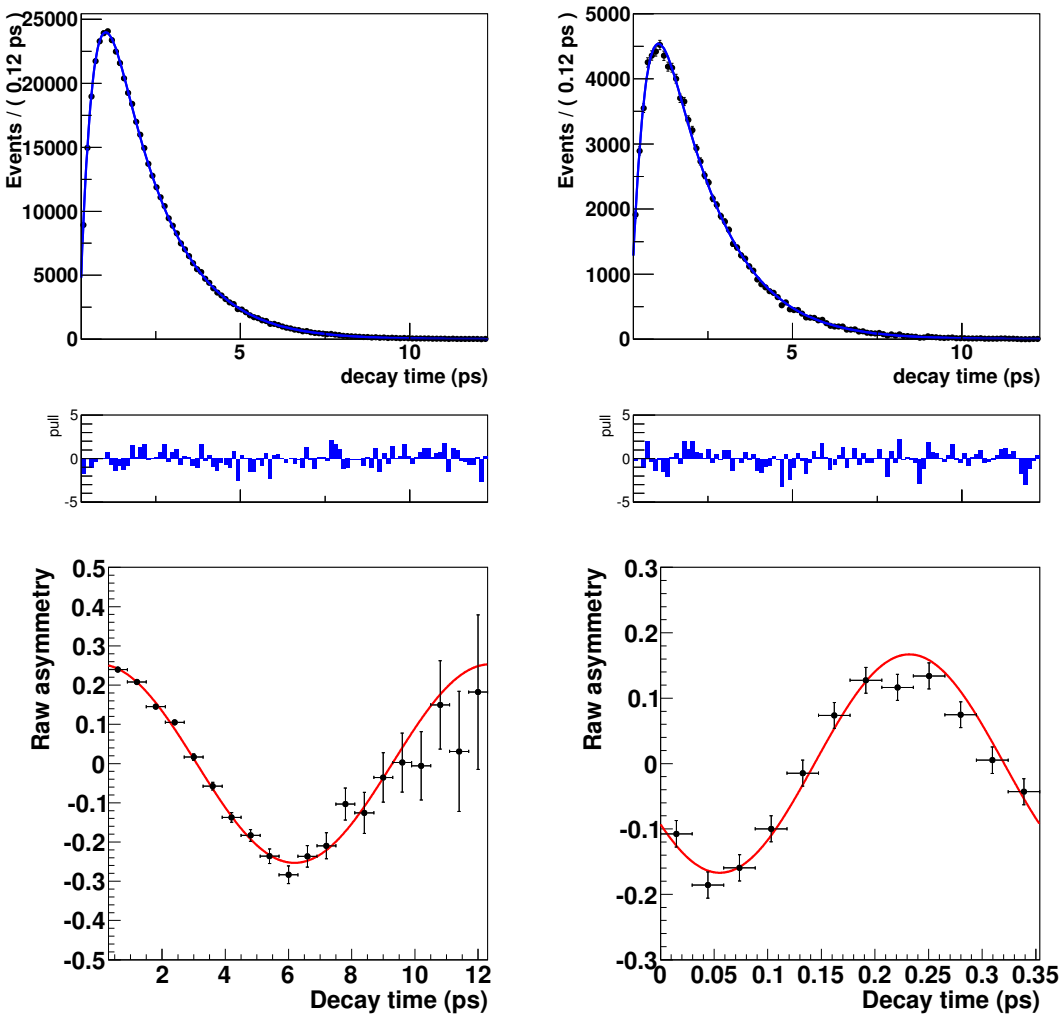

Figure 6.12: *(top) distribution of decay-time and (bottom) time-dependent asymmetries for (left) $B^0 \to D^-\pi^+$ and (right) $B^0_s \to D^-_s\pi^+$ decays. The results of the best fits are superimposed.*

6.8 Decay-time acceptance

In this section, the determination of the decay-time acceptance, *i.e.* the dependence of the reconstruction efficiency on the decay time, for the two-body B decays contributing to the $K^+\pi^-$, $\pi^+\pi^-$ and K^+K^- spectra is presented. The decay-time acceptance is determined in the same way for both signals and cross-feed backgrounds.

In order to determine the decay-time acceptance, $B^0 \to K^+\pi^-$ decays are used, since the untagged time-dependent decay rate is a pure exponential with $\Gamma_d = 0.6588 \pm 0.0017$ ps^{-1} [67] (due to the small value of $\Delta\Gamma_d$). The decay-time distributions of the $K^+\pi^-$, $\pi^+\pi^-$ and K^+K^- spectra are divided into 27 subsamples containing approximately the

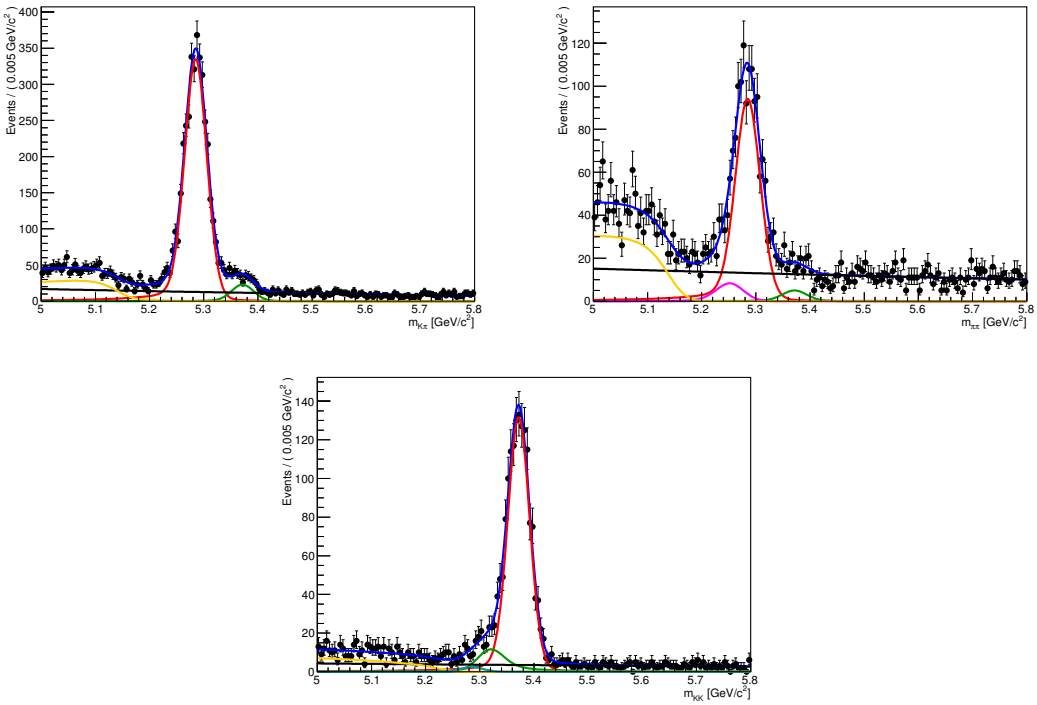

Figure 6.13: *Invariant-mass distribution of the (top left)* $K^+\pi^-$*, (top right)* $\pi^+\pi^-$ *and (bottom)* K^+K^- *spectra in the first bin of decay time, corresponding to the interval* $0.65 < t < 0.78$ *ps. The result of the best fit is overlaid.*

same amount of signal yields in each bin. Then, unbinned maximum likelihood fits to the invariant-mass distributions of the three spectra are performed in each bin, in order to determine the yields of the $B^0 \to K^+\pi^-$ decay. The models used to describe the invariant-mass shapes of the three spectra are those described in Sec. 6.5. As an example, in Fig. 6.13 the invariant-mass distributions of the $K^+\pi^-$, $\pi^+\pi^-$ and K^+K^- spectra in the first bin of decay time (corresponding to the requirement $0.65 < t < 0.78$ ps) are shown, with the result of the best fit overlaid. The yields obtained in each bin are then used to build an histogram representing the decay-time distribution of the $B^0 \to K^+\pi^-$ decays. The histogram is divided by another histogram filled with events generated according to a pure exponential with constant equal to Γ_d. The resulting final histogram represents the decay-time acceptance for the $B^0 \to K^+\pi^-$ decay. For the other decay modes, one needs to determine the ratio between the acceptance of each mode with respect to the $B^0 \to K^+\pi^-$ decay using fully simulated events. In order to take into account possible differences introduced by the PID requirements, the simulated events are weighted according to PID efficiencies on a per-event basis. The ratio of acceptances is then used to rescale the decay-time acceptance of the $B^0 \to K^+\pi^-$ decay obtained from data as described above.

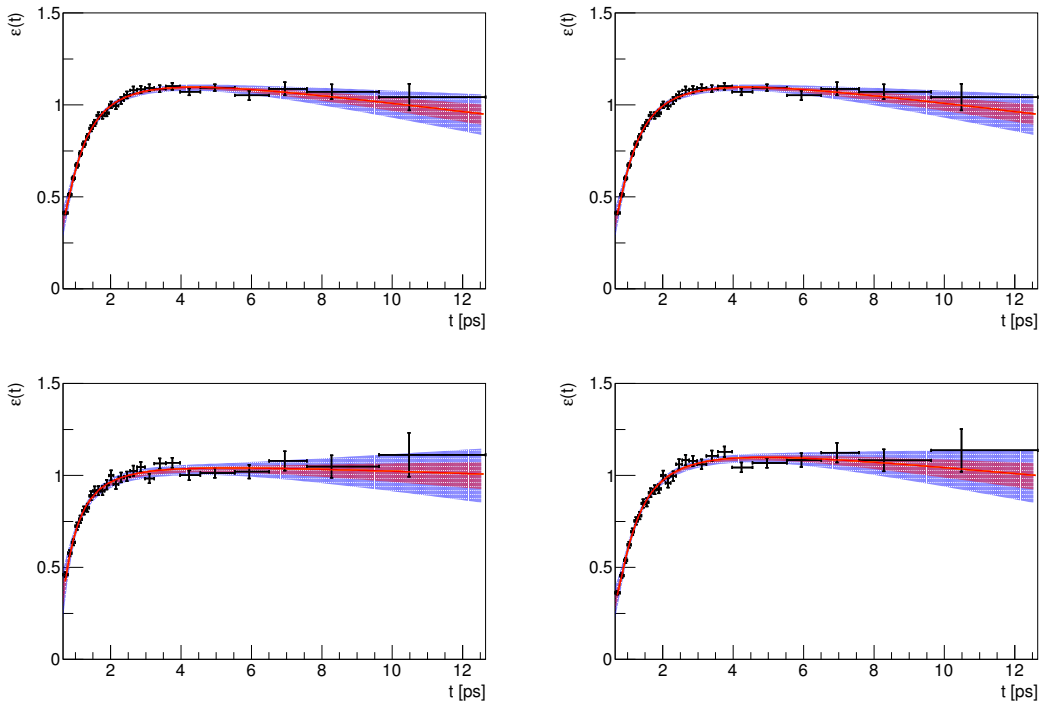

Figure 6.14: *Decay-time acceptances for the two-body B decay modes contributing to the $K^+\pi^-$ spectrum obtained as described in the text. The plots correspond to (top left) $B^0 \to K^+\pi^-$, (top right) $B^0_s \to \pi^+K^-$, (bottom right) $B^0_s \to K^+K^-$ and (bottom right) $B^0 \to \pi^+\pi^-$ decays reconstructed under the $K^+\pi^-$ hypothesis.*

The obtained acceptances are fitted with the effective function

$$\varepsilon_{sig}(t) = \left[b_0 - \mathrm{erf}\left(b_1 t^{b_2}\right)\right]\,(1 - b_3 t)\,, \tag{6.41}$$

where b_i are free parameters in the fit. The acceptance histograms for the various two-body b-hadron decays and final state hypotheses are shown in Figs. 6.14, 6.15 and 6.16, with the result of the best fit with the model described in Eq. (6.41) overlaid. The bands shown in the plots represent the 1σ and 2σ regions obtained from the fit. The results of the fits shown in Figs. 6.14, 6.15 and 6.16 are then used to generate very high statistics samples that are then used to fill histograms. The final histograms are interpolated with cubic splines that are used in the final fit to data.

6.9 Flavour tagging

Two classes of algorithms are used to determine the initial flavour of the signal B meson: the so-called opposite-side (OS) and same-side (SS) taggers [117–119]. Opposite-side taggers [117] exploit the fact that in pp collisions b quarks are mainly produced in $b\bar{b}$ pairs.

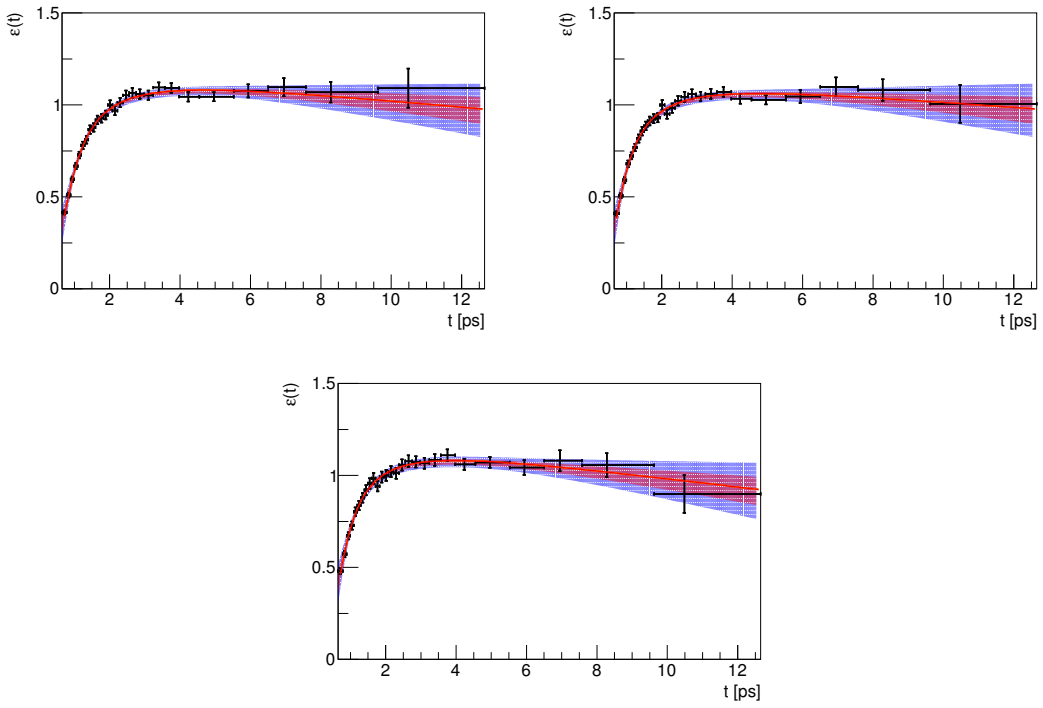

Figure 6.15: *Decay-time acceptances for the two-body B decay modes contributing to the $\pi^+\pi^-$ spectrum obtained as described in the text. The plots correspond to (top left) $B^0 \to \pi^+\pi^-$, (top right) $B_s^0 \to \pi^+\pi^-$ and (bottom) $B^0 \to K^+\pi^-$ decays reconstructed under the $\pi^+\pi^-$ hypothesis.*

Hence flavour tagging is achieved by looking at the charge of the lepton, either muon or electron, originating from semileptonic decays, and of the kaon from the $b \to c \to s$ decay transition of the other b hadron in the event. An additional OS tagger is based on the inclusive reconstruction of the opposite B-decay vertex and on the computation of a p_{T}-weighted average of the charges of all tracks associated to that vertex (vertex-charge tagger). For each tagger, the probability of misidentifying the flavour of the B at the production (mistag probability) is estimated by means of an artificial neural network. When more than one tagger is available per candidate, these probabilities are combined into a single predicted mistag probability η_{OS} and a unique decision per candidate ξ_{OS} is taken.

SS taggers [118,119] are based on the identification of the product of the hadronisation of the B mesons. Differently from OS taggers, that can be applied either on B^0 or B_s^0 mesons, SS taggers depend on the nature of the B meson. The additional $\overline{d}$ (d) and $\overline{s}$ (s) quarks produced in the fragmentation of a B^0 ($\overline{B}^0$) and B_s^0 ($\overline{B}_s^0$) mesons often form pions and protons, in the d quark case, or kaons, in the s quark case. In this thesis the so-called SSπBDT and SSp taggers [118] are used to determine the initial flavour of the B^0 mesons, while the SSkNN [119] algorithm is used to tag the B_s^0 mesons. For simplicity, in this section we will refer to a general SS tagger, representing either the combination of

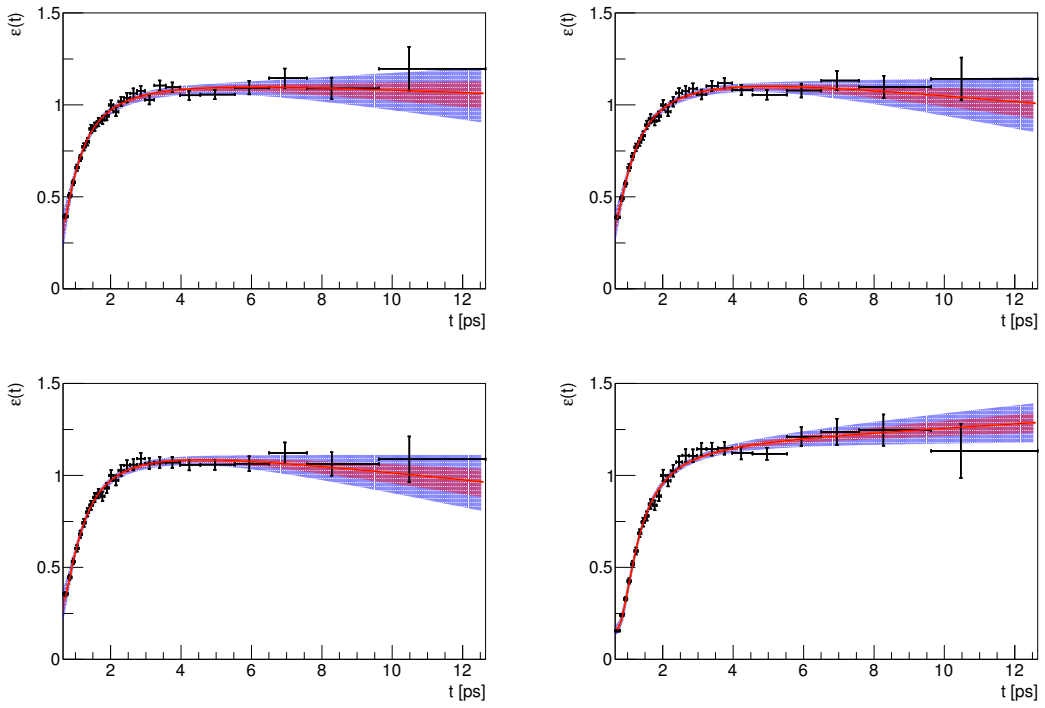

Figure 6.16: *Decay-time acceptances for the two-body B decay modes contributing to the K^+K^- spectrum obtained as described in the text. The plots correspond to (top left) $B^0_s \to K^+K^-$, (top right) $B^0 \to K^+K^-$, (bottom left) $B^0 \to K^+\pi^-$ and (bottom right) $\Lambda^0_b \to pK^-$ decays reconstructed under the K^+K^- hypothesis.*

SSπBDT and SSp algorithms or the SSkNN algorithm alone.

Also already said, each flavour-tagging algorithm assigns to a B candidate a decision $\xi_{\rm tag}$ and a predicted mistag probability $\eta_{\rm tag}$ (tag $=$ OS, SS). The observable $\xi_{\rm tag}$ assumes the discrete value $+1$ when the candidate is tagged as B, -1 when the candidate is tagged as $\overline{B}$ and zero for untagged candidates. The observable $\eta_{\rm tag}$ is a continuous variable in the range $0 \leq \eta_{\rm tag} \leq 0.5$. In order to extract the maximum statistical power from the data, the information is used on a per-event basis. Thus the distribution of $\eta_{\rm tag}$ has to be described for all the components contributing to the spectra. In addition, the functional dependency between $\eta_{\rm tag}$ and the real mistag probability $\omega_{\rm tag}$ has to be calibrated.

In this section the PDFs describing the distributions related to the flavour-tagging observables, $\xi_{\rm tag}$ and $\eta_{\rm tag}$, and the functional dependency between $\eta_{\rm tag}$ and the real mistag probability $\omega_{\rm tag}$ are introduced. Then, in Secs. 6.9.1.2 and 6.9.1.3 the calibration of the SS taggers will be discussed.

6.9.1 Flavour tagging for two-body B decays decays

The probability functions for the observables $\xi_{\rm tag}$ and $\eta_{\rm tag}$ associated to two-body B decays are

$$\begin{aligned}
\Omega^{\rm sig}_{\rm tag}(\xi_{\rm tag},\,\eta_{\rm tag}) &= \delta_{\xi_{\rm tag},\,1}\,\varepsilon^{\rm sig}_{\rm tag}\,(1-\Omega^{\rm sig}_{\rm tag}(\eta_{\rm tag}))\,h^{\rm sig}_{\rm tag}(\eta_{\rm tag}) + \\
&+ \delta_{\xi_{\rm tag},\,-1}\,\varepsilon^{\rm sig}_{\rm tag}\,\Omega^{\rm sig}_{\rm tag}(\eta_{\rm tag})\,h^{\rm sig}_{\rm tag}(\eta_{\rm tag}) + \\
&+ \delta_{\xi_{\rm tag},\,0}\,(1-\varepsilon^{\rm sig}_{\rm tag})\,U(\eta_{\rm tag}), \qquad (6.42)\\
\bar{\Omega}^{\rm sig}_{\rm tag}(\xi_{\rm tag},\,\eta_{\rm tag}) &= \delta_{\xi_{\rm tag},\,-1}\,\bar{\varepsilon}^{\rm sig}_{\rm tag}\,(1-\bar{\omega}^{\rm sig}_{\rm tag}(\eta_{\rm tag}))\,h^{\rm sig}_{\rm tag}(\eta_{\rm tag}) + \\
&+ \delta_{\xi_{\rm tag},\,1}\,\bar{\varepsilon}^{\rm sig}_{\rm tag}\,\bar{\omega}^{sig}_{\rm tag}(\eta_{\rm tag})\,h^{\rm sig}_{\rm tag}(\eta_{\rm tag}) + \\
&+ \delta_{\xi_{\rm tag},\,0}\,(1-\bar{\varepsilon}^{\rm sig}_{\rm tag})\,U(\eta_{\rm tag}), \qquad (6.43)
\end{aligned}$$

where $\delta_{\xi_{\rm tag},\,i}$ is the Kronecker delta function, $\varepsilon^{\rm sig}_{\rm tag}$ ($\bar{\varepsilon}^{\rm sig}_{\rm tag}$) is the efficiency for B ($\overline{B}$) meson to be tagged, $\Omega^{\rm sig}_{\rm tag}(\eta_{\rm tag})$ ($\bar{\omega}^{\rm sig}_{\rm tag}(\eta_{\rm tag})$) is the mistag probability for the B ($\overline{B}$) meson as a function of the predicted mistag $\eta_{\rm tag}$, $h^{\rm sig}_{\rm tag}(\eta_{\rm tag})$ is the PDF of $\eta_{\rm tag}$ up to $\eta_{\rm tag}=0.5$, that is the limit above which the candidate is considered untagged, and $U(\eta_{\rm tag})$ is a uniform distribution of $\eta_{\rm tag}$ in the range $0\leq\eta_{\rm tag}\leq 0.5$. The functional relation between $\eta_{\rm tag}$ and $\omega_{\rm tag}$ is given by

$$\begin{aligned}
\Omega^{\rm sig}_{\rm tag}(\eta_{\rm tag}) &= p_0^{\rm tag} + p_1^{\rm tag}\,(\eta_{\rm tag} - \hat{\eta}_{\rm tag}), \qquad (6.44)\\
\bar{\omega}^{\rm sig}_{\rm tag}(\eta_{\rm tag}) &= \bar{p}_0^{\rm tag} + \bar{p}_1^{\rm tag}\,(\eta_{\rm tag} - \hat{\eta}_{\rm tag}), \qquad (6.45)
\end{aligned}$$

where $\hat{\eta}_{\rm tag}$ is the average value of $\eta_{\rm tag}$ over $h^{\rm sig}_{\rm tag}(\eta_{\rm tag})$. To reduce the correlation among $\varepsilon^{\rm sig}_{\rm tag}$ and $\bar{\varepsilon}^{\rm sig}_{\rm tag}$, and $p_0^{\rm tag}$, $\bar{p}_0^{\rm tag}$, $p_1^{\rm tag}$, and $\bar{p}_1^{\rm tag}$, these variables are parameterised in the following way:

$$\begin{aligned}
\varepsilon^{\rm sig} &= \hat{\varepsilon}^{\rm sig}_{\rm tag}(1+\Delta\varepsilon^{\rm sig}_{\rm tag}), \qquad (6.46)\\
\bar{\varepsilon}^{\rm sig} &= \hat{\varepsilon}^{\rm sig}_{\rm tag}(1-\Delta\varepsilon^{\rm sig}_{\rm tag}), \qquad (6.47)\\
p_0^{\rm tag} &= \hat{p}_0^{\rm tag}(1+\Delta p_0^{\rm tag}), \qquad (6.48)\\
\bar{p}_0^{\rm tag} &= \hat{p}_0^{\rm tag}(1-\Delta p_0^{\rm tag}), \qquad (6.49)\\
p_1^{\rm tag} &= \hat{p}_1^{\rm tag}(1+\Delta p_1^{\rm tag}), \qquad (6.50)\\
\bar{p}_1^{\rm tag} &= \hat{p}_1^{\rm tag}(1-\Delta p_1^{\rm tag}), \qquad (6.51)
\end{aligned}$$

where $\hat{p}^{\rm tag}_{0(1)}$ and $\Delta p^{\rm tag}_{0(1)}$ are the average and the asymmetry between $p^{\rm tag}_{0(1)}$ and $\bar{p}^{\rm tag}_{0(1)}$, respectively, and $\hat{\varepsilon}^{\rm sig}_{\rm tag}$ and $\Delta\varepsilon^{\rm sig}_{\rm tag}$ are the average and the asymmetry between $\varepsilon^{\rm sig}_{\rm tag}$ and $\bar{\varepsilon}^{\rm sig}_{\rm tag}$, respectively. The two distinct PDFs for the OS and SS taggers are then combined into a unique PDF

$$\begin{aligned}
\Omega^{\rm sig}(\xi_{\rm OS},\,\eta_{\rm OS},\,\xi_{\rm SS},\,\eta_{\rm SS}) &= \Omega^{\rm sig}_{\rm OS}(\xi_{\rm OS},\,\eta_{\rm OS})\cdot\Omega^{\rm sig}_{\rm SS}(\xi_{\rm SS},\,\eta_{\rm SS}), \qquad (6.52)\\
\bar{\Omega}^{\rm sig}(\xi_{\rm OS},\,\eta_{\rm OS},\,\xi_{\rm SS},\,\eta_{\rm SS}) &= \bar{\Omega}^{\rm sig}_{\rm OS}(\xi_{\rm OS},\,\eta_{\rm OS})\cdot\bar{\Omega}^{\rm sig}_{\rm SS}(\xi_{\rm SS},\,\eta_{\rm SS}), \qquad (6.53)
\end{aligned}$$

that is an accurate description of the multidimensional distribution, given that $h^{\rm sig}_{\rm OS}(\eta_{\rm OS})$ and $h^{\rm sig}_{\rm SS}(\eta_{\rm SS})$ are uncorrelated. In order to check this assumption, a background-subtracted

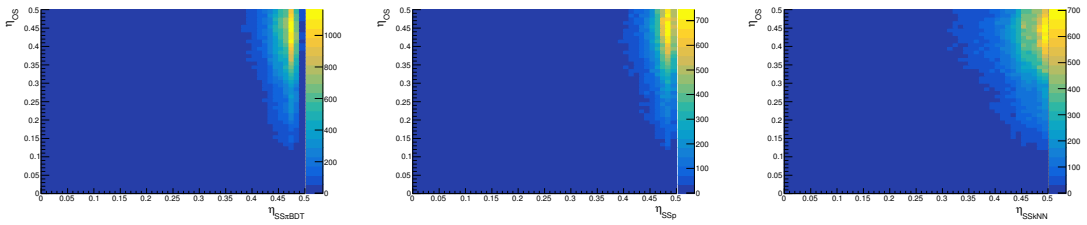

Figure 6.17: *Two-dimensional distributions of the mistag fractions predicted by the various taggers, obtained as described in the text.*

Table 6.13: *Correlation between $\eta_{\rm OS}$ and the SS taggers observables $\eta_{\rm SS\pi BDT}$, $\eta_{{\rm SS}p}$ and $\eta_{\rm SSkNN}$ determined using a background-subtracted sample of two-body B decays, as described in the text. The correlations coefficients are also determined for combinatorial background candidates, selected from the high invariant-mass sideband $m > 5.6\,{\rm GeV}/c^2$.*

Variables	Correlation for signals	Correlation for background
$\eta_{\rm OS}$, $\eta_{\rm SS\pi BDT}$	-0.027	0.000
$\eta_{\rm OS}$, $\eta_{{\rm SS}p}$	0.009	0.053
$\eta_{\rm OS}$, $\eta_{\rm SSkNN}$	0.007	0.058

sample of two-body B decays, obtained with the procedure described in App. D, is used. In Tab. 6.13 the correlations between $\eta_{\rm OS}$ and the three observables for the SS taggers ($\eta_{\rm SS\pi BDT}$, $\eta_{{\rm SS}p}$ and $\eta_{\rm SSkNN}$) are reported, confirming the fact that OS and SS taggers have uncorrelated η distributions. The two-dimensional plots of the flavour tagging observables are shown in Fig. 6.17. The same correlation coefficients are also determined for the combinatorial background, considering only the events with $m > 5.6\,{\rm GeV}/c^2$.

6.9.1.1 Distributions of $\eta_{\rm OS}$ for two-body B decays

The model used to parameterise $h^{\rm sig}_{\rm OS}(\eta)$ is determined from the background-subtracted sample of two-body B decays used to determine the correlations reported in Tab. 6.13. The background subtracted sample is used to create the histograms that are taken as templates to describe the distribution of $\eta_{\rm OS}$ for the two-body B decays. Small differences between the various decay modes and invariant-mass hypotheses could be introduced by the different PID requirements. Indeed, PID requirements modify the $p_{\rm T}$ distributions of the B candidates and this could have an impact on the distribution of $\eta_{\rm OS}$. In order to control this possible effect, the *sWeight* associated to each B candidate by the *sPlot* method is multiplied by the PID efficiency of the candidate as a function of the momentum and pseudorapidity of its final state tracks. In Fig. 6.18 the distribution of $\eta_{\rm OS}$ for different decay modes and different final-state hypotheses is reported. No significant effect is

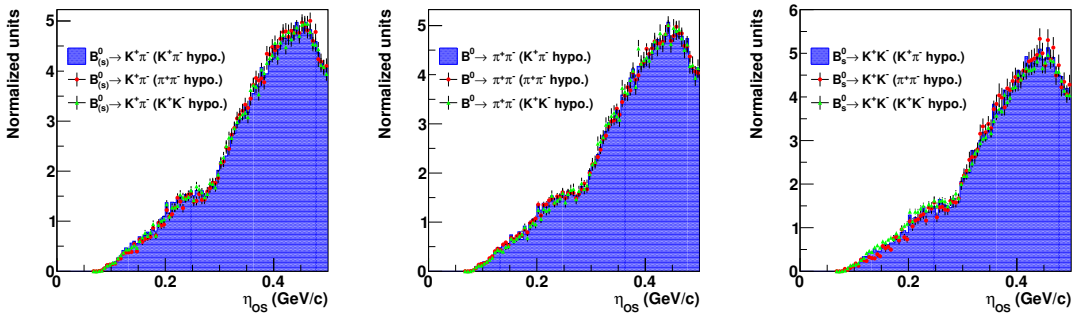

Figure 6.18: *Distributions of the mistag fraction predicted by the OS flavour-tagging algorithms, obtained from background-subtracted two-body B-decay events, as described in App. D. The effect of different PID requirements, labelled in the legends as "h^+h^- hypo" (with $h = K, \pi$) is reproduced by applying an event-per-event weight to the data, as described in the text.*

introduced by the PID requirements, but nevertheless the histograms shown in Fig. 6.18 are used as distributions of $h^{\rm sig}_{\rm OS}(\eta_{\rm OS})$ for the different two-body B decay modes under study. We also found that the average of $\eta_{\rm OS}$ over the distributions of the various two-body b-hadron decay modes is approximately the same, hence in the final fit to data the parameter $\hat{\eta}_{\rm OS}$ will be fixed to this value, corresponding to 0.37.

6.9.1.2 Calibration and combination of SSπBDT and SSp taggers

In the final fit used to determine $C_{\pi^+\pi^-}$ and $S_{\pi^+\pi^-}$ a combination of SSπBDT and SSp taggers is used. In order to combine the two taggers into a unique decision $\xi_{\rm SS}$ and mistag probability $\eta_{\rm SS}$ the responses of the two algorithms need to be calibrated. For this purpose the flavour specific decay $B^0 \to K^+\pi^-$ is used. Signal distributions are isolated from background using the *sPlot* technique by means of a fit to the invariant-mass distribution of the $K^+\pi^-$ spectrum, shown in Fig. 6.19. The PDFs used to describe the various components are those presented in Sec. 6.5. The only difference is that the small contributions of the $B^0 \to \pi^+\pi^-$ and $B^0_s \to K^+K^-$ cross-feed backgrounds (corresponding to less than 1% of the signal yields) are neglected. By means of unbinned maximum likelihood fits to the tagged time-dependent decay rates of the background-subtracted sample it is possible to determine the parameters governing the relation between $\eta_{\rm SS\pi BDT}$ ($\eta_{{\rm SS}p}$) and $\omega^{\rm sig}_{\rm SS\pi BDT}$ ($\omega^{\rm sig}_{{\rm SS}p}$), reported in Eq. (6.44).

In addition, the sample has also been split into various bins of $\eta_{\rm SS\pi BDT(SS}p)$, such that the subsamples in the various bins have approximately the same tagging power. Then, by means of tagged time-dependent fits to the various subsamples, the average mistag fraction in each bin can be determined. In this way it is possible to check if the assumption of a linear dependence between $\eta_{\rm SS}$ and $\omega^{\rm sig}_{\rm SS}$ is correct. At this level the parameters governing possible differences in the flavour-tagging response between B and $\overline{B}$ mesons are neglected, *i.e.* their values are fixed to 0. The determination of these differences between B and

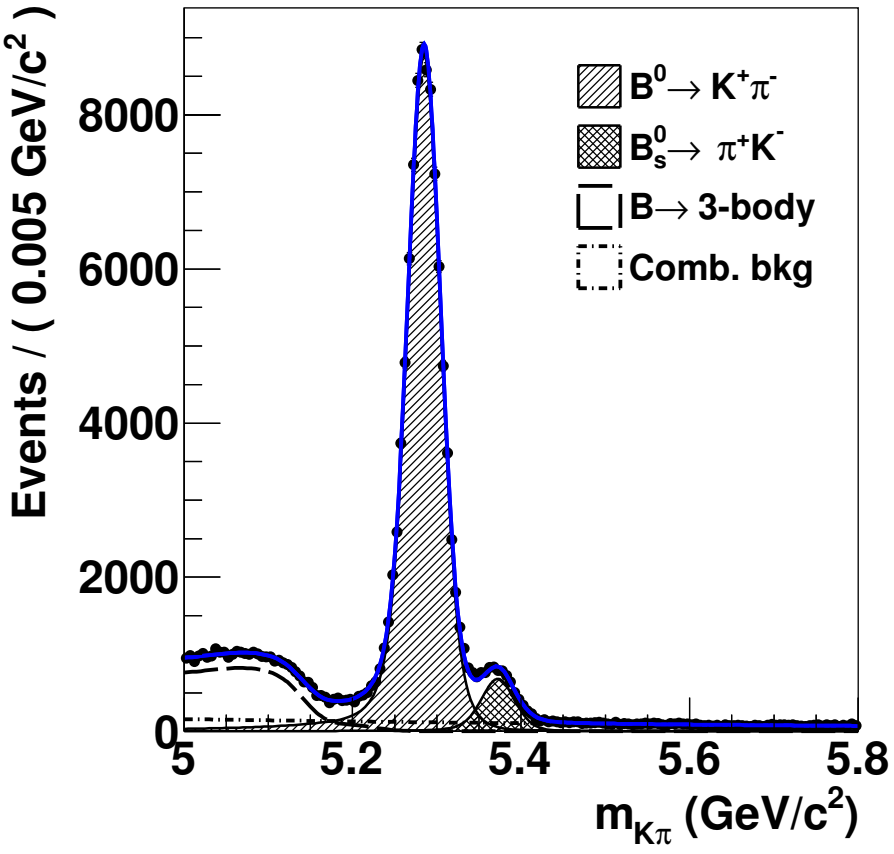

Figure 6.19: *Invariant-mass distribution of candidates reconstructed under the $K^+\pi^-$ or $K^-\pi^+$ final-state hypotheses. The result of the best fit is also shown with the components of the model adapted to the data points.*

$\overline{B}$ will be determined in the final fit, leaving the parameters free to be adjusted. The results of the calibration are reported in Tab. 6.14, whereas calibration plots are shown in Fig. 6.20.

Once the calibration parameters of the SSπBDT and SSp taggers have been determined they are combined into a unique decision ξ_{SScomb} and predicted mistag probability η_{SScomb}, that will be the observable used in the final fit for the determination of $C_{\pi^+\pi^-}$ and $S_{\pi^+\pi^-}$. The final calibration parameters for the SScomb tagger are left free to vary in the final fit, thanks to the presence of the $B^0 \to K^+\pi^-$ decay that allows their determination. However, as a consistency check, the result of the calibration for SScomb are also reported in this section. Finally, the effective tagging power for the SSπBDT, SSp and SScomb taggers are summarised in Tab. 6.15.

The PDFs $h_{sig}(\eta_{\text{SScomb}})$ describing the η_{SScomb} distributions for the various two-body

Table 6.14: *Calibration parameters for the* SSπBDT*,* SSp *and* SScomb *taggers with their statistical uncertainties.*

Tagger	mode	p_0	p_1	$\langle\eta\rangle$	$\rho_{p0,p1}$
SSπBDT	per-event	0.4374 ± 0.0034	0.942 ± 0.085	0.44	-0.377
	category	0.4367 ± 0.0034	0.978 ± 0.091	0.44	-0.405
SSp	per-event	0.4472 ± 0.0046	0.724 ± 0.105	0.44	-0.581
	category	0.4464 ± 0.0048	0.754 ± 0.114	0.44	-0.617
SScomb	per-event	0.4396 ± 0.0030	0.941 ± 0.071	0.44	-0.240
	category	0.4398 ± 0.0030	0.968 ± 0.076	0.44	-0.255

Table 6.15: *Tagging efficiency and tagging power of the* SSπBDT*,* SSp *and* SScomb *algorithms.*

Tagger	ε_{tag} [%]	ε_{eff} [%]
SSπBDT	65.48 ± 0.19	0.81 ± 0.13
SSp	44.73 ± 0.24	0.42 ± 0.17
SScomb	76.82 ± 0.15	1.17 ± 0.11

B decays are determined using a sample of $B^0 \to D^-\pi^+$ data. This sample is provided, already background-subtracted using the *sPlot* technique, by the LHCb flavour tagging group. Since the distribution of η_{SScomb} depends on the kinematic of the B meson, the p_{T} distribution of the $B^0 \to D^-\pi^+$ sample is reweighted in order to match the corresponding distribution of two-body B decays. The p_{T} distributions used as a reference are obtained in the same way as in Sec. 6.9.1.1, to determine the distributions of η_{OS}.

6.9.1.3 Calibration of the SSkNN tagger

In the final fit used to determine $C_{K^+K^-}$, $S_{K^+K^-}$ and $A^{\Delta\Gamma}_{K^+K^-}$, the SS$k$NN tagger is used. In order to calibrate the response of this tagger, the natural control channel would be the $B^0_s \to \pi^+K^-$ decay. However, the signal yield of this decay is approximately 8% with respect to that of the $B^0 \to K^+\pi^-$ decay, and approximately 20% to that of the $B^0_s \to K^+K^-$ decay. As a consequence, the calibration of the SSkNN tagger would suffer from large uncertainties, thus impacting on the precision achievable for the determination of $C_{K^+K^-}$ and $S_{K^+K^-}$. Therefore, to calibrate the SSkNN tagger, a larger sample of $B^0_s \to D^-_s\pi^+$ decays is used. The background is subtracted using the *sPlot* technique, by means of an invariant-mass fit, shown in Fig. 6.21, where the signal is parameterised using a double Gaussian function, while the background is parameterised using an exponential function.

As done for the SSπBDT and SSp taggers, also in this case the calibration of the SSkNN is performed by means of an unbinned maximum likelihood fit to the tagged decay-time distribution of the $B^0_s \to D^-_s\pi^+$ decay. The PFD used to fit the decay-time rates is the same used for the calibration of the SSπBDT and SSp taggers. Also in this case the fit is performed using the flavour tagging information on a per-event basis, determining

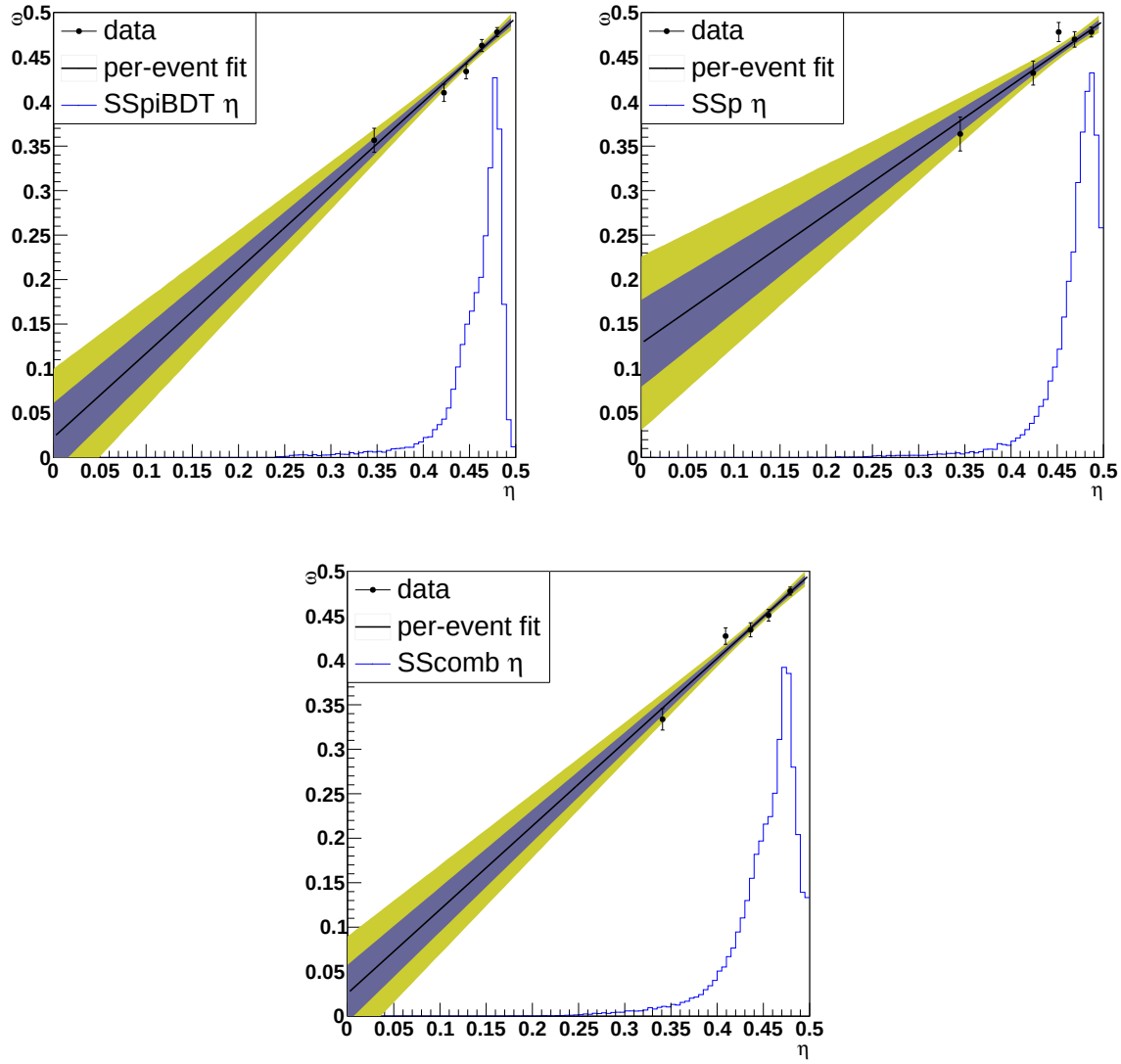

Figure 6.20: *Calibration plots for (left)* SSπBDT *tagger, (right)* SS*p tagger and (bottom) their combination.*

the calibration parameters directly from the fit, and by dividing the sample in bins of $\eta_{\text{SS}k\text{NN}}$ and determining the average $\omega_{\text{SS}k\text{NN}}$ in each bin, in order to check the linearity of the $\eta_{\text{SS}k\text{NN}} - \omega_{\text{SS}k\text{NN}}$ relation.

The portability of the calibration of the SSkNN tagger from the $B^0_s \to D^-_s\pi^+$ to the charmless two-body B-decay sample is achieved by equalising the distributions of the following variables: the p_{T}, the pseudorapidity (η) and the azimuthal angle (ϕ) of the B meson and the number of primary vertices (N_{PV}) and tracks (N_{tracks}) in the event. The reference distributions of charmless two-body B-decay decays, in particular for the p_{T} and η of the B mesons, are determined in the same way as in Sec. 6.9.1.1, for the

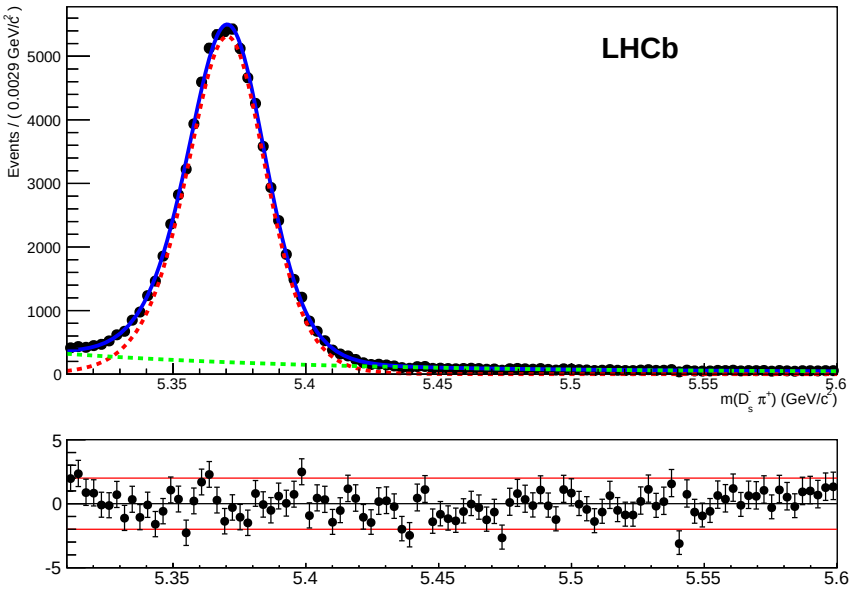

Figure 6.21: *Invariant-mass fit to the* $B_s^0 \to D_s^- \pi^+$ *mass distribution.*

Table 6.16: *Correlation factors of the variables taken into account for the* $B_s^0 \to D_s^- \pi^+$ *reweighting.*

	p_{T}	η	ϕ	N_{tracks}	N_{PV}
p_{T}	1.000	-	-	-	-
η	-0.515	1.000	-	-	-
ϕ	-0.004	0.012	1.000	-	-
N_{tracks}	-0.066	0.035	-0.001	1.000	-
N_{PV}	-0.047	0.019	-0.005	0.609	1.000

determination of the distributions of η_{OS}. Since the variables to be equalised are not completely independent, those showing a correlation factor higher than 10% are reweighted simultaneously. The correlation coefficients are reported in Tab. 6.16. There are two pairs of variables showing a correlation higher than 50%: the p_{T} and η of the B meson, and the N_{PV} with N_{tracks}. For this reason, three different reweightings are performed: a kinematic reweighting including p_{T} and η, an occupancy reweighting for N_{PV} and N_{tracks}, and the reweighting of the azimuthal angle ϕ. The product of these three weights provides the final weight to be applied to data. In Fig. 6.22 the distributions before and after the reweighting procedure are shown.

The calibration of the SSkNN tagger is repeated for all types of reweighting separately, in order to observe any possible deviation from the calibration obtained on the $B_s^0 \to D_s^- \pi^+$ un-reweighted sample. The fit is performed using the per-event mistag and fixing the average value of the mistag $\hat{\eta}_{\mathrm{SS}k\mathrm{NN}} = 0.44$ (to allow an easier comparison of the various calibration parameters). The results are reported in Tab. 6.17. While the reweighting

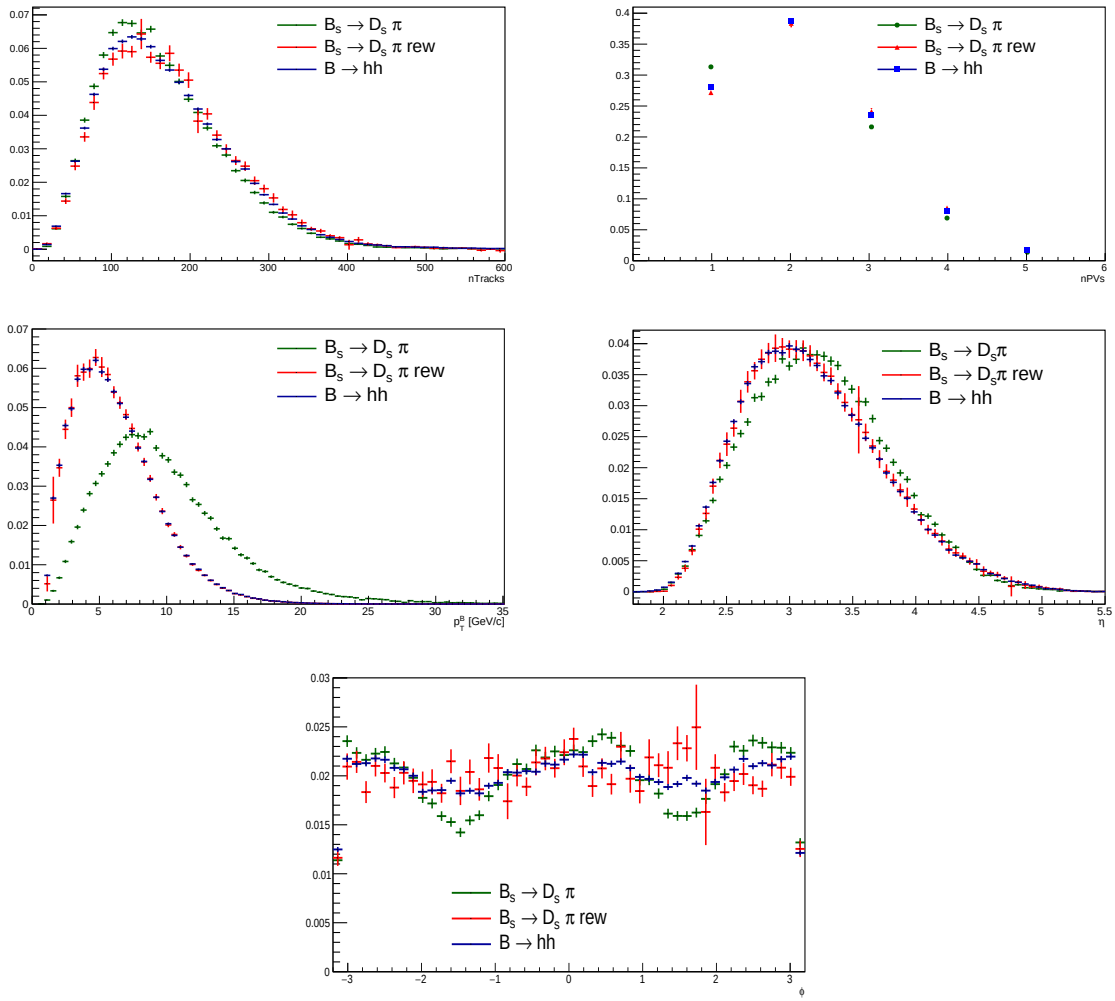

Figure 6.22: *Distribution of (top left) N_{tracks}, (top right) N_{PV}, (middle left) p_{T}, (middle right) η and (bottom) ϕ variables before and after the complete reweighting procedure. In each plot the distributions of the variable in the $B^0_s \to D^-_s\pi^+$ un-reweighted sample, in the $B^0_s \to D^-_s\pi^+$ reweighted sample and in the charmless two-body B-decay sample are shown in green, red and blue, respectively.*

Table 6.17: *Calibration parameters in the $B^0_s \to D^-_s\pi^+$ sample after the kinematic, occupancy and final reweighting.*

Reweighting	p_0	p_1
–	0.4402 ± 0.0047	1.028 ± 0.069
kinematic	0.4552 ± 0.0054	0.752 ± 0.090
occupancy	0.4443 ± 0.0052	0.982 ± 0.052
full	0.4577 ± 0.0054	0.725 ± 0.092

Table 6.18: *Calibration parameters for the* SSkNN *tagger, determined from* $B_s^0 \to D_s^- \pi^+$ *decays with kinematic and occupancy distributions equalised to those of the charmless two-body* B *decays. The value of* $\hat{\eta}$ *is fixed in the fit to* 0.44*. Note that* $\varepsilon^{\rm sig}_{\rm SS\mathit{k}NN}$ *is not reported as it is left free in the final fit.*

Parameter	Value
$\Delta\varepsilon^{sig}_{\rm SS\mathit{k}NN}$	-0.00434 ± 0.00659
$\hat{p}_0^{\rm SS\mathit{k}NN}$	0.45558 ± 0.00502
$\Delta p_0^{\rm SS\mathit{k}NN}$	-0.01082 ± 0.00479
$\hat{p}_1^{\rm SS\mathit{k}NN}$	0.7588 ± 0.0922
$\Delta p_1^{\rm SS\mathit{k}NN}$	0.0341 ± 0.0514

Table 6.19: *Correlation matrix among the calibration parameters of the* SSkNN *tagger determined from* $B_s^0 \to D_s^- \pi^+$ *decays with kinematic and occupancy distributions equalised to those of the charmless two-body* B *decays.*

Parameter	$\Delta\varepsilon^{sig}_{\rm SS\mathit{k}NN}$	$\hat{p}_0^{\rm SS\mathit{k}NN}$	$\Delta p_0^{\rm SS\mathit{k}NN}$	$\hat{p}_1^{\rm SS\mathit{k}NN}$	$\Delta p_1^{\rm SS\mathit{k}NN}$
$\Delta\varepsilon^{sig}_{\rm SS\mathit{k}NN}$	1.000	0.004	0.105	0.009	-0.100
$\hat{p}_0^{\rm SS\mathit{k}NN}$	–	1.000	0.001	-0.114	0.021
$\Delta p_0^{\rm SS\mathit{k}NN}$	–	–	1.000	0.014	-0.171
$\hat{p}_1^{\rm SS\mathit{k}NN}$	–	–	–	1.000	-0.141
$\Delta p_1^{\rm SS\mathit{k}NN}$	–	–	–	–	1.000

related to the occupancy and the azimuthal angle do not affect too much the calibration parameters, the kinematic reweighting changes significantly both $p_0^{\rm SS\mathit{k}NN}$ and $p_1^{\rm SS\mathit{k}NN}$. Further studies are performed to check the observed dependence of the calibration as a function of kinematic reweighting, and are reported in App. D. These studies show a dependency of $p_1^{\rm SS\mathit{k}NN}$ from the average $p_{\rm T}$ of the B meson. Because of this it was decided to use as calibration parameters of the SSkNN tagger those obtained after the kinematic reweighting. In contrast with the case of the SScomb tagger, where all calibration parameters can be determined during the fit thanks to the $B^0 \to K^+\pi^-$ signal, in this case the parameters governing the differences of the calibration between B and $\overline{B}$ mesons are also determined. The values that are fixed in the final fit, are reported in Tab. 6.18. Their uncertainties, together with their correlations (reported in Tab. 6.19), are taken into account when assessing systematic uncertainties.

After the complete reweighting, the tagging power provided by the SSkNN is $\varepsilon_{eff} \simeq 1.26\%$, a value significantly lower with respect to the tagging power evaluated on the sample without any reweighting, $\varepsilon_{eff} \simeq 2.06\%$.

6.9.2 Flavour tagging for combinatorial background

The probability as a function of $\xi_{\rm tag}$ and $\eta_{\rm tag}$ for the combinatorial background is empirically parameterised as

$$\begin{aligned}\Omega^{\rm tag}_{\rm comb}(\xi_{\rm tag},\,\eta_{\rm tag}) =& \delta_{\xi_{\rm tag},\,1}\varepsilon^{\rm tag}_{\rm comb}\,h^{\rm tag}_{\rm comb}(\eta_{\rm tag}) \;+\; \delta_{\xi_{\rm tag},\,-1}\bar{\varepsilon}^{\rm tag}_{\rm comb}\,h^{\rm tag}_{\rm comb}(\eta_{\rm tag}) + \\ & \delta_{\xi_{\rm tag},\,0}\,(1-\varepsilon^{\rm tag}_{\rm comb}-\bar{\varepsilon}^{\rm tag}_{\rm comb})\,U(\eta_{\rm tag}),\end{aligned} \tag{6.54}$$

where tag={OS, SS}, $\varepsilon^{\rm tag}_{\rm comb}$ and $\bar{\varepsilon}^{\rm tag}_{\rm comb}$ are the efficiency to tag a combinatorial background candidate as B or $\overline{B}$ and $h^{\rm tag}_{\rm comb}(\eta)$ is the properly normalised distribution of $\eta_{\rm tag}$ for the combinatorial background events up to $\eta_{\rm tag}=0.5$. As done for the signal model presented in the previous section, the tagging efficiencies are parameterised as

$$\varepsilon^{\rm tag}_{\rm comb} = \frac{\hat{\varepsilon}^{\rm tag}_{\rm comb}}{2}(1+\Delta\varepsilon^{\rm tag}_{\rm comb}), \tag{6.55}$$

$$\bar{\varepsilon}^{\rm tag}_{\rm comb} = \frac{\hat{\varepsilon}^{\rm tag}_{\rm comb}}{2}(1-\Delta\varepsilon^{\rm tag}_{\rm comb}), \tag{6.56}$$

such that the fits determine the average efficiency to tag a combinatorial background as B or $\overline{B}$ ($\hat{\varepsilon}^{\rm tag}_{\rm comb}$) and the asymmetry between the two efficiencies ($\Delta\varepsilon^{\rm tag}_{\rm comb}$). The templates used to parameterise $h^{\rm tag}_{\rm comb}(\eta)$ are histograms filled with candidates taken from the high invariant-mass sidebands ($m > 5.6\,{\rm GeV}/c^2$) for the different spectra, $K^+\pi^-$, $\pi^+\pi^-$ and K^+K^-.

The combined probability function of $\vec{\theta}=\{\xi_{\rm OS},\,\xi_{\rm SS},\,\eta_{\rm OS},\,\eta_{\rm SS}\}$ is given by the product

$$\Omega_{\rm comb}(\vec{\theta}) = \Omega^{\rm OS}_{\rm comb}(\xi_{\rm OS},\,\eta_{\rm OS})\cdot\Omega^{\rm SS}_{\rm comb}(\xi_{\rm SS},\,\eta_{\rm SS}), \tag{6.57}$$

that is a good parameterisation given that the distribution of $\eta_{\rm OS}$ and $\eta_{\rm SS}$ are uncorrelated, as apparent from the correlation coefficients reported in Tab. 6.13.

6.9.2.1 Flavour tagging for partially-reconstructed backgrounds

The probability distribution as a function of $\xi_{\rm tag}$ and $\eta_{\rm tag}$ for partially-reconstructed backgrounds in the $\pi^+\pi^-$ and K^+K^- spectra is empirically parameterised as

$$\begin{aligned}\Omega^{\rm tag}_{\rm phys}(\xi_{\rm tag},\,\eta_{\rm tag}) =& \delta_{\xi_{\rm tag},\,1}\varepsilon^{\rm tag}_{\rm phys}\,h^{\rm tag}_{\rm phys}(\eta_{\rm tag}) \;+\; \delta_{\xi_{\rm tag},\,-1}\bar{\varepsilon}^{\rm tag}_{\rm phys}\,h^{\rm tag}_{\rm phys}(\eta_{\rm tag}) + \\ & \delta_{\xi_{\rm tag},\,0}\,(1-\varepsilon^{\rm tag}_{\rm phys}-\bar{\varepsilon}^{\rm tag}_{\rm phys})\,U(\eta_{\rm tag}),\end{aligned} \tag{6.58}$$

where tag={OS, SS}, $\varepsilon^{\rm tag}_{\rm phys}$ and $\bar{\varepsilon}^{\rm tag}_{\rm phys}$ are the efficiencies to tag a partially reconstructed background candidate as B or $\overline{B}$ and $h^{\rm tag}_{\rm phys}(\eta_{\rm tag})$ is the properly normalised distribution of $\eta_{\rm tag}$ for the partially reconstructed background events up to $\eta_{\rm tag}=0.5$. Also in this case, the tagging efficiencies are parameterised as a function of their average ($\hat{\varepsilon}^{\rm tag}_{\rm phys}$) and their asymmetry ($\Delta\varepsilon^{\rm tag}_{\rm phys}$)

$$\varepsilon^{\rm tag}_{\rm phys} = \frac{\hat{\varepsilon}^{\rm tag}_{\rm phys}}{2}(1+\Delta\varepsilon^{\rm tag}_{\rm phys}), \tag{6.59}$$

$$\bar{\varepsilon}^{\rm tag}_{\rm phys} = \frac{\hat{\varepsilon}^{\rm tag}_{\rm phys}}{2}(1 - \Delta\varepsilon^{\rm tag}_{\rm phys}). \quad (6.60)$$

The templates used to parameterise $h^{\rm tag}_{\rm phys}(\eta_{\rm tag})$ are built from histograms filled with candidates taken from the low invariant-mass sidebands ($m < 5.2\,{\rm GeV}/c^2$) for the different spectra, $K^+\pi^-$, $\pi^+\pi^-$ and K^+K^-.

The residual contamination due to the combinatorial background in the low invariant-mass sideband is subtracted from the histograms. The amount of the contamination is determined from a fit with an exponential function to the high invariant-mass sideband and then rescaling the amount of events to those expected in the low invariant-mass region. The histogram parameterising the $\eta_{\rm tag}$ distribution for combinatorial-background candidates are then subtracted, according to the determined contamination, from those built using the events in the low invariant-mass region. The background-subtracted histograms are used as templates for $h^{\rm tag}_{\rm phys}(\eta_{\rm tag})$. The combined probability function of $\vec{\theta} = \{\xi_{\rm OS}, \xi_{\rm SS}, \eta_{\rm OS}, \eta_{\rm SS}\}$ is given by the product

$$\Omega_{\rm phys}(\vec{\theta}) = \Omega^{\rm OS}_{\rm phys}(\xi_{\rm OS}, \eta_{\rm OS}) \cdot \Omega^{\rm SS}_{\rm phys}(\xi_{\rm SS}, \eta_{\rm SS}). \quad (6.61)$$

As already mentioned in Sec. 6.6.4, in the $K^+\pi^-$ spectrum the partially reconstructed background is parameterised in the same way as for the $B^0 \to K^+\pi^-$ decay, but with independent parameters for the oscillation frequency and flavour-tagging calibration.

6.10 Fit results

In this section the final fit to data is presented. In Figs. 6.25, 6.26, 6.27, 6.28 and 6.29 the results of the unbinned maximum likelihood fits to the data are shown. The following parameters are fixed in the fit

- the parameters governing the tails of the invariant-mass models for the two-body B decays reported in Tab. 6.9;
- the end points of the ARGUS functions governing the mass shapes of partially-reconstructed multi-body B decays; when the model describes B^0 partially-reconstructed decays, the end point is fixed to $5.1446\,{\rm GeV}/c^2$ (corresponding to the known B^0 mass subtracted by the mass of a pion), whereas when the model describes B^0_s partially-reconstructed background the end point is fixed to $5.2318\,{\rm GeV}/c^2$ (analogously for the B^0_s);
- the shapes of the decay-time acceptances for the two-body B decays are fixed from the histograms created following the procedure described in Sec. 6.8;
- the values of Δm_d, Δm_s, $\Delta\Gamma_d$, Γ_s and $\Delta\Gamma_s$ for the B^0 and B^0_s decays taken from HFLAV [67] and summarised in Tab. 6.20. The value of Γ_d is instead left free to be adjusted by the fit as a further cross-check of the validity of the procedure used to describe the decay-time acceptance;

Table 6.20: *Values of the parameters $\Delta\Gamma_d$, Γ_s and $\Delta\Gamma_s$ taken from HFLAV [67] and fixed in the fit to data. For the Γ_s and $\Delta\Gamma_s$ parameters the correlation factor between them is also reported.*

Parameter	Value
Δm_d [ps^{-1}]	0.5065 ± 0.0019
$\Delta\Gamma_d$ [ps^{-1}]	0
$\rho(\Gamma_d, \Delta\Gamma_d)$	0
Δm_s [ps^{-1}]	17.757 ± 0.021
Γ_s [ps^{-1}]	0.6654 ± 0.0022
$\Delta\Gamma_s$ [ps^{-1}]	0.083 ± 0.007
$\rho(\Gamma_s, \Delta\Gamma_s)$	-0.292

- the calibration parameters q_0 and q_1 of the per-event decay time resolution reported in Eq. (6.40) and the parameters $\mu = 0$ fs, $r_\sigma = 3$ and $f_\tau = 0.971$ governing the model describing the decay-time resolution given in Eq. (6.36);
- the PID efficiencies governing the relative yields between the correctly identified and misidentified two-body B decays considered in the model;
- in the case of the measurement of $C_{K^+K^-}$, $S_{K^+K^-}$ and $A^{\Delta\Gamma}_{K^+K^-}$, the parameters governing the calibration of the SSkNN tagger for the B^0_s mesons fixed to those reported in Tab. 6.18.

The fit to data is repeated five times with different flavour-tagging information: once with only OS, SScomb and SSkNN tagger information, once with OS and SScomb tagger information, and once with OS and SSkNN tagger information. In Tab. 6.21 the numerical values for the parameters governing the flavour tagging calibration of the OS and SScomb taggers obtained from the fits are reported.

In Fig. 6.23 the raw time-dependent asymmetry of the $K^\pm\pi^\mp$ spectrum obtained from the invariant-mass region dominated by the $B^0 \to K^+\pi^-$ decay (defined as $5.20 < m < 5.32\,\text{GeV}/c^2$) is shown. The production asymmetries for the B^0 and B^0_s mesons are found to be $A_\text{P}(B^0) = (0.191 \pm 0.596)\%$ and $A_\text{P}(B^0_s) = (2.377 \pm 2.069)\%$, respectively. From the fit it is also possible to determine the raw asymmetries of the $B^0 \to K^+\pi^-$ and $B^0_s \to \pi^+K^-$ decays removing the effect of production asymmetries.

The values of the *CP*-violating parameters determined from the fit are

$$C_{\pi^+\pi^-} = -0.3367 \pm 0.0623, \tag{6.62}$$
$$S_{\pi^+\pi^-} = -0.6261 \pm 0.0538, \tag{6.63}$$
$$C_{K^+K^-} = 0.1968 \pm 0.0584, \tag{6.64}$$
$$S_{K^+K^-} = 0.1816 \pm 0.0586, \tag{6.65}$$
$$A^{\Delta\Gamma}_{K^+K^-} = -0.7876 \pm 0.0730, \tag{6.66}$$

Table 6.21: *Values of the calibration parameters for the flavour tagging obtained from the fits. The value of* $\hat{\eta}_{\rm OS}$ *and* $\hat{\eta}_{\rm SScomb}$ *are fixed to* 0.37 *and* 0.44*, respectively. The calibration parameters are determined from the fits using* OS, SScomb *and* OS +SScomb *only tagger information.*

Parameter	OS	SScomb	OS +SScomb
$\hat{\varepsilon}^{sig}_{\rm OS}$	0.33693 ± 0.00162	–	0.33679 ± 0.00162
$\Delta\varepsilon^{sig}_{\rm OS}$	0.00973 ± 0.00713	–	0.01013 ± 0.00712
$\hat{p}^{\rm OS}_0$	0.38541 ± 0.00431	–	0.38512 ± 0.00424
$\Delta p^{\rm OS}_0$	0.01823 ± 0.00650	–	0.01570 ± 0.00639
$\hat{p}^{\rm OS}_1$	1.0035 ± 0.0452	–	1.0212 ± 0.0444
$\Delta p^{\rm OS}_1$	0.0223 ± 0.0250	–	0.0285 ± 0.0244
$\hat{\eta}_{\rm OS}$	0.37	–	0.37
$\hat{\varepsilon}^{sig}_{\rm SScomb}$	–	0.76528 ± 0.00144	0.76477 ± 0.00144
$\Delta\varepsilon^{sig}_{\rm SScomb}$	–	-0.00463 ± 0.00365	-0.00294 ± 0.00303
$\hat{p}^{\rm SScomb}_0$	–	0.43727 ± 0.00312	0.43826 ± 0.00294
$\Delta p^{\rm SScomb}_0$	–	-0.00200 ± 0.00453	0.00152 ± 0.00420
$\hat{p}^{\rm SScomb}_1$	–	0.9593 ± 0.0749	0.9613 ± 0.0710
$\Delta p^{\rm SScomb}_1$	–	-0.0003 ± 0.0447	-0.0298 ± 0.0428
$\hat{\eta}_{\rm SScomb}$	–	0.44	0.44

$$A_{raw}(B^0 \to K^+\pi^-) = -0.0934 \pm 0.0040, \quad (6.67)$$
$$A_{raw}(B^0_s \to \pi^+K^-) = 0.2227 \pm 0.0153, \quad (6.68)$$

where the $C_{\pi^+\pi^-}$, $S_{\pi^+\pi^-}$, $A_{raw}(B^0 \to K^+\pi^-)$ and $A_{raw}(B^0_s \to \pi^+K^-)$ are obtained from the fit done considering both OS and SScomb tagging information, while $C_{K^+K^-}$, $S_{K^+K^-}$ and $A^{\Delta\Gamma}_{K^+K^-}$ are obtained from the fit done considering both OS and SSkNN tagging information. The statistical-correlation matrix among all the variables is reported in Tab. 6.22. The corrections needed to determine the *CP* asymmetries $A_{CP}(B^0 \to K^+\pi^-)$ and $A_{CP}(B^0_s \to \pi^+K^-)$ from the corresponding raw asymmetries are discussed in Sec. 6.11 and will be used to compute the final values reported in Section 6.13. In Fig. 6.24 the raw time-dependent asymmetries for the $\pi^+\pi^-$ and K^+K^- spectra observed in the invariant-mass windows corresponding to $5.20 < m < 5.35\,{\rm GeV}/c^2$ and $5.30 < m < 5.44\,{\rm GeV}/c^2$ are reported.

6.10.1 Cross-check and validation

As a first cross-check of the results, we compared the values of the *CP*-violating parameters obtained using only OS tagging information, using only SScomb tagging information and using only SSkNN tagging information. The comparison is reported in Tab. 6.23, showing that the values of the parameters are well in agreement.

The stability of the fit is studied by means of pseudo-experiments. The outcome of

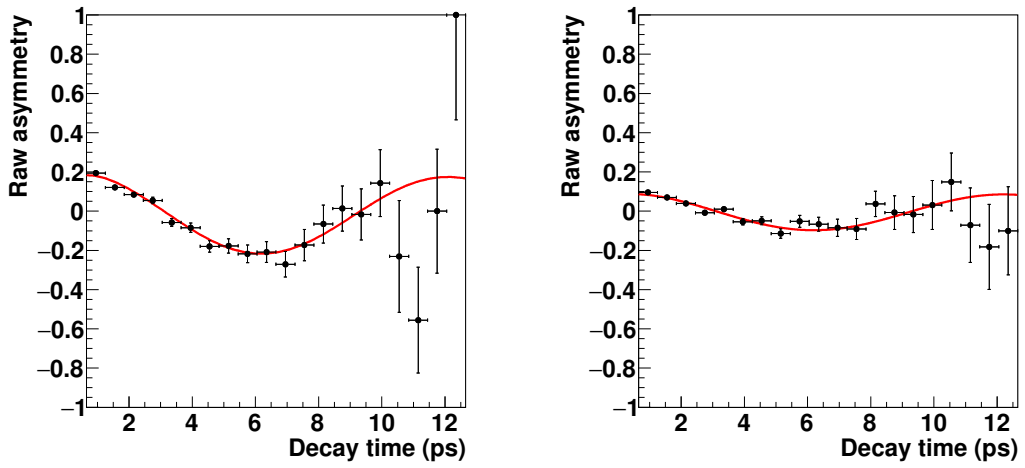

Figure 6.23: *Raw time-dependent asymmetry for the $K^\pm\pi^\mp$ spectrum in the invariant-mass region dominated by the $B^0 \to K^+\pi^-$ decay, defined as $5.23 < m < 5.32\,\text{GeV}/c^2$. On the left the asymmetry observed using the information of the* OS *tagging, while on the right, using that of the* SScomb *tagging.*

Table 6.22: *Statistical correlations among the CP-violating parameters as determined from the fit.*

	$C_{\pi^+\pi^-}$	$S_{\pi^+\pi^-}$	$C_{K^+K^-}$	$S_{K^+K^-}$	$A^{\Delta\Gamma}_{K^+K^-}$	$A_{raw}(B^0 \to K^+\pi^-)$	$A_{raw}(B^0_s \to \pi^+K^-)$
$C_{\pi^+\pi^-}$	1.000	–	–	–	–	–	–
$S_{\pi^+\pi^-}$	0.448	1.000	–	–	–	–	–
$C_{K^+K^-}$	−0.006	−0.040	1.000	–	–	–	–
$S_{K^+K^-}$	−0.009	−0.006	−0.014	1.000	–	–	–
$A^{\Delta\Gamma}_{K^+K^-}$	0.000	0.000	0.025	0.028	1.000	–	–
$A_{raw}(B^0 \to K^+\pi^-)$	−0.009	0.008	0.006	−0.003	0.001	1.000	–
$A_{raw}(B^0_s \to \pi^+K^-)$	0.003	0.000	0.001	0.000	0.000	0.043	1.000

Table 6.23: *Results for the CP-violating parameters obtained from the fits using only* OS *tagging information, using only* SScomb*, only* SSkNN*, only* OS *+*SScomb *and only* OS *+*SSkNN *tagging information.*

Parameter	OS	SScomb	SSkNN	OS +SScomb	OS +SSkNN
$C_{\pi^+\pi^-}$	-0.3392 ± 0.0711	-0.3924 ± 0.1303	–	-0.3367 ± 0.0623	–
$S_{\pi^+\pi^-}$	-0.6884 ± 0.0632	-0.5023 ± 0.1070	–	-0.6261 ± 0.0538	–
$C_{K^+K^-}$	0.2191 ± 0.0654	–	0.057 ± 0.141	–	0.1968 ± 0.0584
$S_{K^+K^-}$	0.2170 ± 0.0653	–	0.099 ± 0.148	–	0.1816 ± 0.0586
$A^{\Delta\Gamma}_{K^+K^-}$	-0.7857 ± 0.0731	–	-0.7966 ± 0.0730	–	-0.7876 ± 0.0730

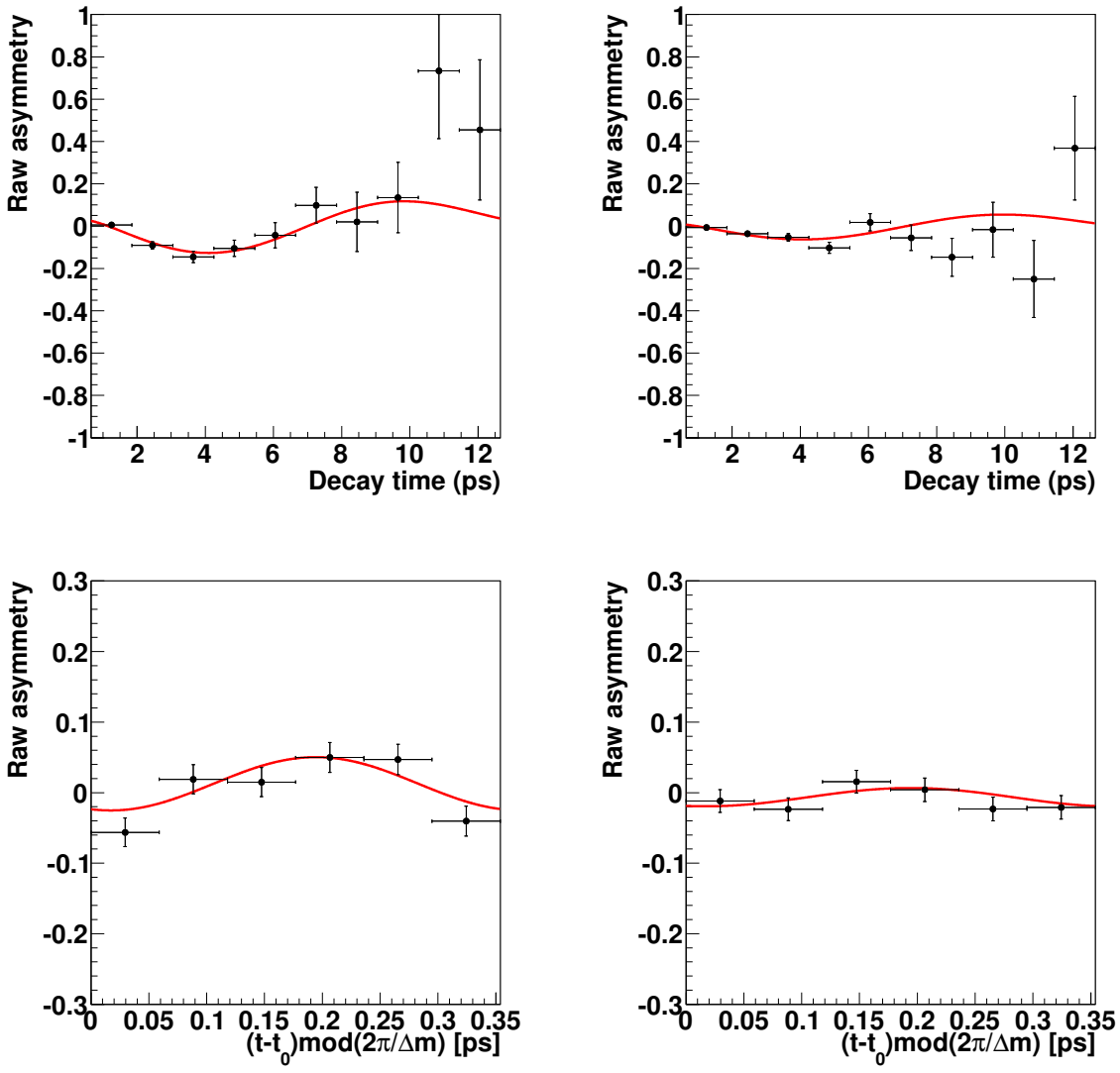

Figure 6.24: *Raw time-dependent asymmetry for the (left)* $\pi^+\pi^-$ *and (right)* K^+K^- *spectra from the invariant-mass regions corresponding to* $5.20 < m < 5.35\,\mathrm{GeV}/c^2$ *and* $5.30 < m < 5.44\,\mathrm{GeV}/c^2$*, respectively.*

the study is reported in App. D and it can be concluded that the fit is stable and returns reliable central values and uncertainties.

As another cross-check a fit to fully simulated events is performed. The sample of fully simulated decays is built in the following way, from the samples summarised in Tab. 6.5

- the sample of fully simulated $B^0 \to K^+\pi^-$ decays is fully exploited, dividing it into three subsamples, one reconstructed as $K^\pm\pi^\mp$ final state, one as $\pi^+\pi^-$ and one as K^+K^-; the relative amount of candidates in each of the three subsamples is the

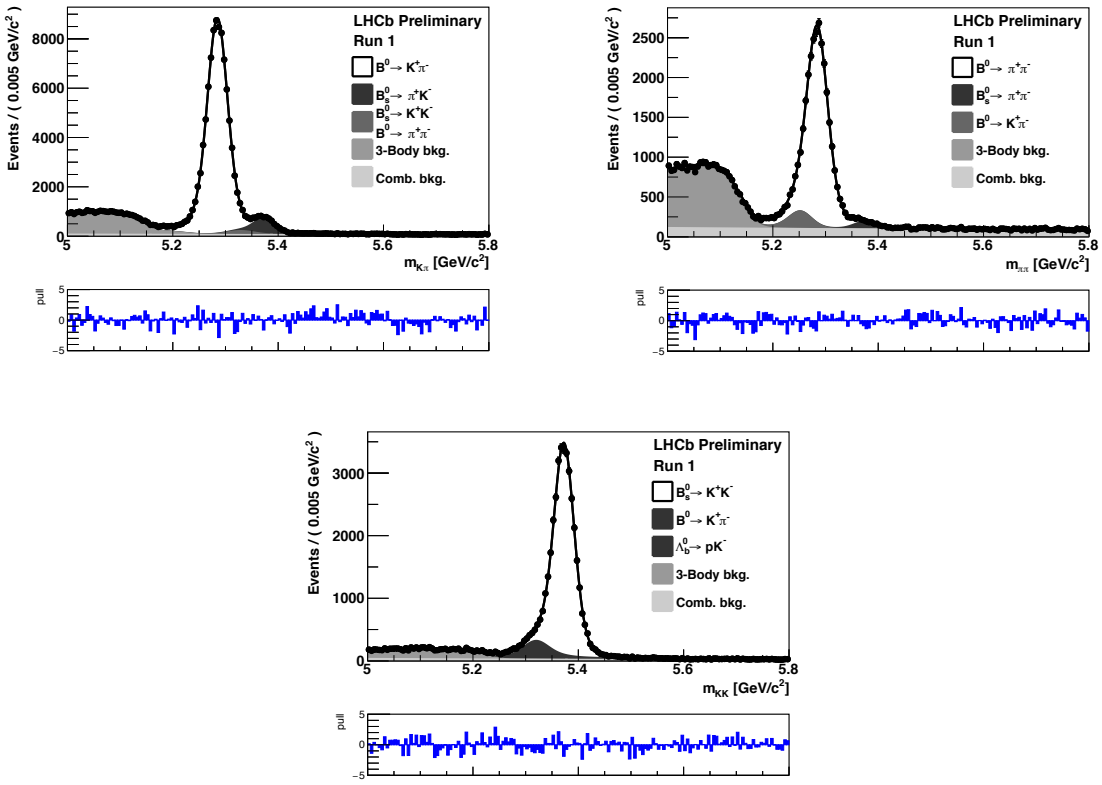

Figure 6.25: *Invariant-mass distributions for events in the (top left) $K^\pm\pi^\mp$, (top right) $\pi^+\pi^-$ and (bottom) K^+K^- spectra. The result of the simultaneous fit is superimposed to data points.*

same between the amount of the $B^0 \to K^+\pi^-$ decays populating the three spectra in real data;

- for the other two-body B decay modes, a proper amount of fully simulated events is used such that the relative fraction of each decay reconstructed in each spectrum corresponds to the relative proportions observed in data;
- no PID requirements are applied, as those would lower significantly the amount of usable simulated candidates available, affecting the precision of the test.

A total amount of about 360000 $B^0 \to K^+\pi^-$ decays are present in the $K^+\pi^-$ spectrum, about 11000 in the $\pi^+\pi^-$ spectrum and about 18000 in the K^+K^- spectrum. All other decay modes contribute to the selected sample with relative proportions equal to those observed in data. The result of the fit to fully simulated events is reported in Tab. 6.24, where we also report the value of the *CP*-violating parameters used in the simulation of the samples. The values of the *CP*-violating parameters determined from the fit are found to be well in agreement with the generated values.

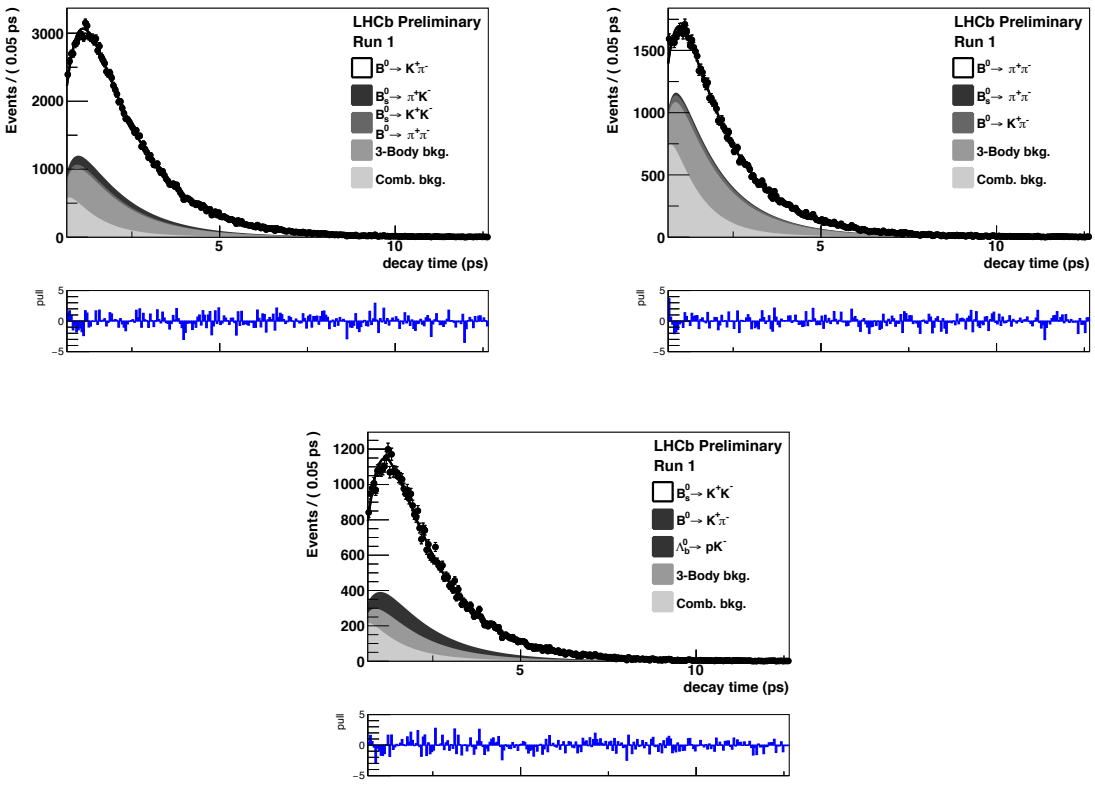

Figure 6.26: *Decay-time distributions for events in the (top left) $K^{\pm}\pi^{\mp}$, (top right) $\pi^+\pi^-$ and (bottom) K^+K^- spectra. The result of the simultaneous fit is superimposed to data points.*

Table 6.24: *Values of the parameters $C_{\pi^+\pi^-}$, $S_{\pi^+\pi^-}$, $C_{K^+K^-}$, $S_{K^+K^-}$ and $A^{\Delta\Gamma}_{K^+K^-}$ as extracted from the fit to fully simulated samples of charmless two-body B decays.*

Parameter	Fit	Generation
$C_{\pi^+\pi^-}$	-0.3878 ± 0.0242	-0.3846
$S_{\pi^+\pi^-}$	-0.6410 ± 0.0220	-0.6403
$C_{K^+K^-}$	0.1311 ± 0.0185	0.1327
$S_{K^+K^-}$	0.2488 ± 0.0185	0.2356
$A^{\Delta\Gamma}_{K^+K^-}$	-0.9708 ± 0.0461	-0.9627
$A_{CP}(B^0 \to K^+\pi^-)$	-0.1024 ± 0.0020	-0.10
$A_{CP}(B^0_s \to \pi^+K^-)$	0.3938 ± 0.0069	0.39

6.10.2 Comparison with previous preliminary results

A consistency check is performed with respect to the preliminary results of Ref. [110], obtained using only OS tagging information. By comparing the results reported in

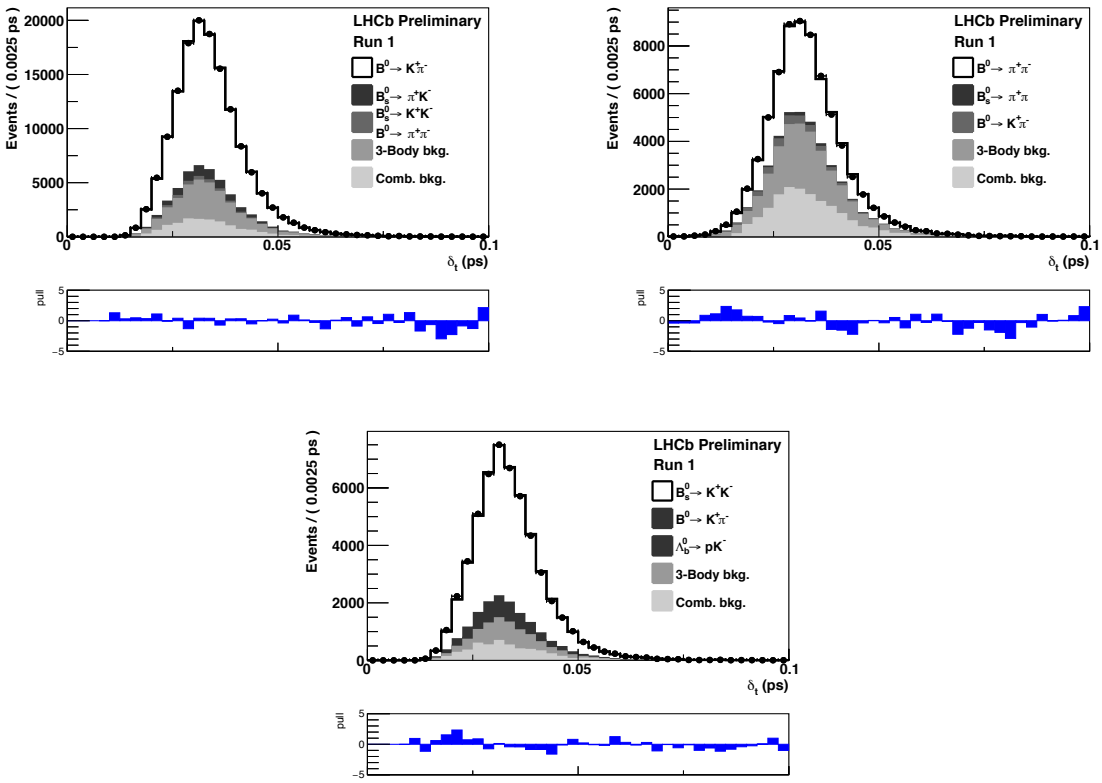

Figure 6.27: *Predicted decay time error (δ_t) distributions for events in the (top left) $K^\pm\pi^\mp$, (top right) $\pi^+\pi^-$ and (bottom) K^+K^- spectra. The result of the simultaneous fit is superimposed to data points.*

Tab. 6.23 with those in Ref. [110] (reported in Tab. 6.1), an apparent discrepancy in the value of $C_{\pi^+\pi^-}$ is observed. After a series of studies, not reported here, the only remaining possibility to investigate has been that of a simple statistical fluctuation. The sample used in Ref. [110] (hereafter referred to as `Old` sample) and the sample used in this analysis (hereafter referred to as `New` sample) are compared. A large fraction of events is found to be in common between the two samples. As an example in Fig. 6.30 the $\pi^+\pi^-$ invariant-mass distribution for events in the common subsample between `Old` and `New`, together with the distributions of the two exclusive samples are shown. A fit to the common sample is also performed in order to compare the $B^0 \to \pi^+\pi^-$ yields, the combinatorial background yields and the flavour-tagging efficiency for the $B^0 \to \pi^+\pi^-$ decay. These values are reported in Tab. 6.25. As it can be seen, approximately 90% of the $B^0 \to \pi^+\pi^-$ decays are in common between the `Old` and `New` samples, whereas approximately 10% of the signal is lost from the `Old` sample and is replaced with a similarly-sized `New` sample. Another variation is the efficiency of the OS tagger that is reduced by approximately an absolute 1%. In addition, the amount of combinatorial background is changed in a relevant way

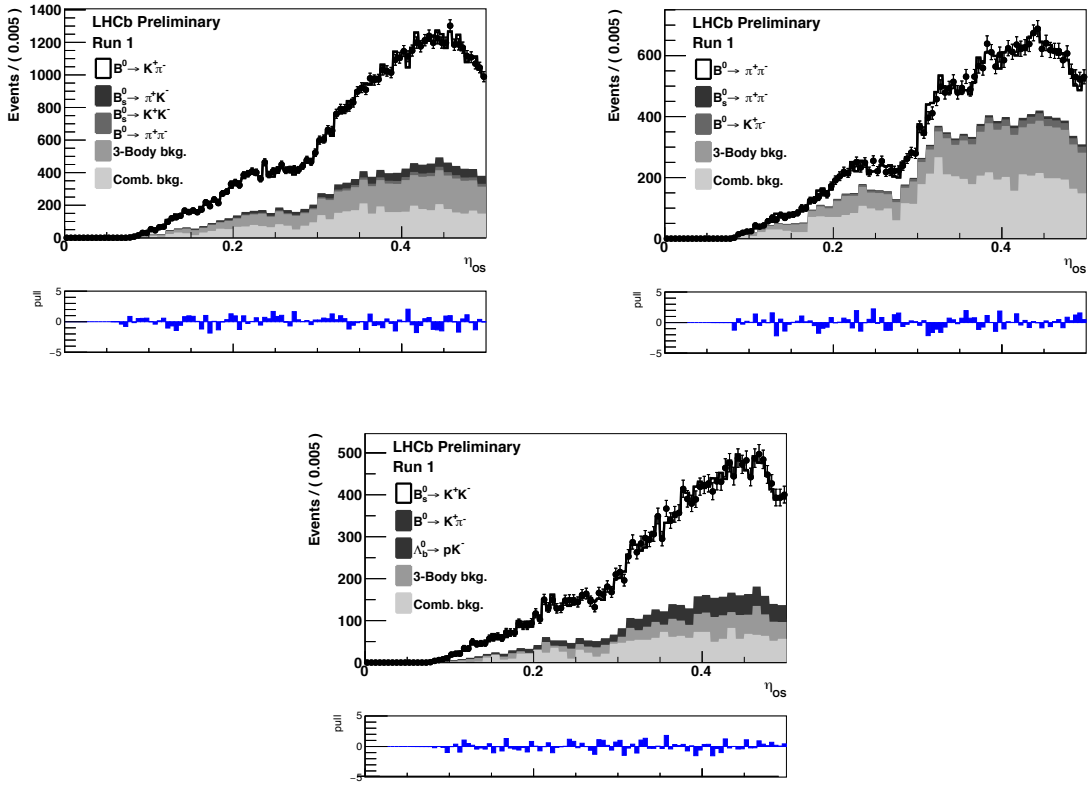

Figure 6.28: *Predicted mistag probability ($\eta_{\rm OS}$) distributions for events in the (top left) $K^{\pm}\pi^{\mp}$, (top right) $\pi^+\pi^-$ and (bottom) K^+K^- spectra. The result of the simultaneous fit is superimposed to data points.*

Table 6.25: *Values for the calibration parameters of the flavour tagging obtained from the fits. The value of $\hat{\eta}_{\rm OS}$ and $\hat{\eta}_{\rm SScomb}$ are fixed in the fit to* 0.37 *and* 0.44*, respectively. The calibration parameters are determined from the fits using* OS *only,* SScomb *only and* OS *+*SScomb *only information.*

Parameter	`Old`	`New`	Common sample
$N(B^0 \to \pi^+\pi^-)$	28600 ± 220	28250 ± 210	28600 ± 190
$N(Comb.bkg.)$	22190 ± 280	17100 ± 270	8600 ± 200
$\varepsilon^{sig}_{\rm OS}(B^0 \to \pi^+\pi^-)$	$(34.4 \pm 0.4)\%$	$(33.9 \pm 0.3)\%$	$(33.5 \pm 0.4)\%$
$\varepsilon^{bkg}_{\rm OS}$	$(62.5 \pm 0.7)\%$	$(62.8 \pm 0.4)\%$	$(62.5 \pm 0.5)\%$

between the `Old` and `New` samples. Two sets of 500 pseudoexperiments are generated: the first one is generated according to the results obtained from the `Old` sample and the

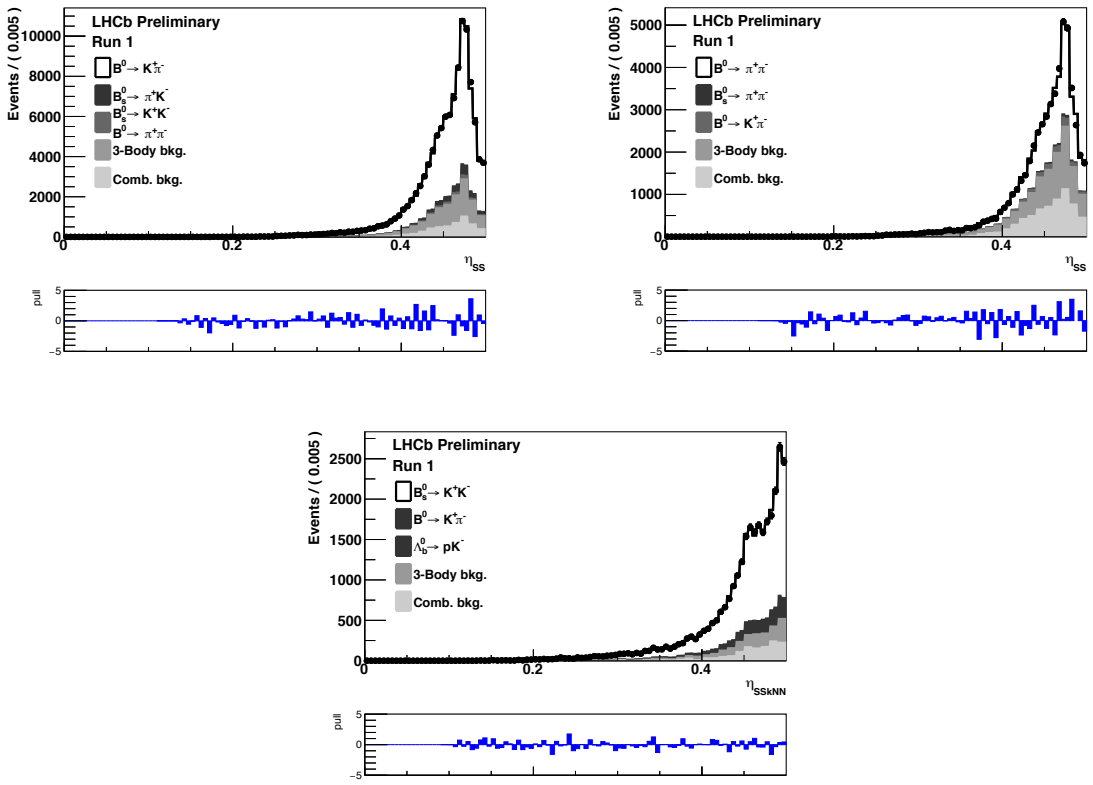

Figure 6.29: *Predicted mistag probability* η_{SScomb} *(*$\eta_{\text{SS}k\text{NN}}$ *for the* K^+K^- *spectrum) distributions for events in the (top left)* $K^\pm\pi^\mp$*, (top right)* $\pi^+\pi^-$ *and (bottom)* K^+K^- *spectra. The result of the simultaneous fit is superimposed to data points.*

second according to the results obtained from the `New` sample. The same values of the *CP*-violating parameters are generated in both sets. Then subsamples are extracted from the first set of pseudoexperiments, taking into account the variation of yields for signal and combinatorial background and the variation of OS tagger efficiencies. From the second set a subsample corresponding to the exclusive sample (shown in red in Fig. 6.30) is extracted. The two set of subsamples are merged into a new set of 500 pseudoexperiments. Then global fits are performed on these new samples and are compared with the results of the fits obtained from the first set of pseudoexperiments. The differences between the values of the *CP*-violationg parameters are computed and their distributions are shown in Fig. 6.31. The root mean squares reported in the plots of Fig. 6.31 correspond to the uncorrelated statistical fluctuation between the result in Ref. [110] and the new ones. The discrepancy between the two values of $C_{\pi^+\pi^-}$ is of about 2.1σ. In Tab. 6.26 we summarise the statistical compatibility for the full set of *CP*-violating parameters. The global χ^2 for the five variables is $\chi^2 = 5.86$, corresponding to a $p-$value of 0.320, that is about 1σ. The χ^2 is also computed without considering the parameter $A^{\Delta\Gamma}_{K^+K^-}$ (as the strategy used

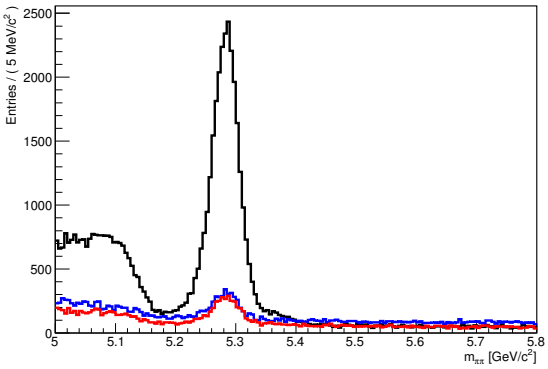

Figure 6.30: *Invariant-mass distribution of the $\pi^+\pi^-$ final state. The common sample of events used in this analysis and those used in Ref. [110] is shown in black. The exclusive sample used in Ref. [110] is shown in blue, whereas the exclusive sample used in this analysis is shown in red.*

Table 6.26: *Summary of the statistical compatibility between the results in Ref. [110] and this analysis.*

Parameter	Ref. [110]	Current	Uncorrelated stat. uncertainty	Discrepancy
$C_{\pi^+\pi^-}$	-0.243 ± 0.069	-0.339 ± 0.071	0.045	2.1σ
$S_{\pi^+\pi^-}$	-0.681 ± 0.060	-0.688 ± 0.063	0.037	0.2σ
$C_{K^+K^-}$	0.236 ± 0.062	0.219 ± 0.065	0.034	0.5σ
$S_{K^+K^-}$	0.212 ± 0.062	0.217 ± 0.065	0.036	0.1σ
$A^{\Delta\Gamma}_{K^+K^-}$	-0.751 ± 0.075	-0.786 ± 0.073	0.035	1.0σ

to determine the decay-time acceptance is rather changed with respect to the preliminary result), obtaining a $p-$value of 0.302.

6.11 Determination of the direct *CP* asymmetries $A_{CP}(B^0 \to K^+\pi^-)$ and $A_{CP}(B_s^0 \to \pi^+K^-)$

In this section the corrections needed to determine $A_{CP}(B^0 \to K^+\pi^-)$ and $A_{CP}(B_s^0 \to \pi^+K^-)$ from the raw asymmetries reported in Eq. (6.62) are discussed and presented. As pointed out in Eq. (6.10), what is actually determined from the fit is $A_{raw} = A_{CP} + A_f$, with A_{CP} and A_f defined in Eqs. (6.14) and (6.15), respectively. The nuisance experimental asymmetry A_f can be written as

$$A_f = A_{\rm PID}(K^-\pi^+) + A_{\rm D}(K^-\pi^+), \tag{6.69}$$

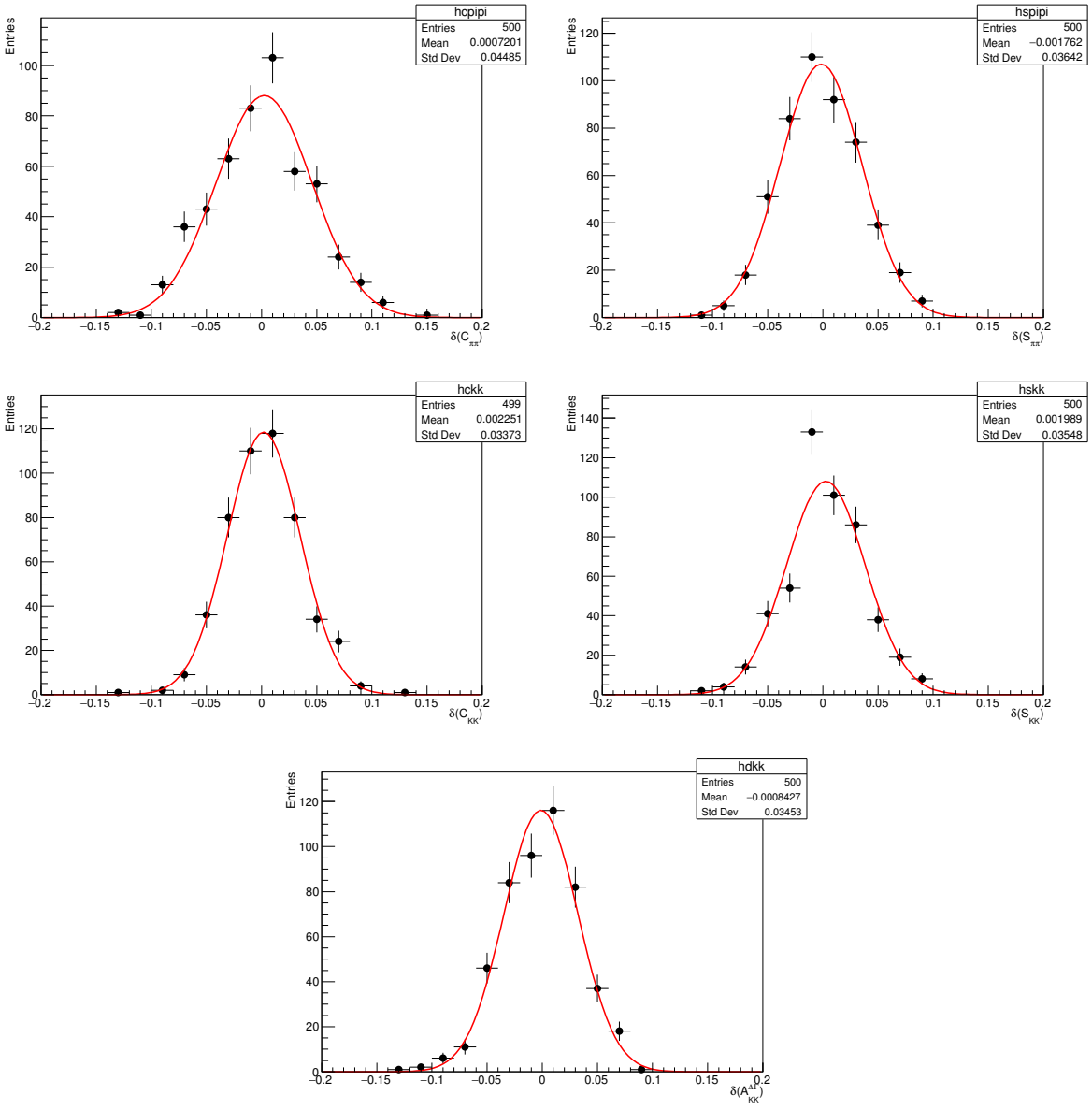

Figure 6.31: *Distributions of the variations of the CP-violating parameters obtained from the pseudoexperiments described in the text.*

where $A_{\rm PID}(K^-\pi^+)$ is the asymmetry between the efficiencies of the PID requirements selecting the $K^+\pi^-$ and π^+K^- final states and $A_{\rm D}(K^-\pi^+)$ is the asymmetry between the reconstruction efficiencies of the $K^+\pi^-$ and π^+K^- final states, before the application of PID requirements. They are defined as

$$A_{\rm D(PID)}(K^-\pi^+) = \frac{\varepsilon_{\rm (PID)}\,(K^-\pi^+) - \varepsilon_{\rm (PID)}\,(K^+\pi^-)}{\varepsilon_{\rm (PID)}\,(K^-\pi^+) + \varepsilon_{\rm (PID)}\,(K^+\pi^-)}, \tag{6.70}$$

where $\varepsilon_{(\mathrm{PID})}$ is the reconstruction (PID) efficiency of the final state. The convention of Eq. (6.70) is followed here for the corrections to be applied to both the raw asymmetries of $B^0 \to K^+\pi^-$ and $B_s^0 \to \pi^+K^-$ decays. However, the *CP* asymmetry for the $B_s^0 \to \pi^+K^-$ is defined conventionally with the opposite order of the final states with respect to Eq. (6.70), hence the value of the *CP* asymmetries for the two modes will be computed as

$$A_{CP} = A_{raw} + \zeta A_{\mathrm{f}}, \tag{6.71}$$

where ζ assume the value -1 for the $B^0 \to K^+\pi^-$ and $+1$ for the $B_s^0 \to \pi^+K^-$ decays, respectively.

6.11.1 Asymmetry induced by PID requirements

The correction due to the asymmetry induced by PID requirements is determined similarly to what is described in Secs. 4 and 7.1.5 of Ref. [106]. PID efficiencies in bins of track momentum (p), pseudorapidity (η), azimuthal angle (ϕ) and number of tracks in the event, are created for kaons and pions (and separated for different charge) from calibration samples of $D^{*+} \to D^0\,(K^-\pi^+)\,\pi^+$. The effect of different event multiplicities (and thus detector occupancies) between the charmless two-body B-decay and calibration samples is corrected for by integrating out the dependence on the number of tracks, following the method described in Ref. [106]. Then PID efficiency maps are used to determine the corresponding maps of PID asymmetry in bins of momentum, pseudorapidity and azimuthal angle of each final state particle (kaon or pion). The PID asymmetry of the $K\pi$ pair as a function of the kinematics of the final-state pair is then defined as

$$A_{\mathrm{PID}}(K^-\pi^+) = \frac{A_{\mathrm{PID}}(K^-)\,(p_K,\,\eta_K,\,\phi_K) - A_{\mathrm{PID}}(\pi^+)\,(p_\pi,\,\eta_\pi,\,\phi_\pi)}{1 - A_{\mathrm{PID}}(K^-)\,(p_K,\,\eta_K,\,\phi_K)\;A_{\mathrm{PID}}(\pi^+)\,(p_\pi,\,\eta_\pi,\,\phi_\pi)}, \tag{6.72}$$

where $A_{\mathrm{PID}}(K(\pi))\left(p_{K(\pi)},\,\eta_{K(\pi)},\,\phi_{K(\pi)}\right)$ is the PID asymmetry of kaons (pions) as a function of particle kinematics. Finally, the PID asymmetry for $K\pi$ pairs as a function of the kinematics of the final-state particles is convolved with the phase space of two-body B decays, in order to obtain the final integrated value of $A_{\mathrm{PID}}^{K\pi}$. The errors on the PID asymmetry are determined summing in quadrature two sources of uncertainties: one related to the statistics of the calibration and of the two-body B-decay samples, and one related to the binning scheme used to divide the phase space. The former source is computed by simply propagating the statistical uncertainties from the efficiency maps and the amount of signals in each bin of the phase space. The latter source (that turns out to be the dominant one) is determined by varying the binning scheme. As a baseline, 71 bins in momentum, 10 in pseudorapidity and 8 in azimuthal angle are used. The binning schemes are varied doubling and halving the number of bins of all the three variables in turn, for a total of 27 different binning schemes. The average and root mean square (RMS) of the 27 results are used as central value and uncertainty for the final integrated correction $A_{\mathrm{PID}}^{K\pi}$. The final result is

$$A_{\mathrm{PID}}(K^-\pi^+) = (-0.04 \pm 0.25)\,\%. \tag{6.73}$$

6.11.2 Final-state detection asymmetry

The final-state detection asymmetry is be obtained by means of $D^+ \to K^-\pi^+\pi^+$ and $D^+ \to \overline{K}^0\pi^+$ control modes. A full discussion on the procedure employed to determine this asymmetry is reported in Sec. 8.1.1 of Ref. [81]. The method consists in combining the raw asymmetries

$$A_{\rm raw}(K\pi\pi) = A_{\rm P}(D^+) + A_{\rm D}(K^-\pi^+) + A_{\rm D}(\pi^+), \quad (6.74)$$
$$A_{\rm raw}(K^0\pi^+) = A_{\rm P}(D^+) + A_{\rm D}(\pi^+) - A_{\rm D}(K^0), \quad (6.75)$$

where $A_{\rm P}(D^+)$ is the production asymmetry of the D^+ meson and the various $A_{\rm D}$ are the detection asymmetries for single particles or combinations of two particles. The difference between Eqs. (6.74) and (6.75) yields to

$$A_{\rm D}(K^-\pi^+) = A_{\rm raw}(K\pi\pi) - A_{\rm raw}(K^0\pi^+) - A_{\rm D}(K^0). \quad (6.76)$$

The quantity $A_{\rm D}(K^0)$ includes *CP* violation in the decay $K^0 \to \pi^+\pi^-$ and the different interaction rates of K^0 and $\overline{K}^0$ with the detector material. Its value was measured in a previous LHCb analysis to be $A_{\rm D}(K^0) = (0.054 \pm 0.014)\,\%$ [68], and it is taken as an external input. In order to ensure the cancellation of $A_{\rm P}(D^+)$ and $A_{\rm D}(\pi^+)$ in the difference in Eq. (6.76), a multidimensional reweighting is performed on p and $p_{\rm T}$ of the D^+ and π^+ mesons in $D^+ \to K^-\pi^+\pi^+$ and $D^+ \to \overline{K}^0\pi^+$ control modes. Finally, since $A_{\rm D}(K^-\pi^+)$ depends on the kaon momentum, due to the different interaction cross sections of K^+ and K^- with the detector material, the correction has been measured in bins of kaon momentum. In Fig. 6.32 the values of $A_{\rm D}(K^-\pi^+)$ as a function of kaon momentum are reported, separately for magnet polarity and year of data taking. In order to compute the final detection asymmetry, the values of $A_{\rm D}(K^-\pi^+)$ reported in Fig. 6.32 are convolved with the momentum distribution of the kaons for $B^0 \to K^+\pi^-$ and $B^0_s \to \pi^+K^-$ decays. The background-subtracted momentum distributions for the two signals are extracted from data using the *sPlot* technique by means of the same invariant-mass fit shown in Fig. 6.19. The results of the invariant-mass fit, separated by magnet polarity and year of data taking are reported in Fig. 6.33. In Fig. 6.34 the distributions of kaon momentum for the $B^0 \to K^+\pi^-$ and $B^0_s \to \pi^+K^-$ decays are shown, separated by magnet polarity and year of data taking. As it can be seen from Fig. 6.34, the measurement of the kaon detection asymmetry is performed up to 70 GeV/c, whereas the distribution of kaon momentum for $B^0 \to K^+\pi^-$ and $B^0_s \to \pi^+K^-$ extends up to 150 GeV/c. In order to take this into account, an additional bin between 70 and 150 GeV/c of kaon momentum is considered, with the same central value of the last bin of the plots in Fig. 6.32 and with twice the error.

The final results for the convolution of the asymmetries in Fig. 6.32 with the momentum distributions of Fig. 6.34 are

$$A_{\rm D}(K^-\pi^+)_{B^0\to K^+\pi^-} = (-0.900 \pm 0.141)\,\%, \quad (6.77)$$
$$A_{\rm D}(K^-\pi^+)_{B^0_s\to \pi^+K^-} = (-0.924 \pm 0.142)\,\%. \quad (6.78)$$

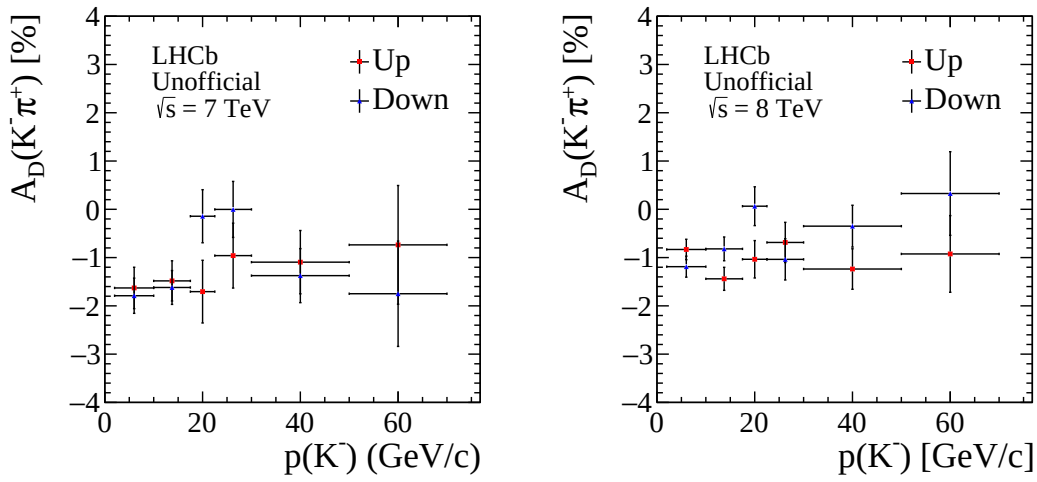

Figure 6.32: *Values of $A_{\rm D}(K^-\pi^+)$ for (left) 2011 and (right) 2012 data as a function of the kaon momentum. Different points are shown for different magnet polarities.*

6.11.3 Results for $A_{CP}(B^0 \to K^+\pi^-)$ and $A_{CP}(B^0_s \to \pi^+K^-)$

Using the values of $A_{raw}(B^0 \to K^+\pi^-)$ and $A_{raw}(B^0_s \to \pi^+K^-)$ reported in Eq. (6.62) and correcting them by $A_{\rm PID}(K^-\pi^+)$ in Eq. (6.73), $A_{\rm D}(K^-\pi^+)_{B^0\to K^+\pi^-}$ in Eq. (6.77) and $A_{\rm D}(K^-\pi^+)_{B^0_s\to\pi^+K^-}$ in Eq. (6.78), the values of $A_{CP}(B^0 \to K^+\pi^-)$ and $A_{CP}(B^0_s \to \pi^+K^-)$ are

$$A_{CP}(B^0 \to K^+\pi^-) = (-8.40 \pm 0.40 \pm 0.25 \pm 0.14)\,\%, \quad (6.79)$$
$$A_{CP}(B^0_s \to \pi^+K^-) = (\ 21.31 \pm 1.53 \pm 0.25 \pm 0.14)\,\%, \quad (6.80)$$

where the first uncertainty is statistical, the second comes from the PID-induced asymmetry and the third from the detection asymmetry between $K^-\pi^+$ and $K^+\pi^-$ final states.

6.12 Systematic uncertainties

In this section the studies done to determine systematic uncertainties affecting the measurements of the *CP*-violating parameters are reported. Two strategies are adopted in order to determine systematics: either the models are fitted to data several times with modified parameters or are generated and baseline and modified models are fitted to the same samples in order to study the differences. In the former case, the sum in quadrature of the mean and the root mean square of the difference between the results of the modified fit to data and the baseline result is taken as a systematic uncertainty. In the latter, the distribution of the difference between the results obtained using the baseline model and the modified model to the same pseudoexperiment is built. Then the sum in quadrature of the mean and root mean square of the distribution is taken as a systematic uncertainty.

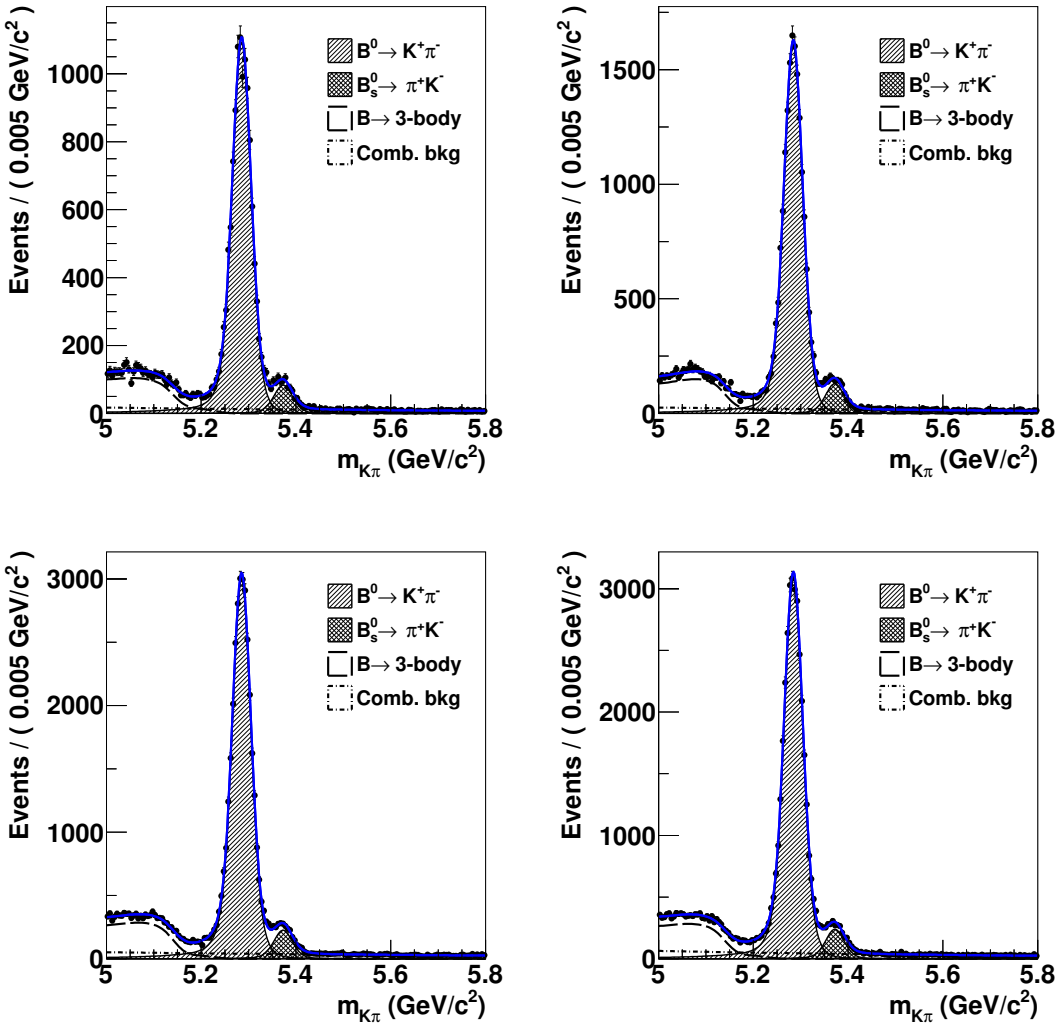

Figure 6.33: *Invariant-mass distributions for candidates selected under the $K^+\pi^-$ and $K^-\pi^+$ final-state and corresponding to (top left) 2011 up, (top right) 2011 down, (bottom left) 2012 up and (bottom right) 2012 down samples. The results of the best fits are superimposed to the data points.*

6.12.1 Invariant-mass model

Systematic uncertainties associated to the models used to describe the invariant-mass shapes are investigated generating 100 pseudoexperiments using the baseline model. The alternative models used to determine the systematic uncertainties are in turn

- the mass resolution for signals and cross-feed backgrounds is substituted with a single Gaussian function;

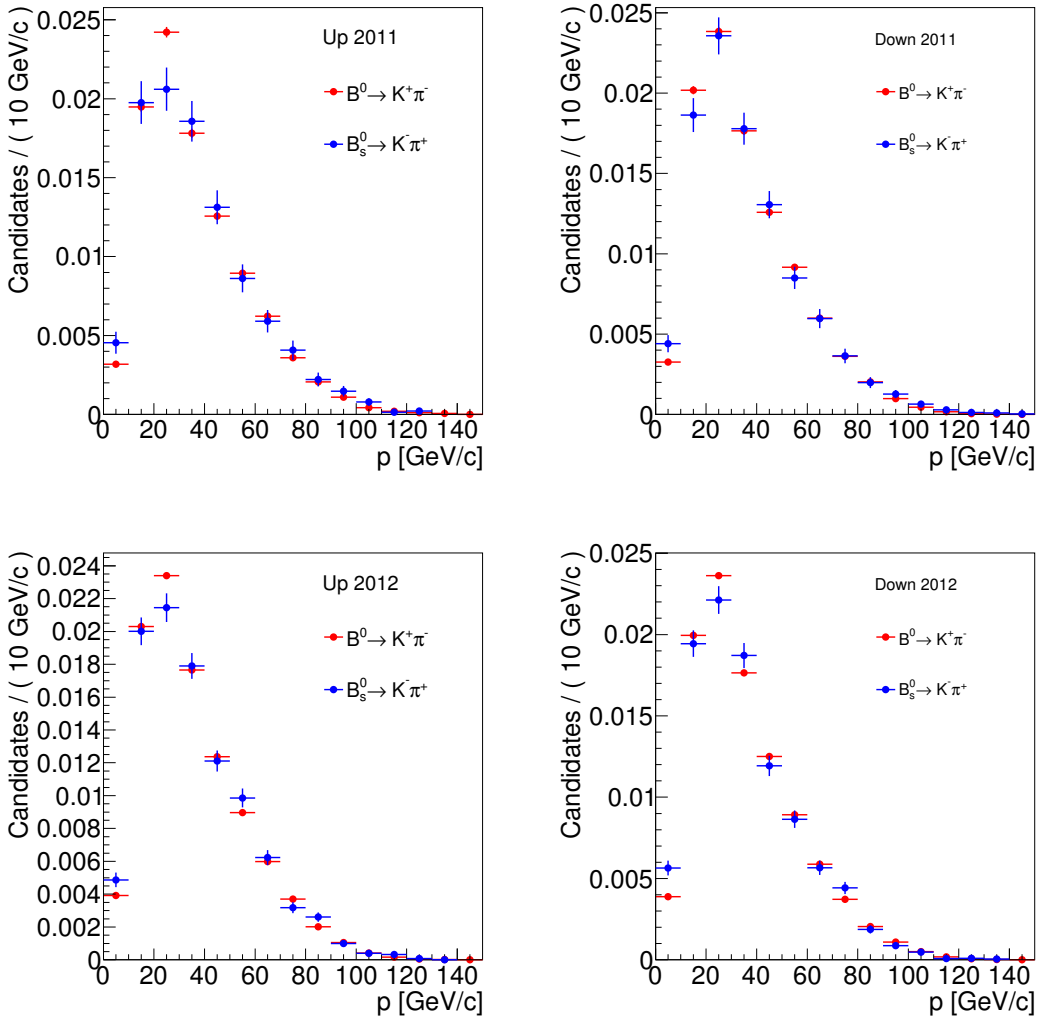

Figure 6.34: *Distributions of kaon momentum for (red)* $B^0 \to K^+\pi^-$ *and (blue)* $B_s^0 \to \pi^+K^-$ *decays obtained from the background subtraction of Fig. 6.33. Histograms are separated by magnet polarity and year of data taking.*

- the parameters governing the tails of the Johnson functions and its relative fraction are fixed to the same values for all signals, namely to those of the $B^0 \to K^+\pi^-$ decay;
- the combinatorial background is parameterised with a straight line instead of an exponential.

6.12.2 Decay-time model

To determine a systematic uncertainty associated to the knowledge of the decay-time acceptance, we generate again 100 different samples with different acceptance functions for each two-body B-decay mode in the fit. Each acceptance is obtained as described in Sec. 6.8, *i.e.* generating a high-statistics histogram on the basis of the effective functions in Figs. 6.14 to 6.16. For each of the 100 different histograms the parameters governing the acceptance are varied by means of a multi-dimensional Gaussian function, according to uncertainties and correlations of the parameters. Then the set of 100 acceptances is used to fit again the data, and the root mean square of the distribution of the fitted parameter is taken as a systematic uncertainty.

The systematic uncertainty associated to the parameterisation of the cross-feed backgrounds is evaluated disabling the oscillating component, that means fixing to 0 the *CP* asymmetry of the $B^0 \to K^+\pi^-$ component in the $\pi^+\pi^-$ and K^+K^- spectra and the C and S parameters of the $B^0 \to \pi^+\pi^-$ and $B^0_s \to K^+K^-$ decays in the $K^\pm\pi^\mp$ spectrum. A set of 100 pseudoexperiments is generated to quantify the size of this uncertainty.

The systematic uncertainty associated to the parameterisation of the decay-time distribution of the combinatorial background is evaluated again using 100 pseudoexperiments. The modified model consists in removing the decay-time acceptance of the combinatorial background.

6.12.3 Partially-reconstructed background

The systematic uncertainty associated to the model describing the partially-reconstructed background is evaluated using 100 pseudoexperiments. The modified model consists in removing the components describing the partially-reconstructed background in the three spectra and to perform the fit only in the invariant mass window above $5.2\,\mathrm{GeV}/c^2$.

6.12.4 Flavour tagging

Most of the systematic uncertainties are expected to cancel in this analysis, since most of the flavour tagging algorithms are calibrated using the $B^0 \to K^+\pi^-$ control mode, that shares the same topology and selection of the $B^0 \to \pi^+\pi^-$ and $B^0_s \to K^+K^-$ signals. The main source of systematic uncertainty stems from the choice of the linear dependence between the predicted mistag probability η and the actual mistag fraction ω. To take this into account, 100 pseudoexperiments are generated according to the baseline model. The modified model consists in changing the linear relation between η and ω with a second order polynomial

$$\omega = p_0^{tag} + p_1^{tag} \cdot (\eta_{tag} - \hat{\eta}_{tag}) + p_2^{tag} \cdot (\eta_{tag} - \hat{\eta_{tag}})^2 \,. \tag{6.81}$$

The systematic uncertainty coming from the SSkNN is determined by fitting the data 100 times with modified values of the calibration parameters of the SSkNN tagger. The values of the parameters are extracted according to a multi-dimensional Gaussian distribution, built according to Tabs. 6.18 and 6.19.

6.12.5 Decay-time resolution

Two sources of systematic uncertainties coming from the decay-time resolution are investigated: those related to the calibration parameters q_0 and q_1 in Eq. (6.40) and to the model used to describe the decay-time resolution. To determine the uncertainties related to the former source, the fit to data is repeated 100 times. In each fit the values of q_0 and q_1 are randomly generated according to a bi-dimensional Gaussian function. The means, widths and correlation are taken from Eq. (6.40), but with inflated uncertainties for q_0 and q_1, to take into account small residual differences between the $B_s^0 \to \pi^+ K^-$ and $B_s^0 \to D_s^- \pi^+$ decays, as observed with simulated events. From Tabs. 6.12 it can be seen that differences with respect to the $B_s^0 \to D_s^- \pi^+$ decay are approximately 1.1 fs for q_0 and 0.1 for q_1. In addition, comparing Tab. 6.12 and Tab. 6.11, a difference of an additional 1 fs for q_0 and 0.05 for q_1 are considered. Instead of summing in quadrature these contributions, we simply add them linearly to the statistical uncertainties of Eqs. (6.40). The values used in the constraint are: $q_0 = 46.1 \pm 4.1$ fs, $q_1 = 0.81 \pm 0.38$ and $\rho(q_0, q_1) = -0.32$.

Systematics related to the latter source are evaluated adding a third Gaussian function to follow the large tails visible in Fig. 6.10. The model is then parameterised with

$$\begin{aligned} R(t-t') =& (1 - f_{tail}) \left[f_\tau \cdot G\left(t - t'; \mu, \sigma_1(\delta_t)\right) + (1 - f_\tau) \cdot G\left(t - t'; \mu, \sigma_2(\delta_t)\right) \right] + \\ & f_{tail} \cdot G\left(t - t'; \mu, \sigma_3(\delta_t)\right), \end{aligned} \tag{6.82}$$

where, as in Eq. (6.37),

$$\sigma_1(\delta_t) = q_0 + q_1 \cdot (\delta_t - \hat{\delta}_t), \tag{6.83}$$

$$\sigma_2(\delta_t) = r_\sigma \cdot \sigma_1(\delta_t), \tag{6.84}$$

$$\sigma_3(\delta_t) = r_{tail} \cdot \sigma_1(\delta_t). \tag{6.85}$$

The same fits of Fig. 6.10 are reported in Fig. 6.35, where the new model for the resolution is used. Numerical results are reported in Tab. 6.27. The fit to the $B^0 \to D^- \pi^+$ and $B_s^0 \to D_s^- \pi^+$ samples is performed again by fixing the values of r_σ, f_τ, r_{tail} and f_{tail} to those in Tab. 6.27, while leaving free to vary q_0 and q_1. The new model and the new calibration parameters are then used to fit again the data. A set of 100 pseudoexperiments is generated according to the baseline fit model and then fitted with both the baseline and modified fitting model. The distribution of the difference between the results of the two fits for each pseudoexperiment is used to determine the systematic uncertainty, evaluated summing in quadrature the mean and the root mean square of the distribution.

Systematics associated due to the description of the distribution of the observable δ_t are determined by changing the histograms used to describe the distributions. Alternative histograms are taken from fully simulated decays reweighted with per-event PID efficiencies. For the combinatorial and partially-reconstructed backgrounds, the same histogram used to parameterise the $B^0 \to K^+ \pi^-$ decay in the $K^\pm \pi^+$ spectrum is employed.

6.12.6 Fixed parameters

A systematic uncertainty associated to the fixed parameters Γ_s, $\Delta\Gamma_s$ and $\Delta m_{d,s}$ is determined by repeating the fit to data 100 times. Each time the values of the parameters

Table 6.27: *Calibration parameters of the decay-time resolution for fully simulated $B^0_s \to \pi^+K^-$ decays. The results are obtained from the unbinned maximum likelihood fit of the model described in Eq.* (6.82)*, to the distributions of fully simulated candidates.*

Parameter	$B^0_s \to \pi^+K^-$
μ [fs]	0.076 ± 0.052
q_0 [fs]	32.68 ± 0.13
q_1	1.0117 ± 0.0058
r_σ	1.776 ± 0.031
f_τ	0.8844 ± 0.0080
r_{tail}	5.20 ± 0.16
f_{tail}	0.0062 ± 0.0005

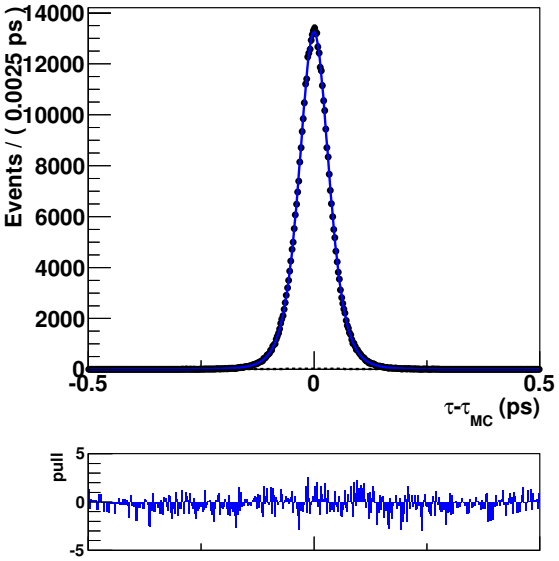

Figure 6.35: *Distribution of $\tau_{err.}$ for fully simulated $B^0_s \to \pi^+K^-$ events. The result of the best fit, using the model described in Eq.* (6.82)*, is superimposed to the data points.*

are randomly extracted according to the central values and uncertainties reported in Tab. 6.20.

6.12.7 Summary of systematics

The full set of systematic uncertainties is summarised in Tab. 6.28.

Table 6.28: *Summary of systematic uncertainties on the CP violation observables, determined as described in Sec. 6.12.*

Parameter	$C_{\pi^+\pi^-}$	$S_{\pi^+\pi^-}$	$C_{K^+K^-}$	$S_{K^+K^-}$	$A^{\Delta\Gamma}_{K^+K^-}$	$A_{CP}(B^0 \to K^+\pi^-)$	$A_{CP}(B^0_s \to \pi^+K^-)$
Time acceptance	0.0011	0.0004	0.0020	0.0017	0.0778	0.0004	0.0002
Time resolution calibration	0.0014	0.0013	0.0108	0.0119	0.0051	0.0001	0.0001
Time resolution model	0.0001	0.0005	0.0002	0.0002	0.0003	negligible	negligible
Input parameters	0.0025	0.0024	0.0092	0.0107	0.0480	negligible	0.0001
OS Tagging calibration	0.0018	0.0021	0.0018	0.0019	0.0001	negligible	negligible
SSkNN Tagging calibration	–	–	0.0061	0.0086	0.0004	–	–
SS Tagging calibration	0.0015	0.0017	–	–	–	negligible	negligible
Cross-feed time model	0.0075	0.0059	0.0022	0.0024	0.0003	0.0001	0.0001
3Body bkg.	0.0070	0.0056	0.0044	0.0043	0.0304	0.0008	0.0043
Comb. bkg. time model	0.0016	0.0016	0.0004	0.0002	0.0019	0.0001	0.0005
Signal mass model (reso.)	0.0027	0.0025	0.0015	0.0015	0.0023	0.0001	0.0041
Signal mass model (tails)	0.0007	0.0008	0.0013	0.0013	0.0016	negligible	0.0003
Comb. bkg. mass model	0.0001	0.0003	0.0002	0.0002	0.0016	negligible	0.0001
PID asymmetry	–	–	–	–	–	0.0025	0.0025
Detection asymmetry	–	–	–	–	–	0.0014	0.0014
Total	0.0115	0.0095	0.0165	0.0191	0.0966	0.0030	0.0066

Table 6.29: *Statistical correlations among the CP violation parameters are determined from the fit.*

	$C_{\pi^+\pi^-}$	$S_{\pi^+\pi^-}$	$C_{K^+K^-}$	$S_{K^+K^-}$	$A^{\Delta\Gamma}_{K^+K^-}$	$A_{raw}(B^0 \to K^+\pi^-)$	$A_{raw}(B^0_s \to \pi^+K^-)$
$C_{\pi^+\pi^-}$	1.000	–	–	–	–	–	–
$S_{\pi^+\pi^-}$	0.448	1.000	–	–	–	–	–
$C_{K^+K^-}$	−0.006	−0.040	1.000	–	–	–	–
$S_{K^+K^-}$	−0.009	−0.006	−0.014	1.000	–	–	–
$A^{\Delta\Gamma}_{K^+K^-}$	0.000	0.000	0.025	0.028	1.000	–	–
$A_{CP}(B^0 \to K^+\pi^-)$	−0.009	0.008	0.006	−0.003	0.001	1.000	–
$A_{CP}(B^0_s \to \pi^+K^-)$	0.003	0.000	0.001	0.000	0.000	0.043	1.000

6.13 Conclusions

The direct and mixing-induced *CP*-violating parameters of the $B^0 \to \pi^+\pi^-$ and $B^0_s \to K^+K^-$ decays have been measured, together with the direct *CP* asymmetries of the $B^0 \to K^+\pi^-$ and $B^0_s \to \pi^+K^-$ decays. The results obtained are

$$\begin{aligned}
C_{\pi^+\pi^-} &= -0.3367 \pm 0.0623 \pm 0.0115, \\
S_{\pi^+\pi^-} &= -0.6261 \pm 0.0538 \pm 0.0095, \\
C_{K^+K^-} &= 0.1968 \pm 0.0584 \pm 0.0165, \\
S_{K^+K^-} &= 0.1816 \pm 0.0586 \pm 0.0191, \\
A^{\Delta\Gamma}_{K^+K^-} &= -0.7876 \pm 0.0730 \pm 0.0966, \\
A_{CP}(B^0 \to K^+\pi^-) &= -0.0840 \pm 0.0040 \pm 0.0030,
\end{aligned}$$

$$A_{CP}(B^0_s \to \pi^+ K^-) \quad = \quad 0.2131 \pm 0.0153 \pm 0.0066,$$

where the first uncertainty is statistical and the second systematic. In Tab. 6.29 the statistical correlations among the parameters are reported.

7 Conclusions

This thesis presents the state-of-the-art for the measurements of b-hadron production asymmetries and CP violation in two-body b-hadron decays at LHCb. These are performed using a data sample corresponding to about $3\,\text{fb}^{-1}$ of integrated luminosity, collected by the experiment during the LHC Run 1 in 2010-2012 at centre-of-mass energies of 7 and 8 TeV. All results here reported are presented for the first time in a thesis and represent original contributions.

Integrating over p_{T} and y, in the range $0 < p_{\text{T}} < 30\,\text{GeV}/c$ and $2.1 < y < 4.5$ for B^+ and B^0 decays, and in the range $2 < p_{\text{T}} < 30\,\text{GeV}/c$ and $2.1 < y < 4.5$ for B_s^0 and Λ_b^0 decays, the following values of the b-hadron production asymmetries are obtained

$$\begin{aligned}
A_{\text{P}}(B^+)_{\sqrt{s}=7\,\text{TeV}} &= -0.002 \pm 0.002 \pm 0.004, \\
A_{\text{P}}(B^+)_{\sqrt{s}=8\,\text{TeV}} &= -0.007 \pm 0.002 \pm 0.003, \\
A_{\text{P}}(B^0)_{\sqrt{s}=7\,\text{TeV}} &= 0.004 \pm 0.009 \pm 0.001, \\
A_{\text{P}}(B^0)_{\sqrt{s}=8\,\text{TeV}} &= -0.014 \pm 0.006 \pm 0.001, \\
A_{\text{P}}(B_s^0)_{\sqrt{s}=7\,\text{TeV}} &= -0.007 \pm 0.029 \pm 0.006, \\
A_{\text{P}}(B_s^0)_{\sqrt{s}=8\,\text{TeV}} &= 0.020 \pm 0.019 \pm 0.006, \\
A_{\text{P}}(\Lambda_b^0)_{\sqrt{s}=7\,\text{TeV}} &= -0.001 \pm 0.025 \pm 0.011, \\
A_{\text{P}}(\Lambda_b^0)_{\sqrt{s}=8\,\text{TeV}} &= 0.034 \pm 0.016 \pm 0.008,
\end{aligned}$$

where the first uncertainties are statistical and the second systematic. The differential measurements, also reported in this thesis, once integrated using appropriate weights for any reconstructed B^+, B^0, B_s^0, Λ_b^0 decay in LHCb, can be used to determine effective production asymmetries, as inputs for CP violation measurements with the LHCb data.

In particular, the measurement of the Λ_b^0 production asymmetry, performed for the first time at a hadron-collider, is a fundamental ingredient to determine the CP asymmetries in $\Lambda_b^0 \to pK^-$ and $\Lambda_b^0 \to p\pi^-$ decays. As reported in this thesis, their values are measured to be

$$A_{CP}(\Lambda_b^0 \to pK^-) = -0.019 \pm 0.013 \pm 0.017,$$

$$A_{CP}(\Lambda_b^0 \to p\pi^-) = -0.035 \pm 0.017 \pm 0.018,$$

where the first uncertainties are statistical and the second systematic. The systematic uncertainties are largely dominated by the knowledge of the Λ_b^0 production asymmetry, hence mostly statistical in nature. For this reason they can be reduced in future updates of these measurements. No evidence for *CP* violation is found. These measurements are the most precise available to date and improve on previous determinations by the CDF collaboration [26].

Finally, *CP* violation arising from decay and from interference between mixing and decay in $B^0 \to \pi^+\pi^-$ and $B_s^0 \to K^+K^-$ are measured, together with the direct *CP* asymmetries in $B^0 \to K^+\pi^-$ and $B_s^0 \to \pi^+K^-$ decays. The results are

$$\begin{aligned}
C_{\pi^+\pi^-} &= -0.34 \pm 0.06 \pm 0.01, \\
S_{\pi^+\pi^-} &= -0.63 \pm 0.05 \pm 0.01, \\
C_{K^+K^-} &= 0.20 \pm 0.06 \pm 0.02, \\
S_{K^+K^-} &= 0.18 \pm 0.06 \pm 0.02, \\
A_{K^+K^-}^{\Delta\Gamma} &= -0.79 \pm 0.07 \pm 0.10, \\
A_{CP}(B^0 \to K^+\pi^-) &= -0.084 \pm 0.004 \pm 0.003, \\
A_{CP}(B_s^0 \to \pi^+K^-) &= 0.213 \pm 0.015 \pm 0.007,
\end{aligned}$$

where the first uncertainties are statistical and the second systematic. These are compatible with the world averages and with previous LHCb determinations [108]. They are the most precise available to date. Together with those from BaBar and Belle, they allow the determination of the unitarity triangle angle γ using decays affected by penguin processes [94, 120, 121]. The comparison to the value of γ determined from tree-level decays will provide a test of the Standard Model and constrain possible non-Standard Model contributions.

As a side measurement, the precise determination of the position of a beryllium-made conical section of the LHCb beampipe is also presented. This measurement will be used to tune the LHCb simulation, and since this section of the beampipe is placed within the acceptance of the LHCb tracking system, the methodology developed in this thesis will enable measurements of cross-sections against fixed target of various particle species produced in the proton-proton collision point to be performed in the future.

Amongst the results presented in this thesis, that on production asymmetries is already published [122]. A further paper on time-dependent and time-integrated *CP* violation in two-body B decays to charged pions and kaons is at the last stage of internal review, and is expected to be published early in 2018. Finally, a paper on *CP* violation in Λ_b^0 two-body decays is also under way, and expected to be published within Winter 2018.

Appendices

A

Tables for $A_{\mathrm{P}}(\Lambda_b^0)$ measurement

A.1 Weights for the determination of $A_{\mathrm{D}}(\pi^+)$

Table A.1: *Weights obtained as a function of pion and kaon momenta used for the determination of the experimental asymmetry $A_{\mathrm{D}}(\pi^+)$. The weights are divided by magnet polarity and year.*

	Kaon bins					
Pion bins	1	2	3	4	5	6
2011 Up						
1	0.00000 ± 0.00000	0.00000 ± 0.00000	0.00000 ± 0.00000	0.00000 ± 0.00000	0.00000 ± 0.00000	0.00000 ± 0.00000
2	0.27532 ± 0.00007	0.13899 ± 0.00002	0.08208 ± 0.00002	0.05641 ± 0.00001	0.02906 ± 0.00001	0.01079 ± 0.00000
3	0.28889 ± 0.00007	0.20372 ± 0.00003	0.14432 ± 0.00002	0.10956 ± 0.00002	0.06967 ± 0.00001	0.03829 ± 0.00001
4	0.30164 ± 0.00008	0.33838 ± 0.00004	0.29872 ± 0.00003	0.26285 ± 0.00002	0.20688 ± 0.00001	0.15402 ± 0.00002
5	0.09599 ± 0.00004	0.17936 ± 0.00003	0.21966 ± 0.00003	0.22150 ± 0.00002	0.21242 ± 0.00001	0.19088 ± 0.00002
6	0.02778 ± 0.00002	0.08100 ± 0.00002	0.12910 ± 0.00002	0.15260 ± 0.00002	0.16900 ± 0.00001	0.17361 ± 0.00002
7	0.01039 ± 0.00001	0.05855 ± 0.00002	0.12611 ± 0.00002	0.19707 ± 0.00002	0.31297 ± 0.00002	0.43240 ± 0.00003
2011 Down						
1	0.00000 ± 0.00000	0.00000 ± 0.00000	0.00000 ± 0.00000	0.00000 ± 0.00000	0.00000 ± 0.00000	0.00000 ± 0.00000
2	0.27727 ± 0.00006	0.14165 ± 0.00002	0.08441 ± 0.00002	0.05849 ± 0.00001	0.03015 ± 0.00000	0.01142 ± 0.00000
3	0.29149 ± 0.00006	0.20639 ± 0.00003	0.14706 ± 0.00002	0.11334 ± 0.00001	0.07222 ± 0.00001	0.04027 ± 0.00001
4	0.30012 ± 0.00006	0.33970 ± 0.00003	0.30229 ± 0.00003	0.26563 ± 0.00002	0.21063 ± 0.00001	0.15586 ± 0.00002
5	0.09423 ± 0.00004	0.17702 ± 0.00002	0.21739 ± 0.00003	0.21963 ± 0.00002	0.21187 ± 0.00001	0.19097 ± 0.00002
6	0.02690 ± 0.00002	0.07853 ± 0.00002	0.12608 ± 0.00002	0.15063 ± 0.00002	0.16797 ± 0.00001	0.17419 ± 0.00002
7	0.00999 ± 0.00001	0.05672 ± 0.00001	0.12277 ± 0.00002	0.19229 ± 0.00002	0.30717 ± 0.00001	0.42729 ± 0.00002
2012 Up						
1	0.00000 ± 0.00000	0.00000 ± 0.00000	0.00000 ± 0.00000	0.00000 ± 0.00000	0.00000 ± 0.00000	0.00000 ± 0.00000
2	0.33189 ± 0.00004	0.17070 ± 0.00001	0.10374 ± 0.00001	0.07238 ± 0.00001	0.03899 ± 0.00000	0.01557 ± 0.00000
3	0.28413 ± 0.00003	0.21204 ± 0.00002	0.15587 ± 0.00001	0.12193 ± 0.00001	0.08138 ± 0.00001	0.04761 ± 0.00001
4	0.27241 ± 0.00003	0.33057 ± 0.00002	0.30250 ± 0.00002	0.27216 ± 0.00001	0.22308 ± 0.00001	0.17152 ± 0.00001
5	0.08079 ± 0.00002	0.16549 ± 0.00001	0.20997 ± 0.00002	0.21538 ± 0.00001	0.21325 ± 0.00001	0.19828 ± 0.00001
6	0.02255 ± 0.00001	0.07125 ± 0.00001	0.11766 ± 0.00001	0.14294 ± 0.00001	0.16192 ± 0.00001	0.17213 ± 0.00001
7	0.00823 ± 0.00001	0.04994 ± 0.00001	0.11026 ± 0.00001	0.17521 ± 0.00001	0.28138 ± 0.00001	0.39490 ± 0.00002
2012 Down						
1	0.00000 ± 0.00000	0.00000 ± 0.00000	0.00000 ± 0.00000	0.00000 ± 0.00000	0.00000 ± 0.00000	0.00000 ± 0.00000
2	0.33103 ± 0.00004	0.16968 ± 0.00001	0.10319 ± 0.00001	0.07197 ± 0.00001	0.03846 ± 0.00000	0.01481 ± 0.00000
3	0.28470 ± 0.00003	0.21164 ± 0.00002	0.15482 ± 0.00001	0.12180 ± 0.00001	0.08084 ± 0.00001	0.04680 ± 0.00001
4	0.27219 ± 0.00003	0.33107 ± 0.00002	0.30198 ± 0.00002	0.27063 ± 0.00001	0.22190 ± 0.00001	0.16988 ± 0.00001
5	0.08114 ± 0.00002	0.16598 ± 0.00001	0.21051 ± 0.00002	0.21573 ± 0.00001	0.21327 ± 0.00001	0.19771 ± 0.00001
6	0.02270 ± 0.00001	0.07164 ± 0.00001	0.11852 ± 0.00001	0.14327 ± 0.00001	0.16260 ± 0.00001	0.17139 ± 0.00001
7	0.00824 ± 0.00001	0.04998 ± 0.00001	0.11099 ± 0.00001	0.17661 ± 0.00001	0.28293 ± 0.00001	0.39941 ± 0.00002

A.2 Weights for the determination of $A_{\rm D}(K^-)$

Table A.2: *Values of the $f_{i,j}$ coefficients for 2011 Up $B^+ \to J/\psi K^+$ decays. K_j stands for the $j-$th momentum bin as defined in Tab. 5.19.*

Bin	K_1	K_2	K_3	K_4	K_5	K_6
A	0.5217 ± 0.0023	0.3900 ± 0.0020	0.0785 ± 0.0009	0.0099 ± 0.0003	0.0000 ± 0.0000	0.0000 ± 0.0000
B	0.3388 ± 0.0024	0.3469 ± 0.0024	0.1776 ± 0.0017	0.1367 ± 0.0016	0.0000 ± 0.0002	0.0000 ± 0.0000
C	0.2449 ± 0.0017	0.3230 ± 0.0020	0.1684 ± 0.0014	0.2128 ± 0.0016	0.0508 ± 0.0009	0.0000 ± 0.0000
D	0.2220 ± 0.0013	0.2771 ± 0.0015	0.1706 ± 0.0012	0.1787 ± 0.0012	0.1516 ± 0.0012	0.0000 ± 0.0000
E	0.1807 ± 0.0011	0.2465 ± 0.0012	0.1352 ± 0.0009	0.2020 ± 0.0011	0.2360 ± 0.0013	0.0004 ± 0.0000
F	0.1250 ± 0.0005	0.1602 ± 0.0005	0.1140 ± 0.0004	0.1647 ± 0.0005	0.3621 ± 0.0008	0.0739 ± 0.0004
G	0.0613 ± 0.0004	0.1038 ± 0.0004	0.0792 ± 0.0004	0.1237 ± 0.0005	0.3642 ± 0.0008	0.2679 ± 0.0008
0	0.4353 ± 0.0012	0.3927 ± 0.0011	0.1041 ± 0.0006	0.0664 ± 0.0005	0.0015 ± 0.0001	0.0000 ± 0.0000
1	0.2697 ± 0.0011	0.3477 ± 0.0013	0.1547 ± 0.0008	0.1618 ± 0.0009	0.0660 ± 0.0006	0.0000 ± 0.0000
2	0.2317 ± 0.0008	0.2798 ± 0.0009	0.1531 ± 0.0007	0.1600 ± 0.0007	0.1754 ± 0.0007	0.0000 ± 0.0000
3	0.1868 ± 0.0006	0.2364 ± 0.0007	0.1490 ± 0.0006	0.1657 ± 0.0006	0.2614 ± 0.0008	0.0008 ± 0.0001
4	0.1636 ± 0.0005	0.2041 ± 0.0006	0.1241 ± 0.0005	0.1661 ± 0.0005	0.3047 ± 0.0008	0.0375 ± 0.0003
5	0.1113 ± 0.0003	0.1444 ± 0.0003	0.1067 ± 0.0003	0.1503 ± 0.0003	0.2966 ± 0.0004	0.1908 ± 0.0004
6	0.0553 ± 0.0002	0.1171 ± 0.0003	0.0850 ± 0.0003	0.1368 ± 0.0004	0.3335 ± 0.0006	0.2723 ± 0.0005
7	0.3053 ± 0.0009	0.3560 ± 0.0010	0.1472 ± 0.0006	0.1366 ± 0.0006	0.0549 ± 0.0004	0.0000 ± 0.0000
8	0.2069 ± 0.0009	0.2608 ± 0.0010	0.1391 ± 0.0007	0.1813 ± 0.0008	0.2120 ± 0.0009	0.0000 ± 0.0000
9	0.1722 ± 0.0007	0.2086 ± 0.0007	0.1240 ± 0.0005	0.1624 ± 0.0006	0.3277 ± 0.0009	0.0051 ± 0.0001
10	0.1404 ± 0.0005	0.1810 ± 0.0006	0.1038 ± 0.0004	0.1410 ± 0.0005	0.3397 ± 0.0008	0.0941 ± 0.0004
11	0.1272 ± 0.0005	0.1532 ± 0.0005	0.0860 ± 0.0004	0.1186 ± 0.0005	0.3248 ± 0.0008	0.1903 ± 0.0006
12	0.1026 ± 0.0003	0.1384 ± 0.0003	0.0877 ± 0.0003	0.1211 ± 0.0003	0.2969 ± 0.0005	0.2532 ± 0.0005
13	0.0686 ± 0.0004	0.1392 ± 0.0005	0.0942 ± 0.0004	0.1450 ± 0.0005	0.3043 ± 0.0008	0.2486 ± 0.0007
14	0.2226 ± 0.0012	0.3067 ± 0.0014	0.1902 ± 0.0011	0.1587 ± 0.0010	0.1216 ± 0.0009	0.0000 ± 0.0000
15	0.1506 ± 0.0011	0.2138 ± 0.0013	0.1188 ± 0.0010	0.1751 ± 0.0011	0.3354 ± 0.0016	0.0063 ± 0.0003
16	0.1194 ± 0.0008	0.1613 ± 0.0010	0.1213 ± 0.0008	0.1562 ± 0.0009	0.3439 ± 0.0014	0.0978 ± 0.0007
17	0.0923 ± 0.0007	0.1360 ± 0.0009	0.1022 ± 0.0008	0.1406 ± 0.0009	0.2971 ± 0.0013	0.2319 ± 0.0011
18	0.1098 ± 0.0008	0.1234 ± 0.0009	0.0886 ± 0.0007	0.1201 ± 0.0008	0.2917 ± 0.0013	0.2664 ± 0.0012
19	0.0867 ± 0.0005	0.1245 ± 0.0006	0.0734 ± 0.0005	0.1143 ± 0.0006	0.3148 ± 0.0010	0.2863 ± 0.0009
20	0.0561 ± 0.0006	0.1254 ± 0.0010	0.0918 ± 0.0008	0.1145 ± 0.0009	0.3299 ± 0.0015	0.2823 ± 0.0014
21	0.1860 ± 0.0011	0.2828 ± 0.0014	0.1599 ± 0.0010	0.1877 ± 0.0011	0.1831 ± 0.0011	0.0006 ± 0.0001
22	0.1356 ± 0.0012	0.1767 ± 0.0014	0.1251 ± 0.0011	0.1892 ± 0.0014	0.3101 ± 0.0018	0.0634 ± 0.0008
23	0.1033 ± 0.0009	0.1316 ± 0.0010	0.0900 ± 0.0008	0.1495 ± 0.0011	0.3554 ± 0.0016	0.1702 ± 0.0011
24	0.1124 ± 0.0009	0.1236 ± 0.0009	0.0889 ± 0.0008	0.1407 ± 0.0010	0.2802 ± 0.0014	0.2542 ± 0.0014
25	0.1069 ± 0.0010	0.1394 ± 0.0011	0.0605 ± 0.0007	0.1206 ± 0.0010	0.3445 ± 0.0017	0.2281 ± 0.0014
26	0.0809 ± 0.0006	0.1024 ± 0.0007	0.0605 ± 0.0005	0.1194 ± 0.0007	0.3502 ± 0.0013	0.2866 ± 0.0011
27	0.0334 ± 0.0007	0.1167 ± 0.0012	0.1000 ± 0.0011	0.1459 ± 0.0013	0.2928 ± 0.0019	0.3112 ± 0.0019
28	0.1492 ± 0.0011	0.2658 ± 0.0014	0.1554 ± 0.0011	0.2018 ± 0.0013	0.2163 ± 0.0013	0.0115 ± 0.0003
29	0.0917 ± 0.0010	0.1618 ± 0.0014	0.0891 ± 0.0010	0.1634 ± 0.0014	0.3639 ± 0.0020	0.1301 ± 0.0012
30	0.0896 ± 0.0009	0.1176 ± 0.0011	0.0822 ± 0.0009	0.1378 ± 0.0011	0.3251 ± 0.0017	0.2476 ± 0.0015
31	0.0884 ± 0.0013	0.1196 ± 0.0015	0.0830 ± 0.0013	0.1227 ± 0.0015	0.3308 ± 0.0024	0.2554 ± 0.0021
32	0.0596 ± 0.0009	0.1125 ± 0.0012	0.0766 ± 0.0010	0.1265 ± 0.0013	0.3646 ± 0.0021	0.2603 ± 0.0018
33	0.0555 ± 0.0007	0.1185 ± 0.0010	0.0613 ± 0.0007	0.1176 ± 0.0010	0.3012 ± 0.0016	0.3458 ± 0.0016
34	0.0495 ± 0.0010	0.1172 ± 0.0015	0.0849 ± 0.0012	0.1560 ± 0.0016	0.3050 ± 0.0023	0.2875 ± 0.0022
35	0.1248 ± 0.0011	0.2240 ± 0.0014	0.1896 ± 0.0013	0.1696 ± 0.0012	0.2600 ± 0.0015	0.0321 ± 0.0005
36	0.1011 ± 0.0012	0.1216 ± 0.0013	0.1019 ± 0.0012	0.1453 ± 0.0014	0.3406 ± 0.0022	0.1895 ± 0.0016
37	0.1086 ± 0.0014	0.1502 ± 0.0016	0.0866 ± 0.0012	0.1294 ± 0.0015	0.2738 ± 0.0022	0.2513 ± 0.0021
38	0.0711 ± 0.0012	0.1047 ± 0.0014	0.1115 ± 0.0015	0.1596 ± 0.0018	0.2801 ± 0.0024	0.2730 ± 0.0023
39	0.1071 ± 0.0016	0.1348 ± 0.0017	0.0487 ± 0.0010	0.1174 ± 0.0016	0.3595 ± 0.0028	0.2324 ± 0.0022
40	0.0585 ± 0.0009	0.0918 ± 0.0011	0.0737 ± 0.0010	0.1323 ± 0.0013	0.3483 ± 0.0021	0.2954 ± 0.0019
41	0.0210 ± 0.0010	0.1799 ± 0.0024	0.0327 ± 0.0010	0.1290 ± 0.0020	0.3551 ± 0.0033	0.2823 ± 0.0029
42	0.1081 ± 0.0008	0.2089 ± 0.0010	0.1303 ± 0.0008	0.1873 ± 0.0010	0.2971 ± 0.0012	0.0683 ± 0.0006
43	0.0927 ± 0.0010	0.1068 ± 0.0011	0.0761 ± 0.0009	0.1237 ± 0.0011	0.3148 ± 0.0018	0.2860 ± 0.0018
44	0.0658 ± 0.0009	0.1364 ± 0.0012	0.0697 ± 0.0009	0.1242 ± 0.0012	0.3279 ± 0.0019	0.2760 ± 0.0018
45	0.0548 ± 0.0009	0.0984 ± 0.0012	0.0678 ± 0.0010	0.1536 ± 0.0016	0.3226 ± 0.0022	0.3028 ± 0.0022
46	0.0229 ± 0.0008	0.1303 ± 0.0016	0.1197 ± 0.0015	0.1293 ± 0.0016	0.3328 ± 0.0026	0.2650 ± 0.0023
47	0.0422 ± 0.0008	0.0986 ± 0.0011	0.0570 ± 0.0008	0.1265 ± 0.0012	0.3388 ± 0.0020	0.3370 ± 0.0020
48	0.0605 ± 0.0014	0.0955 ± 0.0018	0.0592 ± 0.0013	0.1168 ± 0.0018	0.3077 ± 0.0029	0.3602 ± 0.0031
49	0.0855 ± 0.0007	0.1631 ± 0.0009	0.1162 ± 0.0007	0.1790 ± 0.0009	0.3271 ± 0.0013	0.1290 ± 0.0008
50	0.1190 ± 0.0015	0.1163 ± 0.0015	0.0746 ± 0.0012	0.1339 ± 0.0016	0.2856 ± 0.0023	0.2706 ± 0.0022
51	0.0510 ± 0.0013	0.1246 ± 0.0018	0.0829 ± 0.0015	0.1849 ± 0.0022	0.2772 ± 0.0026	0.2794 ± 0.0026
52	0.0925 ± 0.0017	0.1317 ± 0.0020	0.0998 ± 0.0018	0.1134 ± 0.0019	0.2627 ± 0.0028	0.2999 ± 0.0030
53	0.0331 ± 0.0013	0.0828 ± 0.0018	0.1147 ± 0.0023	0.1547 ± 0.0025	0.3300 ± 0.0037	0.2847 ± 0.0034
54	0.0723 ± 0.0013	0.1038 ± 0.0015	0.0318 ± 0.0008	0.1421 ± 0.0018	0.3435 ± 0.0027	0.3066 ± 0.0026
55	0.0081 ± 0.0012	0.0435 ± 0.0020	0.1134 ± 0.0030	0.1553 ± 0.0033	0.2716 ± 0.0042	0.4082 ± 0.0053

Table A.3: *Values of the $f_{i,j}$ coefficients for 2011 Down $B^+ \to J/\psi K^+$ decays. K_j stands for the $j-th$ momentum bin as defined in Tab. 5.19.*

Bin	K_1	K_2	K_3	K_4	K_5	K_6
A	0.5224 ± 0.0019	0.3849 ± 0.0017	0.0825 ± 0.0008	0.0102 ± 0.0003	0.0000 ± 0.0000	0.0000 ± 0.0000
B	0.3221 ± 0.0019	0.3815 ± 0.0021	0.1879 ± 0.0015	0.1073 ± 0.0012	0.0012 ± 0.0002	0.0000 ± 0.0000
C	0.2538 ± 0.0015	0.3277 ± 0.0017	0.1725 ± 0.0012	0.1957 ± 0.0013	0.0503 ± 0.0007	0.0000 ± 0.0000
D	0.1997 ± 0.0011	0.2556 ± 0.0012	0.1743 ± 0.0010	0.2115 ± 0.0011	0.1589 ± 0.0010	0.0000 ± 0.0000
E	0.1791 ± 0.0009	0.2205 ± 0.0010	0.1489 ± 0.0008	0.1983 ± 0.0009	0.2538 ± 0.0012	0.0006 ± 0.0000
F	0.1246 ± 0.0004	0.1533 ± 0.0004	0.1117 ± 0.0004	0.1637 ± 0.0004	0.3607 ± 0.0007	0.0860 ± 0.0004
G	0.0627 ± 0.0003	0.1003 ± 0.0004	0.0736 ± 0.0003	0.1254 ± 0.0004	0.3513 ± 0.0007	0.2867 ± 0.0007
0	0.4317 ± 0.0010	0.3988 ± 0.0010	0.1057 ± 0.0005	0.0619 ± 0.0004	0.0018 ± 0.0001	0.0000 ± 0.0000
1	0.2656 ± 0.0009	0.3355 ± 0.0010	0.1601 ± 0.0007	0.1746 ± 0.0008	0.0642 ± 0.0005	0.0000 ± 0.0000
2	0.2314 ± 0.0007	0.2903 ± 0.0008	0.1499 ± 0.0006	0.1765 ± 0.0006	0.1519 ± 0.0006	0.0000 ± 0.0000
3	0.1952 ± 0.0005	0.2376 ± 0.0006	0.1421 ± 0.0005	0.1633 ± 0.0005	0.2615 ± 0.0007	0.0002 ± 0.0000
4	0.1546 ± 0.0004	0.2026 ± 0.0005	0.1182 ± 0.0004	0.1627 ± 0.0004	0.3262 ± 0.0006	0.0357 ± 0.0002
5	0.1081 ± 0.0002	0.1471 ± 0.0002	0.1014 ± 0.0002	0.1520 ± 0.0003	0.3053 ± 0.0004	0.1861 ± 0.0003
6	0.0542 ± 0.0002	0.1113 ± 0.0003	0.0876 ± 0.0002	0.1316 ± 0.0003	0.3484 ± 0.0005	0.2670 ± 0.0004
7	0.3070 ± 0.0008	0.3523 ± 0.0008	0.1505 ± 0.0005	0.1357 ± 0.0005	0.0544 ± 0.0003	0.0000 ± 0.0000
8	0.2004 ± 0.0007	0.2433 ± 0.0008	0.1438 ± 0.0006	0.1879 ± 0.0007	0.2246 ± 0.0007	0.0000 ± 0.0000
9	0.1816 ± 0.0006	0.2150 ± 0.0006	0.1214 ± 0.0005	0.1630 ± 0.0005	0.3089 ± 0.0007	0.0101 ± 0.0001
10	0.1520 ± 0.0005	0.1741 ± 0.0005	0.1036 ± 0.0004	0.1486 ± 0.0004	0.3429 ± 0.0007	0.0787 ± 0.0003
11	0.1202 ± 0.0004	0.1485 ± 0.0004	0.0931 ± 0.0003	0.1337 ± 0.0004	0.3080 ± 0.0006	0.1965 ± 0.0005
12	0.0970 ± 0.0002	0.1396 ± 0.0003	0.0996 ± 0.0002	0.1225 ± 0.0003	0.2856 ± 0.0004	0.2556 ± 0.0004
13	0.0651 ± 0.0003	0.1460 ± 0.0004	0.0830 ± 0.0003	0.1213 ± 0.0004	0.3206 ± 0.0006	0.2640 ± 0.0006
14	0.2162 ± 0.0009	0.3077 ± 0.0011	0.1723 ± 0.0008	0.1659 ± 0.0008	0.1379 ± 0.0007	0.0000 ± 0.0000
15	0.1639 ± 0.0010	0.2011 ± 0.0011	0.1253 ± 0.0008	0.1813 ± 0.0010	0.3192 ± 0.0014	0.0092 ± 0.0002
16	0.1325 ± 0.0008	0.1550 ± 0.0008	0.1111 ± 0.0007	0.1535 ± 0.0008	0.3442 ± 0.0012	0.1036 ± 0.0007
17	0.1146 ± 0.0007	0.1382 ± 0.0007	0.0852 ± 0.0006	0.1314 ± 0.0007	0.3256 ± 0.0011	0.2050 ± 0.0009
18	0.1216 ± 0.0007	0.1312 ± 0.0007	0.0727 ± 0.0005	0.1028 ± 0.0006	0.3094 ± 0.0011	0.2623 ± 0.0010
19	0.0751 ± 0.0004	0.1335 ± 0.0006	0.0856 ± 0.0004	0.1009 ± 0.0005	0.3204 ± 0.0009	0.2845 ± 0.0008
20	0.0602 ± 0.0006	0.1049 ± 0.0007	0.0911 ± 0.0007	0.1256 ± 0.0008	0.3056 ± 0.0012	0.3125 ± 0.0013
21	0.1753 ± 0.0009	0.2710 ± 0.0011	0.1739 ± 0.0009	0.1916 ± 0.0009	0.1882 ± 0.0009	0.0000 ± 0.0000
22	0.1092 ± 0.0008	0.1729 ± 0.0010	0.1273 ± 0.0009	0.1561 ± 0.0010	0.3699 ± 0.0015	0.0646 ± 0.0006
23	0.1303 ± 0.0009	0.1389 ± 0.0009	0.0974 ± 0.0008	0.1663 ± 0.0010	0.2996 ± 0.0013	0.1676 ± 0.0010
24	0.1089 ± 0.0008	0.1240 ± 0.0008	0.0715 ± 0.0006	0.1228 ± 0.0008	0.3161 ± 0.0013	0.2567 ± 0.0012
25	0.0788 ± 0.0007	0.1187 ± 0.0009	0.0989 ± 0.0008	0.1339 ± 0.0009	0.3060 ± 0.0014	0.2637 ± 0.0013
26	0.0870 ± 0.0006	0.1321 ± 0.0007	0.0768 ± 0.0005	0.1258 ± 0.0007	0.3053 ± 0.0011	0.2730 ± 0.0010
27	0.0465 ± 0.0007	0.1092 ± 0.0010	0.0961 ± 0.0009	0.1396 ± 0.0011	0.3139 ± 0.0017	0.2947 ± 0.0016
28	0.1522 ± 0.0009	0.2676 ± 0.0012	0.1655 ± 0.0009	0.1798 ± 0.0010	0.2241 ± 0.0011	0.0107 ± 0.0002
29	0.0968 ± 0.0009	0.1557 ± 0.0012	0.1185 ± 0.0010	0.1460 ± 0.0011	0.3465 ± 0.0017	0.1364 ± 0.0011
30	0.0818 ± 0.0007	0.1217 ± 0.0009	0.0889 ± 0.0008	0.1169 ± 0.0009	0.3527 ± 0.0015	0.2380 ± 0.0013
31	0.1029 ± 0.0009	0.1272 ± 0.0010	0.0601 ± 0.0007	0.1168 ± 0.0010	0.3198 ± 0.0016	0.2732 ± 0.0014
32	0.0591 ± 0.0008	0.1046 ± 0.0010	0.0895 ± 0.0009	0.1086 ± 0.0010	0.3385 ± 0.0018	0.2997 ± 0.0017
33	0.0734 ± 0.0007	0.1203 ± 0.0008	0.0638 ± 0.0006	0.1186 ± 0.0008	0.3274 ± 0.0014	0.2965 ± 0.0013
34	0.0432 ± 0.0008	0.1212 ± 0.0013	0.0953 ± 0.0011	0.0914 ± 0.0011	0.3440 ± 0.0021	0.3049 ± 0.0020
35	0.1624 ± 0.0010	0.2422 ± 0.0012	0.1202 ± 0.0009	0.1919 ± 0.0011	0.2433 ± 0.0012	0.0401 ± 0.0005
36	0.0969 ± 0.0010	0.1286 ± 0.0012	0.0970 ± 0.0010	0.1474 ± 0.0012	0.3106 ± 0.0018	0.2195 ± 0.0015
37	0.0747 ± 0.0009	0.1411 ± 0.0012	0.1029 ± 0.0010	0.1279 ± 0.0012	0.2805 ± 0.0017	0.2729 ± 0.0017
38	0.0726 ± 0.0010	0.1295 ± 0.0013	0.0669 ± 0.0010	0.1428 ± 0.0014	0.2851 ± 0.0019	0.3031 ± 0.0020
39	0.0728 ± 0.0010	0.1208 ± 0.0013	0.0680 ± 0.0010	0.1188 ± 0.0013	0.3389 ± 0.0022	0.2807 ± 0.0020
40	0.0623 ± 0.0008	0.1210 ± 0.0011	0.0732 ± 0.0009	0.1244 ± 0.0011	0.3037 ± 0.0017	0.3154 ± 0.0018
41	0.0231 ± 0.0009	0.0960 ± 0.0015	0.1097 ± 0.0015	0.1083 ± 0.0015	0.2861 ± 0.0024	0.3768 ± 0.0028
42	0.1018 ± 0.0006	0.2111 ± 0.0009	0.1382 ± 0.0007	0.1837 ± 0.0008	0.2866 ± 0.0010	0.0786 ± 0.0005
43	0.0794 ± 0.0009	0.1385 ± 0.0011	0.1183 ± 0.0010	0.1291 ± 0.0011	0.3054 ± 0.0017	0.2293 ± 0.0015
44	0.0920 ± 0.0009	0.0919 ± 0.0009	0.0776 ± 0.0008	0.1493 ± 0.0011	0.3274 ± 0.0017	0.2619 ± 0.0015
45	0.0547 ± 0.0008	0.0912 ± 0.0010	0.0781 ± 0.0009	0.1507 ± 0.0013	0.3441 ± 0.0019	0.2812 ± 0.0018
46	0.0928 ± 0.0011	0.1069 ± 0.0012	0.0843 ± 0.0011	0.1442 ± 0.0014	0.2962 ± 0.0020	0.2756 ± 0.0020
47	0.0505 ± 0.0007	0.1045 ± 0.0010	0.0663 ± 0.0008	0.1267 ± 0.0011	0.3329 ± 0.0017	0.3191 ± 0.0016
48	0.0719 ± 0.0013	0.0988 ± 0.0015	0.0794 ± 0.0014	0.1170 ± 0.0016	0.3447 ± 0.0027	0.2881 ± 0.0025
49	0.0959 ± 0.0006	0.1671 ± 0.0008	0.1097 ± 0.0006	0.1637 ± 0.0008	0.3364 ± 0.0011	0.1273 ± 0.0007
50	0.0880 ± 0.0011	0.1342 ± 0.0014	0.0907 ± 0.0011	0.1357 ± 0.0014	0.3065 ± 0.0020	0.2449 ± 0.0018
51	0.0727 ± 0.0011	0.1095 ± 0.0013	0.0969 ± 0.0012	0.1185 ± 0.0014	0.3236 ± 0.0023	0.2788 ± 0.0021
52	0.0856 ± 0.0014	0.1216 ± 0.0016	0.0996 ± 0.0015	0.1560 ± 0.0019	0.2539 ± 0.0024	0.2834 ± 0.0025
53	0.0792 ± 0.0013	0.0567 ± 0.0011	0.0737 ± 0.0013	0.1055 ± 0.0016	0.2892 ± 0.0025	0.3956 ± 0.0030
54	0.0615 ± 0.0011	0.1067 ± 0.0014	0.0694 ± 0.0011	0.1243 ± 0.0015	0.3288 ± 0.0025	0.3093 ± 0.0024
55	0.0227 ± 0.0012	0.0414 ± 0.0013	0.0931 ± 0.0020	0.1530 ± 0.0025	0.3386 ± 0.0037	0.3512 ± 0.0038

Table A.4: *Values of the $f_{i,j}$ coefficients for 2012 Up $B^+ \to J/\psi K^+$ decays. K_j stands for the $j-th$ momentum bin as defined in Tab. 5.19.*

Bin	K_1	K_2	K_3	K_4	K_5	K_6
A	0.5284 ± 0.0014	0.3851 ± 0.0011	0.0782 ± 0.0005	0.0082 ± 0.0002	0.0000 ± 0.0000	0.0000 ± 0.0000
B	0.3331 ± 0.0015	0.3754 ± 0.0015	0.1863 ± 0.0011	0.1040 ± 0.0008	0.0012 ± 0.0001	0.0000 ± 0.0000
C	0.2567 ± 0.0012	0.3482 ± 0.0013	0.1775 ± 0.0009	0.1812 ± 0.0010	0.0364 ± 0.0005	0.0000 ± 0.0000
D	0.2068 ± 0.0009	0.2821 ± 0.0010	0.1749 ± 0.0008	0.2105 ± 0.0009	0.1257 ± 0.0007	0.0000 ± 0.0000
E	0.1611 ± 0.0007	0.2316 ± 0.0008	0.1467 ± 0.0006	0.2023 ± 0.0007	0.2583 ± 0.0008	0.0002 ± 0.0000
F	0.1142 ± 0.0003	0.1686 ± 0.0004	0.1201 ± 0.0003	0.1731 ± 0.0004	0.3560 ± 0.0005	0.0680 ± 0.0003
G	0.0514 ± 0.0002	0.0994 ± 0.0003	0.0749 ± 0.0003	0.1217 ± 0.0003	0.3645 ± 0.0006	0.2882 ± 0.0005
0	0.4162 ± 0.0007	0.3998 ± 0.0006	0.1160 ± 0.0003	0.0652 ± 0.0003	0.0028 ± 0.0001	0.0000 ± 0.0000
1	0.2826 ± 0.0007	0.3220 ± 0.0007	0.1515 ± 0.0005	0.1803 ± 0.0005	0.0636 ± 0.0003	0.0000 ± 0.0000
2	0.2268 ± 0.0005	0.2765 ± 0.0005	0.1535 ± 0.0004	0.1717 ± 0.0004	0.1715 ± 0.0004	0.0000 ± 0.0000
3	0.1857 ± 0.0004	0.2392 ± 0.0004	0.1424 ± 0.0003	0.1704 ± 0.0004	0.2612 ± 0.0005	0.0011 ± 0.0000
4	0.1568 ± 0.0003	0.2084 ± 0.0004	0.1307 ± 0.0003	0.1610 ± 0.0003	0.3045 ± 0.0005	0.0386 ± 0.0002
5	0.1084 ± 0.0002	0.1564 ± 0.0002	0.1086 ± 0.0002	0.1498 ± 0.0002	0.3066 ± 0.0003	0.1702 ± 0.0002
6	0.0637 ± 0.0002	0.1124 ± 0.0002	0.0918 ± 0.0002	0.1319 ± 0.0002	0.3457 ± 0.0004	0.2545 ± 0.0003
7	0.2912 ± 0.0005	0.3474 ± 0.0006	0.1610 ± 0.0004	0.1461 ± 0.0004	0.0543 ± 0.0002	0.0000 ± 0.0000
8	0.2069 ± 0.0005	0.2429 ± 0.0005	0.1450 ± 0.0004	0.1805 ± 0.0005	0.2247 ± 0.0005	0.0000 ± 0.0000
9	0.1636 ± 0.0004	0.2081 ± 0.0004	0.1241 ± 0.0003	0.1673 ± 0.0004	0.3271 ± 0.0005	0.0098 ± 0.0001
10	0.1417 ± 0.0003	0.1817 ± 0.0004	0.1095 ± 0.0003	0.1453 ± 0.0003	0.3373 ± 0.0005	0.0845 ± 0.0002
11	0.1207 ± 0.0003	0.1530 ± 0.0003	0.1013 ± 0.0003	0.1327 ± 0.0003	0.3082 ± 0.0004	0.1841 ± 0.0004
12	0.0948 ± 0.0002	0.1402 ± 0.0002	0.0942 ± 0.0002	0.1222 ± 0.0002	0.2986 ± 0.0003	0.2499 ± 0.0003
13	0.0638 ± 0.0002	0.1315 ± 0.0003	0.0933 ± 0.0003	0.1332 ± 0.0003	0.3214 ± 0.0005	0.2568 ± 0.0004
14	0.2065 ± 0.0006	0.2970 ± 0.0008	0.1752 ± 0.0006	0.1894 ± 0.0006	0.1318 ± 0.0005	0.0000 ± 0.0000
15	0.1358 ± 0.0006	0.2016 ± 0.0007	0.1281 ± 0.0006	0.1770 ± 0.0007	0.3479 ± 0.0009	0.0096 ± 0.0002
16	0.1217 ± 0.0005	0.1509 ± 0.0006	0.0994 ± 0.0004	0.1588 ± 0.0006	0.3692 ± 0.0009	0.1000 ± 0.0004
17	0.1008 ± 0.0004	0.1180 ± 0.0005	0.0916 ± 0.0004	0.1479 ± 0.0005	0.3205 ± 0.0008	0.2213 ± 0.0006
18	0.0917 ± 0.0004	0.1262 ± 0.0005	0.0712 ± 0.0004	0.1236 ± 0.0005	0.3187 ± 0.0008	0.2686 ± 0.0007
19	0.0810 ± 0.0003	0.1194 ± 0.0004	0.0783 ± 0.0003	0.1187 ± 0.0004	0.3135 ± 0.0006	0.2892 ± 0.0006
20	0.0609 ± 0.0004	0.1359 ± 0.0006	0.0858 ± 0.0005	0.1312 ± 0.0006	0.3068 ± 0.0009	0.2794 ± 0.0008
21	0.1651 ± 0.0006	0.2756 ± 0.0008	0.1727 ± 0.0006	0.1832 ± 0.0006	0.2019 ± 0.0006	0.0014 ± 0.0001
22	0.1229 ± 0.0006	0.1723 ± 0.0007	0.1177 ± 0.0006	0.1705 ± 0.0007	0.3462 ± 0.0010	0.0703 ± 0.0005
23	0.0941 ± 0.0005	0.1514 ± 0.0006	0.0985 ± 0.0005	0.1388 ± 0.0006	0.3243 ± 0.0009	0.1928 ± 0.0007
24	0.0865 ± 0.0005	0.1312 ± 0.0006	0.0830 ± 0.0005	0.1211 ± 0.0006	0.3200 ± 0.0009	0.2581 ± 0.0008
25	0.0748 ± 0.0005	0.1184 ± 0.0006	0.0804 ± 0.0005	0.1173 ± 0.0006	0.3114 ± 0.0010	0.2977 ± 0.0009
26	0.0658 ± 0.0004	0.1247 ± 0.0005	0.0801 ± 0.0004	0.1183 ± 0.0005	0.3001 ± 0.0007	0.3110 ± 0.0007
27	0.0541 ± 0.0005	0.1518 ± 0.0008	0.0653 ± 0.0005	0.1257 ± 0.0007	0.3086 ± 0.0011	0.2945 ± 0.0011
28	0.1444 ± 0.0006	0.2573 ± 0.0008	0.1545 ± 0.0006	0.1993 ± 0.0007	0.2359 ± 0.0007	0.0085 ± 0.0001
29	0.0971 ± 0.0006	0.1639 ± 0.0008	0.1240 ± 0.0007	0.1483 ± 0.0008	0.3384 ± 0.0012	0.1283 ± 0.0007
30	0.0881 ± 0.0005	0.1153 ± 0.0006	0.0883 ± 0.0005	0.1436 ± 0.0007	0.3116 ± 0.0010	0.2531 ± 0.0009
31	0.0809 ± 0.0006	0.1083 ± 0.0007	0.0875 ± 0.0006	0.1124 ± 0.0007	0.3459 ± 0.0011	0.2650 ± 0.0010
32	0.0697 ± 0.0006	0.1085 ± 0.0007	0.0977 ± 0.0007	0.0938 ± 0.0007	0.3353 ± 0.0012	0.2949 ± 0.0012
33	0.0813 ± 0.0005	0.1068 ± 0.0006	0.0838 ± 0.0005	0.1119 ± 0.0006	0.3157 ± 0.0010	0.3006 ± 0.0009
34	0.0327 ± 0.0006	0.1306 ± 0.0010	0.0953 ± 0.0008	0.1322 ± 0.0010	0.3297 ± 0.0015	0.2795 ± 0.0014
35	0.1291 ± 0.0006	0.2270 ± 0.0008	0.1463 ± 0.0006	0.1818 ± 0.0007	0.2831 ± 0.0009	0.0326 ± 0.0003
36	0.1080 ± 0.0008	0.1428 ± 0.0009	0.1091 ± 0.0008	0.1251 ± 0.0008	0.3156 ± 0.0013	0.1994 ± 0.0010
37	0.0772 ± 0.0006	0.0981 ± 0.0007	0.0833 ± 0.0006	0.1422 ± 0.0008	0.3250 ± 0.0013	0.2741 ± 0.0011
38	0.0739 ± 0.0007	0.1111 ± 0.0008	0.0705 ± 0.0007	0.1291 ± 0.0009	0.3560 ± 0.0015	0.2595 ± 0.0012
39	0.0854 ± 0.0008	0.1085 ± 0.0009	0.0685 ± 0.0007	0.1391 ± 0.0010	0.2984 ± 0.0014	0.3001 ± 0.0014
40	0.0548 ± 0.0005	0.1012 ± 0.0007	0.0970 ± 0.0007	0.1059 ± 0.0007	0.3216 ± 0.0012	0.3194 ± 0.0012
41	0.0464 ± 0.0008	0.1191 ± 0.0012	0.0917 ± 0.0010	0.1075 ± 0.0010	0.3287 ± 0.0018	0.3066 ± 0.0018
42	0.1162 ± 0.0004	0.1982 ± 0.0006	0.1356 ± 0.0005	0.1857 ± 0.0005	0.2933 ± 0.0007	0.0711 ± 0.0003
43	0.0921 ± 0.0006	0.1316 ± 0.0007	0.0950 ± 0.0006	0.1167 ± 0.0006	0.3043 ± 0.0010	0.2603 ± 0.0010
44	0.0858 ± 0.0006	0.1208 ± 0.0007	0.0711 ± 0.0005	0.1341 ± 0.0007	0.3425 ± 0.0012	0.2457 ± 0.0010
45	0.0779 ± 0.0007	0.1148 ± 0.0008	0.0971 ± 0.0007	0.1237 ± 0.0008	0.3117 ± 0.0013	0.2749 ± 0.0012
46	0.0803 ± 0.0008	0.1069 ± 0.0008	0.0688 ± 0.0007	0.1302 ± 0.0009	0.3517 ± 0.0015	0.2621 ± 0.0013
47	0.0575 ± 0.0005	0.1049 ± 0.0007	0.0755 ± 0.0006	0.1264 ± 0.0007	0.3345 ± 0.0012	0.3012 ± 0.0011
48	0.0350 ± 0.0006	0.1084 ± 0.0010	0.0668 ± 0.0008	0.1165 ± 0.0010	0.3484 ± 0.0018	0.3248 ± 0.0017
49	0.0940 ± 0.0004	0.1597 ± 0.0005	0.1221 ± 0.0004	0.1685 ± 0.0005	0.3140 ± 0.0007	0.1418 ± 0.0005
50	0.0788 ± 0.0007	0.1376 ± 0.0009	0.0944 ± 0.0008	0.1423 ± 0.0009	0.2990 ± 0.0014	0.2478 ± 0.0012
51	0.0756 ± 0.0008	0.1222 ± 0.0009	0.0799 ± 0.0008	0.1346 ± 0.0010	0.3316 ± 0.0015	0.2561 ± 0.0013
52	0.0832 ± 0.0009	0.0965 ± 0.0010	0.0770 ± 0.0008	0.1088 ± 0.0010	0.3181 ± 0.0017	0.3165 ± 0.0017
53	0.0588 ± 0.0009	0.1217 ± 0.0012	0.0989 ± 0.0011	0.1091 ± 0.0012	0.3105 ± 0.0020	0.3011 ± 0.0019
54	0.0411 ± 0.0006	0.1156 ± 0.0009	0.0906 ± 0.0008	0.0909 ± 0.0009	0.3370 ± 0.0016	0.3248 ± 0.0016
55	0.0065 ± 0.0006	0.0839 ± 0.0013	0.0697 ± 0.0012	0.1500 ± 0.0017	0.3573 ± 0.0026	0.3327 ± 0.0025

Table A.5: *Values of the $f_{i,j}$ coefficients for 2012 Down $B^+ \to J/\psi K^+$ decays. K_j stands for the $j-th$ momentum bin as defined in Tab. 5.19.*

Bin	K_1	K_2	K_3	K_4	K_5	K_6
A	0.5285 ± 0.0013	0.3838 ± 0.0011	0.0761 ± 0.0005	0.0115 ± 0.0002	0.0000 ± 0.0000	0.0000 ± 0.0000
B	0.3143 ± 0.0014	0.4028 ± 0.0015	0.1818 ± 0.0010	0.1000 ± 0.0008	0.0011 ± 0.0001	0.0000 ± 0.0000
C	0.2527 ± 0.0011	0.3281 ± 0.0012	0.1881 ± 0.0009	0.1941 ± 0.0010	0.0370 ± 0.0004	0.0000 ± 0.0000
D	0.2177 ± 0.0009	0.2635 ± 0.0009	0.1778 ± 0.0008	0.2111 ± 0.0008	0.1299 ± 0.0007	0.0000 ± 0.0000
E	0.1790 ± 0.0007	0.2304 ± 0.0008	0.1555 ± 0.0006	0.1993 ± 0.0007	0.2361 ± 0.0008	0.0003 ± 0.0000
F	0.1175 ± 0.0003	0.1656 ± 0.0004	0.1205 ± 0.0003	0.1689 ± 0.0003	0.3614 ± 0.0005	0.0660 ± 0.0003
G	0.0471 ± 0.0002	0.1001 ± 0.0003	0.0745 ± 0.0002	0.1264 ± 0.0003	0.3700 ± 0.0005	0.2819 ± 0.0005
0	0.4263 ± 0.0007	0.3822 ± 0.0006	0.1215 ± 0.0003	0.0671 ± 0.0003	0.0030 ± 0.0001	0.0000 ± 0.0000
1	0.2756 ± 0.0007	0.3297 ± 0.0007	0.1548 ± 0.0005	0.1723 ± 0.0005	0.0676 ± 0.0003	0.0000 ± 0.0000
2	0.2225 ± 0.0005	0.2841 ± 0.0005	0.1514 ± 0.0004	0.1691 ± 0.0004	0.1729 ± 0.0004	0.0000 ± 0.0000
3	0.1830 ± 0.0004	0.2402 ± 0.0004	0.1464 ± 0.0003	0.1678 ± 0.0004	0.2618 ± 0.0005	0.0008 ± 0.0000
4	0.1507 ± 0.0003	0.2030 ± 0.0004	0.1330 ± 0.0003	0.1666 ± 0.0003	0.3101 ± 0.0005	0.0367 ± 0.0002
5	0.1080 ± 0.0002	0.1570 ± 0.0002	0.1092 ± 0.0002	0.1492 ± 0.0002	0.3008 ± 0.0003	0.1757 ± 0.0002
6	0.0585 ± 0.0002	0.1129 ± 0.0002	0.0853 ± 0.0002	0.1391 ± 0.0002	0.3406 ± 0.0004	0.2637 ± 0.0003
7	0.2883 ± 0.0005	0.3418 ± 0.0005	0.1638 ± 0.0004	0.1494 ± 0.0004	0.0568 ± 0.0002	0.0000 ± 0.0000
8	0.2005 ± 0.0005	0.2361 ± 0.0005	0.1392 ± 0.0004	0.1895 ± 0.0005	0.2346 ± 0.0005	0.0000 ± 0.0000
9	0.1702 ± 0.0004	0.2084 ± 0.0004	0.1223 ± 0.0003	0.1621 ± 0.0004	0.3277 ± 0.0005	0.0093 ± 0.0001
10	0.1436 ± 0.0003	0.1798 ± 0.0004	0.1138 ± 0.0003	0.1426 ± 0.0003	0.3433 ± 0.0005	0.0770 ± 0.0002
11	0.1148 ± 0.0003	0.1561 ± 0.0003	0.0926 ± 0.0002	0.1329 ± 0.0003	0.3176 ± 0.0004	0.1860 ± 0.0003
12	0.0945 ± 0.0002	0.1455 ± 0.0002	0.0872 ± 0.0002	0.1247 ± 0.0002	0.2969 ± 0.0003	0.2512 ± 0.0003
13	0.0609 ± 0.0002	0.1381 ± 0.0003	0.0950 ± 0.0003	0.1351 ± 0.0003	0.3164 ± 0.0005	0.2544 ± 0.0004
14	0.1986 ± 0.0006	0.3080 ± 0.0007	0.1717 ± 0.0006	0.1807 ± 0.0006	0.1410 ± 0.0005	0.0000 ± 0.0000
15	0.1395 ± 0.0006	0.1805 ± 0.0007	0.1287 ± 0.0006	0.1904 ± 0.0007	0.3508 ± 0.0009	0.0101 ± 0.0002
16	0.1123 ± 0.0005	0.1516 ± 0.0005	0.1070 ± 0.0004	0.1496 ± 0.0005	0.3730 ± 0.0008	0.1065 ± 0.0005
17	0.1088 ± 0.0004	0.1350 ± 0.0005	0.0863 ± 0.0004	0.1328 ± 0.0005	0.3301 ± 0.0008	0.2069 ± 0.0006
18	0.0849 ± 0.0004	0.1163 ± 0.0005	0.0766 ± 0.0004	0.1259 ± 0.0005	0.3231 ± 0.0008	0.2731 ± 0.0007
19	0.0765 ± 0.0003	0.1198 ± 0.0004	0.0858 ± 0.0003	0.1245 ± 0.0004	0.3093 ± 0.0006	0.2841 ± 0.0006
20	0.0558 ± 0.0004	0.1259 ± 0.0006	0.0858 ± 0.0005	0.1414 ± 0.0006	0.3204 ± 0.0009	0.2708 ± 0.0008
21	0.1692 ± 0.0006	0.2717 ± 0.0007	0.1675 ± 0.0006	0.1922 ± 0.0006	0.1979 ± 0.0006	0.0016 ± 0.0001
22	0.1117 ± 0.0006	0.1728 ± 0.0007	0.1180 ± 0.0006	0.1665 ± 0.0007	0.3559 ± 0.0010	0.0751 ± 0.0005
23	0.0993 ± 0.0005	0.1293 ± 0.0006	0.0994 ± 0.0005	0.1558 ± 0.0006	0.3421 ± 0.0009	0.1741 ± 0.0007
24	0.0916 ± 0.0005	0.1277 ± 0.0006	0.0896 ± 0.0005	0.1359 ± 0.0006	0.2958 ± 0.0009	0.2594 ± 0.0008
25	0.0695 ± 0.0004	0.1254 ± 0.0006	0.0887 ± 0.0005	0.1223 ± 0.0006	0.3159 ± 0.0009	0.2782 ± 0.0009
26	0.0695 ± 0.0004	0.1209 ± 0.0005	0.0852 ± 0.0004	0.1151 ± 0.0004	0.3242 ± 0.0007	0.2851 ± 0.0007
27	0.0475 ± 0.0005	0.1144 ± 0.0007	0.0829 ± 0.0006	0.1273 ± 0.0007	0.3399 ± 0.0012	0.2881 ± 0.0011
28	0.1420 ± 0.0006	0.2484 ± 0.0007	0.1647 ± 0.0006	0.1858 ± 0.0006	0.2503 ± 0.0007	0.0088 ± 0.0001
29	0.1066 ± 0.0006	0.1465 ± 0.0007	0.0957 ± 0.0006	0.1622 ± 0.0008	0.3471 ± 0.0011	0.1419 ± 0.0007
30	0.0838 ± 0.0005	0.1289 ± 0.0006	0.0729 ± 0.0005	0.1421 ± 0.0007	0.3200 ± 0.0010	0.2524 ± 0.0009
31	0.0700 ± 0.0005	0.1204 ± 0.0007	0.0851 ± 0.0006	0.1313 ± 0.0007	0.3177 ± 0.0011	0.2754 ± 0.0010
32	0.0720 ± 0.0006	0.0977 ± 0.0007	0.0868 ± 0.0007	0.1350 ± 0.0008	0.3020 ± 0.0012	0.3065 ± 0.0012
33	0.0728 ± 0.0005	0.1199 ± 0.0006	0.0792 ± 0.0005	0.1169 ± 0.0006	0.3154 ± 0.0010	0.2958 ± 0.0009
34	0.0462 ± 0.0006	0.1209 ± 0.0009	0.0909 ± 0.0008	0.1410 ± 0.0010	0.2901 ± 0.0014	0.3109 ± 0.0014
35	0.1173 ± 0.0006	0.2537 ± 0.0008	0.1600 ± 0.0007	0.1880 ± 0.0007	0.2505 ± 0.0008	0.0304 ± 0.0003
36	0.0968 ± 0.0007	0.1421 ± 0.0008	0.0960 ± 0.0007	0.1381 ± 0.0008	0.3287 ± 0.0012	0.1984 ± 0.0010
37	0.0800 ± 0.0007	0.1035 ± 0.0008	0.1231 ± 0.0008	0.1514 ± 0.0009	0.2928 ± 0.0013	0.2492 ± 0.0012
38	0.0850 ± 0.0008	0.0909 ± 0.0008	0.0987 ± 0.0008	0.1323 ± 0.0009	0.3297 ± 0.0014	0.2635 ± 0.0012
39	0.0675 ± 0.0007	0.1325 ± 0.0010	0.0484 ± 0.0006	0.1236 ± 0.0009	0.3520 ± 0.0015	0.2760 ± 0.0014
40	0.0567 ± 0.0006	0.1019 ± 0.0007	0.0821 ± 0.0006	0.1251 ± 0.0008	0.3289 ± 0.0012	0.3052 ± 0.0012
41	0.0343 ± 0.0007	0.1193 ± 0.0011	0.0797 ± 0.0009	0.1318 ± 0.0012	0.3174 ± 0.0018	0.3175 ± 0.0018
42	0.1102 ± 0.0004	0.2004 ± 0.0006	0.1366 ± 0.0005	0.1775 ± 0.0005	0.3079 ± 0.0007	0.0674 ± 0.0003
43	0.0953 ± 0.0006	0.1346 ± 0.0007	0.0934 ± 0.0006	0.1462 ± 0.0008	0.3156 ± 0.0011	0.2149 ± 0.0009
44	0.0744 ± 0.0006	0.1204 ± 0.0007	0.0797 ± 0.0006	0.1442 ± 0.0008	0.3225 ± 0.0011	0.2588 ± 0.0010
45	0.0828 ± 0.0007	0.1227 ± 0.0008	0.0790 ± 0.0006	0.1185 ± 0.0008	0.3215 ± 0.0013	0.2755 ± 0.0012
46	0.0582 ± 0.0007	0.1121 ± 0.0008	0.0873 ± 0.0008	0.0995 ± 0.0008	0.3520 ± 0.0015	0.2908 ± 0.0013
47	0.0604 ± 0.0005	0.1200 ± 0.0007	0.0719 ± 0.0005	0.1230 ± 0.0007	0.3112 ± 0.0011	0.3136 ± 0.0011
48	0.0232 ± 0.0005	0.1008 ± 0.0010	0.0675 ± 0.0008	0.1371 ± 0.0011	0.3058 ± 0.0017	0.3656 ± 0.0018
49	0.0969 ± 0.0004	0.1568 ± 0.0005	0.1191 ± 0.0004	0.1471 ± 0.0005	0.3296 ± 0.0007	0.1505 ± 0.0005
50	0.0698 ± 0.0007	0.1295 ± 0.0009	0.0913 ± 0.0007	0.1114 ± 0.0008	0.3232 ± 0.0014	0.2748 ± 0.0013
51	0.0770 ± 0.0007	0.1177 ± 0.0009	0.0831 ± 0.0007	0.1218 ± 0.0009	0.3081 ± 0.0014	0.2924 ± 0.0014
52	0.0538 ± 0.0007	0.1459 ± 0.0011	0.0814 ± 0.0009	0.1354 ± 0.0011	0.2842 ± 0.0016	0.2993 ± 0.0016
53	0.0541 ± 0.0008	0.1016 ± 0.0011	0.0951 ± 0.0011	0.1112 ± 0.0011	0.3286 ± 0.0020	0.3092 ± 0.0019
54	0.0338 ± 0.0006	0.0983 ± 0.0009	0.0714 ± 0.0007	0.1239 ± 0.0010	0.3347 ± 0.0016	0.3379 ± 0.0016
55	0.0242 ± 0.0007	0.0782 ± 0.0013	0.0768 ± 0.0012	0.1319 ± 0.0016	0.3700 ± 0.0027	0.3189 ± 0.0025

A.3 $A_{\rm D}(K^-)$ in B^+ kinematic bins

Table A.6: *Kaon detection asymmetries for 2011 data samples, divided by magnet polarities and calculated for every kinematic bin defined in Tab. 3.12.*

2011 Up				2011 Down			
Bin	$A^i_{\rm D}(K^-)(\%)$	Bin	$A^i_{\rm D}(K^-)(\%)$	Bin	$A^i_{\rm D}(K^-)(\%)$	Bin	$A^i_{\rm D}(K^-)(\%)$
0	-1.426 ± 0.294	28	-1.386 ± 0.290	0	-1.627 ± 0.248	28	-1.163 ± 0.245
1	-1.410 ± 0.271	29	-1.330 ± 0.368	1	-1.280 ± 0.230	29	-1.208 ± 0.310
2	-1.404 ± 0.273	30	-1.302 ± 0.436	2	-1.246 ± 0.230	30	-1.283 ± 0.377
3	-1.396 ± 0.296	31	-1.304 ± 0.444	3	-1.223 ± 0.250	31	-1.342 ± 0.396
4	-1.373 ± 0.310	32	-1.297 ± 0.463	4	-1.218 ± 0.271	32	-1.288 ± 0.426
5	-1.326 ± 0.377	33	-1.272 ± 0.528	5	-1.238 ± 0.325	33	-1.319 ± 0.420
6	-1.295 ± 0.464	34	-1.286 ± 0.471	6	-1.250 ± 0.402	34	-1.302 ± 0.432
7	-1.416 ± 0.271	35	-1.399 ± 0.302	7	-1.377 ± 0.229	35	-1.202 ± 0.248
8	-1.390 ± 0.283	36	-1.323 ± 0.394	8	-1.196 ± 0.244	36	-1.242 ± 0.351
9	-1.383 ± 0.321	37	-1.308 ± 0.421	9	-1.230 ± 0.264	37	-1.267 ± 0.387
10	-1.355 ± 0.336	38	-1.300 ± 0.450	10	-1.250 ± 0.283	38	-1.290 ± 0.417
11	-1.327 ± 0.384	39	-1.299 ± 0.434	11	-1.282 ± 0.331	39	-1.309 ± 0.409
12	-1.309 ± 0.430	40	-1.285 ± 0.491	12	-1.287 ± 0.372	40	-1.299 ± 0.432
13	-1.304 ± 0.431	41	-1.275 ± 0.483	13	-1.291 ± 0.390	41	-1.260 ± 0.490
14	-1.420 ± 0.272	42	-1.360 ± 0.318	14	-1.232 ± 0.230	42	-1.149 ± 0.270
15	-1.377 ± 0.327	43	-1.293 ± 0.468	15	-1.184 ± 0.271	43	-1.238 ± 0.357
16	-1.355 ± 0.343	44	-1.293 ± 0.463	16	-1.221 ± 0.293	44	-1.254 ± 0.392
17	-1.314 ± 0.412	45	-1.275 ± 0.492	17	-1.288 ± 0.343	45	-1.232 ± 0.415
18	-1.306 ± 0.441	46	-1.311 ± 0.459	18	-1.357 ± 0.383	46	-1.265 ± 0.395
19	-1.295 ± 0.468	47	-1.268 ± 0.531	19	-1.321 ± 0.406	47	-1.290 ± 0.444
20	-1.301 ± 0.470	48	-1.267 ± 0.546	20	-1.269 ± 0.430	48	-1.291 ± 0.418
21	-1.397 ± 0.280	49	-1.337 ± 0.354	21	-1.153 ± 0.240	49	-1.197 ± 0.303
22	-1.358 ± 0.322	50	-1.296 ± 0.444	22	-1.180 ± 0.294	50	-1.268 ± 0.370
23	-1.323 ± 0.386	51	-1.280 ± 0.458	23	-1.230 ± 0.312	51	-1.272 ± 0.404
24	-1.304 ± 0.427	52	-1.303 ± 0.467	24	-1.319 ± 0.381	52	-1.236 ± 0.393
25	-1.305 ± 0.424	53	-1.296 ± 0.479	25	-1.254 ± 0.386	53	-1.330 ± 0.508
26	-1.287 ± 0.481	54	-1.264 ± 0.502	26	-1.303 ± 0.393	54	-1.295 ± 0.433
27	-1.287 ± 0.492	55	-1.261 ± 0.599	27	-1.233 ± 0.418	55	-1.189 ± 0.480

Bin	$A^i_{\rm D}(K^-)(\%)$	Bin	$A^i_{\rm D}(K^-)(\%)$
A	-1.435 ± 0.317	A	-1.775 ± 0.267
B	-1.429 ± 0.283	B	-1.396 ± 0.240
C	-1.400 ± 0.280	C	-1.228 ± 0.235
D	-1.405 ± 0.274	D	-1.137 ± 0.239
E	-1.381 ± 0.294	E	-1.152 ± 0.254
F	-1.356 ± 0.344	F	-1.196 ± 0.295
G	-1.297 ± 0.470	G	-1.280 ± 0.419

Table A.7: *Kaon detection asymmetries for 2012 data samples, divided by magnet polarities and calculated for every kinematic bin defined in Tab. 3.12.*

2012 Up				2012 Down			
Bin	$A_{\rm D}^i(K^-)(\%)$	Bin	$A_{\rm D}^i(K^-)(\%)$	Bin	$A_{\rm D}^i(K^-)(\%)$	Bin	$A_{\rm D}^i(K^-)(\%)$
0	-1.118 ± 0.155	28	-1.223 ± 0.172	0	-0.689 ± 0.158	28	-0.302 ± 0.178
1	-1.134 ± 0.151	29	-1.275 ± 0.212	1	-0.533 ± 0.155	29	-0.070 ± 0.229
2	-1.181 ± 0.156	30	-1.268 ± 0.267	2	-0.429 ± 0.160	30	0.070 ± 0.284
3	-1.217 ± 0.172	31	-1.290 ± 0.280	3	-0.344 ± 0.176	31	0.124 ± 0.300
4	-1.240 ± 0.182	32	-1.300 ± 0.296	4	-0.248 ± 0.189	32	0.160 ± 0.319
5	-1.261 ± 0.220	33	-1.283 ± 0.296	5	-0.040 ± 0.233	33	0.147 ± 0.313
6	-1.292 ± 0.275	34	-1.308 ± 0.288	6	0.129 ± 0.297	34	0.175 ± 0.321
7	-1.146 ± 0.150	35	-1.244 ± 0.180	7	-0.538 ± 0.154	35	-0.261 ± 0.179
8	-1.194 ± 0.165	36	-1.270 ± 0.235	8	-0.383 ± 0.172	36	0.009 ± 0.252
9	-1.240 ± 0.188	37	-1.274 ± 0.283	9	-0.297 ± 0.192	37	0.096 ± 0.279
10	-1.258 ± 0.196	38	-1.292 ± 0.280	10	-0.174 ± 0.203	38	0.120 ± 0.294
11	-1.261 ± 0.226	39	-1.268 ± 0.294	11	-0.031 ± 0.241	39	0.116 ± 0.307
12	-1.275 ± 0.261	40	-1.298 ± 0.310	12	0.060 ± 0.278	40	0.183 ± 0.323
13	-1.290 ± 0.271	41	-1.308 ± 0.303	13	0.104 ± 0.285	41	0.201 ± 0.331
14	-1.178 ± 0.156	42	-1.246 ± 0.187	14	-0.422 ± 0.161	42	-0.178 ± 0.196
15	-1.254 ± 0.196	43	-1.277 ± 0.268	15	-0.257 ± 0.204	43	0.023 ± 0.259
16	-1.265 ± 0.211	44	-1.283 ± 0.268	16	-0.097 ± 0.222	44	0.094 ± 0.290
17	-1.262 ± 0.250	45	-1.280 ± 0.280	17	0.008 ± 0.256	45	0.114 ± 0.299
18	-1.280 ± 0.276	46	-1.287 ± 0.280	18	0.108 ± 0.298	46	0.183 ± 0.317
19	-1.284 ± 0.288	47	-1.295 ± 0.301	19	0.128 ± 0.304	47	0.170 ± 0.326
20	-1.290 ± 0.282	48	-1.315 ± 0.320	20	0.126 ± 0.298	48	0.261 ± 0.366
21	-1.213 ± 0.165	49	-1.262 ± 0.212	21	-0.365 ± 0.169	49	-0.042 ± 0.228
22	-1.257 ± 0.199	50	-1.274 ± 0.261	22	-0.148 ± 0.210	50	0.134 ± 0.299
23	-1.276 ± 0.235	51	-1.285 ± 0.272	23	-0.016 ± 0.243	51	0.137 ± 0.309
24	-1.283 ± 0.270	52	-1.283 ± 0.307	24	0.075 ± 0.284	52	0.139 ± 0.311
25	-1.286 ± 0.294	53	-1.296 ± 0.296	25	0.131 ± 0.301	53	0.203 ± 0.326
26	-1.289 ± 0.301	54	-1.318 ± 0.317	26	0.144 ± 0.307	54	0.239 ± 0.349
27	-1.302 ± 0.292	55	-1.313 ± 0.329	27	0.170 ± 0.313	55	0.246 ± 0.343

Bin	$A_{\rm D}^i(K^-)(\%)$	Bin	$A_{\rm D}^i(K^-)(\%)$
A	-1.083 ± 0.164	A	-0.786 ± 0.168
B	-1.132 ± 0.155	B	-0.575 ± 0.160
C	-1.144 ± 0.156	C	-0.513 ± 0.161
D	-1.164 ± 0.159	D	-0.434 ± 0.163
E	-1.214 ± 0.176	E	-0.355 ± 0.175
F	-1.262 ± 0.202	F	-0.158 ± 0.210
G	-1.306 ± 0.299	G	0.175 ± 0.316

A.4 $A_{\rm PID}(B^+ \to J/\psi K^+)$

Table A.8: *PID asymmetries induced by PID cuts on the final state kaons for $B^+ \to J/\psi K^+$ 2011 dataset, divided by magnet polarity and calculated for every kinematic bin defined in Tab. 3.12.*

2011 Up				2011 Down			
Bin	$A_{\rm PID}(B^+ \to J/\psi K^+)(\%)$	Bin	$A_{\rm PID}(B^+ \to J/\psi K^+)(\%)$	Bin	$A_{\rm PID}(B^+ \to J/\psi K^+)(\%)$	Bin	$A_{\rm PID}(B^+ \to J/\psi K^+)(\%)$
0	0.0624 ± 0.0398	28	0.0670 ± 0.0578	0	0.0729 ± 0.0302	28	-0.0126 ± 0.0466
1	0.0925 ± 0.0408	29	0.0866 ± 0.0850	1	0.0563 ± 0.0294	29	0.0160 ± 0.0718
2	-0.0008 ± 0.0365	30	0.0397 ± 0.1100	2	-0.0035 ± 0.0289	30	0.0895 ± 0.0854
3	0.0567 ± 0.0348	31	0.1519 ± 0.1208	3	-0.0045 ± 0.0270	31	0.0864 ± 0.0960
4	0.1483 ± 0.0345	32	0.1227 ± 0.1256	4	0.0023 ± 0.0265	32	-0.0760 ± 0.1076
5	0.0312 ± 0.0228	33	-0.0327 ± 0.1057	5	-0.0392 ± 0.0175	33	0.0093 ± 0.0811
6	-0.0108 ± 0.0285	34	-0.0459 ± 0.1373	6	-0.0404 ± 0.0238	34	-0.1354 ± 0.1103
7	0.1990 ± 0.0385	35	-0.0831 ± 0.0583	7	0.0355 ± 0.0279	35	-0.0454 ± 0.0540
8	0.1404 ± 0.0444	36	-0.0731 ± 0.1403	8	0.0457 ± 0.0317	36	-0.0951 ± 0.0996
9	0.0535 ± 0.0377	37	0.1953 ± 0.1386	9	0.0186 ± 0.0322	37	-0.2067 ± 0.1021
10	0.0533 ± 0.0377	38	0.0036 ± 0.1279	10	0.0008 ± 0.0303	38	0.1130 ± 0.1129
11	0.0705 ± 0.0414	39	0.4415 ± 0.1803	11	-0.0034 ± 0.0312	39	-0.0237 ± 0.1374
12	0.0005 ± 0.0305	40	0.0926 ± 0.1341	12	0.0125 ± 0.0242	40	-0.1415 ± 0.1069
13	0.0126 ± 0.0409	41	0.1251 ± 0.1759	13	-0.0659 ± 0.0327	41	0.2280 ± 0.1683
14	0.0155 ± 0.0511	42	0.0382 ± 0.0490	14	0.0190 ± 0.0372	42	0.0393 ± 0.0402
15	0.1091 ± 0.0700	43	0.1404 ± 0.1312	15	-0.0748 ± 0.0526	43	0.0503 ± 0.0960
16	0.1013 ± 0.0639	44	0.1753 ± 0.1308	16	0.0075 ± 0.0487	44	0.1401 ± 0.1082
17	0.1070 ± 0.0760	45	0.0573 ± 0.1446	17	0.0464 ± 0.0620	45	-0.3046 ± 0.1094
18	-0.0110 ± 0.0821	46	0.1870 ± 0.1276	18	-0.0513 ± 0.0723	46	0.4487 ± 0.1155
19	0.1592 ± 0.0604	47	0.0938 ± 0.1211	19	-0.0894 ± 0.0517	47	-0.1288 ± 0.0965
20	-0.1798 ± 0.0766	48	-0.0751 ± 0.1804	20	0.0315 ± 0.0735	48	0.1022 ± 0.1615
21	0.1277 ± 0.0547	49	0.0749 ± 0.0551	21	0.0571 ± 0.0369	49	-0.0639 ± 0.0523
22	0.0651 ± 0.0789	50	-0.1018 ± 0.1731	22	0.0276 ± 0.0557	50	-0.1428 ± 0.1306
23	-0.0964 ± 0.0738	51	0.0484 ± 0.1444	23	0.0003 ± 0.0651	51	-0.1118 ± 0.1479
24	-0.0203 ± 0.0945	52	0.4825 ± 0.1724	24	0.0198 ± 0.0805	52	0.1467 ± 0.1442
25	0.1456 ± 0.0981	53	-0.1935 ± 0.2136	25	-0.0221 ± 0.0848	53	-0.3679 ± 0.2464
26	0.0683 ± 0.0850	54	0.1373 ± 0.1476	26	-0.0243 ± 0.0635	54	-0.1471 ± 0.1429
27	-0.1153 ± 0.1078	55	0.0360 ± 0.0266	27	-0.1586 ± 0.0923	55	0.0805 ± 0.2558

Bin	$A_{\rm PID}(B^+ \to J/\psi K^+)(\%)$	Bin	$A_{\rm PID}(B^+ \to J/\psi K^+)(\%)$
A	-0.0221 ± 0.0636	A	0.0739 ± 0.0473
B	0.1170 ± 0.0738	B	-0.0139 ± 0.0523
C	0.0073 ± 0.0581	C	-0.0013 ± 0.0452
D	-0.0064 ± 0.0544	D	0.0096 ± 0.0426
E	0.1341 ± 0.0529	E	-0.0797 ± 0.0437
F	0.0828 ± 0.0327	F	-0.0902 ± 0.0252
G	0.0386 ± 0.0400	G	-0.0434 ± 0.0334

Table A.9: *PID asymmetries induced by PID cuts on the final state kaons for $B^+ \to J/\psi K^+$ 2012 dataset, divided by magnet polarity and calculated for every kinematic bin defined in Tab. 3.12.*

2012 Up				2012 Down			
Bin	$A_{\rm PID}(B^+ \to J/\psi K^+)(\%)$	Bin	$A_{\rm PID}(B^+ \to J/\psi K^+)(\%)$	Bin	$A_{\rm PID}(B^+ \to J/\psi K^+)(\%)$	Bin	$A_{\rm PID}(B^+ \to J/\psi K^+)(\%)$
0	-0.0183 ± 0.0228	28	0.0017 ± 0.0327	0	-0.1321 ± 0.0252	28	-0.0636 ± 0.0346
1	-0.0172 ± 0.0266	29	-0.0184 ± 0.0472	1	-0.0848 ± 0.0278	29	-0.1891 ± 0.0558
2	-0.0537 ± 0.0237	30	-0.0582 ± 0.0637	2	-0.0934 ± 0.0249	30	-0.1471 ± 0.0634
3	0.0026 ± 0.0225	31	0.0671 ± 0.0775	3	-0.1088 ± 0.0237	31	-0.0801 ± 0.0740
4	-0.0382 ± 0.0216	32	0.0262 ± 0.0843	4	-0.1120 ± 0.0230	32	-0.1770 ± 0.0870
5	0.0247 ± 0.0147	33	0.1705 ± 0.0597	5	-0.1015 ± 0.0155	33	-0.1653 ± 0.0609
6	0.0606 ± 0.0196	34	0.1136 ± 0.0843	6	-0.1043 ± 0.0200	34	-0.1928 ± 0.0863
7	0.0027 ± 0.0212	35	-0.0594 ± 0.0363	7	-0.0447 ± 0.0224	35	-0.0887 ± 0.0380
8	-0.0111 ± 0.0259	36	0.1852 ± 0.0738	8	-0.1151 ± 0.0274	36	-0.1572 ± 0.0706
9	-0.0091 ± 0.0229	37	0.0806 ± 0.0856	9	-0.1265 ± 0.0265	37	-0.0787 ± 0.0791
10	-0.0054 ± 0.0228	38	0.0793 ± 0.0968	10	-0.0822 ± 0.0259	38	-0.1420 ± 0.0891
11	0.0487 ± 0.0252	39	0.1296 ± 0.0963	11	-0.0847 ± 0.0261	39	-0.2828 ± 0.1036
12	0.0447 ± 0.0191	40	0.0159 ± 0.0765	12	-0.1165 ± 0.0196	40	-0.1184 ± 0.0786
13	0.0618 ± 0.0259	41	-0.0596 ± 0.1225	13	-0.1200 ± 0.0248	41	-0.2268 ± 0.1104
14	0.0247 ± 0.0286	42	0.0733 ± 0.0288	14	-0.0847 ± 0.0314	42	-0.0419 ± 0.0327
15	-0.0581 ± 0.0376	43	0.0757 ± 0.0728	15	-0.0753 ± 0.0411	43	-0.1381 ± 0.0713
16	0.0212 ± 0.0415	44	0.0087 ± 0.0725	16	-0.0536 ± 0.0393	44	-0.1770 ± 0.0735
17	0.0355 ± 0.0433	45	-0.1273 ± 0.0849	17	-0.1159 ± 0.0460	45	-0.2192 ± 0.0941
18	-0.0283 ± 0.0539	46	0.0066 ± 0.0983	18	-0.0602 ± 0.0538	46	-0.1107 ± 0.0960
19	-0.0086 ± 0.0387	47	0.0122 ± 0.0751	19	-0.1073 ± 0.0399	47	-0.0612 ± 0.0735
20	0.0537 ± 0.0530	48	0.0654 ± 0.1094	20	-0.0747 ± 0.0500	48	-0.0473 ± 0.1170
21	0.0104 ± 0.0303	49	0.0509 ± 0.0357	21	-0.0243 ± 0.0310	49	-0.0788 ± 0.0392
22	0.0316 ± 0.0441	50	0.1177 ± 0.0898	22	-0.1034 ± 0.0479	50	-0.1792 ± 0.0920
23	-0.0005 ± 0.0477	51	0.0319 ± 0.0956	23	-0.1000 ± 0.0500	51	-0.2532 ± 0.0919
24	0.0622 ± 0.0602	52	0.1722 ± 0.1180	24	-0.1463 ± 0.0600	52	-0.2839 ± 0.1053
25	0.1381 ± 0.0670	53	0.1094 ± 0.1256	25	-0.0941 ± 0.0666	53	-0.3299 ± 0.1269
26	0.0292 ± 0.0511	54	0.0443 ± 0.1011	26	-0.2206 ± 0.0489	54	-0.1618 ± 0.1029
27	0.1211 ± 0.0703	55	0.7701 ± 0.1785	27	-0.1775 ± 0.0677	55	-0.2164 ± 0.1567
Bin		$A_{\rm PID}(B^+ \to J/\psi K^+)(\%)$		Bin		$A_{\rm PID}(B^+ \to J/\psi K^+)(\%)$	
A		0.0407 ± 0.0384		A		-0.1036 ± 0.0394	
B		0.1098 ± 0.0491		B		-0.0477 ± 0.0445	
C		0.0453 ± 0.0392		C		-0.0858 ± 0.0408	
D		0.0218 ± 0.0366		D		-0.0168 ± 0.0405	
E		-0.0171 ± 0.0339		E		0.0102 ± 0.0399	
F		-0.0339 ± 0.0214		F		-0.0864 ± 0.0238	
G		-0.0127 ± 0.0302		G		-0.1370 ± 0.0286	

A.5 Efficiencies and weights for integration

Table A.10: *Values of efficiencies,* ω_i^{data} *and* ω_i *from simulation for* $B^+ \to J/\psi K^+$ *2011 decays.* δ *is the difference between* ω_i^{data} *and* ω_i *divided by the square root of the sum of the squared errors.*

Bin	ε^{sel}	ε^{PID}	ε^{trig}	ω_i^{data}	ω_i
A	0.1314 ± 0.0020	0.9954 ± 0.0152	0.3609 ± 0.0092	0.0442 ± 0.0007	0.0576 ± 0.0003
B	0.2934 ± 0.0062	0.9946 ± 0.0211	0.4585 ± 0.0143	0.0109 ± 0.0002	0.0133 ± 0.0001
C	0.3301 ± 0.0067	0.9938 ± 0.0203	0.4671 ± 0.0140	0.0109 ± 0.0002	0.0128 ± 0.0001
D	0.3670 ± 0.0073	0.9933 ± 0.0197	0.4878 ± 0.0139	0.0104 ± 0.0003	0.0121 ± 0.0001
E	0.3938 ± 0.0077	0.9935 ± 0.0196	0.5105 ± 0.0141	0.0097 ± 0.0003	0.0115 ± 0.0001
F	0.3779 ± 0.0049	0.9880 ± 0.0128	0.5258 ± 0.0094	0.0251 ± 0.0007	0.0280 ± 0.0002
G	0.1928 ± 0.0028	0.9448 ± 0.0141	0.5450 ± 0.0111	0.0377 ± 0.0004	0.0428 ± 0.0003
0	0.1365 ± 0.0014	0.9946 ± 0.0102	0.4102 ± 0.0065	0.1165 ± 0.0023	0.1233 ± 0.0004
1	0.2904 ± 0.0043	0.9934 ± 0.0148	0.4851 ± 0.0104	0.0286 ± 0.0004	0.0273 ± 0.0002
2	0.3221 ± 0.0046	0.9925 ± 0.0144	0.5101 ± 0.0103	0.0280 ± 0.0005	0.0261 ± 0.0002
3	0.3431 ± 0.0049	0.9947 ± 0.0143	0.5185 ± 0.0103	0.0286 ± 0.0006	0.0248 ± 0.0002
4	0.3549 ± 0.0052	0.9899 ± 0.0146	0.5283 ± 0.0107	0.0274 ± 0.0007	0.0228 ± 0.0002
5	0.3371 ± 0.0033	0.9819 ± 0.0097	0.5599 ± 0.0074	0.0657 ± 0.0024	0.0537 ± 0.0003
6	0.1751 ± 0.0020	0.8882 ± 0.0109	0.5724 ± 0.0093	0.0976 ± 0.0024	0.0744 ± 0.0003
7	0.1747 ± 0.0018	0.9920 ± 0.0105	0.4737 ± 0.0073	0.0796 ± 0.0014	0.0900 ± 0.0004
8	0.3371 ± 0.0055	0.9929 ± 0.0162	0.5409 ± 0.0120	0.0193 ± 0.0004	0.0197 ± 0.0002
9	0.3798 ± 0.0060	0.9930 ± 0.0158	0.5521 ± 0.0118	0.0182 ± 0.0005	0.0184 ± 0.0002
10	0.3957 ± 0.0064	0.9946 ± 0.0160	0.5758 ± 0.0122	0.0172 ± 0.0006	0.0171 ± 0.0002
11	0.3967 ± 0.0066	0.9902 ± 0.0166	0.5697 ± 0.0127	0.0166 ± 0.0005	0.0158 ± 0.0002
12	0.3790 ± 0.0043	0.9689 ± 0.0112	0.5844 ± 0.0088	0.0399 ± 0.0012	0.0356 ± 0.0002
13	0.2225 ± 0.0029	0.7890 ± 0.0118	0.5958 ± 0.0115	0.0509 ± 0.0007	0.0446 ± 0.0003
14	0.2059 ± 0.0035	0.9896 ± 0.0171	0.5120 ± 0.0124	0.0238 ± 0.0000	0.0286 ± 0.0002
15	0.3463 ± 0.0098	0.9855 ± 0.0282	0.5783 ± 0.0217	0.0056 ± 0.0003	0.0063 ± 0.0001
16	0.3600 ± 0.0104	0.9909 ± 0.0287	0.5827 ± 0.0221	0.0057 ± 0.0003	0.0058 ± 0.0001
17	0.4093 ± 0.0116	0.9952 ± 0.0283	0.5895 ± 0.0218	0.0046 ± 0.0003	0.0053 ± 0.0001
18	0.3977 ± 0.0120	0.9801 ± 0.0297	0.6087 ± 0.0237	0.0047 ± 0.0003	0.0049 ± 0.0001
19	0.3762 ± 0.0078	0.9412 ± 0.0200	0.6026 ± 0.0165	0.0112 ± 0.0004	0.0109 ± 0.0001
20	0.2293 ± 0.0056	0.7262 ± 0.0209	0.6015 ± 0.0223	0.0132 ± 0.0002	0.0127 ± 0.0001
21	0.2159 ± 0.0043	0.9891 ± 0.0199	0.5374 ± 0.0148	0.0172 ± 0.0001	0.0201 ± 0.0002
22	0.3577 ± 0.0123	0.9882 ± 0.0341	0.5850 ± 0.0264	0.0039 ± 0.0002	0.0042 ± 0.0001
23	0.4174 ± 0.0137	0.9903 ± 0.0327	0.5904 ± 0.0254	0.0034 ± 0.0002	0.0039 ± 0.0001
24	0.4044 ± 0.0140	0.9905 ± 0.0343	0.5938 ± 0.0267	0.0036 ± 0.0003	0.0036 ± 0.0001
25	0.4066 ± 0.0148	0.9774 ± 0.0360	0.6046 ± 0.0287	0.0031 ± 0.0002	0.0032 ± 0.0001
26	0.3729 ± 0.0095	0.9097 ± 0.0244	0.5863 ± 0.0205	0.0080 ± 0.0003	0.0072 ± 0.0001
27	0.2562 ± 0.0075	0.6780 ± 0.0240	0.6030 ± 0.0275	0.0077 ± 0.0002	0.0080 ± 0.0001
28	0.2418 ± 0.0055	0.9870 ± 0.0227	0.5537 ± 0.0171	0.0111 ± 0.0001	0.0139 ± 0.0001
29	0.3631 ± 0.0150	0.9828 ± 0.0411	0.6329 ± 0.0333	0.0026 ± 0.0002	0.0028 ± 0.0001
30	0.3993 ± 0.0163	0.9866 ± 0.0406	0.5855 ± 0.0315	0.0026 ± 0.0002	0.0026 ± 0.0001
31	0.4139 ± 0.0172	0.9775 ± 0.0412	0.6135 ± 0.0330	0.0022 ± 0.0002	0.0024 ± 0.0001
32	0.3905 ± 0.0175	0.9479 ± 0.0436	0.5497 ± 0.0341	0.0024 ± 0.0002	0.0022 ± 0.0001
33	0.3997 ± 0.0123	0.8802 ± 0.0288	0.5638 ± 0.0246	0.0049 ± 0.0002	0.0046 ± 0.0001
34	0.2661 ± 0.0098	0.6315 ± 0.0294	0.5532 ± 0.0346	0.0059 ± 0.0002	0.0048 ± 0.0001
35	0.2641 ± 0.0071	0.9811 ± 0.0267	0.5422 ± 0.0200	0.0081 ± 0.0001	0.0091 ± 0.0001
36	0.4173 ± 0.0198	0.9910 ± 0.0472	0.5636 ± 0.0358	0.0018 ± 0.0002	0.0019 ± 0.0001
37	0.3959 ± 0.0196	0.9779 ± 0.0490	0.5628 ± 0.0376	0.0019 ± 0.0002	0.0018 ± 0.0001
38	0.4253 ± 0.0217	0.9896 ± 0.0508	0.6132 ± 0.0402	0.0014 ± 0.0002	0.0016 ± 0.0001
39	0.4238 ± 0.0230	0.9705 ± 0.0535	0.5441 ± 0.0407	0.0016 ± 0.0001	0.0014 ± 0.0001
40	0.4113 ± 0.0153	0.8275 ± 0.0339	0.5580 ± 0.0306	0.0033 ± 0.0002	0.0031 ± 0.0001
41	0.2924 ± 0.0131	0.5803 ± 0.0341	0.5986 ± 0.0455	0.0031 ± 0.0001	0.0030 ± 0.0001
42	0.3022 ± 0.0066	0.9738 ± 0.0217	0.5316 ± 0.0163	0.0104 ± 0.0002	0.0119 ± 0.0001
43	0.3934 ± 0.0164	0.9601 ± 0.0408	0.5334 ± 0.0311	0.0025 ± 0.0002	0.0026 ± 0.0001
44	0.4738 ± 0.0194	0.9580 ± 0.0401	0.5517 ± 0.0311	0.0021 ± 0.0002	0.0022 ± 0.0001
45	0.4760 ± 0.0202	0.9658 ± 0.0417	0.5541 ± 0.0321	0.0018 ± 0.0002	0.0020 ± 0.0001
46	0.4725 ± 0.0221	0.8838 ± 0.0440	0.5335 ± 0.0364	0.0018 ± 0.0002	0.0017 ± 0.0001
47	0.4218 ± 0.0141	0.7762 ± 0.0294	0.5481 ± 0.0280	0.0040 ± 0.0002	0.0037 ± 0.0001
48	0.2761 ± 0.0118	0.4945 ± 0.0300	0.5478 ± 0.0449	0.0043 ± 0.0002	0.0035 ± 0.0001
49	0.3596 ± 0.0080	0.8824 ± 0.0208	0.4813 ± 0.0164	0.0095 ± 0.0002	0.0099 ± 0.0001
50	0.5087 ± 0.0216	0.8827 ± 0.0399	0.4663 ± 0.0309	0.0019 ± 0.0001	0.0019 ± 0.0001
51	0.4270 ± 0.0203	0.8801 ± 0.0446	0.4833 ± 0.0352	0.0020 ± 0.0001	0.0018 ± 0.0001
52	0.4678 ± 0.0230	0.8261 ± 0.0447	0.5059 ± 0.0385	0.0015 ± 0.0001	0.0015 ± 0.0001
53	0.5169 ± 0.0265	0.7853 ± 0.0453	0.5033 ± 0.0410	0.0011 ± 0.0001	0.0013 ± 0.0001
54	0.4427 ± 0.0176	0.6262 ± 0.0314	0.4584 ± 0.0340	0.0030 ± 0.0001	0.0025 ± 0.0001
55	0.3525 ± 0.0179	0.4119 ± 0.0327	0.4717 ± 0.0545	0.0022 ± 0.0002	0.0019 ± 0.0001

Table A.11: *Values of efficiencies, $\omega_i^{\rm data}$ and ω_i from simulation for $B^+ \to J/\psi K^+$ 2012 decays. δ is the difference between $\omega_i^{\rm data}$ and ω_i divided by the square root of the sum of the squared errors*

Bin	ε^{sel}	$\varepsilon^{\rm PID}$	ε^{trig}	$\omega_i^{\rm data}$	ω_i
A	0.1117 ± 0.0018	0.9973 ± 0.0163	0.3910 ± 0.0103	0.0420 ± 0.0007	0.0554 ± 0.0003
B	0.2591 ± 0.0058	0.9950 ± 0.0224	0.4172 ± 0.0145	0.0101 ± 0.0001	0.0127 ± 0.0001
C	0.3095 ± 0.0065	0.9952 ± 0.0208	0.4303 ± 0.0137	0.0094 ± 0.0002	0.0123 ± 0.0001
D	0.3322 ± 0.0069	0.9961 ± 0.0207	0.4263 ± 0.0135	0.0096 ± 0.0002	0.0117 ± 0.0001
E	0.3573 ± 0.0073	0.9925 ± 0.0203	0.4305 ± 0.0134	0.0089 ± 0.0002	0.0112 ± 0.0001
F	0.3292 ± 0.0044	0.9876 ± 0.0134	0.4342 ± 0.0090	0.0235 ± 0.0004	0.0276 ± 0.0002
G	0.1725 ± 0.0026	0.9453 ± 0.0146	0.4566 ± 0.0104	0.0335 ± 0.0002	0.0426 ± 0.0003
0	0.1151 ± 0.0013	0.9943 ± 0.0110	0.4466 ± 0.0074	0.1191 ± 0.0018	0.1181 ± 0.0004
1	0.2563 ± 0.0040	0.9926 ± 0.0154	0.4817 ± 0.0108	0.0270 ± 0.0003	0.0270 ± 0.0002
2	0.2922 ± 0.0043	0.9945 ± 0.0148	0.4953 ± 0.0105	0.0262 ± 0.0004	0.0257 ± 0.0002
3	0.3119 ± 0.0046	0.9939 ± 0.0147	0.4934 ± 0.0104	0.0265 ± 0.0005	0.0243 ± 0.0002
4	0.3275 ± 0.0049	0.9922 ± 0.0148	0.5022 ± 0.0106	0.0245 ± 0.0005	0.0228 ± 0.0002
5	0.3164 ± 0.0031	0.9806 ± 0.0098	0.4956 ± 0.0070	0.0610 ± 0.0014	0.0535 ± 0.0003
6	0.1669 ± 0.0019	0.8864 ± 0.0108	0.5008 ± 0.0086	0.0896 ± 0.0014	0.0754 ± 0.0003
7	0.1487 ± 0.0017	0.9942 ± 0.0112	0.5070 ± 0.0080	0.0866 ± 0.0011	0.0880 ± 0.0003
8	0.3028 ± 0.0051	0.9932 ± 0.0168	0.5356 ± 0.0124	0.0196 ± 0.0004	0.0193 ± 0.0002
9	0.3392 ± 0.0056	0.9932 ± 0.0164	0.5483 ± 0.0122	0.0186 ± 0.0006	0.0181 ± 0.0002
10	0.3655 ± 0.0060	0.9933 ± 0.0163	0.5435 ± 0.0121	0.0174 ± 0.0006	0.0170 ± 0.0002
11	0.3810 ± 0.0063	0.9853 ± 0.0165	0.5418 ± 0.0123	0.0162 ± 0.0006	0.0158 ± 0.0002
12	0.3567 ± 0.0040	0.9635 ± 0.0111	0.5556 ± 0.0086	0.0383 ± 0.0009	0.0365 ± 0.0002
13	0.1985 ± 0.0026	0.7730 ± 0.0117	0.5550 ± 0.0112	0.0521 ± 0.0005	0.0474 ± 0.0003
14	0.1669 ± 0.0031	0.9944 ± 0.0186	0.5368 ± 0.0137	0.0284 ± 0.0001	0.0284 ± 0.0002
15	0.3079 ± 0.0091	0.9956 ± 0.0295	0.5771 ± 0.0226	0.0062 ± 0.0003	0.0062 ± 0.0001
16	0.3360 ± 0.0097	0.9874 ± 0.0288	0.5642 ± 0.0219	0.0059 ± 0.0003	0.0059 ± 0.0001
17	0.3380 ± 0.0101	0.9865 ± 0.0298	0.5738 ± 0.0229	0.0056 ± 0.0003	0.0055 ± 0.0001
18	0.3576 ± 0.0109	0.9853 ± 0.0301	0.5770 ± 0.0232	0.0050 ± 0.0003	0.0050 ± 0.0001
19	0.3519 ± 0.0073	0.9333 ± 0.0199	0.5828 ± 0.0163	0.0112 ± 0.0004	0.0111 ± 0.0001
20	0.1955 ± 0.0048	0.6921 ± 0.0205	0.5753 ± 0.0225	0.0150 ± 0.0002	0.0139 ± 0.0001
21	0.1837 ± 0.0039	0.9901 ± 0.0211	0.5595 ± 0.0159	0.0193 ± 0.0001	0.0201 ± 0.0002
22	0.3356 ± 0.0113	0.9852 ± 0.0335	0.5813 ± 0.0259	0.0042 ± 0.0003	0.0043 ± 0.0001
23	0.3439 ± 0.0119	0.9928 ± 0.0345	0.5707 ± 0.0263	0.0040 ± 0.0003	0.0040 ± 0.0001
24	0.3696 ± 0.0130	0.9802 ± 0.0348	0.5593 ± 0.0266	0.0037 ± 0.0003	0.0036 ± 0.0001
25	0.3746 ± 0.0136	0.9696 ± 0.0358	0.5853 ± 0.0283	0.0032 ± 0.0003	0.0034 ± 0.0001
26	0.3459 ± 0.0088	0.8890 ± 0.0240	0.5869 ± 0.0207	0.0077 ± 0.0003	0.0074 ± 0.0001
27	0.2214 ± 0.0064	0.6658 ± 0.0237	0.6068 ± 0.0277	0.0084 ± 0.0001	0.0089 ± 0.0001
28	0.2012 ± 0.0049	0.9869 ± 0.0243	0.5617 ± 0.0184	0.0140 ± 0.0001	0.0138 ± 0.0001
34	0.2533 ± 0.0088	0.6124 ± 0.0273	0.5357 ± 0.0326	0.0059 ± 0.0001	0.0054 ± 0.0001
35	0.2259 ± 0.0063	0.9819 ± 0.0278	0.5373 ± 0.0208	0.0095 ± 0.0001	0.0093 ± 0.0001
36	0.3783 ± 0.0174	0.9747 ± 0.0454	0.5433 ± 0.0343	0.0019 ± 0.0002	0.0021 ± 0.0001
37	0.3863 ± 0.0190	0.9734 ± 0.0486	0.5423 ± 0.0367	0.0019 ± 0.0002	0.0018 ± 0.0001
38	0.3760 ± 0.0192	0.9636 ± 0.0500	0.5472 ± 0.0384	0.0018 ± 0.0002	0.0017 ± 0.0001
39	0.4410 ± 0.0233	0.9359 ± 0.0511	0.5863 ± 0.0418	0.0014 ± 0.0002	0.0014 ± 0.0001
40	0.3814 ± 0.0139	0.8358 ± 0.0334	0.5288 ± 0.0291	0.0034 ± 0.0002	0.0033 ± 0.0001
41	0.2559 ± 0.0110	0.5413 ± 0.0315	0.5763 ± 0.0442	0.0036 ± 0.0001	0.0035 ± 0.0001
42	0.2568 ± 0.0058	0.9683 ± 0.0223	0.5317 ± 0.0168	0.0127 ± 0.0002	0.0126 ± 0.0001
43	0.3757 ± 0.0155	0.9624 ± 0.0406	0.5115 ± 0.0301	0.0029 ± 0.0002	0.0026 ± 0.0001
44	0.4112 ± 0.0170	0.9676 ± 0.0406	0.5432 ± 0.0309	0.0024 ± 0.0002	0.0024 ± 0.0001
45	0.4161 ± 0.0185	0.9546 ± 0.0434	0.5300 ± 0.0331	0.0022 ± 0.0002	0.0020 ± 0.0001
46	0.4466 ± 0.0205	0.8877 ± 0.0434	0.5704 ± 0.0369	0.0017 ± 0.0002	0.0018 ± 0.0001
47	0.3911 ± 0.0126	0.7492 ± 0.0280	0.5523 ± 0.0278	0.0042 ± 0.0002	0.0041 ± 0.0001
48	0.2777 ± 0.0107	0.5141 ± 0.0276	0.5274 ± 0.0390	0.0042 ± 0.0001	0.0040 ± 0.0001
49	0.3214 ± 0.0071	0.8907 ± 0.0208	0.4684 ± 0.0160	0.0114 ± 0.0002	0.0106 ± 0.0001
50	0.4214 ± 0.0183	0.8523 ± 0.0402	0.4933 ± 0.0331	0.0021 ± 0.0002	0.0021 ± 0.0001
51	0.4099 ± 0.0192	0.8681 ± 0.0437	0.4861 ± 0.0351	0.0021 ± 0.0001	0.0018 ± 0.0001
52	0.4371 ± 0.0212	0.8349 ± 0.0444	0.4661 ± 0.0363	0.0018 ± 0.0001	0.0016 ± 0.0001
53	0.4300 ± 0.0221	0.7566 ± 0.0447	0.5559 ± 0.0441	0.0013 ± 0.0001	0.0015 ± 0.0001
54	0.4286 ± 0.0157	0.6064 ± 0.0285	0.4857 ± 0.0327	0.0029 ± 0.0001	0.0029 ± 0.0001
55	0.3078 ± 0.0145	0.3831 ± 0.0292	0.4826 ± 0.0530	0.0024 ± 0.0001	0.0024 ± 0.0001

Table A.12: *Values of efficiencies and* ω_i^{data} *for* $B^0 \to J/\psi K^{*0}$ *2011 decays using the* B^0 *binning scheme.*

Bin	ε^{sel}	ε^{PID}	$\varepsilon^{\text{trig}}$	ω_i^{data}	ω_i
A	0.0366 ± 0.0011	0.6619 ± 0.0237	0.3755 ± 0.0219	0.0388 ± 0.0022	0.0579 ± 0.0003
B	0.0921 ± 0.0035	0.7079 ± 0.0319	0.5285 ± 0.0328	0.0106 ± 0.0003	0.0135 ± 0.0001
C	0.1161 ± 0.0041	0.7141 ± 0.0296	0.5361 ± 0.0303	0.0106 ± 0.0003	0.0126 ± 0.0001
D	0.1401 ± 0.0046	0.7270 ± 0.0277	0.5488 ± 0.0283	0.0107 ± 0.0004	0.0121 ± 0.0001
E	0.1438 ± 0.0047	0.7369 ± 0.0281	0.5835 ± 0.0291	0.0112 ± 0.0005	0.0117 ± 0.0001
F	0.1474 ± 0.0031	0.7593 ± 0.0181	0.6137 ± 0.0187	0.0269 ± 0.0009	0.0282 ± 0.0002
G	0.0727 ± 0.0018	0.7454 ± 0.0208	0.6506 ± 0.0225	0.0411 ± 0.0003	0.0426 ± 0.0003
0	0.0401 ± 0.0008	0.7425 ± 0.0164	0.4754 ± 0.0152	0.0990 ± 0.0024	0.1235 ± 0.0004
1	0.0960 ± 0.0025	0.7485 ± 0.0226	0.5899 ± 0.0232	0.0281 ± 0.0002	0.0273 ± 0.0002
2	0.1166 ± 0.0028	0.7723 ± 0.0213	0.6116 ± 0.0216	0.0296 ± 0.0007	0.0261 ± 0.0002
3	0.1328 ± 0.0031	0.7778 ± 0.0205	0.6129 ± 0.0206	0.0278 ± 0.0009	0.0250 ± 0.0002
4	0.1404 ± 0.0033	0.7855 ± 0.0209	0.6411 ± 0.0213	0.0267 ± 0.0011	0.0229 ± 0.0002
5	0.1428 ± 0.0022	0.7792 ± 0.0135	0.6556 ± 0.0140	0.0651 ± 0.0032	0.0535 ± 0.0003
6	0.0720 ± 0.0013	0.7674 ± 0.0161	0.6599 ± 0.0170	0.0964 ± 0.0031	0.0737 ± 0.0003
7	0.0647 ± 0.0011	0.7936 ± 0.0157	0.5563 ± 0.0148	0.0756 ± 0.0014	0.0890 ± 0.0004
8	0.1432 ± 0.0036	0.7985 ± 0.0225	0.6638 ± 0.0229	0.0192 ± 0.0009	0.0198 ± 0.0002
9	0.1724 ± 0.0041	0.7967 ± 0.0213	0.6903 ± 0.0222	0.0180 ± 0.0012	0.0182 ± 0.0002
10	0.1823 ± 0.0043	0.8176 ± 0.0216	0.6918 ± 0.0220	0.0183 ± 0.0013	0.0172 ± 0.0002
11	0.1920 ± 0.0047	0.8449 ± 0.0223	0.6971 ± 0.0221	0.0174 ± 0.0014	0.0158 ± 0.0002
12	0.1865 ± 0.0030	0.8237 ± 0.0148	0.7055 ± 0.0151	0.0428 ± 0.0027	0.0361 ± 0.0003
13	0.1011 ± 0.0020	0.7132 ± 0.0168	0.6883 ± 0.0195	0.0549 ± 0.0014	0.0448 ± 0.0003
14	0.0848 ± 0.0023	0.7781 ± 0.0239	0.6402 ± 0.0246	0.0246 ± 0.0002	0.0288 ± 0.0002
15	0.1727 ± 0.0071	0.8135 ± 0.0370	0.6963 ± 0.0379	0.0064 ± 0.0007	0.0062 ± 0.0001
16	0.1943 ± 0.0078	0.8395 ± 0.0367	0.7342 ± 0.0375	0.0060 ± 0.0008	0.0057 ± 0.0001
17	0.1984 ± 0.0082	0.8078 ± 0.0371	0.7200 ± 0.0389	0.0064 ± 0.0009	0.0053 ± 0.0001
18	0.2161 ± 0.0089	0.8297 ± 0.0374	0.7459 ± 0.0389	0.0053 ± 0.0009	0.0049 ± 0.0001
19	0.2069 ± 0.0058	0.8404 ± 0.0259	0.7550 ± 0.0268	0.0125 ± 0.0014	0.0109 ± 0.0001
20	0.1236 ± 0.0042	0.6938 ± 0.0282	0.7174 ± 0.0344	0.0158 ± 0.0005	0.0126 ± 0.0001
21	0.1048 ± 0.0031	0.8248 ± 0.0267	0.6715 ± 0.0265	0.0165 ± 0.0004	0.0198 ± 0.0002
22	0.1924 ± 0.0090	0.8370 ± 0.0429	0.7395 ± 0.0441	0.0041 ± 0.0007	0.0042 ± 0.0001
23	0.2035 ± 0.0096	0.8680 ± 0.0441	0.7371 ± 0.0436	0.0040 ± 0.0007	0.0039 ± 0.0001
24	0.2267 ± 0.0106	0.8581 ± 0.0433	0.7837 ± 0.0447	0.0036 ± 0.0008	0.0036 ± 0.0001
25	0.2249 ± 0.0108	0.8647 ± 0.0445	0.7904 ± 0.0458	0.0034 ± 0.0008	0.0035 ± 0.0001
26	0.2176 ± 0.0074	0.8662 ± 0.0316	0.7910 ± 0.0324	0.0081 ± 0.0012	0.0071 ± 0.0001
27	0.1394 ± 0.0057	0.6694 ± 0.0334	0.7980 ± 0.0446	0.0090 ± 0.0006	0.0077 ± 0.0001
28	0.1177 ± 0.0039	0.8086 ± 0.0299	0.7209 ± 0.0314	0.0119 ± 0.0006	0.0138 ± 0.0001
29	0.2326 ± 0.0123	0.8361 ± 0.0482	0.7674 ± 0.0505	0.0027 ± 0.0007	0.0028 ± 0.0001
30	0.2091 ± 0.0118	0.8631 ± 0.0524	0.8007 ± 0.0544	0.0028 ± 0.0007	0.0027 ± 0.0001
31	0.2459 ± 0.0136	0.8415 ± 0.0507	0.7971 ± 0.0537	0.0026 ± 0.0008	0.0024 ± 0.0001
32	0.2393 ± 0.0141	0.8461 ± 0.0544	0.8347 ± 0.0587	0.0022 ± 0.0007	0.0021 ± 0.0001
33	0.2382 ± 0.0095	0.8365 ± 0.0366	0.7835 ± 0.0387	0.0052 ± 0.0010	0.0047 ± 0.0001
34	0.1484 ± 0.0074	0.5704 ± 0.0375	0.7403 ± 0.0566	0.0071 ± 0.0004	0.0049 ± 0.0001
35	0.1340 ± 0.0050	0.8267 ± 0.0343	0.7440 ± 0.0357	0.0079 ± 0.0006	0.0094 ± 0.0001
36	0.2260 ± 0.0144	0.8000 ± 0.0571	0.7908 ± 0.0635	0.0018 ± 0.0006	0.0019 ± 0.0001
37	0.2612 ± 0.0165	0.8406 ± 0.0579	0.7725 ± 0.0605	0.0018 ± 0.0006	0.0017 ± 0.0001
38	0.2236 ± 0.0156	0.8585 ± 0.0647	0.7954 ± 0.0672	0.0019 ± 0.0006	0.0016 ± 0.0001
39	0.2271 ± 0.0169	0.8122 ± 0.0670	0.7687 ± 0.0723	0.0018 ± 0.0006	0.0014 ± 0.0001
40	0.2503 ± 0.0121	0.8353 ± 0.0443	0.8085 ± 0.0477	0.0032 ± 0.0008	0.0030 ± 0.0001
41	0.1663 ± 0.0101	0.5846 ± 0.0464	0.8365 ± 0.0725	0.0032 ± 0.0003	0.0029 ± 0.0001
42	0.1511 ± 0.0047	0.8351 ± 0.0286	0.7744 ± 0.0302	0.0109 ± 0.0009	0.0121 ± 0.0001
43	0.2335 ± 0.0132	0.8571 ± 0.0522	0.8074 ± 0.0547	0.0027 ± 0.0008	0.0024 ± 0.0001
44	0.2596 ± 0.0144	0.8769 ± 0.0519	0.8316 ± 0.0540	0.0024 ± 0.0008	0.0022 ± 0.0001
45	0.2370 ± 0.0143	0.8681 ± 0.0564	0.8101 ± 0.0585	0.0024 ± 0.0007	0.0021 ± 0.0001
46	0.2764 ± 0.0163	0.8715 ± 0.0550	0.8725 ± 0.0590	0.0018 ± 0.0007	0.0019 ± 0.0001
47	0.2612 ± 0.0112	0.7719 ± 0.0375	0.8487 ± 0.0448	0.0042 ± 0.0010	0.0038 ± 0.0001
48	0.1884 ± 0.0099	0.5452 ± 0.0386	0.8292 ± 0.0645	0.0043 ± 0.0005	0.0035 ± 0.0001
49	0.2059 ± 0.0060	0.8139 ± 0.0265	0.8180 ± 0.0294	0.0091 ± 0.0011	0.0101 ± 0.0001
50	0.2975 ± 0.0164	0.8135 ± 0.0499	0.8609 ± 0.0569	0.0020 ± 0.0008	0.0020 ± 0.0001
51	0.3013 ± 0.0180	0.8530 ± 0.0553	0.8445 ± 0.0596	0.0019 ± 0.0008	0.0017 ± 0.0001
52	0.2820 ± 0.0183	0.8361 ± 0.0593	0.8191 ± 0.0642	0.0019 ± 0.0007	0.0015 ± 0.0001
53	0.2834 ± 0.0194	0.8411 ± 0.0627	0.8611 ± 0.0692	0.0014 ± 0.0006	0.0014 ± 0.0001
54	0.3087 ± 0.0151	0.6388 ± 0.0391	0.8464 ± 0.0563	0.0028 ± 0.0008	0.0024 ± 0.0001
55	0.2603 ± 0.0160	0.4302 ± 0.0403	0.7983 ± 0.0837	0.0018 ± 0.0003	0.0018 ± 0.0001

Table A.13: *Values of efficiencies and $\omega_i^{\rm data}$ for $B^0 \to J/\psi K^{*0}$ 2012 decays using the B^0 binning scheme.*

Bin	$\varepsilon^{\rm sel}$	$\varepsilon^{\rm PID}$	$\varepsilon^{\rm trig}$	$\omega_i^{\rm data}$	ω_i
A	0.0163 ± 0.0006	0.6589 ± 0.0310	0.4624 ± 0.0320	0.0478 ± 0.0030	0.0554 ± 0.0003
B	0.0417 ± 0.0021	0.7445 ± 0.0426	0.5163 ± 0.0411	0.0110 ± 0.0004	0.0130 ± 0.0001
C	0.0495 ± 0.0023	0.7328 ± 0.0397	0.4824 ± 0.0377	0.0115 ± 0.0004	0.0123 ± 0.0001
D	0.0528 ± 0.0024	0.7548 ± 0.0399	0.4622 ± 0.0360	0.0138 ± 0.0004	0.0118 ± 0.0001
E	0.0563 ± 0.0026	0.7643 ± 0.0396	0.5415 ± 0.0381	0.0112 ± 0.0003	0.0114 ± 0.0001
F	0.0604 ± 0.0017	0.7585 ± 0.0248	0.5229 ± 0.0236	0.0268 ± 0.0002	0.0270 ± 0.0002
G	0.0316 ± 0.0010	0.7366 ± 0.0270	0.5390 ± 0.0269	0.0387 ± 0.0011	0.0421 ± 0.0002
0	0.0247 ± 0.0005	0.7367 ± 0.0181	0.5455 ± 0.0182	0.1320 ± 0.0031	0.1192 ± 0.0003
1	0.0680 ± 0.0018	0.7851 ± 0.0238	0.5991 ± 0.0235	0.0290 ± 0.0006	0.0267 ± 0.0002
2	0.0795 ± 0.0020	0.7747 ± 0.0224	0.5767 ± 0.0219	0.0310 ± 0.0009	0.0256 ± 0.0002
3	0.0915 ± 0.0022	0.7821 ± 0.0216	0.5959 ± 0.0213	0.0271 ± 0.0011	0.0242 ± 0.0002
4	0.0961 ± 0.0024	0.7936 ± 0.0220	0.6177 ± 0.0218	0.0255 ± 0.0013	0.0224 ± 0.0002
5	0.0946 ± 0.0015	0.8003 ± 0.0144	0.5972 ± 0.0139	0.0649 ± 0.0027	0.0539 ± 0.0003
6	0.0538 ± 0.0010	0.7595 ± 0.0158	0.5992 ± 0.0161	0.0832 ± 0.0018	0.0746 ± 0.0003
7	0.0484 ± 0.0008	0.7774 ± 0.0155	0.6445 ± 0.0159	0.0873 ± 0.0017	0.0885 ± 0.0003
8	0.1138 ± 0.0028	0.7860 ± 0.0215	0.7031 ± 0.0229	0.0191 ± 0.0015	0.0197 ± 0.0002
9	0.1399 ± 0.0032	0.7998 ± 0.0204	0.6654 ± 0.0208	0.0191 ± 0.0018	0.0181 ± 0.0001
10	0.1455 ± 0.0033	0.8279 ± 0.0208	0.7147 ± 0.0212	0.0166 ± 0.0018	0.0174 ± 0.0001
11	0.1615 ± 0.0036	0.8337 ± 0.0206	0.6980 ± 0.0206	0.0158 ± 0.0019	0.0160 ± 0.0001
12	0.1593 ± 0.0024	0.8134 ± 0.0136	0.7065 ± 0.0140	0.0358 ± 0.0030	0.0363 ± 0.0002
13	0.0883 ± 0.0016	0.7060 ± 0.0150	0.6927 ± 0.0176	0.0467 ± 0.0015	0.0470 ± 0.0002
14	0.0711 ± 0.0018	0.7927 ± 0.0227	0.6966 ± 0.0239	0.0255 ± 0.0009	0.0284 ± 0.0002
15	0.1523 ± 0.0056	0.8265 ± 0.0337	0.7500 ± 0.0354	0.0058 ± 0.0011	0.0063 ± 0.0001
16	0.1778 ± 0.0063	0.8316 ± 0.0326	0.7730 ± 0.0344	0.0050 ± 0.0012	0.0058 ± 0.0001
17	0.2056 ± 0.0072	0.8525 ± 0.0321	0.7716 ± 0.0331	0.0043 ± 0.0012	0.0053 ± 0.0001
18	0.2106 ± 0.0074	0.8323 ± 0.0321	0.7716 ± 0.0339	0.0041 ± 0.0012	0.0050 ± 0.0001
19	0.1931 ± 0.0048	0.8247 ± 0.0224	0.7704 ± 0.0239	0.0101 ± 0.0017	0.0112 ± 0.0001
20	0.1176 ± 0.0034	0.6486 ± 0.0232	0.7728 ± 0.0315	0.0111 ± 0.0008	0.0134 ± 0.0001
21	0.0894 ± 0.0024	0.8154 ± 0.0245	0.7591 ± 0.0262	0.0170 ± 0.0011	0.0199 ± 0.0002
22	0.1829 ± 0.0075	0.8203 ± 0.0369	0.8053 ± 0.0404	0.0036 ± 0.0010	0.0043 ± 0.0001
23	0.1863 ± 0.0077	0.8345 ± 0.0379	0.7769 ± 0.0401	0.0039 ± 0.0011	0.0041 ± 0.0001
24	0.2195 ± 0.0089	0.8415 ± 0.0371	0.7981 ± 0.0394	0.0031 ± 0.0011	0.0037 ± 0.0001
25	0.2128 ± 0.0091	0.8517 ± 0.0395	0.8151 ± 0.0419	0.0027 ± 0.0010	0.0034 ± 0.0001
26	0.2165 ± 0.0061	0.8408 ± 0.0259	0.8021 ± 0.0276	0.0063 ± 0.0015	0.0076 ± 0.0001
27	0.1265 ± 0.0043	0.6313 ± 0.0273	0.7929 ± 0.0385	0.0075 ± 0.0008	0.0088 ± 0.0001
28	0.1031 ± 0.0031	0.8217 ± 0.0275	0.7741 ± 0.0294	0.0120 ± 0.0011	0.0139 ± 0.0001
29	0.2006 ± 0.0095	0.8307 ± 0.0433	0.7853 ± 0.0462	0.0025 ± 0.0009	0.0029 ± 0.0001
30	0.2226 ± 0.0104	0.8162 ± 0.0423	0.8499 ± 0.0477	0.0023 ± 0.0010	0.0027 ± 0.0001
31	0.2184 ± 0.0108	0.8382 ± 0.0453	0.8099 ± 0.0487	0.0023 ± 0.0010	0.0025 ± 0.0001
32	0.2447 ± 0.0120	0.8541 ± 0.0452	0.8319 ± 0.0483	0.0019 ± 0.0009	0.0022 ± 0.0001
33	0.2427 ± 0.0081	0.8025 ± 0.0299	0.8220 ± 0.0338	0.0041 ± 0.0013	0.0049 ± 0.0001
34	0.1510 ± 0.0060	0.5805 ± 0.0304	0.8050 ± 0.0470	0.0047 ± 0.0006	0.0055 ± 0.0001
35	0.1313 ± 0.0043	0.8380 ± 0.0300	0.7644 ± 0.0313	0.0077 ± 0.0011	0.0093 ± 0.0001
36	0.2345 ± 0.0126	0.8052 ± 0.0480	0.8612 ± 0.0554	0.0015 ± 0.0008	0.0020 ± 0.0001
37	0.2227 ± 0.0125	0.8805 ± 0.0526	0.8250 ± 0.0543	0.0017 ± 0.0009	0.0019 ± 0.0001
38	0.2547 ± 0.0141	0.8549 ± 0.0514	0.8376 ± 0.0550	0.0014 ± 0.0008	0.0017 ± 0.0001
39	0.2307 ± 0.0141	0.8459 ± 0.0564	0.7689 ± 0.0585	0.0015 ± 0.0008	0.0015 ± 0.0000
40	0.2549 ± 0.0102	0.7701 ± 0.0352	0.8413 ± 0.0419	0.0026 ± 0.0010	0.0032 ± 0.0001
41	0.1658 ± 0.0080	0.5399 ± 0.0356	0.8044 ± 0.0591	0.0027 ± 0.0005	0.0034 ± 0.0001
42	0.1437 ± 0.0039	0.8093 ± 0.0243	0.8049 ± 0.0269	0.0108 ± 0.0015	0.0126 ± 0.0001
43	0.2340 ± 0.0108	0.8372 ± 0.0421	0.8611 ± 0.0466	0.0022 ± 0.0010	0.0027 ± 0.0001
44	0.2455 ± 0.0119	0.8821 ± 0.0456	0.8503 ± 0.0477	0.0021 ± 0.0010	0.0023 ± 0.0001
45	0.2442 ± 0.0121	0.8452 ± 0.0456	0.8663 ± 0.0502	0.0019 ± 0.0010	0.0022 ± 0.0001
46	0.2825 ± 0.0143	0.8499 ± 0.0465	0.8353 ± 0.0500	0.0016 ± 0.0010	0.0018 ± 0.0001
47	0.2596 ± 0.0093	0.7727 ± 0.0314	0.8645 ± 0.0378	0.0034 ± 0.0012	0.0040 ± 0.0001
48	0.1640 ± 0.0073	0.4920 ± 0.0313	0.8016 ± 0.0570	0.0042 ± 0.0006	0.0040 ± 0.0001
49	0.1952 ± 0.0049	0.8030 ± 0.0224	0.8315 ± 0.0254	0.0095 ± 0.0018	0.0108 ± 0.0001
50	0.2972 ± 0.0141	0.7964 ± 0.0422	0.8736 ± 0.0495	0.0018 ± 0.0011	0.0020 ± 0.0001
51	0.2796 ± 0.0137	0.8461 ± 0.0451	0.8239 ± 0.0484	0.0019 ± 0.0010	0.0020 ± 0.0001
52	0.2805 ± 0.0147	0.8154 ± 0.0474	0.8547 ± 0.0537	0.0016 ± 0.0009	0.0017 ± 0.0001
53	0.2739 ± 0.0157	0.7928 ± 0.0511	0.8672 ± 0.0600	0.0014 ± 0.0009	0.0015 ± 0.0000
54	0.2895 ± 0.0115	0.6389 ± 0.0317	0.8501 ± 0.0457	0.0026 ± 0.0010	0.0029 ± 0.0001
55	0.2443 ± 0.0117	0.3995 ± 0.0302	0.8857 ± 0.0711	0.0019 ± 0.0005	0.0024 ± 0.0001

Table A.14: *Values of ω_i for $B_s^0 \to D_s^- \pi^+$ 2011 and 2012 decays determined from simulation using the B_s^0 binning scheme.*

Bin	$\omega_i^{B_s^0 \to D_s^- \pi^+}$ (2011)	Bin	$\omega_i^{B_s^0 \to D_s^- \pi^+}$ (2012)
0	0.36648 ± 0.00021	0	0.35546 ± 0.00021
1	0.09728 ± 0.00011	1	0.09560 ± 0.00011
2	0.25154 ± 0.00017	2	0.25454 ± 0.00018
3	0.08500 ± 0.00010	3	0.08474 ± 0.00010
4	0.02098 ± 0.00005	4	0.02161 ± 0.00005
5	0.04817 ± 0.00008	5	0.05066 ± 0.00008
6	0.03987 ± 0.00007	6	0.04033 ± 0.00007
7	0.00947 ± 0.00003	7	0.00976 ± 0.00003
8	0.01966 ± 0.00005	8	0.02109 ± 0.00005
9	0.03865 ± 0.00007	9	0.04037 ± 0.00007
10	0.00848 ± 0.00003	10	0.00901 ± 0.00003
11	0.01443 ± 0.00004	11	0.01682 ± 0.00005

A.6 Systematic uncertainties in kinematic bins

Table A.15: *Systematic uncertainties on $A_{\rm P}(B^+)$ from $B^+ \to J/\psi K^+$ 2011 decays corresponding to each kinematic bin. No value is reported when it turns out to be less than* 0.0001. *The various acronyms refer to: signal mass shape (SMS), combinatorial background mass shape (BMS) and final state radiation (FSR).*

Bin	SMS	BMS	FSR	Bin	SMS	BMS	FSR
0	–	–	–	28	0.0001	–	–
1	–	–	–	29	0.0002	–	–
2	–	–	–	30	–	–	–
3	–	–	–	31	0.0005	–	–
4	–	–	–	32	0.0008	–	–
5	–	–	–	33	0.0007	–	–
6	–	–	–	34	0.0005	0.0007	–
7	0.0002	–	–	35	0.0007	–	–
8	0.0001	–	–	36	0.0002	0.0003	–
9	0.0003	–	–	37	0.0005	0.0001	–
10	–	–	–	38	0.0006	–	–
11	–	–	–	39	0.0006	0.0002	–
12	–	–	–	40	0.0015	–	–
13	–	–	–	41	–	–	–
14	0.0003	–	–	42	0.0004	–	–
15	0.0001	–	–	43	0.0003	–	–
16	0.0005	–	–	44	0.0004	–	–
17	0.0006	–	–	45	0.0003	–	–
18	0.0002	–	–	46	0.0002	0.0004	–
19	–	–	–	47	0.0011	0.0004	–
20	0.0005	–	–	48	0.0004	–	–
21	–	–	–	49	0.0002	0.0002	–
22	–	–	–	50	0.0005	–	–
23	0.0004	0.0002	–	51	0.0011	0.0006	–
24	–	0.0033	–	52	0.0003	–	–
25	0.0004	–	–	53	0.0019	0.0004	–
26	0.0002	–	–	54	0.0002	0.0012	–
27	0.0001	–	–	55	0.0002	0.0027	–

Bin	SMS	BMS	FSR
A	–	–	–
B	0.0003	–	–
C	0.0001	–	–
D	–	–	–
E	–	–	–
F	–	–	–
G	–	–	–

Table A.16: *Systematic uncertainties on $A_{\rm P}(B^+)$ from $B^+ \to J/\psi K^+$ 2012 decays corresponding to each kinematic bin. No value is reported when it turns out to be less than* 0.0001*. The various acronyms refer to: signal mass shape (SMS), combinatorial background mass shape (BMS) and final state radiation varied (FSR).*

Bin	SMS	BMS	FSR	Bin	SMS	BMS	FSR
0	–	–	–	28	0.0001	–	–
1	–	–	–	29	0.0002	0.0001	–
2	–	–	–	30	0.0002	–	–
3	–	–	–	31	0.0004	0.0002	–
4	–	–	–	32	–	–	–
5	–	–	–	33	0.0002	0.0001	–
6	–	–	–	34	0.0003	0.0002	–
7	–	–	–	35	0.0004	0.0001	–
8	–	–	–	36	0.0003	0.0001	–
9	0.0002	–	–	37	0.0002	–	–
10	–	–	–	38	0.0004	0.0002	–
11	0.0001	–	–	39	0.0002	0.0003	–
12	–	–	–	40	0.0003	0.0001	–
13	–	–	–	41	–	–	–
14	0.0001	–	–	42	–	–	–
15	0.0002	0.0001	–	43	0.0008	–	–
16	0.0001	–	–	44	0.0005	–	–
17	0.0002	–	–	45	0.0009	0.0004	–
18	0.0003	0.0001	–	46	0.0003	–	–
19	0.0001	–	–	47	0.0003	0.0001	–
20	–	–	–	48	–	–	–
21	0.0001	–	–	49	–	–	–
22	0.0002	–	–	50	0.0005	0.0002	–
23	0.0002	–	–	51	0.0012	0.0001	–
24	0.0001	–	–	52	0.0002	–	–
25	0.0002	–	–	53	0.0003	–	–
26	0.0002	–	–	54	–	0.0003	–
27	–	–	–	55	0.0004	0.0004	–

Bin	SMS	BMS	FSR
A	–	–	–
B	–	–	–
C	0.0001	–	–
D	0.0002	–	–
E	–	–	–
F	–	–	–
G	–	–	–

Table A.17: *Systematic uncertainties on $A_{\rm P}(B^0)$ from $B^0 \to J/\psi\, K^{*0}$ 2011 decays corresponding to each kinematic bin. No value is reported when it turns out to be less than* 0.0001. *The various acronyms refer to: signal mass shape (SMS), decay time bias (DTB), decay time resolution (DTR), final state radiation (FSR), decay time acceptance (DTA), combinatorial background mass shape (CMS). In the last column we report the total systematic uncertainty.*

Bin	SMS	DTB	Δm_d	$\lvert q/p\rvert_{B^0}$	DTR	FSR	DTA	CMS	Total
0	0.0013	-	0.0005	0.0009	-	0.0005	0.0002	-	0.0017
1	0.0007	0.0003	0.0003	0.0009	0.0003	0.0002	0.0003	0.0003	0.0013
2	-	0.0002	0.0002	0.0009	0.0001	0.0002	0.0002	0.0001	0.0010
3	-	-	0.0002	0.0009	-	-	-	-	0.0009
4	0.0011	0.0001	0.0002	0.0009	0.0001	-	0.0003	0.0001	0.0015
5	0.0027	-	-	0.0009	-	-	-	-	0.0028
6	0.0010	-	0.0001	0.0009	-	-	-	-	0.0013
7	0.0038	-	0.0002	0.0009	-	0.0002	0.0003	-	0.0039
8	-	-	0.0004	0.0009	-	0.0001	-	-	0.0010
9	0.0016	-	0.0002	0.0009	-	0.0002	-	-	0.0019
10	0.0011	-	0.0002	0.0009	-	0.0008	0.0001	-	0.0016
11	0.0011	-	0.0001	0.0009	-	0.0004	-	-	0.0015
12	0.0005	-	-	0.0009	-	0.0002	-	-	0.0010
13	0.0009	-	-	0.0009	-	0.0003	0.0002	-	0.0013
14	0.0018	-	-	0.0009	-	0.0010	-	0.0010	0.0025
15	0.0004	-	0.0005	0.0009	-	0.0012	0.0006	-	0.0017
16	0.0029	-	0.0005	0.0009	-	0.0002	0.0002	0.0002	0.0031
17	0.0046	-	0.0002	0.0009	-	0.0004	-	-	0.0047
18	0.0036	0.0003	0.0003	0.0009	0.0003	0.0008	0.0003	0.0003	0.0039
19	0.0015	0.0001	0.0002	0.0009	-	0.0001	0.0002	0.0001	0.0018
20	0.0007	-	-	0.0009	-	0.0013	-	0.0003	0.0018
21	0.0086	-	0.0003	0.0009	-	0.0003	0.0004	0.0002	0.0087
22	0.0025	0.0001	0.0003	0.0009	-	0.0005	0.0005	-	0.0028
23	0.0040	-	-	0.0009	-	0.0011	0.0005	-	0.0043
24	0.0011	0.0003	0.0002	0.0009	0.0002	0.0018	0.0004	0.0003	0.0024
25	0.0002	0.0001	0.0003	0.0009	0.0001	0.0007	0.0001	0.0007	0.0014
26	0.0030	0.0001	0.0002	0.0009	0.0001	0.0003	0.0002	0.0001	0.0032
27	0.0020	0.0001	0.0002	0.0009	0.0002	0.0009	0.0007	0.0002	0.0025
28	0.0088	-	0.0002	0.0009	-	0.0006	0.0003	-	0.0089
29	0.0030	0.0009	0.0006	0.0009	0.0010	0.0007	0.0007	0.0006	0.0036
30	0.0011	-	0.0002	0.0009	-	0.0009	0.0001	-	0.0017
31	0.0012	0.0002	0.0011	0.0009	0.0001	0.0012	0.0004	0.0002	0.0023
32	0.0004	-	-	0.0009	-	-	0.0006	0.0001	0.0012
33	0.0007	-	0.0006	0.0009	-	0.0008	0.0006	-	0.0016
34	0.0017	-	0.0004	0.0009	-	0.0007	0.0001	-	0.0021
35	0.0011	-	-	0.0009	-	0.0017	0.0002	0.0004	0.0023
36	0.0019	-	0.0009	0.0009	-	0.0008	-	0.0037	0.0044
37	0.0038	0.0002	0.0006	0.0009	0.0002	0.0003	0.0001	-	0.0040
38	0.0015	-	0.0005	0.0009	-	0.0010	0.0009	0.0007	0.0024
39	0.0022	-	0.0004	0.0009	-	0.0003	0.0007	0.0002	0.0025
40	0.0028	-	0.0003	0.0009	-	0.0021	0.0003	0.0007	0.0037
41	-	-	0.0005	0.0009	-	0.0014	0.0003	-	0.0018
42	0.0007	0.0019	0.0020	0.0009	0.0018	0.0003	0.0001	0.0018	0.0039
43	0.0039	0.0001	0.0009	0.0009	0.0001	0.0006	0.0001	0.0001	0.0042
44	0.0014	0.0014	0.0014	0.0009	0.0012	0.0032	0.0016	0.0008	0.0046
45	0.0024	-	0.0001	0.0009	-	0.0009	0.0007	0.0029	0.0040
46	0.0004	0.0004	0.0008	0.0009	0.0004	0.0019	0.0017	0.0003	0.0029
47	0.0018	-	0.0003	0.0009	-	0.0003	0.0001	-	0.0021
48	0.0001	0.0001	0.0002	0.0009	0.0001	0.0008	0.0008	0.0027	0.0031
49	0.0009	-	0.0001	0.0009	-	0.0005	0.0002	-	0.0014
50	0.0032	-	0.0005	0.0009	-	0.0002	-	0.0004	0.0034
51	0.0020	-	-	0.0009	-	0.0021	0.0001	0.0039	0.0049
52	0.0010	0.0002	0.0004	0.0009	0.0002	0.0019	0.0011	0.0002	0.0026
53	0.0004	-	0.0003	0.0009	-	0.0015	0.0003	0.0001	0.0018
54	0.0022	0.0004	0.0005	0.0009	0.0004	0.0008	0.0005	0.0006	0.0027
55	0.0023	-	0.0003	0.0009	-	0.0008	0.0014	0.0005	0.0030
A	0.0001	0.0001	0.0001	0.0009	0.0001	0.0002	0.0004	-	0.0010
B	-	-	0.0002	0.0009	-	0.0017	0.0004	-	0.0020
C	0.0022	-	0.0001	0.0009	-	0.0004	0.0001	-	0.0024
D	0.0034	0.0002	0.0005	0.0009	0.0003	0.0011	0.0003	0.0002	0.0038
E	0.0033	-	0.0002	0.0009	0.0001	0.0003	0.0003	0.0005	0.0035
F	0.0005	-	-	0.0009	-	-	0.0003	-	0.0011
G	-	-	0.0003	0.0009	-	0.0006	0.0006	0.0003	0.0013

Table A.18: *Systematic uncertainties on $A_{\rm P}(B^0)$ from $B^0 \to J/\psi\, K^{*0}$ 2012 decays corresponding to each kinematic bin. No value is reported when it turns out to be less than* 0.0001. *The various acronyms refer to: signal mass shape (SMS), decay time bias (DTB), decay time resolution (DTR), final state radiation (FSR), decay time acceptance (DTA), combinatorial background mass shape (CMS). In the last column we report the total systematic uncertainty.*

Bin	SMS	DTB	Δm_s	$\lvert q/p\rvert_{B^0}$	DTR	FSR	DTA	CMS	Total
0	0.0010	-	-	0.0009	-	-	-	-	0.0013
1	-	-	-	0.0009	-	-	-	-	0.0009
2	-	-	0.0001	0.0009	-	-	0.0001	-	0.0009
3	-	-	0.0001	0.0009	-	-	0.0002	-	0.0009
4	-	0.0002	0.0004	0.0009	0.0002	0.0003	0.0004	0.0003	0.0012
5	-	-	-	0.0009	-	-	-	-	0.0009
6	-	-	-	0.0009	-	-	-	-	0.0009
7	0.0026	-	-	0.0009	-	-	-	-	0.0028
8	0.0025	-	0.0003	0.0009	-	-	0.0001	-	0.0027
9	0.0027	-	-	0.0009	-	-	0.0001	-	0.0028
10	0.0018	-	-	0.0009	-	-	-	-	0.0020
11	0.0004	-	0.0002	0.0009	-	-	-	-	0.0010
12	0.0003	-	0.0001	0.0009	-	-	-	-	0.0010
13	0.0005	-	0.0002	0.0009	-	-	-	-	0.0010
14	0.0027	-	0.0001	0.0009	-	-	-	-	0.0028
15	0.0011	-	-	0.0009	-	-	0.0002	-	0.0014
16	0.0022	0.0002	0.0006	0.0009	0.0002	0.0002	0.0004	0.0002	0.0025
17	0.0008	-	0.0002	0.0009	-	-	-	-	0.0012
18	0.0009	-	-	0.0009	-	-	-	-	0.0013
19	0.0043	0.0002	0.0004	0.0009	0.0002	0.0002	0.0004	0.0002	0.0044
20	0.0020	0.0001	0.0001	0.0009	-	0.0001	0.0002	-	0.0022
21	0.0014	-	-	0.0009	-	-	-	-	0.0017
22	0.0008	-	0.0002	0.0009	-	-	0.0005	-	0.0013
23	0.0005	-	-	0.0009	-	-	-	-	0.0010
24	0.0021	-	-	0.0009	-	-	0.0003	-	0.0023
25	0.0009	0.0007	0.0011	0.0009	0.0007	0.0008	0.0011	0.0008	0.0025
26	0.0001	-	0.0002	0.0009	-	-	0.0001	-	0.0009
27	0.0033	-	-	0.0009	-	-	0.0001	-	0.0034
28	0.0020	-	0.0001	0.0009	-	-	-	-	0.0022
29	0.0048	-	-	0.0009	-	-	-	0.0010	0.0050
30	0.0018	-	0.0003	0.0009	-	-	0.0003	-	0.0021
31	0.0058	0.0001	0.0004	0.0009	-	0.0001	0.0004	-	0.0059
32	0.0033	-	0.0003	0.0009	-	-	-	-	0.0034
33	0.0009	-	0.0002	0.0009	-	-	0.0002	-	0.0013
34	0.0024	-	0.0002	0.0009	-	-	0.0003	-	0.0026
35	0.0055	-	-	0.0009	-	-	0.0002	-	0.0056
36	0.0024	-	0.0003	0.0009	-	-	0.0001	-	0.0026
37	0.0065	-	0.0002	0.0009	-	-	-	0.0001	0.0066
38	0.0007	-	0.0002	0.0009	-	-	-	0.0001	0.0012
39	0.0039	-	0.0004	0.0009	-	-	0.0004	-	0.0040
40	0.0082	0.0001	0.0002	0.0009	-	-	0.0001	-	0.0083
41	-	-	-	0.0009	-	-	-	-	0.0009
42	0.0005	-	-	0.0009	-	-	0.0001	-	0.0010
43	0.0023	-	0.0006	0.0009	0.0001	-	0.0003	-	0.0026
44	0.0002	-	0.0002	0.0009	-	-	0.0003	-	0.0010
45	0.0014	-	0.0001	0.0009	-	-	0.0002	-	0.0017
46	0.0019	-	0.0002	0.0009	-	-	0.0001	0.0003	0.0021
47	0.0044	-	0.0002	0.0009	-	-	-	-	0.0045
48	0.0021	0.0005	0.0010	0.0009	0.0005	0.0005	0.0005	0.0004	0.0027
49	0.0008	-	-	0.0009	-	-	0.0002	-	0.0012
50	0.0037	-	0.0001	0.0009	-	-	0.0001	-	0.0038
51	0.0017	-	0.0002	0.0009	-	-	0.0006	-	0.0020
52	0.0013	-	0.0002	0.0009	-	-	-	0.0003	0.0016
53	0.0023	-	-	0.0009	-	-	-	0.0001	0.0025
54	0.0009	-	0.0002	0.0009	-	-	0.0002	0.0002	0.0013
55	0.0040	0.0003	0.0006	0.0009	0.0003	-	0.0002	0.0008	0.0042
A	-	-	0.0001	0.0009	-	-	-	-	0.0009
B	-	0.0005	0.0009	0.0009	0.0005	0.0004	0.0007	0.0005	0.0017
C	-	-	0.0002	0.0009	-	-	0.0006	-	0.0011
D	-	0.0013	0.0014	0.0009	0.0013	0.0013	0.0014	0.0012	0.0034
E	-	0.0004	0.0007	0.0009	0.0004	0.0003	0.0009	0.0003	0.0016
F	-	-	0.0003	0.0009	-	-	-	-	0.0009
G	-	-	-	0.0009	-	-	0.0003	0.0001	0.0010

Table A.19: *Systematic uncertainties on* $A_{\rm P}(B_s^0)$ *from* $B_s^0 \to D_s^-\pi^+$ *2011 decays corresponding to each kin ematic bin. No value is reported when it turns out to be less than* 0.0001*. The various acronyms refer to: signal mass shape (SMS), decay time bias (DTB), decay time resolution (DTR), final state radiation (FSR), decay time acceptance (DTA), combinatorial background mass shape (CMS) and partially reconstructed background mass shape (PMS). In the last column we report the total systematic uncertainty.*

Bin	SMS	DTB	$\Delta\Gamma_s$	Δm_s	$\lvert q/p\rvert_{B_s^0}$	DTR	FSR	DTA	CMS	PMS	Total
0	0.0105	0.0010	-	0.0021	0.0021	0.0016	-	-	0.0006	0.0058	0.0125
1	0.0034	0.0068	0.0002	0.0114	0.0021	0.0047	0.0002	-	0.0002	0.0038	0.0151
2	0.0010	0.0003	-	0.0020	0.0021	0.0101	-	0.0001	0.0008	0.0079	0.0132
3	0.0009	0.0038	-	0.0040	0.0021	0.0029	-	-	0.0005	0.0013	0.0068
4	0.0030	0.0007	0.0001	0.0019	0.0021	0.0018	0.0001	-	-	0.0119	0.0127
5	0.0075	0.0018	-	0.0030	0.0021	0.0002	-	-	0.0004	0.0025	0.0089
6	0.0009	0.0008	-	0.0028	0.0021	0.0007	0.0002	-	0.0001	0.0115	0.0121
7	0.0010	0.0005	0.0002	0.0018	0.0021	0.0122	0.0003	-	0.0022	0.0125	0.0179
8	-	0.0005	0.0002	0.0022	0.0021	0.0070	-	-	0.0116	0.0160	0.0212
9	0.0011	0.0013	-	0.0015	0.0021	0.0038	-	-	0.0003	0.0037	0.0061
10	0.0080	0.0008	-	0.0001	0.0021	0.0065	0.0002	-	0.0011	0.0009	0.0106
11	0.0023	0.0033	0.0024	0.0012	0.0021	0.0100	0.0025	0.0023	0.0029	0.0088	0.0150

Table A.20: *Systematic uncertainties on* $A_{\rm P}(B_s^0)$ *from* $B_s^0 \to D_s^-\pi^+$ *2012 decays corresponding to each kin ematic bin. No value is reported when it turns out to be less than* 0.0001*. The various acronyms refer to: signal mass shape (SMS), decay time bias (DTB), decay time resolution (DTR), final state radiation (FSR), decay time acceptance (DTA), combinatorial background mass shape (CMS) and partially reconstructed background mass shape (PMS). In the last column we report the total systematic uncertainty.*

Bin	SMS	DTB	$\Delta\Gamma_s$	Δm_s	$\lvert q/p\rvert_{B_s^0}$	DTR	FSR	DTA	CMS	PMS	Total
0	0.0046	0.0052	0.0031	0.0067	0.0021	0.0082	0.0032	0.0030	0.0025	0.0050	0.0150
1	0.0028	0.0027	0.0005	0.0035	0.0021	0.0042	0.0005	0.0020	0.0005	0.0028	0.0079
2	0.0018	0.0015	0.0014	0.0036	0.0021	0.0029	0.0014	0.0013	0.0013	0.0068	0.0092
3	0.0017	0.0009	0.0003	0.0012	0.0021	0.0057	0.0004	0.0002	0.0003	0.0017	0.0067
4	0.0035	0.0012	0.0005	0.0042	0.0021	0.0115	0.0004	0.0071	0.0022	0.0040	0.0155
5	0.0006	0.0011	0.0005	0.0028	0.0021	0.0050	0.0005	0.0025	0.0025	0.0033	0.0079
6	0.0044	0.0012	0.0009	0.0014	0.0021	0.0014	0.0010	0.0027	0.0008	0.0006	0.0063
7	0.0065	0.0029	0.0022	0.0064	0.0021	0.0077	0.0024	0.0090	0.0066	0.0008	0.0171
8	0.0021	0.0010	0.0006	0.0032	0.0021	0.0065	0.0006	0.0044	0.0019	0.0046	0.0104
9	0.0003	0.0013	0.0005	0.0009	0.0021	0.0013	0.0005	0.0006	0.0005	0.0039	0.0050
10	0.0030	0.0023	0.0009	0.0034	0.0021	0.0056	0.0008	0.0042	0.0034	0.0131	0.0162
11	0.0050	0.0035	0.0014	0.0045	0.0021	0.0077	0.0014	0.0054	0.0002	-	0.0124

A.7 Correlation matrices for $A_{\rm P}(\Lambda_b^0)$

Table A.21: *Correlations amongst the bins for the measurement of the Λ_b^0 production asymmetry, using data collected at $\sqrt{s} = 7$ TeV.*

Bin	0	1	2	3	4	5	6	7	8	9	10	11
0	1.000	0.008	0.005	0.006	0.009	0.007	0.005	0.001	0.009	0.008	0.009	0.010
1	0.008	1.000	0.012	0.008	0.010	0.009	0.012	0.002	-0.001	0.005	0.006	0.011
2	0.005	0.012	1.000	0.011	0.007	0.009	0.006	0.007	0.004	0.011	0.001	0.008
3	0.006	0.008	0.011	1.000	0.008	0.006	0.002	0.005	0.001	0.009	-0.001	0.007
4	0.009	0.010	0.007	0.008	1.000	0.007	0.008	0.005	0.008	0.007	0.008	0.003
5	0.007	0.009	0.009	0.006	0.007	1.000	0.005	0.013	0.007	0.017	0.007	-0.003
6	0.005	0.012	0.006	0.002	0.008	0.005	1.000	0.001	0.007	0.010	0.007	0.004
7	0.001	0.002	0.007	0.005	0.005	0.013	0.001	1.000	0.003	0.006	0.009	0.006
8	0.009	-0.001	0.004	0.001	0.008	0.007	0.007	0.003	1.000	0.006	0.003	0.001
9	0.008	0.005	0.011	0.009	0.007	0.017	0.010	0.006	0.006	1.000	0.007	0.006
10	0.009	0.006	0.001	-0.001	0.008	0.007	0.007	0.009	0.003	0.007	1.000	-0.003
11	0.010	0.011	0.008	0.007	0.003	-0.003	0.004	0.006	0.001	0.006	-0.003	1.000

Table A.22: *Correlations amongst the bins for the measurement of the Λ_b^0 production asymmetry, using data collected at $\sqrt{s} = 8$ TeV.*

Bin	0	1	2	3	4	5	6	7	8	9	10	11
0	1.000	0.040	0.050	0.034	0.029	0.031	0.034	0.018	0.022	0.038	0.026	0.024
1	0.040	1.000	0.044	0.032	0.022	0.023	0.030	0.015	0.014	0.028	0.020	0.021
2	0.050	0.044	1.000	0.040	0.029	0.037	0.026	0.020	0.021	0.038	0.017	0.023
3	0.034	0.032	0.040	1.000	0.018	0.022	0.018	0.015	0.014	0.024	0.008	0.015
4	0.029	0.022	0.029	0.018	1.000	0.019	0.020	0.014	0.017	0.021	0.012	0.011
5	0.031	0.023	0.037	0.022	0.019	1.000	0.019	0.019	0.018	0.030	0.012	0.004
6	0.034	0.030	0.026	0.018	0.020	0.019	1.000	0.007	0.014	0.023	0.016	0.009
7	0.018	0.015	0.020	0.015	0.014	0.019	0.007	1.000	0.007	0.014	0.013	0.011
8	0.022	0.014	0.021	0.014	0.017	0.018	0.014	0.007	1.000	0.017	0.004	0.006
9	0.038	0.028	0.038	0.024	0.021	0.030	0.023	0.014	0.017	1.000	0.016	0.016
10	0.026	0.020	0.017	0.008	0.012	0.012	0.016	0.013	0.004	0.016	1.000	0.000
11	0.024	0.021	0.023	0.015	0.011	0.004	0.009	0.011	0.006	0.016	0.000	1.000

Table A.23: *Correlations amongst the bins used for the measurement of the Λ_b^0 production asymmetry as a function of $p_{\rm T}$ of the Λ_b^0, for data collected at (left) $\sqrt{s} = 7$ TeV and (right) $\sqrt{s} = 8$ TeV.*

Bin	0	1	2	3	0	1	2	3
0	1.000	0.020	0.019	0.022	1.000	0.054	0.046	0.050
1	0.020	1.000	0.010	0.018	0.054	1.000	0.035	0.041
2	0.019	0.010	1.000	0.013	0.046	0.035	1.000	0.033
3	0.022	0.018	0.013	1.000	0.050	0.041	0.033	1.000

Table A.24: *Correlations amongst the bins used for the measurement of the Λ_b^0 production asymmetry as a function of y of the Λ_b^0, for data collected at (left) $\sqrt{s} = 7$ TeV and (right) $\sqrt{s} = 8$ TeV.*

Bin	0	1	2	0	1	2
0	1.000	0.022	0.022	1.000	0.049	0.056
1	0.022	1.000	0.016	0.049	1.000	0.040
2	0.022	0.016	1.000	0.056	0.040	1.000

A.8 Fits to $A_{\rm P}(\Lambda_b^0)$ dependencies on $p_{\rm T}$ and y

Table A.25: *Parameters obtained from the fit to the data points for each mode using a constant or a straight line.*

	$\Lambda_b^0(2011)$	$\Lambda_b^0(2012)$
Fit p_T		
Constant		
q	0.008 ± 0.026	0.036 ± 0.017
χ^2	4.1	0.8
d.o.f.	3	3
$p-value$	0.25	0.84
Line		
m [c/Gev]	0.001 ± 0.006	0.003 ± 0.003
q	0.007 ± 0.050	0.012 ± 0.032
$\rho(m,q)$	-0.85	-0.84
χ^2	4.1	0.04
d.o.f.	2	2
$p-value$	0.13	0.98
Fit y		
Constant		
q	0.023 ± 0.025	0.045 ± 0.017
χ^2	4.6	4.5
d.o.f.	2	2
$p-value$	0.10	0.11
Line		
m [c/Gev]	0.081 ± 0.042	0.047 ± 0.028
q	-0.24 ± 0.13	-0.11 ± 0.09
$\rho(m,q)$	-0.98	-0.98
χ^2	0.9	1.5
d.o.f.	1	1
$p-value$	0.35	0.22

B

Beampipe position plots

B.1 Difference between nominal and fitted position

We report in Figs. from B.1 to B.16 on the difference between the measured radial distance obtained by Eq. (4.6) and the design one as a function of the z coordinate, separately for each data-taking year, magnet polarity and angular sector. The coloured bands correspond to the uncertainty on the fitted radius obtained by propagating the uncertainties relative to the m and q parameters and reported in Tabs. 4.6 and 4.7.

B.2 Comparison between nominal and fitted transverse slices

In order to obtain a measure of the radius of the beampipe and of the possible displacement of the center of the beampipe from the design position (*i.e.* the point with coordinates $x = 0$ mm and $y = 0$ mm), we need to fit the radial distances in each z slice with a circle. The circle is parameterised as

$$r^2 - 2r\sqrt{x_0^2 + y_0^2}\cos(\phi - \text{atan2}(y, x)) + x_0^2 + y_0^2 = R^2 \ , \tag{B.1}$$

where r is the measured radial distance, x_0 and y_0 are the parameters describing the displacement of the circle center and R is circle radius. We perform a χ^2 fit, minimising the function

$$\chi^2 = \sum_i \frac{(r_i - r(x_0, y_0, R))^2}{\sigma_{r_i}^2} \ , \tag{B.2}$$

where r_i is the measured radial distance, σ_{r_i} is its uncertainty and the index i runs over the ϕ sectors. The measured radial distances in bins of the z coordinate with the result of the fit overlaid are here reported in Figs. from B.17 to B.44. As the value of the z coordinate increases, the displacement from the design position is more and more evident.

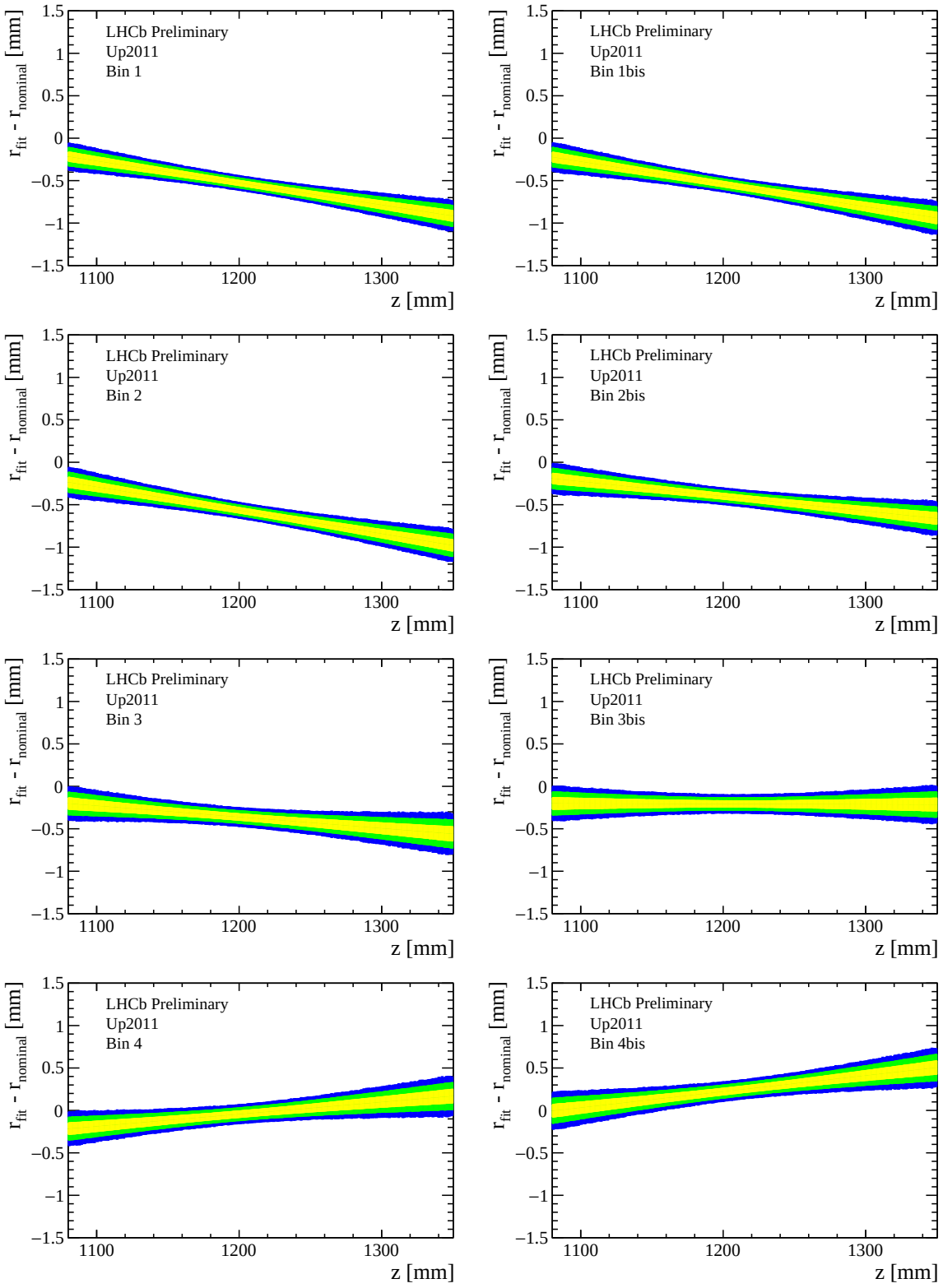

Figure B.1: *Difference between the measured and the design radial distance of the beampipe position in the various ϕ sectors as a function of the z coordinate for the Up2011 data sample. The yellow, green and blue bands represent the 1σ, 2σ and 3σ contours.*

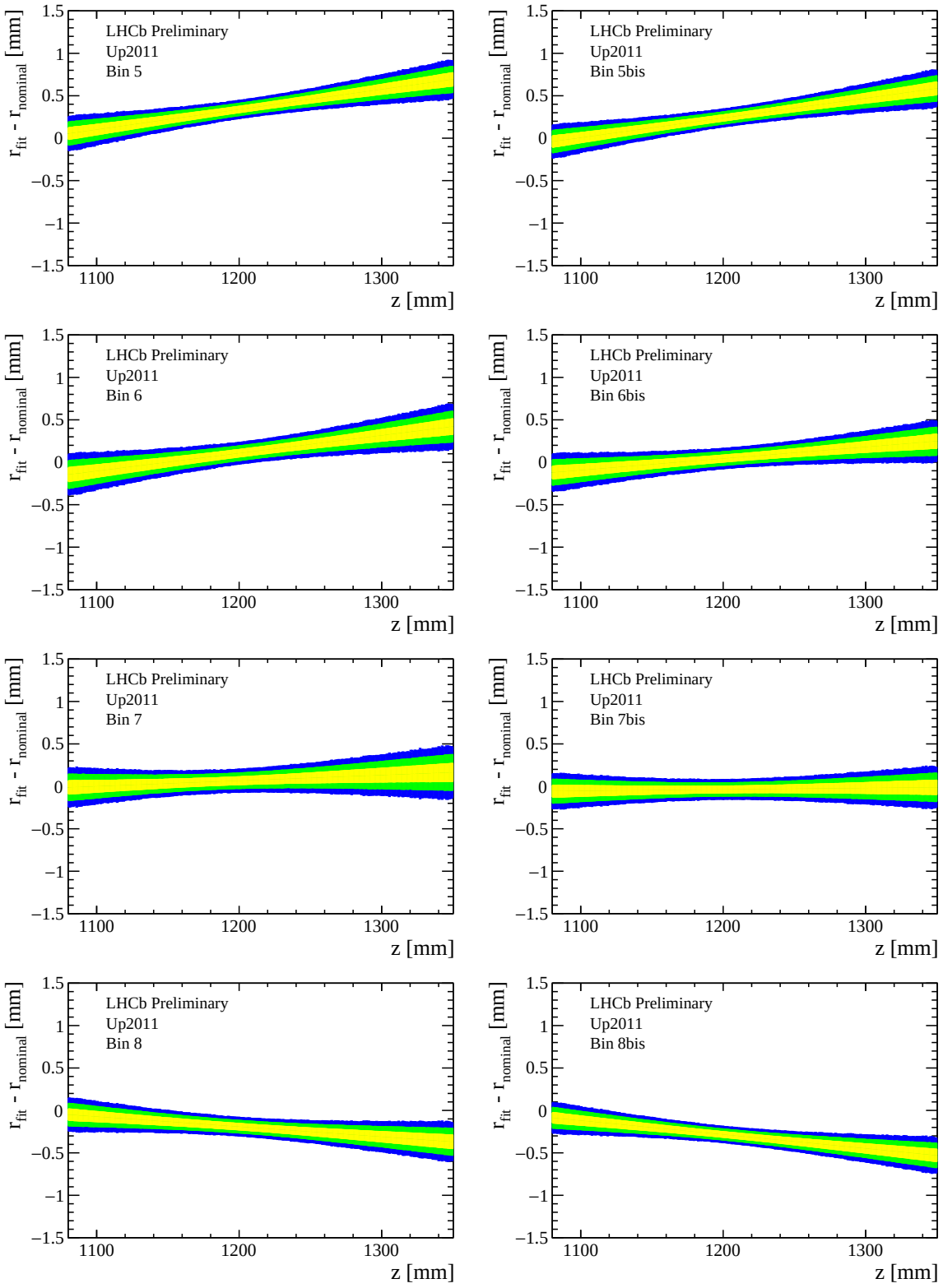

Figure B.2: *Difference between the measured and the design radial distance of the beampipe position in the various ϕ sectors as a function of the z coordinate for the Up2011 data sample. The yellow, green and blue bands represent the 1σ, 2σ and 3σ contours.*

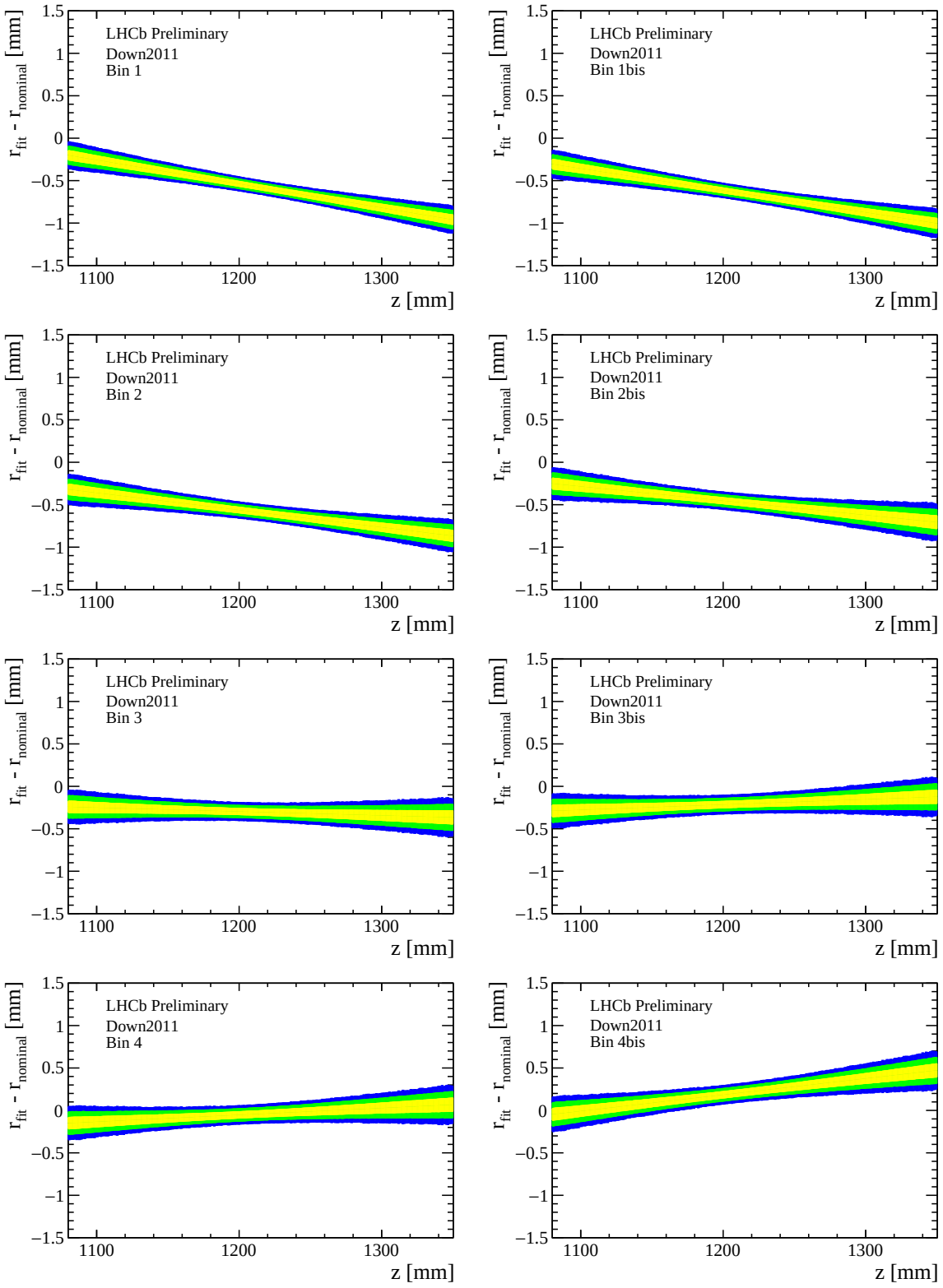

Figure B.3: *Difference between the measured and the design radial distance of the beampipe position in the various ϕ sectors as a function of the z coordinate for the Down2011 data sample. The yellow, green and blue bands represent the 1σ, 2σ and 3σ contours.*

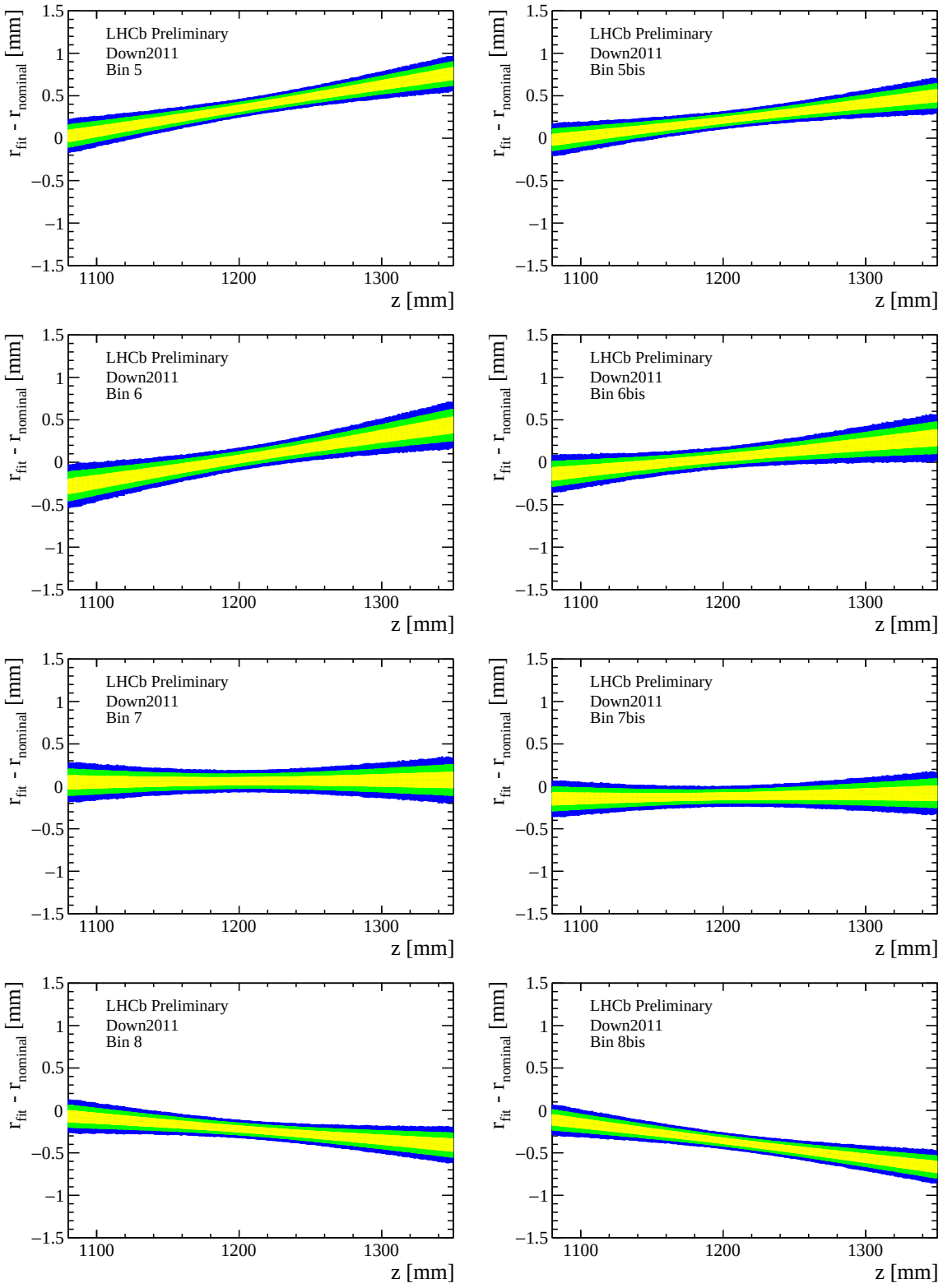

Figure B.4: *Difference between the measured and the design radial distance of the beampipe position in the various ϕ sectors as a function of the z coordinate for the Down2011 data sample. The yellow, green and blue bands represent the 1σ, 2σ and 3σ contours.*

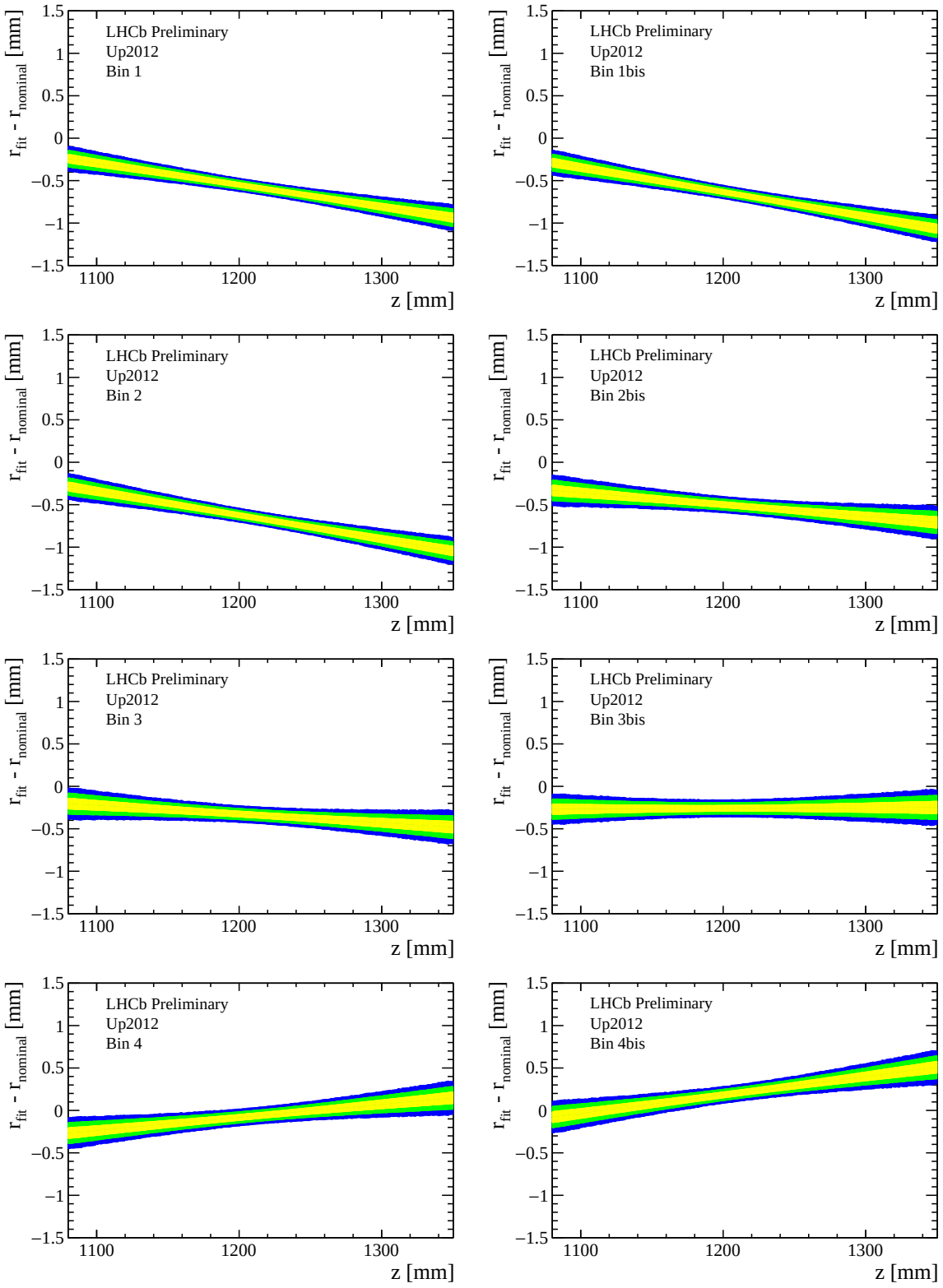

Figure B.5: *Difference between the measured and the design radial distance of the beampipe position in the various ϕ sectors as a function of the z coordinate for the Up2012 data sample. The yellow, green and blue bands represent the 1σ, 2σ and 3σ contours.*

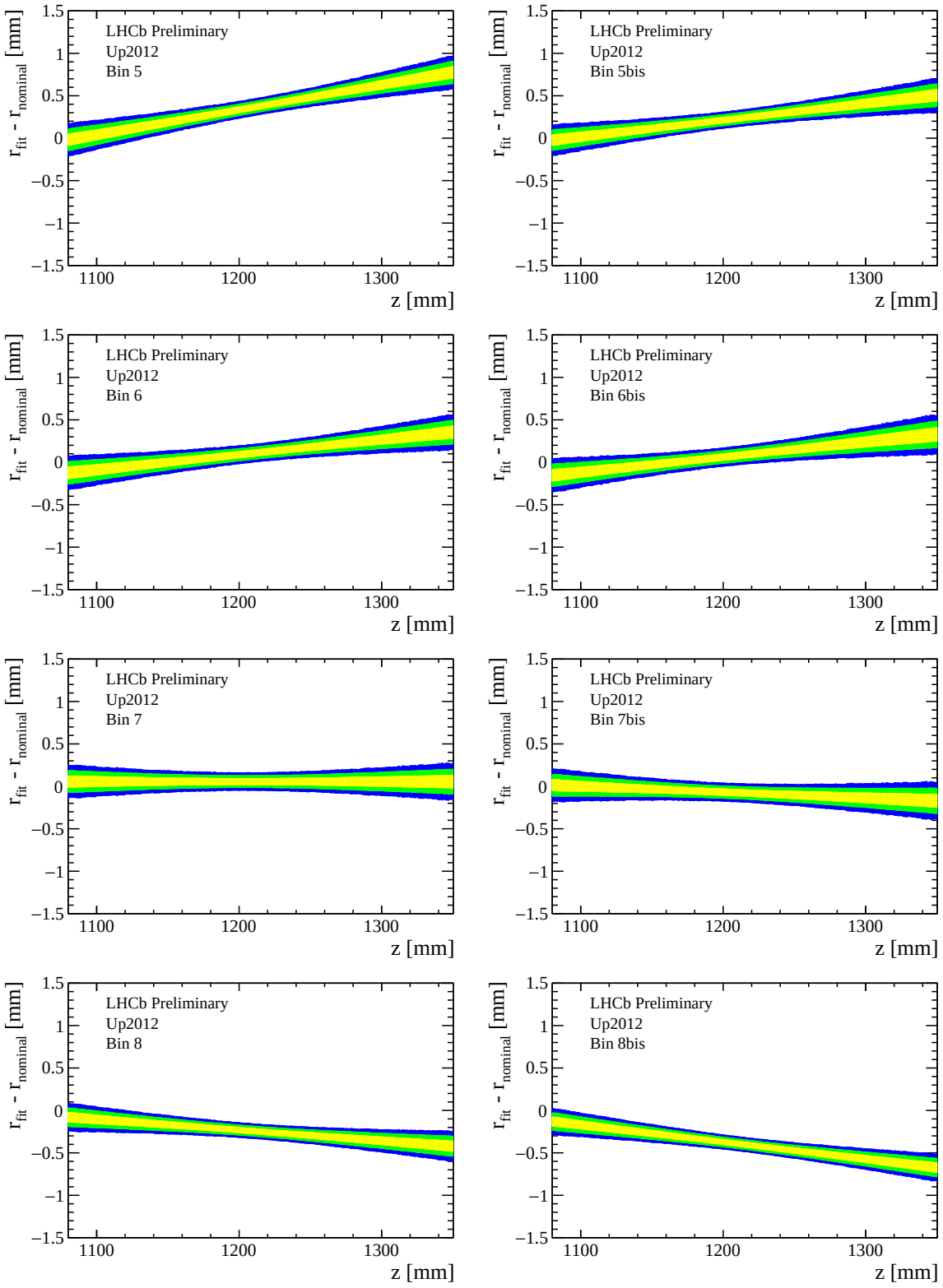

Figure B.6: *Difference between the measured and the design radial distance of the beampipe position in the various ϕ sectors as a function of the z coordinate for the Up2012 data sample. The yellow, green and blue bands represent the 1σ, 2σ and 3σ contours.*

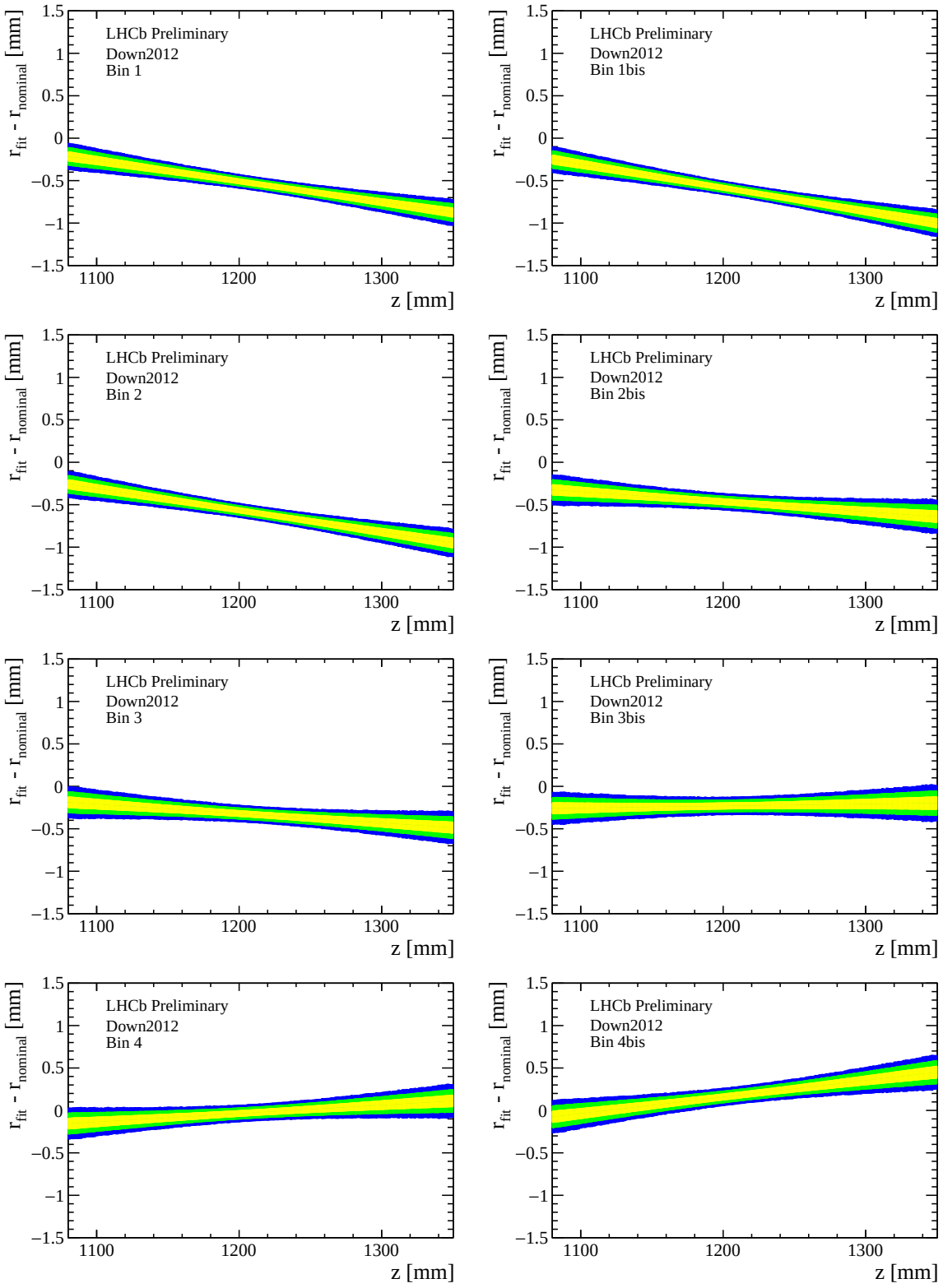

Figure B.7: *Difference between the measured and the design radial distance of the beampipe position in the various ϕ sectors as a function of the z coordinate for the Down2012 data sample. The yellow, green and blue bands represent the 1σ, 2σ and 3σ contours.*

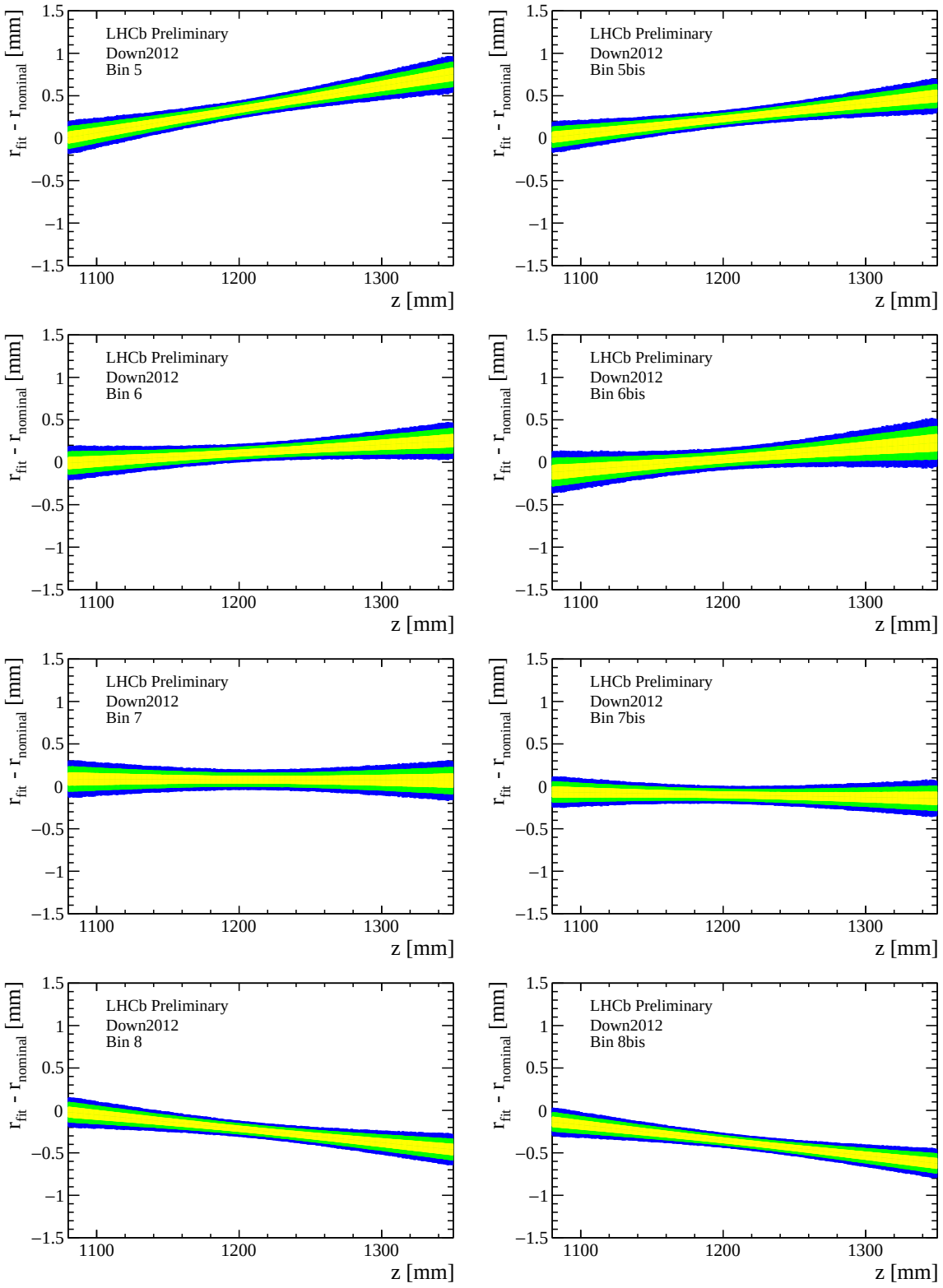

Figure B.8: *Difference between the measured and the design radial distance of the beampipe position in the various ϕ sectors as a function of the z coordinate for the Down2012 data sample. The yellow, green and blue bands represent the 1σ, 2σ and 3σ contours.*

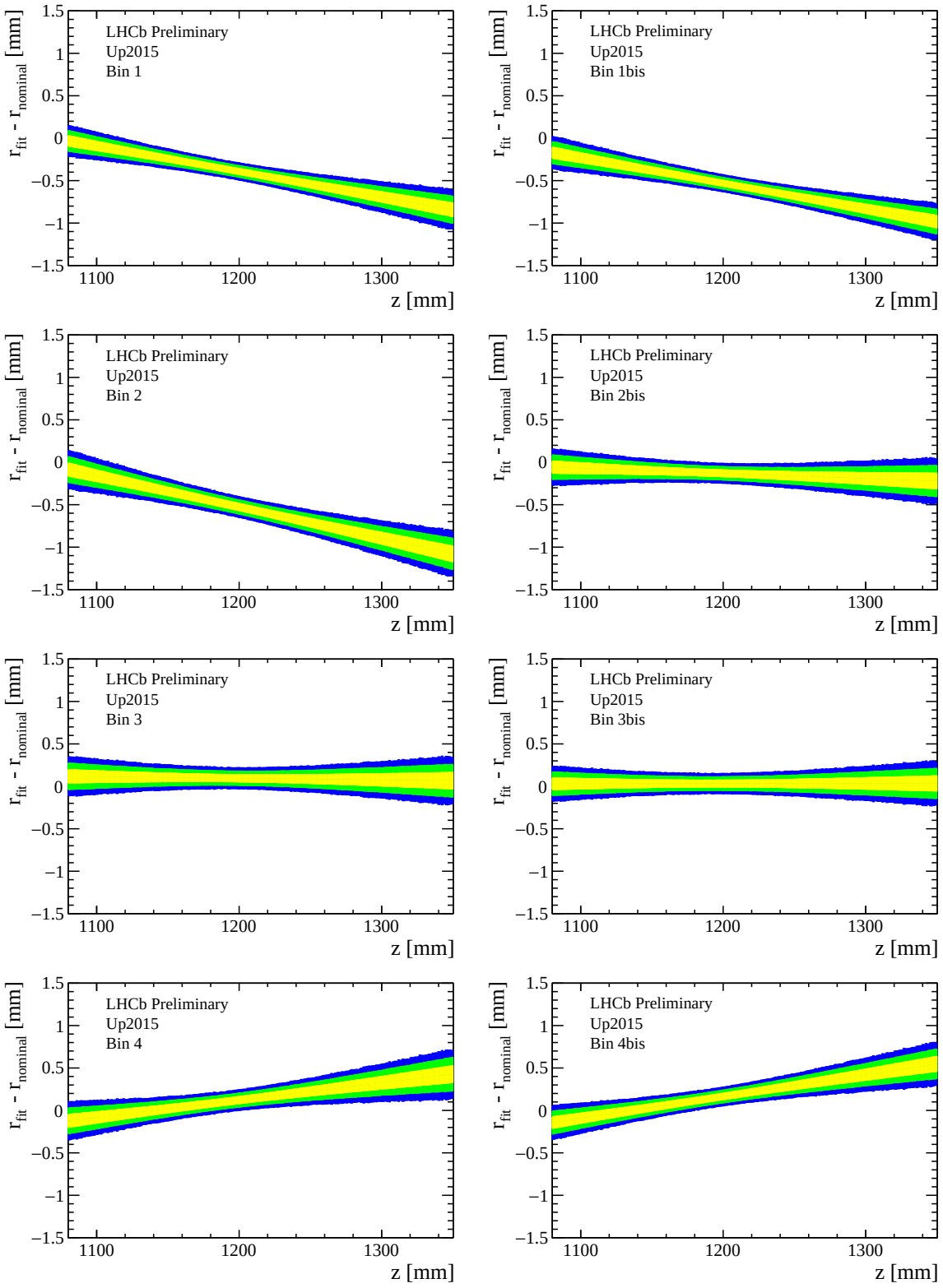

Figure B.9: *Difference between the measured and the design radial distance of the beampipe position in the various ϕ sectors as a function of the z coordinate for the Up2015 data sample. The yellow, green and blue bands represent the 1σ, 2σ and 3σ contours.*

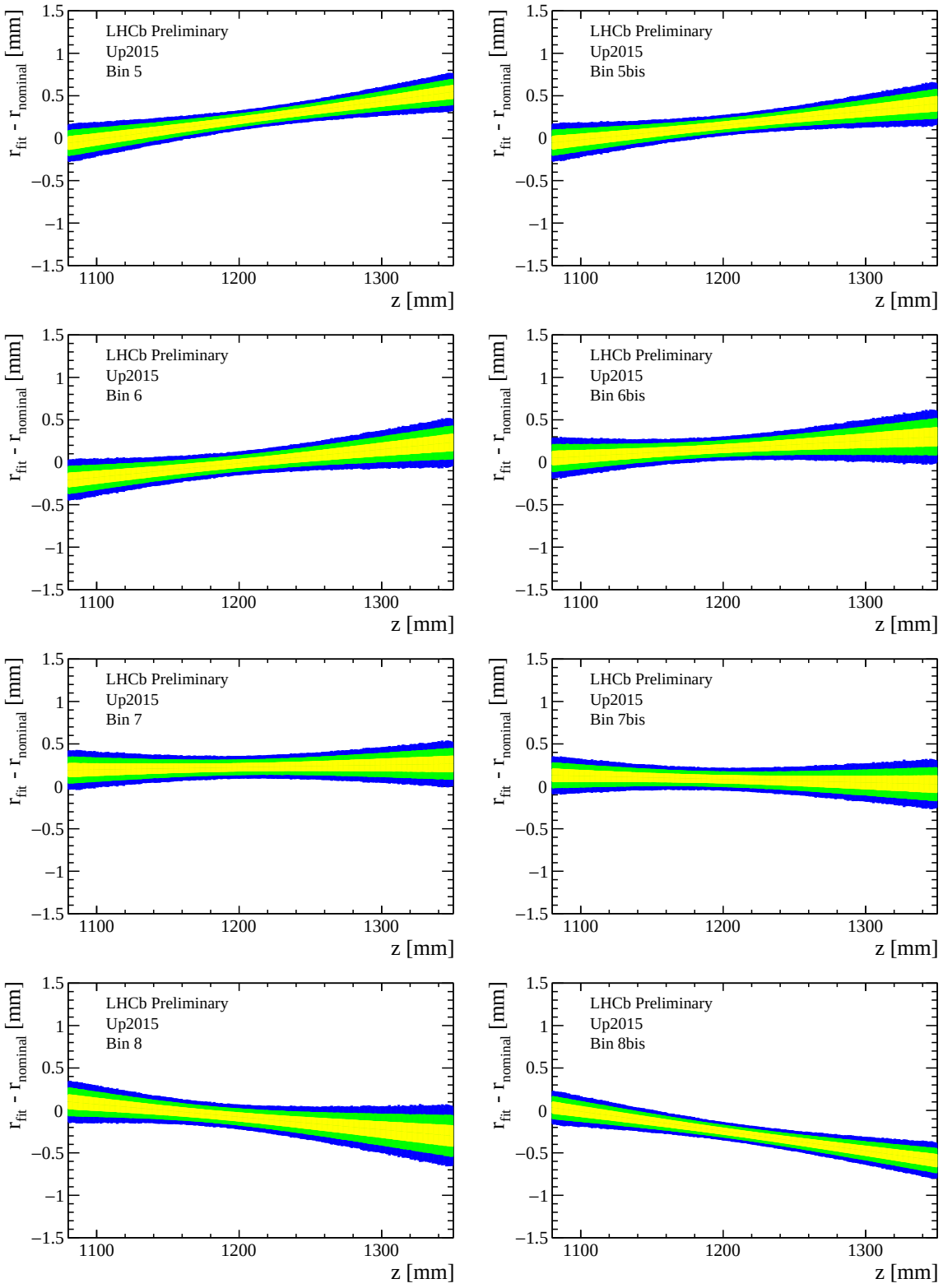

Figure B.10: *Difference between the measured and the design radial distance of the beampipe position in the various ϕ sectors as a function of the z coordinate for the Up2015 data sample. The yellow, green and blue bands represent the 1σ, 2σ and 3σ contours.*

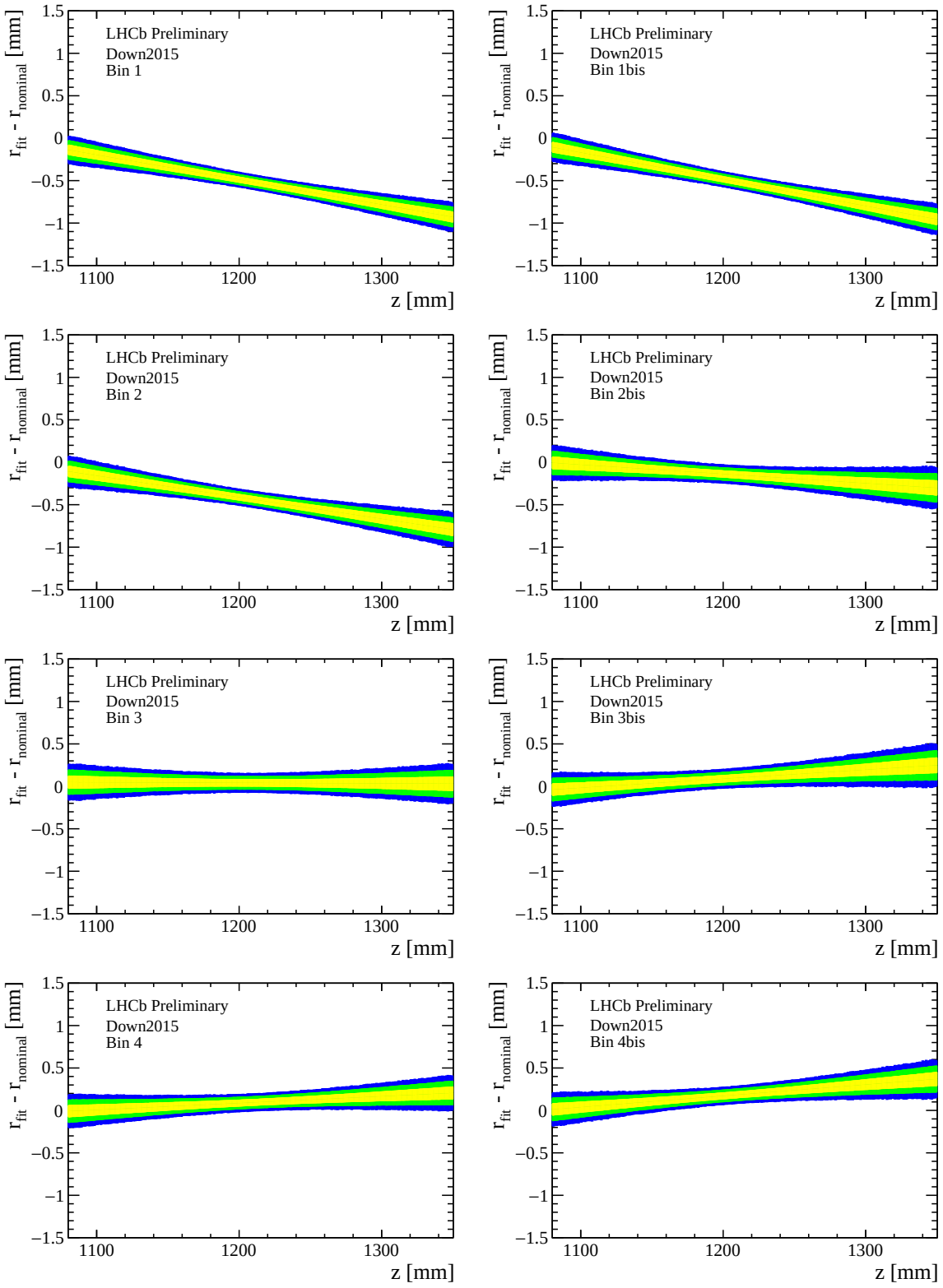

Figure B.11: *Difference between the measured and the design radial distance of the beampipe position in the various ϕ sectors as a function of the z coordinate for the Down2015 data sample. The yellow, green and blue bands represent the 1σ, 2σ and 3σ contours.*

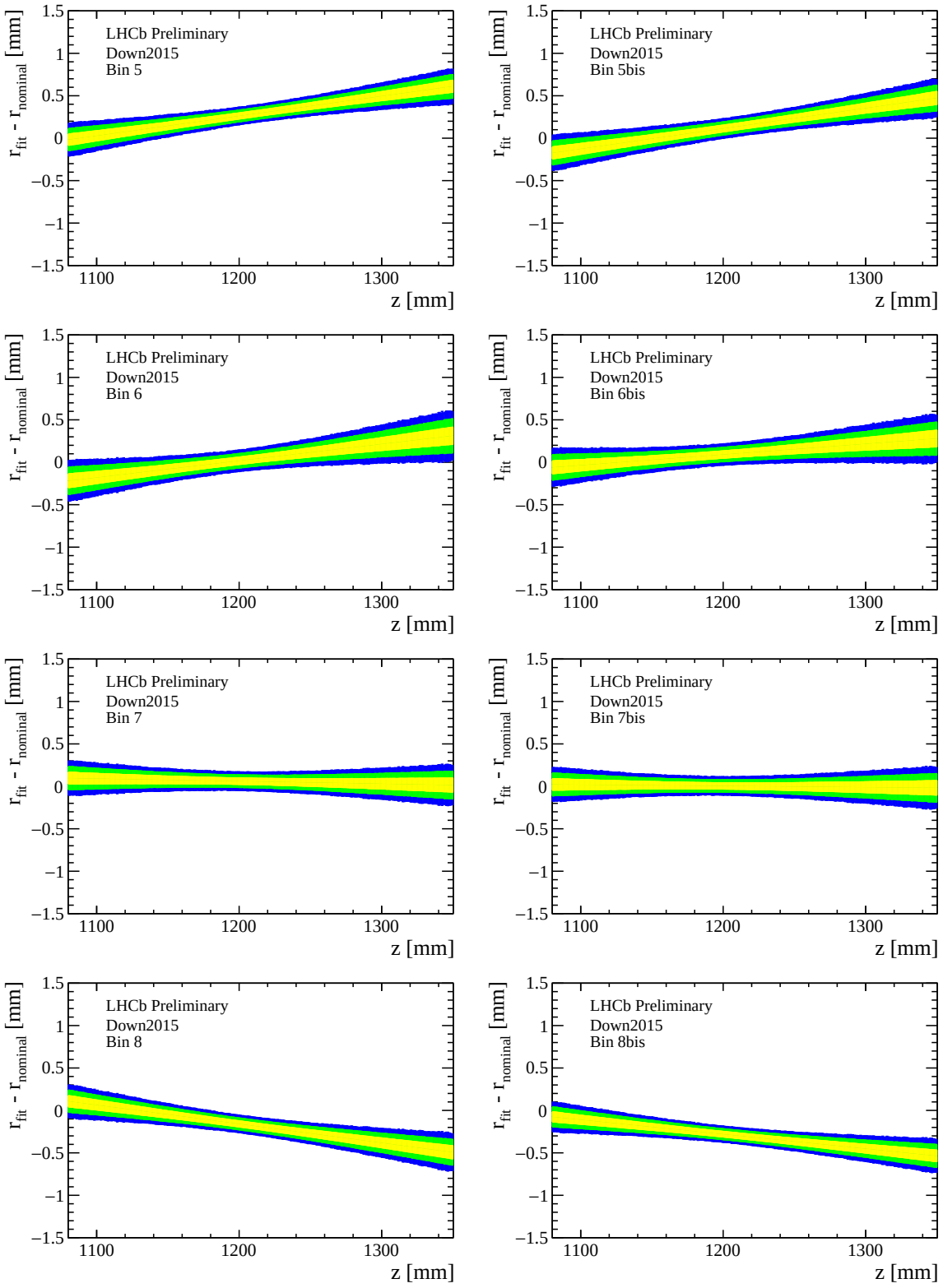

Figure B.12: *Difference between the measured and the design radial distance of the beampipe position in the various ϕ sectors as a function of the z coordinate for the Down2015 data sample. The yellow, green and blue bands represent the 1σ, 2σ and 3σ contours.*

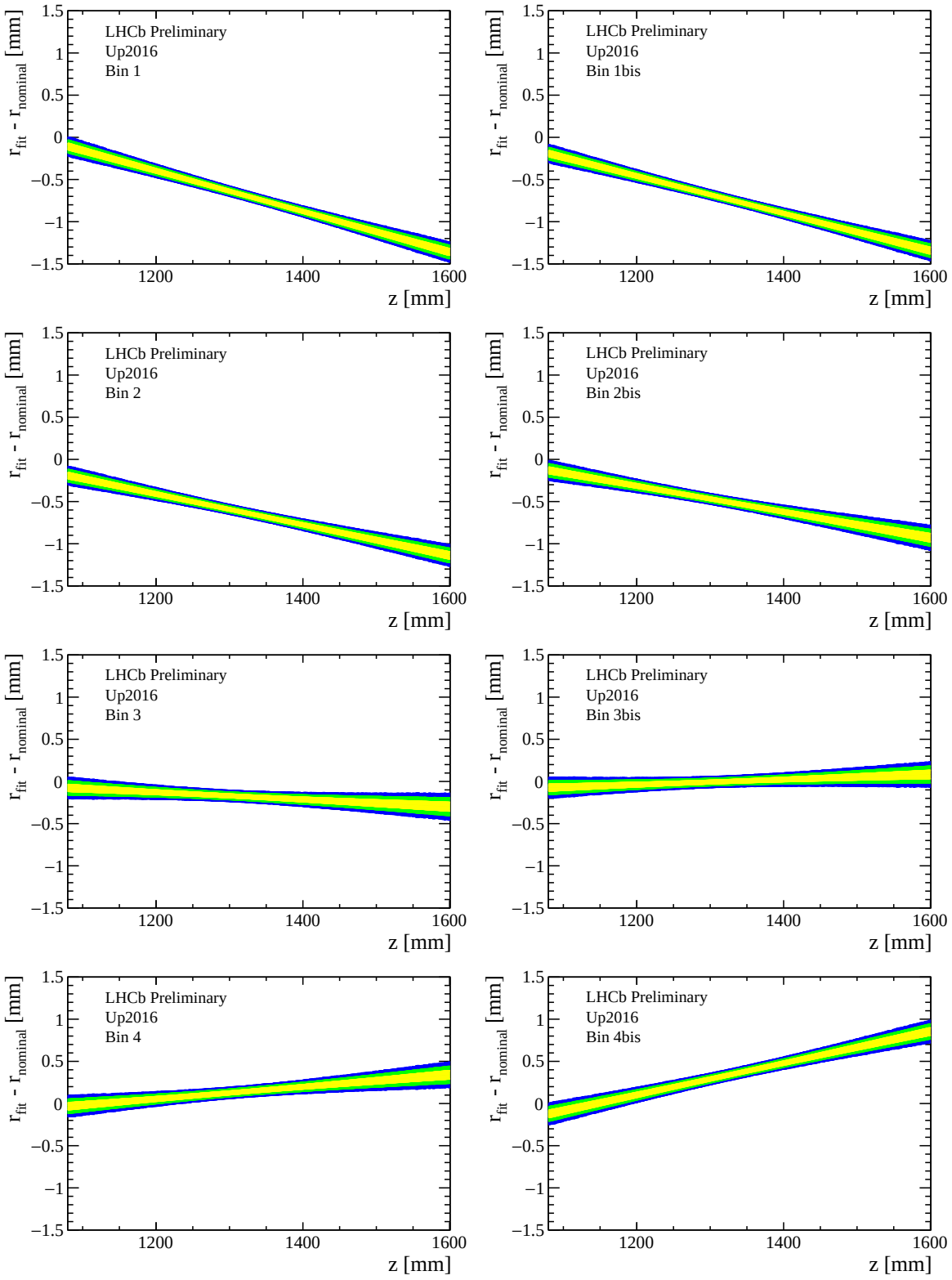

Figure B.13: *Difference between the measured and the design radial distance of the beampipe position in the various ϕ sectors as a function of the z coordinate for the Up2016 data sample. The yellow, green and blue bands represent the 1σ, 2σ and 3σ contours.*

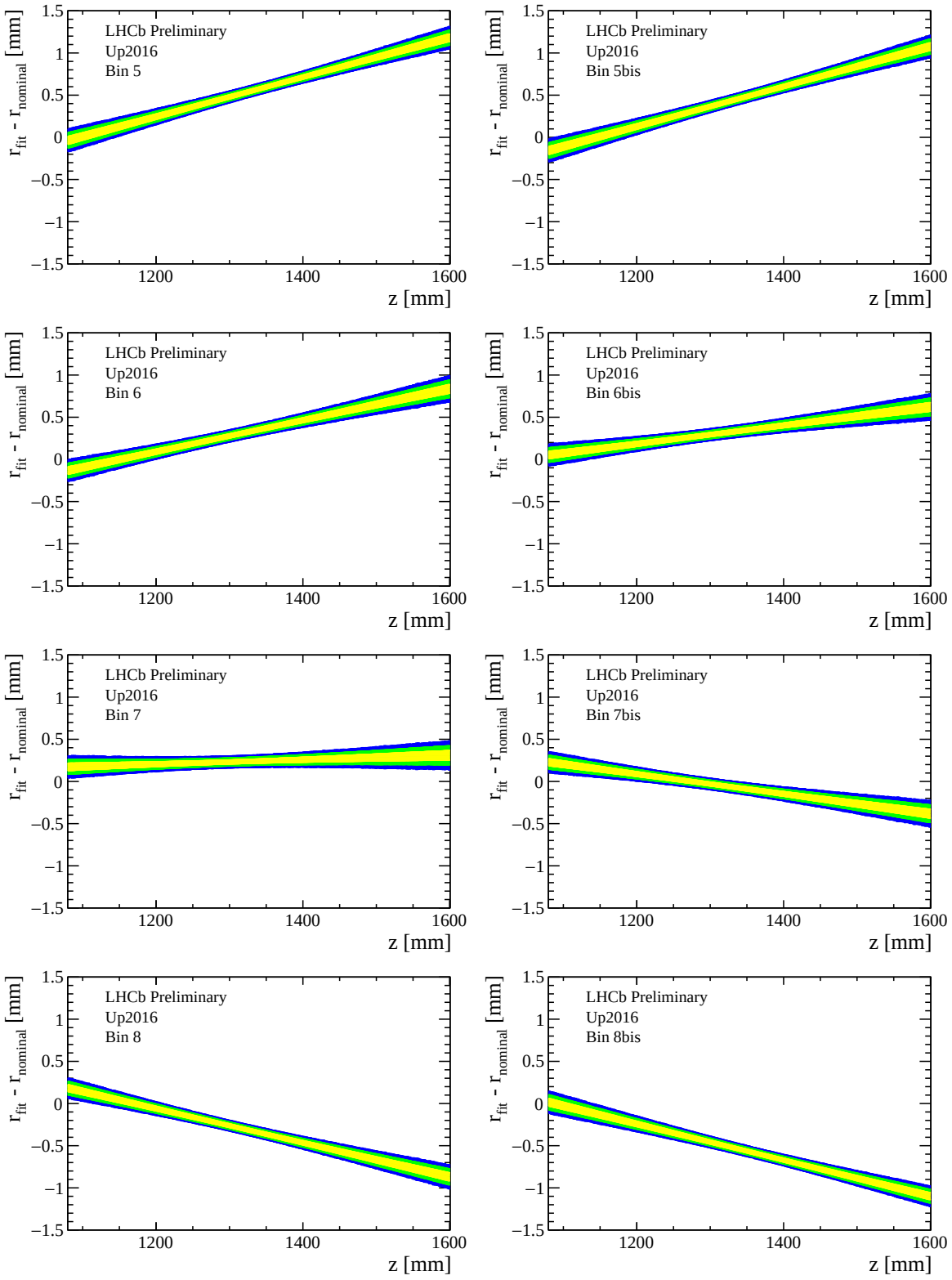

Figure B.14: *Difference between the measured and the design radial distance of the beampipe position in the various ϕ sectors as a function of the z coordinate for the Up2016 data sample. The yellow, green and blue bands represent the 1σ, 2σ and 3σ contours.*

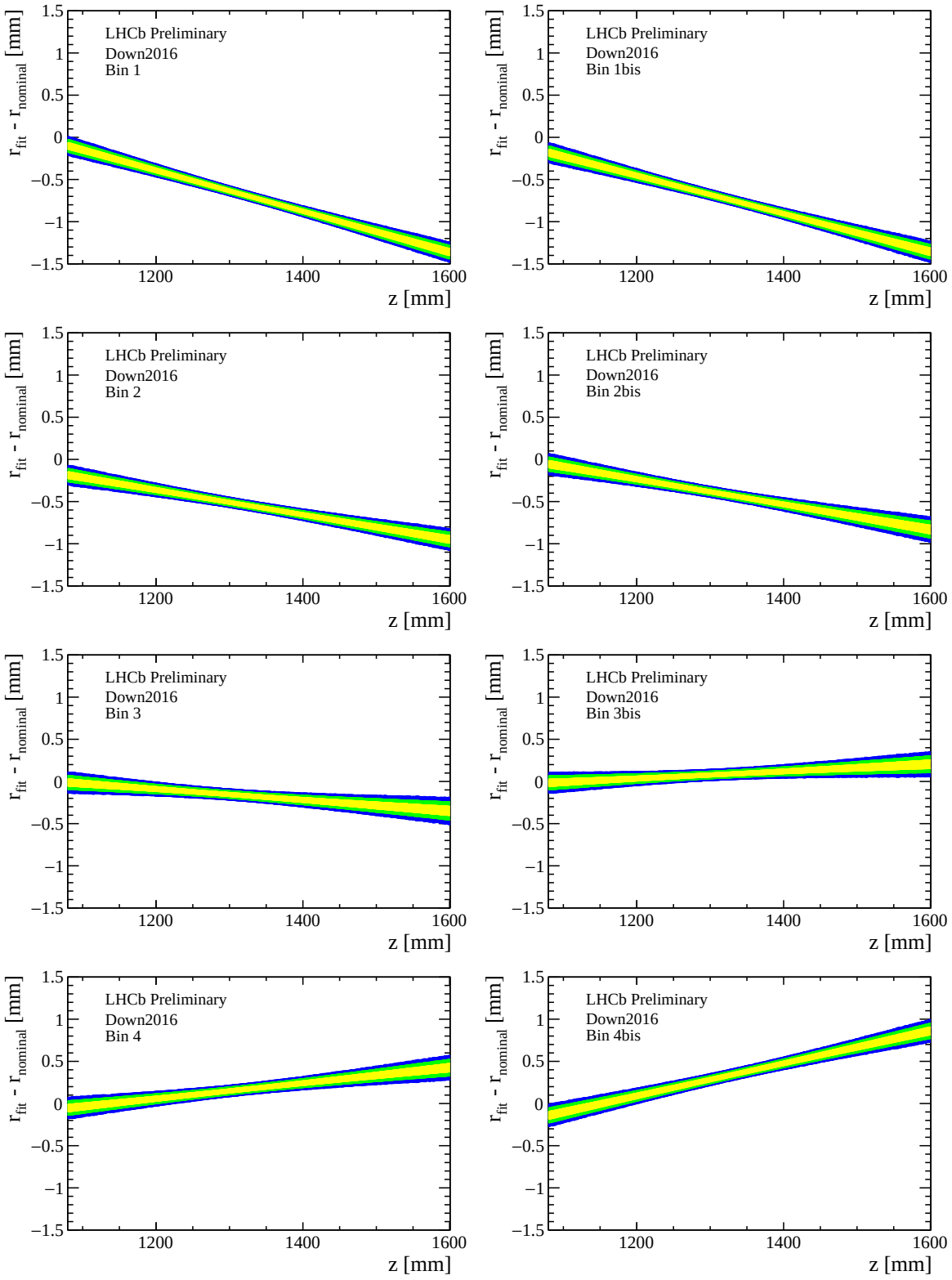

Figure B.15: *Difference between the measured and the design radial distance of the beampipe position in the various ϕ sectors as a function of the z coordinate for the Down2016 data sample. The yellow, green and blue bands represent the 1σ, 2σ and 3σ contours.*

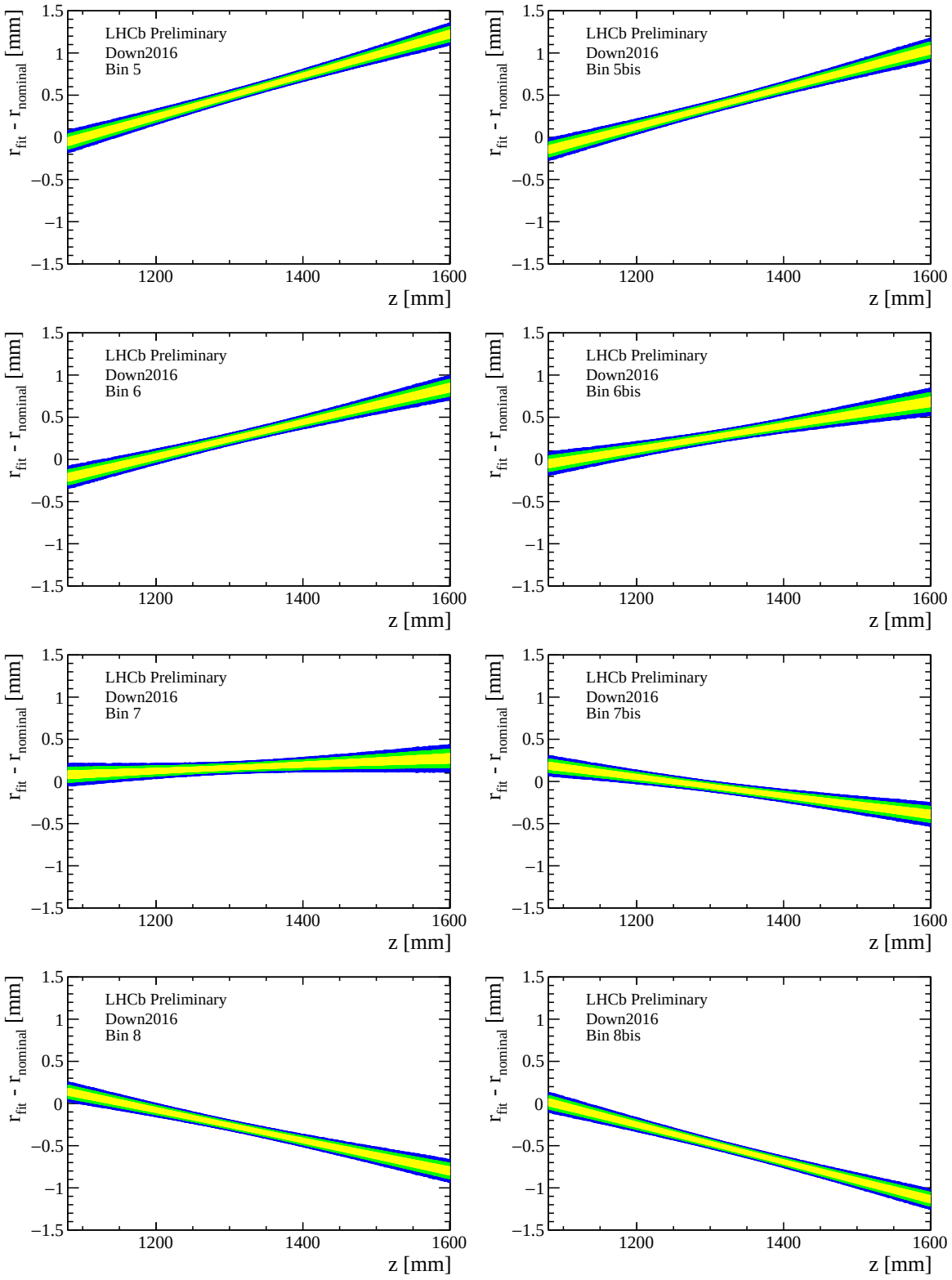

Figure B.16: *Difference between the measured and the design radial distance of the beampipe position in the various ϕ sectors as a function of the z coordinate for the Down2016 data sample. The yellow, green and blue bands represent the 1σ, 2σ and 3σ contours.*

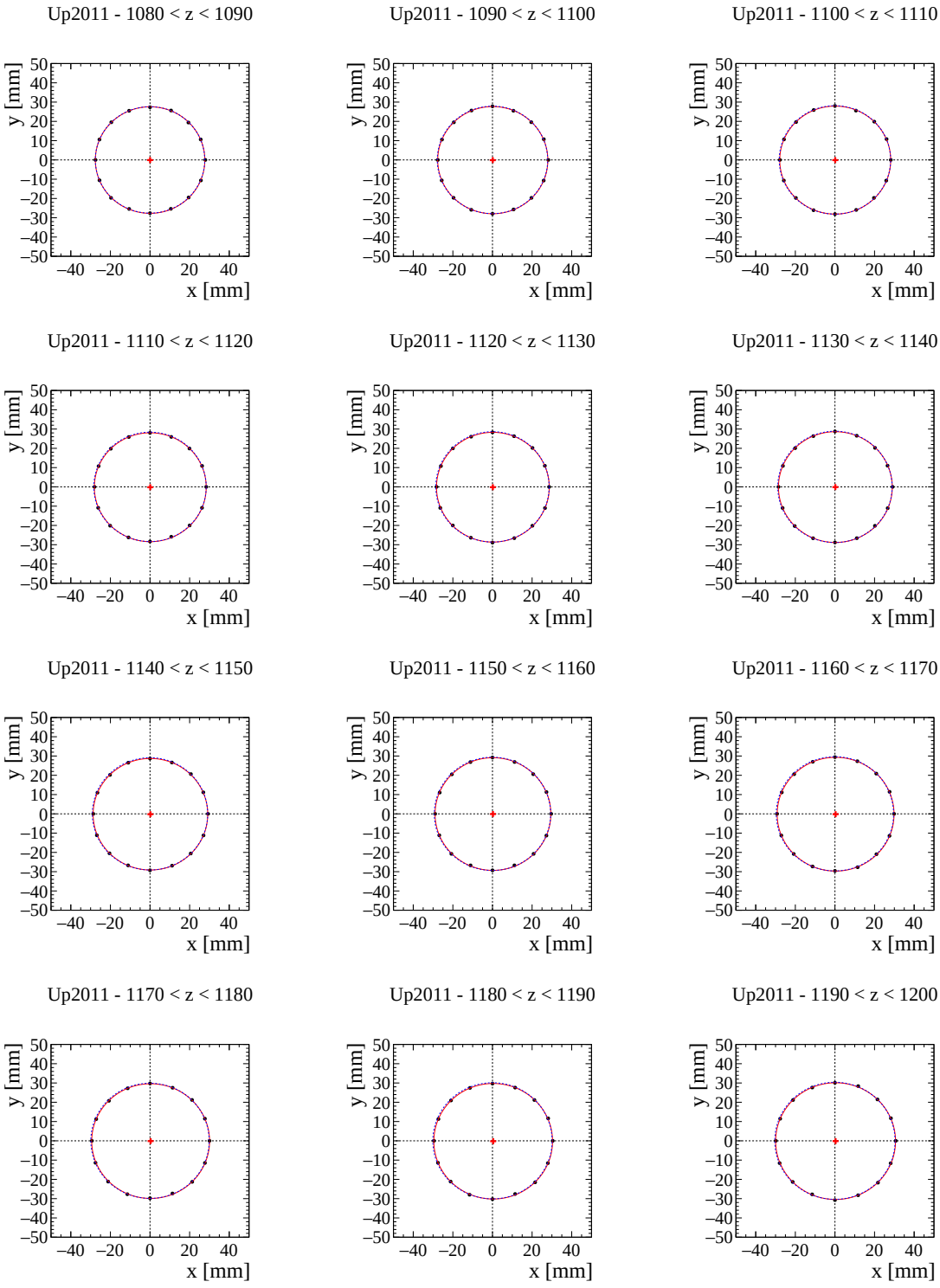

Figure B.17: *Measured radial distance in bins of the z coordinate for the Up 2011 sample. The red solid line corresponds to the fitted circle, whereas the blue dashed line is the design reference. The red cross represents the position of the center of the fitted circle. The uncertainties on the radial distances are not shown.*

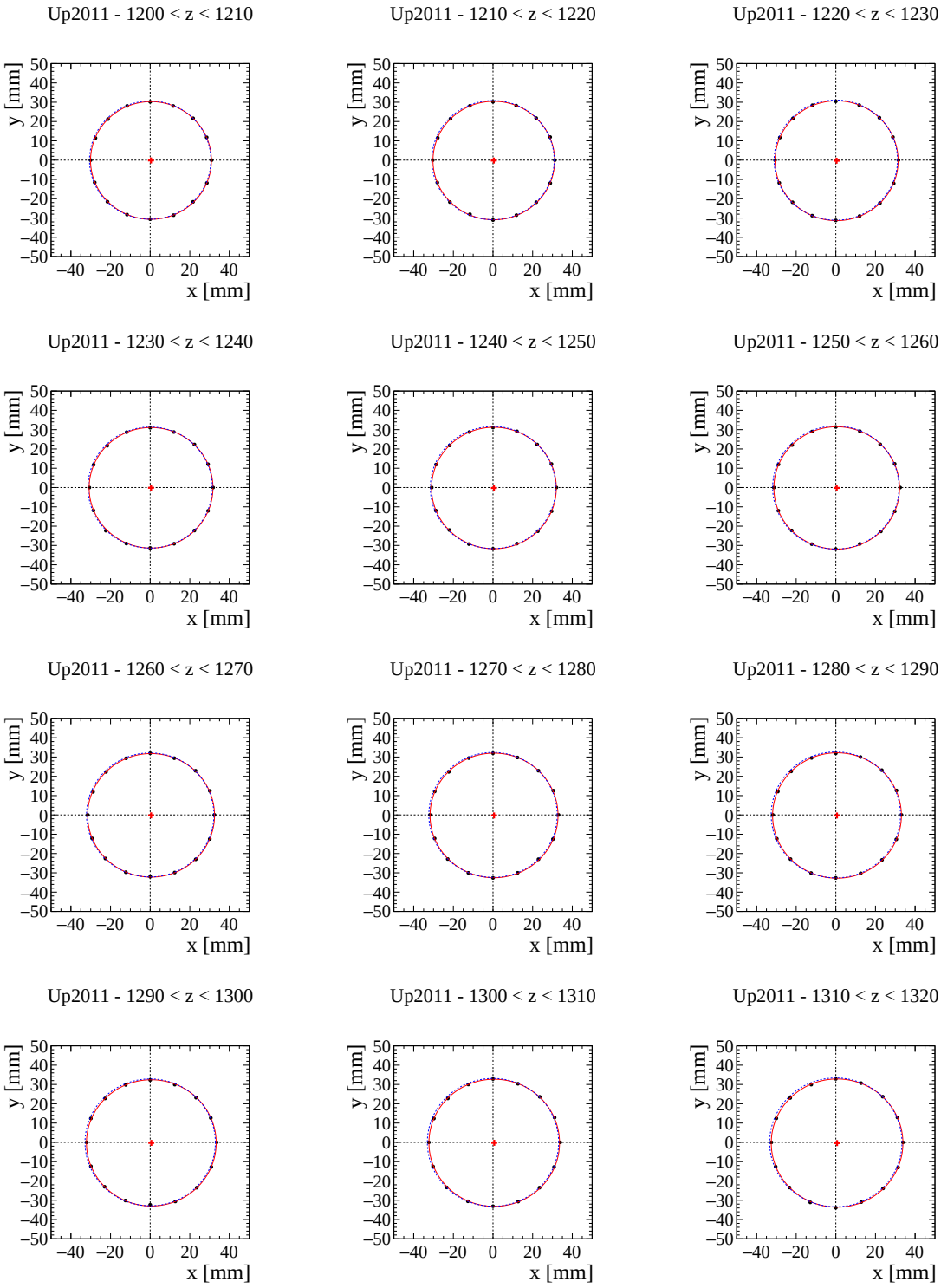

Figure B.18: *Measured radial distance in bins of the z coordinate for the Up 2011 sample. The red solid line corresponds to the fitted circle, whereas the blue dashed line is the design reference. The red cross represents the position of the center of the fitted circle. The uncertainties on the radial distances are not shown.*

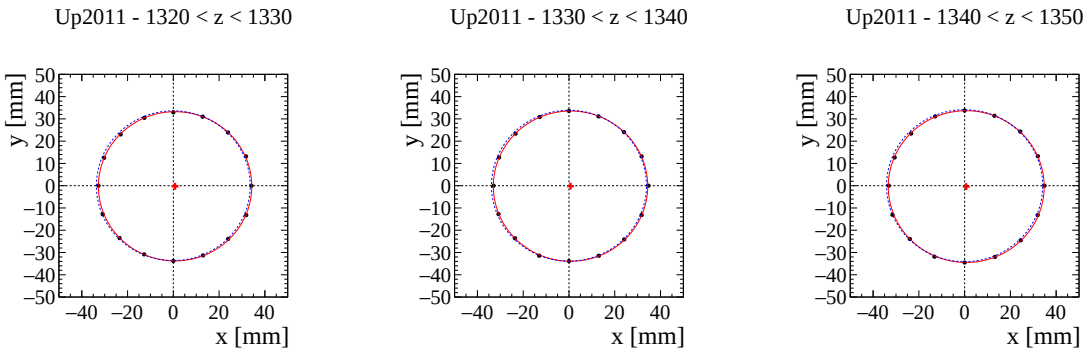

Figure B.19: *Measured radial distance in bins of the z coordinate for the Up 2011 sample. The red solid line corresponds to the fitted circle, whereas the blue dashed line is the design reference. The red cross represents the position of the center of the fitted circle. The uncertainties on the radial distances are not shown.*

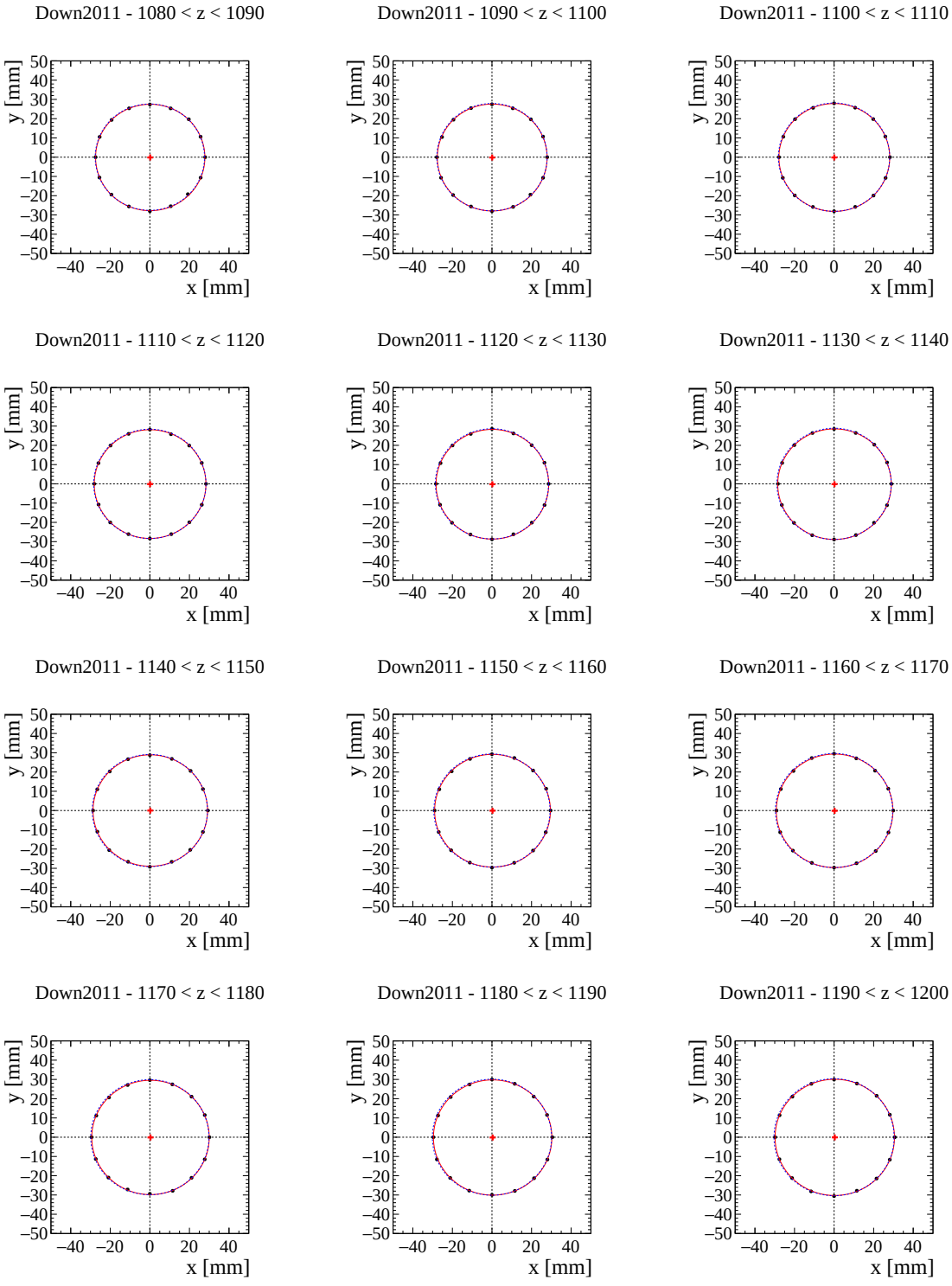

Figure B.20: *Measured radial distance in bins of the z coordinate for the Down 2011 sample. The red solid line corresponds to the fitted circle, whereas the blue dashed line is the design reference. The red cross represents the position of the center of the fitted circle. The uncertainties on the radial distances are not shown.*

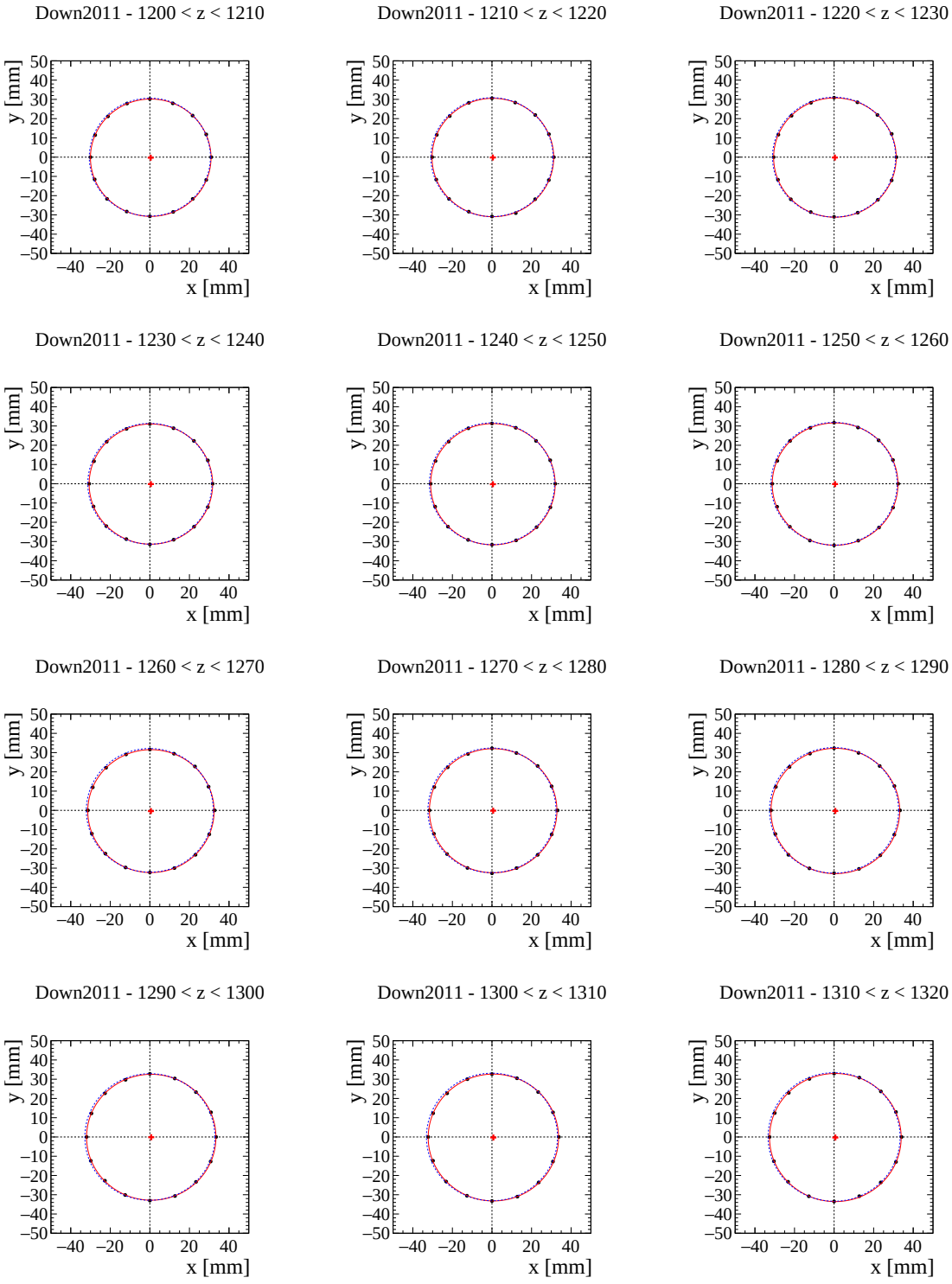

Figure B.21: *Measured radial distance in bins of the z coordinate for the Down 2011 sample. The red solid line corresponds to the fitted circle, whereas the blue dashed line is the design reference. The red cross represents the position of the center of the fitted circle. The uncertainties on the radial distances are not shown.*

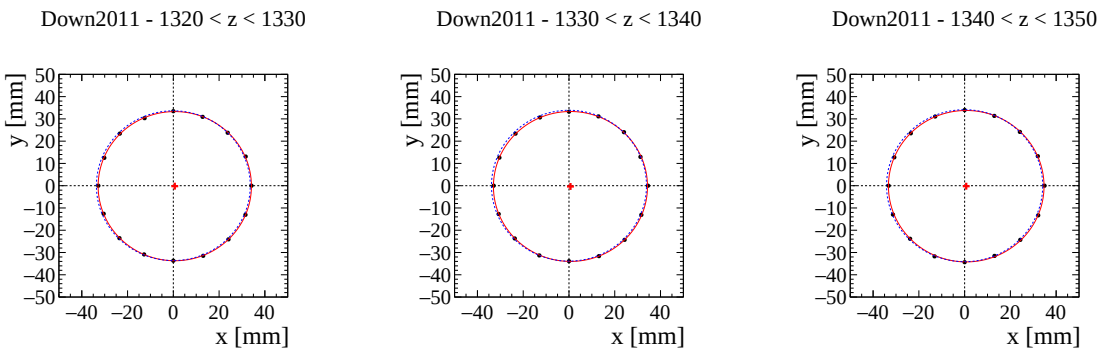

Figure B.22: *Measured radial distance in bins of the z coordinate for the Down 2011 sample. The red solid line corresponds to the fitted circle, whereas the blue dashed line is the design reference. The red cross represents the position of the center of the fitted circle. The uncertainties on the radial distances are not shown.*

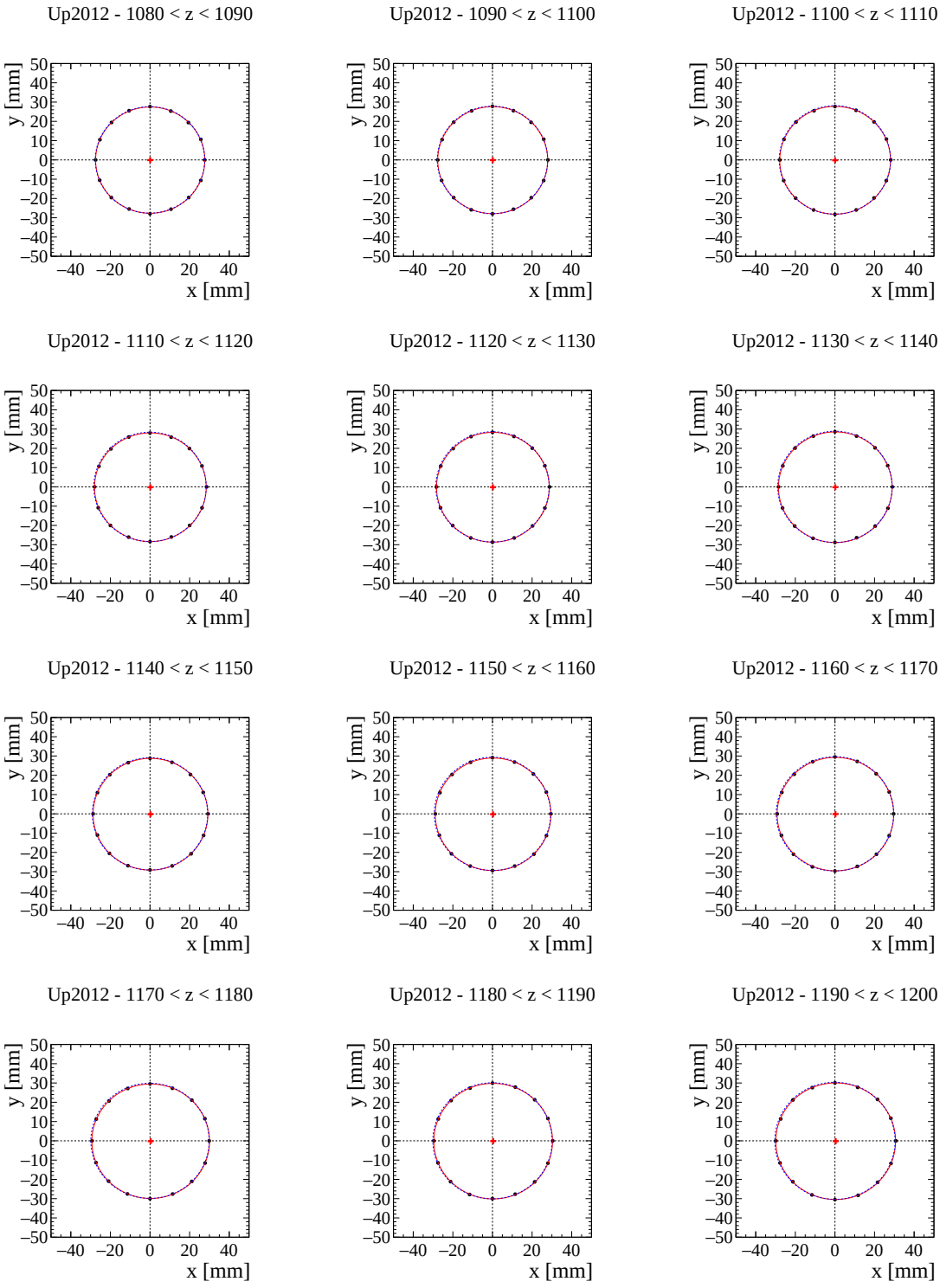

Figure B.23: *Measured radial distance in bins of the z coordinate for the Up 2012 sample. The red solid line corresponds to the fitted circle, whereas the blue dashed line is the design reference. The red cross represents the position of the center of the fitted circle. The uncertainties on the radial distances are not shown.*

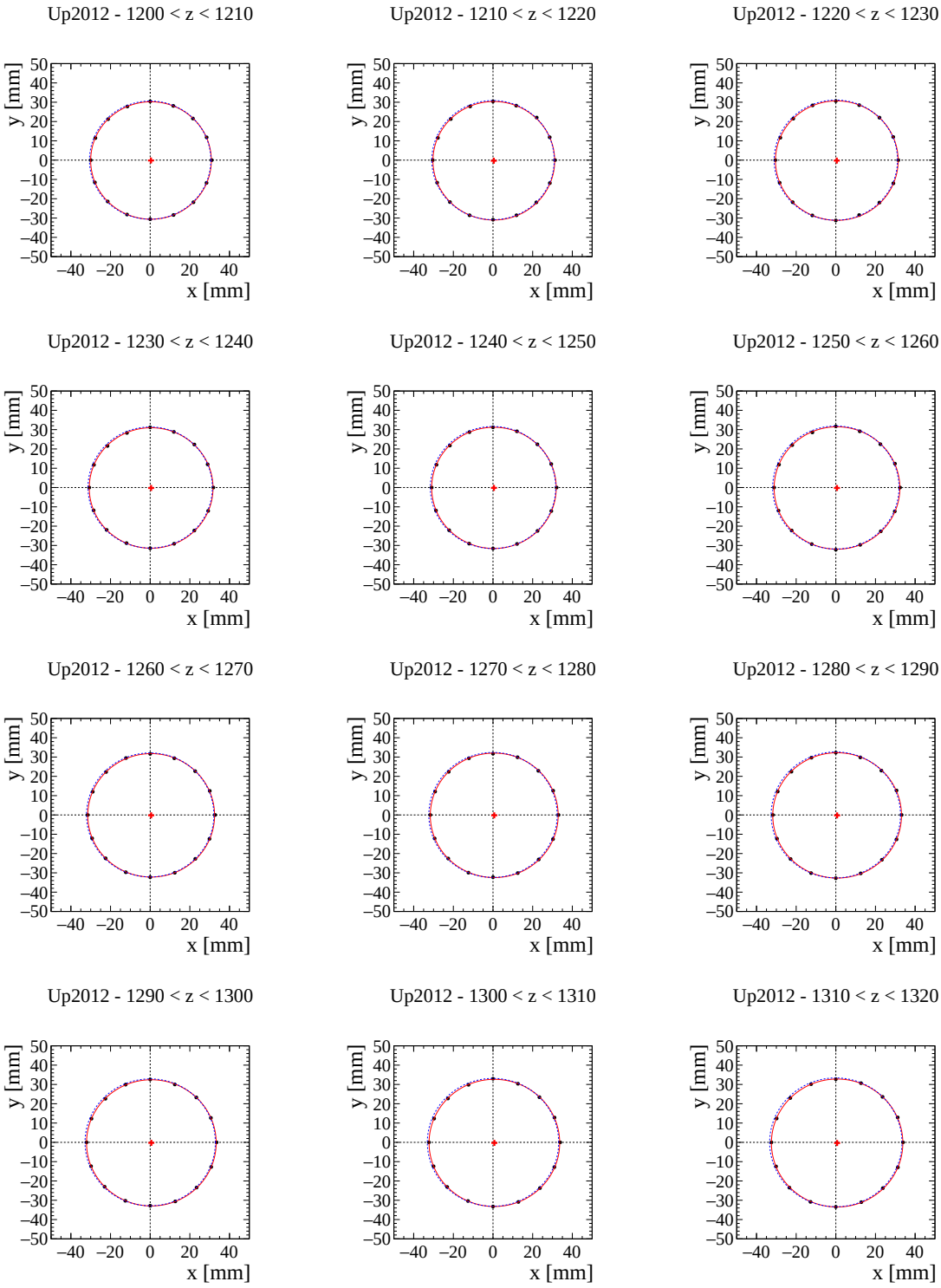

Figure B.24: *Measured radial distance in bins of the z coordinate for the Up 2012 sample. The red solid line corresponds to the fitted circle, whereas the blue dashed line is the design reference. The red cross represents the position of the center of the fitted circle. The uncertainties on the radial distances are not shown.*

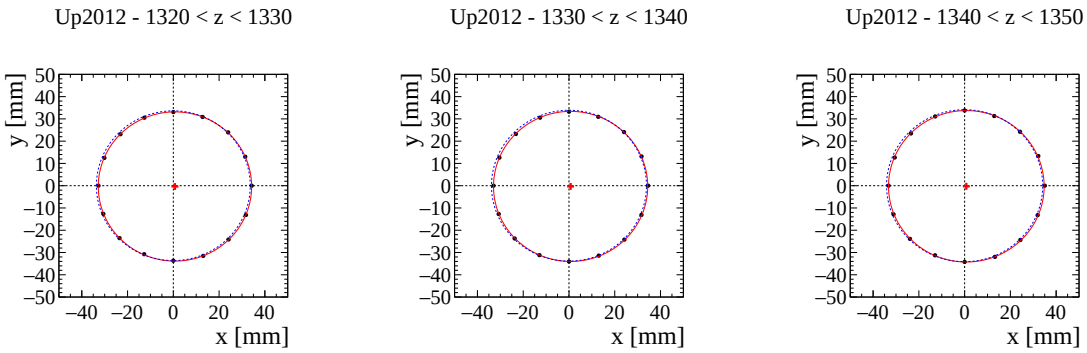

Figure B.25: *Measured radial distance in bins of the z coordinate for the Up 2012 sample. The red solid line corresponds to the fitted circle, whereas the blue dashed line is the design reference. The red cross represents the position of the center of the fitted circle. The uncertainties on the radial distances are not shown.*

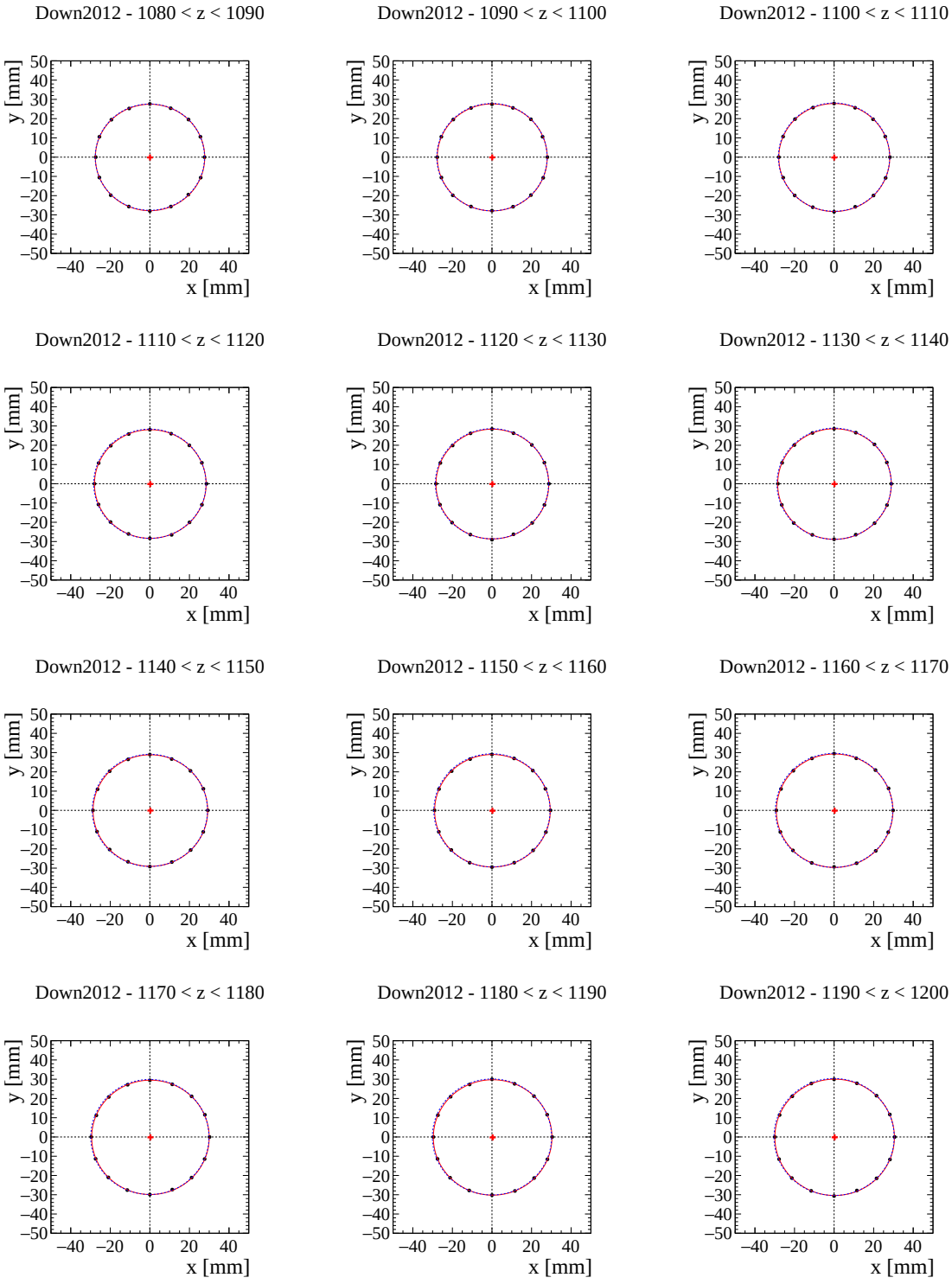

Figure B.26: *Measured radial distance in bins of the z coordinate for the Down 2012 sample. The red solid line corresponds to the fitted circle, whereas the blue dashed line is the design reference. The red cross represents the position of the center of the fitted circle. The uncertainties on the radial distances are not shown.*

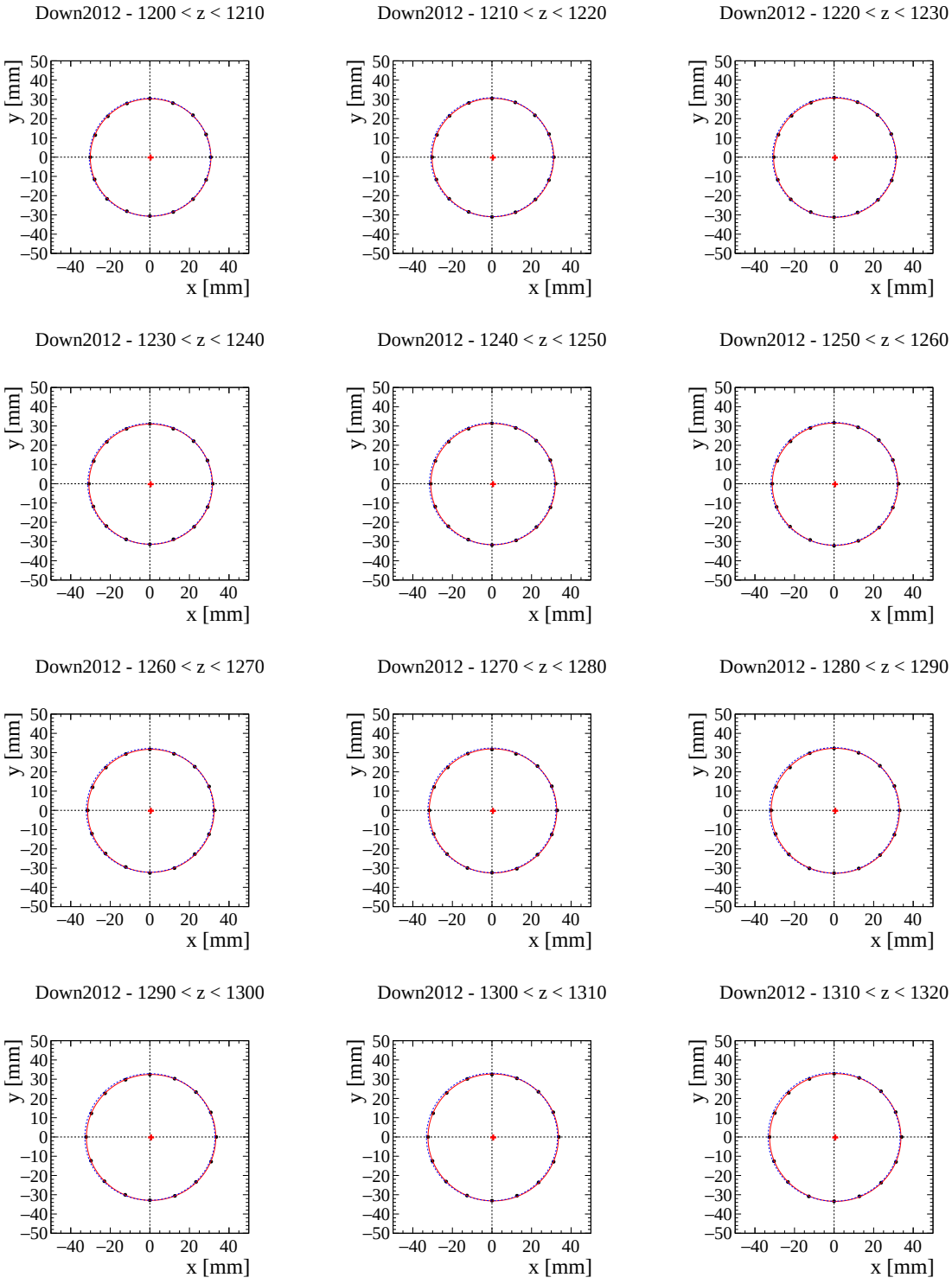

Figure B.27: *Measured radial distance in bins of the z coordinate for the Down 2012 sample. The red solid line corresponds to the fitted circle, whereas the blue dashed line is the design reference. The red cross represents the position of the center of the fitted circle. The uncertainties on the radial distances are not shown.*

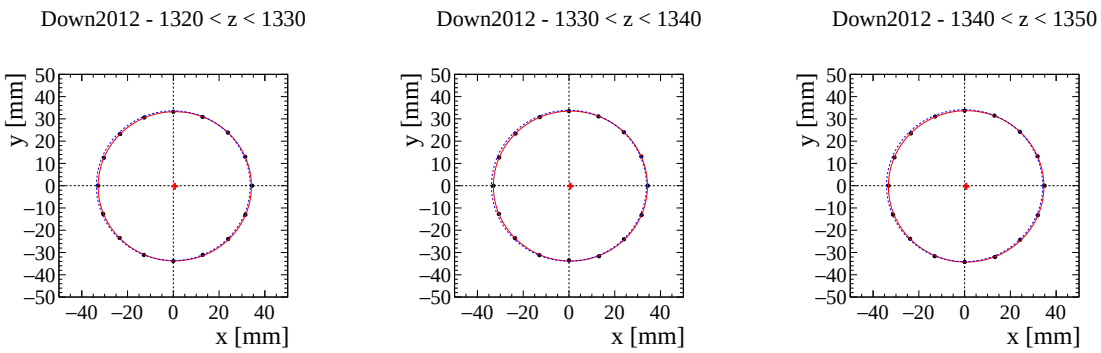

Figure B.28: *Measured radial distance in bins of the z coordinate for the Down 2012 sample. The red solid line corresponds to the fitted circle, whereas the blue dashed line is the design reference. The red cross represents the position of the center of the fitted circle. The uncertainties on the radial distances are not shown.*

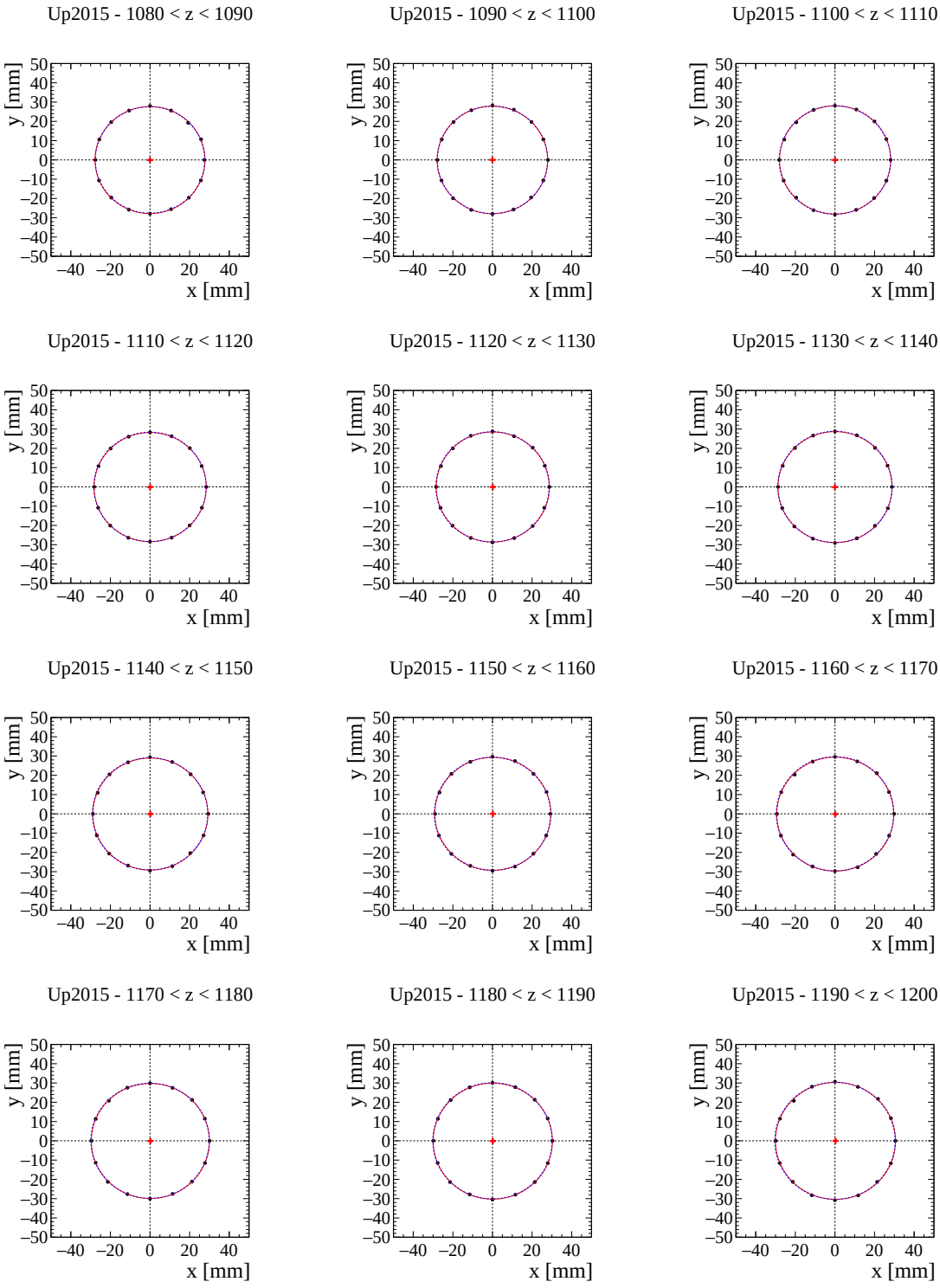

Figure B.29: *Measured radial distance in bins of the z coordinate for the Up 2015 sample. The red solid line corresponds to the fitted circle, whereas the blue dashed line is the design reference. The red cross represents the position of the center of the fitted circle. The uncertainties on the radial distances are not shown.*

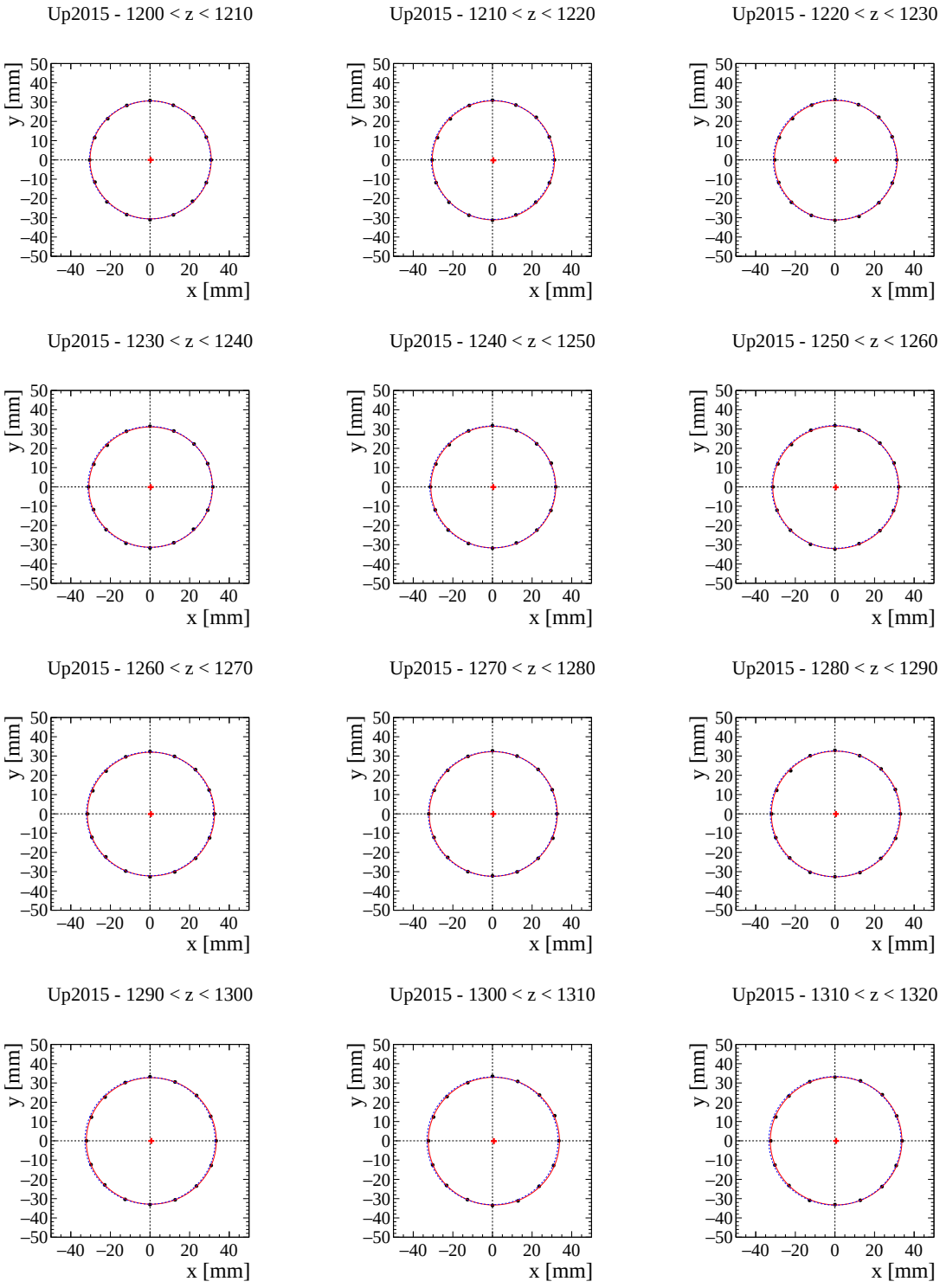

Figure B.30: *Measured radial distance in bins of the z coordinate for the Up 2015 sample. The red solid line corresponds to the fitted circle, whereas the blue dashed line is the design reference. The red cross represents the position of the center of the fitted circle. The uncertainties on the radial distances are not shown.*

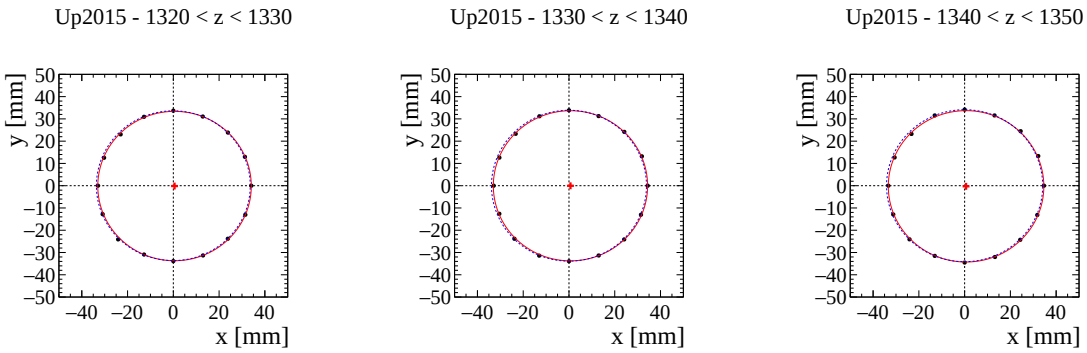

Figure B.31: *Measured radial distance in bins of the z coordinate for the Up 2015 sample. The red solid line corresponds to the fitted circle, whereas the blue dashed line is the design reference. The red cross represents the position of the center of the fitted circle. The uncertainties on the radial distances are not shown.*

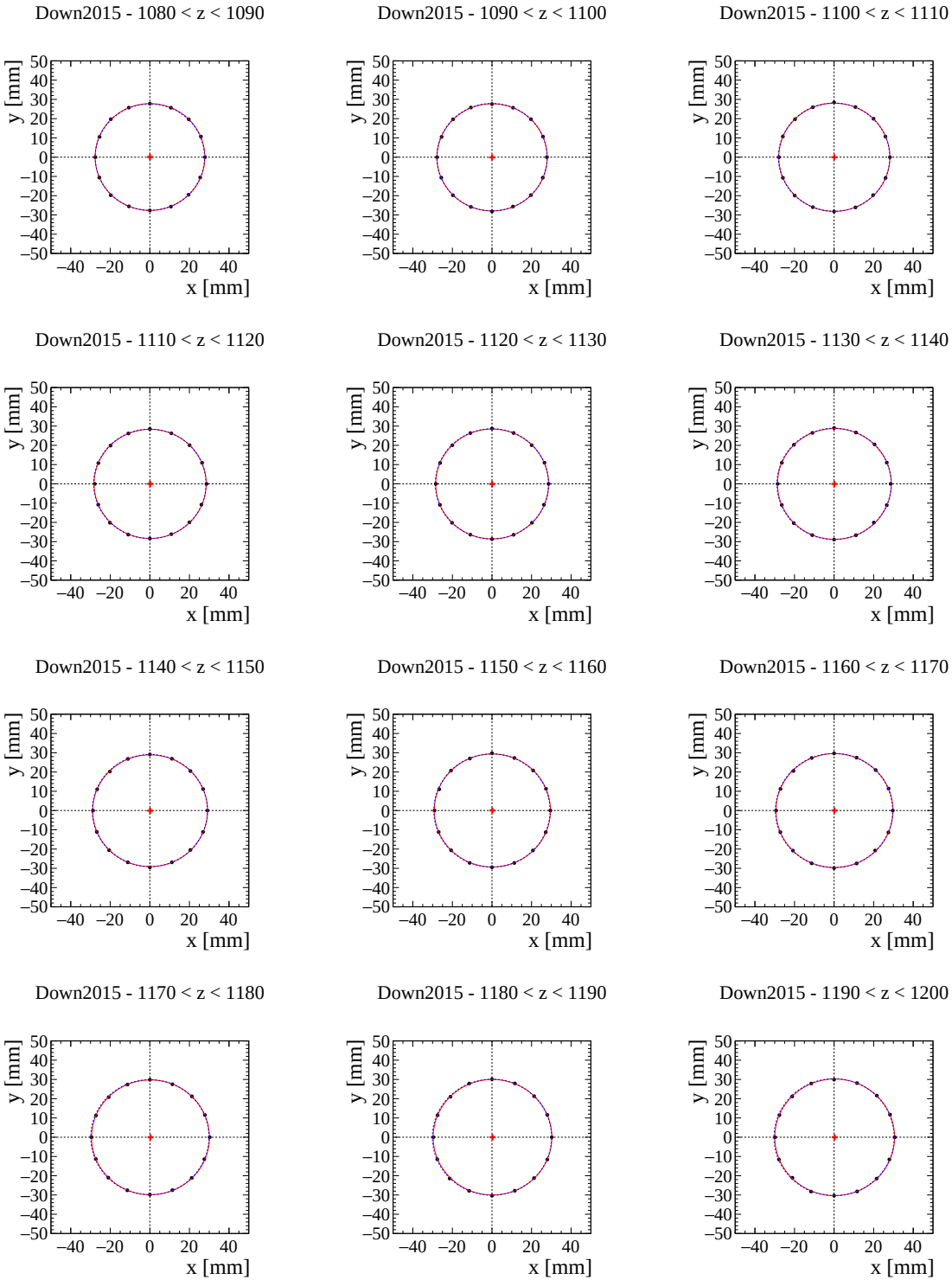

Figure B.32: *Measured radial distance in bins of the z coordinate for the Down 2015 sample. The red solid line corresponds to the fitted circle, whereas the blue dashed line is the design reference. The red cross represents the position of the center of the fitted circle. The uncertainties on the radial distances are not shown.*

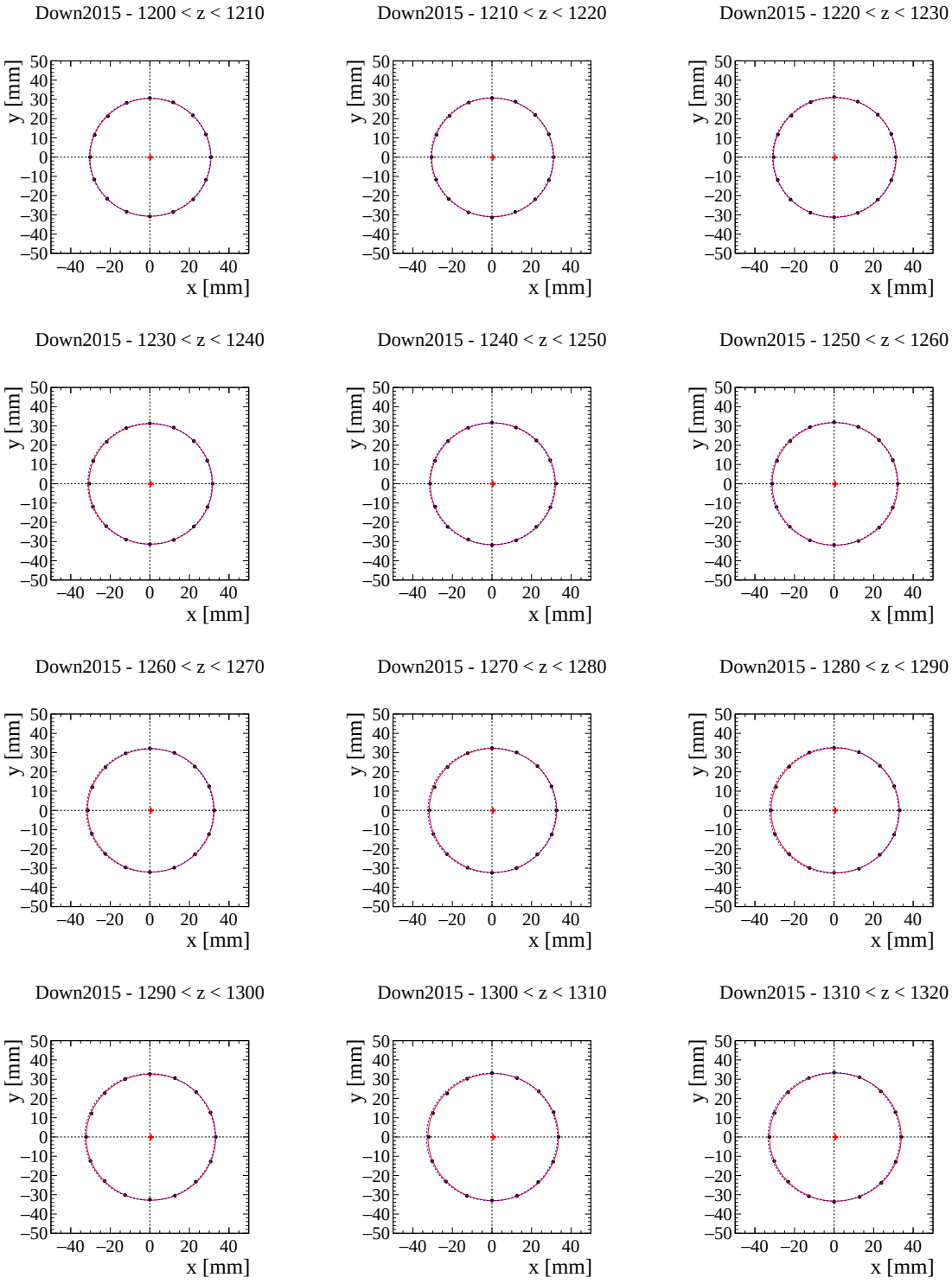

Figure B.33: *Measured radial distance in bins of the z coordinate for the Down 2015 sample. The red solid line corresponds to the fitted circle, whereas the blue dashed line is the design reference. The red cross represents the position of the center of the fitted circle. The uncertainties on the radial distances are not shown.*

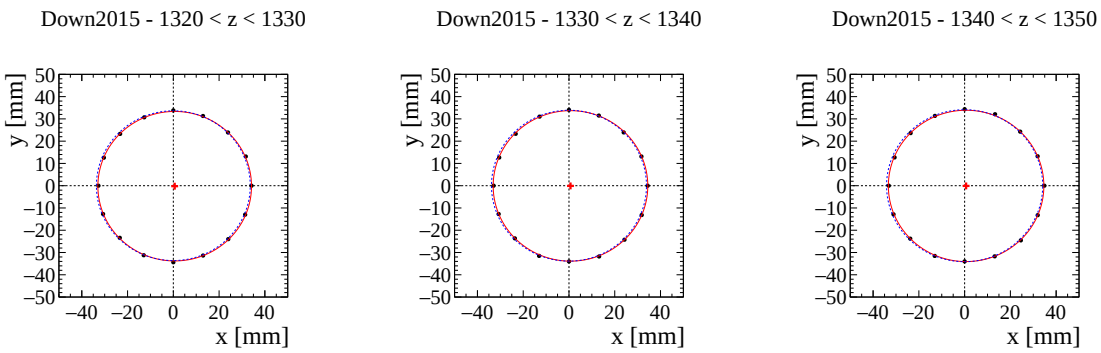

Figure B.34: *Measured radial distance in bins of the z coordinate for the Down 2015 sample. The red solid line corresponds to the fitted circle, whereas the blue dashed line is the design reference. The red cross represents the position of the center of the fitted circle. The uncertainties on the radial distances are not shown.*

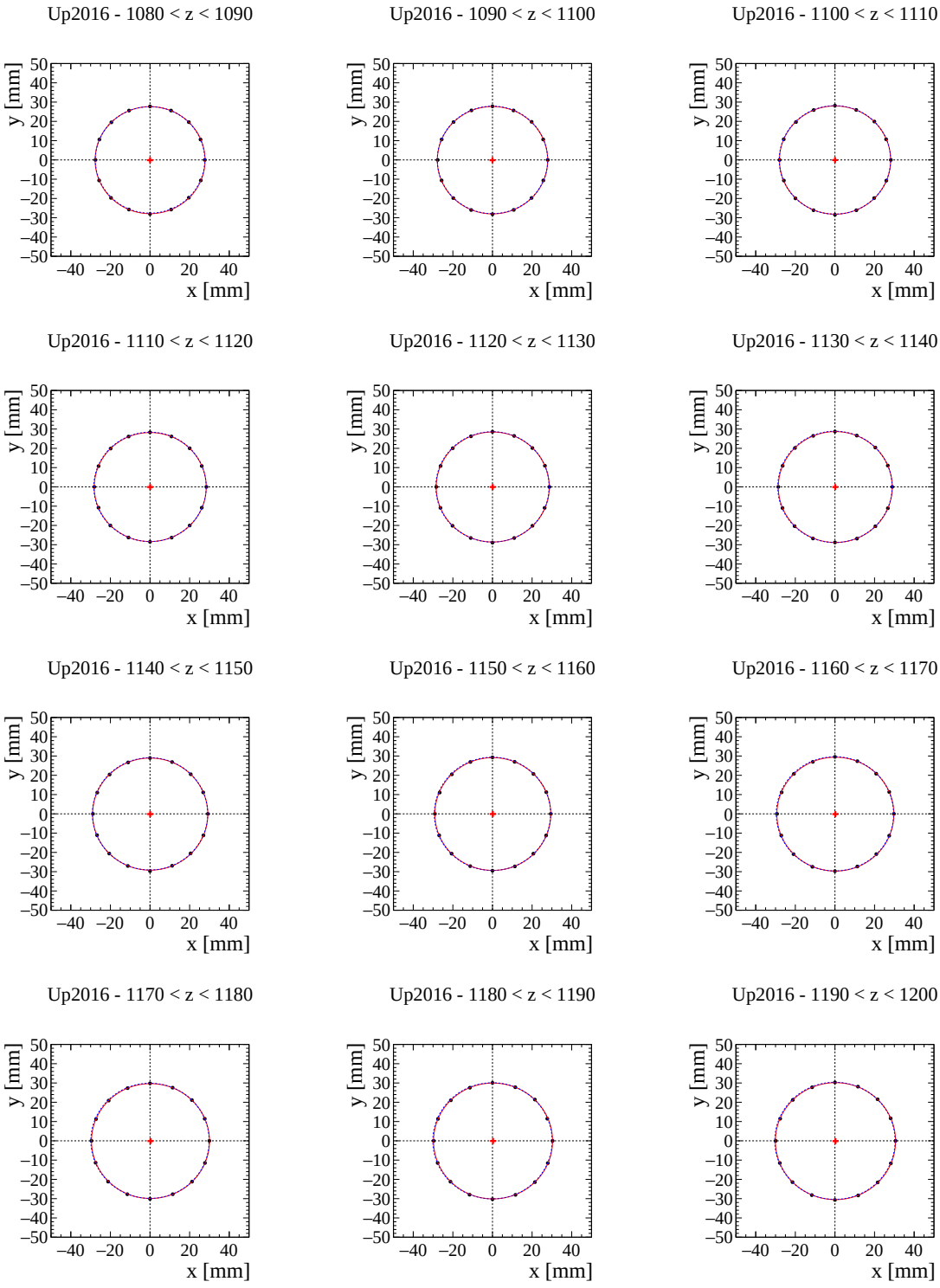

Figure B.35: *Measured radial distance in bins of the z coordinate for the Up 2016 sample. The red solid line corresponds to the fitted circle, whereas the blue dashed line is the design reference. The red cross represents the position of the center of the fitted circle. The uncertainties on the radial distances are not shown.*

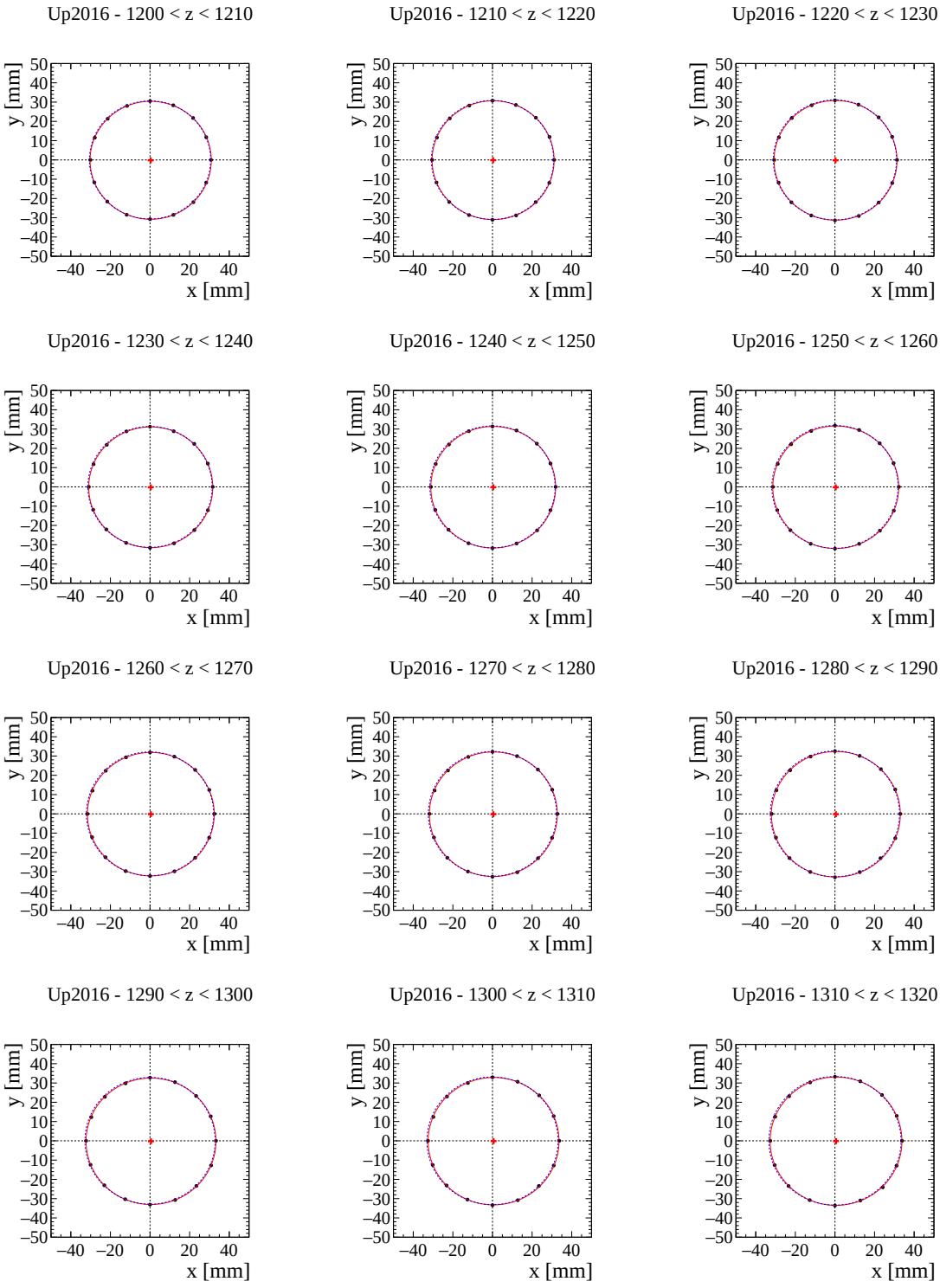

Figure B.36: *Measured radial distance in bins of the z coordinate for the Up 2016 sample. The red solid line corresponds to the fitted circle, whereas the blue dashed line is the design reference. The red cross represents the position of the center of the fitted circle. The uncertainties on the radial distances are not shown.*

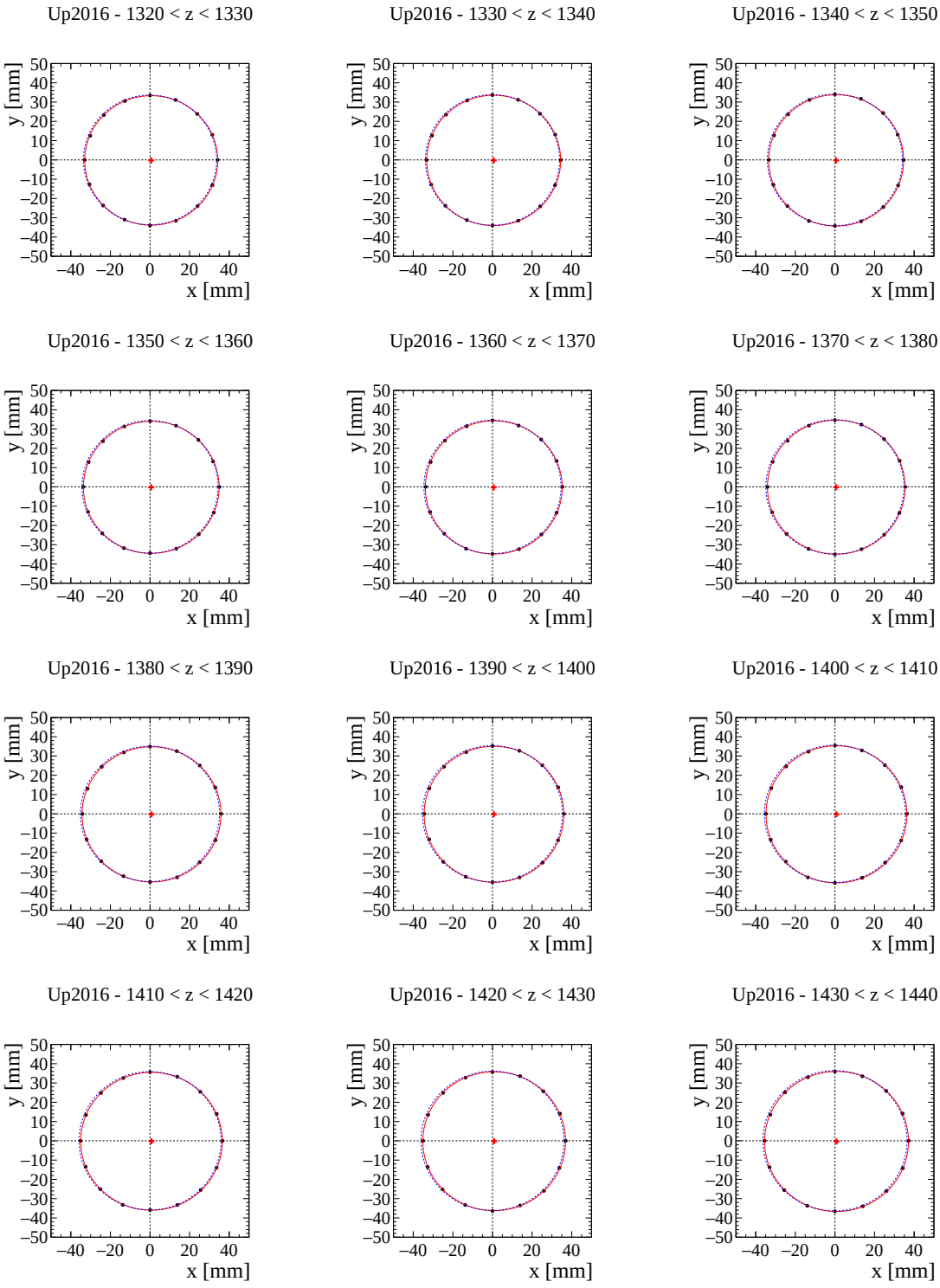

Figure B.37: *Measured radial distance in bins of the z coordinate for the Up 2016 sample. The red solid line corresponds to the fitted circle, whereas the blue dashed line is the design reference. The red cross represents the position of the center of the fitted circle. The uncertainties on the radial distances are not shown.*

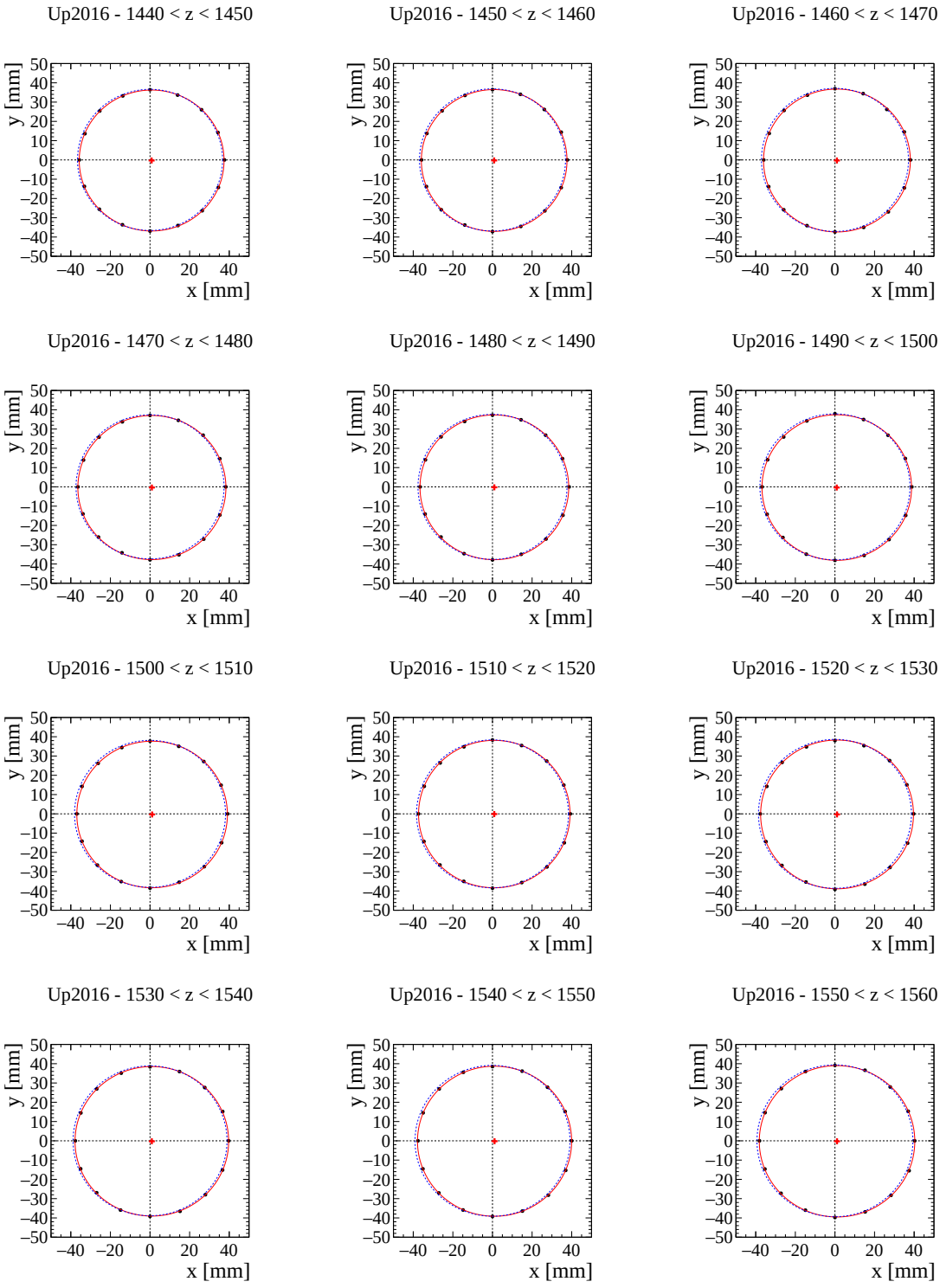

Figure B.38: *Measured radial distance in bins of the z coordinate for the Up 2016 sample. The red solid line corresponds to the fitted circle, whereas the blue dashed line is the design reference. The red cross represents the position of the center of the fitted circle. The uncertainties on the radial distances are not shown.*

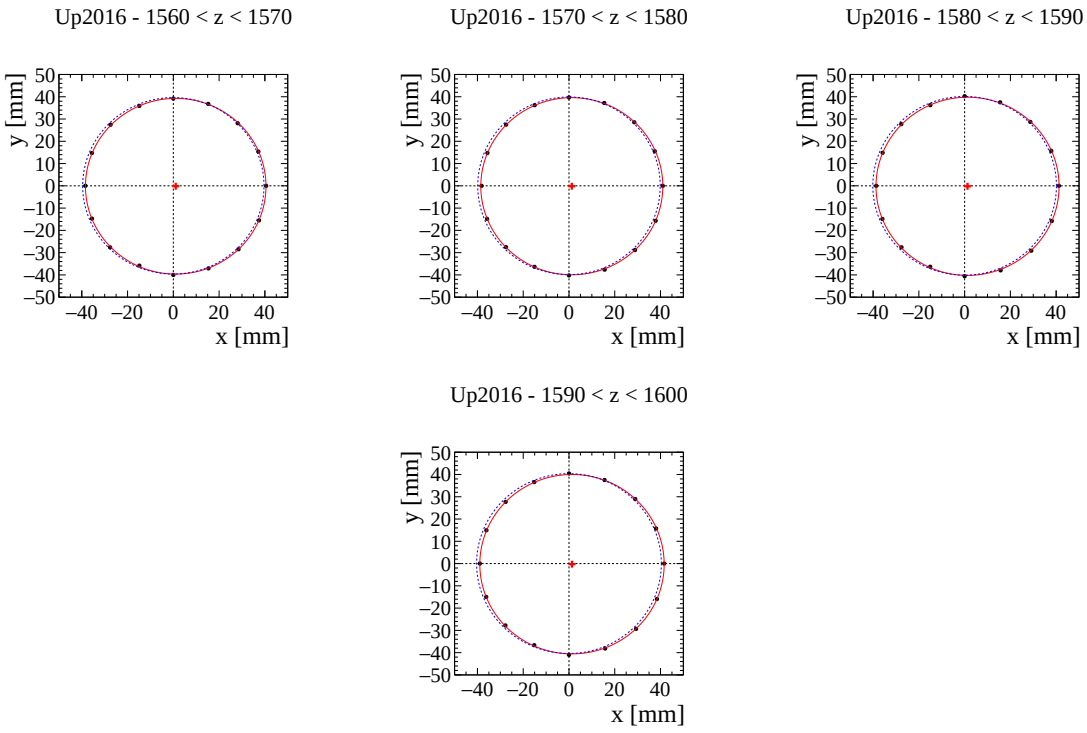

Figure B.39: *Measured radial distance in bins of the z coordinate for the Up 2016 sample. The red solid line corresponds to the fitted circle, whereas the blue dashed line is the design reference. The red cross represents the position of the center of the fitted circle. The uncertainties on the radial distances are not shown.*

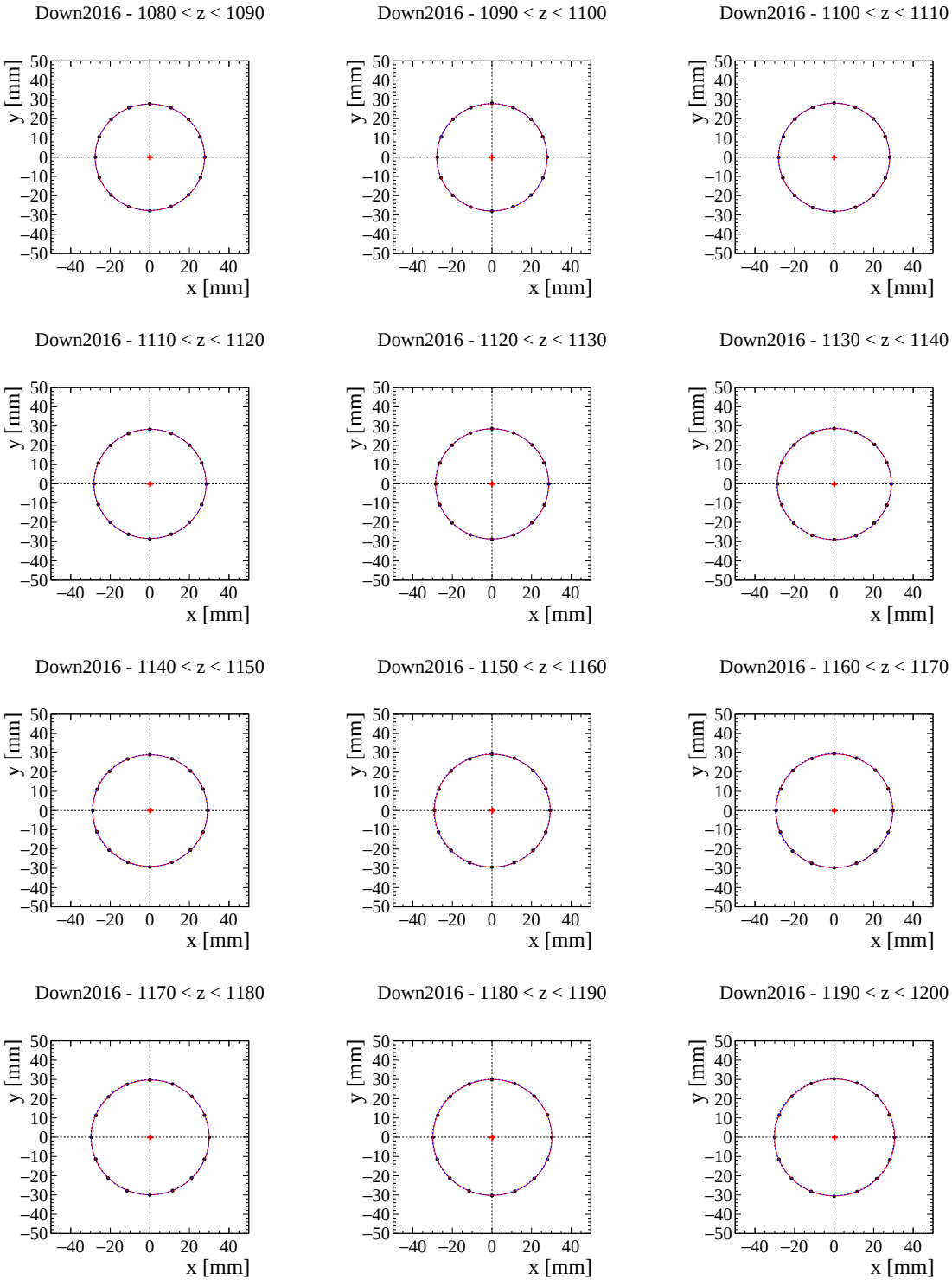

Figure B.40: *Measured radial distance in bins of the z coordinate for the Down 2016 sample. The red solid line corresponds to the fitted circle, whereas the blue dashed line is the design reference. The red cross represents the position of the center of the fitted circle. The uncertainties on the radial distances are not shown.*

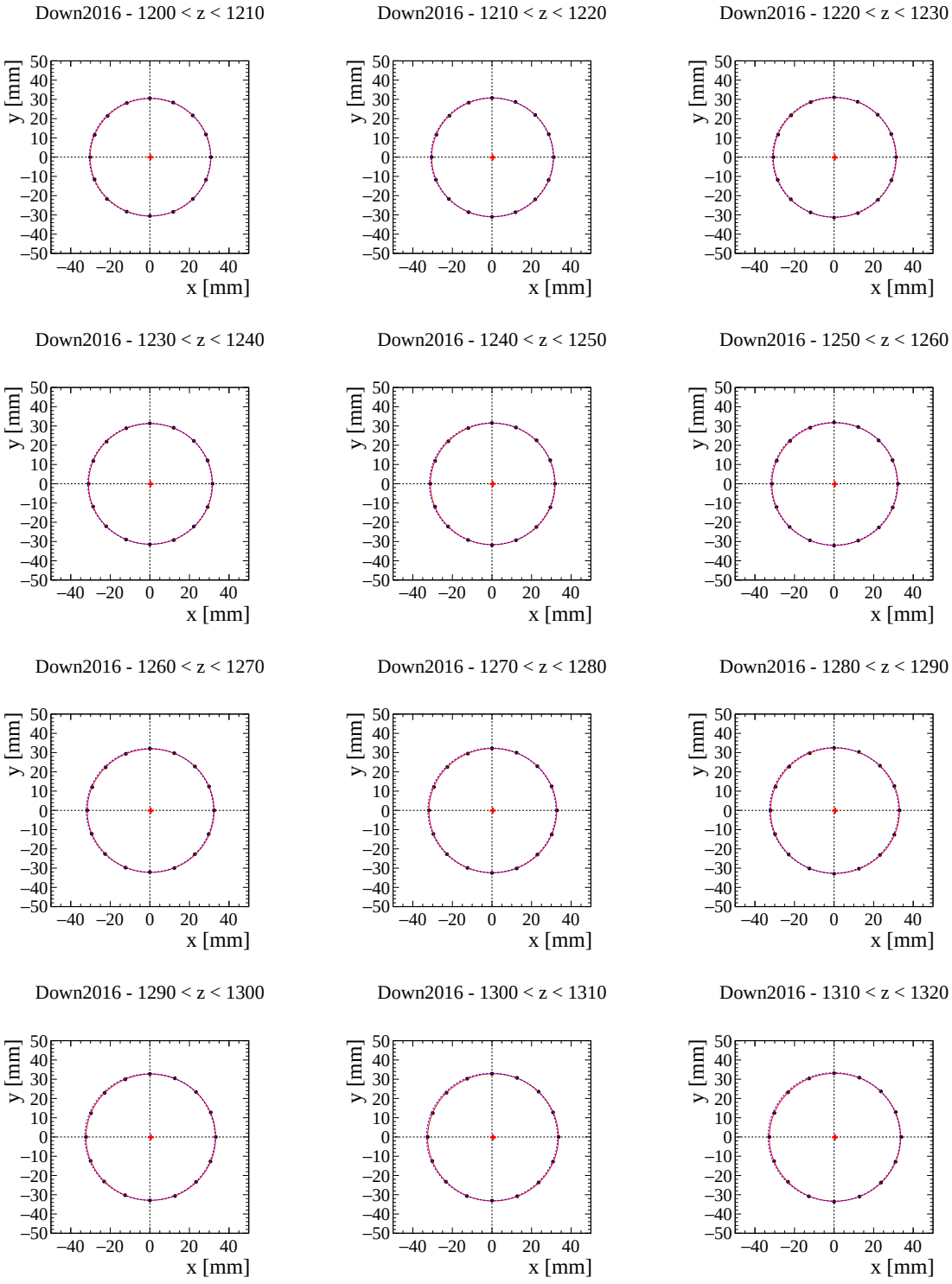

Figure B.41: *Measured radial distance in bins of the z coordinate for the Down 2016 sample. The red solid line corresponds to the fitted circle, whereas the blue dashed line is the design reference. The red cross represents the position of the center of the fitted circle. The uncertainties on the radial distances are not shown.*

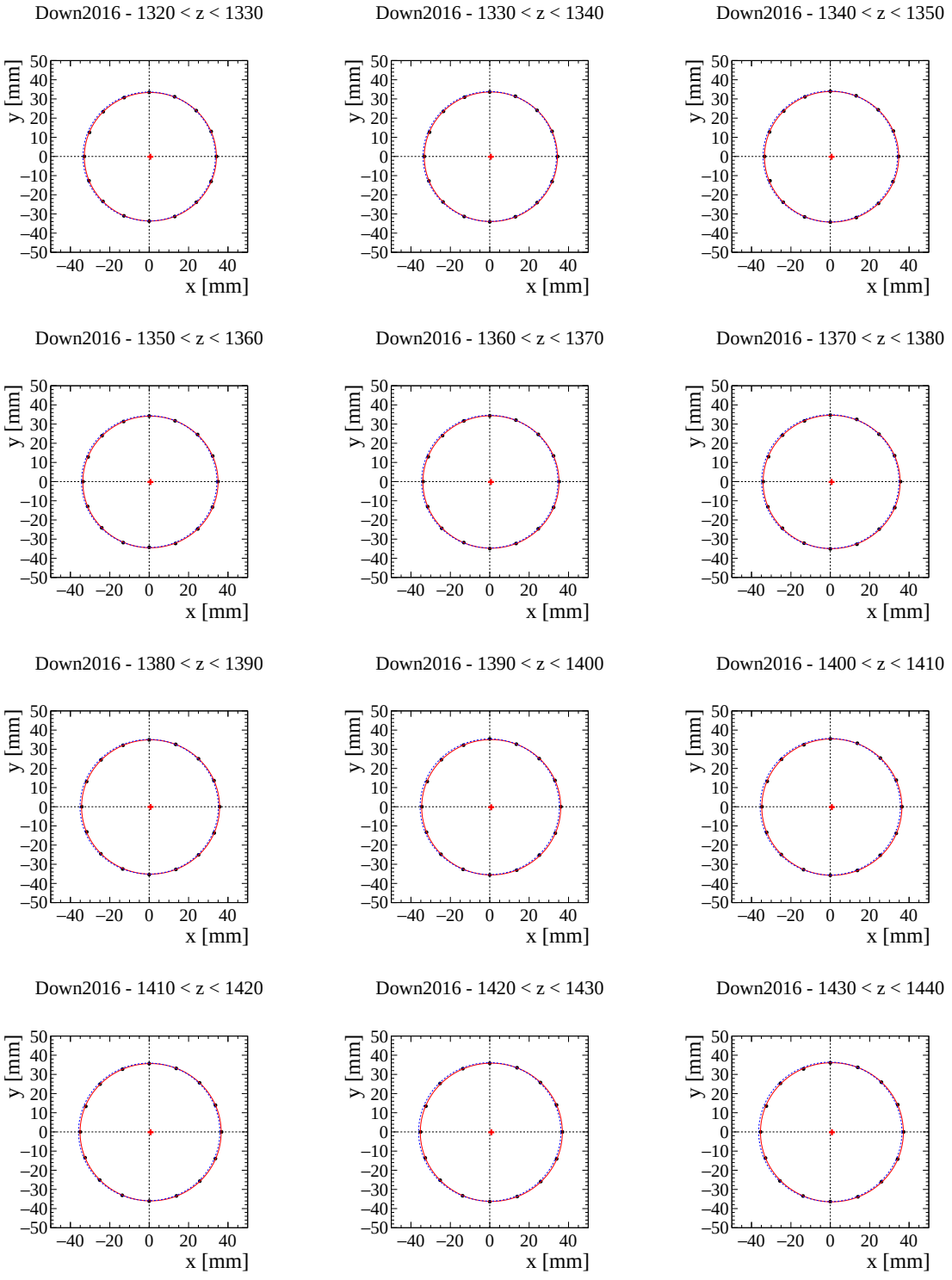

Figure B.42: *Measured radial distance in bins of the z coordinate for the Down 2016 sample. The red solid line corresponds to the fitted circle, whereas the blue dashed line is the design reference. The red cross represents the position of the center of the fitted circle. The uncertainties on the radial distances are not shown.*

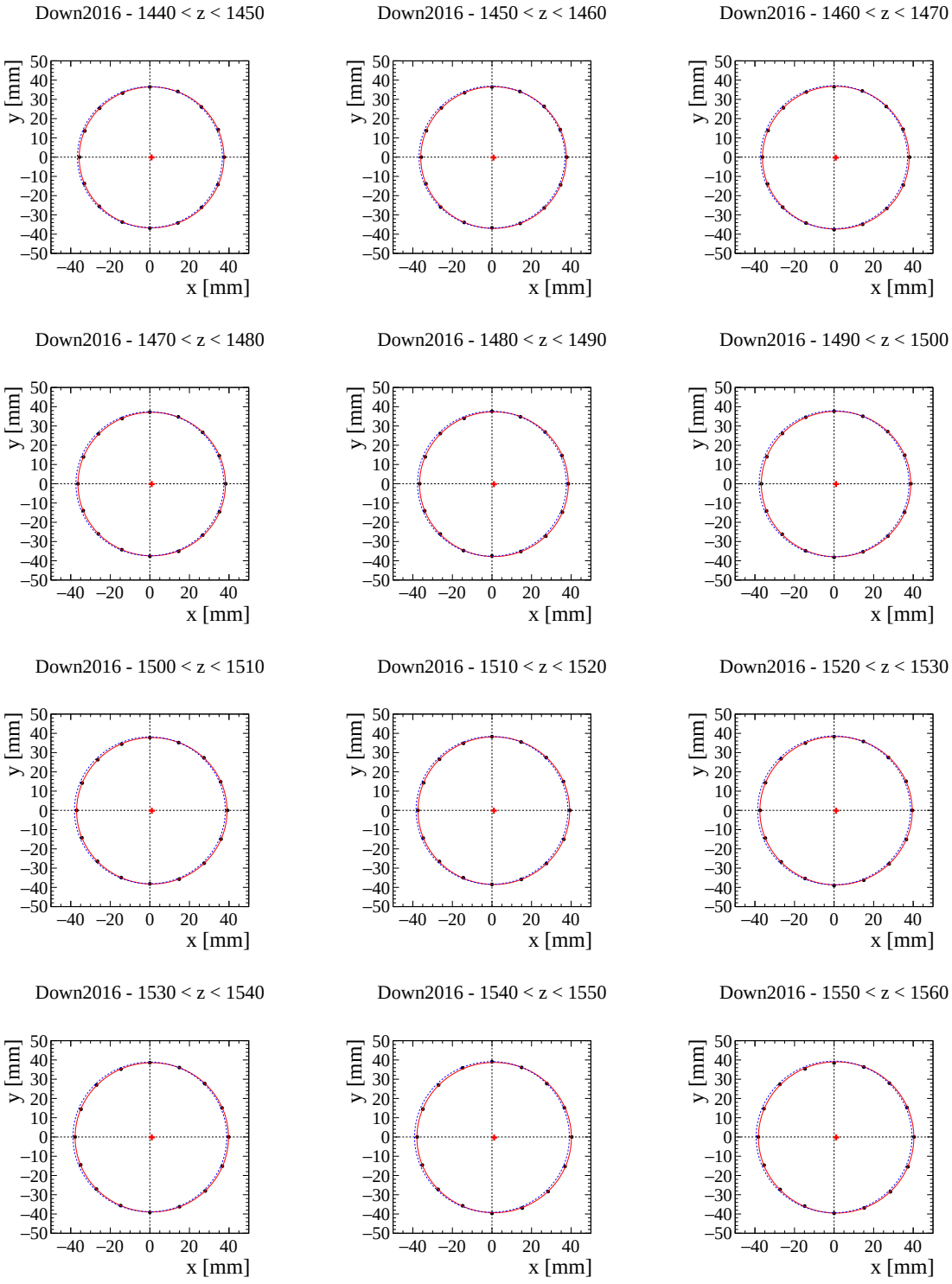

Figure B.43: *Measured radial distance in bins of the z coordinate for the Down 2016 sample. The red solid line corresponds to the fitted circle, whereas the blue dashed line is the design reference. The red cross represents the position of the center of the fitted circle. The uncertainties on the radial distances are not shown.*

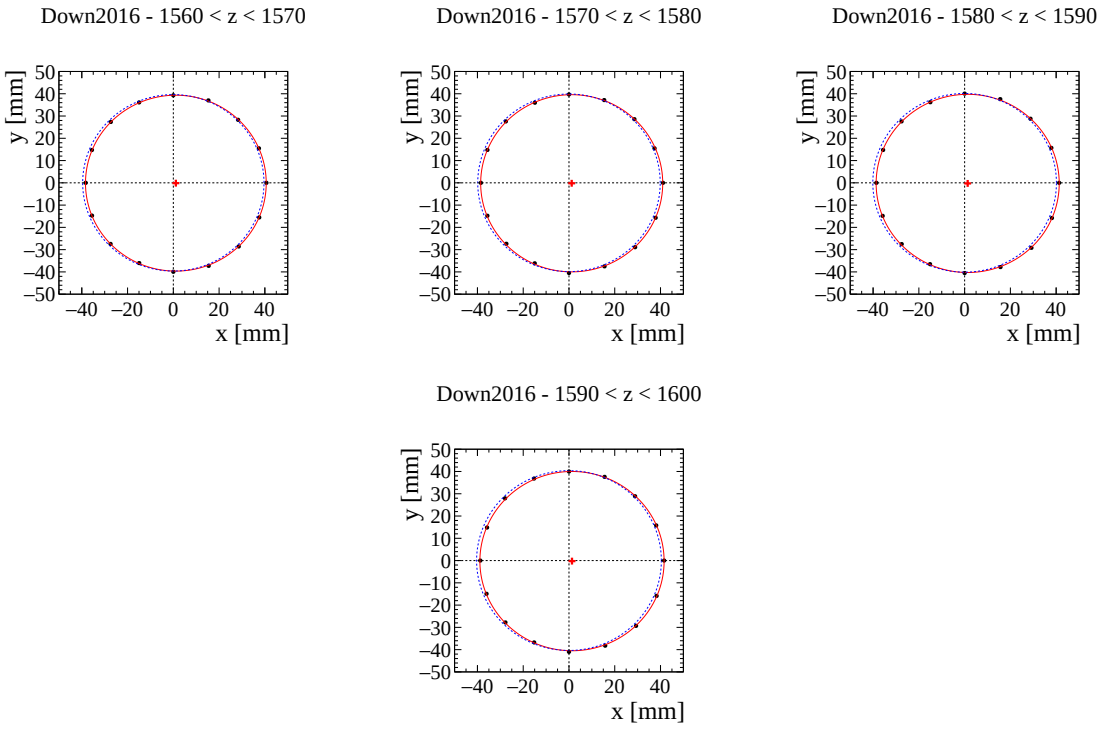

Figure B.44: *Measured radial distance in bins of the z coordinate for the Down 2016 sample. The red solid line corresponds to the fitted circle, whereas the blue dashed line is the design reference. The red cross represents the position of the center of the fitted circle. The uncertainties on the radial distances are not shown.*

C Additional studies with $\Lambda_b^0 \to pK^-$ and $\Lambda_b^0 \to p\pi^-$ decays

C.1 Validation of the cross-feed background model

A sample of $K^+\pi^-$ events is selected with very tight requirements in order to remove almost all the combinatorial background and the contamination from charmless two-body b-hadron decays different from the $B^0 \to K^+\pi^-$ and $B_s^0 \to \pi^+K^-$ channels (the values of the requirements are reported in Tab. C.1).

Table C.1: *Selection requirements used to select the sample shown in Fig. C.1. This selection is applied in order to remove as much combinatorial background as possible and to select only $K^+\pi^-$ (or $K^-\pi^+$) pairs of tracks.*

Requirement type	Value
BDT	> 0.4
$\Delta \log \mathcal{L}_{K-\pi}\ (K)$	> 7
$\Delta \log \mathcal{L}_{K-p}\ (K)$	> 0
$\Delta \log \mathcal{L}_{K-\pi}\ (\pi)$	< -7
$\Delta \log \mathcal{L}_{p-\pi}\ (\pi)$	< 0

To determine the amount of the various contributions, an invariant-mass fit of the $K^+\pi^-$ spectrum is performed. The signals are parameterised as described in Sec. 5.5.1, whereas the combinatorial background is described with an exponential function. In the case of partially-reconstructed backgrounds we consider two sources, one coming from multibody decays of the B^0 meson and one coming from the multibody decays of the B_s^0 meson, as done in Ref. [103]. Both contributions are modelled with an ARGUS function convolved with the same resolution function used for the signals. The end points of the two ARGUS functions are fixed to the values $m_{B^0} - m_{\pi^0}$ and $m_{B_s^0} - m_{\pi^0}$, where m_{B^0},

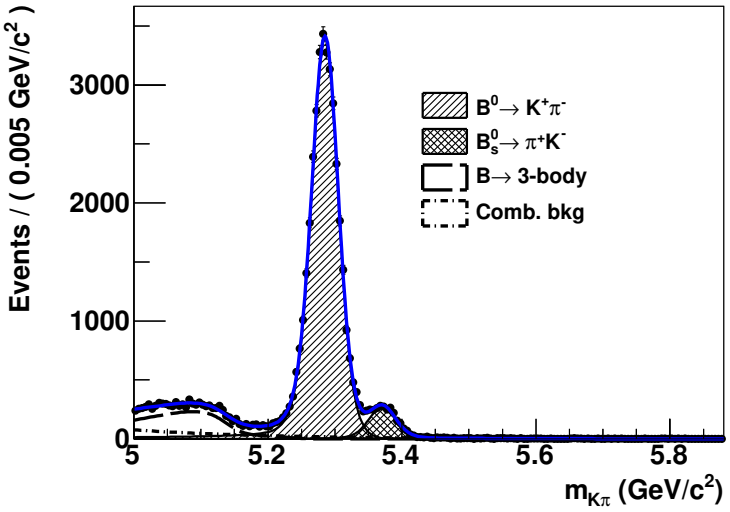

Figure C.1: *Invariant $K\pi$ mass distribution for events passing the preselection described in Sec. 5.3 and the requirements reported in Tab. C.1. The result of the best fit is superimposed to the data points. The description of the fit model is reported in the text.*

$m_{B_s^0}$ and m_{π^0} are the masses of the B^0, B_s^0 and π^0 mesons, as reported in Ref. [17]. The other parameter governing the shape of the ARGUS function is in common between the B^0 and B_s^0 components and left free in the fit. In Fig. C.1 we report the distribution of $m_{K^+\pi^-}$ with the result of the best fit superimposed. The invariant mass computed under the K^+K^- hypothesis for the same sample is reported in Fig. C.2 (black histogram). The distribution of $m_{K^+K^-}$ for fully simulated samples of $B^0 \to K^+\pi^-$ (red filled histogram) and $B_s^0 \to \pi^+K^-$ decays (green filled histogram) are superimposed. The two histograms are rescaled in order to match the yields extracted from the fit of Fig. C.1. To reproduce the invariant-mass resolution induced by the detector, we add a smearing to the wrong mass of each event, randomly extracted according to a double Gaussian function with the parameters determined from the fit shown in Fig. C.1. Note that in Fig. C.2 we report the case where the PID weights w_i are not considered when creating the signal histograms (left) and the case where PID effect has been taken into account (right). The improved agreement apparent in the right-hand plot, with respect to that on the left, demonstrates the impact of PID in the parameterisation of cross-feed backgrounds.

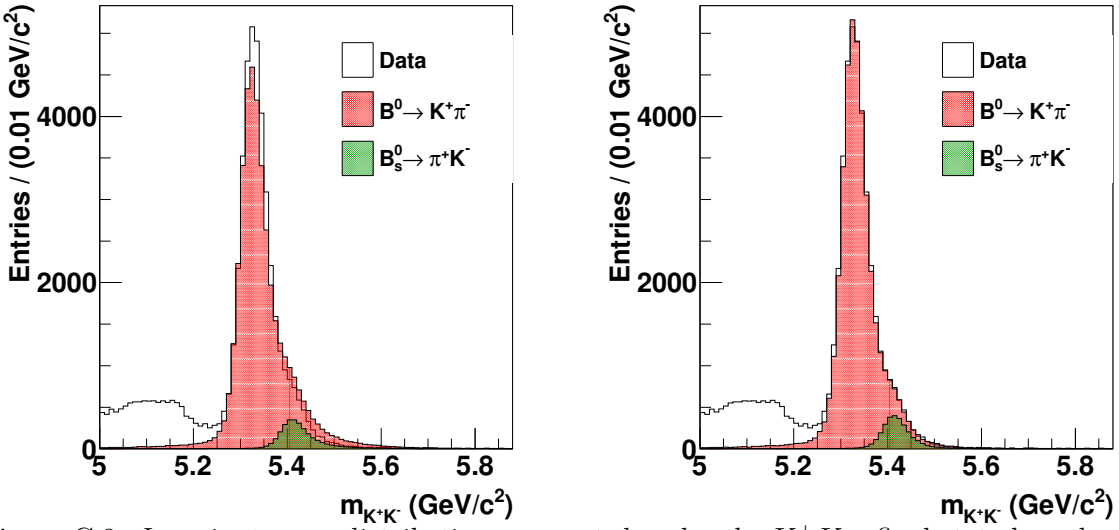

Figure C.2: *Invariant-mass distributions computed under the K^+K^- final state hypothesis for event passing the preselection described in Sec. 5.3 and the requirements reported in Tab. C.1. The template histograms describing the shapes of (filled red) $B^0 \to K^+\pi^-$ and (filled green) $B_s^0 \to \pi^+K^-$ decays are obtained from fully simulated events and rescaled to the yields extracted from the fit shown in Fig. C.1. On the left the template histograms are created without taking into account the effect of PID requirements, while the template histograms on the right take this effect into account.*

D

Additional studies with $B \to h^+h'^-$ decays

D.1 Study of the differences between 2011 and 2012 data

The distributions of the variables listed in Tab. 6.7 and their correlations are studied. Background events are selected from the high invariant-mass sideband, $m > 5.6\,\text{GeV}/c^2$ (for the K^+K^- and $\pi^+\pi^-$ spectra), after applying the PID requirements reported in Tab. 6.6 and used to separate K^+K^- and $\pi^+\pi^-$ final states. The distributions are reported for the total sample in Figs. D.1 and D.4 (for the K^+K^- and $\pi^+\pi^-$ cases, respectively), for 2011 only (Figs. D.2 and D.5) and for 2012 only (Figs. D.3 and D.6). Figures D.7 and D.8 show the correlation between the variables for signal-like and background-like for the training of the BDT used to select the $B_s^0 \to K^+K^-$ and the $B^0 \to \pi^+\pi^-$ samples. The same tables are shown separately for the total sample, 2011 sample only and 2012 sample only. No significant differences are observed in the distributions or in the correlations of the variables between the different data taking periods.

As a further check to confirm that separate optimisations for 2011 and 2012 data are not needed, the optimisation of the BDT selection, from the training of the multivariate classifier to the definition of the optimal requirement on the BDT output, as described in Sec. 6.4.2, is performed using 2011 and 2012 samples separately. In Figs. D.9 and D.10 the $\xi = S/\sqrt{S+B}$ value as a function of the requirement on the BDT variable is reported for the optimisation performed separately using 2011 and 2012 samples, together with the one already shown in Fig. 6.5. In the same figure the simplified fits of Fig. 6.4, but applied to the data surviving the BDT requirements that gives the largest value of ξ are also reported, again separately for the 2011, 2012 and total optimisation. The same optimal requirement is found from the different optimisations for the $B_s^0 \to K^+K^-$ and $B^0 \to \pi^+\pi^-$ decays. Finally, in Tab. D.1 the maximum value of ξ as obtained from the optimisation procedure is compared to that determined from the fits shown in Figs. D.9 and D.10. Very similar maximum values of ξ are found between the optimisation procedure and the simplified fits. In addition, in the same table the yields of the two signals obtained from the fits are reported. It is worth noting that the sum of the yields obtained from the 2011 and 2012

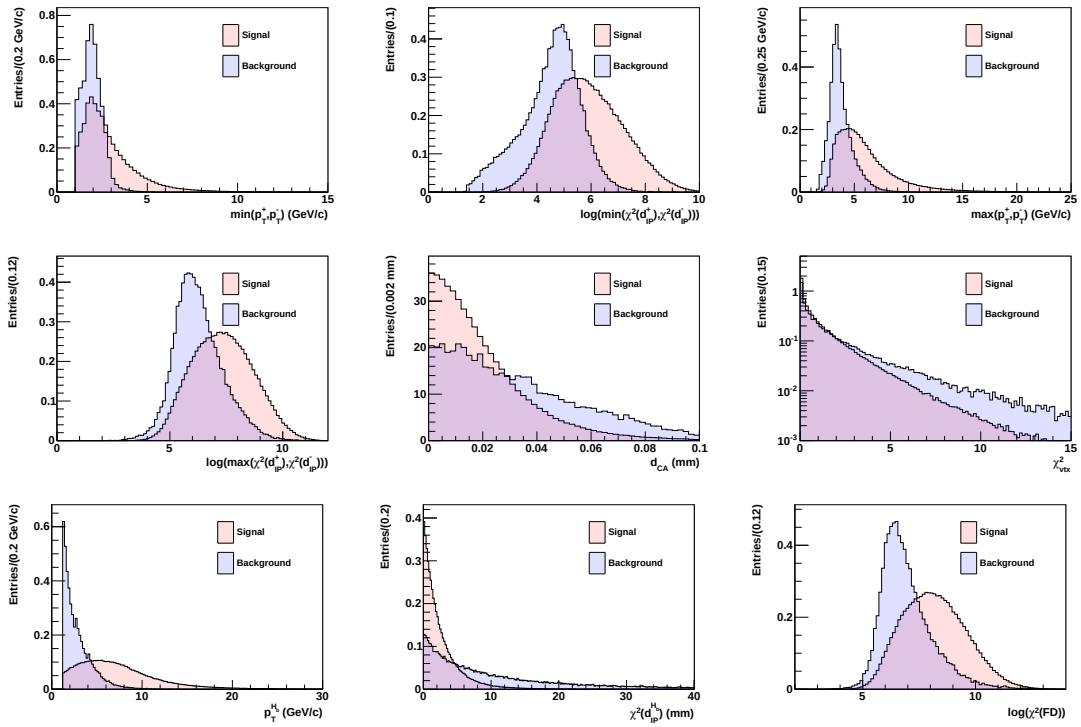

Figure D.1: *Distributions of the variables used in the training of the BDT algorithms for (red histogram) $B_s^0 \to K^+K^-$ decays and (blue histogram) high invariant-mass sideband events. The sum of 2011 and 2012 samples is used to produce the histograms.*

Table D.1: *Maximum values of the figure of merit $\xi = S/\sqrt{S+B}$ obtained from the optimisation of the BDT selection and from unbinned maximum likelihood fits to the invariant-mass spectra of selected candidates. The comparison between the optimisations of the selections performed using 2011, 2012 and total sample is reported.*

Year	$B_s^0 \to K^+K^-$			$B^0 \to \pi^+\pi^-$		
	Yields	ξ_{max}^{fit}	ξ_{max}^{opt}	Yields	ξ_{max}^{fit}	ξ_{max}^{opt}
2011	13145 ± 130	109.583	110.436	8680 ± 109	88.2714	90.9677
2012	29350 ± 198	162.137	163.919	19409 ± 168	130.864	130.666
Total	42462 ± 236	195.869	197.371	28014 ± 199	158.024	160.499

optimisations is very well in agreement with the yields obtained when merging 2011 and 2012 samples.

Finally, in Fig. D.11 the correlations among the variables used to train the BDT and those in the final fit to determine the *CP*-violating observables are reported.

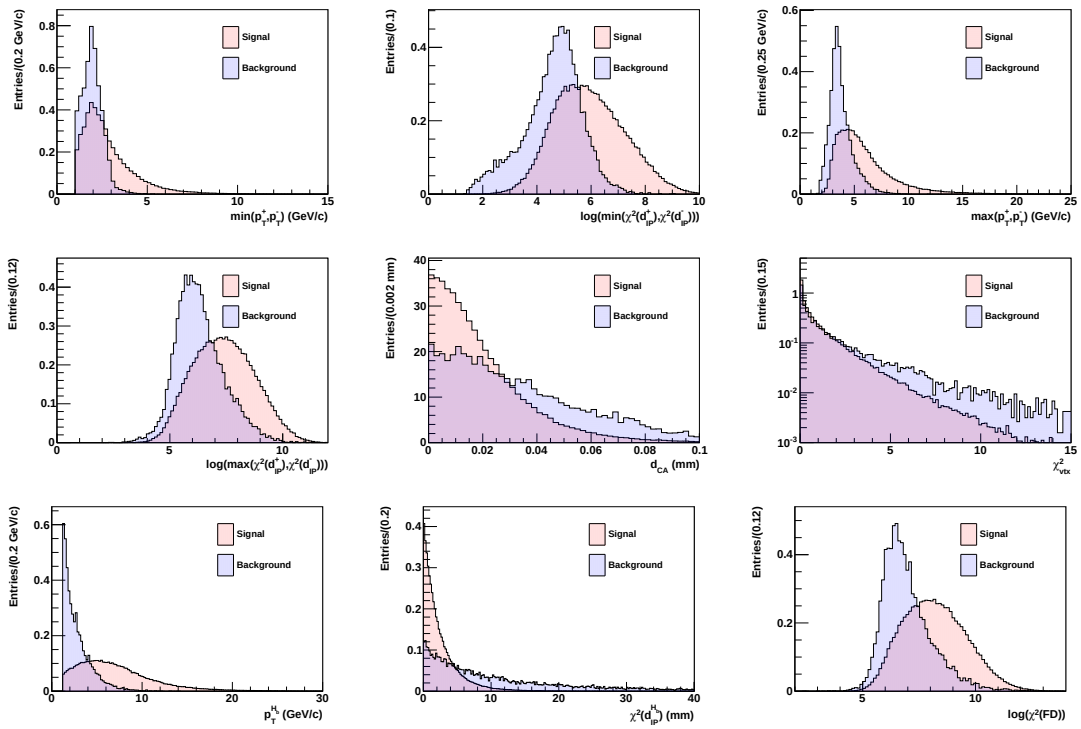

Figure D.2: *Distributions of the variables used in the training of the BDT algorithms for (red histogram) $B_s^0 \to K^+K^-$ decays and (blue histogram) high invariant-mass sideband events. Only 2011 samples are used to produce the histograms.*

D.2 Background subtraction

The background subtraction of for two-body b-hadron decay events is performed using the *sPlot* technique [85], by fitting the invariant mass computed assuming both final state particles to be pions ($m_{\pi\pi}$). Events are selected applying the BDT requirements corresponding to $BDT_{\pi^+\pi^-}$. The shapes of signal contributions have been parameterised applying a Kernel Estimation Method [89] to the distribution of $m_{\pi^+\pi^-}$ for fully simulated events, where $m_{\pi^+\pi^-}$ has been computed assuming perfect invariant-mass resolution. The obtained non-parametric distributions are then convolved with a Gaussian resolution model with free mean and width. The relative fractions between the various two-body decays are fixed to the values measured by LHCb in Ref. [105]. In the case of Λ_b^0 decays, the world averages of the absolute branching ratios computed by the Heavy Flavour Averaging Group (HFLAV) are used; they are reported in Ref. [67]. The value of the hadronisation fraction for Λ_b^0 baryons is taken from the LHCb measurement of $f_{\Lambda_b^0}/(f_d + f_u)$, published in Ref. [123], assuming also $f_d \approx f_u$. The measurement is dominated by the external input of $\mathcal{B}$ $(\Lambda_c^+ \to pK^-\pi^+)$, and the central value is with a good approximation inversely proportional to this branching ratio. Hence the value of $f_{\Lambda_b^0}/(f_d + f_u)$ is rescaled by the ratio between the input used in the LHCb paper, and the updated value published by Belle in Ref. [124]. The contribution due to combinatorial background has been parameterized

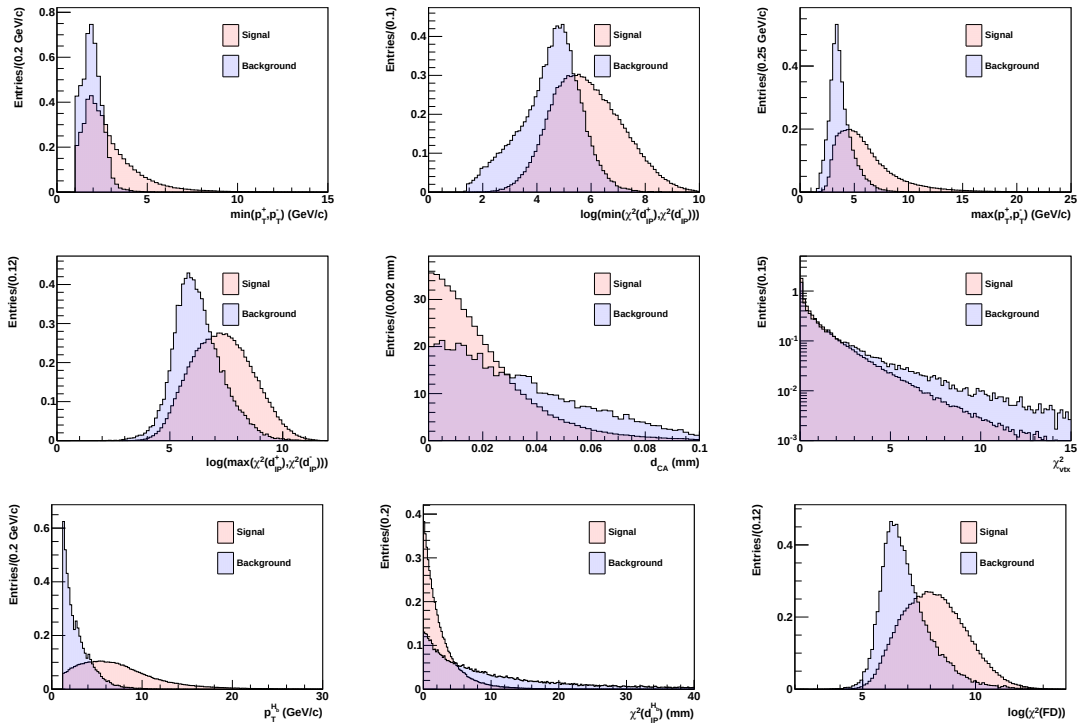

Figure D.3: *Distributions of the variables used in the training of the BDT algorithms for (red histogram) $B_s^0 \to K^+K^-$ decays and (blue histogram) high invariant-mass sideband events. Only 2012 samples are used to produce the histograms.*

with an exponential function, while the component coming from partially reconstructed 3-body B decays is described using an ARGUS function [114] convolved with the same Gaussian resolution model used for the signal shapes

$$f(m) = A \cdot \left[m' \sqrt{1 - \frac{m'^2}{m_0^2}} \Theta(m_0 - m') e^{c\frac{m'}{m_0}} \right] \otimes G(m - m'; \delta_m, \sigma_1), \tag{D.1}$$

where A is a normalisation constant, m_0 is the end-point of the ARGUS function, c is a parameter governing the shape of the function, G is a Gaussian resolution model and $\otimes$ stands for the convolution product. The $m_{\pi\pi}$ distribution is reported in Fig. D.12 with the result of the fit overlaid.

D.3 Distribution of pull variables

The results of the fast pseudoexperiment studies performed to validate the fitting code are reported. Two set of of pseudoexperiments are performed: one reproducing the fit including the OS+SScomb tagging information, that is used for the pulls of $C_{\pi^+\pi^-}$ and $S_{\pi^+\pi^-}$, and one including the information of OS+SSkNN, that is used for the pulls of $C_{K^+K^-}$, $S_{K^+K^-}$ and $A^{\Delta\Gamma}_{K^+K^-}$.

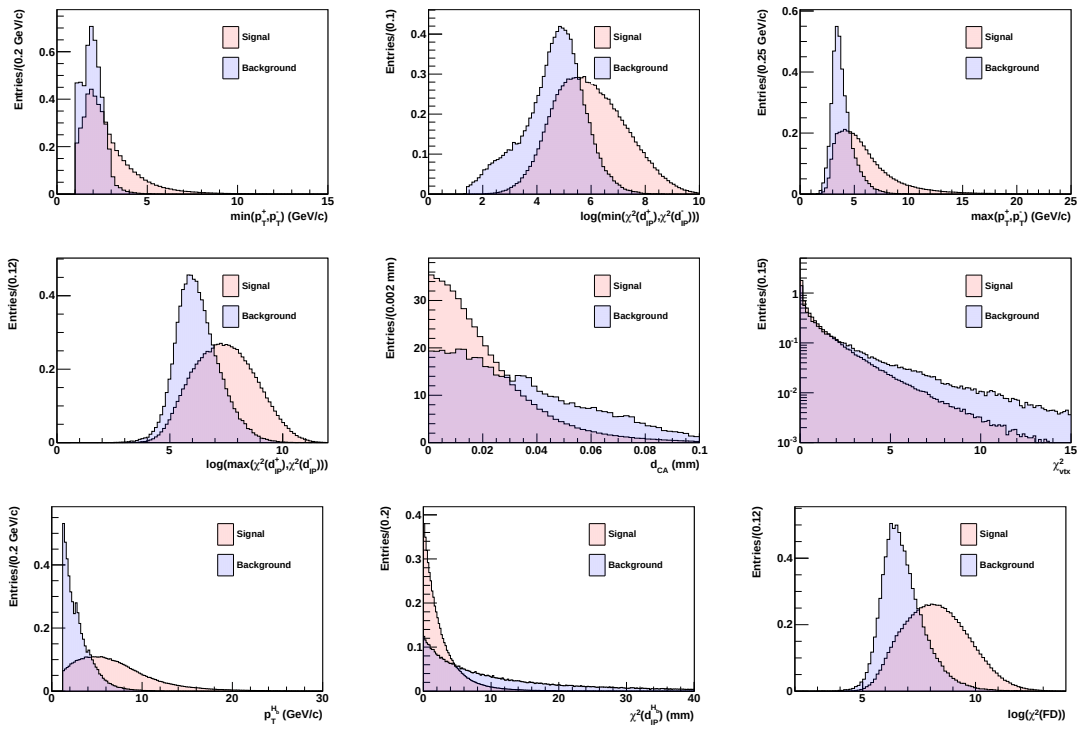

Figure D.4: *Distributions of the variables used in the training of the BDT algorithms for (red histogram) $B^0 \to \pi^+\pi^-$ decays and (blue histogram) high invariant-mass sideband events. The sum of 2011 and 2012 samples is used to produce the histograms.*

D.4 Studies of SSkNN tagging

D.4.1 SSkNN tagging calibration in simulated events

To better understand the dependence of the the SSkNN calibration parameters on the event kinematics a detailed study is performed on a simulated sample of $B_s^0 \to D_s^-\pi^+$ events corresponding to the luminosity of $3\,\text{fb}^{-1}$. This study aims at verifying if the fit is able to retrieve the correct mistag ω. First the generated true decay-time is used, avoiding in this way any effect on the determination of ω due to the decay-time resolution. The sample is split in two bins of B transverse momentum, by requiring $p_{\text{T}}^B > (<) 9\,\text{GeV}/c$. The calibration fit is performed both splitting the sample in η categories and using a per-event mistag. The first fit choice enables the linearity of the relation between ω and η to be measured, while with the second it is possible to obtain more precise results. In both the methods the average of η is fixed to 0.44. The fit results are reported in Tab. D.2. The linear relation of ω as a function of η is shown in Fig. D.14, where both ω value estimated from the per-event fit and the one evaluated using the Monte Carlo truth information are shown. The difference between the calibration functions in the two kinematic regions is reported in Fig. D.15. In each sample the ω values obtained from the fit are in good agreement with the Monte Carlo truth information. However, a small trend is observed in

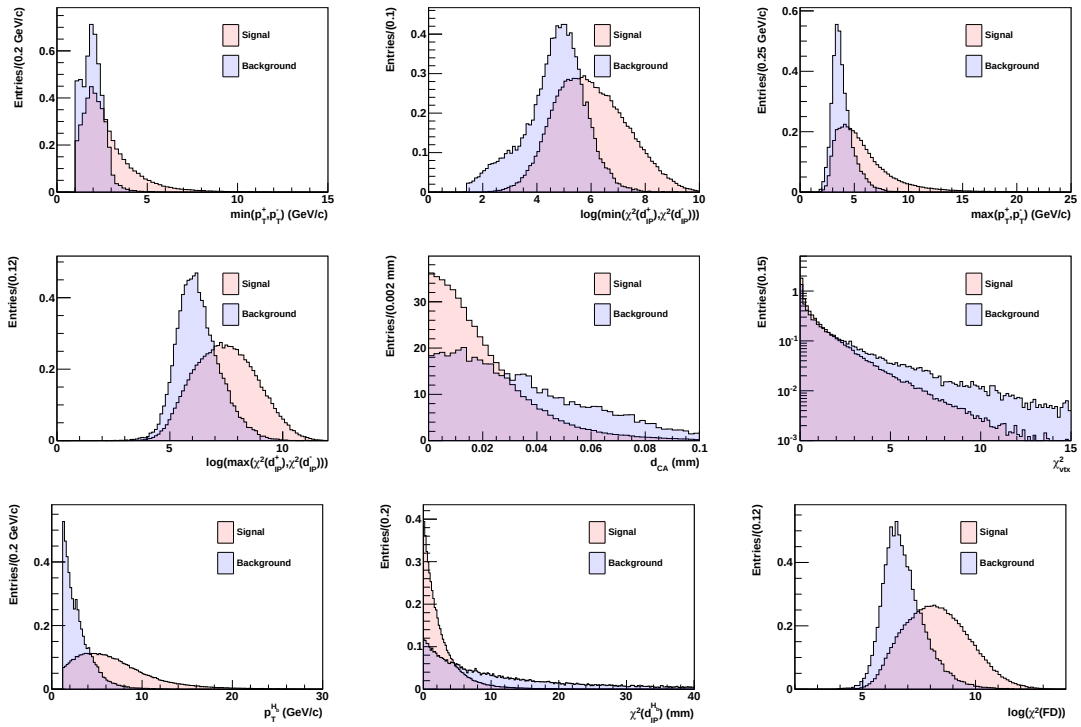

Figure D.5: *Distributions of the variables used in the training of the BDT algorithms for (red histogram) $B^0 \to \pi^+\pi^-$ decays and (blue histogram) high invariant-mass sideband events. Only 2011 samples are used to produce the histograms.*

Table D.2: *Calibration parameters for the* SSkNN *tagging response in different kinematic regions, using the true decay-time in the fit.*

$p_{\rm T}^B$	Category			Event		
	p_0 [fs]	p_1	$\rho(p0,p1)$	p_0 [fs]	p_1	$\rho(p0,p1)$
–	0.4410 ± 0.0014	0.952 ± 0.015	0.270	0.4409 ± 0.0014	0.953 ± 0.015	0.246
< 9	0.4423 ± 0.0017	0.906 ± 0.023	0.130	0.4423 ± 0.0017	0.917 ± 0.023	0.123
> 9	0.4389 ± 0.0025	0.970 ± 0.019	0.434	0.4389 ± 0.0025	0.975 ± 0.021	0.403

p_1, increasing between the two kinematic bins, as reported in Tab. D.2.

A second check is performed using the reconstructed decay-time and including the decay-time resolution in the calibration fit. Also in this case the fit is repeated both using a per-category and a per-event mistag, keeping the same split in two kinematic regions. The decay-time resolution is considered as a per-event observable, as done with data, and the average value of η is fixed to 0.44. The fit results are reported in Tab. D.3 whereas the plots of the ω vs η dependence and of the difference between the calibrations in the two $p_{\rm T}^B$ bins are shown in Figs. D.16 and D.15, respectively. Also in this case, the response of the SSkNN tagger is in very good agreement with the expected Monte Carlo truth value. The same dependence of the calibration parameters on the B transverse momentum is

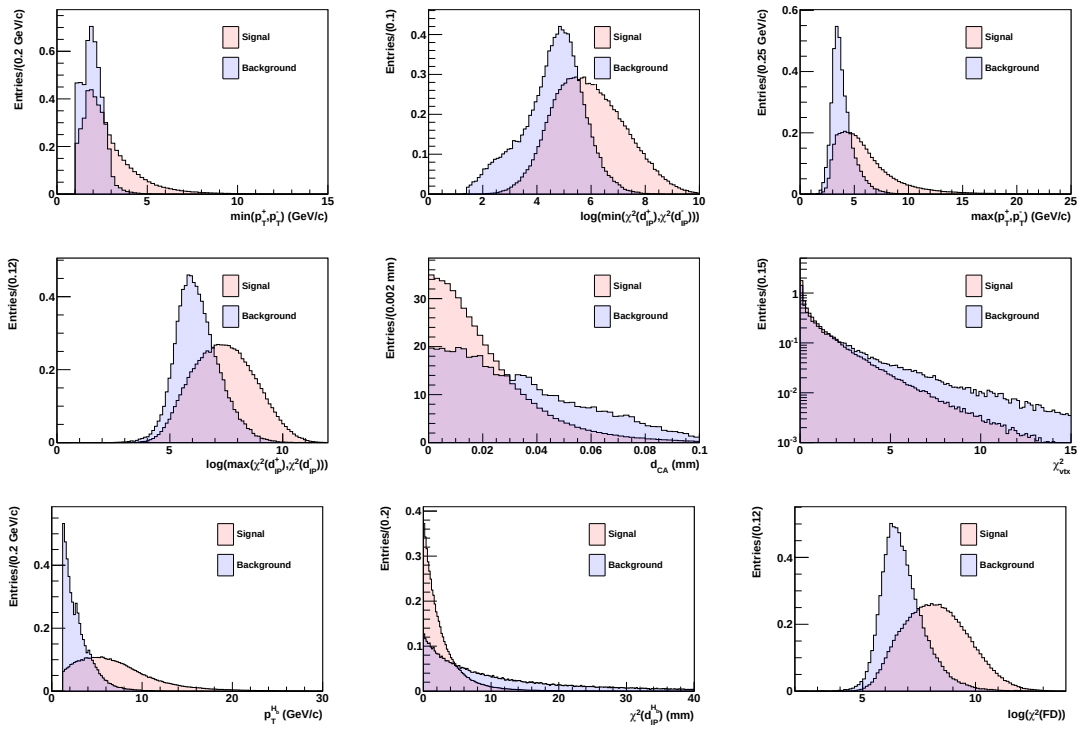

Figure D.6: *Distributions of the variables used in the training of the BDT algorithms for (red histogram) $B^0 \to \pi^+\pi^-$ decays and (blue histogram) high invariant-mass sideband events. Only 2012 samples are used to produce the histograms.*

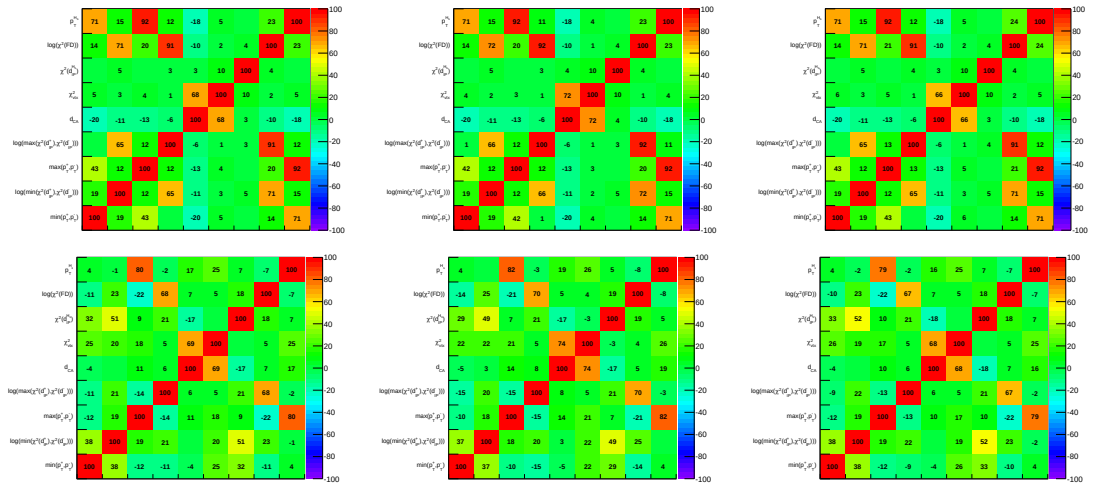

Figure D.7: *Correlations among the variables used to train the BDT algorithms for (top) $B_s^0 \to K^+K^-$ simulated events and (bottom) high invariant-mass sideband. From left to right: the sum of 2011 and 2012 samples is used, only 2011 samples are used, and only 2012 samples are used.*

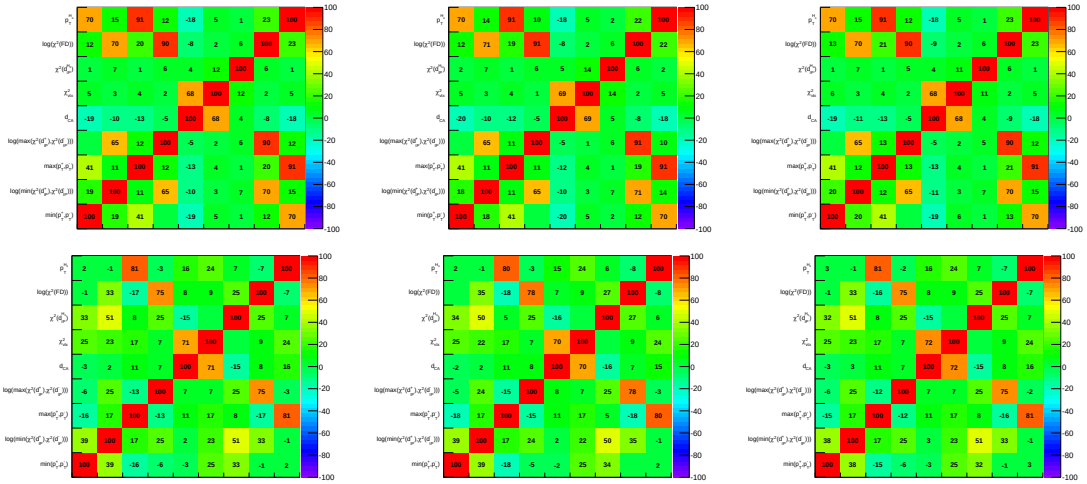

Figure D.8: *Correlations among the variables used to train the BDT algorithms for (top) $B^0 \to \pi^+\pi^-$ simulated events and (bottom) high invariant-mass sideband. From left to right: the sum of 2011 and 2012 samples is used, only 2011 samples are used, and only 2012 samples are used.*

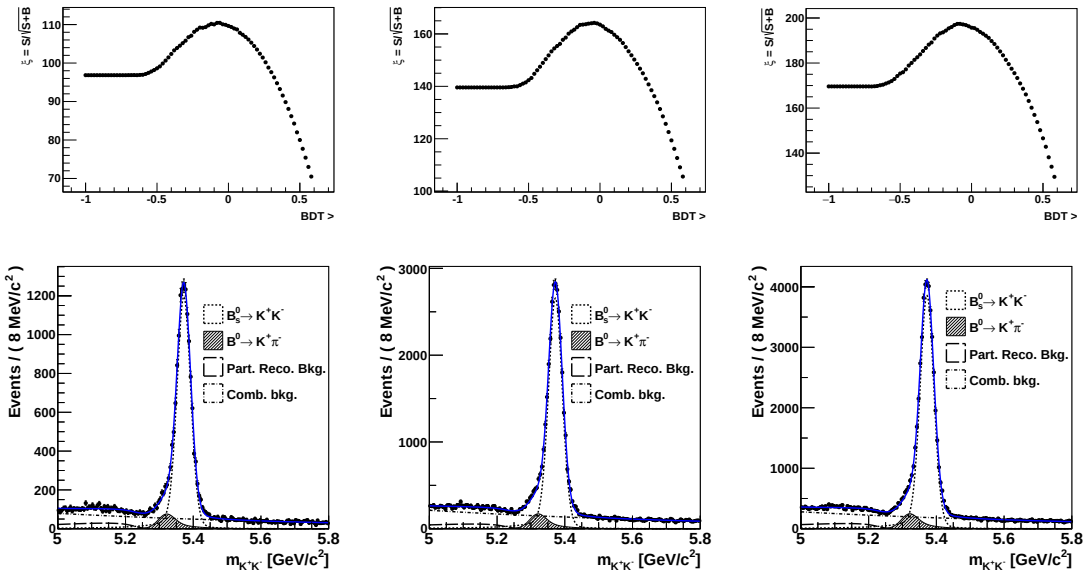

Figure D.9: *Top row: value of the figure of merit $\xi = S/\sqrt{S+B}$ as a function of the requirement on the BDT output corresponding to $BDT_{K^+K^-}$. Bottom row: fits to the K^+K^- invariant-mass distribution used to determine the values of ξ reported in Tab. D.1. From left to right, the result of the optimisation using 2011, 2012 and the total sample are reported.*

observed and also the differences between the two calibrations have similar slopes.

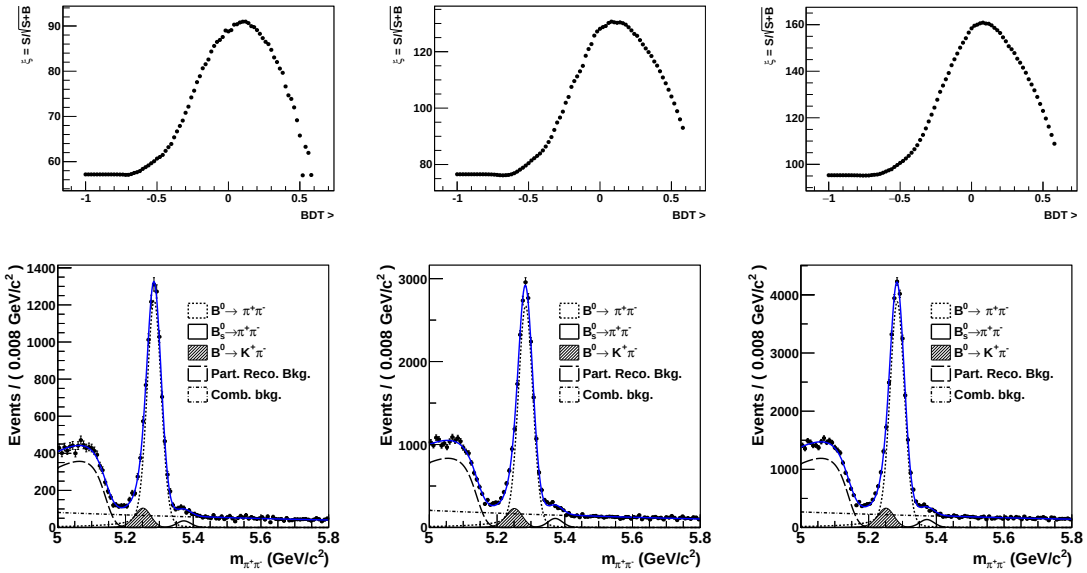

Figure D.10: *Top row: value of the figure of merit $\xi = S/\sqrt{S+B}$ as a function of the requirement on the BDT output corresponding to $BDT_{\pi^+\pi^-}$. Bottom row: fits to the $\pi^+\pi^-$ invariant-mass distribution used to determine the values of ξ reported in Tab. D.1. From left to right, the result of the optimisation using 2011, 2012 and the total sample are reported.*

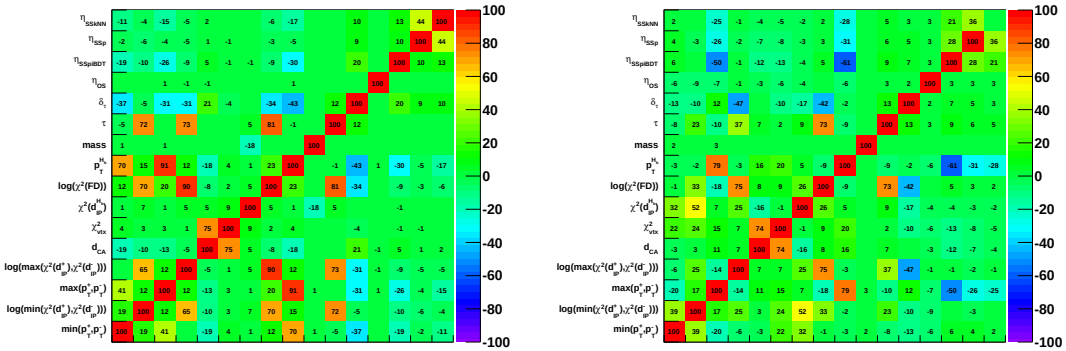

Figure D.11: *Correlations among the variables used to train the BDT algorithms for (left) $B^0 \to \pi^+\pi^-$ simulated events and (right) high invariant-mass sideband. In addition to the variables used to train the BDT, also the variables used in the final fit to determine the CP-violating observables are reported.*

Table D.3: *Calibration parameters for the* SS*k*NN *response in different kinematic regions, using the reconstructed decay-time in the fit and including a per-event decay-time resolution.*

$p_{\rm T}^B$ [GeV/c]	Category			Event		
	p_0 [fs]	p_1	$\rho(p0,p1)$	p_0 [fs]	p_1	$\rho(p0,p1)$
–	0.4427 ± 0.0018	0.969 ± 0.019	0.266	0.4427 ± 0.0019	0.964 ± 0.020	0.242
< 9	0.4460 ± 0.0022	0.914 ± 0.031	0.119	0.4460 ± 0.0022	0.921 ± 0.031	0.112
> 9	0.4376 ± 0.0030	0.976 ± 0.024	0.416	0.4376 ± 0.0030	0.978 ± 0.027	0.385

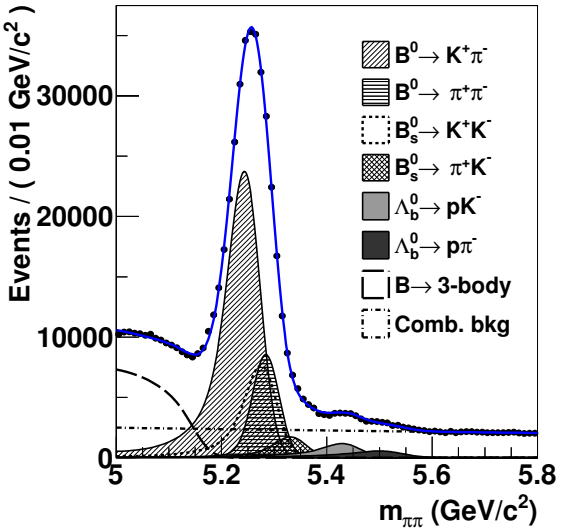

Figure D.12: *Distribution of invariant mass under the $\pi^+\pi^-$ final state hypothesis for the events surviving the BDT requirements corresponding to $BDT_{\pi^+\pi^-}$. The result of the best fit used to determine the weights for charmless two-body b-hadron decays is overlaid to the data points.*

Table D.4: *Calibration parameters for the* SSkNN *response in different kinematic regions using a data sample of $B^0_s \to D^-_s\pi^+$ decays.*

$p_{\rm T}^B$ [GeV/c]	Category			Event		
	p_0 [fs]	p_1	$\rho(p0,p1)$	p_0 [fs]	p_1	$\rho(p0,p1)$
–	0.4401 ± 0.0047	1.028 ± 0.071	0.087	0.4402 ± 0.0047	1.028 ± 0.069	0.112
< 9	0.4451 ± 0.0075	0.664 ± 0.144	-0.087	0.4450 ± 0.0075	0.713 ± 0.138	-0.048
> 9	0.4384 ± 0.0061	1.154 ± 0.082	0.170	0.4386 ± 0.0061	1.141 ± 0.080	0.218

D.4.2 SSkNN tagging calibration in $p_{\rm T}^B$ bins in data

A final cross-check is done to verify that what observed in the simulated sample has a true correspondence in the real data, using a $B^0_s \to D^-_s\pi^+$ decays sample. The kinematic splitting and the calibration fit are performed following the same procedure described in the previous section. In Tab. D.4 the fit results are reported while the linear plots and the differences between the calibrations in the two kinematic regions are shown in Figs. D.17 and D.18.

The same dependence observed in the simulation, regarding a trend in the SSkNN calibration while increasing the B transverse momentum is observed also in data. However in this case the effect seems to be more significant than what found in the simulated sample.

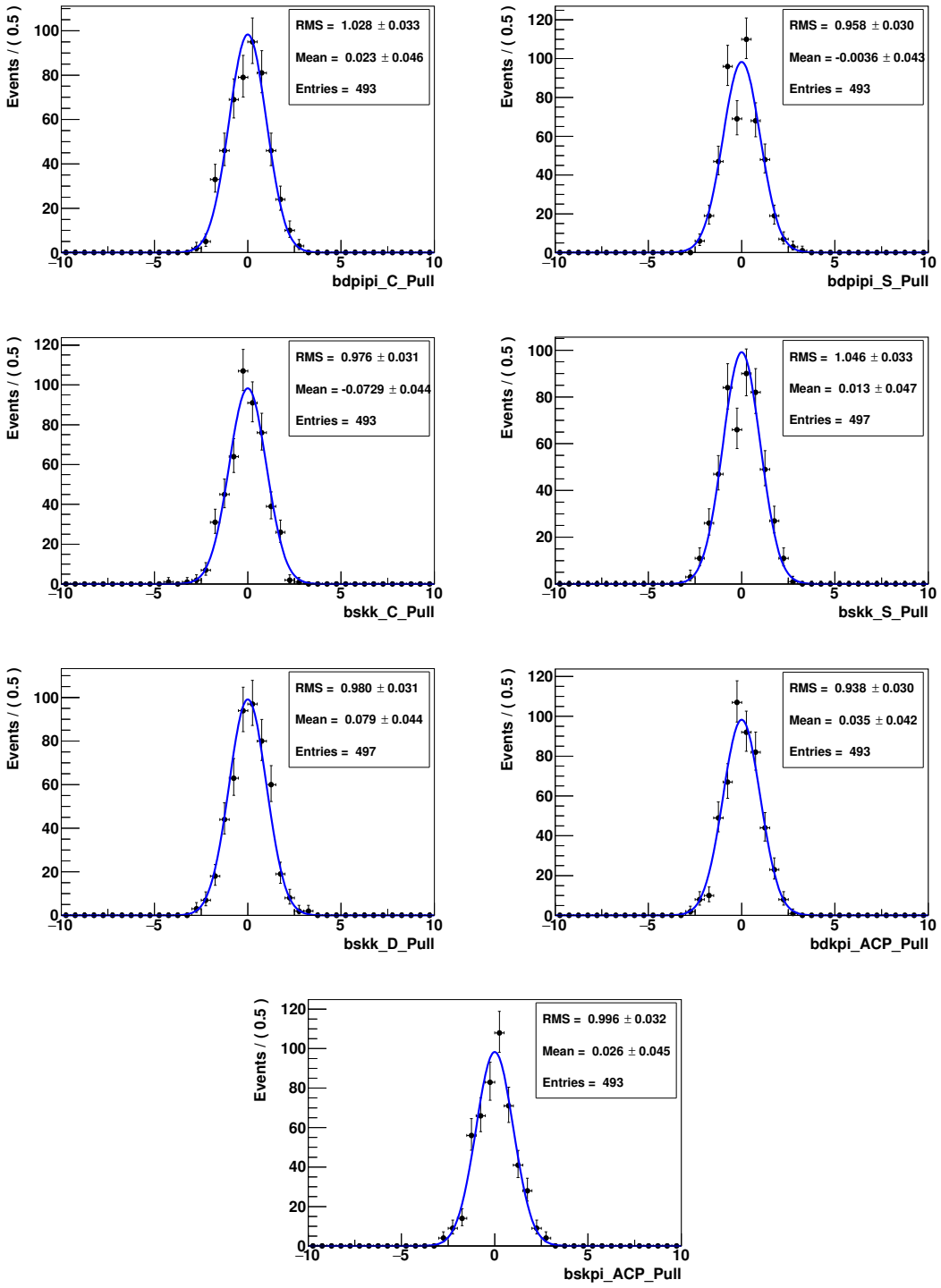

Figure D.13: *Pull distributions for (top left) $C_{\pi^+\pi^-}$, (top right) $S_{\pi^+\pi^-}$, (middle left) $C_{K^+K^-}$, (middle right) $S_{K^+K^-}$, (bottom left) $A^{\Delta\Gamma}_{K^+K^-}$, (bottom right) $A_{CP}(B^0 \to K^+\pi^-)$ and (bottom) $A_{CP}(B^0_s \to \pi^+K^-)$.*

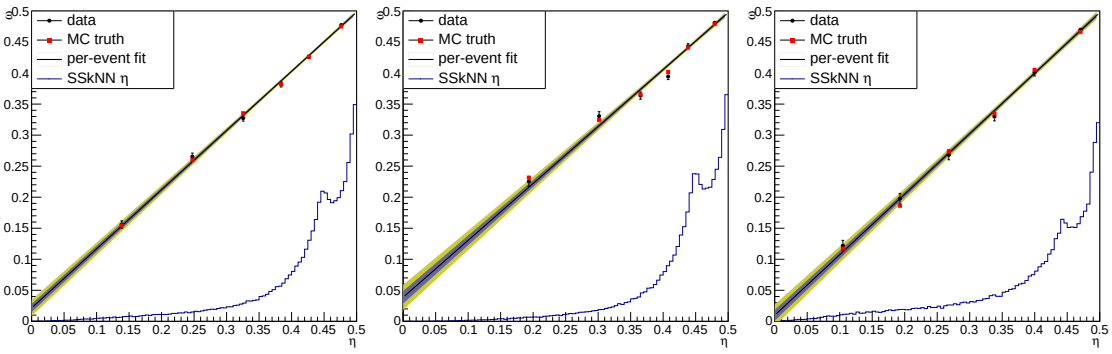

Figure D.14: *Calibration plots for the* SSkNN *tagger in different kinematic regions: (left) whole sample, (center) sub-sample with* $p_{\mathrm{T}}^{B} < 9\,\mathrm{GeV}/c$ *and (right) sub-sample with* $p_{\mathrm{T}}^{B} > 9\,\mathrm{GeV}/c$*. The* ω *values estimated from the per-event fit using the true decay-time are reported in black, while the true mistag obtained from the MC truth is drawn in red. The two bands in blue and in yellow represent the 66% and 95% of confidence level. The* SSkNN η *distribution is also shown.*

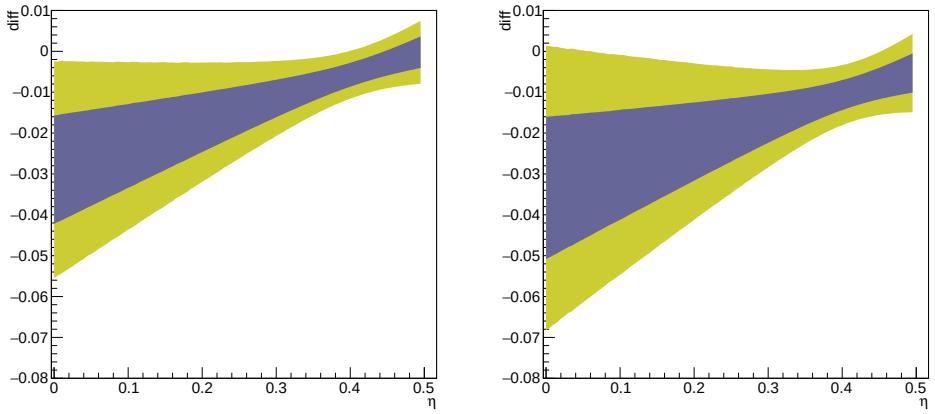

Figure D.15: *Differences between the calibration functions in the two kinematic regions,* $p_{\mathrm{T}}^{B} < 9\,\mathrm{GeV}/c$ *and* $p_{\mathrm{T}}^{B} > 9\,\mathrm{GeV}/c$*, using (left) the true decay-time and (right) the reconstructed decay-time in the fit.*

D.4.3 Final SS tagging calibrations

The SS taggers are used in the final fit to reduce the statistical uncertainties on the *CP*-violating observables. Indeed, the combination of the SSπBDT and SSp taggers can provide an additional 1.17% to the tagging power obtained from the OS tagger. The SSkNN can add a further 1.26% to the whole tagging power as well. In order to use them in a proper way, they need to be calibrated on the two-body B-decay sample, as described in the previous sections. The parameters used to calibrate the SS taggers are summarized in Tab. D.5. The response of the SScomb tagger is calibrated directly during the simultaneous fit, exploiting the $B^0 \to K^+\pi^-$ decay, as well as the OS tagger.

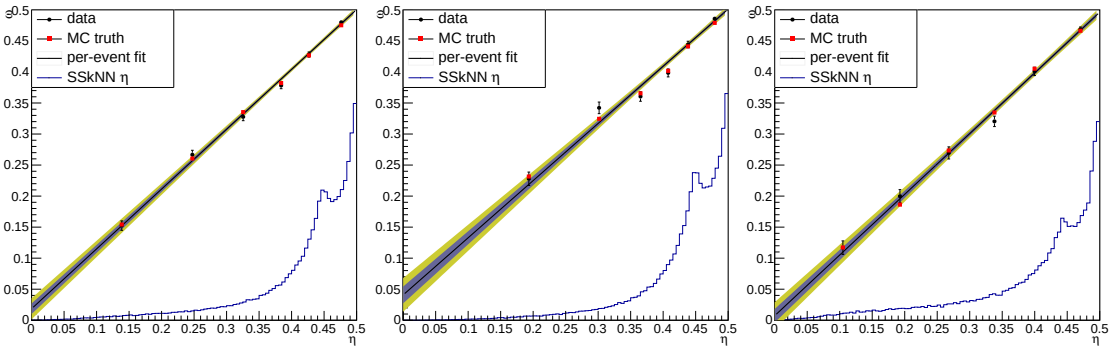

Figure D.16: *Calibration plots for* SSkNN *tagger in different kinematic regions: (left) whole sample, (center) sub-sample with* $p_{\mathrm{T}}^B < 9\,\mathrm{GeV}/c$ *and (right) sub-sample with* $p_{\mathrm{T}}^B > 9\,\mathrm{GeV}/c$*. The* ω *values estimated from the per-event fit using the reconstructed decay-time are reported in black, while the true mistag obtained from the Monte Carlo truth information is drawn in red. The two bands in blue and in yellow represent the 66% and 95% of confidence level. The* SSkNN η *distribution is also shown.*

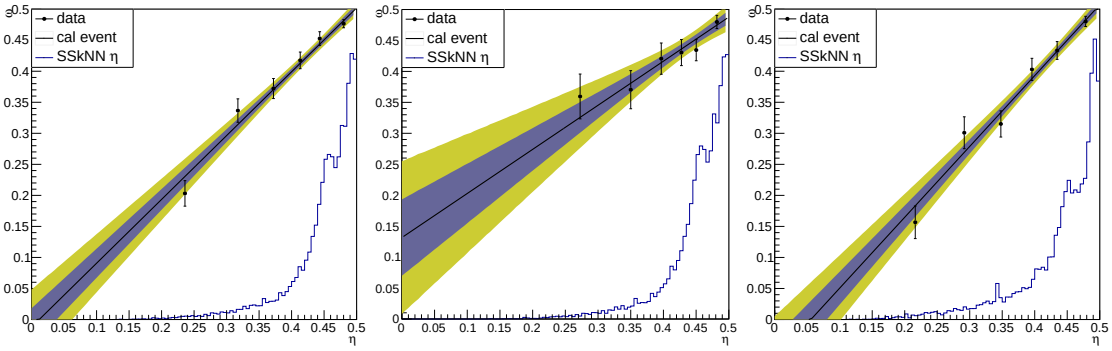

Figure D.17: *Calibration plots for the* SSkNN *tagger using the* $B_s^0 \to D_s^-\pi^+$ *data sample. Different kinematic regions are shown: (left) whole sample, (center) sub-sample with* $p_{\mathrm{T}}^B < 9\,\mathrm{GeV}/c$ *and (right) sub-sample with* $p_{\mathrm{T}}^B > 9\,\mathrm{GeV}/c$*. The two bands in blue and in yellow represent the 66% and 95% of confidence level. The* SSkNN η *distribution is also shown.*

Table D.5: *Calibration parameters for the SS taggers.*

Tagger	p_0 [fs]	p_1	$\langle\eta\rangle$
SSπBDT	0.4529 ± 0.0031	0.939 ± 0.084	0.4565
SSp	0.4668 ± 0.0038	0.714 ± 0.105	0.4664
SSkNN	0.4577 ± 0.0054	0.725 ± 0.092	0.44

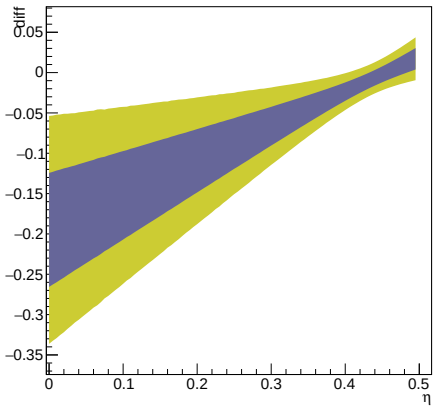

Figure D.18: *Differences between the calibrations in the two kinematic regions,* $p_{\mathrm{T}}^{B} < 9\,\mathrm{GeV}/c$ *and* $p_{\mathrm{T}}^{B} > 9\,\mathrm{GeV}/c$*, using a data sample of* $B_s^0 \to D_s^- \pi^+$ *decays.*

Bibliography

[1] C. S. Wu *et al.*, *Experimental test of parity conservation in beta decay*, Phys. Rev. **105** (1957) 1413.

[2] M. Goldhaber, L. Grodzins, and A. W. Sunyar, *Helicity of neutrinos*, Phys. Rev. **109** (1958) 1015.

[3] J. H. Christenson, J. W. Cronin, V. L. Fitch, and R. Turlay, *Evidence for the* 2π *decay of the* K_2^0 *meson*, Phys. Rev. Lett. **13** (1964) 138.

[4] S. L. Glashow, J. Iliopoulos, and L. Maiani, *Weak interactions with lepton-hadron symmetry*, Phys. Rev. D **2** (1970) 1285.

[5] J. J. Aubert *et al.*, *Experimental observation of a heavy particle* J, Phys. Rev. Lett. **33** (1974) 1404.

[6] J. E. Augustin *et al.*, *Discovery of a narrow resonance in* e^+e^- *annihilation*, Phys. Rev. Lett. **33** (1974) 1406, [Adv. Exp. Phys.5,141(1976)].

[7] M. Kobayashi and T. Maskawa, *CP violation in the renormalizable theory of weak interaction*, Prog. Theor. Phys. **49** (1973) 652.

[8] S. W. Herb *et al.*, *Observation of a dimuon resonance at 9.5-GeV in 400-GeV proton-nucleus collisions*, Phys. Rev. Lett. **39** (1977) 252.

[9] CDF collaboration, F. Abe *et al.*, *Observation of top quark production in* $\overline{p}p$ *collisions with the collider detector at fermilab*, Phys. Rev. Lett. **74** (1995) 2626.

[10] D0 collaboration, S. Abachi *et al.*, *Observation of the top quark*, Phys. Rev. Lett. **74** (1995) 2632.

[11] ARGUS collaboration, H. Albrecht *et al.*, *Observation of* $B^0 - \overline{B}^0$ *Mixing*, Phys. Lett. **B192** (1987) 245.

[12] CDF collaboration, A. Abulencia *et al.*, *Observation of $B_s^0 - \overline{B}_s^0$ oscillations*, Phys. Rev. Lett. **97** (2006) 242003.

[13] LHCb collaboration, R. Aaij *et al.*, *Observation of $D^0 - \overline{D}^0$ oscillations*, Phys. Rev. Lett. **110** (2013) 101802.

[14] BaBar collaboration, B. Aubert *et al.*, *Observation of CP violation in the B^0 meson system*, Phys. Rev. Lett. **87** (2001) 091801.

[15] Belle collaboration, K. Abe *et al.*, *Observation of large CP violation in the neutral B meson system*, Phys. Rev. Lett. **87** (2001) 091802.

[16] LHCb collaboration, R. Aaij *et al.*, *First observation of CP violation in the decays of B_s^0 mesons*, Phys. Rev. Lett. **110** (2013) 221601.

[17] Particle Data Group, C. Patrignani *et al.*, *Review of particle physics*, Chin. Phys. **C40** (2016) 100001.

[18] L. Wolfenstein, *Parametrization of the Kobayashi-Maskawa matrix*, Phys. Rev. Lett. **51** (1983) 1945.

[19] UTfit collaboration, M. Bona *et al.*, *http://www.utfit.org/*, 2017.

[20] R. Fleischer, *B physics and CP violation*, Lect. Notes Phys. **647** (2004) 42, arXiv:hep-ph/0210323.

[21] G. Buchalla, A. J. Buras, and M. E. Lautenbacher, *Weak decays beyond leading logarithms*, Rev. Mod. Phys. **68** (1996) 1125, arXiv:hep-ph/9512380.

[22] BaBar collaboration, J. P. Lees *et al.*, *Measurement of CP asymmetries and branching fractions in charmless two-body B-meson decays to pions and kaons*, Phys. Rev. **D87** (2013) 052009, arXiv:1206.3525.

[23] Belle collaboration, I. Adachi *et al.*, *Measurement of the CP violation parameters in $B^0 \to \pi^+\pi^-$ decays*, Phys. Rev. **D88** (2013) 092003, arXiv:1302.0551.

[24] LHCb collaboration, R. Aaij *et al.*, *First measurement of time-dependent CP violation in $B_s^0 \to K^+K^-$ decays*, JHEP **10** (2013) 183, arXiv:1308.1428.

[25] Belle collaboration, Y.-T. Duh *et al.*, *Measurements of branching fractions and direct CP asymmetries for $B \to K\pi$, $B \to \pi\pi$ and $B \to KK$ decays*, Phys. Rev. **D87** (2013) 031103, arXiv:1210.1348.

[26] CDF collaboration, T. A. Aaltonen *et al.*, *Measurements of direct* CP-violating *asymmetries in charmless decays of bottom baryons*, Phys. Rev. Lett. **113** (2014) 242001, arXiv:1403.5586.

[27] LHCb collaboration, R. Aaij *et al.*, *First observation of CP violation in the decays of B_s^0 mesons*, Phys. Rev. Lett. **110** (2013) 221601, arXiv:1304.6173.

[28] CDF collaboration, T. Aaltonen *et al.*, *Observation of new charmless decays of bottom hadrons*, Phys. Rev. Lett. **103** (2009) 031801, arXiv:0812.4271.

[29] LHCb collaboration, R. Aaij *et al.*, *Observation of the annihilation decay mode $B^0 \to K^+K^-$*, Phys. Rev. Lett. **118** (2017) 081801, arXiv:1610.08288.

[30] Y. K. Hsiao and C. Q. Geng, *Direct CP violation in Λ_b decays*, Phys. Rev. **D91** (2015), no. 11 116007, arXiv:1412.1899.

[31] A. Ali, G. Kramer, and C.-D. Lu, *Experimental tests of factorization in charmless nonleptonic two-body B decays*, Phys. Rev. **D58** (1998) 094009, arXiv:hep-ph/9804363.

[32] C.-D. Lu *et al.*, *Anatomy of the pQCD Approach to the Baryonic Decays $\Lambda_b^0 \to p\pi^-$, pK^-*, Phys. Rev. **D80** (2009) 034011, arXiv:0906.1479.

[33] L. Evans and P. Bryant, *LHC Machine*, JINST **3** (2008) S08001.

[34] LHCb collaboration, A. A. Alves Jr. *et al.*, *The LHCb detector at the LHC*, JINST **3** (2008) S08005.

[35] LHCb collaboration, R. Aaij *et al.*, *Measurement of the b-quark production cross-section in 7 and 13 TeV pp collisions*, Phys. Rev. Lett. **118** (2017) 052002, arXiv:1612.05140.

[36] LHCb collaboration, R. Aaij *et al.*, *Prompt charm production in pp collisions at $\sqrt{s} = 7$ TeV*, Nucl. Phys. **B871** (2013) 1, arXiv:1302.2864.

[37] LHCb collaboration, R. Aaij *et al.*, *Measurements of prompt charm production cross-sections in pp collisions at $\sqrt{s} = 13$ TeV*, JHEP **03** (2016) 159, arXiv:1510.01707, [Erratum: JHEP **05** (2017) 074].

[38] LHCb collaboration, *LHCb VELO TDR: Vertex locator. Technical design report*, CERN-LHCC-2001-011 (2001).

[39] R. Aaij *et al.*, *Performance of the LHCb Vertex Locator*, JINST **9** (2014) 09007, arXiv:1405.7808.

[40] LHCb collaboration, *LHCb: Inner tracker technical design report*, CERN-LHCC-2002-029 (2002).

[41] LHCb collaboration, *LHCb: Outer tracker technical design report*, CERN-LHCC-2001-024 (2001).

[42] LHCb collaboration, *LHCb magnet: Technical design report*, CERN-LHCC-2000-007

(2000).

[43] A. Jaeger *et al.*, *Measurement of the track finding efficiency*, LHCb-PUB-2011-025, CERN-LHCb-PUB-2011-025 (2012).

[44] LHCb collaboration, R. Aaij *et al.*, *Measurement of the track reconstruction efficiency at LHCb*, JINST **10** (2015), no. 02 P02007, arXiv:1408.1251.

[45] LHCb collaboration, *LHCb: RICH technical design report*, CERN-LHCC-2000-037 (2000).

[46] LHCb RICH Group, M. Adinolfi *et al.*, *Performance of the LHCb RICH detector at the LHC*, Eur. Phys. J. **C73** (2013) 2431, arXiv:1211.6759.

[47] LHCb collaboration, *LHCb calorimeters: Technical design report*, CERN-LHCC-2000-036 (2000).

[48] W. R. Leo, *Techniques for nuclear and particle physics experiments: a how to approach*, Ed. Springer (1987) 368 p.

[49] H. Fessler *et al.*, *A scintillator-lead photon calorimeter using optical fiber readout systems*, Nucl. Instrum. Meth. **A240** (1985) 284.

[50] LHCb collaboration, *LHCb muon system technical design report*, CERN-LHCC-2001-010 (2001).

[51] F. Archilli *et al.*, *Performance of the Muon Identification at LHCb*, JINST **8** (2013) P10020, arXiv:1306.0249.

[52] R. Aaij *et al.*, *The LHCb Trigger and its Performance in 2011*, JINST **8** (2013) P04022, arXiv:1211.3055.

[53] M. Chaichian and A. Fridman, *On a possibility for measuring effects of CP violation at pp colliders*, Phys. Lett. **B298** (1993) 218.

[54] E. Norrbin and R. Vogt, *Bottom production asymmetries at the LHC*, arXiv:hep-ph/0003056.

[55] E. Norrbin and T. Sjostrand, *Production and hadronization of heavy quarks*, Eur. Phys. J. **C17** (2000) 137, arXiv:hep-ph/0005110.

[56] LHCb collaboration, R. Aaij *et al.*, *Search for direct CP violation in* $D^0 \to h^-h^+$ *modes using semileptonic* B *decays*, Phys. Lett. **B723** (2013) 33, arXiv:1303.2614.

[57] D0 collaboration, V. M. Abazov *et al.*, *Measurement of direct CP violation parameters in* $B^\pm \to J/\psi K^\pm$ *and* $B^\pm \to J/\psi\pi^\pm$ *decays with 10.4* fb^{-1} *of Tevatron data*, Phys. Rev. Lett. **110** (2013) 241801, arXiv:1304.1655.

[58] Belle collaboration, K. Sakai *et al.*, *Search for CP violating charge asymmetry in $B^\pm \to J/\psi K^\pm$ decays*, Phys. Rev. **D82** (2010) 091104, arXiv:1008.2567.

[59] BaBar collaboration, B. Aubert *et al.*, *Measurement of branching fractions and charge asymmetries for exclusive B decays to charmonium*, Phys. Rev. Lett. **94** (2005) 141801, arXiv:hep-ex/0412062.

[60] LHCb collaboration, R. Aaij *et al.*, *Measurement of the $B^\pm$ production asymmetry and the CP asymmetry in $B^\pm \to J/\psi K^\pm$ decays*, Phys. Rev. **D95** (2017) 052005, arXiv:1701.05501.

[61] LHCb collaboration, R. Aaij *et al.*, *Measurement of the fragmentation fraction ratio f_s/f_d and its dependence on B meson kinematics*, JHEP **04** (2013) 001, arXiv:1301.5286.

[62] LHCb collaboration, R. Aaij *et al.*, *Study of the kinematic dependences of Λ_b^0 production in pp collisions and a measurement of the $\Lambda_b^0 \to \Lambda_c^+\pi^-$ branching fraction*, JHEP **08** (2014) 143, arXiv:1405.6842.

[63] L. Breiman, J. H. Friedman, R. A. Olshen, and C. J. Stone, *Classification and regression trees*, Wadsworth international group, Belmont, California, USA, 1984.

[64] B. P. Roe *et al.*, *Boosted decision trees as an alternative to artificial neural networks for particle identification*, Nucl. Instrum. Meth. **A543** (2005) 577, arXiv:physics/0408124.

[65] A. Carbone *et al.*, *Measurement of time-dependent CP-violating asymmetries in $B^0 \to \pi^+\pi^-$ and $B_s^0 \to K^+K^-$ decays at LHCb*, LHCb-ANA-2013-040. LHCb internal documentation, can be partially made available on request.

[66] K. S. Cranmer, *Kernel estimation in high-energy physics*, Comput. Phys. Commun. **136** (2001) 198, arXiv:hep-ex/0011057.

[67] Heavy Flavor Averaging Group, Y. Amhis *et al.*, *Averages of b-hadron, c-hadron, and τ-lepton properties as of summer 2014*, arXiv:1412.7515, updated results and plots available at http://www.slac.stanford.edu/xorg/hflav/.

[68] LHCb collaboration, R. Aaij *et al.*, *Measurement of CP asymmetry in $D^0 \to K^-K^+$ and $D^0 \to \pi^-\pi^+$ decays*, JHEP **07** (2014) 041, arXiv:1405.2797.

[69] M. Stahl and M. Vesterinen, *Tracking asymmetry measurement with $J/\psi \to \mu^+\mu^-$ decays*, Tech. Rep. LHCb-INT-2015-012. CERN-LHCb-INT-2015-012, CERN, Geneva, Feb, 2016. LHCb internal documentation, can be partially made available on request.

[70] LHCb collaboration, R. Aaij *et al.*, *Study of the kinematic dependences of Λ_b^0 production in pp collisions and a measurement of the $\Lambda_b^0 \to \Lambda_c^+ \pi^-$ branching fraction*, JHEP **08** (2014) 143, arXiv:1405.6842.

[71] G. Corti, T. Latham, and C. Wallace, *Determination of the global position of the VELO*, Tech. Rep. LHCb-INT-2014-013. CERN-LHCb-INT-2014-013, CERN, Geneva, Apr, 2014. LHCb internal documentation, can be partially made available on request.

[72] D. Dossett *et al.*, *Mapping the material in the LHCb vertex locator using secondary hadronic interactions*, Tech. Rep. LHCb-DP paper to be submitted to JINST, in preparation, CERN, Geneva.

[73] M. Ferro-Luzzi, T. Latham, and C. Wallace, *Determination of the aperture of the LHCb VELO RF foil*, Tech. Rep. LHCb-PUB-2014-012. CERN-LHCb-PUB-2014-012, CERN, Geneva, Apr, 2014.

[74] LHCb, *https://twiki.cern.ch/twiki/bin/view/LHCb/DaVinci*, 2017.

[75] G. Dujany and B. Storaci, *Real-time alignment and calibration of the LHCb Detector in Run II*, J. Phys. Conf. Ser. **664** (2015) 082010.

[76] N. L. Johnson, *Systems of frequency curves generated by methods of translation*, Biometrika **36** (1949).

[77] J. H. Christenson, J. W. Cronin, V. L. Fitch, and R. Turlay, *Evidence for the* 2π *decay of the* K_2^0 *meson*, Phys. Rev. Lett. **13** (1964) 138.

[78] BaBar collaboration, B. Aubert *et al.*, *Observation of CP violation in the* B^0 *meson system*, Phys. Rev. Lett. **87** (2001) 091801, arXiv:hep-ex/0107013.

[79] Belle collaboration, K. Abe *et al.*, *Observation of large CP violation in the neutral B meson system*, Phys. Rev. Lett. **87** (2001) 091802, arXiv:hep-ex/0107061.

[80] LHCb collaboration, R. Aaij *et al.*, *Measurement of matter-antimatter differences in beauty baryon decays*, Nature Phys. **13** (2017) 391, arXiv:1609.05216.

[81] LHCb collaboration, R. Aaij *et al.*, *Measurement of* B^0*,* B_s^0*,* B^+ *and* Λ_b^0 *production asymmetries in 7 and 8 TeV proton-proton collisions*, Phys. Lett. **B774** (2017) 139, arXiv:1703.08464.

[82] M. Artuso *et al.*, *Measurement of the CP violating asymmetry* a_{sl}^s, LHCb-ANA-2016-004. LHCb internal documentation, can be partially made available on request.

[83] M. Adinolfi *et al.*, *Performance of the LHCb RICH detector at the LHC*, Eur. Phys. J. **C73** (2013) 2431, arXiv:1211.6759.

[84] A. Carbone *et al.*, *Search for the* $B^0 \to K^+K^-$ *decay with* $\int \mathcal{L}\, dt = 3\ fb^{-1}$, LHCb-ANA-2016-016. LHCb internal documentation, can be partially made available on request.

[85] M. Pivk and F. R. Le Diberder, *sPlot: A statistical tool to unfold data distributions*, Nucl. Instrum. Meth. **A555** (2005) 356, arXiv:physics/0402083.

[86] E. Baracchini and G. Isidori, *Electromagnetic corrections to non-leptonic two-body B and D decays*, Phys. Lett. **B633** (2006) 309.

[87] P. Golonka and Z. Was, *PHOTOS Monte Carlo: A precision tool for QED corrections in Z and W decays*, Eur. Phys. J. **C45** (2006) 97, arXiv:hep-ph/0506026.

[88] A. Carbone *et al.*, *Invariant mass line shape of $B \to PP$ decays at LHCb*, LHCb-PUB-2009-031.

[89] K. S. Cranmer, *Kernel estimation in high-energy physics*, Comput. Phys. Commun. **136** 198.

[90] LHCb collaboration, Aaij, R. and others, *Measurement of b-hadron branching fractions for two-body decays into charmless charged hadrons*, JHEP **10** (2012) 037.

[91] E. M. Gersabeck *et al.*, *Measurement of the time-integrated CP violation in $D^0 \to K^-K^+$ decays using prompt $D^{*\pm} \to D^0(K^-K^+)\pi^\pm$ decays with 3 fb^{-1}*, LHCb-ANA-2016-007. LHCb internal documentation, can be partially made available on request.

[92] CDF collaboration, T. Aaltonen *et al.*, *Measurements of direct cp-violating asymmetries in charmless decays of bottom baryons*, Phys. Rev. Lett. **113** (2014) 242001.

[93] N. Cabibbo, *Unitary Symmetry and Leptonic Decays*, Phys. Rev. Lett. **10** (1963) 531.

[94] R. Fleischer, *New strategies to extract β and γ from $B_d \to \pi^+\pi^-$ and $B_s \to K^+K^-$*, Phys. Lett. **B459** (1999) 306, arXiv:hep-ph/9903456.

[95] M. Gronau and J. L. Rosner, *The role of $B_s \to K\pi$ in determining the weak phase γ*, Phys. Lett. **B482** (2000) 71, arXiv:hep-ph/0003119.

[96] H. J. Lipkin, *Is observed direct CP violation in $B_d \to K^+\pi^-$ due to new physics? Check standard model prediction of equal violation in $B_s \to K^-\pi^+$*, Phys. Lett. **B621** (2005) 126, arXiv:hep-ph/0503022.

[97] R. Fleischer, *$B_{s,d} \to \pi\pi, \pi K, KK$: status and prospects*, Eur. Phys. J. **C52** (2007) 267.

[98] R. Fleischer and R. Kneigjens, *In pursuit of new physics with $B_s^0 \to K^+K^-$*, Eur. Phys. J. **C71** (2011) .

[99] A. Carbone *et al.*, *Measurement of direct CP violation in charmless charged two-body B decays at LHCb using 2010 data*, LHCb-ANA-2011-023. LHCb internal documentation, can be partially made available on request.

[100] A. Carbone *et al.*, *Charmless charged two-body B decays at LHCb with 2011 data*, LHCb-ANA-2011-060. LHCb internal documentation, can be partially made available on request.

[101] A. Carbone *et al.*, *First observation of direct CP violation in $B_s^0 \to \pi^+ K^-$ decays*, LHCb-ANA-2012-055. LHCb internal documentation, can be partially made available on request.

[102] LHCb collaboration, R. Aaij *et al.*, *First evidence of direct CP violation in charmless two-body decays of B_s^0 mesons*, Phys. Rev. Lett. **108** (2012) 201601, arXiv:1202.6251.

[103] LHCb collaboration, R. Aaij *et al.*, *First observation of CP violation in the decays of B_s^0 mesons*, Phys. Rev. Lett. **110** (2013) 221601, arXiv:1304.6173.

[104] A. Carbone *et al.*, *Measurement of the branching fractions of charmless charged two-body decays of bottom hadrons*, LHCb-ANA-2012-019. LHCb internal documentation, can be partially made available on request.

[105] LHCb collaboration, R. Aaij *et al.*, *Measurement of b-hadron branching fractions for two-body decays into charmless charged hadrons*, JHEP **10** (2012) 037, arXiv:1206.2794.

[106] A. Carbone *et al.*, *Search for the $B^0 \to K^+K^-$ decay with $\int \mathcal{L}\, dt = 3\ fb^{-1}$*, LHCb-ANA-2016-016. LHCb internal documentation, can be partially made available on request.

[107] A. Carbone *et al.*, *Measurement of time-dependent CP violation in charmless charged two-body B decays*, LHCb-ANA-2012-020. LHCb internal documentation, can be partially made available on request.

[108] LHCb collaboration, R. Aaij *et al.*, *First measurement of time-dependent CP violation in $B_s^0 \to K^+K^-$ decays*, JHEP **10** (2013) 183, arXiv:1308.1428.

[109] LHCb collaboration, R. Aaij *et al.*, *Determination of γ and $-2\beta_s$ from charmless two-body decays of beauty mesons*, Phys. Lett. **B739** (2015) 1, arXiv:1408.4368.

[110] LHCb collaboration, *Measurement of time-dependent CP violating asymmetries in $B^0 \to \pi^+\pi^-$ and $B_s^0 \to K^+K^-$ decays at LHCb*, LHCb-CONF-2016-018.

[111] A. Puig, *The LHCb trigger in 2011 and 2012*, Tech. Rep. LHCb-PUB-2014-046. CERN-LHCb-PUB-2014-046, CERN, Geneva, Nov, 2014.

[112] A. Hocker *et al.*, *TMVA - Toolkit for Multivariate Data Analysis*, PoS **ACAT** (2007) 040, arXiv:physics/0703039.

[113] Y. Freund and R. E. Schapire, *A decision-theoretic generalization of on-line learning and an application to boosting*, J. Comput. Syst. Sci. **55** (1997) 119.

[114] ARGUS collaboration, H. Albrecht *et al.*, *Measurement of the polarization in the decay $B \to J/\psi K^*$*, Phys. Lett. **B340** (1994) 217.

[115] A. Carbone *et al.*, *Measurement of time-dependent CP-violating asymmetries in $B^0 \to \pi^+\pi^-$ and $B_s^0 \to K^+K^-$ decays at LHCb*, LHCb-ANA-2016-070. LHCb internal documentation, can be partially made available on request.

[116] T. M. Karbach, G. Raven, and M. Schiller, *Decay time integrals in neutral meson mixing and their efficient evaluation*, Tech. Rep. LHCb-INT-2013-043. CERN-LHCb-INT-2013-043, CERN, Geneva, Jul, 2013. LHCb internal documentation, can be partially made available on request.

[117] LHCb, R. Aaij *et al.*, *Opposite-side flavour tagging of B mesons at the LHCb experiment*, Eur. Phys. J. **C72** (2012) 2022, arXiv:1202.4979.

[118] LHCb, R. Aaij *et al.*, *New algorithms for identifying the flavour of* B^0 *mesons using pions and protons*, Eur. Phys. J. **C77** (2017), no. 4 238, arXiv:1610.06019.

[119] LHCb, R. Aaij *et al.*, *A new algorithm for identifying the flavour of B_s^0 mesons at LHCb*, JINST **11** (2016), no. 05 P05010, arXiv:1602.07252.

[120] M. Ciuchini, E. Franco, S. Mishima, and L. Silvestrini, *Testing the Standard Model and searching for new physics with $B^0 \to \pi^+\pi^-$ and $B_s^0 \to K^+K^-$ decays*, JHEP **10** (2012) 029, arXiv:1205.4948.

[121] LHCb, R. Aaij *et al.*, *Determination of γ and -2β_s from charmless two-body decays of beauty mesons*, Phys. Lett. **B741** (2015) 1, arXiv:1408.4368.

[122] LHCb collaboration, R. Aaij *et al.*, *Measurement of B^0, B_s^0, B^+ and Λ_b^0 production asymmetries in 7 and 8 TeV proton-proton collisions*, Phys. Lett. **B774** (2017) 139, arXiv:1703.08464.

[123] LHCb collaboration, R. Aaij *et al.*, *Measurement of b hadron production fractions in 7 TeV pp collisions*, Phys. Rev. **D85** (2012) 032008, arXiv:1111.2357.

[124] Belle collaboration, A. Zupac *et al.*, *Measurement of the branching fraction $\mathcal{B}(\Lambda_c^+ \to pK^-\pi^+)$*, Phys. Rev. Lett. **113** (2014) 042002, arXiv:1312.7826.